CRANFIELD UNIVERSITY

Michael J Taylor

Plasma Propellant Interactions in an Electrothermal-Chemical Gun

ROYAL MILITARY COLLEGE OF SCIENCE

PhD THESIS

CRANFIELD UNIVERSITY

ROYAL MILITARY COLLEGE OF SCIENCE

DEPARTMENT OF ENVIRONMENTAL AND ORDNANCE SYSTEMS

PhD THESIS

Academic Year 2002-2003

Michael J Taylor

Plasma Propellant Interactions in an Electrothermal-Chemical Gun

Supervisor: Prof A Crowley

September 2002

Intellectual Property Department, QinetiQ ltd, Cody Technology Park, Farnborough, Hampshire GU14 0LX

Abstract

This Thesis covers work conducted to understand the mechanisms underpinning the operation of the electrothermal-chemical gun. The initial formation of plasma from electrically exploding wires, through to the development of plasma venting from the capillary and interacting with a densely packed energetic propellant bed is included. The prime purpose of the work has been the development and validation of computer codes designed for the predictive modelling of the electrothermal-chemical (ETC) gun.

Two main discussions in this Thesis are:

- a proposed electrically insulating vapour barrier located around condensed exploding conductors and

- the deposition of metallic vapour resulting in a high energy flux to the surface of propellant, leading to propellant ignition.

The vapour barrier hypothesis is important in a number of fields where the passage of current through condensed material or through plasma is significant. The importance may arise from the need to disrupt the fragments by applying strong magnetic fields (as in the disruption of metallic shaped charge jets); in the requirement to generate a metallic vapour efficiently from electrically exploding wires (as per ETC ignition

systems); or in the necessity to re-use the condensed material after a discharge (as with lightning divertor strips).

The ignition by metallic vapour deposition hypothesis relies on the transfer of latent heat during condensation. It is important for the efficient transfer of energy from an exploded wire (or other such metallic vapour generating device) to the surface of energetic material. This flux is obtained far more efficiently through condensation than from radiative energy transfer, because the energy required to evaporate copper is far less than that required to heat it to temperatures at which significant radiative flux would be emitted.

Introduction

The work contained in this Thesis was supported entirely by the UK Ministry of Defence (MoD) through the electrothermal-chemical (ETC) gun project 06/08/02/008/2000. This Thesis is an unclassified document; some aspects of the Author's work cannot be discussed here, however. Nonetheless, it is one of the stated aims of the MoD (Corporate Research) that scientific work conducted under its jurisdiction should be disseminated widely. Therefore, as much detailed information as possible on the work conducted by the Author has been included in this Thesis.

The Author's employer is QinetiQ, which was formerly part of the Defence Evaluation and Research Agency (DERA) until July 2001, when it was divided into Defence Systems Technology Laboratories (DSTL) and QinetiQ. Hence, some of the Author's work is referenced as being performed within DERA, and other work for QinetiQ.

Work discussed within this Thesis is still very much in progress. The subject matter is associated with defence issues, specifically large calibre artillery guns and the application of electrical energy to such launch systems. Behind the work was (and still is) a drive to understand the entire ETC process from initial electrical explosion of a plasma initiation wire, through the interaction of plasma with energetic material for ignition and combustion control, to the continued control of projectile acceleration in the gun tube once all propellant has burnt.

The work is mainly experimental, but paying due regard to underlying theory and computer simulation for corroboration of hypotheses formulated as a result of experimental observation. The more fundamental aspects of plasma formation and plasma/propellant interaction are covered here, although the work has had to remain within the limits of practical application - i.e. the requirement to progress towards a fieldable ETC gun system.

This Thesis covers a time-span of around four years, and is mainly concerned with the contribution made by the Author.

The structure of the Thesis consists of chapters that, although reasonably independent from one another, do run in a linear manner. The first chapter discusses the concept of artillery guns, briefly exploring the history and recent developments in electric guns in the context of today's armed forces – bearing in mind that the Author is neither an historian nor a gunner. The second chapter then outlines the benefits of the ETC gun concept and describes some plasma generator designs. The third chapter briefly describes the computer simulation models used to further the progress of ETC fundamental work, and in more detail the capillary plasma generator (CPG) model, EDENET, and its successor, EDEN-IB. The fourth chapter then explores the work conducted by the Author to improve the understanding of the operation of plasma generators and thus improve the predictive nature of EDENET. This part of the work concentrates on the electrical explosion

of metallic conductors and energy transfer processes occurring within CPGs. In particular, it seeks to explain the diversion of electrical current around condensed fragments of conductor and describes the Author's hypothesis that this effect is due to thermal boundary layers of poorly conducting metallic vapour at the condensed material/plasma interface. The fifth chapter goes on to describe attempts by the Author to measure the energy partition associated with the plasma plume that vents from a CPG. Chapter 6 details the energy transfer processes from such expanding plasma plumes to their surroundings, as well as some of the other properties of the plume plasma. Chapter 7 describes the energy transfer processes to energetic gun propellant under standard temperature and pressure (STP) conditions. In particular, this chapter discusses the mechanisms responsible for the ignition of the energetic material. Chapter 8 summarises work by other groups in this area, and details small-scale work performed to test the Author's hypothesis that ignition is primarily the result of latent heat transfer due to metallic vapour deposition, rather than radiative energy transfer. Finally, Chapter 9 discusses the application of the ignition theories to large calibre chambers under realistic loading conditions. References for individual chapters are given at the end of that chapter.

A brief summary and two appendixes are included at the end of the Thesis. Appendix A discusses the Author's contribution to the spectroscopic metrology of ETC plasma propellant interactions, detailing data acquisition and calibration techniques new to the field of

ETC research. Appendix B provides details of photographic capture and analytical techniques used on digital images.

Notation

A	Transition probability that a particular decay will occur
A	Area of the projectile base
a	Least squares regression line intercept coefficient
b	Least squares regression line slope coefficient
c	Speed of light in a vacuum
C	Constant associated with the Boltzmann's Plot method of temperature determination from a spectral line
c	Specific heat
c_l	Specific heat capacity of liquid
C_p	Constant pressure specific heat
c_s	Specific heat capacity of solid
C_v	Constant volume specific heat
d_c	Diameter of condensed copper fragment
d_p	Diameter of copper plasma column
e	Electronic charge
E	Young's modulus
E_s	Total work done during expansion
E_u	Energy of the upper level (in electron volts)
F	Propellant force constant
f	Ultranac camera geometrical calibration factor
G	Spectral radiant energy collected from heated graphite sample during calibration process
g	Gravitational field strength
g_u	Statistical weight of the upper energy level of the electron decay orbit
h	Planck's constant
h	Heat transfer coefficient

I	Spectral line intensity
I	Transmitted radiation flux density
k	Boltzmann's constant
$k\ (\lambda)$	Spectral transmittance
K_L	Thermal conductivity
k_{NPL}	Constant associated with the collection parameters of NPL's calibration lamp irradiance measurement
l	Horizontal slant length of frustum of a cone
ℓ	Length of propellant cord
l_c	Length of condensed copper fragment
L_m	Specific latent heat of melting
l_p	Length of copper plasma column
L_v	Specific latent heat of vaporisation
M	Total charge mass
m_{Cu}	Mass per unit area of condensed copper deposit
m_p	Projectile mass
m_x	Mass of heated propellant to a depth x
n	Number of observations
n_e	Free electron number density
P	Chamber pressure (in megapascals) at time t
p	Number of pixels in a given length of digital image
$P(s)$	Projectile base pressure
P_{max}	Peak working pressure
P_s	Projectile base pressure upon exit of shot
$P_T(s)$	Theoretical maximum projectile base pressure
Q_c	Energy liberated within a gun

Q_0	Total flux transferred
R	Major radii of frustum of a cone
R	Correlation coefficient
R	Inverse of the spectrograph detector relative spectral response
R	Radius of propellant cord
r	Residual standard deviation
r	Radius of unheated propellant cord
r	Minor radii of frustum of a cone
r'_{in}	Final capillary inner radius (after compression)
r_{in}	Initial capillary inner radius
r_{out}	Capillary outer radius
s	Projectile shot travel
S	Burning surface area at time t
s	Sample standard deviation
S_P	Standard deviation in the abscissa values
S_ε	Standard deviation in the ordinate values
t	Time
t	Thickness of thermal metallic vapour boundary layer
t	Value from statistical t-table (quoted with a 95% confidence interval unless stated otherwise)
T_c	Temperature of condensed copper
t_g	Known exposure time of the graphite acquisition
T_p	Temperature of copper plasma
T_s	Surface temperature
T_{sat}	Saturation temperature
T_v	Temperature of copper vapour
t_W	Known exposure time of the tungsten irradiance lamp acquisition

T_∞	Bulk temperature
V	Volume
V_0	Initial volume
$V_0\,(t)$	Free volume of the chamber at time t
V_T	Volume at temperature T
W_c	Spectral radiant energy collected from the tungsten irradiance lamp
X	Upper energy level value
x	Transparent sample thickness
x_{Cu}	Thickness of copper vapour deposit
x_p	Heated skin depth
$\bar{x}$	Sample mean
Z	Ion charge number
Z_σ	Corrected value of the ionisation Z allowing for an increase in resistivity due to electron-electron collisions
ΔE	Difference between the upper and lower energy levels of the electronic transition from which an emitted photon originates
Δ_r	Capillary plasma transition region thickness
E	Total energy radiated from an entire body
Φ	Radiant flux density or radiant power density
Φ_B	Blackbody radiant flux density
Φ_n	Radiant flux density incident on slice *n*
Φ_{n-1}	Radiant flux density transmitted from slice *n-1*
Λ	Fraction of emitted light collected by the spectroscope objective fibre optic from the solid angle of 2π
Λ_c	Coulomb logarithm
Λ_w	Fraction of emitted light from the tungsten irradiance lamp collected by the monochromator

Λ_W	Fraction of emitted light collected by the monochromator from the solid angle of 2π
T	Thermodynamic temperature
T_1	Initial temperature
T_2	Final temperature
T_b	Brightness (or blackbody) temperature
T_c	Colour temperature
T_e	Electron temperature in electronvolts
T_γ	Capillary plasma core temperature
α	Absorption coefficient
α	Burn rate pressure index of the propellant
α_L	Linear expansion coefficient of liquid
α_S	Linear expansion coefficient of solid
β	Burn-rate coefficient of the propellant
ε	Radiated energy density
ε	Discharged electrical energy
$\varepsilon(\lambda, T)$	Emissivity
ε'	Frequency and temperature independent emissivity
ε_0	Permittivity of free space
ε_g	Spectral emissivity of graphite
ε_t	Threshold energy value for radiation damage
ϕ	Spectral radiant flux density or spectral power density
ϕ_0	Measured incident spectral radiant flux density
ϕ_B	Blackbody spectral radiant flux density
ϕ_g	Spectral radiant flux density of heated graphite sample during calibration process

ϕ_{NPL}	Spectral radiant flux density of calibration lamp as measured by National Physical Laboratories (NPL)
ϕ_T	Transmitted spectral radiant flux density
ϕ_W	Spectral radiant flux density of tungsten irradiance lamp
η	Compression
η_b	Percentage ballistic efficiency
η_p	Piezometric efficiency
η_d	Gun design efficiency
κ_r	Radiative conductivity of the capillary plasma transition zone
λ	Wavelength of the electromagnetic energy
λ	Thermal conductivity
λ_0	Wavelength at which transmittance goes to zero
λ_r	Rosseland mean free path for photons
μ_L	Viscosity
ν	Frequency
v_m	Projectile muzzle velocity
θ	Thermodynamic temperature
ρ	Density
ρ_{Cu}	Density of copper
σ	Stefan-Boltzmann constant
σ	Poisson's ratio
σ_e	Electrical conductivity
τ	Duration
τ	Optical depth

Abbreviation

1.5D	1.5 dimensional
1D	One-dimensional
2D	Two-dimensional
ARC	Acton research corporation
AWE	Atomic weapons establishment
CBPFN	Capacitor-based pulse forming networks
CCD	Charge-coupled device
CI	Current injection
CPG	Capillary plasma generator
DDE	Direct data exchange
DERA	Defence Evaluation and Research Agency
DSTL	Defence systems technology laboratories
EGGR	Enhanced gas generation rate
EGGRDED	Enhanced gas generation rate during electrical discharge
EM	Electromagnetic
EMP	Electromagnetic pulse
EOS	Equation of state
ET	Electrothermal
ETC	Electrothermal-chemical
FOOB	Fire out of battery
GP	Gunpowder
HMX	1,3,5,7-tetranitro-1,3,5,7-tetroazacyclo-octane
IB	Internal ballistics
ICPAES	Inductively coupled plasma atomic emission spectrometer
ICT	Fraunhofer-Institut für Chemische Technologien
ISL	Institute of Saint Louis

Abbreviation

KE	Kinetic-energy
LCR	Inductance, capacitance and resistance
LOVA	Low vulnerability ammunition
LP	Liquid propellant
LTE	Local thermal equilibrium
met	Meteorological conditions
MHD	Magnetohydrodynamic
MoD	Ministry of Defence
MSTV	Medium scale test vessel
MV	Muzzle velocity
NC	Nitrocellulose
NG	Nitroglycerine
NPL	National physical laboratory
PEDEGGR	Post electrical discharge enhanced gas generation rate
PPS	Pulsed power supply
RDX	1,3,5-trinitro-1,3,5-triazacyclohexane
SEM	Scanning electron microscopy
SEM-EDX	Scanning electron microscope with energy dispersive x-ray microanalysis
SHC	Specific heat capacity
SPLP	Solid propellant/liquid propellant
STP	Standard temperature and pressure
TZN	Technologiezentrum nord
UPCS	Unimodular propellant charge system
UV	Universal vessel
w/w	Amount weight by weight
Z	Ion charge number

Contents

Chapter 1 – Guns

1 Introduction

1.1 Definition of a gun

1.1.1 A gun can be described as a mechanical device for projecting a mass (known as the projectile, round or shot) over some distance. Guns are *transducers* which change potential energy (conventionally chemical) to kinetic with associated system losses such as heat, light and sound.

1.1.2 A strict definition of a gun is hard to achieve, as the functionality and physics of the gun are shared with other devices. For example internal combustion engines, jets and rockets could all fall under the above definition. However, for the purposes of this work, a gun is defined here as a transducer device designed to transfer stored energy to a projectile within a short time-scale (i.e. tens of milliseconds) before the projectile leaves the device. Energy transfers to the projectile after it leaves the gun would then be considered separately from the gun.

1.2 Generic gun design

1.2.1 Gun systems can have very different designs with little in common. Early systems for projecting a mass would have involved throwing or launching by hand, e.g. the javelin. Less basic but still primitive would have been the semi-mechanical bow and arrow and also the catapult. The introduction of gunpowder from China by Dutch sailors in the early 13th century permitted a design identifiable with a modern-day gun. Gunpowder is thought to have been invented by Chinese alchemists seeking an elixir for immortality. They began to recognise the

characteristics of saltpetre (potassium nitrate) and sulphur, two ingredients essential for gunpowder. Some historians date the invention of gunpowder to 850 AD when a Taoist book warned of three specific elixir formulae too dangerous for experimentation.

1.2.2 Basic understanding of the science of projectiles (ballistics) and guns (internal ballistics) allowed gun design to improve. Over the centuries, extension of the gun barrel, obturation (sealing of pressurised gases) and rear breech designs allowed the gun to be loaded and fired more efficiently. Such guns have been used extensively by the British military for several centuries. At the rear of the gun is the breech (a gas sealed door) which opens into a chamber, the front end of which leads into a cylindrical bore tube (the gun tube or barrel). A projectile can be loaded into the gun through the open breech and rammed into the barrel. A solid chemical 'propelling charge' (the propellant) is inserted into the chamber via the breech, which is then closed. The propellant is ignited by some means and burns rapidly (in tens of milliseconds) with the hot combustion gases pressurising the chamber. During the burning process, at some given (shot start) pressure, the projectile starts to accelerate up the barrel and exits from the gun at the barrel muzzle. The propellant needs to have burnt completely before the projectile exits if the gun is to operate efficiently. The velocity with which the projectile exits the barrel is known as the muzzle velocity (MV). More recent technological advances have resulted in new concepts to emerge, such as electric guns. Here, electrical energy may be used

alone or in conjunction with generic chemical energy based gun either to ignite the charge and/or to improve the gun efficiency by controlling the propellant gas generation rate.

1.3 Uses of guns

1.3.1 Guns are frequently associated with maiming or killing but can have other purposes. Even large calibre guns used in military engagements are not always used simply to harm, but can be used in bombardment to induce attrition, undermining the enemy's cohesion or causing an enemy to surrender with minimal loss of life, as well as being used to deploy flares, smoke etc. A political requirement of modern warfare is to increase lethality to a target at minimal cost in terms of collateral damage to civilian life and property and to reduce burdens on military resources.

1.3.2 Guns can be broadly categorised into two groups: guns for direct battlefield engagement (direct fire) or for indirect battlefield engagement (indirect fire). Direct fire (small-arms and large calibre tank) guns engage targets they can directly see, whereas indirect fire (artillery) guns engage targets that cannot be seen directly by the firer but the location is known from observation by a third party. Design criteria differ for the two categories. The basic requirements for direct fire guns are high projectile energy and accuracy, whilst indirect fire guns have the added requirement for muzzle velocity reproducibility (for consistency of projectile shot fall). A few percent muzzle velocity

variation between consecutive rounds is less significant to direct fire, but for indirect fire this could mean the difference between hitting a target or overshooting/undershooting by hundreds of metres, causing untold collateral damage. Further, direct fire guns tend to use a single propellant design and full propellant charge regardless of the situation, whereas indirect fire guns will use different propellant designs and less 'charge weight' for different range work (zoning). This has repercussions for the internal ballistics of the gun (below). An indirect fire gun only utilises its maximum safe working pressure for maximum range work.

1.4 Precision, efficiency and safe design of the gun

1.4.1 Early guns had many problems associated with their precision, efficiency and safety of operation. Precision of a gun concerns different things dependent on whether the target is being engaged directly or indirectly. A direct fire gun needs accuracy of aim, but an indirect fire gun further requires reproducibility of projectile muzzle velocity (i.e. the velocity with which the projectile leaves the barrel). One advance in accuracy was the introduction of rifling, which causes the projectile to spin coaxially; conservation of angular momentum stabilises the projectile and causes it to maintain a more predictable path. Some designs of gun projectiles rely on fins rather than spin to stabilise their flight. Projectiles are grouped as 'spin-stabilised' or 'fin-stabilised'. Modern 'smart' projectiles have movable fins which can be guided

either by an onboard electronics (e.g. heat seeker) or remotely by an operator.

1.4.2 Poor reproducibility is usually associated with poor internal gun ballistics (i.e. the way the propellant burns within the gun chamber), gun design or projectile design. Good ignition of the charge is central to achieving consistent internal ballistics.

1.4.3 Efficiency is discussed in detail along with the internal ballistics of guns later (Section 2). Problems in both efficiency and safety stem from the extreme pressure regimes under which guns perform. Pressures attained in a gun are typically in the region of hundreds of megapascals (one atmosphere pressure is equivalent to one tenth of a megapascal). An optimised gun design has the advantage that energy transfer processes are safe and efficient, meaning that the gun system can have a smaller calibre (i.e. be less massive) to meet the requirements of the gunner. New roles also appear for the larger calibre guns that have increased range and lethality. Early improvements to the efficiency and safety of a gun included a lengthening of the barrel and a reduction in gas leakage both around the projectile using soft leather or metallic driving bands and, where fitted, through the breech.

1.5 Improvements to modern conventional direct fire guns

1.5.1 There are two main areas for improvement in modern direct fire guns. The first is centred upon increased projectile penetration to both counter improvements in target armour and to allow a reduction in the

calibre of guns for current mass criteria. The second is the design of propellant compositions with a low vulnerability to attack (the so-called LOVA propellants).

1.5.2 Projectile penetration can be improved both through projectile design and the increased MV of the projectile round. Projectile design is beyond the scope of this Thesis. Increasing the MV can be achieved by improving the gun design to enhance the internal ballistics (i.e. the way the propellant burns within the gun chamber) within the limitations of a given gun design (Section 2). Little can be done to improve the already optimised modern gun design without some great advance in materials science. Improvements to propellant compositions for further optimisation of gun internal ballistics are under development but conventional means of propellant ignition are believed to be inadequate for many new compositions. One development is disc propellant [1], which may consist of two (or more) propellant compositions – a slow burning propellant around the outside of the disc which burns away to reveal a faster burning higher energy propellant within it. Another is the solid propellant/liquid propellant concept [2] which has a central core of solid propellant within the chamber burning away to reveal a high energy fast burning liquid propellant. A third is the consolidated charge – a disc arrangement composed of pressed grains of propellant [3].

1.5.3 Much research into LOVA propellant design has been carried out in the last decade. However, these compositions appeared difficult to ignite

by conventional means: long and variable ignition delays have been experienced. Future development of such propellants would require new means of ignition to provide reproducible internal ballistics with an igniter which itself would have low vulnerability to attack.

1.6 Improvements to conventional indirect fire guns

1.6.1 LOVA propellants would be almost as beneficial to indirect fire guns as to the direct fire variety. Other improvements to indirect fire guns would be based on increased range and precision. Improvements to projectile range can be made both through projectile design and an increase in the muzzle velocity of the projectile round. Increasing the muzzle velocity can be achieved by the use of advanced charge design or improving the efficiency of the gun. The same problem with ignition of advanced propellant concepts applies.

1.6.2 Indirect fire guns require accuracy and reproducibility of shot fall. Increasing the range of a projectile has adverse effects on the shot fall reproducibility. Various factors cause the location of shot fall to differ between seemingly identical rounds. These can be broadly categorised into two main groups: variability in the operation of the gun subsystems and variability in the meteorological conditions (met) whilst the round is in flight.

1.6.3 Met measurements can be obtained and predictive methods exist to reduce variability due to met. Current estimations suggest that,

dependent upon weather conditions and range, around 40% of all irreproducibility results from met [4].

1.6.4 The gun subsystems that affect reproducibility can again be divided into two classes: shot to shot and systematic variability. Causes of shot to shot variability include variations in the projectile temperature and mass, the chamber and barrel temperature, as well as the propellant temperature, composition and mass. Poor propellant production metrics and changes to the propellant composition during storage also contribute. Another principle cause of shot to shot variability would appear to be associated with the engraving process of the projectile driving bands into the gun barrel rifling. This may be related to ignition processes [5]. Causes of systematic variability include chamber and barrel wear. Small changes to any of these parameters will have a significant effect on shot fall. Systematic changes to the gun can be allowed for with careful record-keeping by the gunner and calibration of the system over time. Some of the shot to shot variability can also be allowed for if knowledge of the subsystem temperatures and masses are known. However, much of the shot to shot variability still remains unpredictable.

1.7 UPCS for indirect fire guns

1.7.1 The unimodular propellant charge system (UPCS) is an experimental concept designed to reduce the logistical burden upon the indirect fire gun and the supporting supply chain [6]. Current in-service propellant

charge systems require different propellant geometry designs for so-called low-zone and high-zone engagement. Low-zone propellant charges (bottom charges) are designed to burn efficiently at low pressure and are used when engaging close targets (several kilometres distant). High-zone propellant charges (top charges) are designed to burn efficiently at higher pressures and may act to supplement the low-zone charges when engaging targets at greater distances (up to nearly forty kilometres). A vehicle needs to be equipped with a full stock of all charges when on active duty, as a pre-knowledge of possible combat scenarios is unlikely. If, however, low-zone engagement occurs then the higher charge supplements become obsolete and are later disposed of (usually burnt).

1.7.2 The cost of propellant production and supply could be significantly reduced with the development of a UPCS that simply uses a greater number of identical modules for a top charge than for a bottom charge. However, problems with the internal ballistics of such UPCS bottom charges have been encountered and these are discussed in more detail in Chapter 3.

2 Internal ballistics of guns

2.1 Gun efficiency

2.1.1 The efficiency with which the stored energy (chemical or otherwise) is transferred to a projectile in a gun system can be defined in various

ways. The simplest approach is through the definition of percentage ballistic efficiency, η_b:

$$\eta_b = 100 \times \frac{1}{2} m_p v_m^2 / Q_c \qquad \textbf{Equation 1.1}$$

where

m_p is the projectile mass,

v_m is the projectile muzzle velocity and

Q_c is the energy liberated within the gun.

2.1.2 This is the ratio of the energy transferred to the projectile to the energy available for transfer. The value of the ballistic efficiency varies from system to system, but for a conventional medium calibre weapon a figure of around 32% is given in [7]. Of the remaining energy, around 3% is transferred to the motion of the propellant gases, 3% into frictional losses, 20% into heat loss to the gun and projectile, while a further 42% is heat retained by the propellant gases. Within this, a further 0.15% is transferred as rotational motion to the projectile (for spin stabilised rounds) and 0.2% as recoil motion of the gun.

2.1.3 A high proportion of the potential chemical energy within a propellant charge will still be stored within the combustion by-products after the projectile has exited the barrel. Such by-products as hydrogen and carbon monoxide will oxidise upon entrainment of the oxygen from the air into the gases as they exit the barrel behind the projectile. The temperature of the gases will be close to around 2000 K and thus they will spontaneously ignite to give the characteristic muzzle flash seen

from a gun. This energy is unrecoverable within the ballistic cycle unless more oxygen is added to the propellant composition. However, this would increase the heat transfer to the chamber and barrel and make erosion unacceptable [8].

2.1.4 A more complex but more useful definition of gun efficiency is the piezometric efficiency, η_p. This relates to the performance of the gun, propellant charge and projectile system itself without reference to how much of the propellant energy is converted. (In practice, the amount of energy transferred to the projectile is the important factor rather than the percentage available for transfer.) The piezometric efficiency is the ratio of the calculated mean pressure required to achieve the measured muzzle velocity to the measured peak chamber pressure, P_{max}: this definition is known as 'the ratio of the mean to peak pressure' [9]. The value of the piezometric efficiency changes surprisingly little for a given gun and projectile if smaller charge weights are used: a reduction in charge weight will lead to a proportionally reduced muzzle velocity and peak chamber pressure. This definition of efficiency is useful for *relative* comparisons between gun systems.

2.1.5 However, the piezometric efficiency takes no account of the changes in gun design strength with shot travel and so would give lower efficiency values than if gun design strength was considered (at least, in all cases except one: if the gun strength were constant from the chamber to the muzzle in which case the values would be the same). Because of this,

the definition for piezometric efficiency is lacking when the performance of a given gun system requires to be measured *absolutely*. For example, a gun with a slender (low mass) design barrel may use a fast-burning propellant to give a high peak pressure early in the shot travel. In this instance, the piezometric efficiency of the gun will be low although the gun may be performing to its maximum design: in terms of muzzle velocity, relative to other gun systems it is a poorly performing gun, but in terms of itself this particular gun might be very efficient indeed. Another definition, formalised here by the Author and coined as the gun design efficiency, η_d is provided by Equation 1.2, given here as the ratio of work done on a projectile to the maximum theoretical work which could be done on it within the (safe and desirable) bounds of the given gun system:

$$\eta_d = \int_0^s AP(s)ds \,/\, \int_0^s AP_T(s)ds \qquad \textbf{Equation 1.2}$$

where

A is the area of the projectile base,

$P(s)$ is the actual projectile base pressure,

$P_T(s)$ is the theoretical maximum (permissible) projectile base pressure given by the gun design and various safety considerations and

s is the projectile shot travel.

2.1.6 Figure 1.1 shows some pressure-space curves for a given gun system. Actual pressure-space curves are given for hot, ambient and cold charges respectively. The gun design efficiency is given as the ratio of

the area beneath the actual pressure space curve to the maximum area permissible by the gun design (P_T is here an hypothetical value). The value P_T varies in a real gun as a function of position as the thickness of the chamber wall reduces into the lesser thickness of the gun barrel, the thickness of which is tapered down its length. A normalised shot base pressure of unity represents the idealised (launch velocity) maximum working shot base pressure of the gun system in the case where $P(s) = P_{max} = P_T$.

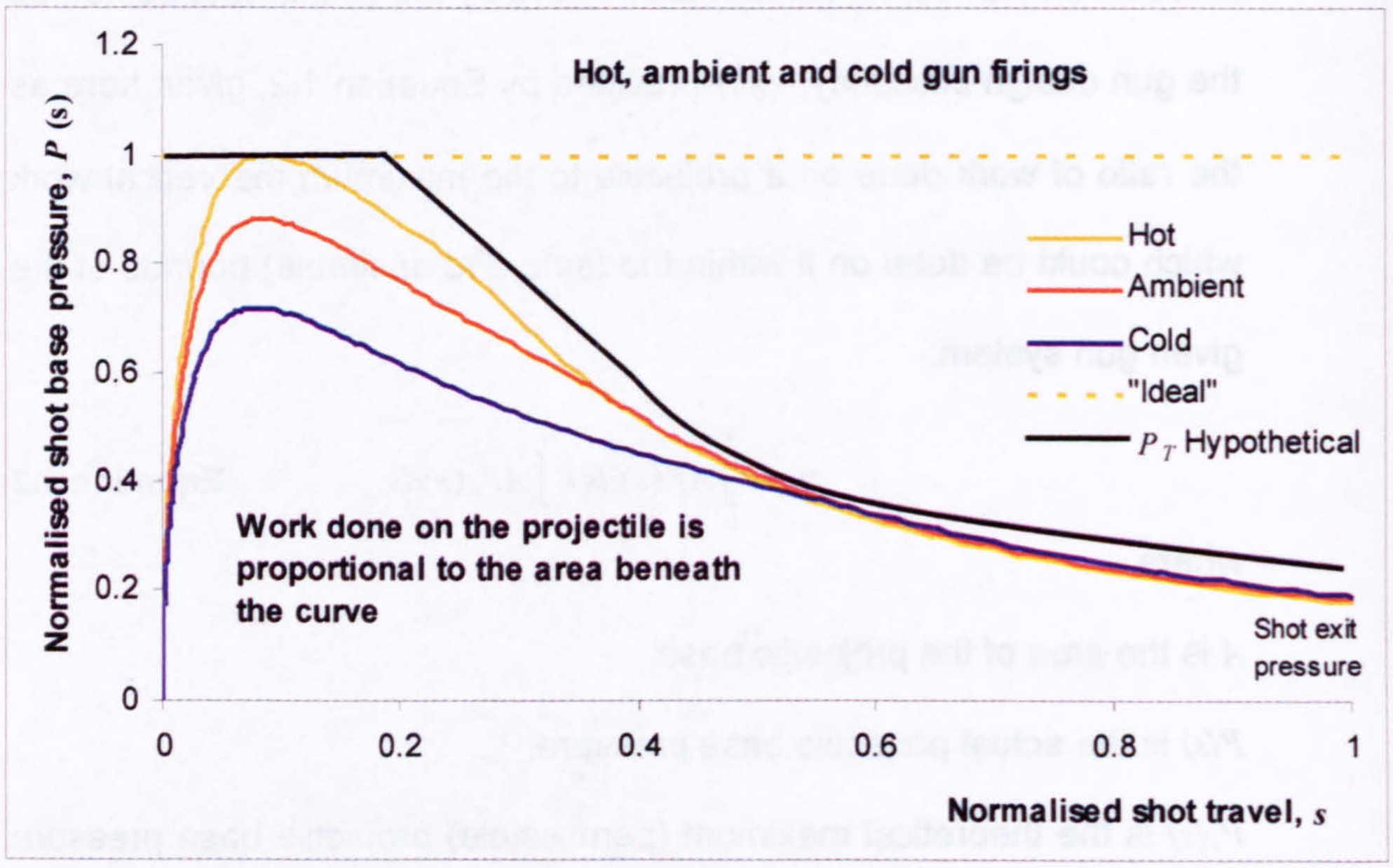

Figure 1.1 Idealised, hypothetical and actual shot base pressure vs. shot travel curves for hot, ambient and cold propellant charges

2.1.7 In Figure 1.1, the piezometric efficiency for the hot charge is given by the ratio of the area beneath the actual to the constant ideal pressure-space curves and can be seen to be in the typical range of 0.3 - 0.4. (Ambient and cold charges will have separate constant pressure values

but a similar piezometric efficiency.) The gun design efficiency can be seen in the figure to be far higher, closer to 0.9. (Ambient and cold charges will have the same variable pressure to work with and thus a lower gun design efficiency.)

2.1.8 An idealised gun would have an instantaneous rise in pressure and maintain the gun elastic strength pressure for the duration of the ballistic cycle. However, constraints apply to the operation of a real gun. The safe and desirable gun strength is reduced for reasons of safety (there is a certain standard deviation applicable to attained peak pressure) and increased barrel operational life-expectancy (a propellant charge is designed such that P_{max} is around 30% less than the elastic strength of the gun; when a new gun is commissioned, proofing shots are fired which take the gun to its theoretical peak in elastic strength, but repeatedly doing so would cause excessive fatigue to the gun subsystems). In practice, the pressurisation rate is limited by the propellant burning characteristics and geometry, and in some cases by the round itself (e.g. sensitive 'smart' munitions) with a limited tolerance to jerk. As the shot leaves the barrel, the expansion of the pressurised propellant gases produces a blast wave that can lead to (un)friendly collateral damage. Strict limitations are set upon the shot exit pressure. Further, as the projectile accelerates up the barrel and the volume available for the propellant gases to expand into enlarges at an increasingly rapid rate, the propellant gas generation rate cannot keep pace and hence the base pressure falls. Further, most of the propellant

will continue to burn within the chamber rather than in the barrel, subsequently reducing the propellant's ability to maintain the peak projectile base pressure.

2.1.9 The Author's definition for gun efficiency came about due to the requirement to increase the absolute performance of a given gun system. Often, gun design strength allows for a higher down-bore shot base pressure even when the safety and desirability aspects are accounted for. Hence, there is the potential with some guns to increase their absolute efficiency, and the piezometric efficiency failed to give a useful measurement of the gun's absolute capability. The maximum value of $\eta_d = 1$.

2.1.10 Designing a propellant which increases the burning surface area or in any other way increases the gas generation rate after P_{max} will help to maintain a higher base pressure and thus increase the gun design efficiency of the gun system. One of the Author's contributions to gun system development has been in the area of enhancing the gas generation rates of propellants with the use of electrothermal plasma. (This work is briefly referred to in later chapters, but limitations on length means that this work is not discussed in any depth here.)

2.1.11 An obvious way to increase the gun design efficiency might seem to be to design a propellant that continues to burn until shot exit, in a way so as to maintain the pressure at the ideal gun design value. Even if a propellant could be designed to do so, this would lead to excessive

barrel wear and nonuniform muzzle velocities [10, 11]. A further limitation on complex propellant design is that of cost, both for production and logistics when the gun needs to be used for a multitude of tasks – a specialist propellant composition may be optimal for one P_{max} value but not another, causing the gun system to require a supply of a multitude of propellant designs which may or may not be used in the field.

2.1.12 The integral of the pressure versus shot travel profile is seen from Figure 1.1 to change in practice depending on the initial temperature of the propellant [12]. Propellant charges are required to perform satisfactorily over a wide range of ambient temperatures, typically - 40 °C to +60 °C. Propellant burn rate at a given pressure increases with temperature and so a higher peak is achieved with a hotter propellant. The gun system must be designed to stay below the safe maximum working pressure, P_{max} when the propellant charge is conditioned (firing) hot and to have propellant all-burnt sufficiently early in the shot travel to produce consistent projectile velocity when conditioned cold. Therefore, even with an idealised propellant, the gun may be used in most instances (at 21 °C) well below its peak gun design efficiency, as the propellant charges are not pre-heated prior to combat. Only in the tropics or sub-tropics is the gun system likely to achieve peak absolute performance.

2.1.13 The elastic strength of the gun will generally reduce with distance down the barrel, forcing the requirement of the reduction in shot base pressure [10]. The gun design value of P_{max} is governed by engineering constraints: the value could be indefinitely increased by an equally indefinite increase in thickness of chamber and barrel wall. A balance between a maximum overall gun mass and a minimum value of P_{max} is achieved by judicious choice of material (gun steel) and other features such as tapering of the barrel external diameter beyond the point where P_{max} occurs. Pre-stressing the gun barrel during manufacture (autofrettage) will allow a further reduction in barrel mass. Gun balance is also an issue.

2.1.14 The length of the barrel can be increased, thus allowing the pressure to act upon the projectile for longer. (Early guns had very short barrels and simply lobbed the projectile a short distance in a general direction.) However, the theoretical limitation on barrel length results from the retarding forces (friction between projectile and barrel) becoming greater than the accelerating forces due to the pressurised gases when the gas pressure falls below a certain limit. In the case of indirect fire guns, this problem is compounded by the necessity to admit lower charge weights. Practical limitations on lengthening the barrel are weight, manoeuvrability and 'barrel droop' whereby the barrel becomes so massive and long that it droops excessively under the weight; in practice, this length is never approached.

2.2 Propellant design

2.2.1 Modern gun propellants, as opposed to rocket propellants, are often referred to as smokeless powders. This refers to smoky gunpowder (or black powder, the modern equivalent) with a mixture of saltpetre, charcoal and sulphur in an approximate ratio of 15:75:10, used for rockets and some igniters in guns [7]. These gunpowders give off up to half of their mass as solid products (smoke) [11]. Central to the internal ballistics of guns is the design of the propellant (often referred to as a grain or powder, although many propellant compositions are neither granular nor powdery). As mentioned above, there are engineering and logistical limitations on the way in which propellant design can be used to maximise the gun design efficiency of a given gun, but certain propellants have been designed to increase efficiency.

2.2.2 A propellant is akin to an explosive. The distinguishing feature between the two is the rate at which energy is liberated during the various exothermic reactions. An explosive releases energy during a detonation: the explosive is ignited, the ignition grows to deflagration (fast burning) and this growth into a full burn to detonation as a shock wave passes through the explosive medium faster than the local sound speed, stimulating the chemical combustion reactions by adiabatic (non-thermal energy transfer) compression [13]. A propellant is derived from similar explosive constituents but the composition or geometry is such that, upon ignition, the propellant will deflagrate without normally burning to detonation.

2.2.3 Propellant comes in many compositions and shapes [7]. The three conventional propellant composition types are single-based, double-based and triple-based. Single-based propellants consist primarily (over 98%) of nitrocellulose, NC (gun cotton), dissolved in alcohol, with the remainder consisting of additives to reduce muzzle flash for example. These compositions are relatively less energetic than the other two. Double-based propellants consist mainly of NC (around 60%) dissolved in nitroglycerine, NG (around 30%), although the quantities differ widely. Double-based propellants are more powerful (i.e. release energy at a greater rate) than single-based compositions, but have a higher flame temperature (3609 K compared with 2820 K for typical double- and single-based compositions respectively [14]) which greatly increases barrel wear. Triple-based propellant compositions have cool burning nitroguanidine added (up to 55%, with around 20% NC and NG). This has the effect of reducing the flame temperature to that of single-based propellants whilst maintaining the power of double-based propellants through increasing the burn rate.

2.2.4 Graphite coatings are often applied to propellants to provide some protection against electrostatic build-up. Other components are commonly used to prevent accidental ignition by electrostatic discharge, friction or (for LOVA propellant) impact from hot fragments [15]. 1,3,5-trinitro-1,3,5-triazacyclohexane (RDX) and 1,3,5,7-tetranitro-1,3,5,7-tetroazacyclo-octane (HMX) are used in some modern LOVA

propellants having little or no NG/NC content, but consisting mainly of one or other of these less-sensitive energetic mixes.

2.2.5 The geometry of propellants can be designed to benefit internal ballistics. A non-porous propellant is assumed to burn in parallel layers (known as Piobert's Law, in honour of his work in 1839). A cylinder of propellant will remain a cylinder until it is completely burnt. Hence, the burning surface area may decrease (degressive burn), remain the same (neutral burn) or increase (progressive burn) during combustion depending on the initial geometry. This has an effect on the gas generation rates. A propellant with a progressive burn after P_{max} will increase the gun design efficiency of the gun system. A simple cylindrical cord will have a degressive burn; a cylindrical tube will be approximately neutral (as the increasing area of the central hole compensates for the decreasing area of the outer surface) and a cylinder with many holes (multi-perf propellant) will have a progressive burn until the holes join up into slivers with a degressive property.

2.3 Propellant ignition

2.3.1 Ignition of propellants is a complex topic. The performance of the entire gun system is reliant upon good ignition characteristics [16]: ideally, uniform and simultaneous ignition throughout the entire bed of propellant [17], or at least along the central or outer length of the chamber is highly desirable to prevent axial pressure oscillations. The flame spread velocity at atmospheric pressure of the propellant would

be too slow to allow hot-wire or match-head ignition at a single point within the bed. This would cause part of the bed to produce hot gas at an accelerated rate due to the relatively higher pressure build-up at that location before other parts have ignited. The resulting pressure gradients would intensify during the ballistic cycle, and pressure waves would be reflected back and forth through the bed, with consequential variations in muzzle velocity and gun recoil. Poor ignition is very pronounced with low loading densities (i.e. in large calibre direct fire guns when bottom charges are used [7]) or LOVA compositions. It has been shown that LOVA propellants require approximately twice the ignition energy compared with conventional nitrocellulose-based propellants [17]. Poor ignition may lead to hangfires (an excessive delay in the time between the start of the ignition sequence and the rise in chamber pressure to the megapascal range) and stickers (a projectile which does not leave the barrel during the ballistic cycle).

2.3.2 The transfer of energy to ignite the propellant bed is conventionally achieved through the use of a primer charge. There are numerous primer designs but a common device in service with the British MoD operates either with black powder, which is ignited by percussion (small hammer), or an electrically heated wire. The hot gases and incandescent particles transfer energy onto the surface of the charge. A certain pressure associated with the primer helps to propel the burning gases/particles down the length of, and a short distance into, the bed, increases the heat transfer coefficients [18] and aids to

increase the propellant initial burn rate. The energy is transferred from the gaseous primer products to the propellant grain surfaces by convection and from the solid burning particulates by conduction, with conduction into the propellant grain itself if the grain is non-porous. In the case of a porous bed where the inter-grain distance is of the same order of magnitude as the flame structure, both convection and compaction play important roles in the deep penetration of energy during the ignition phase [19]. Thermal radiation at these temperatures is insignificant. A constant energy transfer (flux) of 20 MW m^{-2} is typical for a gunpowder (GP) igniter [20]; the contribution from the radiative component will be around 1 MW m^{-2} (from the Stefan-Boltzmann radiation law for a radiator with an emissivity of unity at 2000 K). Thermal contours around spherical gunpowder particles will have spherical symmetry, whilst those of the gases will be linear and thus more effective at energy transfer. Figure 1.2 illustrates the simplified process.

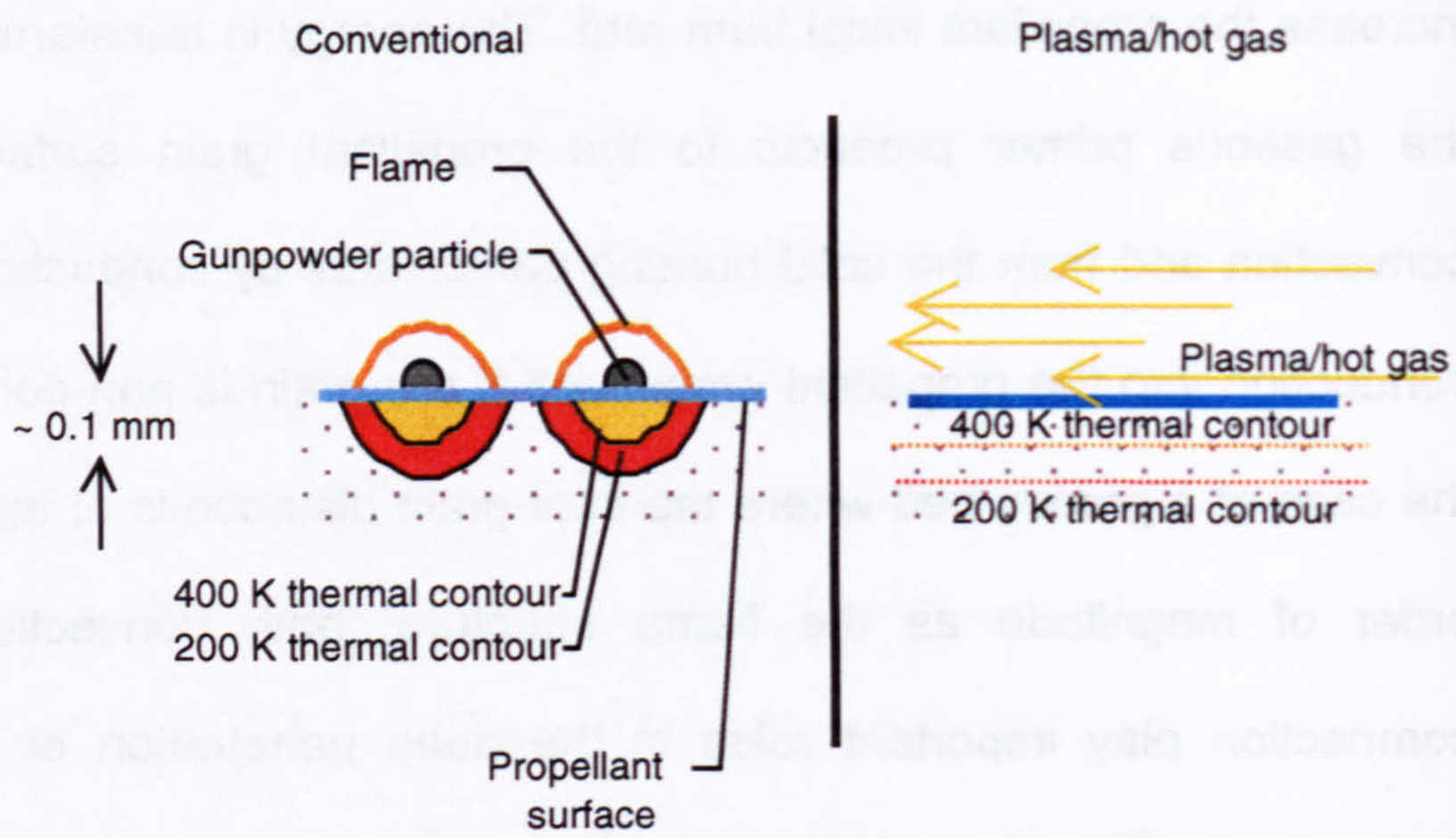

Figure 1.2 Diagrammatic representation of conventional ignition processes

2.3.3 During energy transfer from the primer products to the propellant surface, luminous exothermic chemical reactions have been recorded at or a few micrometers below the surface [21, 22]. If energy transfer from the primer source were removed at this point, then a go/no-go ignition situation would develop where the propellant bed either would or would not undergo self-sustaining combustion [23]. Various "hot-spot" mechanisms have been proposed including the formation of discrete critical ignition sites whose size, duration and temperature would be interdependent [13]. Typical dimensions, times and temperatures have been quoted as 0.1-10 μm, 0.01-1 ms and around 700 K respectively [24, 25]. Non-critical hot-spots would produce some decomposition of the grain surface and subsurface, but the energy transferred from the site would be greater than that liberated, thus quenching the site before self-sustaining combustion could take hold. This situation has been shown to occur with small quantities of

propellant surrounded by inert material, even at a very high ignition flux (see Chapter 9). Here, the net heat transfer from the ignition sites is due to the isolation of the energetic material. This implies that propellant loading density is also a prime factor in go/no-go situation.

2.3.4 It is possible for propellants to self-ignite if loaded into a hot gun and left for a long time (the propellant is said to "cookoff"). The combination of external heat from the hot chamber walls and self-heating of an energetic material produces a sudden rapid rise in the propellant temperature. The length of time a given propellant can be left at a given temperature within the chamber can be predicted [26].

2.3.5 The temperature which a propellant surface has to reach before self-sustaining combustion occurs is often taken as a single value for modelling purposes, based on the assumption that enough heat has propagated to a depth of tens of microns to ensure self-sustained combustion. Typical temperatures are 450 – 600 K [27]. However, this assumption neglects the finding that the ignition temperature is dependent on the type of heat transfer (conductive, radiative and so forth) [17]. Ignition energy transfer processes are discussed further in the chapters on plasma ignition.

2.4 Sustained combustion

2.4.1 Once self-sustained combustion has taken hold, energy transfer processes from the exothermically reacting products at the surface occur, possibly together with subsurface condensed [28] or mixed

phase [29] exothermic reactions. The importance of subsurface reactions is not clear: Davidson and Beckstead suggested such solid phase reactions are negligible [28]. Schroeder et al [22] cited various papers suggesting that less than 10% of decomposition occurs in the condensed phases. However, the Author has performed some (unreported) work to show that condensed phase reactions may be crucial to burning behaviour of solid propellant at atmospheric pressure. In the work conducted by the Author, propellant of a particular composition could be made to *smoulder* with a surface regression rate between 0.2 to 0.4 times that of when flaming combustion occurred. Spectroscopic measurements of the condensed surface showed the thermodynamic temperature to be around 1100 K maintained (in free air) for 5 s. This was similar to the findings of Howard et al [30], where a hang-fire situation occurred during thermometric tests. Howard measured a surface temperature of 1200 K, decaying to 900 K over 40 ms.

2.4.2 The transfer processes from the exothermic reactions occurring in the flame above the surface are dominated by convection and conduction, with radiation probably contributing a small proportion of the total energy transferred. The flame chemistry is not well understood, having complex spatial and temporal reaction zones. Figure 1.3 shows a typical flame zone for a double-based propellant. The propellant grain is pre-heated by both radiation from the flames and conduction from the superficial degradation layer.

2.4.3 As the gun chamber pressure increases, the combustion zones are pushed closer to the propellant surface, increasing the rate of transfer of energy to the condensed propellant and thus the gas generation rate.

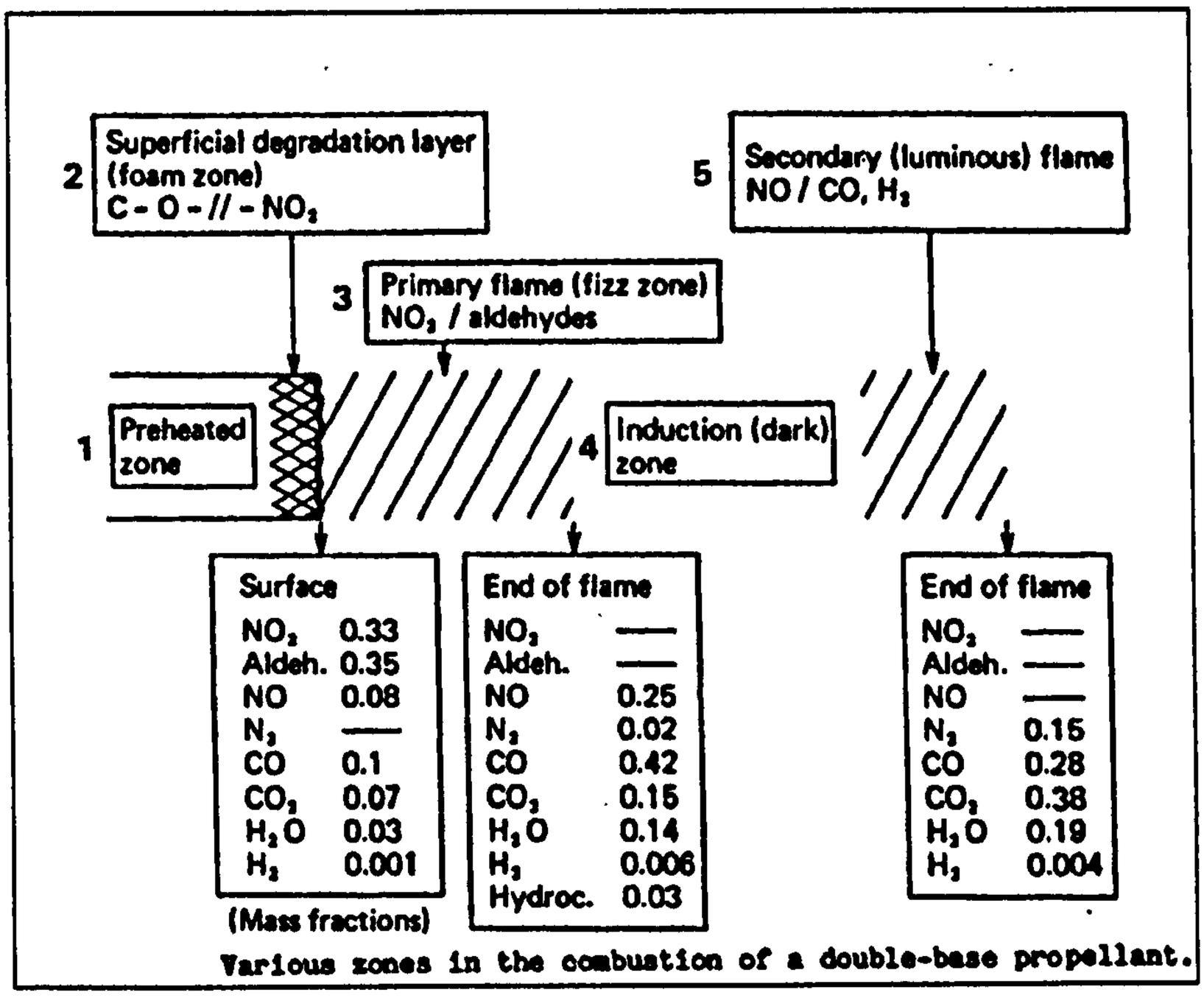

Various zones in the combustion of a double-base propellant.

Figure 1.3 Flame structure of a typical double-based propellant composition [31]

2.5 Closed vessel experimentation

2.5.1 The way propellant characteristics change during the combustion cycle can be studied in closed vessel (closed bomb) experiments. Here, the volume of the chamber remains constant (apart from a small change due to the effective space taken up by the propellant gas molecules being greater than that of the propellant molecules in the solid phase), making modelling less complex. The pressure of the chamber is measured as a function of time (with for example piezoelectric pressure

transducers) and isobaric conditions are sometimes assumed to prevail.

2.5.2 The pressurisation $P(t)$ and rate of increase in mass of gas, dm/dt within a closed bomb chamber during the combustion of solid propellant are related (assuming the ideal gas law) by the semi-empirical law:

$$P(t) = \frac{F}{V_0}\int_0^t \frac{dm}{dt}dt = \frac{F\rho}{V_0}\int_0^t S\beta P^{\alpha}dt \qquad \textbf{Equation 1.3}$$

where

P is the chamber pressure (in megapascals) at time t,

F is known as the force constant of the propellant,

V_0 is the free volume of the chamber at time t,

ρ is the density of the solid propellant,

S is the burning surface area at time t,

β is known as the burn-rate coefficient of the propellant and

α is known as the burn rate pressure index of the propellant.

2.5.3 The force constant, measured in units of J kg^{-1}, is related to the integrated energy liberated from the propellant grain surface and is thus a property of the propellant composition (vis the chemical reactions at the burning surface). The force constant (as with the propellant density) is not a function of time unless multi-layered propellant compositions are used. Double and triple-based propellants have a higher force constant than the energetic single-based compositions.

2.5.4 The free volume of the closed bomb is the chamber volume minus the volume taken up by the propellant molecules (or co-volume). As hot gas phase particles have a greater effective cross-sectional area than cold condensed phase molecules, V_0 generally reduces with time.

2.5.5 The burning surface area is strongly time-dependent, as already mentioned above. An equation relating the proportion of burnt propellant to the remaining grain size is called the form function, and depends solely on propellant grain geometry.

2.5.6 The burn rate coefficient is defined as the surface regression velocity per unit (pressure)$^{\alpha}$ with pressure being measured in megapascals. It is a property of the propellant composition rather than the geometry. This value is known to be temperature sensitive [7] and is responsible for the reduction in the gun design efficiency when cold propellant is used. Values of β for gun propellants are around 0.1 – 0.2 cm s^{-1} MPa^{-1} [11].

2.5.7 Even if the grain surface area is constant, the rate of change of pressure is not usually directly proportional to the pressure at any given time. The burn rate pressure index is a constant close to unity and allows for the slight deviation from direct proportionality.

2.5.8 βP^{α} is often referred to as the propellant burn rate and is thus directly proportional to the rate of change of pressure within the chamber if everything else remains constant. A plot of dP/dt or βP^{α} (i.e. the burn rate) against P will give an approximately straight line relationship for α

close to unity, and reasonably constant S and V_0. This is known as Vieille's law of burning.

2.5.9 Figure 1.4 shows an experimental baseline plot of dP/dt (in absolute units) against P for an RDX and NC based propellant and for Vieille's law (in arbitrary units) in a closed vessel [32, 33].

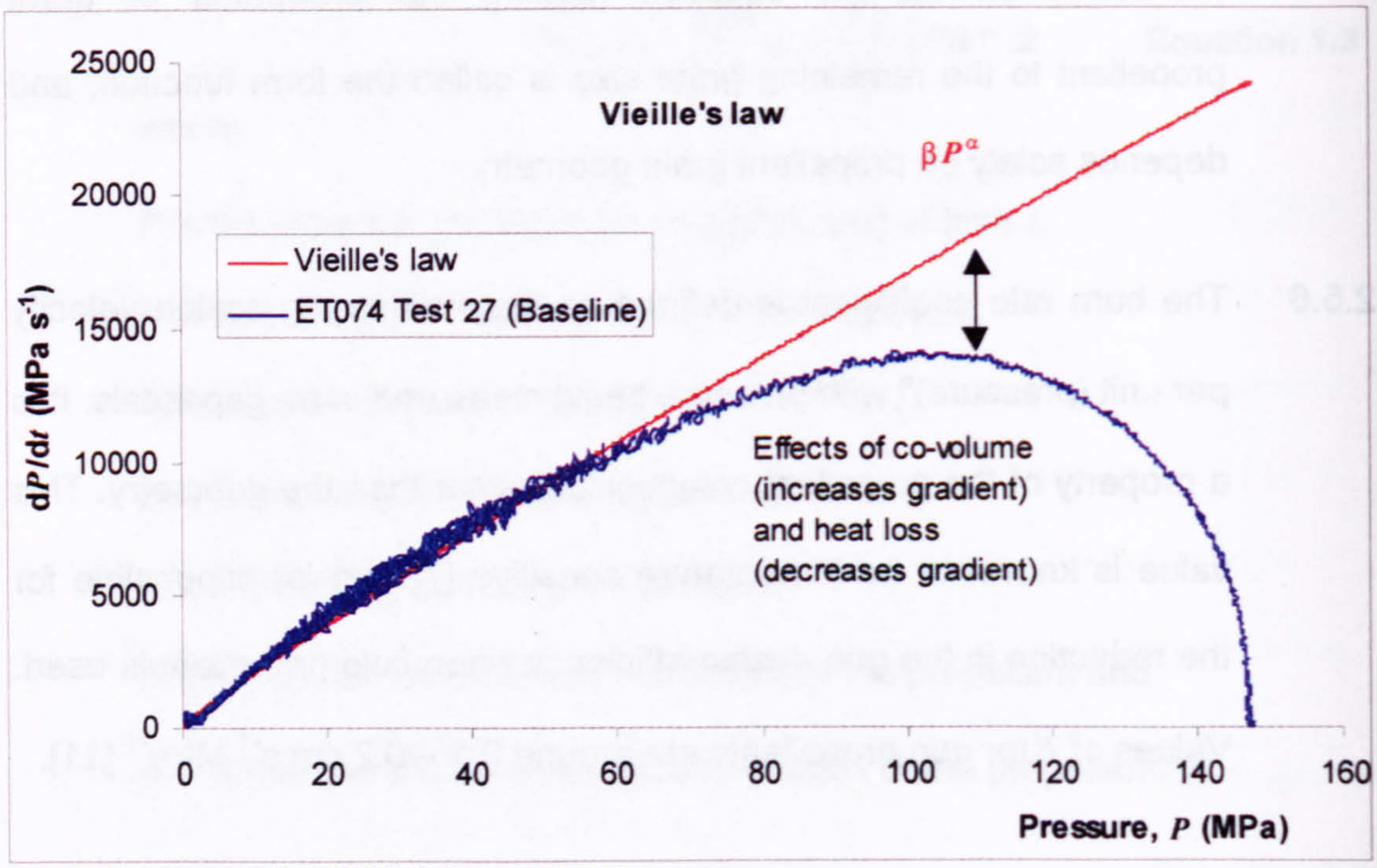

Figure 1.4 Experimental and theoretical application of Vieille's law

2.5.10 No account has been taken of atmospheric pressure (i.e. P = 0.1 MPa at t = 0), heat loss to the chamber walls or the decrease in V_0. The heat loss will tend to decrease dP/dt and the decrease in V_0 will tend to increase dP/dt. The divergence of Vieille's law from the baseline test after around 60 MPa is mainly due to the heat loss term, which is more significant than the co-volume. These differences are allowed for in the full closed bomb analysis. When these differences are allowed for, the

plot of Vieille's law would be coincident with *dP/dt* for the baseline test. The values of α and β and the other constants can be determined by curve-fitting techniques. Changes to the propellant composition or the ballistic cycle can be made and any differences in the values computed.

3 Non-conventional improvements to guns

3.1 Introduction

3.1.1 Conventional guns firing solid propellants are all but optimised [34], although small improvements to the ballistic cycle are still possible with new propellant compositions.

3.1.2 Much work has been done over the past decade or two on non-conventional concepts for increasing muzzle energies and decreasing the round to round variability in muzzle velocities. Four of these concepts are briefly introduced below.

3.2 The electromagnetic (EM) gun

3.2.1 The idea of using electrical energy for gun propulsion is almost as old as the discovery of the electromagnetic force. In 1844, *the newly invented electric gun* "SIVA" (The Destroyer) was claimed by a Mr Benningfield to be able to *fire a continuous stream of balls at a rate of more than 2000 min $^{-1}$ and kill at a distance greater than a mile* [35]. Nothing much is known about the device or how it operated, but the concept is suggested using electrical energy to provide the propulsive

force for driving projectiles in military applications. Today, many workers are still applying efforts to field an all-electric vehicle with an EM gun as the main armament [36] and projectile velocities of up to 3 km s^{-1} [37] for direct fire applications.

3.2.2 There are a number of different designs for EM guns. The coil gun uses the magnetic field generated in a series string of solenoids to induce a magnetic field within the steel projectile and propel it at great speeds (several kilometres per second) directly at a target. The rail gun uses the principle of the Lorentz force generated on a freely running armature placed between two parallel conducting rails. References to the modern work in such guns can be found in reference [38].

3.2.3 The main advantages of EM guns are the entire lack of propellant charges, together with the control and ideally unlimited energy densities of electrical power supplies. The main drawbacks are the engineering constraints of modern capacitors and rotating machines. These are proposed to store and supply the prodigious quantities of energy (around 32 MJ) needed to launch a projectile with muzzle energies of around 9 MJ as required by such practical weapons [36]. Hence, the requirement for EM guns has been a main driving force behind much of the developmental work in pulsed power supply (PPS) and materials science.

3.2.4 Such guns, when finally developed, will not only radically alter the direction of modern warfare but have non-military applications in such areas as satellite and aircraft launchers.

3.3 Liquid propellant (LP) guns

3.3.1 Liquid propellant (LP) guns were considered to have the potential for high loading densities and low molecular weight combustion products. This would allow high combustion gas velocities to be achieved; in addition, they would have the benefit for extra propellant to be added during the combustion cycle. However, work is not currently being carried out (at least in the UK) on LP guns due to the production of pressure waves of a dangerous amplitude within the gun chamber and other engineering factors [39]. Work is still in progress elsewhere [40] involving a solid propellant/liquid propellant (SPLP) hybrid, which would use electrothermal energy (see below) to ignite a core of low force constant solid propellant surrounded by high force constant liquid propellant. Such a system could conceivably make substantial improvements to the design efficiency of a gun system.

3.4 The electrothermal (ET) gun

3.4.1 LP ignition using electrical energy in the form of electrical plasmas has been considered for some time [2]. This led to the concept of introducing electrical energy to vaporise an endothermic (e.g. water) or slightly exothermic working fluid [41, 42] (e.g. hydrogen [43]) within the chamber of the gun. In another design, aluminium electrical plasmas

were injected into water – the exothermic reduction/oxidation reaction of the aluminium and water adding to the electrothermal energy from the power supply.

3.4.2 This system shared many of the same advantages and disadvantages of the LP gun. The added benefits were the potential for a cheap and totally inert propellant immune to attack and the real-time control which electrical energy offers; the drawback was the requirement for excessive quantities of electrical energy. At around 10-30 MJ for large calibre, exothermic LP guns [42, 44, 45] and up to 150 MJ for water [42] and with firing rates of around three shots in ten seconds, this made the idea impractical [46].

3.4.3 The conclusion has been that, due to the size and mass of the required power supply, the performance enhancements over conventional guns would only be modest and therefore there was no incentive to embark on new LP technologies [44].

3.4.4 Pure ET launchers have also been studied for applications other than weaponry. Small masses have been accelerated to velocities in the region of tens of kilometres per second for research into impacts of space debris [47].

3.5 The electrothermal-chemical (ETC) gun

3.5.1 The ETC gun concept is similar to some of the ET guns discussed above, ETC technology having evolved directly from ET technology

[40]. An exothermic working fluid – either solid, liquid, slurry or gel – provides the bulk of the energy required for projectile acceleration. The electrical energy is used for ignition, to enhance the burn rate characteristics and/or augment the thermal energy of the system, thus reducing the burden on the PPS.

3.5.2 Solid propellant ETC guns are designed to improve on conventional solid propellant guns through the introduction of electrical energy into the combustion cycle. The idea of using electrical energy to ignite a solid propellant charge and augment the combustion ballistics of conventional guns was being promoted before the end of the 1980's [36]. Although less radical than the EM, LP or ET guns, the ETC gun has the advantages of working within a mature area of ballistics. ETC also has low pulsed power requirements of less than a few megajoules and an achievable fieldable weapons system [48], together with the high energy densities of the chemical propellant (typically 3-5 kJ g^{-1} [49]). A direct fire ETC weapon may be in service by 2017 with a projectile muzzle energy of around 9 MJ, developed by Rheinmetall's TZN and MaK subsidiaries [50].

3.5.3 The following chapters will exploring the ETC concepts in some detail, including advances in the understanding of the formation of the electrical plasma and the interactions between the plasma and the solid energetic materials used in ETC gun technology.

1 A. M. Voronov, H. K. Haak and Th. H. G. G. Weise, "The Interaction of Electrothermally Supplied Energy with Compact Solid Propellants", IEEE Transactions on Magnetics, Vol. 35, 1, January 1999

2 A. Chaboki, S. Zelenak and B. Isle, "Recent Advances in Electrothermal-Chemical Gun Propulsion at United Defence, L.P.", IEEE Transactions on Magnetics, Vol. 33, 1, January 1997

3 A. Kay, J. Raupp, D. Mura, C. Steinbach, D. Hensel and H. Peter, "Plasma Ignition of Consolidated Propellants in a 60 mm ETC Gun", 19th International Symposium of Ballistics, Interlaken, Switzerland, 7th – 11th May 2001

4 S. R. Fuller, M. Firth and C. R. Woodley, "Interim Smart Gun Report", unpublished DERA/MoD report, June 1997

5 M. J. Taylor, "Consideration of the Energy Transfer Mechanisms Involved in SPETC Ignition Systems", 11th Electromagnetic launch Symposium, St. Louis, France, 14th – 17th May 2002

6 C. R. Woodley and S. J. Billett, "Modelling Enhanced Gas Generation Rates in a 155 mm ETC Gun", IEEE Transactions on Magnetics, Vol. 37, No. 1, January 2001

7 C. L. Farrar and D. W. Leeming Royal Military College of Science (RMCS), Shrivenham, UK "Military Ballistics – A Basic Manual", Brassey's Battlefield Weapons Systems and Technology, Vol. X, Brassey's Defence Publishers, 1982

8 J. M. Bellerby, Environmental and Chemical Systems Department, RMCS, "Gun Propellants", Internal Ballistics Course Notes, 1996

9 J. Corner, "Theory of the Interior Ballistics of Guns", John Wiley and Son, Inc. Publishers, 1950

10 H. Krier and M. J. Adams, "Interior Ballistics of Guns, Progress in Astronautics and Aeronautics, Vol. 66, 1978

11 A. Crowley, RMCS, "Introduction", Internal Ballistics Course Notes, 1996

12 M. A. Firth et al, "Electrothermal-Chemical Launchers", DERA internal report DRA/DWS/WX6/CR97188, 1997

13 J. F. Field, "Hot Spot Ignition Mechanisms for Explosives", Accounts of Chemical Research, 25, N°. 11, 1992

14 D. Debenham, A. Edwards, C. Woodley, DERA internal memo, 1997

15 E. S. Kim and S. T. Thynell, "Condensed-Phase Kinetics of Cyclotetra-methylenetetranitramine from Confined Rapid Thermolysis/FTIR Spectroscopy" , American Institute of Aeronautics and Astronautics, 1997

16 A. E. Wildegger-Gaissmaier, I. R. Johnson and G. Teague, "Flame Spread in a LOVA Charge: An Experimental Study", Propellants, Explosives, Pyrotechnics, Vol. 20, pp 139-143, 1995

17 A. E. Wildegger-Gaissmaier, I. R. Johnson, "Ignition of a Granular Propellant Bed", Combustion and Flame, Vol. 106, pp 219-230, 1996

18 D. Zoler and S. Cuperman, "Two-dimensional Modeling of Propellant Ignition by a Plasma Jet", 17th International Symposium on Ballistics, Midrand, South Africa, March 1998

19 B. W. Asay, S. F. Son and J. B. Bdzil, "The Role of Gas Permeation in Convective Burning", Int. J. Multiphase Flow, Vol.22, No. 5, pp 923-952, 1996

20 C. R. Woodley, Private communication, Land and Weapons Systems Sector, Defence Evaluation and Research Agency (DERA), UK

21 H. Mach, "Measurements of the Threshold Energies for Reliable Ignition of Solid Propellants Using a Pulsed Nd-Glass Laser", 14th International Symposium on Ballistics, Quebec, Canada, 26th – 29th September 1993

22 M. A. Schroeder, R. A. Fifer, M. S. Miller, R. A. Pesche-Rodriguez, C. J. S. McNesby, G. Singh and J. M. Widder, 'Condensed-phase Processes During Combustion of Solid Gun Propellants II Nitramine Composite Propellants' Combustion and Flame Vol. 126, p1577, 2001

23 K. K. Kuo, J. U. Kim, B. L. Fetherolf and T. Torikai, "Preignition Dynamics of RDX-Based Energetic Materials Under CO^2 Laser Heating", Combustion and Flame Vol. 95, pp 351-361, 1993

24 F. P. Bowden, A. D. Yoffe, "Initiation and Growth of Explosives in Liquids and Solids", Cambridge University Press, Cambridge 1952 (reprinted in 1989)

25 F. P. Bowden, A. D. Yoffe, "Fast Reactions in Solids", Butterworths, London 1958

26 A. C. Victor, "Equations for Predicting Cookoff Ignition Temperatures, Heating Times and Violence", Propellants, Explosives and Pyrotechnics 22, pp 59-64, 1997

27 J. M. Bellerby, Environmental and Chemical Systems Department, RMSC, "Gun Propellants", Internal Ballistics Course notes, 1996

28 Y. C. Laiu and V. Yang, J. Propulsion Power Vol. 11, pp 729-739, 1995 (cited reference 7 in J. E. Davidson and M. W. Beckstead, "A Three-phase Model of HMX Combustion", 26th Symposium (International) on Combustion, Combustion Institute, pp 1989-1996, 1996)

29 R. L. Hatch, "Chemical Kinetics Model of the NG/binder System"

30 S. L. Howard, L-M Chang and D. E. Kooker, "Thermocouple Sensor for Rapid Temperature Measurement during Ignition and Early Phase Combustion of Packed Propellant Beds", Rev. Sci. Instrum. 66 (8), pp 4259-4266, August 1995

31 Kuo & Summerfield, "Fundamentals of Solid Propellant Combustion", Progress in Astronautics and Aeronautics, Vol. 90, 1984

32 M. J. Taylor, "Power Threshold of PEDEGGR for LOVA Propellants", Experiment ET092, DERA internal document WSS/WX6/01-ETG/ERD022, June 2000

33 M. J. Taylor and C. R. Woodley, "Variation in enhanced gas generation rates in electrothermal-chemical closed chamber studies", Proc. 19th International Symposium on Ballistics, 1, pp 179 – 186, 7th – 11th May 2001

34 C. R. Woodley and S. R. Fuller, "The Effect of Plasma on the Combustion Rates of Solid Propellants", The International Autumn Seminar on Propellants, Explosives and Pyrotechnics, Shenzen, China, 8th – 11th October 1997

35 I. R. McNab, "Early Electric Gun Research", IEEE Transactions on Magnetics, Vol. 35, No. 1, January 1999

36 R. M. Ogorkiewicz, "In Search of Lighter, Smaller Electric Guns for Future Tanks", Jane's International Defence Review, Vol. 32, February 1999

37 A. P. Noel, A. Challita and D. P. Bauer, "A Novel Railgun Launch Package Concept", IEEE Transactions on Magnetics, Vol. 37, 1, January 2001

38 Various authors, IEEE Transactions on Magnetics, Vol. 37, No. 1, January 2001

39 M. A. Firth, C. R. Woodley, A. W. Edwards and J. Fellows, "Electrothermal-Chemical Launchers", DERA internal report DRA/DWS/WX6/CR97188, 1997

40 A. Chaboki, S. Zelenak and B. Isle, "Recent Advances in Electrothermal-Chemical Gun Propulsion at United Defence, L.P.", IEEE Transactions on Magnetics, Vol. 33, 1, January 1997

41 L. Thornhill, J. Batteh, J. Scanlon and D. Cook, "End-to-End Modelling of Electrothermal Launchers", IEEE Transactions on Magnetics, Vol. 29, 1, January 1993

42 C. R. Woodley, Parametric Study for an Electrothermal-Chemical Artillery Weapon", IEEE Transactions on Magnetics, Vol. 29, 1, January 1993

43 D. A. Tidman and D. W. Massey, "Electrothermal Light Gas Gun", IEEE Transactions on Magnetics, Vol. 29, 1, January 1993

44 C. R. Woodley and S. R. Lumley, "DRA Modelling Activities on Electrothermal Guns", 15th International Symposium on Ballistics, Jerusalem, Israel, 21th – 24th May, 1995

45 N. Silvestre, D. Hensel and K. Darée, "A Comprehensive, Numerical Model of Electro-Thermal Propulsion", IEEE Transactions on Magnetics, Vol. 29, 1, January 1993

46 S. R. Fuller, "Pulsed Power Supply Integration Study for a Naval ETC Gun", M.Sc. Dissertation, University of Salford, 1998

47 M. Rott, "The LRT/TUM Small Calibre Electrothermal Accelerator", IEEE Transactions on Magnetics, Vol. 29, 1, January 1993

48 J. R. Greig et al, "Investigation of Plasma-Augmented Solid Propellant Interior Ballistic Processes", IEEE Transactions on Magnetics, Vol. 29, 1, January 1993

49 Z. Kaplan et al, "Electrothermal Augmentation of a Solid Propellant Launcher", IEEE Transactions on Magnetics, Vol. 29, 1, January 1993

50 R. Pengelley and M Hewish, "Updates and Upgrades Defer the Arrival of the New Technology Tank", Jane's International Defence Review, Vol. 33, April 2000

Chapter 2 - ETC guns

1.1 Benefits of ETC gun systems

1.1.1 An ETC gun system benefits from the advantages of stored chemical energy in the propellant of around three to four megajoules per kilogram compared with an energy density of capacitor based systems of a few tens of kilojoules per kilogram [1], whilst still retaining the control aspects of an electrical system.

1.1.2 Such benefits of an ETC gun system over conventional weapons systems are still largely perceived. Furthermore, ETC technology is immature and the interaction between the electrical energy and energetic propellant is not well understood at higher pressures. The defence applications of ETC technology are still under review. Understanding the ETC plasma-propellant interaction is the key to optimisation and reduction of the pulsed power burden [2] and may well ultimately determine the cost effectiveness of ETC gun systems.

1.1.3 The perceived benefits of ETC technology for direct and/or indirect battlefield engagement large calibre gun systems are:

- Improvement in the performance of the gun system through increasing its muzzle energy.
- Ignition and control of the combustion of new propellant formulations, e.g. low vulnerability 'LOVA' propellants and solid propellant/liquid propellant (SPLP) hybrids, and unimodular propellant charge systems (UPCS).

- Optimisation of the projectile launch to match given projectile characteristics (e.g. lower acceleration for smart projectiles).

- Reduction in the shot to shot variations in muzzle velocity due to, for example, first round effects and variable shot start conditions.

- Compensation for the variation in gun performance with propellant temperature.

1.1.4 The performance of the gun system would be improved by increasing its gun design efficiency (see Chapter 1). Just using electro-thermal energy to augment the chemical energy within the combustion chamber shortly after P_{max} alone, would be highly desirable. However, thermal augmentation is very much a perceived benefit as the quantity of electrical energy required would be prodigious (in the region of 5 - 10 MJ [3]). The practicality of this must be considered in the light of the fact that 0.37 m^3 MJ^{-1} are required for a simple theoretical capacitor-based storage system, [4]. However, there have been reports from the UK, USA and Sweden of an apparently enhanced gas generation rate (EGGR) of propellant compositions stimulated by the discharge of an ETC plasma [1,2,5,6,7,8,9] both during electrical discharge (EGGRDED) and post electrical discharge (PEDEGGR) [10, 11]. This phenomenon could be used to increase the gun design efficiency of a gun and thus increase the muzzle velocities. EGGR is not discussed in depth in this Thesis due to length limitations, but the Author's contributions to EGGR include an experimental demonstration that PEDEGGR is a statistically real effect

for some propellants only, and that the propellants tested exhibit EGGRDED to the same degree. The conclusion that EGGRDED may be propellant composition independent was new to the field [11]. Another project concerned the Author's attempt to detect any catalytic [11, 12] or shock [13] mechanisms in the EGGR process. There was no statistical evidence to suggest that either mechanism was responsible for EGGR. Work by the Author is currently in hand to measure the radiative flux transfer to propellant from an electrothermal plasma during the combustion processes, as well as direct measurement of propellant surface regression rates using new probe designs.

1.1.5 Due to their mobility within a bed of propellant, ETC plasmas have been shown to give almost simultaneous and uniform ignition in beds of solid propellant charge compositions such as high loading density discs [14] and insensitive munitions [9, 15]. Good ignition reproducibility for bottom charge UPCS and consistent muzzle velocities are attained where conventional ignition techniques are unsatisfactory [9, 16]. As stated in the previous chapter, the ability to solve the UPCS problems would provide benefits both in terms of cost-saving and logistics. For given gun systems, the potential to ignite higher loading densities with ETC plasmas can result in a 16 - 25% gain over an optimised conventional gun [9, 16]. In addition, the potential exists for use of non-conventional geometries such as multi-layered disc propellants, and others that are programmed to undergo a radical change in form function with the application of an electrothermal plasma. Further, the rapid rise in the

pressure possible with plasma ignition may lead to improvements in the gun design efficiency of the system. The energy transfer mechanisms involved in ignition are considered in depth later in the Thesis.

1.1.6 So-called 'soft launch' for advanced sensitive smart munitions could be achieved by flattening and extending of the pressure versus time curve through EGGR or pure thermal augmentation [5]. This concept, although having been around for a decade or so, has yet to be supported by demonstrable evidence.

1.1.7 Muzzle velocity control has been shown possible by the introduction of electrical energy after all the propellant has burnt via a concept known as the 'Smart gun' [17, 18, 19, 20]. A pressure wave generated by the electrical discharge within a capillary plasma generator (CPG) after propellant all-burnt has been shown to affect the acceleration of a projectile before it leaves the barrel. Electrical noise resistant fibre optic strain gauges, developed at QinetiQ [17], have successfully measured the initial acceleration of the projectile. (Strain within the barrel results from the progress of the projectile as it moves along the length.) The acceleration (and hence muzzle velocity) will vary randomly from round to round due to small differences in propellant temperature, packing and composition, as well as the gun condition (for example barrel temperature or first round effects of 'gun memory' or oil within the barrel). In the Smart gun concept, if the projectile is found to deviate from a pre-determined upper limit acceleration, then a pre-programmed electrical

discharge can be fired at a computed time to counter the small effects. The smaller the difference in acceleration then the later the discharge occurs. Any round with an acceleration equal to or greater than that predetermined would need no 'smart' discharge to occur. Some experimental work has been done at QinetiQ for Smart gun proof of principle [17, 18].

1.1.8 Figure 2.1 shows the Smart gun muzzle velocity in the case of a conventional 155 mm artillery gun [17].

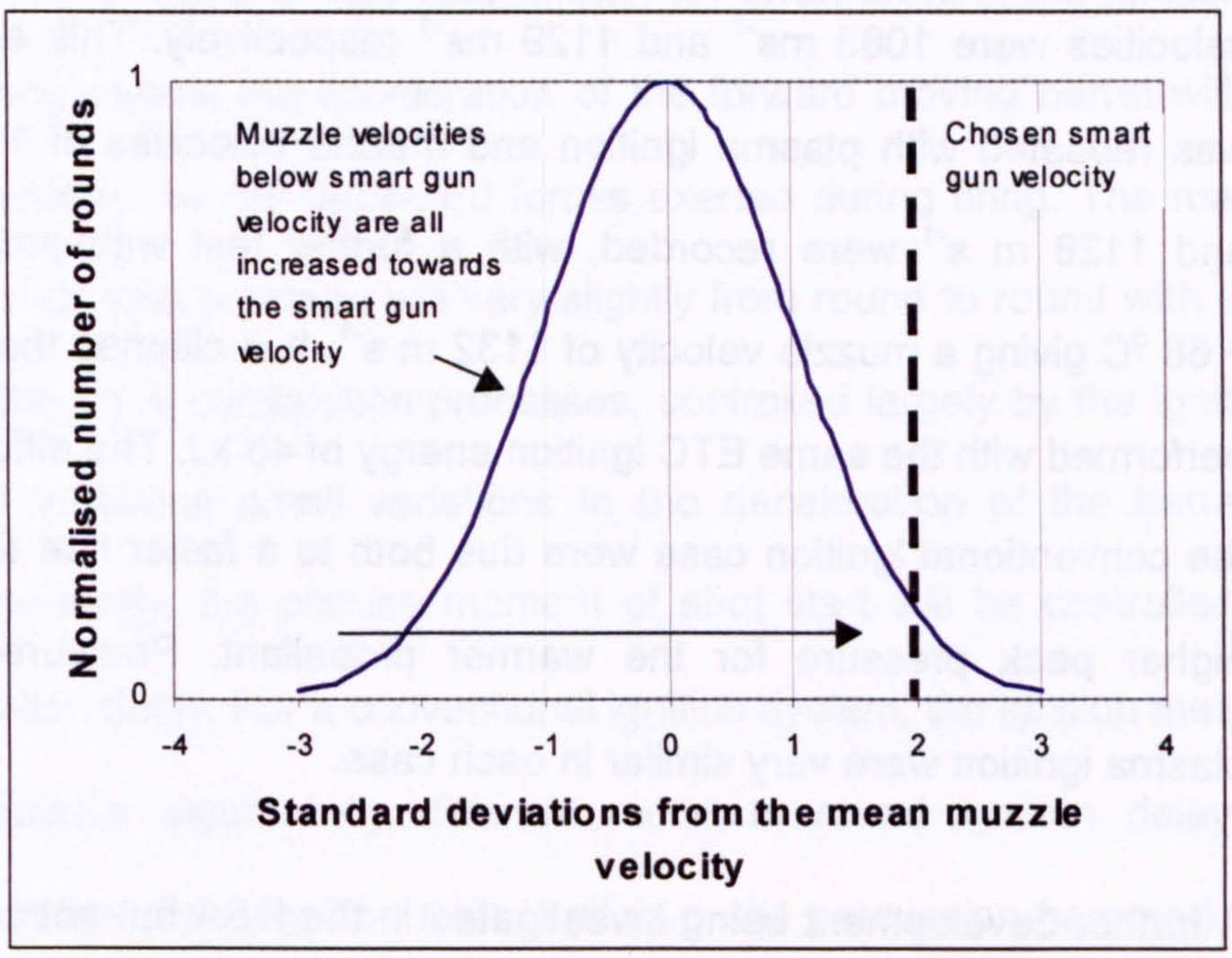

Figure 2.1 Conventional and 'Smart gun' muzzle velocity distribution

1.1.9 Assuming a perfect smart gun system, then a choice of smart gun velocity two standard deviations above the mean would result in around 98% of all projectiles leaving the gun with this velocity and the remaining 2% having slightly too much energy. Dispersion at the target would thus be much reduced.

1.1.10 As mentioned previously, the propellant burn rate at a given pressure increases with temperature and so a higher peak is achieved with a hotter propellant. Therefore, the gun may be used in most instances (at 21 °C) well below its peak gun design efficiency since the propellant charges are not pre-heated prior to combat. However, it has been demonstrated by United Defense, LP, Armament Systems Division that ETC plasmas can compensate for temperature variability in experimental 30 mm gun firings [9]. With conventional ignition, propellant was preconditioned at temperatures of - 9 °C and + 25 °C; the muzzle velocities were 1063 ms^{-1} and 1129 ms^{-1} respectively. This experiment was repeated with plasma ignition and muzzle velocities of 1132 m s^{-1} and 1128 m s^{-1} were recorded, with a further test with propellant at + 68 °C giving a muzzle velocity of 1132 m s^{-1}. It is claimed that this was performed with the same ETC ignition energy of 43 kJ. The differences in the conventional ignition case were due both to a faster rise time and a higher peak pressure for the warmer propellant. Pressures for the plasma ignition were very similar in each case.

1.1.11 A further development being investigated in the USA but not currently in the UK, utilises the short and predictable 'ignition delay' (the time required to attain a given pressure) that ETC plasmas can provide. This is the 'fire out of battery' (FOOB) approach [21], which involves locking the gun at the rear out-of-battery position and pre-accelerating the gun forward by letting it go free. The gun fires when it reaches half the normal recoil speed and then decelerates to rest at the out-of-battery position. A

locking mechanism holds the gun in this position ready for the next round. The advantage is a significant reduction in trunnion pull, which allows for a reduction in the parasitic mass of the vehicle design. This has demonstrated a 40% reduction in trunnion force compared with the case of a conventional arrangement firing 17 standard M724 kinetic-energy (KE) training rounds in FOOB mode from a 105 mm M35 cannon with a modified recoil system.

1.1.12 The FOOB approach relies on very accurate predictability of shot start pressure: there is very little margin for error. Getting the ignition timing wrong means the acceleration of the forward moving barrel will not be countered by the backward forces exerted during firing. The magnitude of shot start pressure will vary slightly from round to round with variation in the early combustion processes, controlled largely by the igniter. This will introduce small variations in the deceleration of the barrel. More importantly, the precise moment of shot start will be controlled by the ignition delay. For a conventional ignition system, the ignition method can introduce significantly different round to round ignition delays, both because of the ignition train itself (e.g. the percussion hammer) and the variability in energy transfer processes from igniter material to propellant. Plasma ignition has been shown not to suffer from either of these two disadvantages, making ETC technology attractive as an igniter for FOOB guns.

1.1.13 Figure 2.2 illustrates the variation in ignition delay between similar conventional and plasma ignition tests [22].

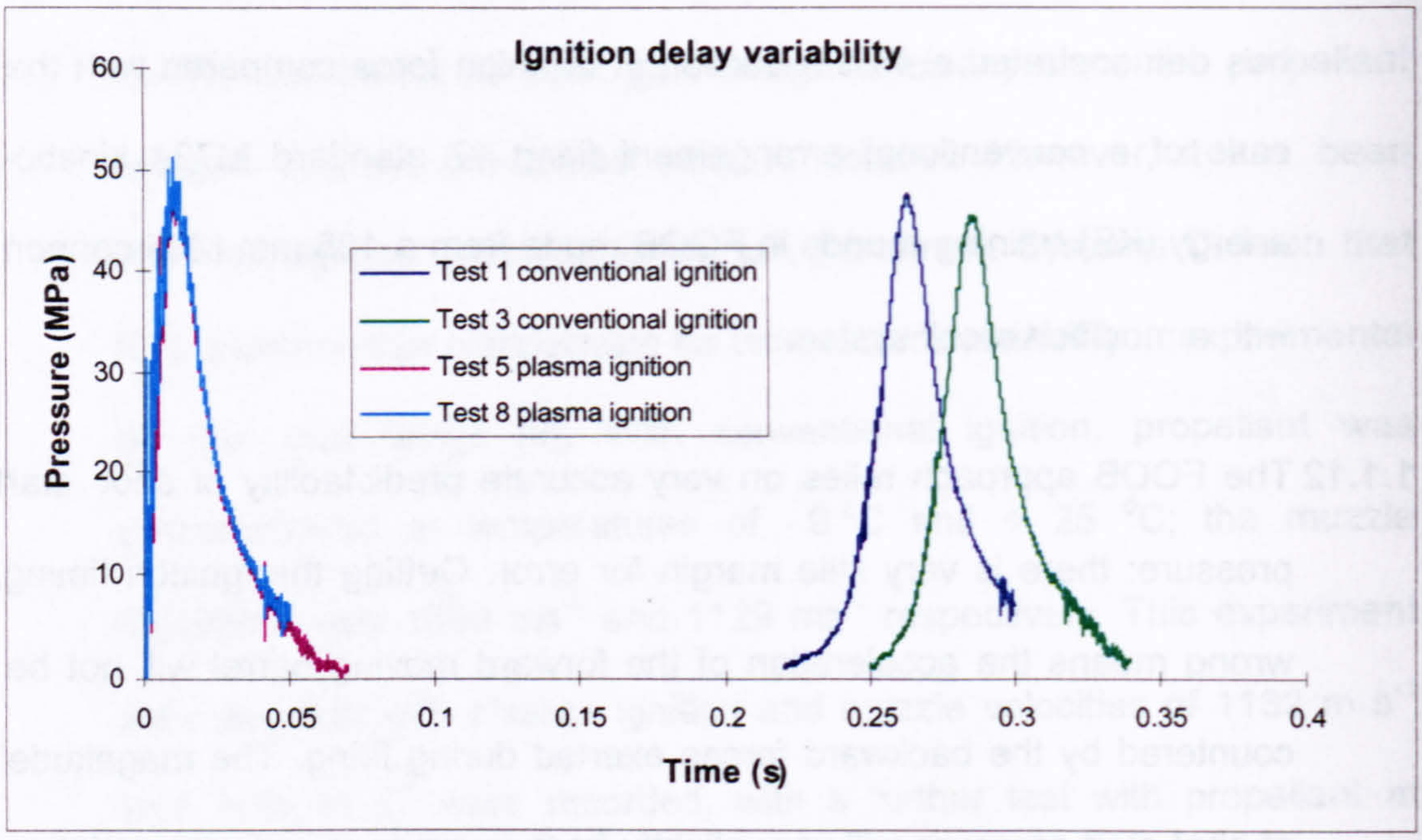

Figure 2.2 Variability in plasma and conventional ignition delays for a 155 mm gun

1.1.14 Although the FOOB concept has not been studied in the UK, some work has been done by the Author relating to the ignition delay of a plasma igniter in a 155 mm gun [23]. This latter work is not discussed in depth in the Thesis due to limitations on length, but ignition delay measurements are described for small-scale closed vessel tests and 155 mm gun chamber simulator tests in Chapters 7 – 9. The conclusions from the 155 mm gun work were that the ignition delay from different plasma discharge energies is predictable and may be a function of charge design. Further, it was found that the lower the discharge energy the higher the muzzle velocity for a given propellant charge weight. This latter conclusion is somewhat counter-intuitive; it was found that there

was a possible correlation between muzzle velocity, discharge energy and shot-start processes, indicating that shot-start pressure may be responsible for this result. Another study conducted by the Author, also partly reported in [23] but not discussed in depth here, concerned the damage to the integrity of the propellant bed during high electric al energy and high discharge power ignition tests at 155 mm. This work used large calibre visualisation tests with macaroni as an inert propellant simulant [24], x-radiographic and fast cine photography [25] and modelling [24]. Standing pressure oscillations occurring along a central ullage tube caused the combustible tube material to burst approximately half-way along the charge, dividing it into two and compacting one portion against the projectile, with the other against the breech face.

1.2 Design of ETC gun systems

1.2.1 An ETC gun is essentially a conventional weapon with some means of introducing electrical energy into the system. Various designs of plasma generator which act as an electrothermal transducer are discussed below. The design actively being pursued at QinetiQ is the capillary plasma generator (CPG) [26]. Figure 2.3 is a schematic diagram of an ETC CPG 155 mm gun system.

1.2.2 The gun system comprises three main elements: the pulsed power supply (PPS), the plasma generator and the plasma/propellant interaction. Options for the PPS will be briefly examined, but this research is still in its infancy and much of the information is restricted.

The plasma generator will be reviewed with emphasis on the work conducted recently within the UK. The plasma/propellant interactions will be identified but discussed in depth in later chapters of the Thesis.

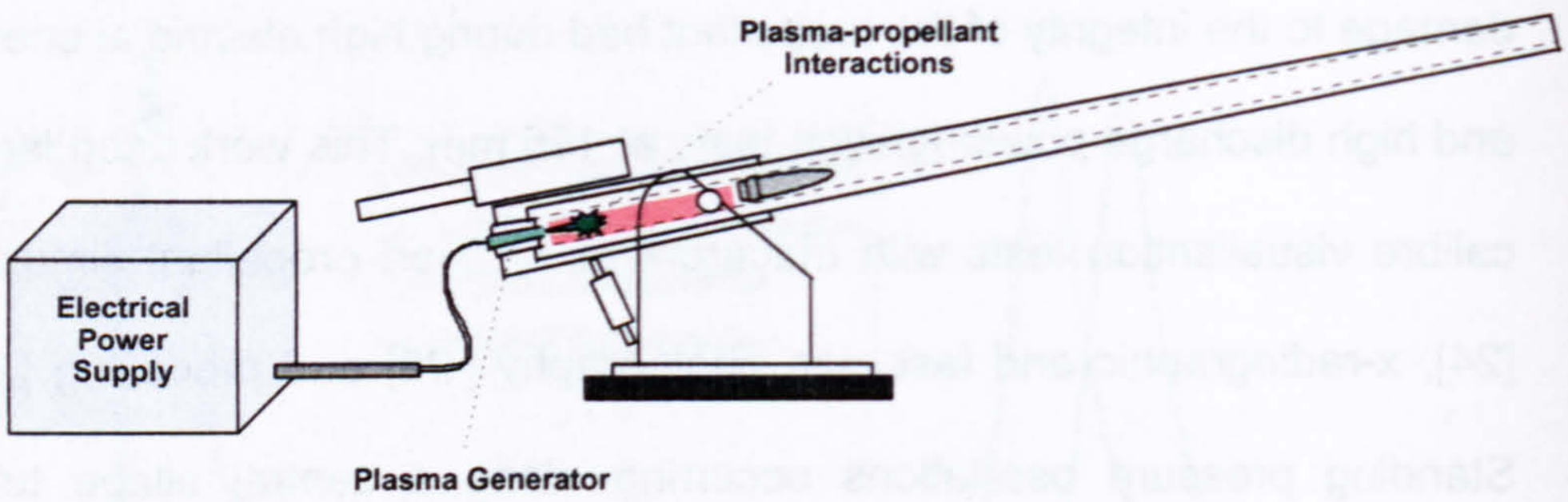

Figure 2.3 Diagrammatic representation of a typical capillary plasma generator ETC gun system

1.3 Pulsed power supply options for the ETC gun

1.3.1 Decisions on which PPS to use with an ETC gun system depend on factors such as space availability, system requirements (energy per round and rate of fire), integration and mobility. A PPS suitable for a main battle tank where plasma ignition alone is required would be different from that in a naval application where the rate of fire and the energy per round may be greater and electrical thermal augmentation is required to maximise the range for naval ground support.

1.3.2 The PPS would require a source of electrical energy referred to as the prime mover [27]. This might be the platform main engine or a dedicated supply such as a diesel generator. If a maximum energy of 10 MJ were used at a rate of two rounds in ten seconds, the prime mover would need to generate more than 2 MW of electric power unless the PPS could

store more than 20 MJ. For a modern warship, this would equate to half the total supply capability of its diesel generators [28]. Transmission of the power from the prime mover to the PPS could be problematic if the main engine is the prime mover. Thermal management of the prime mover is also an issue in a 'silent watch' battle scenario.

1.3.3 Options for the various types of platform PPS are currently under review and a UK integration development programme is underway for both direct and indirect battlefield gun systems. The options include capacitor-based pulse forming networks (CBPFN), rotating machines, inductive (superconducting) storage systems and explosively-driven linear flux compressors. A CBPFN is probably the most advanced solution to an ETC PPS. Current state-of-the-art capacitors have an energy density of around 2.7 MJ m^{-3} (0.37 m^3 MJ^{-1}) [4]. Rotating machines have the greatest potential for energy storage density but the technology is still in the developmental stages; they suffer from excessive vibration and component wear [29]. Superconducting magnetic inductive storage devices require cooling systems and have limited energy storage densities, but may be a long-term solution. The reusable linear flux compressor is a device that reduces the length of a current-carrying solenoid with a piston driven by some chemical energy based engine. The reduction in length amplifies the current due to the conservation of magnetic flux. These devices have the advantages both of high energy densities and an indefinite 'silent watch' capability [30].

1.3.4 The integration of the PPS into a weapons platform would include the incorporation of switching and power transfer systems. The inclusion of smart gun technology would additionally require a fire control system [17].

1.4 ETC plasmas

1.4.1 Electrical energy is transferred to the chamber of a gun via electrical plasma. The plasma forms due to ohmic heating of a conducting plasma initiator: this initiator often takes the form of a length of copper fuse wire or copper strips. Plasma is an ionised gas generally composed of equal numbers of positive ions and free electrons: plasmas are therefore electrically neutral overall but charged on a local scale. The scale length over which separation of charges becomes important is known as the Debye length. An ideal plasma (non-colliding particles) can be defined in terms of the Debye length:

$$\lambda_D = \sqrt{\frac{\varepsilon_0 k T_e}{n_e e^2}} \qquad \textbf{Equation 2.1}$$

where

ε_0 is the permittivity of free space,

k is Boltzmann's constant,

T_e is the electron temperature in electron-volts (the thermodynamic temperature in kelvin divided by 11600 K eV^{-1}),

n_e is the free electron number density and

e is the electronic charge.

1.4.2 A fully ionised ideal plasma's electrical properties can be predicted from the Spitzer expression [31]:

$$\sigma_e = 1.9 \times 10^4 \frac{T_e^{3/2}}{Z_\sigma \ln \Lambda_c} \qquad \textbf{Equation 2.2}$$

where

σ_e is the electrical conductivity,

Z_σ is a corrected value of the ionisation, Z (ion charge number) allowing for an increase in resistivity due to electron-electron collisions and

Λ_c is known as the Coulomb logarithm.

1.4.3 The Coulomb logarithm is related to the collision interactions of the electrons and ions and so depends upon the electron number density, n_e and the plasma electron temperature (often far higher than the ion temperature due to the electric fields accelerating the electrons far more efficiently than the massive ions). It is a very slowly varying function of the plasma parameters. The value of $\ln \Lambda_c$ for solar wind plasmas (with $n_e = 10^7$ m^{-3} and $T_e = 10$ eV) is 26, and for fusion reactors plasmas (with $n_e = 10^{20}$ m^{-3} and $T_e = 1000$ eV) is 18 [32].

1.4.4 ETC plasmas can have number densities greater than 10^{25} m^{-3} and temperatures less than 3 eV [33]. These very low temperatures and high densities make such plasmas difficult to define in terms of plasma theoretical models. The ETC plasmas are non-ideal in that they have very low ionisation due to the low temperature, and the densities of the plasmas produce electron-ion collisions resulting in a higher resistivity than Equation 2.2 might suggest [34]. However, attempts have been

made to correct the Spitzer law for the non-ideal nature of ETC plasmas [35]. It is assumed that the free electron distribution is Maxwellian, and local thermal equilibrium (LTE) conditions prevail. As can be seen, temperature and density (pressure) are important parameters within both gun systems and plasmas.

1.5 Plasma generator options for the ETC gun

1.5.1 The plasma initiator is located either within the gun chamber itself or recessed within a capillary in the breech. There is strong synergy with a conventional igniter over the location of the plasma generator. An electrical pulse, several hundred microseconds to tens of milliseconds in duration, melts and vaporises the plasma initiator. The vapour is poorly conducting and so high voltages are required to break it down into ions and free electrons. The resistance of the plasma rises until the breakdown is complete: this process is studied in more detail in Chapter 4. Once the breakdown is complete, the plasma voltage and resistance fall and remain relatively steady for the duration of the discharge or until events within the chamber (e.g. pressurisation) cause the voltage to change. The discharge will end when its power becomes too low to sustain the plasma arc temperature (and hence conductivity). If the PPS is regenerated by, for instance, the addition of further capacitor banks to the discharge then the latter could feasibly be maintained (or sustained) for a long period of time. Fresh material for the plasma from the plasma generator components (the electrodes or capillary liner) replaces material venting away from the discharge region.

1.5.2 Through the judicious choice of PPS design, one plasma generator can thus be used for ignition, combustion control and post all-burnt thermal augmentation. Igniting a propellant charge is accomplished with a low power discharge. The plasma can then be sustained until just after P_{max} with an even lower power discharge, and combustion controlled (enhancement of the burn rate) with a high powered boost. This may then be followed by a further low powered sustain pulse and finally a high powered 'smart' discharge to complete a full ETC plasma cycle. The ignition sequence may require several tens of kilojoules of electrical energy (half a megajoule if temperature compensation is required); the sustain sequences may require a megajoule each and the enhance and the smart pulses several megajoules each. Hence, around 10 MJ of electrical energy may be required for the full range of ETC options.

1.5.3 Design criteria of a plasma generator must take into account this full cycle of events, plus be optimised for both long low-powered and short high-powered discharges. The components must be re-usable or else easily replaceable for each round. The plasma generator must be able to withstand the pressures in excess of 600 MPa developed in a gun system, as well as be able to discharge electrical energy at these pressures without pressure or electrical failure. Electrical discharges must not interfere with the chamber wall (erosion) or projectile operation (especially with smart munitions). The electrical connections must be able to withstand the recoil forces of the gun. Further, for ignition, the propellant must not constrict the plasma from expanding freely , otherwise

the propellant bed itself may suffer from the forces governing the plasma expansion process [24]. This aspect is revisited in Chapter 7.

1.5.4 Generally, there are two generic types of plasma generator: radial and axial discharge devices. With the criteria listed above, the natural location for a plasma generator is within a conventional disposable metallic cartridge case containing the propellant (plus possibly the projectile). These are currently used by many non-UK military forces and the UK navy. The UK army, however, tends to favour combustible cartridge cases for 155 mm calibre artillery which are cheaper and lack the very hot metal needing disposal between each round. A cartridge case could be pre-assembled incorporating a new plasma generator for each round. The rear face of the metallic cartridge offers a natural contact for the electrical supply and thanks to the incorporation of an insulating section, the cylindrical body provides a return path. The interior of the cartridge would offer protection from the plasma discharge for the chamber walls. Further, it is believed that the plasma-propellant interactions are optimised when developed within the bed of propellant, rather than in a separate chamber.

1.5.5 The method for discharging electrical energy directly into the propellant bed in a radial direction is referred to here as current injection (CI). The CI plasma generator is being investigated by many research groups around the world [36, 37, 38]. The disadvantage of CI is exposure of the plasma to the high pressure propellant gases, which may not be ideal for

the properties of the plasma required. To sustain an arc tens of centimetres long within this environment requires high voltages and currents and therefore more energy. Further, the radial venting of the discharge might not suit a smart gun system in which an axial pressure pulse is required. An alternative type of plasma generator is the capillary plasma generator (CPG) whereby the electrical discharge occurs within a separate chamber or capillary. An electrode is located at the rear of the capillary and the plasma vents axially from an annular nozzle located centrally within the breech of the gun, which also acts as the second electrode. This capillary might be over 150 mm in length and 20 mm diameter. CPGs are also being researched by various groups [39, 40, 41]. The CPG could be renewed for each round in a similar fashion to a conventional breech igniter.

1.5.6 A Piccolo Tube is a radially discharging plasma generator designed to overcome the disadvantage of CI devices. It provides a metallic chamber running the entire length of the combustion chamber axis in which the plasma initiation wire is located. The plasma can develop and be sustained within this chamber. Holes located at regular intervals down the length of the Piccolo tube allow the plasma to vent into the combustion chamber. The Piccolo tube concept is utilised by some conventional igniter designs, but there are no reports of this concept being taken forward beyond conception for ETC gun research, although a perforated central ullage tube is often used in conjunction with CPGs.

1.5.7 The Discharge Rod is a similar device to the Piccolo tube, in that it is located on the central axis of the combustion chamber. This is more exposed to the propellant gases but, due to the design having a number of short plasma initiators, energies required to sustain the plasma can be reduced. This design is being taken forward by some researchers [42].

1.5.8 A type of axially discharging plasma generator which is located on the face of the breech (and resembles a very short CPG) is the Lorentz Force Generator (LFG). This consists of a central electrode surrounded by an annulus. The Lorentz force generated on the plasma arc directs the plasma into the chamber, thus increasing its resistance. This allows more energy to be discharged than the short electrode separation might otherwise suggest. When the arc length increases, a new arc is struck at the LFG module. The plasma can be initiated with very low voltages (possibly without the need for an initiating wire) and sustained with very small power levels because of the short distance between terminals. The device may be used repeatedly with no maintenance if a self-replacing spring-loaded central electrode is used. Due to proximity of the propellant, this device is thought to be just as efficient as a CI method, but as yet no experimental work in the UK has been performed to confirm it. LFG designs are being pursued for some ET 30 mm calibre cannon designs [43].

1.5.9 Although very general figures have been given for the energy requirements of an ignite/sustain/ enhance/sustain and smart discharge,

little work has been reported on real energy requirements for any single plasma generator design, and certainly none for comparative purposes. Work is in progress at QinetiQ with other UK collaborators to determine the requirements of a CPG, mainly resulting from earlier work done on the LP and ET guns [44]. However, designs have been produced at QinetiQ for all of the above concepts and these have been tested on a small (30 mm) scale or at least in the open air. The designs for several radial and axial discharge devices are reviewed below: they are experimental and designed to fit various vessels for small scale QinetiQ ETC studies. These vessels are known as either the Universal vessel (UV) – with an approximate volume of 400 cm^3 dependent upon instrumentation – and the medium scale test vessel (MSTV) – with an approximate volume of 900 cm^3. The vessels have a number of co-planar instrumentation ports for pressure gauges, sapphire windows and burster discs (for vented vessel work). Conventional ignition can be performed with a Gevelot gunpowder primer together with extra small quantities of gunpowder, located within one of the instrumentation ports at the vessels base.

1.6 The current injection plasma generator

1.6.1 Figure 2.4 illustrates one configuration of the UV in CI mode. A barrel is fitted to the front face in this diagram but this can be removed to fit either a sealed face or a closed secondary chamber. Electrical current flows through the positive rear end electrode which has a pressure sealed design. The standard length of the axial initiation wire is around 20 mm,

but this can be varied to almost any length within the 120 mm long chamber. If the electrode separation distance is close to that between the end electrode and the chamber wall, then the current may arc to the chamber wall in an uncontrolled manner. A high density polyethylene liner can be inserted into the vessel to prevent this, but at a reduction to the vessel volume. The side electrode juts into the vessel and acts as a cathode, whilst the body of the vessel is held at earth potential and acts as a return path for the current. The polarity of the electrodes can be reversed if required.

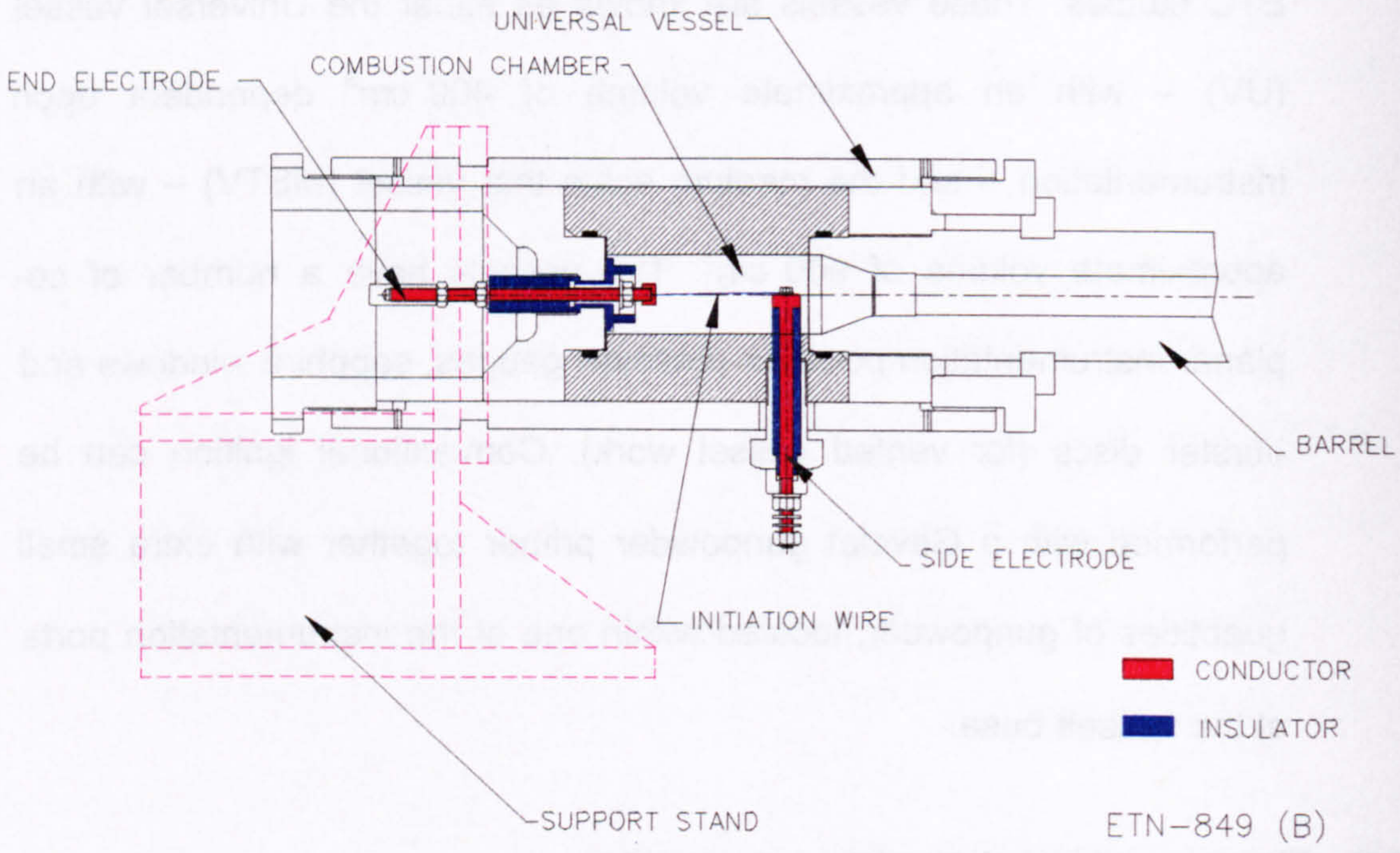

Figure 2.4 Current injection within the Universal test vessel

1.6.2 Although not suitable for a working gun system, the UV in CI closed vessel mode has been used for most of the EGGR studies at QinetiQ because the EGGR effect seems to be enhanced by a factor of around four when compared with CPG tests, making the study more feasible.

However, a high degree of variability has been measured recently [11, 12] which may be due to the set-ups asymmetry. The region of the discharge is unknown, although some work is in hand at QinetiQ to model this. It might be that only a small proportion of the propellant is affected by a 20 mm discharge within a 120 mm long vessel. A further disadvantage of the UV in CI closed vessel mode is that the initiation wire is exposed to the hot combustion gases if under conventional ignition; some doubt has been demonstrated over the condition of the wire at higher discharge pressures of 35 MPa [12]. Measurements made during non-ETC tests showed that wires in CI configuration were susceptible to loss of electrical continuity.

1.6.3 Typically around 48 g mass of propellant gives an effective loading density of around 0.13 g cm^{-3} in the UV. With a high energy discharge, the electrical energy can easily be up to four times greater than the available chemical energy. Although this is an unlikely scenario for a real gun system, it is sometimes desirable in research investigations.

1.7 The Piccolo Tube plasma generator

1.7.1 Figure 2.5 demonstrates the arrangement of a Piccolo Tube plasma generator design. This device represents an attempt to produce a working system from an axially radiating CI plasma generator. The initiation wire is contained within a separate chamber, which may extend for the entire length of the combustion chamber. The rear electrode again acts as an anode and the front face of the piccolo as the cathode. The

discharge is isolated from the main combustion process and the plasma vents through small holes along the length of the piccolo. If the plasma is not used for ignition then the propellant gases initially fill the piccolo ullage. This system has been little researched at QinetiQ due to the perceived disadvantage that the space required for this plasma generator would reduce the propellant loading density.

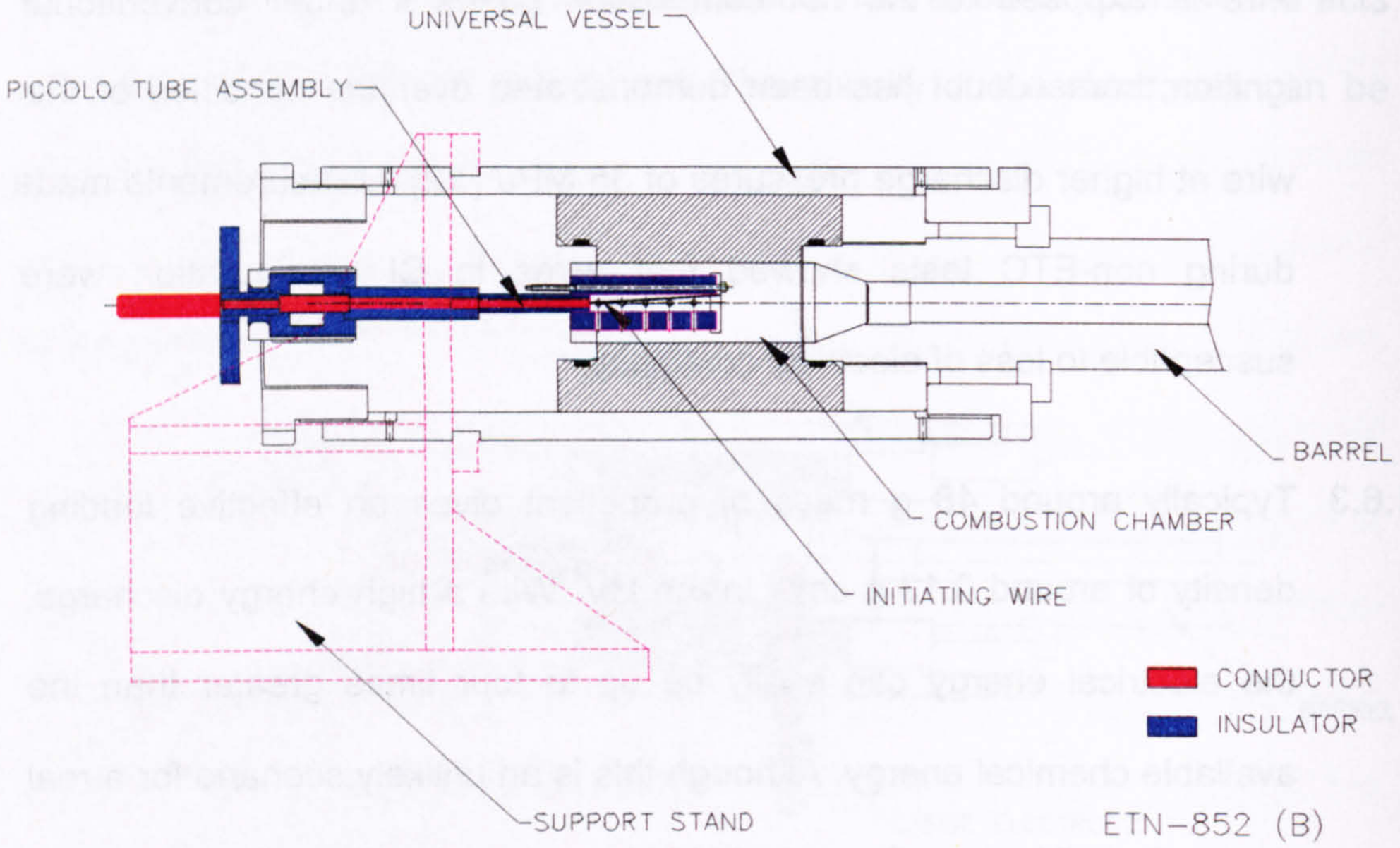

Figure 2.5 Piccolo Tube within the Universal test vessel

1.8 The Discharge Rod plasma generator

1.8.1 Figure 2.6 illustrates the Discharge Rod plasma generator design, which was developed in parallel with the Piccolo Tube as a potential practical large calibre ETC gun system plasma generator.

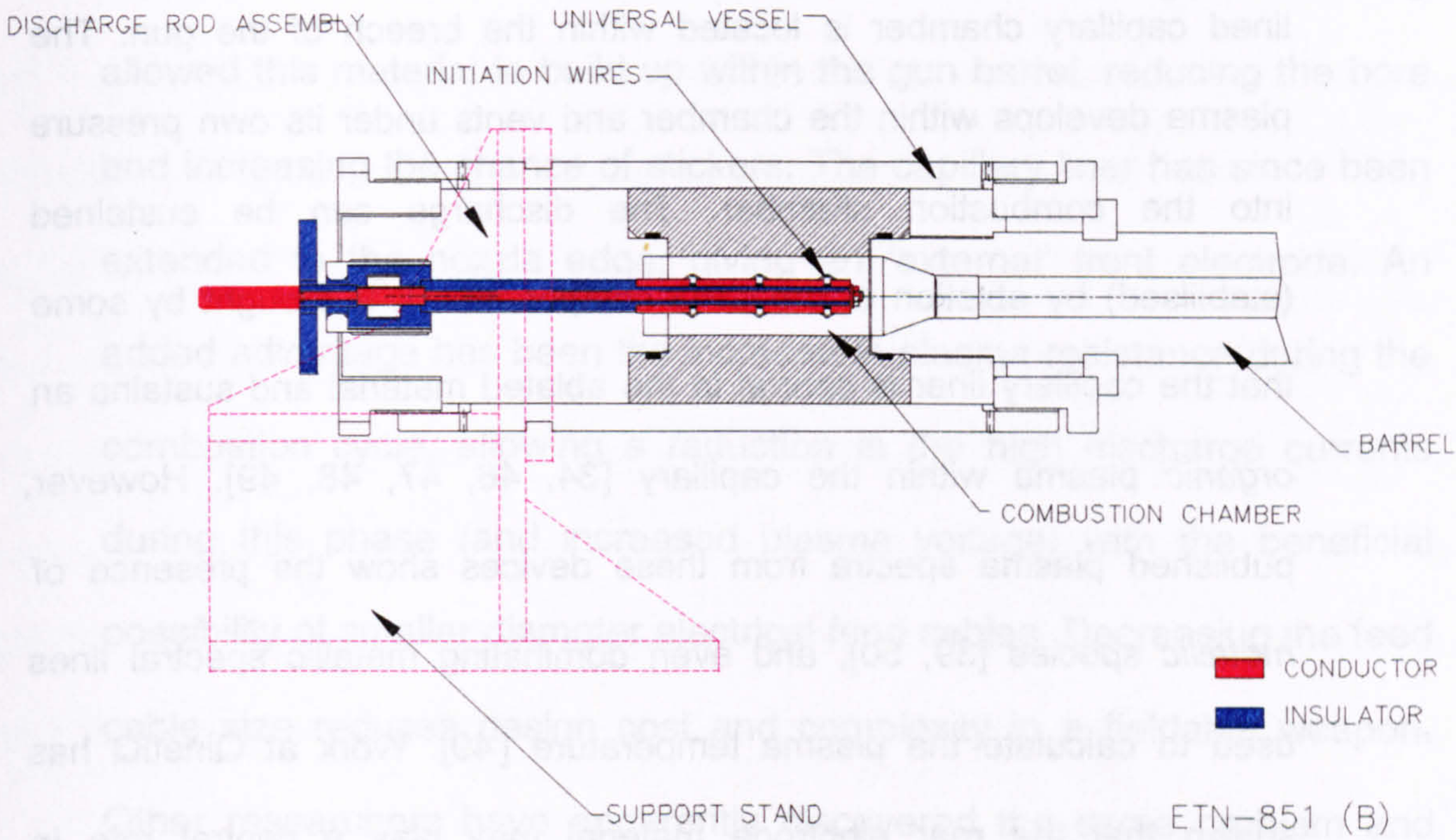

Figure 2.6 Discharge Rod within the Universal test vessel

1.8.2 One single plasma initiation wire is replaced by several short lengths interconnected in series with solid copper washers. The current flows along a central insulated conductor and returns through a number of parallel initiating wire networks. The perceived advantage is that the plasma discharge would be more evenly distributed along the length of the charge, and the plasma could be sustained with a reduction in applied voltage and thus energy. Open air tests have shown an even distribution of plasma plumes radiating from the wire locations, but the device has yet to be tested within a closed vessel.

1.9 The capillary plasma generator

1.9.1 The so-called ablation stabilised arcs [34] are probably the earliest experimental plasma generator designs to be studied for ETC [45]. In the CPG design, a high density polyethylene (known as Lexan in the US)

lined capillary chamber is located within the breech of the gun. The plasma develops within the chamber and vents under its own pressure into the combustion chamber. The discharge can be sustained (stabilised) by ablation of the CPG components. It is thought by some that the capillary liner is central to the ablated material and sustains an *organic* plasma within the capillary [34, 46, 47, 48, 49]. However, published plasma spectra from these devices show the presence of *metallic* species [39, 50], and even dominating metallic spectral lines used to calculate the plasma temperature [49]. Work at QinetiQ has shown that the rear electrode material may play a central role in contributing metallic species to the plasma [51]. Further, Chapter 4 describes the Author's work showing that the plasma initiation wire condensed material remains for a prolonged period of time within the plasma, acting as a metallic mass source. Chapter 6 and Appendix A of this Thesis detail the spectra associated with such plasma.

1.9.2 Figure 2.7 shows the design used for much of the experimentation at QinetiQ: this system has been studied in depth in open air and on small, medium and large scale 155 mm calibre gun firings. The form of the capillary has gone through many evolutions as design implications have arisen. The design in the figure has a parallel capillary, but high pressures tend to distort the capillary rear; a tapered capillary, narrower at the rear, has been used recently. Further, it was found that the mass of material ablated from the nozzle (around 60 g of iron per shot) produced an aerosol of slow-moving iron droplets up to a millimetre in

diameter. Constant use of the CPG in a 155 mm ETC gun eventually allowed this material to build up within the gun barrel, reducing the bore and increasing the chance of stickers. The capillary liner has since been extended to the nozzle edge, giving an 'external' front electrode. An added advantage has been the increase in plasma resistance during the combustion cycle, allowing a reduction in the high discharge currents during this phase (and increased plasma voltage) with the beneficial possibility of smaller diameter electrical feed cables. Decreasing the feed cable size reduces design cost and complexity in a fieldable weapon. Other researchers have apparently discovered the same problem and have recently changed their designs [39, 48].

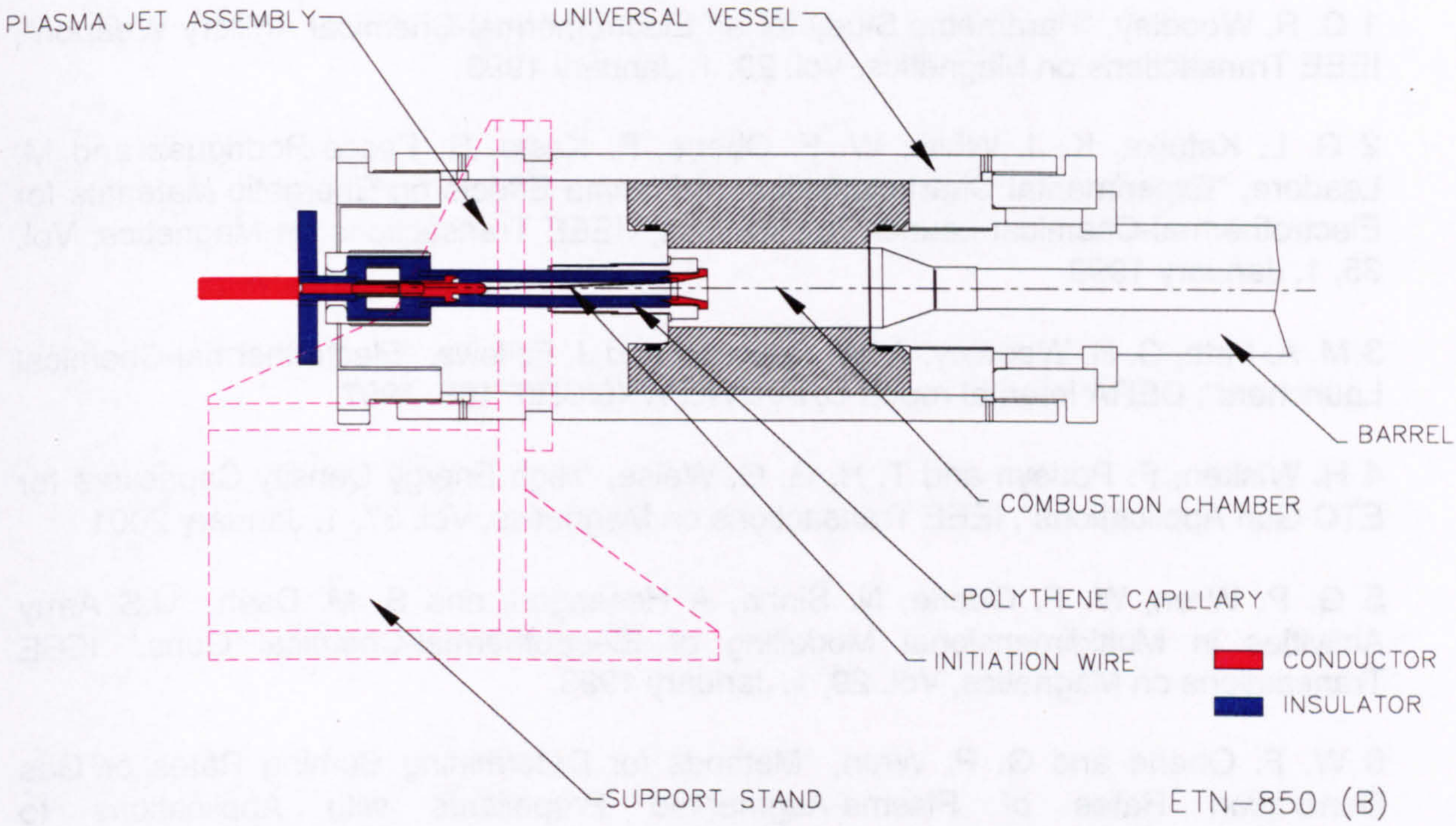

Figure 2.7 Capillary Plasma Generator within the Universal test vessel

1.10 ETC gun development

1.10.1 The cornerstone of fundamental ETC research has been the development of predictive computer models for simulating the operation of various plasma generator designs; eventually these will be included in a fully integrated ETC gun hydrocode model. The CPG has been chosen for incorporation in the plasma generator model EDENET. This code is modular and can therefore be extended to any of the plasma generator designs outlined above. The next chapter looks at the physics underlying EDENET, and its extension to the internal ballistics (IB) of the gun with EDEN-IB.

---

1 C. R. Woodley, "Parametric Study for an Electrothermal-Chemical Artillery Weapon", IEEE Transactions on Magnetics, Vol. 29, 1, January 1993

2 G. L. Katulka, K. J. White, W. F. Oberle, P. Kaste, R. Pesce-Rodriguez and M. Leadore, "Experimental Characterisation of Plasma Effects on Energetic Materials for Electrothermal-Chemical Launch Applications," IEEE Transactions on Magnetics, Vol. 35, 1, January 1999

3 M. A. Firth, C. R. Woodley, A. W. Edwards and J. Fellows, "Electrothermal-Chemical Launchers", DERA internal report DRA/DWS/WX6/CR97188, 1997

4 H. Wisken, F. Podeyn and T. H. G. G. Weise, "High Energy Density Capacitors for ETC Gun Applications", IEEE Transactions on Magnetics, Vol. 37, 1, January 2001

5 G. P. Wren, W. F. Oberle, N. Sinha, A Hosangadi and S. M. Dash, "U.S Army Activities in Multidimensional Modelling of Electrothermal-Chemical Guns," IEEE Transactions on Magnetics, Vol. 29, 1, January 1993

6 W. F. Oberle and G. P. Wren, "Methods for Determining Burning Rates or Gas Generation Rates of Plasma-Augmented Propellants with Applications to Electrothermal-Chemical (ETC) Guns", IEEE Transactions on Magnetics, Vol. 31, 1, January 1995

7 C. R. Woodley, S. J. Billett, "Modelling of Enhanced Gas Generation Rates in a 155 mm ETC gun," IEEE Transactions on Magnetics, Vol. 37, 1, January 2001

8 S. Andreasson and M. U. Carlson, "Results from Initial ETC Closed Vessel Experiments", IEEE Transactions on Magnetics, Vol. 35, 1, January 1999

9 A. Chaboki, S. Zelenak and B. Isle, "Recent Advances in Electrothermal-Chemical Gun Propulsion at United Defence, L.P.", IEEE Transactions on Magnetics, Vol. 33, 1, January 1997

10 C. R. Woodley and S. R. Fuller, "The Effect of Plasma on the Combustion Rates of Solid Propellants", The International Autumn Seminar on Propellants, Explosives and Pyrotechnics, Shenzen, China, 8th – 11th October 1997

11 M. J. Taylor and C. R. Woodley, "Variation in Enhanced Gas Generation Rates in Electrothermal-chemical Closed Vessel Studies", 19th International Symposium on Ballistics, pp 179-186, Interlaken, Switzerland, 7th – 11th May 2001

12 K. Godfrey and M. J. Taylor, "Investigation Into Catalytic Cause Of EGGR" Experiment ET086, unpublished DERA report WSS/WX6/01-ETG/ERD018, May 1999

13 M. J. Taylor, "ET081 - Shocking of Propellant to Measure Enhanced Burn Rate", unpublished DERA report WSS/WX6/01/ERD013, September 1999

14 A. M. Voronov, H. K. Haak and Th. H. G. G. Weise, "The Interaction of Electrothermally Supplied Energy with Compact Solid Propellants", IEEE Transactions on Magnetics, Vol. 35, 1, January 1999

15 C. R. Woodley and S. R. Lumley, "DRA Modelling Activities on Electrothermal Guns", 15th International Symposium on Ballistics, Jerusalem, Israel, 21 – 24th May 1995

16 W. F. Oberle and B. D. Goodell, "The Role of Electrothermal-Chemical (ETC) Gun Propulsion in Enhanced Direct-Fire Gun Lethality", 16th International Symposium on Ballistics, San Francisco, CA, 23rd – 28th September 1996

17 S. R. Fuller and C. R. Woodley, "'Smart Gun' For Artillery Muzzle Velocity Control: Simulations And Experimental Proof Of Principle", IEEE Transactions on Magnetics, Vol. 37, 1, January 2001

18 S. R. Fuller, "ET131 - Smart Gun Ignite and Sustain Capability Test", DERA internal report WSS/WS4/01-ETG/ERD046/1), April 2000

19 S. R. Fuller, S. Gilbert, R. Mills and D. Edwards, "Means for Controlling the Muzzle Velocity of a Projectile (Smart Gun)", UK patent application Number 9622615.4, October 1996

20 S. R. Fuller, C. R. Woodley and C. R. Inglis, "Results from a full scale 'smart gun' trial", 11th Electromagnetic launch Symposium, St. Louis, France, 14th – 17th May 2002

21 "ETC Gun/ammunition Suite on Track for FCS", Jane's International Defence Review, 20th June 2001

22 Grant Savell, DERA internal reports ET102 and ET108, 1999 .

23 M. J. Taylor, "Consideration of the Energy Transfer Mechanisms Involved in SPETC Ignition Systems", 11th Electromagnetic launch Symposium, St. Louis, France, 14th – 17th May 2002

24 M. J. Taylor, "ET136 - Ignition by Copper Vapour Deposition: 155 mm Simulation", unpublished DERA report DERA/WSS/WS4/58-ETL/ERD010

25 M. J. Taylor, "ET157 - Visualisation of the Ignition by Plasma of a UPCS in a Transparent 155 mm Simulator", Unpublished DERA report LWS/WS4/58-ETL/ERD018, April 2001

26 D. C. Haugh and M. A. Firth, "The UK Electric Gun Programme for the Millennium", IEEE Transactions on Magnetics, Vol. 37, 1, January 2001

27 S. Fuller, "Pulsed Power Supply Integration Study for a Naval ETC Gun", MSc Dissertation, University of Salford, 1998

28 D. Miller, "Surface Warship Propulsion", Jane's International Defence Review, 10, November 1994

29 M. Pichot et al, "Active Magnetic Bearings for Energy Storage Systems for Combat Vehicles", IEEE Transactions on Magnetics, Vol. 37, 1, January 2001

30 Y. Wang, J. Li, Z. Wang, M. Gao and Y. Cao, "A Mathematical Model of the Reusable Linear Flux compressor", IEEE Transactions on Magnetics, Vol. 37, 1, January 2001

31 I. H. Hutchinson, "Principles of Plasma Diagnostics", Cambridge University Press, Cambridge, 1987, p18

32 R. J. Goldston and P. H. Rutherford, "Introduction to Plasma Physics", Institute of Physics Publishing, Bristol, 1995, p170

33 J. Batteh, J. Powell, D. Sink and L. Thornhill, "A Methodology for Computing Thermodynamic and Transport Properties of Plasma Mixtures in ETC Injectors", IEEE Transactions on Magnetics, Vol. 31, 1, January 1999

34 J. D. Powell and A. E. Zielinski, "Capillary Discharge in the Electrothermal Gun", IEEE Transactions on Magnetics, Vol. 29, 1, January 1993

35 L. L. Raja, P. L. Varghese and D. E. Wilson, "Modeling of the Electrothermal Ignitor Metal Vapor Plasma for Electrothermal-Chemical Guns", IEEE Transactions on Magnetics, Vol. 33, 1, January 1997

36 K. Gruber, K. Kappen, A. Voronov and H. Haaks, "Radiation Absorption of Propellant Gas", IEEE Transactions on Magnetics, Vol. 37, 1, January 2001

37 S. Andreasson and M. U. Carlson, "Results from Initial ETC Closed Vessel Experiments", IEEE Transactions on Magnetics, Vol. 35, 1, January 1999

38 J. Jung, Y. Lee, K. Yang, J. Kim and J. Chu, "Overview of ETC Program in Korea", IEEE Transactions on Magnetics, Vol. 37, 1, January 2001

39 R. Alimi, A. Borenstein, C. Goldenberg, L. Perelmutter, A. Pokryvailo, N. Shafir, S. Wald, E. Weiss, D. Zoler and M. Shapira, "ETC research at Soreq NRC, Israel, IEEE Transactions on Magnetics, Vol. 37, 1, January 2001

40 H. D. Fair, "The Science and Technology of Electric Launch", IEEE Transactions on Magnetics, Vol. 37, 1, January 2001

41 D. C. Haugh and M. A. Firth, "The Electric Gun UK National Overview", IEEE Transactions on Magnetics, Vol. 37, 1, January 2001

42 A. Kay, J. Raupp, D. Mura, C. Steinbach, D. Hensel and H. Peter, "Plasma ignition of consolidated propellants in a 60 mm ETC gun", 19th International Symposium of Ballistics, Interlaken, Switzerland, May 2001

43 A. V. Budin, A. A. Bogomaz, V. A. Kolikov, Ph. G. Rutberg and A. F. Savvateev, "Multipulse Discharge in the Chamber of Electric Discharge Launcher", IEEE Transactions on Magnetics, Vol. 35, 1, January 1999

44 G. Savell, "Liquid Propellant Gun Performance", DRA internal report DRA-MIL-GWP-15-91-WS5, 1991

45 E. Z. Ibrahim, "The Ablation Dominated Polymethylmethacrylate Arc", J. Phys. D: Appl. Phys. 13, p 2045, 1980

46 W. F. Oberle and G. P. Wren, "Further studies concerning the energy distribution in the ETC closed chamber and the impact on observed propellant burn rate", IEEE Transactions on Magnetics, Vol. 37, 1, January 2001

47 M. J. Nusca, M. J. McQuaid and W. R. Anderson, "Development and Validation of a Comprehensive Model of the Plasma Jet Generated by an Electrothermal-chemical Igniter", 19th International Symposium of Ballistics, Interlaken, Switzerland, May 2001

48 L. Perelmutter, M. Sudi, C. Goldenberg, D. Kimhe, Z. Zvi, S. Arie, M. Melnik and D. Melnik, "Temperature Compensation by Controlled Ignition Power in SPETC Guns", 16th International Symposium on Ballistics, San Francisco, CA, September 1996

49 J. Caillard, C. Delzarra and L. Brunet, "Experimental Assessment of a 1 kJ Electro-pyrotechnic Device Ignited in the 300-1000 V Range for ETC Studies", IEEE Transactions on Magnetics, Vol. 37, 1, January 2001

50 J. M. Kohel, L. K. Su, N. T. Clemens and P. L. Varghese, "Emission Spectroscopic Measurements and Analysis of a Pulsed Plasma Jet", IEEE Transactions on Magnetics, Vol. 35, 1, January 1999

51 M. J. Taylor, "Measurement of the Properties of Plasma from ETC Capillary Plasma Generators", IEEE Transactions on Magnetics, Vol. 37, 1, January 2001

Chapter 3 – Modelling

1 Introduction

1.1 Benefits

1.1.1 The progression from development of a new concept to an optimised device requires a thorough understanding of the underlying physics. This understanding comes primarily from physical experimentation designed to test hypotheses regarding the nature of pertinent physical interactions. Often, such experimentation is resource expensive, and many of the physical characteristics prove difficult to measure. A predictive modelling capability, however, allows 'virtual' experimentation to be accomplished more cost-effectively than test firings alone, as well as providing information on the various properties that are difficult to measure directly.

1.1.2 Gun research is a very demanding area of study: many of the basic physical and chemical interactions are not well understood. This is partly because in the past there has been so much room for improvement in gun design that refined understanding was not necessary. The extreme physical conditions of pressure, temperature and timescale have also meant that metrology has simply not been possible. Gun systems are now so fully optimised, however, that further improvement requires ever greater effort. With the advent of ETC research, the subject's complexity has increased even further, especially as so little is known about organometallic plasma at the phase conditions pertinent to ETC technology. It is becoming

increasingly important to understand how conventional gun systems operate, in order to comprehend the perturbation of electrical energy on the system. Thus, computer simulation of internal ballistic events together with codes describing the operation of plasma generators are needed to assist in the understanding and eventual optimisation of ETC weaponry.

1.1.3 Various internal ballistic and propellant burn models have been employed for the work described in this Thesis. These are described here very briefly, as the Thesis aims to provide a description of the development of ETC rather than conventional guns. However, rather more attention is paid to the capillary plasma generator codes, whose development into a fully predictive ETC model is a main impetus behind the experimental work described in later chapters.

2 Internal ballistics modelling

2.1 Introduction

2.1.1 Interior ballistics codes have been used for several decades to further the understanding of the fluid dynamics of gun systems. Four interior ballistics codes used with some regularity within QinetiQ are:

- CTA1V2 [1]
- WAFBC1CHEM [2, 3]
- FHIBS [4]
- BRLCB version 3 [5, 6]

2.1.2 No input to these codes is required other than defining tasks to be completed by modelling staff. It is their decision as to which model is most appropriate, but then the Author must interpret the output from the models. The following paragraphs briefly summarise the codes listed.

2.2 CTA1V2

2.2.1 This one-dimensional (1D) multiphase computer fluid dynamic code solves equations for mass, momentum and energy for both solid and gas phases. It simulates both conventional and ETC guns. The projectile shot motion is predicted from the following: defined igniter, propellant combustion (Vieille's law), interphase drag (i.e. effect of combustion gases upon the condensed propellant, and pressure oscillations within the gun chamber), intergranular stresses, projectile engraving process (shot start pressure), heat transfer to the barrel and fume extraction. The ETC discharge is modelled from a tabular input of electrical power and location of the input within the gun chamber. One of the assumed energy transfer mechanisms from the plasma to the propellant is radiative, and so the Stefan-Boltzmann radiation law is used.

2.3 WAFBC1CHEM

2.3.1 This 1D code is similar to CTA1, with the addition of modelling interphase heat transfer and gas phase chemistry. The model assumes heat transfer to the propellant through conduction, convection and radiation. The gas phase chemistry sublimates the solid propellant

endothermically to form a reactive fuel and oxidiser mixture. This mixture reacts to release thermal energy and (unspecified) inert product gases with global properties.

2.4 FHIBS

2.4.1 The Fort Halstead Internal Ballistics Software is a two-dimensional (2D) multiphase model. It is otherwise similar to WAFBC1CHEM.

2.5 BRLCB

2.5.1 This code was obtained from the Army Research Laboratory of the United States, under a technical co-operation programme. It is a lumped parameter 0D code capable of closed vessel and vented vessel work but, unlike the codes referred to above, it cannot model guns.

3 Thermochemical and chemical kinetics codes

3.1.1 The internal ballistics codes introduced above use semi-empirical burning models. The fit of physical experimental metrics such as chamber pressure and projectile acceleration allow other parameters to be deduced such as solid propellant surface regression (i.e. burn) rates, heat transfer and the way these parameters vary under differing conditions. The internal ballistics codes used for the work described here do not attempt to model the propellant burn in any detail; there is no discrete nature to the propellant burn zone, for example.

3.1.2 Development work is being undertaken, however, on theoretical propellant chemistry to deduce the burn rate of propellants from their

chemical composition. This is important because there are many variables in internal ballistics codes, and when electrical energy is introduced, various perturbations to the combustion system can be explained by more than one parametric change. It thus becomes difficult to assess which interaction processes may be responsible for these perturbations. With thermochemical and chemical kinetics schemes, the list of important parameters becomes more obvious, enabling a greater chance of optimising the system.

3.1.3 The development of thermochemical kinetics codes is still in its infancy and little of the Thesis work is concerned with its progress. However, the eventual aim is to unite various internal ballistics codes with plasma generator codes as well as reduced chemical kinetics schemes. The codes used for this work are CHEETAH [7] and CHEMKIN [8], both commercially available. CHEETAH is a thermochemical equilibrium code capable of simulating reactions, predicting the products and liberated energy, but not the reaction pathways themselves. CHEMKIN is a chemical kinetics code for predicting reaction rates, reaction pathways and products. CHEMKIN is a 1D temporal and spatial code.

4 Plasma generator modelling

4.1 Introduction

4.1.1 The eventual development of the ETC gun system is likely to be heavily dependent upon optimisation of ETC subsystems. These include prime

energy source and PPS design, energy transfer systems, plasma generator design and plasma-propellant interactions.

4.1.2 Many researchers have been developing models for ETC research over a decade [9, 10, 11]. The most recent work has attempted predictions of plasma radiation absorption in pressurised propellant gases [12] and distribution of the current pathways throughout a CI mode ETC plasma discharge [13, 14].

4.1.3 The Author has been heavily involved in the development of EDENET for four years. It is clearly stated in this Chapter which improvements are directly attributable to the Author. In addition, the Author has made many contributions towards the development that are less direct and less easy to separate from the contributions of others.

4.2 Capillary plasma generator modelling at QinetiQ – EDENET

4.2.1 The QinetiQ ETC modelling programme has been under development since the early 1990s, based on code developments for the LP and ET projects [15]. Development work has been contracted to Fluid Gravity Engineering Ltd.

4.2.2 The physics of the CPG is strongly 2D, with the physical properties having gradients in both the axial and radial directions. However, a fully 2D model would be expensive in computer processing unit time; a 1.5' dimensional (1.5D) approach allows the modelling to be complet ed in a few hours on a conventional desk-top personal computer. With the

1.5D approach, radial and axial components are run separately but the results from one component can be used as inputs to the other. The multi-species Eulerian hydrodynamics codes, still under development, currently support a 1.5D modular model called EDENET [16]. The hydrocode concept is based on calculating the physical properties of one cell and passing these to adjacent cells. Each main model comprises a number of sub-models or subroutines responsible for different subsystems within the CPG. This modular nature permits extensions and alterations for different plasma generator designs with the addition of separate models for the chemical kinetics of the combustion chamber.

4.2.3 Figure 3.1 shows a schematic diagram of the salient physics features in EDENET version 4 axial mode. EDENETs main features are:

- an electrical circuit (PPS) model
- joule heating effects
- wire vaporisation model
- magnetic diffusion (1D radial)
- thermal and radiative diffusion models (1D radial)
- electrode erosion
- Desjarlais [17] experimentally validated [18] electrical conductivity data in the liquid vapour transition region and
- SESAME [19] tabular equation of state (EOS).

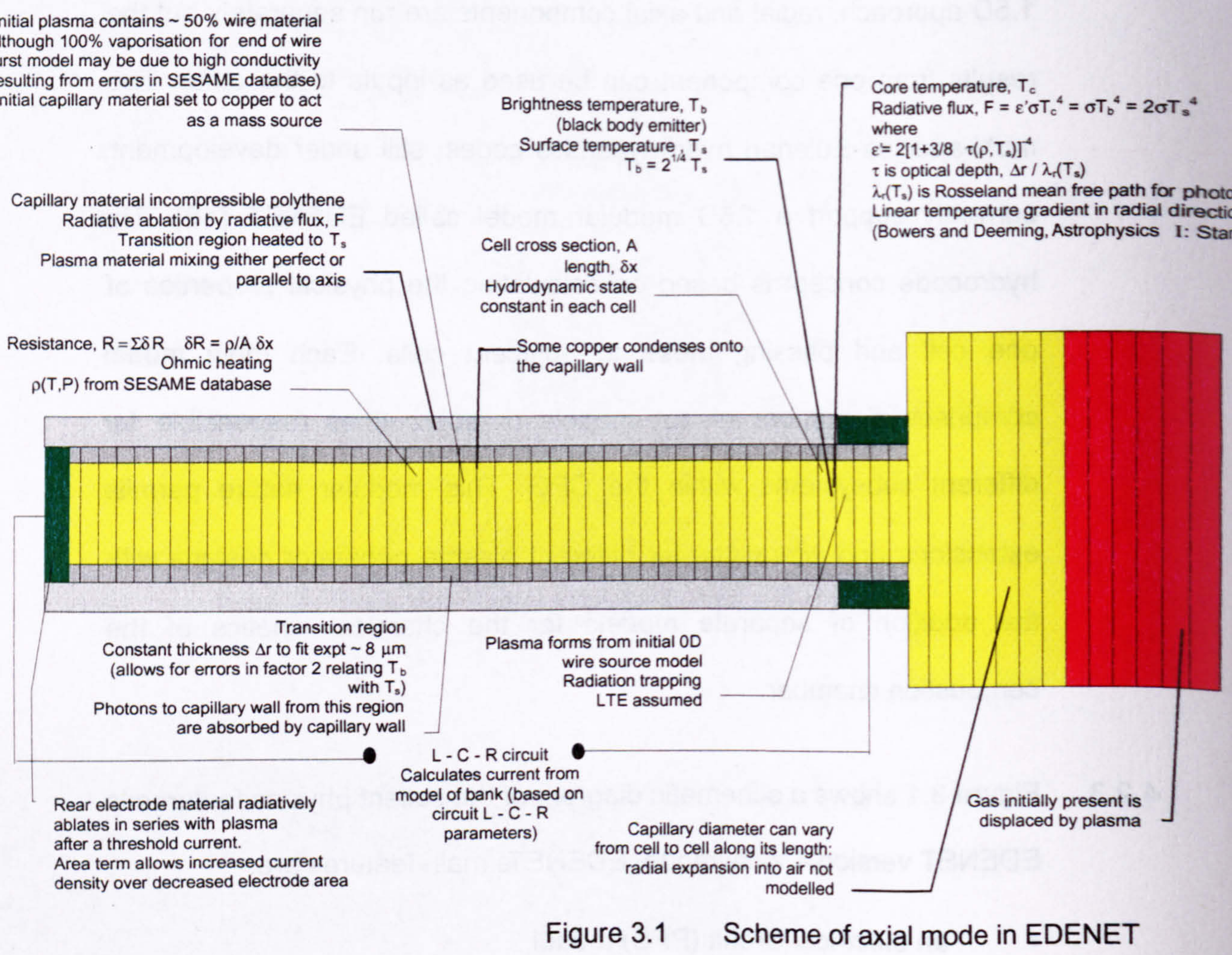

Figure 3.1 Scheme of axial mode in EDENET

4.2.4 EDENET has to fit several experimental metrics: current, voltage, capillary pressure, plasma brightness temperature and component integrated erosion. If these parameters can be matched for a wide range of test conditions without recourse to manually input scaling factors, then the model can be described as predictive. Predicted mass and energy flux venting from the capillary could then be input parameters for internal ballistics codes.

4.2.5 Typical voltage and current profiles from exploding wire experiments appear in Figure 3.2. Although the details change with the test

conditions, there are some general features that are common to most tests.

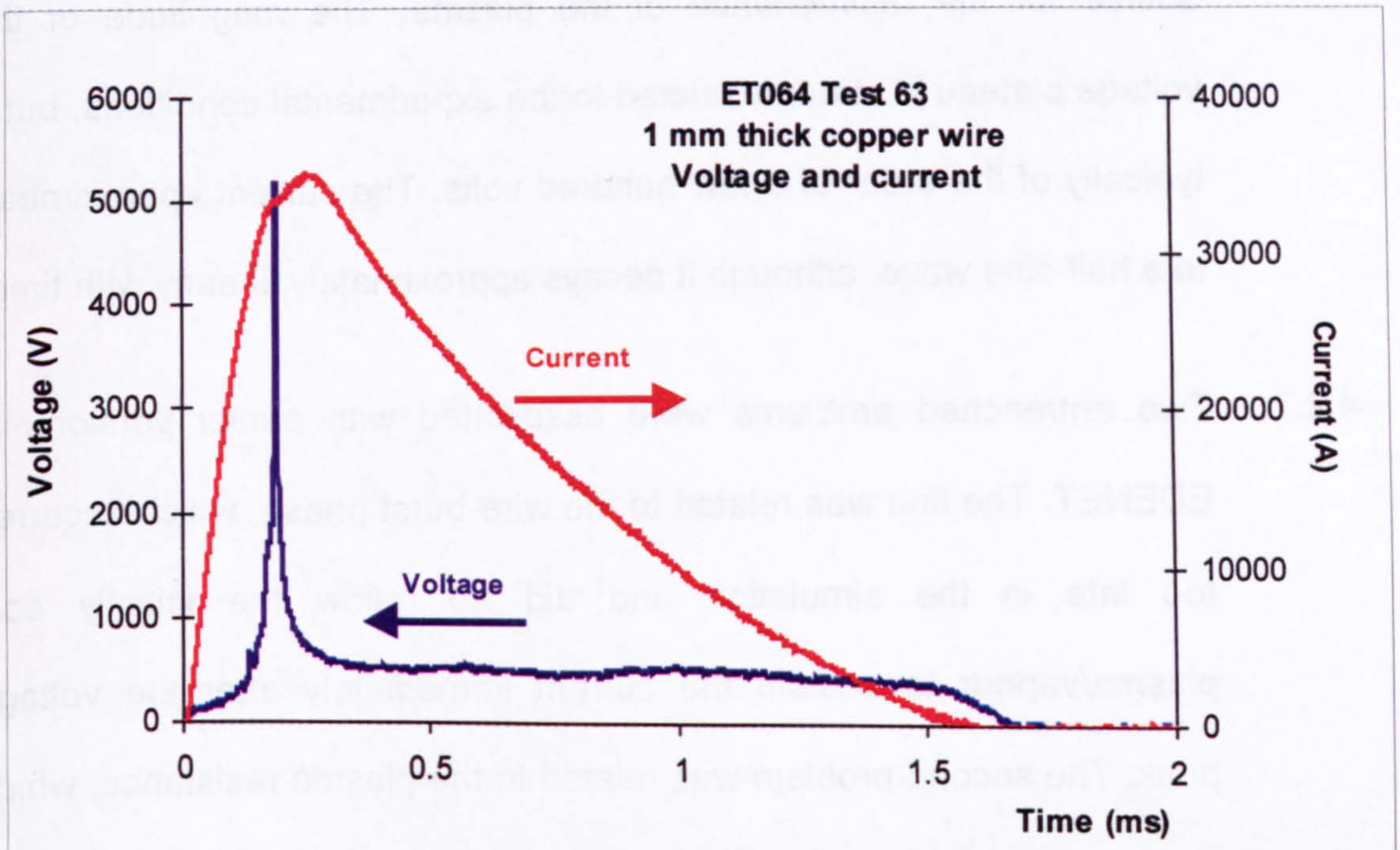

Figure 3.2 Typical voltage and current profiles for exploding wires under ETC conditions

4.2.6 In brief, the voltage initially rises slowly in a manner associated with inductive effects and ohmic heating of the wire. The spike in the voltage trace has been identified as relating to fragmentation of, and plasma development around, the wire and begins shortly after the melt phase (see Chapter 4). The rapid rise and fall in voltage results from changes in plasma resistance, as the current over this period is reasonably constant. This peak in the voltage (resistance) is known as the 'wire-burst'; the wire fragmentation is accompanied by a small inflection in the current profile. For unconfined wire explosions in air, the voltage spike is followed by a voltage plateau which has been sustained for

experimental purposes through the discharge of additional capacitor modules, with material ablated from the electrodes acting as a mass source for the maintenance of the plasma. The magnitude of this voltage plateau is strongly related to the experimental conditions, but is typically of the order of a few hundred volts. The current approximates to a half-sine wave, although it decays approximately linearly with time.

4.2.7 Two entrenched problems were associated with earlier versions of EDENET. The first was related to the wire-burst phase, which occurred too late in the simulation and did not allow the initially cool plasma/vapour to sustain the current immediately after the voltage peak. The second problem was related to the plasma resistance, which was too low after peak current and did not allow for a match with the linear decay in current.

4.2.8 The time to wire-burst has previously been corrected for by applying two scaling factors. The first involved pre-warming the wire so that less energy was required to vaporise it, and the second was to fix the initial conductivity (i.e. temperature) of the plasma to ensure that it could support the current.

4.2.9 Currently, the computed plasma resistance is 'fixed' to match observed values of current decay by adding polythene - notionally ablated from the capillary wall - to enter the flow. The polythene's relatively high specific heat acts to constrain the temperature of the plasma and (by extension) its conductivity. Although this technique is generally

successful in matching current data, it is consistently accompanied by over-predicting capillary pressure, suggesting that in fact too much mass is entering the flow. Obviously, these fixes are artificial and so properties such as mass flow and energy flux from the capillary are likely to be erroneous (this is further investigated below). Details of various sub-models within EDENET are now described.

4.3 Electrical circuit model

4.3.1 The electrical circuit model comprising inductance, capacitance and resistance (LCR) treats the CPG as a variably resisting load. This part of the model is easily validated experimentally by replacing the CPG with a constant resistance load. The PPS used for experimental research at QinetiQ is an 800 μF, 500 kJ capacitor bank composed of ten identical modules [20]: system inductance can be varied from tens to thousands of microhenries. EDENET has been shown to have a predictive capability for the PPS.

4.4 Wire explosion model

1.1.1 Current from the PPS passes through the plasma initiator. The development of this sub-model has been one of the successes of the work conducted by the Author. This experimental work is described in detail in Chapter 4 but the evolution of the sub-model is outlined here.

4.4.2 A previous 'wire burst' model where the evaporation of the wire was treated zero dimensionally in the axial mode proved to be physically incorrect. In this model the material was treated as homogeneous and

could be any specified material of any dimension. The wire was heated uniformly and its density remained constant until all the wire had evaporated. The resistance of the wire increased due to the increased heating rather than any reduction in wire diameter. Once enough energy had been transferred to evaporate the entire wire, the wire burst model was turned off and the system hydrodynamics treated as for a uniform plasma. The sudden switch in state-space was accompanied by a sudden drop in circuit resistance, which poorly matched experimentation. However, the experimental conductivities were approached more closely if the amount of internal energy of the wire was artificially increased, causing the resistance peak to occur slightly earlier.

4.4.3 Once the wire had evaporated totally, the internal energy of the system was re-adjusted. Further, the mass of wire material needed to match the data was adjusted so that only 50% produced the plasma. The justification for this mass adjustment was that wire material (copper) could be evaporating from the wire and condensing partly onto the capillary. Re-evaporation was modelled by making the capillary wall material from copper rather than high density polyethylene. No physical justification was possible for increasing and decreasing the internal energy.

4.4.4 In the improved 'wire source' model, some specified fraction of the wire was allowed to evaporate with no hydrodynamics or electrical

conduction in the vapour. At this point, the plasma hydrodynamics were calculated but electrical conduction in the reduced residual wire was also taken into account. This situation remained until all the wire material had evaporated. However, the wire source model provided very little improvement over the wire burst model. It was hoped that the only free parameter would be the fraction of the wire evaporated, but the mass and energy still needed adjustment to fit experimentation and the capillary wall material was still set to that of the wire.

4.4.5 One problem remaining with the scheme was that material from the wire instantaneously and uniformly filled all the cells and as the hydrodynamic state of each cell was constant, excessive evaporation from one segment of the wire did not produce a high density in that region of the capillary. This unphysical situation needed refinement. Further, the inaccuracies in the material properties at that time, especially the transport properties of electrical and heat conductivities, were likely to obscure small improvements to the model.

4.4.6 It is stated in reference [21] that the electrical conductivity of the metal vapour under exploding wire conditions was the most difficult part of the process to model. Previously, EDENET made exclusive use of SESAME's ('Rinker') transport data. The SESAME tables consist of a library of data obtained from both experiments and theoretical calculations, created by Los Alamos National Laboratory. The tables are used regularly within ETC codes [10, 22, 23], their applicability in

ETC work (particularly the wire-burst phase) is questionable – in many instances extrapolation is required to compute data at states attained by the CPG plasma. A particular example of this problem is the calculation of electrical conductivity for the condensed wire, which is clearly orders of magnitude out when extrapolated from SESAME data. Further, the vapour phase for copper was treated as a perfect insulator, requiring the model to transition between condensed phase and plasma whilst avoiding the vapour stage to avoid infinite resistance. Thus, low confidence in the materials data has led to low confidence in the predictive capability of EDENET, and instead towards a possible means of improvement.

4.4.7 Recently published work by Desjarlais [17] has provided experimentally validated electrical conductivity data [18] in the liquid vapour transition region that improve on this situation by allowing some current to flow through the copper vapour; Rinker data treat the vapour as a perfect electrical insulator. The conductivity of liquid copper at atmospheric pressure as calculated from Desjarlais'work is in excellent agreement with that from Dyos [24].

4.4.8 Figure 3.3a shows copper conductivity data by Rinker with the data as presented in the work by Desjarlais in Figure 3.3b. The Rinker data show zero conductivity in the region where copper vapour exists (cross in figure), whilst Desjarlais'data show continuity in finite conductivity for all state space.

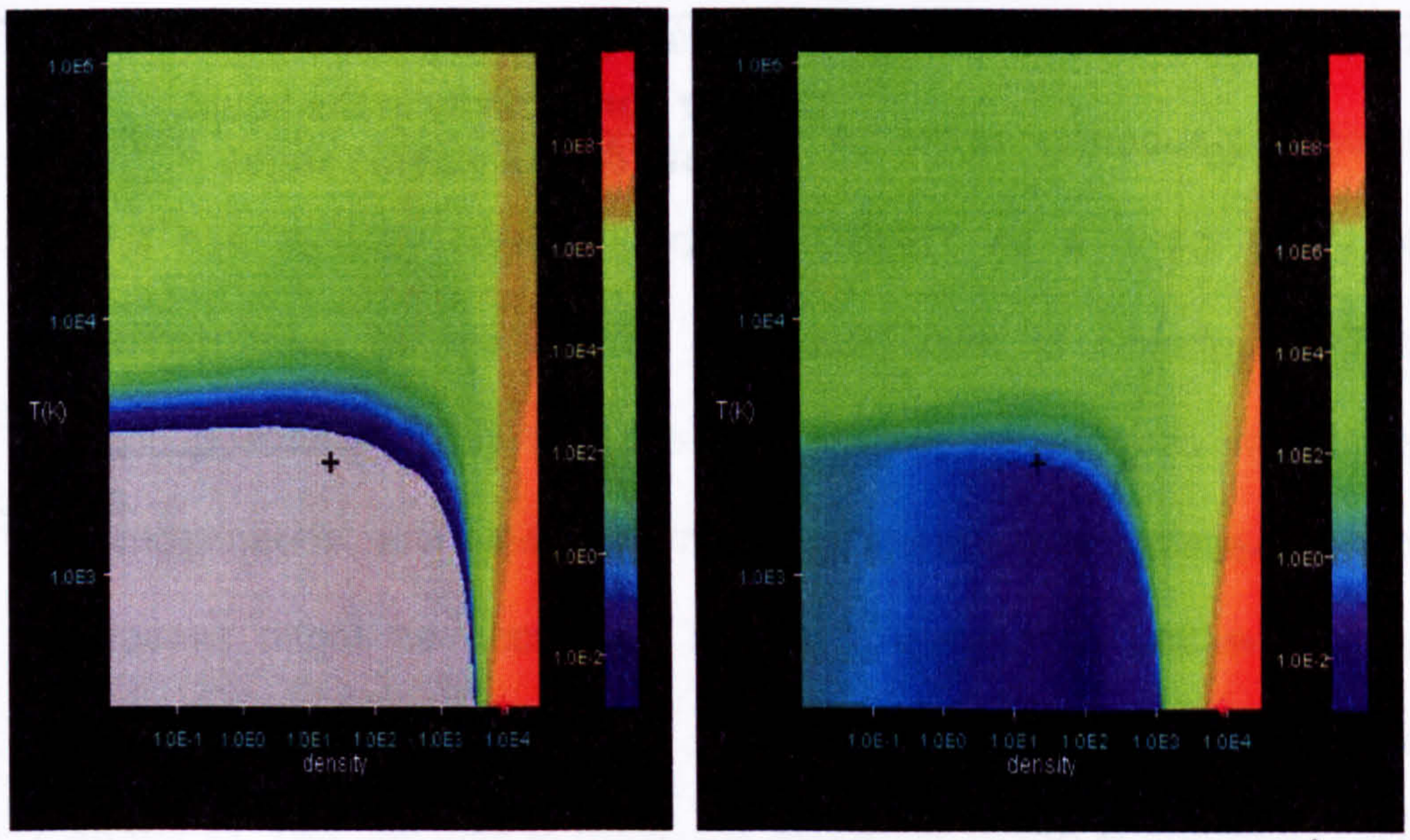

Figure 3.3 (a) Rinker [19] and (b) Desjarlais [17] electrical conductivity data for copper

4.4.9 Figure 3.4 and Figure 3.5 show these data interpreted by the Cu_3 EOS within SESAME at atmospheric pressure. The thermal conductivity can be estimated from the electrical conductivity. Desjarlais' transport data allowed a reasonable current to be supported immediately after the wire-burst without the need for conductivity scaling, although the inflection in the current was still larger than would be measured experimentally.

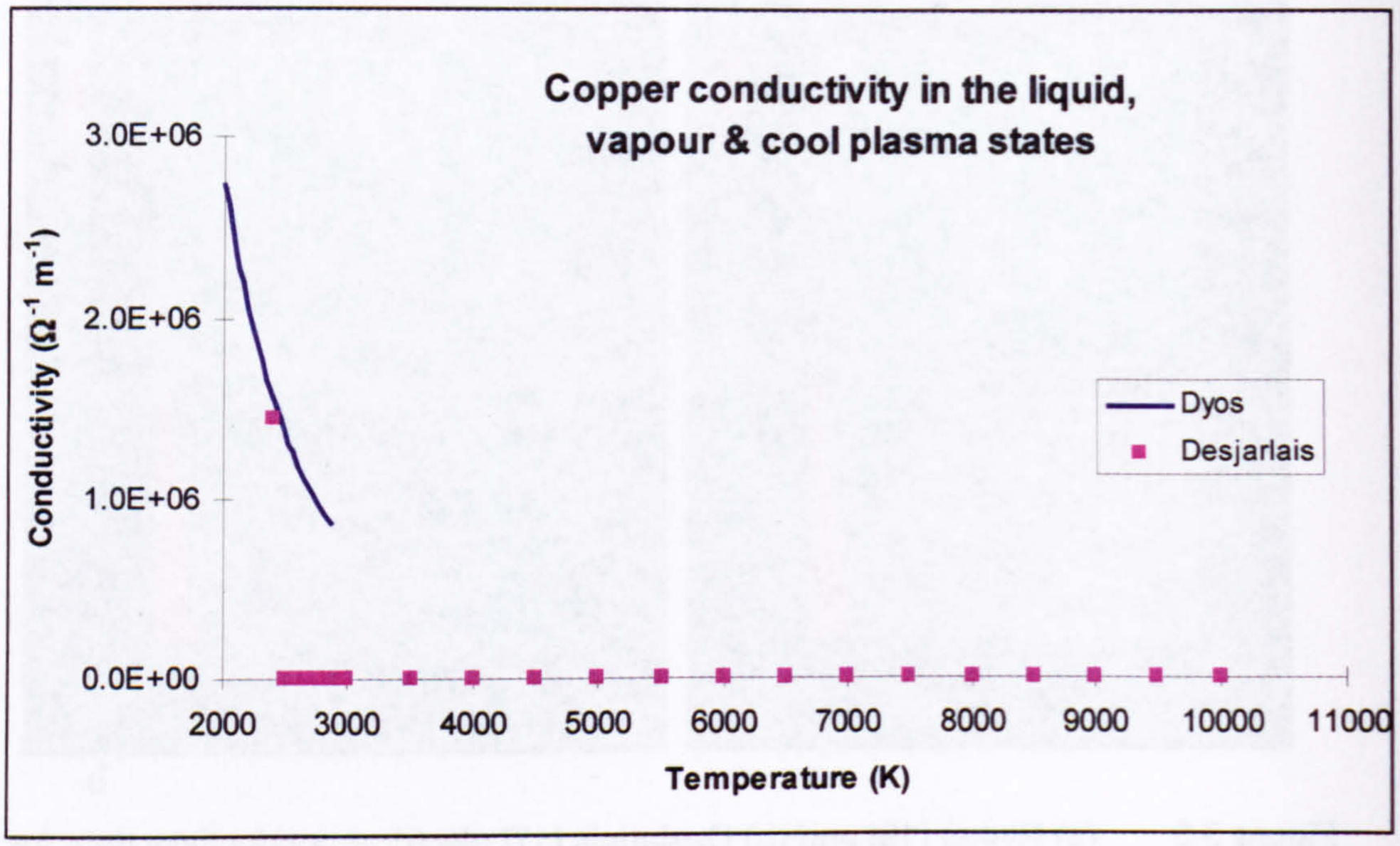

Figure 3.4 Conductivity of liquid, vapour and plasma states from Desjarlais interpreted by Cu_3 EOS within SESAME – Copper liquid, vapour and plasma

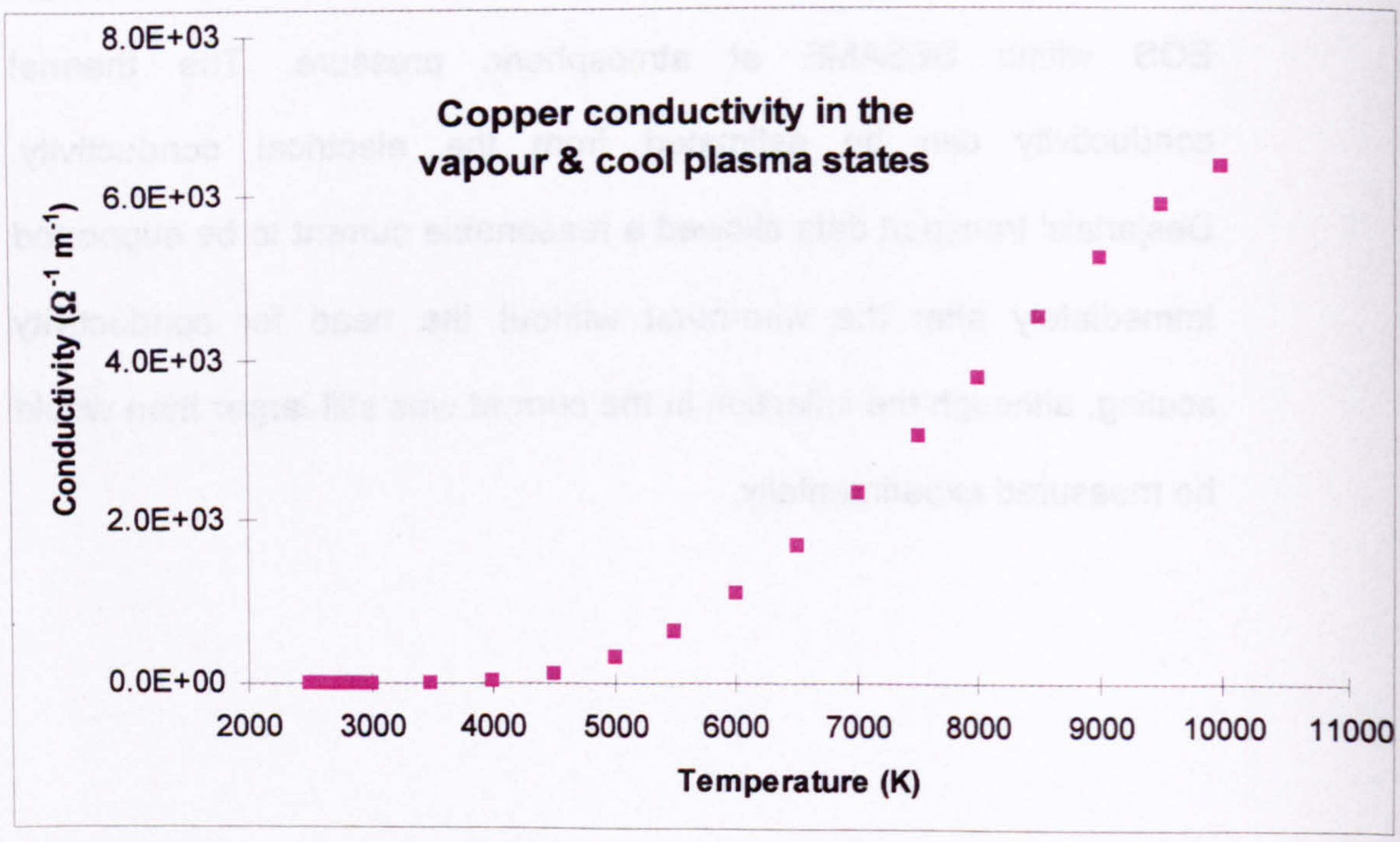

Figure 3.5 Conductivity vapour and plasma states of from Desjarlais interpreted by Cu_3 EOS within SESAME – Copper vapour and plasma

4.4.10 The wire itself was previously treated to heat up uniformly and, upon reaching boiling, vaporised immediately. An inhomogeneous wire-burst model has recently been added to EDENET as a direct result of experimentation by the Author, discussed later in Chapter 4. The Author postulated [25] that the wire explosion process might be inhomogeneous and that an inhomogeneous mechanism for the processes might be occurring. This hypothesis was backed up by experimental work carried out [26, 27, 28] and described (see Chapter 4). The aim was to make the modelling of the evaporating fuse wire emulate experimental observation: that is, instead of the computed wire vaporising in a uniform fashion over its entire length and within a short period of time, the wire would burst in different places at different times, with electrical conduction shared between an initial (and increasing) mass of plasma and the remaining fragments of still-condensed wire. The hope was that, by making the mode of wire explosion more realistic, the remaining correction factors might be explained or eliminated. The latest version of EDENET treats the condensed wire as a series of individual segments, each with its own radius, temperature, density, conductivity and opacity. The wire is initially assumed to have an inhomogeneous radius along its length, analogous to notching a real wire. The depth and spacing of the 'notches' are varied and the model is run without either of the non-physical scaling factors mentioned above for the wire-burst. By appropriate use of the 'notch' depth and spacing, the time of wire-burst

can be matched exactly. Further, the simulation predicts that the wire will fragment in a manner similar to what is observed experimentally. Although this solution still produces a non-predictive wire-burst, it does at least have the advantage of being based upon observed physical mechanisms, which adds to confidence in its predictive capability for mass and energy flow from the system.

4.5 SESAME materials database

4.5.1 As already mentioned, the SESAME tables created by Los Alamos National Laboratory comprise a library of data obtained from both experiments and theoretical calculations. The tables consist of EOS, resistivity and opacity data. Although these tables are used regularly within ETC codes, other thermochemical codes exist to calculate material functions in plasmas, an example being PLASMADAT [29]. Further, alternative methods of evaluating plasma properties, based upon the Spitzer expression [30, 31] treat the plasma as an immobile substance with a constant, known conductivity [14].

4.5.2 As mentioned earlier, the SESAME transport equations (electrical conductivity, heat conductivity and radiation) and some opacity data (for tungsten, the material often used in the rear electrode of the CPG) were, as mentioned above, found to have large errors [32] when compared with experimental results at atmospheric temperatures and pressures. This could be due to the fact that the SESAME database (as well as possibly others) was devised for high temperature, high

pressure nuclear fusion and fission plasmas and thus was not normalised to STP. Although the plasmas formed within the capillary are relatively cool and low pressure, SESAME is thought to be reasonably appropriate for this region of state-space, unlike the condensed phases. Whether the same problems exist with PLASMADAT and other tables is unknown, but it is probable.

4.5.3 To assist with work relating to ignition of propellant by copper vapour deposition (Chapters 7 - 9), the Author requested the boiling point of copper as a function of pressure to be extracted from the SESAME database. It was then found that the latest SESAME database predicts the boiling point of copper to be around 500 K higher than experimentation suggests. This was of some concern as the same database was to be used for energy transfer calculations within the gun chamber. If the boiling point was inconsistent, then the predicted latent heat energy transferred during condensation would be wrong. This has serious implications because metallic vapour deposition has been shown by the Author to be the main energy transfer process [33, 34]. Hence, the Author applied to the Atomic Weapons Establishment (AWE) at Aldermaston, UK, for data on the boiling point of copper as a function of pressure. The Author was aware that AWE's GENERA' code [35] contained such information; indeed, GENERA was calibrated using copper as one of its primary materials. The data resulting from this enquiry appear (by kind permission of AWE) in Figure 3.6 along with data from SESAME.

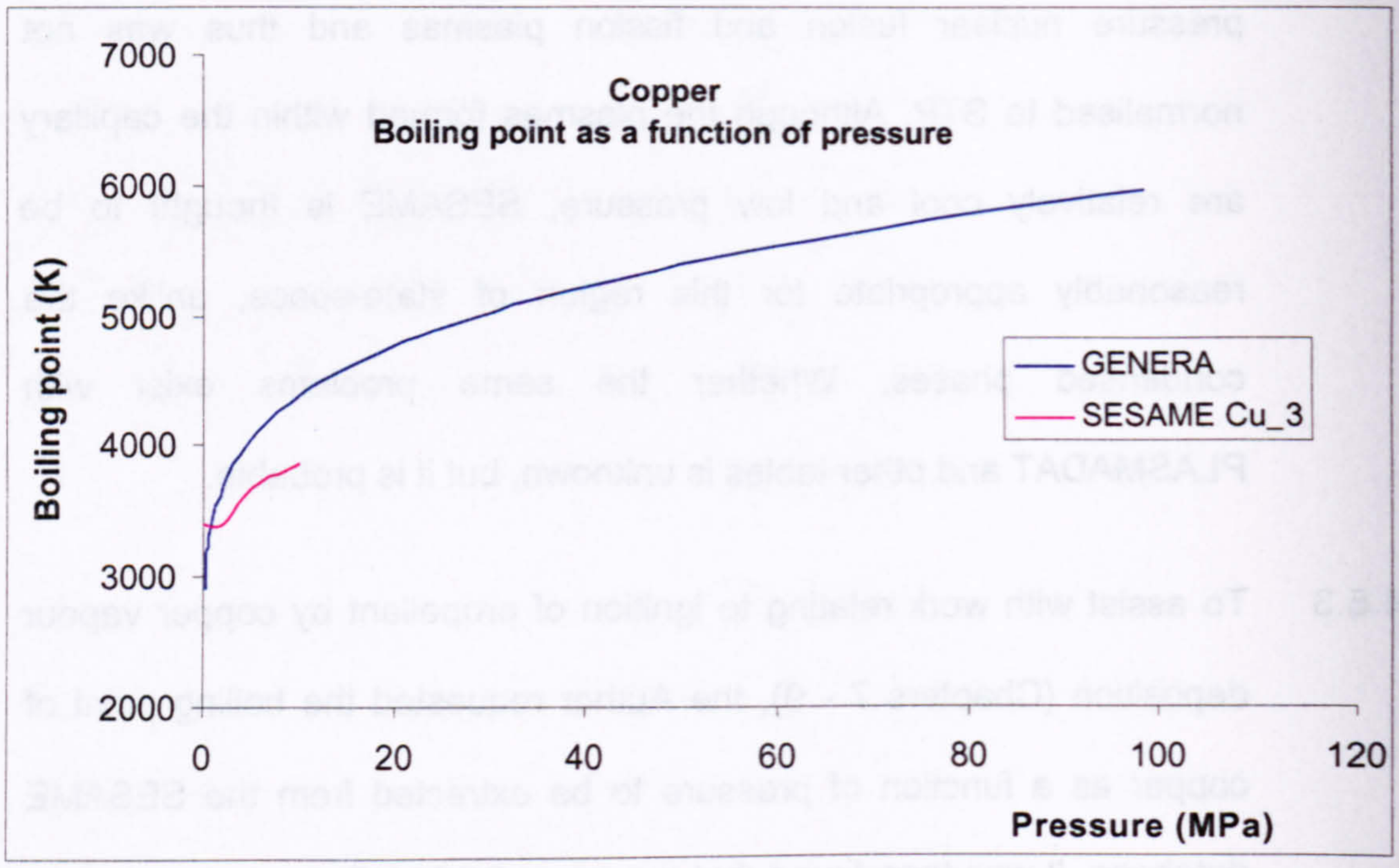

Figure 3.6 Boiling point of copper as a function of pressure (GENERA and SESAME)

4.5.4 It is clear not only that SESAME fails to predict the boiling point of copper at atmospheric pressure, but it disagrees with GENERA at higher pressures. GENERA data will be used as input for the boiling point of copper in EDENET future developments.

4.6 Energy transfer processes within the model

4.6.1 A 'multi-zone' capability has now been incorporated into the axial model, i.e. different states can exist in the radial direction of the axial model (not to be confused with the radial model itself). This consists of a central plasma core with a transition region between it and the residual condensed wire, and with another transition region between the core and the capillary wall. The thicknesses of the transition regions are constant and are represented by a free parameter, usually of the

order of 8 μm. Temperature gradients across the transition regions are assumed to be linear. Energy transfer (both radiative and conductive) from the core and residual wire is dependent upon the properties of the transition regions. The core energy gains are offset by the surface energy losses. This relationship is now set out below.

4.6.2 The radiating flux, Φ, the transition region brightness temperature, T_b and the transition region (surface) temperature, T_s are related by the simple expression [25] :

$$\Phi = \sigma T_b^4 = 2\sigma T_s^4 \qquad \textbf{Equation 3.1}$$

and thus

$$T_b = 2^{1/4} T_s \qquad \textbf{Equation 3.2}$$

where

σ is the Stefan-Boltzmann constant. The factor two accounts for the photons escaping from a short distance within the plasma.

4.6.3 Because the temperature gradient, ∇T is assumed to be linear, the core temperature, T_γ and the surface temperature T_s are related by:

$$\nabla T \approx -\frac{T_\gamma - T_s}{\Delta r} \qquad \textbf{Equation 3.3}$$

where

Δr is the transition region thickness.

4.6.4 The flux can also be written in terms of the temperature gradient:

$$\Phi = -\kappa_r \nabla T \qquad \textbf{Equation 3.4}$$

where

κ_r is the radiative conductivity of the transition zone given by [25, 36]:

$$\kappa_r = \frac{16}{3}\lambda_r \sigma T_s^3 \qquad \textbf{Equation 3.5}$$

λ_r is the Rosseland mean free path for the photons.

4.6.5 Equating the flux gives an implicit relationship between the core and surface temperature:

$$T_\gamma = \left[1 + \frac{3}{8}\frac{\Delta r}{\lambda_r}\right] T_s \qquad \textbf{Equation 3.6}$$

4.6.6 Given that the surface temperature, T_s can be found, it could be used to calculate radiative heat losses and thus cool the core temperature, T_γ.

4.6.7 In earlier versions of EDENET, a constant 'greying' factor or emissivity, ε was used to reduce the radiative heat losses from the plasma. That the plasma surface was not radiating as a blackbody within the capillary had been considered by workers since the early 1990s [37]. The factor acted as an emissivity for the core plasma temperature such that:

$$\Phi = \varepsilon\sigma T_\gamma^4 \qquad \textbf{Equation 3.7}$$

4.6.8 From Equation 3.1 and Equation 3.7:

$$\Phi = \varepsilon\sigma T_\gamma^4 = 2\sigma T_s^4 \qquad \textbf{Equation 3.8}$$

But from Equation 3.6:

$$2\sigma T_s^4 = 2\sigma T_\gamma^4 \left[1 + \frac{3}{8}\frac{\Delta r}{\lambda_r}\right]^{-4} = \varepsilon'\sigma T_\gamma^4 \qquad \textbf{Equation 3.9}$$

where

$$\varepsilon' = 2\left[1 + \frac{3}{8}\tau\right]^{-4} \qquad \textbf{Equation 3.10}$$

τ is known as optical depth and Δr / λ_r is a measure of the insulation given to the core plasma by the transition region [25, 36].

4.6.9 ε' replaces ε in Equation 3.7 for later versions of EDENET. It is a photon frequency independent quantity, in the same way that both the Rosseland mean free path and the thickness of the boundary layer are frequency independent. This may not reflect the true physical situation, however. Further, either or both expressions in Equation 3.4 or Equation 3.5 may be wrongly applied to the plasma transition zone in this case since the Authors experimental measurements of the brightness temperature at the capillary wall have shown a far cooler surface than T_s predicted by EDENET. This subject is revisited later in Chapters 4 and 5.

4.7 Capillary ablation

1.1.1 Material ablation from the capillary results from heat transfer causing evaporation, as well as scouring due to friction of fast flowing fluids. The volume of the capillary will change due to ablated mass loss, affecting the density and other properties of the plasma. It is thus important to model ablation rates accurately.

4.7.2 Scouring has not yet been considered in EDENET, but its effect may be dominant towards the nozzle.

4.7.3 Initial investigations into the effects of thermal conductivity on the evaporation rates within the capillary suggested that these effects were

small, with various changes in the thermal conductivity of the various materials changing the total measured ablated mass by only 1 in 1000 [38].

4.7.4 Radiative evaporation of the polyethylene capillary liner will be a function of both the surface temperature of the transition zone and the optical properties of the liner, and thus will be highly susceptible to impurities and reflections. The energy is likely to be deposited in the order of millimetres in depth into the translucent liner for visible and infrared radiation, but only at the surface for ultraviolet radiation. If condensation from the wire and rear electrode is occurring then this will greatly alter the situation, as the condensate is likely to be optically thick. Hence, radiative evaporation is not easy to model. However, the radiation reaching the surface of the liner can be measured directly and energy transfers can be estimated with knowledge of the absorptance and scattering of the material. This has been attempted by the Author and the work will be discussed in Chapter 5.

4.8 Pressure expansion of the capillary

4.8.1 The motion of the capillary wall under pressure will affect the interior volume of the capillary. The properties of the plasma are sensitive to its density and so any small change in the interior volume will have a significant effect on the model. Some tapered capillaries designed for a 155 mm gun – 15 mm diameter at the rear and 18 mm at the front – allowed for these effects. Inspection of the capillaries following high

energy discharge has shown that they became reasonably parallel due to such distortion.

4.8.2 The Author has performed some initial calculations to determine whether the volume increase warranted consideration by Fluid Gravity. This calculation involved consideration of the material density at different pressures and is shown below.

4.8.3 Figure 3.7 represents a cross section of the capillary; it is assumed tightly encased in incompressible steel.

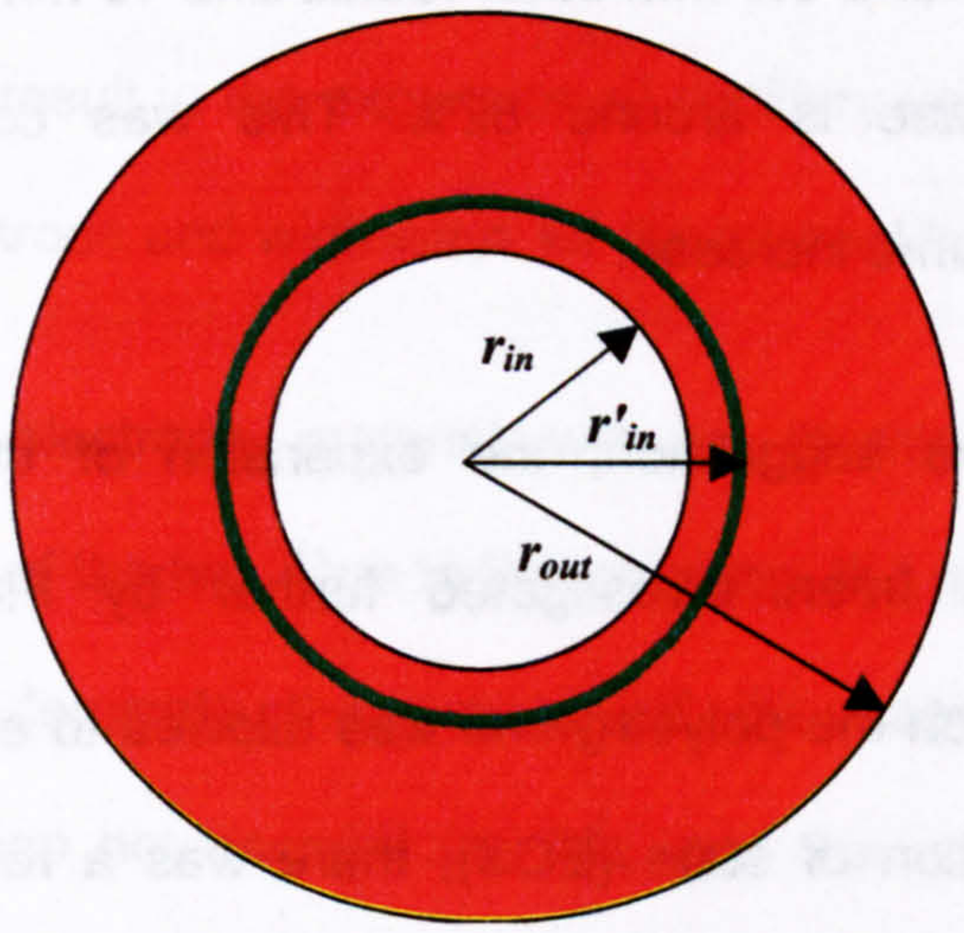

Figure 3.7 Expansion of the capillary

4.8.4 The ratio of the compressed to the uncompressed volumes is known as the compression, η. Hence:

$$\eta = \frac{r_{out}^2 - r_{in}^2}{r_{out}^2 - r_{in}'^2} \qquad \textbf{Equation 3.11}$$

where r_{in}, is the capillary initial inner radius, r'_{in} is the capillary expanded inner radius and r_{out} is the (fixed) capillary outer radius as defined in Figure 3.7 above.

4.8.5 The Steinberg compendium [39] contains an equation of state for high density polyethylene and this has been used to obtain the densities of the material at pressures representative of a high energy plasma discharge [32, 40]. At atmospheric pressure, the density of the capillary material is given as 0.95 g cm^{-3} and at 600 MPa it is 1.01 g cm^{-3}. This is a compression of 1.06 and with an initial inner radius of 18 mm and outer radius of 28 mm (10 mm wall thickness), the compressed inner radius will be around 18.7 mm. This translates to a capillary volume increase of around 8%. For capillaries of smaller inner radii, the effect is far greater; for a 3.5 mm inner radius and 10 mm wall thickness, the volume increase is around 82%. This was considered to be a significant volume increase.

4.8.6 At the Authors suggestion, the expansion of the capillary under pressure has been investigated further by Fluid Gravity, using EDENET. When the polyethylene was allowed to expand according to a given equation of state (EOS), there was a reduction in capillary density and temperature, resulting in a decrease in pressure of around 30% for a 7 mm capillary during a typical low energy plasma discharge. Although this is significant, the reduction was insufficient to increase plasma resistance and thus account for the poor fit of current to experimental data after the current peak (Section 4.2.9). However, the effect of capillary expansion has been added to later versions of EDENET.

4.9 Electrode erosion model

4.9.1 The physics involved in erosion of the rear electrode will be different from that affecting the front electrode. Visual observation of the rear electrode shows pitting whilst that of the front electrode indicates scouring. The CPG design with an extended capillary liner and external front electrode (Chapter 2, Section 1.10.2) shows slight pitting on the front electrode. The contribution to the capillary plasma from the front electrode material is going to be vastly different from that of the rear, with little material ablated from the front electrode entering the bulk plasma within the capillary. Electrode erosion, similar to capillary erosion, will result in the expansion of capillary volume (lengthways for the rear electrode and widthways for the internal front electrode).

4.9.2 Erosion of electrode material will be thermal, mechanical or a combination of the two. Due to the scouring, the mechanical process is thought to dominate the erosion of the internal front electrode. EDENET does not account for this, and the requirement has since disappeared with the introduction of the extended liner.

4.9.3 Thermal erosion is modelled by both ohmic heating within the bulk and at the surface due to contact resistance and ballistic heating of bombarding ions and electrons, in addition to conductive and radiative heat transfers. The rear electrode is explicitly modelled within EDENET. Earlier versions indicated that the ablation from the rear electrode would be related to the current density, and so a current

threshold and an area term were introduced for each electrode to allow some control over an otherwise constant ablation rate. However, this failed to give good agreement with experimental measurements of the integrated mass loss and so its use as a predictive tool was nullified. Radiative ablation, whereby the radiated energy from the plasma surface was absorbed by the electrode was equated with the enthalpy of the ablated material. However, this gave worse agreement with experiment.

4.9.4 Therefore, contact resistance and ballistic effects have been incorporated. Contact resistance occurs where two conductors with different charge carrier properties meet. The materials may have the same electrical conductivity but different charge carrier densities and energies; energy transfer from one conductor to the next may be inefficient and the resultant energy losses emerge as heat. The energy will be liberated within a few atomic spacings of the interface and is thus difficult to incorporate accurately into a hydrocode model with large cell sizes (hundreds of microns). EDENET has four free parameters (resistances) for each interface: two for each material dependent upon the direction of current flow. The extra resistance is added to the first cells either side of the interface.

4.9.5 The ballistic effect occurs when electrons collide with the anode and ions with the cathode. The kinetic energy of the particles is liberated as heat at the surface; further, it will be polarity dependent as the

electrons generally have more kinetic energy than the ions when particle acceleration from field effects occur. At present, this method is implicitly modelled with the contact resistance but it may be investigated further on a finer scale at a later date.

4.9.6 Limiting the current flow after peak current can be achieved in several ways. As mentioned above, EDENET achieves this by using ablated wall material to constrain the plasma temperature (Section 4.2.9). However, alternative physical changes have been explored with the same outcome. The first method allowed the capillary to expand as the high density polyethylene compressed under pressure (Section 4.8.6). This increased the capillary volume and thus decreased the plasma density and temperature. The overall effect on plasma resistance and pressure was studied, and the result permitted a match to the current profile with a significantly reduced capillary pressure. However, the simulation still required some over-pressurisation to match the experimental current and voltage. An alternative hypothesis [41] introduced a cool, thin boundary layer between the rear electrode and the plasma. This boundary layer consisted of metallic vapour and was proposed by the Author [27] to exist between condensed metal and plasma (see Chapter 4). The effect was to introduce a highly (but not perfectly) insulating layer in series with the plasma. Formerly, use of the Rinker data required the ablated material to be heated immediately to plasma temperature, or else a perfect insulator would be introduced in series with the plasma, reducing the current instantly to zero. With

the Desjarlais data, a vapour layer can exist and still conduct. The questions asked were what thickness of boundary layer was required to reduce the overall resistance and how did the subsequently computed ablation of the rear electrode compare with experimental results.

4.9.7 To commence investigations of these issues, a simulation was set up with the rear electrode modelled explicitly as finely zoned copper. Allowing the plasma to ablate the electrode resulted in the desired effect on the current. Interrogation of EDENET showed that the mass of ablated material was around 0.5 g, which is similar to experimentally observed values. Initial modelling had used a mesh size of 100 μm for the cells at the condensed copper/plasma interface. This is considered too coarse for proper modelling of boundary layer physics and so refined mesh-size computations are currently in hand.

4.10 Divergence of the nozzle

4.10.1 Little experimental work has been conducted on effects of the nozzle geometry on the capillary plasma properties. However, some work has involved EDENET in modelling the initial expansion flow from the capillary by continuing the nozzle beyond the front (internal) annular electrode, with a 45° expansion. This work is covered in Section 4.1.2 of Chapter 5.

5 Coupling plasma generator and internal ballistics codes – EDEN-IB

5.1.1 This section looks at the future extension of EDENET beyond the capillary nozzle and into a gun chamber. Currently, the plasma generator in EDENET routinely discharges into an infinitely long chamber of the same internal diameter as the capillary itself. However, work is in hand to extend EDENET into a new 2-D model, EDEN-IB. This will use EDENET but discharge into a chamber of defined length and radius. Further, the chamber will have the option of being loaded with grains of energetic propellant having chemical and physical properties specified by the user. Codes from EDENET will specify the mass and energy flux venting from the CPG, and pressure and material will feed back into the capillary from the combusting material. Both the material ignition and combustion will be modelled. Further, EDEN-IB will go on to model the projectile acceleration up the gun tube.

5.1.2 The aim of EDEN-IB is to understand further the physical mechanisms involved in ETC plasma propellant interaction processes, in particular the mechanisms for plasma enhanced gas generation.

5.1.3 Much of the work that follows will be used in the development and validation of EDEN-IB. In particular, the experimental work described in Chapter 9 was carried out specifically for primary validation of the model.

1 C. R. Woodley, "Development of a One-dimensional Internal Ballistics Model of a Cased Telescoped Ammunition Gun", 15th International Symposium on Ballistics, Jerusalem, May 1995

2 C. A. Lowe, "The WAFBC1CHV2.5 Code", COA report 9803, College of Aeronautics, Cranfield University, 1998

3 C. R. Woodley, "Modelling Heat Transfer from Conventional and Plasma Igniters to Solid Propellant", 20th International Symposium on Ballistics, Orlando, FL. September 2002

4 C. R. Woodley and S. J. Billett, "Modelling Enhanced Gas Generation Rates in a 155 mm ETC Gun", IEEE Transactions on Magnetics, Vol. 37, 1, January 2001

5 W. F. Oberle and D. E. Kooker, "BRLCB: A Closed-chamber Data Analysis Program: Part 1 - Theory and Users Manual", ARL Technical Report ARL-TR-36, US Army Research Laboratory, Aberdeen Proving Ground, MD, January 1993

6 M. J. Taylor and C. R. Woodley, "Variation in Enhanced Gas Generation Rates in Electrothermal-chemical Closed Chamber Studies", 19th International Symposium of Ballistics, Interlaken, Switzerland, May 2001

7 L. E. Fried, W. M. Howard and P. C. Souers, Lawrence Livermore National Laboratory, USA

8 R. J. Kee, F. M. Rupley and J. A. Millar, "CHEMKIN II: A Fortran Chemical Kinetics Package for the Analysis of Gas Phase Chemical Kinetics", Sandia report SAND89-8009B UC-706

9 G. P. Wren and W. F. Oberle, "U.S. Army Activities in Multidimensional Modelling of Electrothermal-Chemical Guns", IEEE Transactions on Magnetics, Vol. 29, 1, January 1993

10 J. Ashkenazy, "The Effect of External Pressure on the Internal Conditions Inside the Discharge Tube", IEEE Transactions on Magnetics, Vol. 29, 1, January 1993

11 N. Silvestre, D. Hensel and K. Darée, "A Comprehensive, Numerical Model of Electro-Thermal Propulsion", IEEE Transactions on Magnetics, Vol. 29, No. 1, January 1993

12 K. Gruber, K. Kappen, A. Voronov and H. Haak, "Radiation Absorption of Propellant Gas", IEEE Transactions on Magnetics, Vol. 37, 1, January 2001

13 K. Kappen and U. H. Bauder, "Calculation of Plasma Radiation Transport for Description of Propellant Ignition and Simulation of Interior Ballistics in ETC Guns", IEEE Transactions on Magnetics, Vol. 37, 1, January 2001

14 J. D. Powell and L. D. Thornhill, "Current Distribution and Plasma Properties in Injectors for Electrothermal-Chemical Launch", IEEE Transactions on Magnetics, Vol. 37, 1, January 2001

15 C. R. Woodley, "A Parametric Study for an Electrothermal-Chemical Artillery Weapon", IEEE Transactions on Magnetics, Vol. 29, 1, January 1993

16 D. C. Swift, "Hydrocode Modelling of Plasma Capillaries", APS Plasma Physics Meeting, New Orleans, 1998

17 M. P. Desjarlais, "Practical Improvements to the Lee-More Conductivity near the Metal-insulator Transition", Contributions To Plasma Physics, 41, 2-3, pp 267-270, January 2001

18 A. W. DeSilva and J. D. Katsouros, "Electrical Conductivity Measurement in Dense Metal Plasmas: Comparisons of Several Metals", Journal de Physique IV, 10 (P5), pp 209-214, 2000

19 SESAME EOS database, Los Alamos National Laboratory, USA

20 B. Augsburger et al, "DRA 500 kJ Multi-module Capacity Bank", IEEE Transactions on Magnetics, Vol. 31, 1, January 1995

21 Y. Me-Bar and R. Harel, "Electrical Explosions of Segmented Wires", J. Appl. Phys. Vol. 79, 4, pp 1864-1868, 1996

22 J. Ashkenazy, "The Effect of External Pressure on the Internal Conditions Inside the Discharge Tube", IEEE Transactions on Magnetics, Vol. 29, 1, 1993

23 D. Hensel, K. Darée and N. Silvestre, "ET-Guns with Working Media of Low Molecular Weight: A Numerical Study", IEEE Transactions on Magnetics, Vol. 31, 1, January 1995

24 G. T. Dyos and T. Farrell, "Electrical Resistivity Handbook", London: Peter Peregrinus, 1992

25 D. C. Swift, "Capillary Plasma Generator Modelling Using EDEN-ET: Final Report on Phase 1 of Contract WSS/R6991", DERA Internal Report, April 1998

26 M. J. Taylor, "Measurement of the Properties of Plasma from ETC Capillary Plasma Generators", IEEE Transactions on Magnetics, Vol. 37, 1, January 2001

27 M. J. Taylor, "Formation of Plasma Around Wire Fragments Created by Electrically Exploded Copper Wire", J. Phys. D: Appl. Phys, Vol. 35, 7, pp 700-709, 2002

28 M. J. Taylor and J. Dunnett, "A Description of the Wire Explosion Process for ETC Plasma Generators", 11th Electromagnetic Launch Symposium, Saint-Louis, France, May 14th –17th, 2002

29 K. Kappen and U. H. Bauder, "Simulation of Plasma Radiation in Electrothermal-Chemical Accelerators", IEEE Transactions on Magnetics, Vol. 35, 1, January 1999

30 J. D. Powell and A. E. Zielinski, "Capillary Discharge in the Electrothermal Gun", IEEE Transactions on Magnetics, Vol. 29, 1, January 1993

31 R. J. Zollweg and R. W. Liebermann, "Electrical Conductivity of Non-Ideal Plasmas", J. Appl. Phys., Vol. 62, p 3621, 1987

32 D. C. Swift, "Progress Report 3 for Contract WSS/R6991 Phase 2", DERA internal report, May 1999

33 M. J. Taylor, "Ignition of Propellant by Metallic Vapour Deposition for an ETC Gun System", Propellants, Explosives, Pyrotechnics, 26, pp 137–143, 2001

34 M. J. Taylor, "Consideration of the Energy Transfer Mechanisms Involved in SPETC Ignition Systems", 11th Electromagnetic Launch Symposium, Saint-Louis, France, May 14th –17th, 2002

35 G. P. Parish, "Thermodynamic and Interatomic Potential Data Generator for Equations of State of Solid Elements (GENERA-S), AWE report AWC 01/95, 1995

36 R. L. Bowers and T. Deeming, "Astrophysics I: Stars", Jones and Bartlett, 1984

37 R. B. Mohanti and J. G. Gilligan, "Time Dependent Simulation of the Plasma Discharge in an Electrothermal Launcher", IEEE Transactions on Magnetics, Vol. 29, 1, January 1993

38 D. C. Swift and J. D. Dunnett, "Capillary Plasma Generator Modelling using EDENET: Final report on Phase 2 of Contract WSS/R6991", DERA internal report, March 2000

39 D. J. Steinberg, "Equation of State and Strength Properties of Selected Materials", Lawrence Livermore National Laboratory Report UCRL-MA-106439 change 1, 1996

40 D. C. Swift, 'ELECTRA' program for analysing equations of state, 1997

41 J. Dunnett, personal communication, September 2001

Chapter 4 - Plasma initiation

1 Introduction

1.1 Energy transfers

1.1.1 Electrical energy is transformed into thermal energy within the capillary of a CPG via ohmic dissipation within the plasma initiation wire and subsequent plasma material. The amount of the electrical power transferred to the system is often measured in terms of gigawatts in large calibre 155 mm ETC gun firings. More commonly in small-scale fundamental ETC studies it is measured in terms of tens or hundreds of megawatts. In all cases, the effect of the discharge is to add energy to the CPG at a rate far greater than it can be transferred away, resulting in a considerable rise in temperature and pressure of the capillary's interior material.

1.1.2 The electrical energy is transferred firstly to the plasma initiator wire, where the conduction electrons collide with the atomic lattice and hence transfer energy through their collisions (ohmic dissipation). The atomic lattice structure bonds break because of the thermal excitation produced by the energy transfer and the material initially melts; the molten material, being a conductor, continues to heat until it vaporises. This occurs so quickly that gravitational effects which would normally cause the molten wire to drip onto the capillary floor have no time to act and so the wire integrity is retained in a liquid column. This Chapter explores the development of the liquid column as it fragments, vaporises and heats to plasma temperatures.

1.2 Exploding wire history

1.2.1 Historically, the scientific investigation of electrically exploded wires goes back as far as 1774 when E. Nairne proved for the first time that the current in a series circuit is the same at all points around it [1]. However, the subject attracted little attention until the twentieth century: much progress was made during the late 1950s and early 1960s, with contemporary work being published in a series of four books of proceedings from the 'Exploding Wire Phenomenon' symposium, edited by W. G. Chace and H. K. Moore [2]. Work continued during the 1970s [3], 1980s [4] and 1990s [5, 6, 7] as more applications for exploding wires were found. However, despite all the efforts to date, understanding of the wire explosion process is still far from complete. This is partly because the wire experiences the explosion process differently depending upon the experimental parameters involved, which vary with each application.

1.3 Applications

1.3.1 Currently, applications for exploding wire technology include circuit breakers, segmented lightning divertor strips for aircraft radomes, disruptors for metallic 'shaped charge' jets [7, 8], plasma armatures for electromagnetic railguns and plasma generators for electrothermal-chemical (ETC) guns. Some applications require the efficient transfer of energy to the condensed phases of the wire explosion, while others rely on the establishment of current-carrying plasma around the condensed material.

1.3.2 This Chapter is concerned with recent work undertaken by the Author on processes occurring during the establishment of a current path through electrical plasma around condensed fragments of electrically exploded wires under certain conditions. First, the parameter ranges involved in various experiments undertaken for this study are discussed, followed by the observations made during the experiments. An hypothesis is then offered to explain the apparently anomalous electric current path and, finally, supporting evidence is presented for this hypothesis.

1.4 Exploding wire studies (conducted by the Author)

1.4.1 The exploding wire studies described in this Chapter were undertaken by the Author (unless otherwise indicated) in the context of developing capillary plasma generators (CPGs) for electrothermal-chemical (ETC) guns [9]. CPGs used here were typically polyethylene tubes 100 mm in length and 10 mm in diameter, with a copper rear electrode and internal annular front electrode connected via a copper wire ranging in diameter from 0.5 to 1 mm [10]. The CPG assembly was encased in a vessel body made from either steel or filament-wound glass. Both bodies could be interfaced with closed vessels of various volumes, maintained with a high pressure gas seal. The steel body was capable of withholding pressures up to 400 MPa in vented vessel mode (where the pressure is released rapidly by a rupturing disc), and around 200 MPa in closed vessel mode (where the pressure is released far more slowly by a vent-bolt driven by a remotely operated electric motor). The filament-wound body was only capable of operating at up to around half the pressures of the steel body,

but this body design is compatible with piezoelectric pressure transducers which need to be electrically insulated. Such insulation is difficult to achieve using the earthed steel vessel body. Figure 4.1 is a photograph of a CPG body design with the capillary, *c* rear electrode, *e* and front annular electrode, *f* removed; a biro pen is laid alongside for scale.

Figure 4.1 Capillary plasma generator components

1.5 Experimental parameters

1.5.1 Unless stated otherwise, a single module of a ten module, 500 kJ, 800 μF capacitor-based pulsed power supply [11] was used for the investigation of the wire explosion process described in this chapter. This single module was connected in series with an inductor and the exploding wire load. Inductance ranged from around 26 μH to 800 μH. The inductance ensured that current continually flowed with no current 'dwell' – much debated in earlier exploding wire work where circuit inductance was far lower [2]. During this so-called current dwell, the electric current reduced to very low values, whilst the voltage across the wire remained uniform as the resistance approached very high values. In the system described here, the current continued flowing with only a

small inflection, whilst the voltage increased often beyond that used to charge the capacitor. A crowbar diode fitted within the module ensured there was no current reversal. The discharged current approximated to a half-sinusoidal waveform. The capacitor bank could be operated in two voltage modes with the twin capacitors in each module operating in parallel (11 kV mode) or series (22 kV mode). The charge voltage for these experiments was generally around 10 kV for both modes. Depending on the test conditions, between 1.5 kJ and 30 kJ of electrical energy were discharged into the load, over times varying between 0.8 ms to 10 ms. Load voltage varied during the tests, giving peak electrical discharge powers between 0.4 MW and 250 MW.

1.5.2 Exploding wires were tested in free air and also confined within capillary tubes. Wire material was high purity (99.9%) copper of 1.0 mm thickness, cut from a reel. The wires were pulled hand-tight between electrodes with 150 – 180 mm separation. The electrodes had either a simple square clamp or round-ended cylindrical design with an axial hole through which the wire was threaded. For x-radiological and photographic studies, the wires were suspended in a 'semi-balanced field' assembly to reduce the non-axial magnetic field produced by the supply cables, thus reducing the off-axis Lorentz forces on the current-carrying material during the wire explosion. Figure 4.2 is a schematic diagram of the balanced field rig assembly. The rig comprises a rectangular frame made from aluminium, in which an aluminium spur runs from the centre of the top downwards and in the plane of the frame: this forms the anode

connection for the load wire. The aluminium cathode connection, which is very well insulated electrically from the anode frame, passes into the frame plane from below. The load wire is connected to the anode and cathode by any suitable means. The dimensions of the rig are variable depending upon the application and the magnetic fields are balanced approximately within the plane of the rectangular rig.

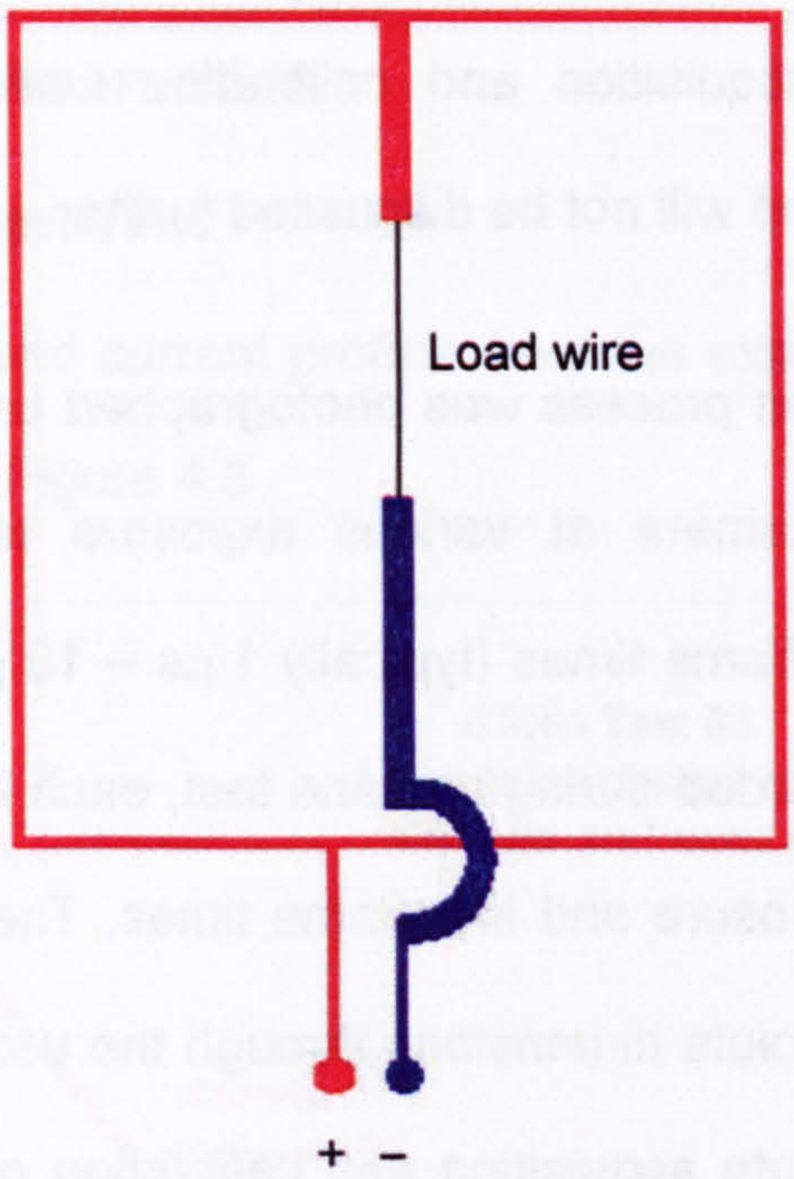

Figure 4.2 Layout of the 'balanced field rig' assembly used in exploding wire studies

1.5.3 Time-resolved measurement of the voltage across the wire was achieved using a calibrated 3000:1 voltage divider. The experimental copper wires were run through axial holes incorporated in the electrode design, and crocodile clips attached to them acted as connections to the terminals of the voltage divider without measuring the electrode connection voltage drop. These wire ends were always found to be largely unaffected after the discharge, with the crocodile clips still attached firmly.

1.5.4 Time-resolved current flowing through the wire was deduced from the measurement of the rate of change of current, using a calibrated Rogowski coil around the electrical supply cables. The load resistance, discharged energy and power could be deduced from the time-resolved voltage and current. Electrical data acquisition rates were either 1 MHz or 10 MHz.

1.5.5 Electrical data acquisition and calibration were the responsibility of laboratory staff and will not be discussed further.

1.5.6 The wire explosion process was photographed using an intensified fast-framing digital camera at various exposure times (typically around 100 ns) and interframe times (typically 1 μs – 10 μs). Between 8 and 24 images were recorded during any one test, each image being separately controlled for exposure and interframe times. The camera images were calibrated for absolute dimensions through the use of a test card. All set-up parameters, data acquisition and calibration of photographic images were the responsibility of the Author. A description of the camera and its operation can be found in Appendix B.

1.5.7 A 150 kV Hewlett-Packard flash X-ray system, fitted with a beryllium window, was used to obtain details of the wire structure hidden by the expanding plasma. This system was operated by laboratory staff, so no further description will be given.

1.5.8 Absolutely calibrated time-resolved spectra of the plasma were recorded in some tests by the methods described in Appendix A. All set-up parameters, data acquisition and calibration of spectrographic data were the responsibility of the Author. For measurements made during the wire explosion process, the plasma is dense and approximates to a blackbody emitter.

2 Experimental Observations

2.1 Electrical considerations

2.1.1 Typical voltage and current profiles from the exploding wire experiments are illustrated in Figure 4.3.

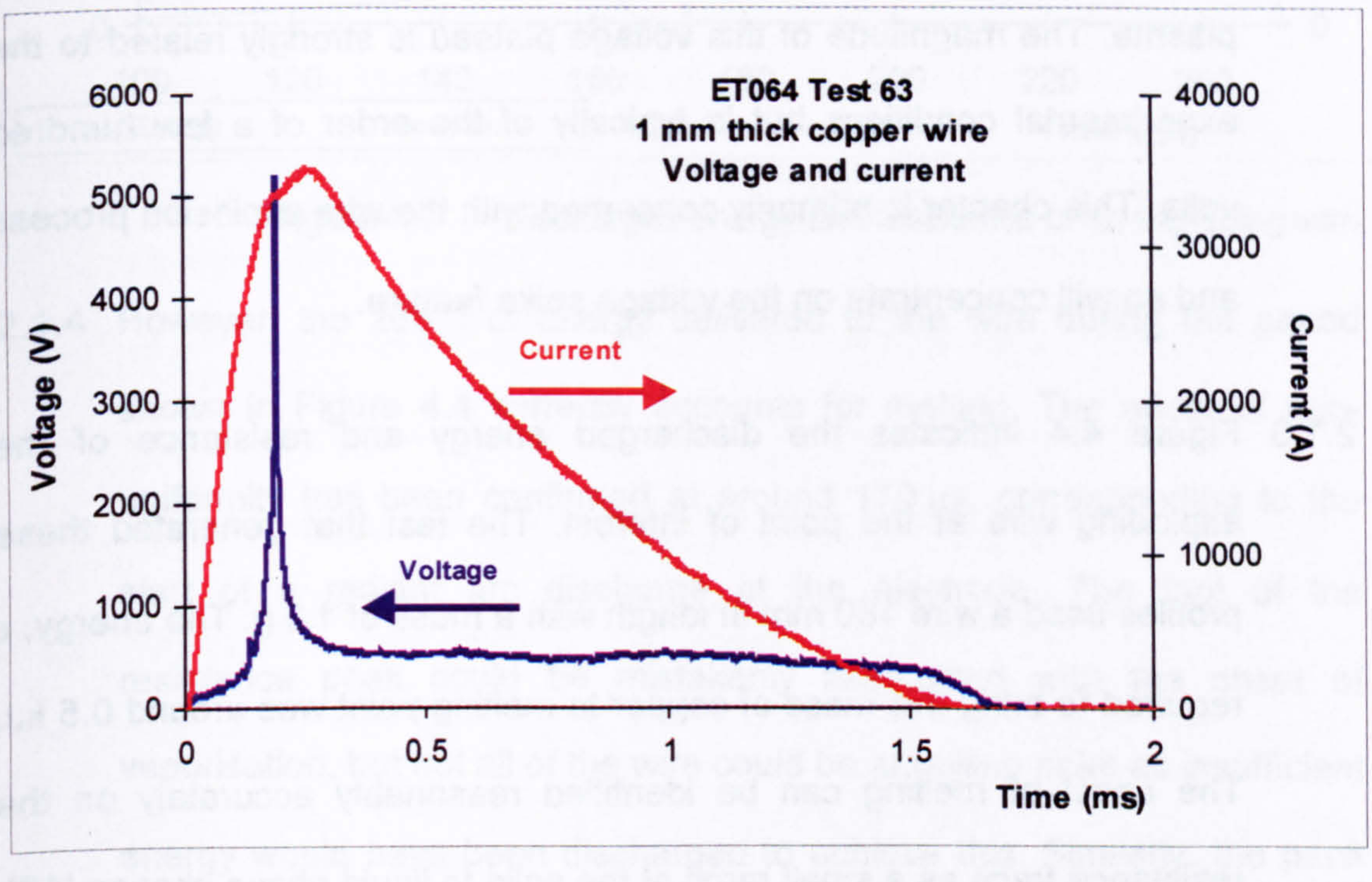

Figure 4.3 Typical current and voltage profiles from an exploding wire in air

2.1.2 Although the details change (depending upon the test conditions), some general features are common to most tests. In brief, the voltage initially

rises slowly in a manner associated with inductive effects and ohmic heating of the wire. It is shown later that there is reasonably uniform heating of the wire until it has melted. The spike in the voltage trace has been identified as related to the fragmentation of the wire with plasma development around it, and this begins shortly after melt. The wire fragmentation is accompanied by a small inflection in the current profile, where presumably the current 'dwell' would occur in systems with far lower inductance. For unconfined wire explosions in air, the voltage spike is followed by a voltage plateau which has been sustained experimentally by the discharge of additional capacitor modules, with material ablated from the electrodes acting as a mass source for the maintenance of the plasma. The magnitude of this voltage plateau is strongly related to the experimental conditions but is typically of the order of a few hundred volts. This chapter is primarily concerned with the wire explosion process and so will concentrate on the voltage spike feature.

2.1.3 Figure 4.4 indicates the discharged energy and resistance of the exploding wire at the point of interest. The test that generated these profiles used a wire 180 mm in length with a mass of 1.3 g. The energy, ε required to bring this mass of copper to melting point was around 0.5 kJ. The onset of melting can be identified reasonably accurately on the resistance trace as a small ramp at the solid to liquid phase change [12]. The energy discharged at that point was greater than the 0.5 kJ needed to reach melting and the resistance value (0.029 Ω) was just above that of the solid wire [13] at melting point (0.023 Ω). These higher values are

probably due to a combination of non-perfect uniformity of heating (especially at the electrodes) with inductive effects.

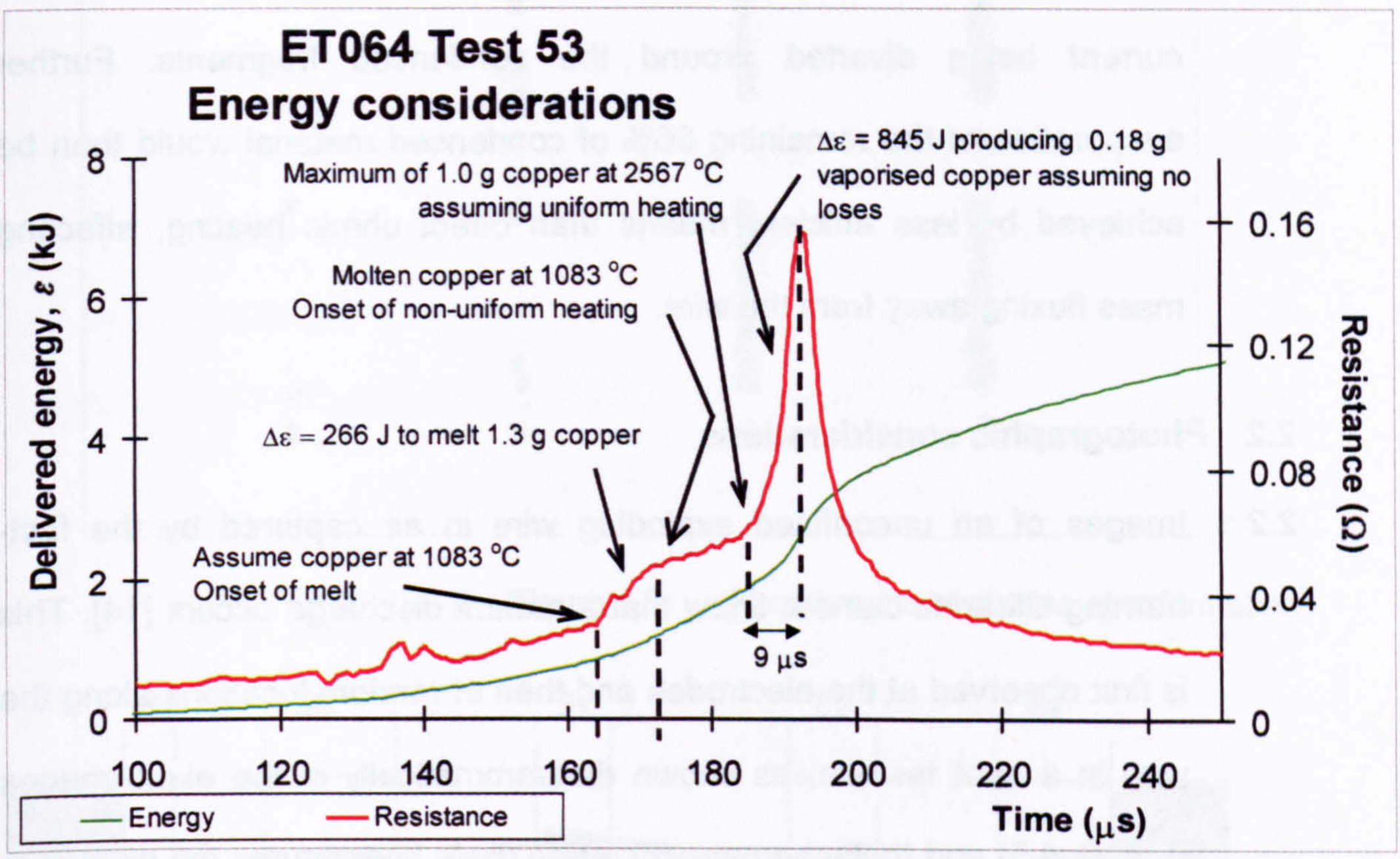

Figure 4.4 Discharged energy and resistance of an exploding wire

2.1.4 However, the 266 J of energy delivered to the wire during the period shown in Figure 4.4 correctly accounts for melting. The onset of non-uniformity has been confirmed at around 170 μs, corresponding to the start of a radiant arc discharge at the electrode. The foot of the resistance peak could be mistakenly associated with the onset of vaporisation, but not all of the wire could be at boiling point as insufficient energy would have been discharged to achieve this. Similarly, the peak in resistance could be mistaken for the end of the vaporisation process, but only sufficient energy to vaporise 0.18 g of the wire mass would have been discharged by this time. An upper limit to the fraction of condensed

wire mass vaporised, assuming uniform heating, at the resistance peak for this test is thus around 14%. This is significant, as it is argued later that negligible current flows through the condensed wire remnants, with current being diverted around the condensed fragments. Further evaporation of the remaining 86% of condensed material would then be achieved by less efficient means than direct ohmic heating, affecting mass fluxing away from the wire.

2.2 Photographic considerations

2.2.1 Images of an unconfined exploding wire in air captured by the fast-framing Ultranac camera show that a radiant discharge occurs [14]. This is first observed at the electrodes and then at random locations along the wire in a spot fashion, as shown diagrammatically in the eight images (Figure 4.5) and the schematic (Figure 4.6). In both figures the plasma is represented by negative images acquired from an actual wire explosion. In Figure 4.5 the wire is vertical and its ends are located at the two spots in image 1. Image 1 was captured at a time corresponding to the end of melt; image 6 represents the resistance peak and image 8 the start of the voltage plateau. In Figure 4.6 the wire is shown for location only.

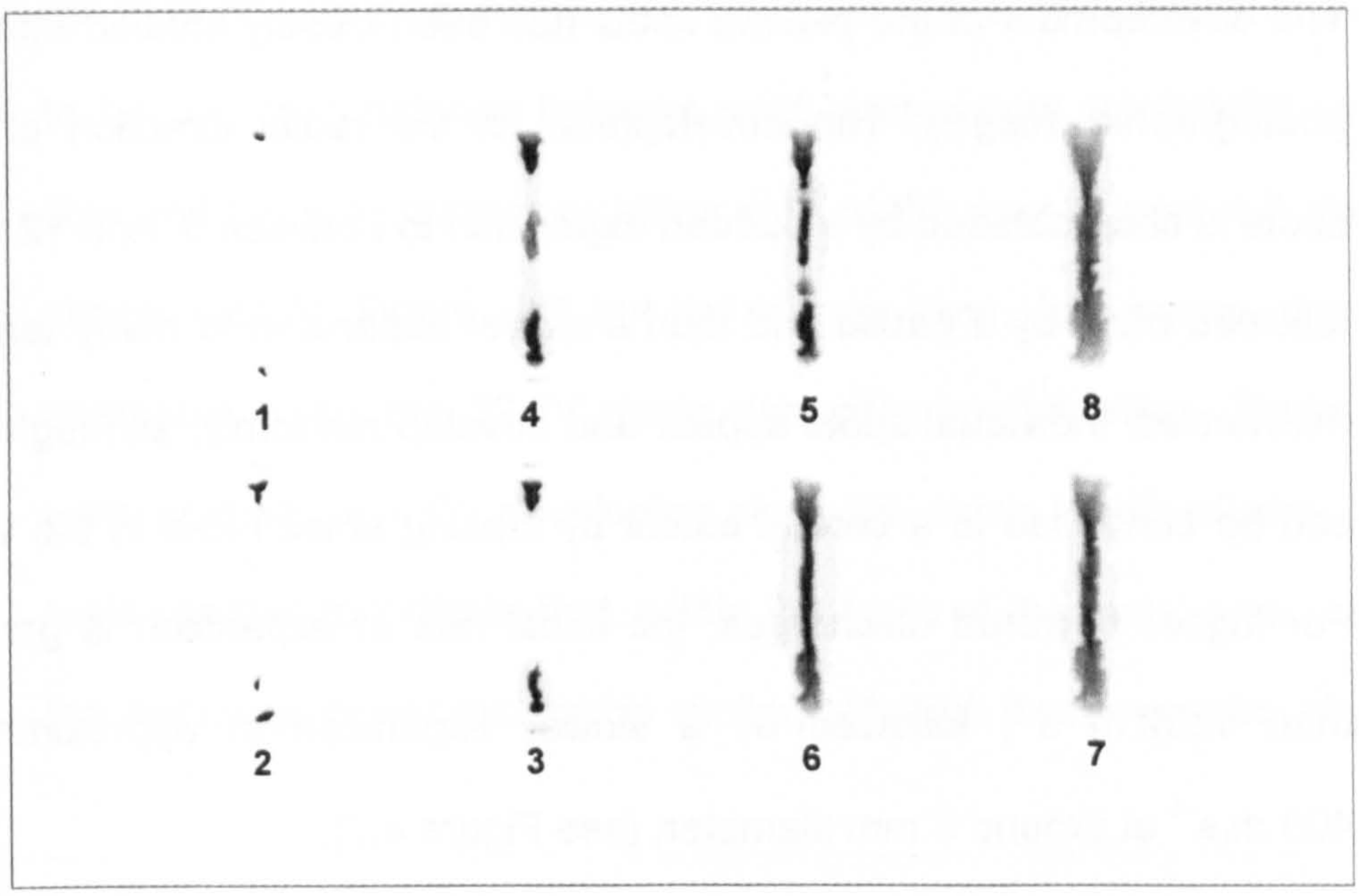

Figure 4.5 Photographs of plasma spot formation

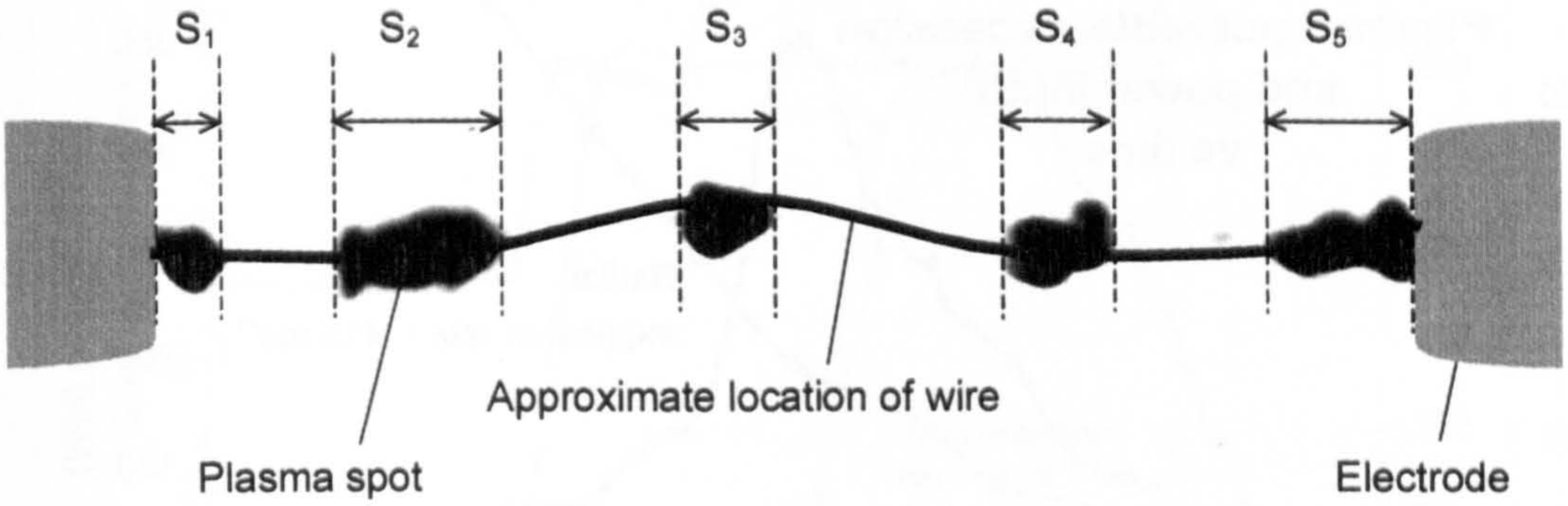

Figure 4.6 Schematic of plasma spot formation

2.2.2 The radiant emittance of the molten portion of the wire is low in comparison with the bright spots developing in the images. The location of condensed portions of the wire cannot be seen on the photographic images. Spectra recorded from such spots reveal that the radiant parts represent copper plasma, with a brightness and colour temperature of around 16 000 K in higher powered tests. When the peak in resistance occurs, the entire wire appears to be shrouded in radiant plasma.

2.2.3 The development of the plasma spots has been closely studied through photographic images. The development in the radial direction of the spots is characterised by a sudden expansion to between 5 and 12 mm, followed often by a pause and then a slower expansion to many tens of millimetres. Individual spots appear and develop randomly, although this can be controlled to a certain extent by making small nicks in the wire. For higher powered discharges, the initial rate of expansion is greater than 1200 m s^{-1}, followed by a slower expansion of approximately 400 m s^{-1} at around 8 mm diameter, (see Figure 4.7).

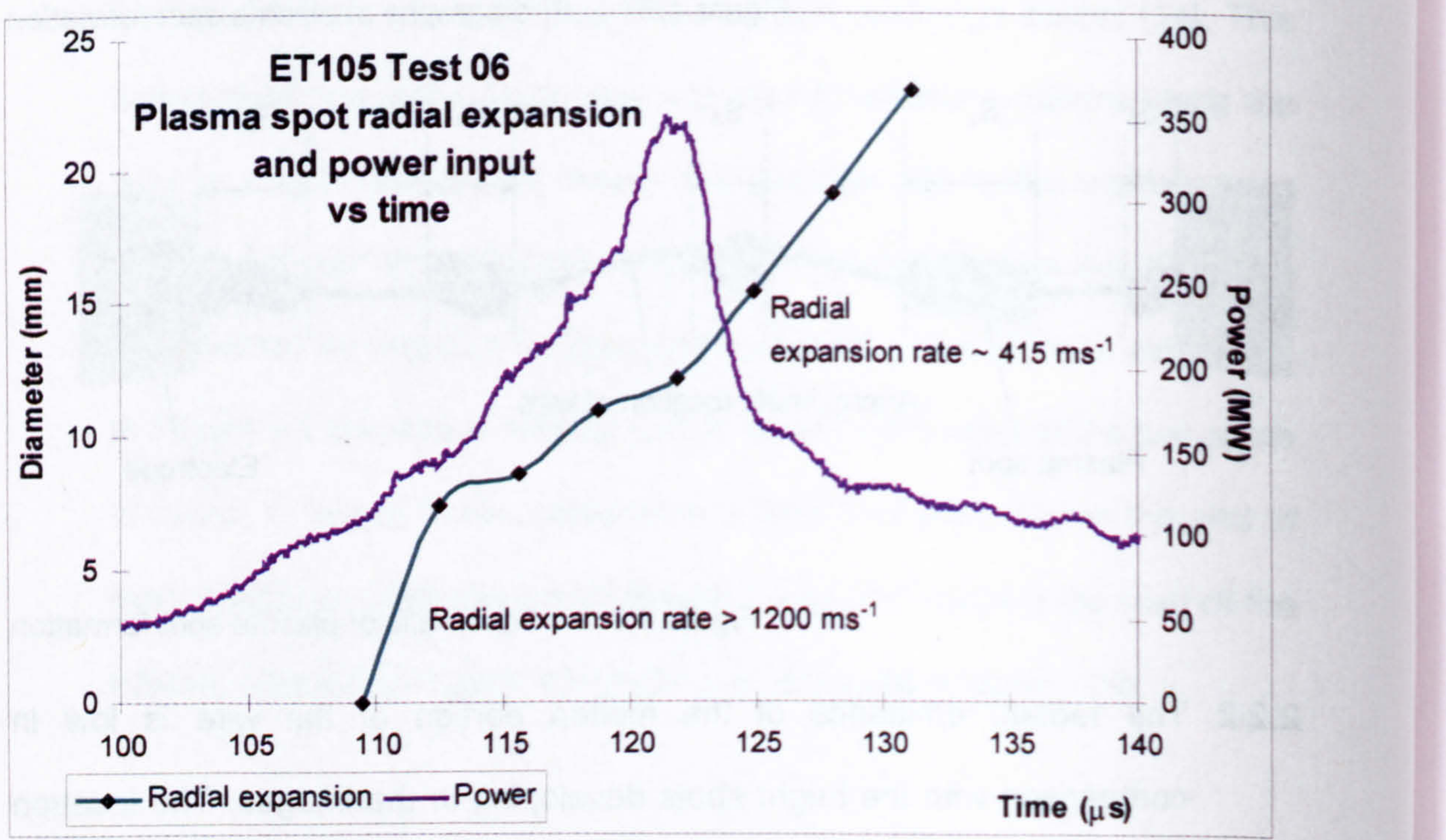

Figure 4.7 Plasma radial expansion rate and discharge power for high powered discharge

2.2.4 For a very low power discharge, the rate of expansion was dramatically lower (around 14 m s^{-1}) and the length of the pause was considerable, although the spot diameter at the pause at 9 mm was similar to that of

the high powered discharge. The pause at this spot diameter is thought to be due to a balance between spot temperature (resistivity), current flow and the wire resistance either side of the spot. Figure 4.8 shows a similar plot to Figure 4.7 but for a very long, low power discharge attainable using the 22 kV mode capacitor configuration. Three spots were studied, (A – C), developing along the same length of wire. These tests seemed to indicate that, within the limits of the tests, a reduction in the discharge power resulted in similar, although less energetic, physics.

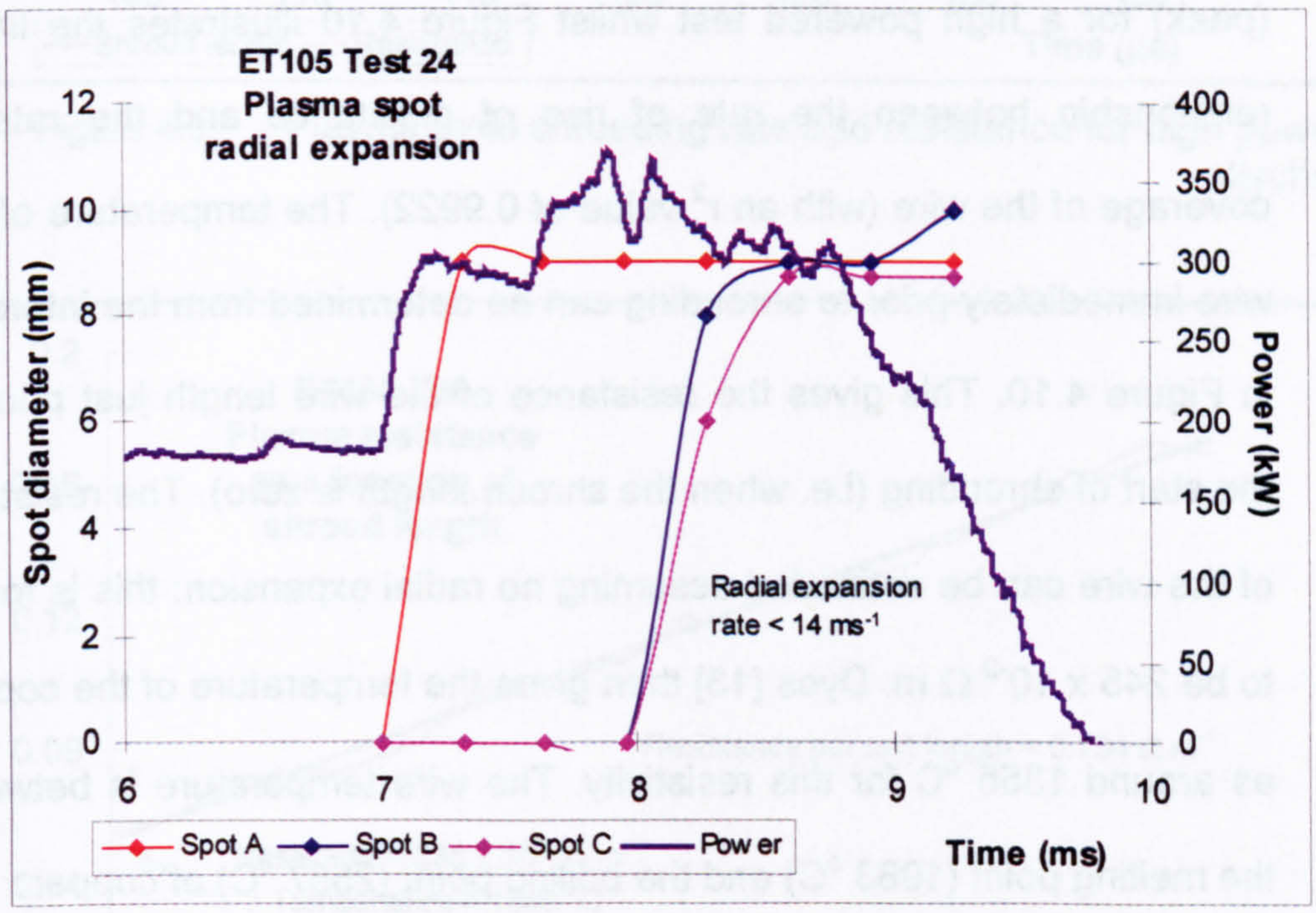

Figure 4.8 Plasma radial expansion rate and discharge power for low powered discharge

2.2.5 Individual spots tend to expand and coalesce with axial development. The total length of the plasma (here called the shroud length) can be measured from the photographic images, shown in Figure 4.6 as the sum of the individual lengths S_1 to S_5. The edges of the plasma spot

boundaries are poorly defined, but the digital images allow an edge to be objectively determined within one pixel of error. The image pixels are defined in 'counts': the higher the count, the brighter the image. The plasma edge can thus be defined in terms of a particular count (see appendix B Section 3.1.6).

2.2.6 It is evident from measurement of the shroud length that a strong relationship exists between it and the resistance of the wire/plasma system. Figure 4.9 shows the shroud length along with the resistance (peak) for a high powered test whilst Figure 4.10 illustrates the linear relationship between the rate of rise of resistance and the rate of coverage of the wire (with an r^2 value of 0.9922). The temperature of the wire immediately prior to shrouding can be determined from the intercept in Figure 4.10. This gives the resistance of the wire length just prior to the start of shrouding (i.e. when the shroud length is zero). The resistivity of the wire can be estimated assuming no radial expansion: this is found to be 245×10^{-9} Ω m. Dyos [13] then gives the temperature of the copper as around 1355 °C for this resistivity. The wire temperature is between the melting point (1083 °C) and the boiling point (2567 °C) of copper.

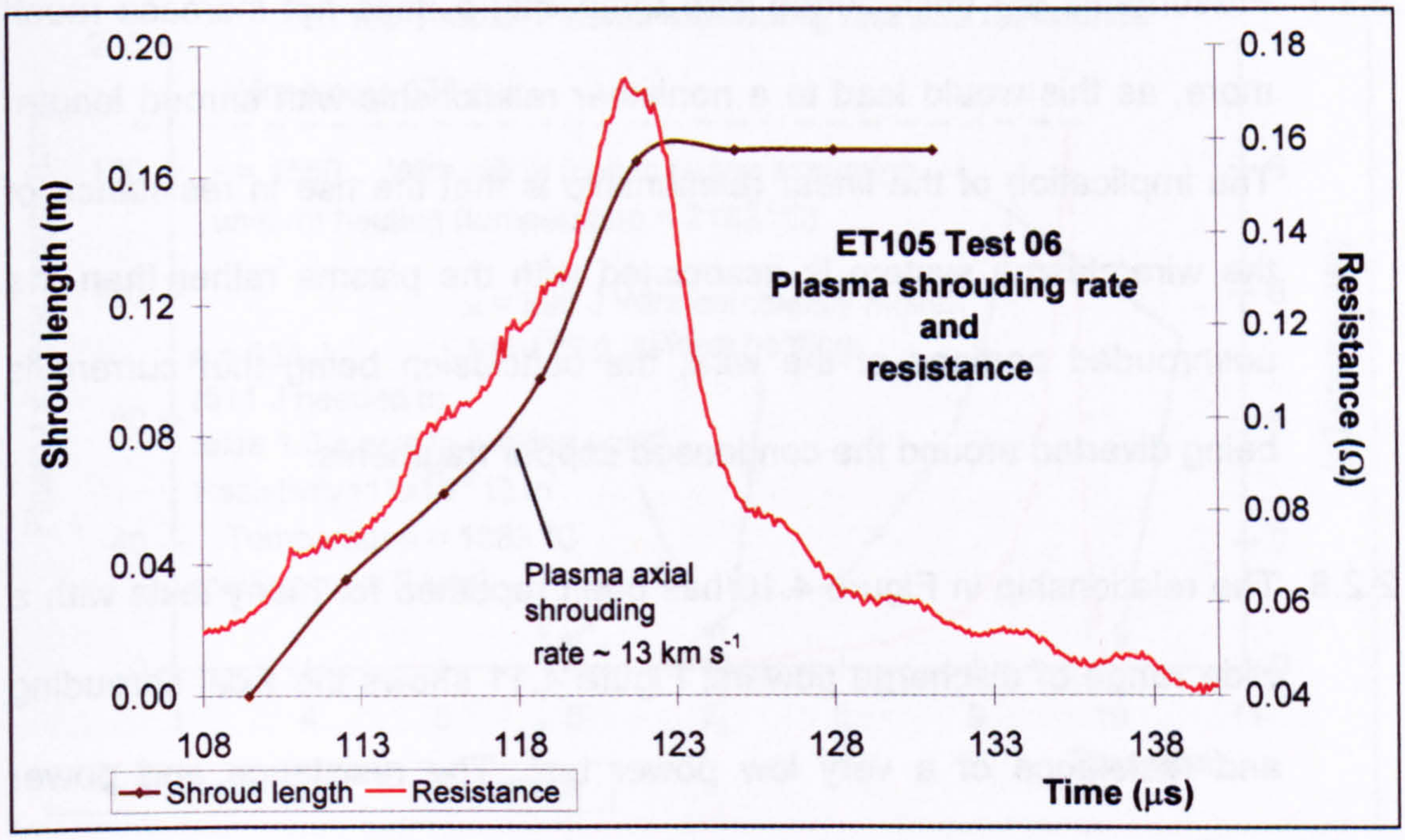

Figure 4.9 Plasma axial shrouding rate and resistance for high powered discharge

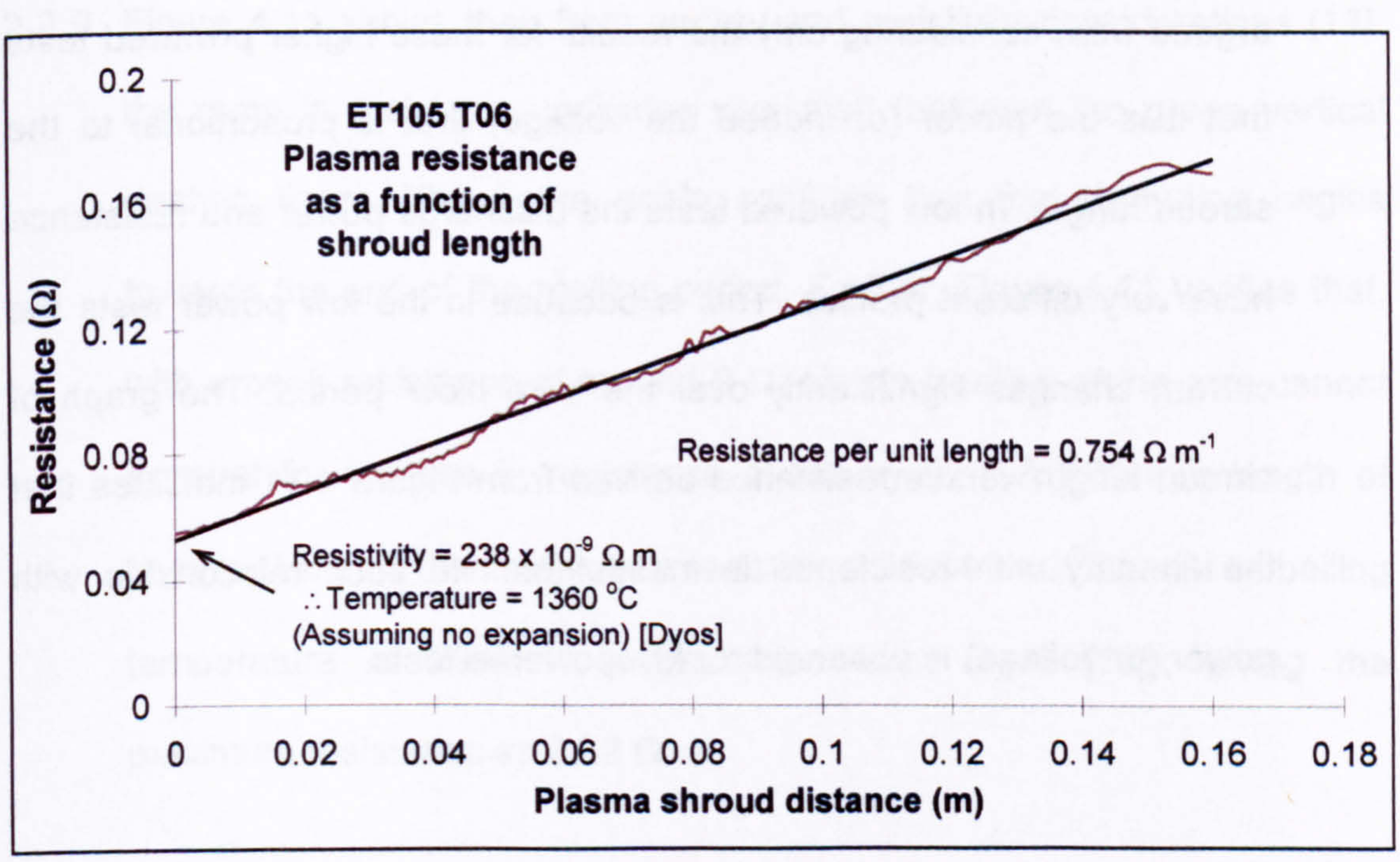

Figure 4.10 Plasma shroud length versus resistance for high powered discharge

2.2.7 Presumably the unshrouded wire temperature does not increase much more, as this would lead to a nonlinear relationship with shroud length. The implication of the linear relationship is that the rise in resistance of the wire/plasma system is associated with the plasma rather than the unshrouded portions of the wire, the conclusion being that current is being diverted around the condensed copper fragments.

2.2.8 The relationship in Figure 4.10 has been repeated for many tests with a wide range of discharge powers; Figure 4.11 shows the axial shrouding and resistance of a very low power test. The resistance and power profiles are very similar in the higher powered tests due to the current being reasonably constant for this period of the discharge. It could be argued from considering only the results for these higher powered tests that it is the power (or indeed the voltage) that is proportional to the shroud length. In low powered tests the discharge power and resistance have very different profiles. This is because in the low power tests the current changes significantly over the 'wire blow' period. The graph of shroud length versus resistance derived from Figure 4.11 indicates that the linearity with resistance is maintained. No such relationship with power (or voltage) is observed for low powered tests.

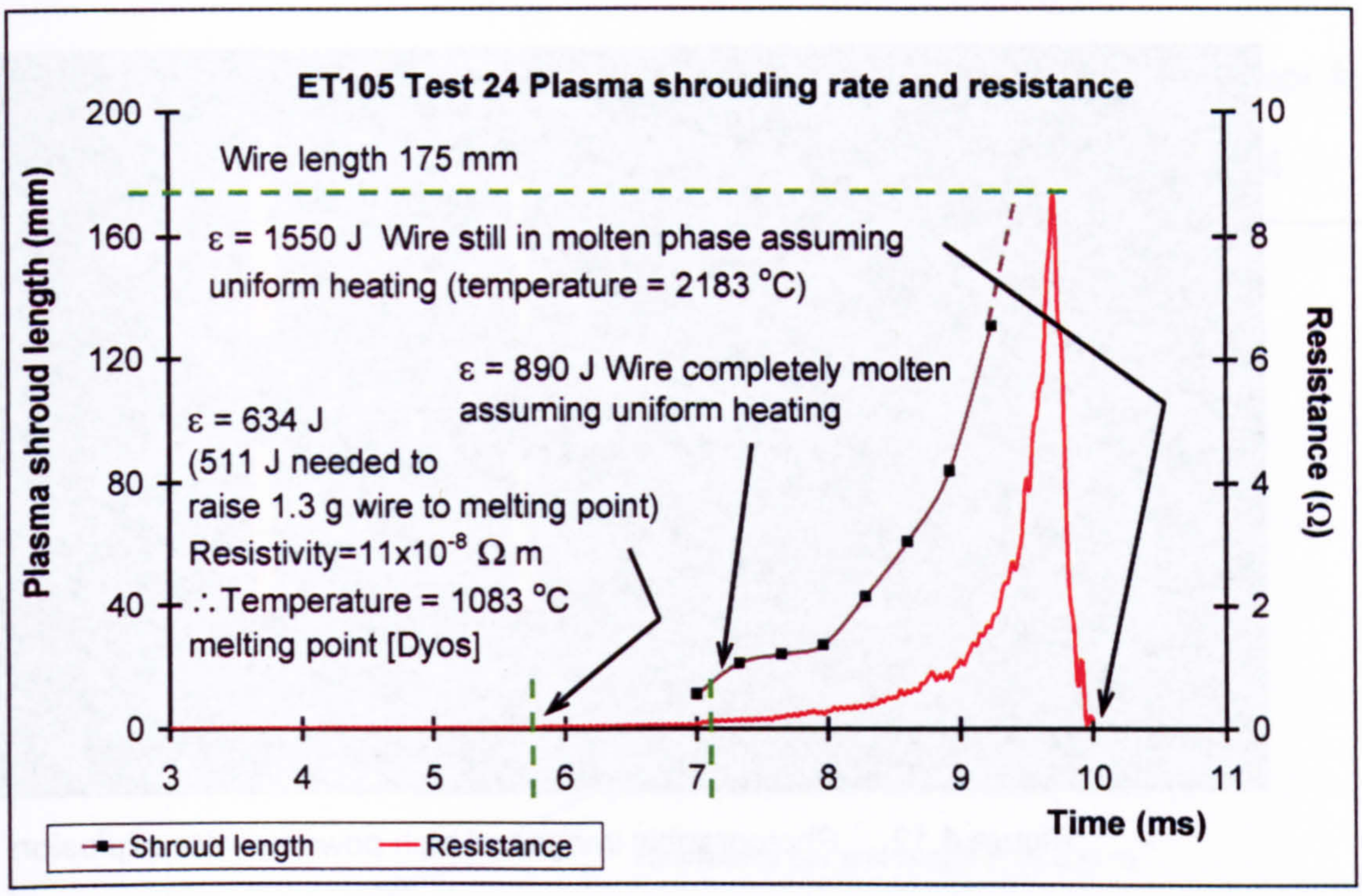

Figure 4.11 Plasma axial shroud length versus resistance for low powered discharge

2.2.9 Figure 4.11 shows that, from energy and resistivity considerations [13], the ramp in resistance indicates wire melt (between the green vertical dashed lines). The figure again confirms that the shrouding begins towards the end of the melting period. Further, Figure 4.11 verifies that, with a peak resistance of around 9 Ω, simple heating of the wire cannot account for the rise in resistance of the system. A 180 mm length of copper, 1 mm in diameter has a resistivity of 5.64×10^{-6} Ω m at its boiling temperature of 2840 K (extrapolated from Dyos [13]), giving the maximum resistance as 0.32 Ω.

2.2.10 Figure 4.12 and Figure 4.13 are false colour photographs of a high and a low powered wire explosion respectively, using the same setting for exposure time.

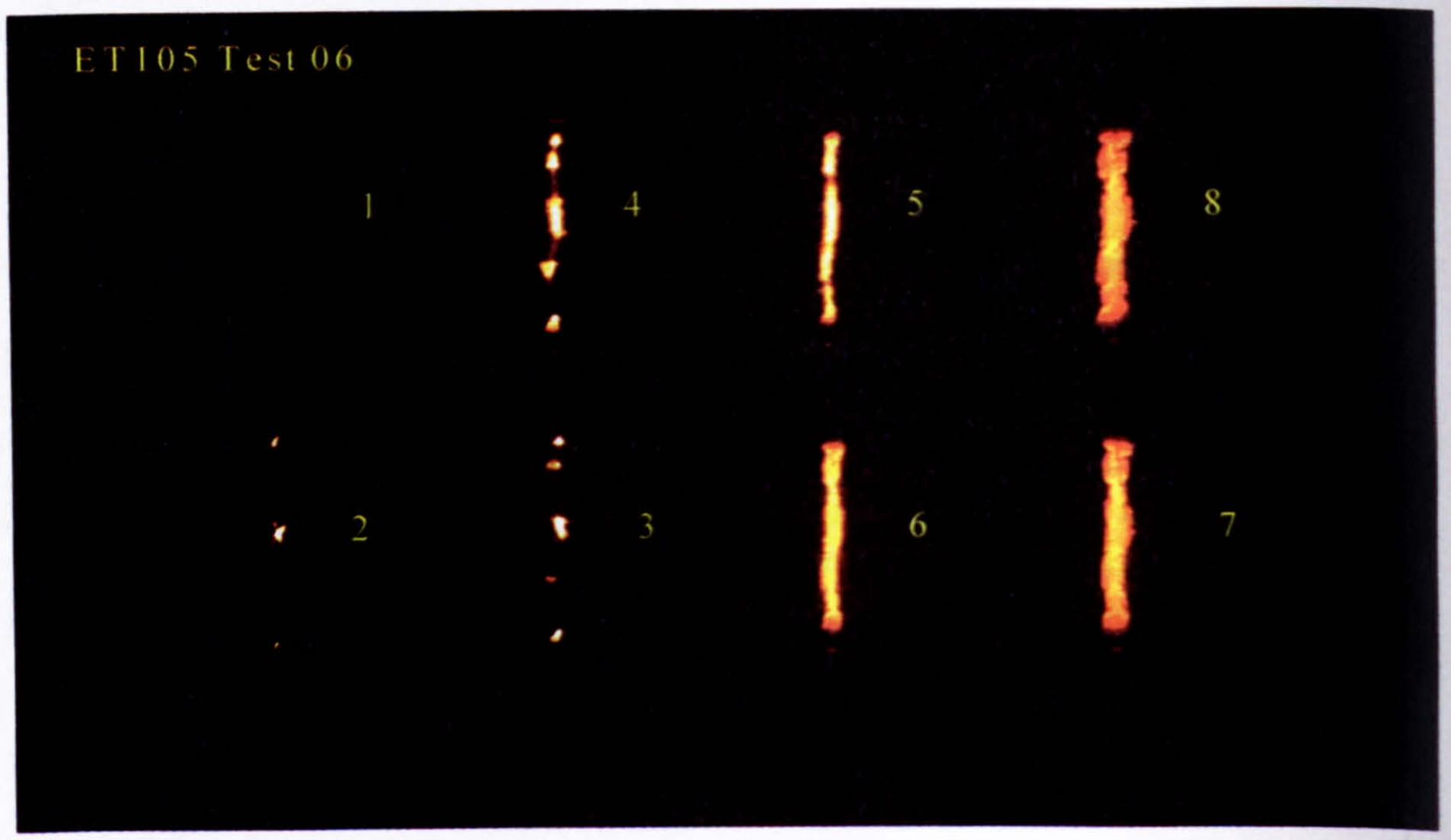

Figure 4.12 Photographic images of high powered wire explosion

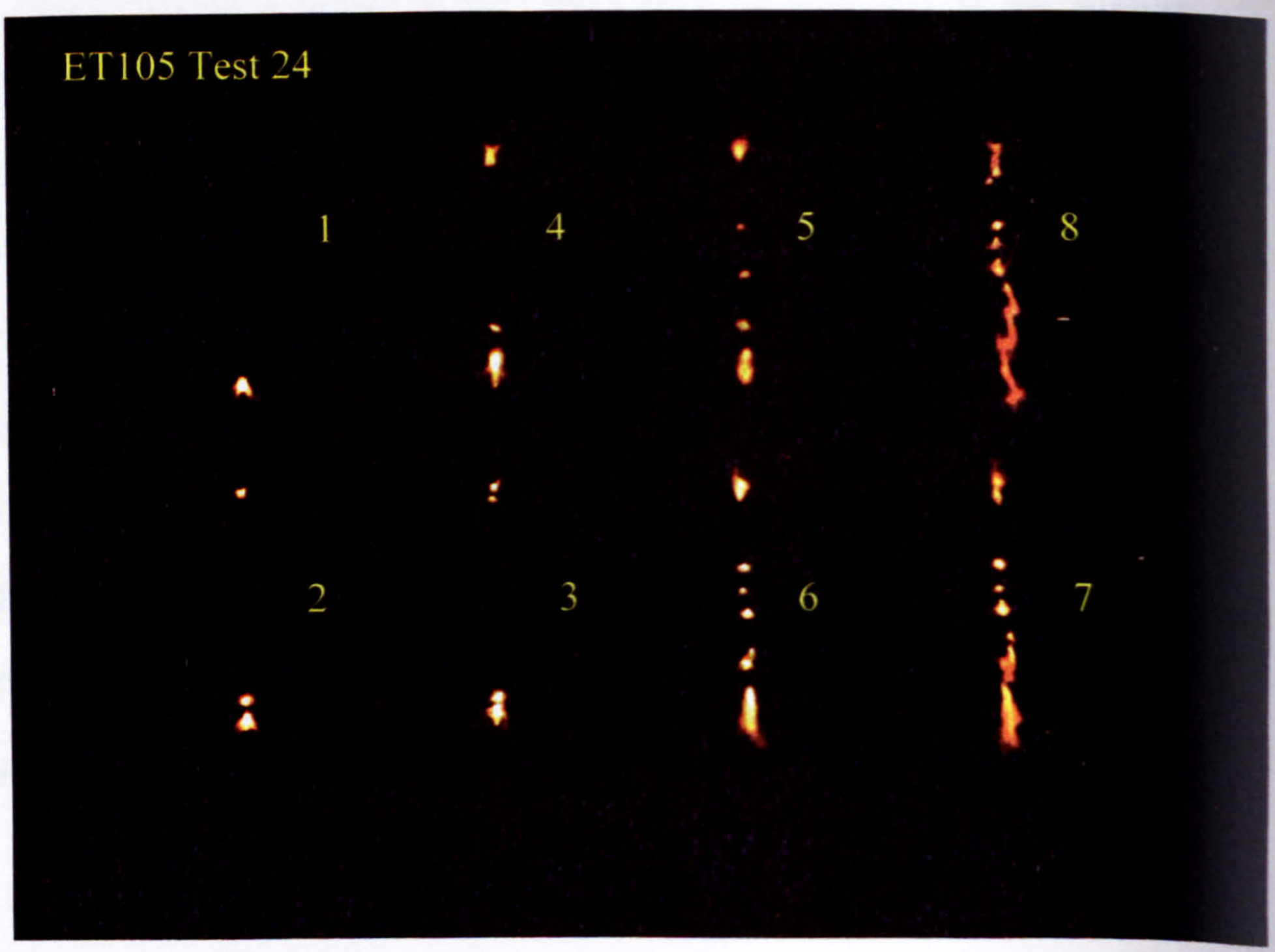

Figure 4.13 Photographic images of low powered wire explosion

2.2.11 In the low powered test, the photographed plasma boundary was fuzzy, making it difficult to determine the shroud length accurately. This resulted

in a poorer correlation (r^2 value of 0.973) and a negative intercept for axial shroud length versus resistance plots, as shown in Figure 4.14.

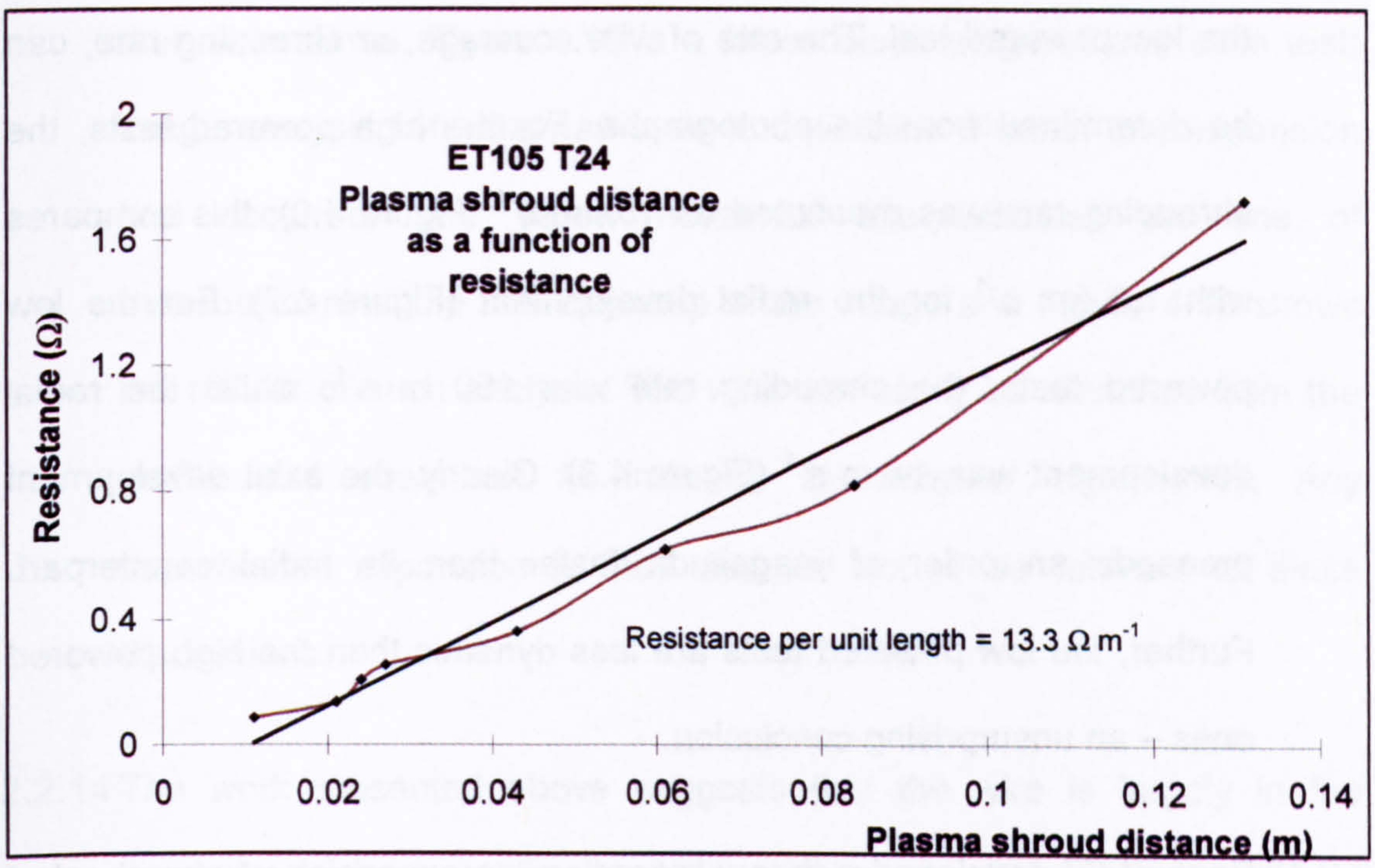

Figure 4.14 Plasma shroud length versus resistance for a low powered discharge

2.2.12 The resistance per unit length of the plasma column for the low powered discharge (given by the gradient of the line in Figure 4.14) is 13.3 Ω m^{-1}: this compares with 0.745 Ω m^{-1} for high powered tests (Figure 4.10). Given an homogenous plasma with an even current density, the plasma temperature could be calculated from the gradient of such lines. However, the situation here is complex, with condensed fragments carrying at least a small fraction of the current and an inhomogeneous plasma system, making any attempt at measuring the plasma temperature susceptible to large, undetermined errors. However, assuming uniform plasma columns of 10 mm diameter, and employing

plasma conductivities from Marshall [15], the plasma temperatures are determined at around 6500 K for the high powered test and 5500 K for the low powered test. The rate of wire coverage, or shrouding rate, can be determined from the photographs. For the high powered tests, the shrouding rate was measured as 13 km s^{-1} (Figure 4.9); this compares with 1.2 km s^{-1} for the radial development (Figure 4.7). For the low powered tests, the shrouding rate was 150 m s^{-1}, whilst the radial development was 14 m s^{-1} (Figure 4.8). Clearly, the axial development proceeds an order of magnitude faster than its radial counterpart. Further, the low powered tests are less dynamic than the high powered ones – an unsurprising conclusion.

2.2.13 Bennett [3] developed a theory regarding the expansion of superheated wires for the early phase of the wire explosion event. The experimental parameters for his work were very different, however. In particular, Bennett used thin wire of around a hundred microns diameter, with very low circuit inductance and no crowbar diode to prevent current reversal. Thus, the current could reduce to very low values and even undergo polarity reversal. Bennett's theories developed to explain a rapid expansion of the condensed phase of the wire that occurred before a plasma discharge formed, which had been noticed during exploding wire studies. The easiest way to show this expansion was to back-light the exploding wire and then photograph it. This work was performed by the Author, under experimental conditions pertinent to ETC technology [14]. A piece of stiff, white card was placed behind the wire with the aim of

using the plasma light itself to back-light the exploding wire. The expansion rate of the unshrouded wire, which could be easily seen, was then determined. Figure 4.15 is a false colour image of one such test; image analysis software was used to determine whether any expansion had occurred. The yellow horizontal line indicates the line of measurement of the intensity map of the image and Figure 4.16 shows the results of such analysis. The wire can easily be identified from the profile and seen not to increase in diameter significantly. Any superheated expansion is thus deemed not to be relevant to these discussions.

2.2.14 The work presented above suggests that the wire is largely in the condensed phase at the peak in resistance, with a plasma shroud covering it. It is presumed from the linear resistance relationship that the electrical current is largely being conducted through this plasma. If it were not, then the linear relationship between resistance and shroud length, as well as the energy transfer processes required for the maintenance of the plasma temperature would both need an explanation. The conclusion from these arguments is that current is being diverted around the fragments preferring a path through the plasma.

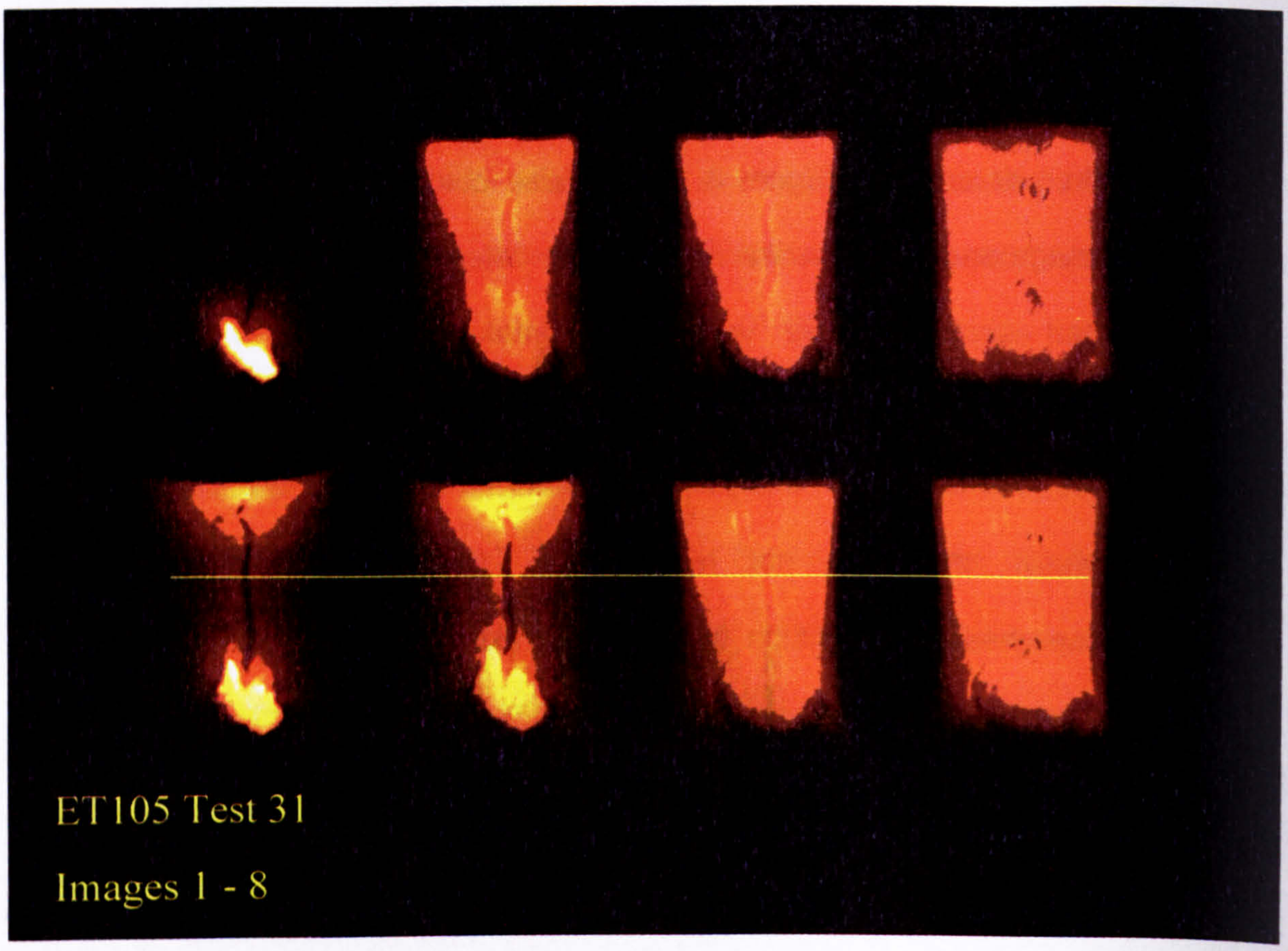

Figure 4.15 False colour images of back-lit exploding wire

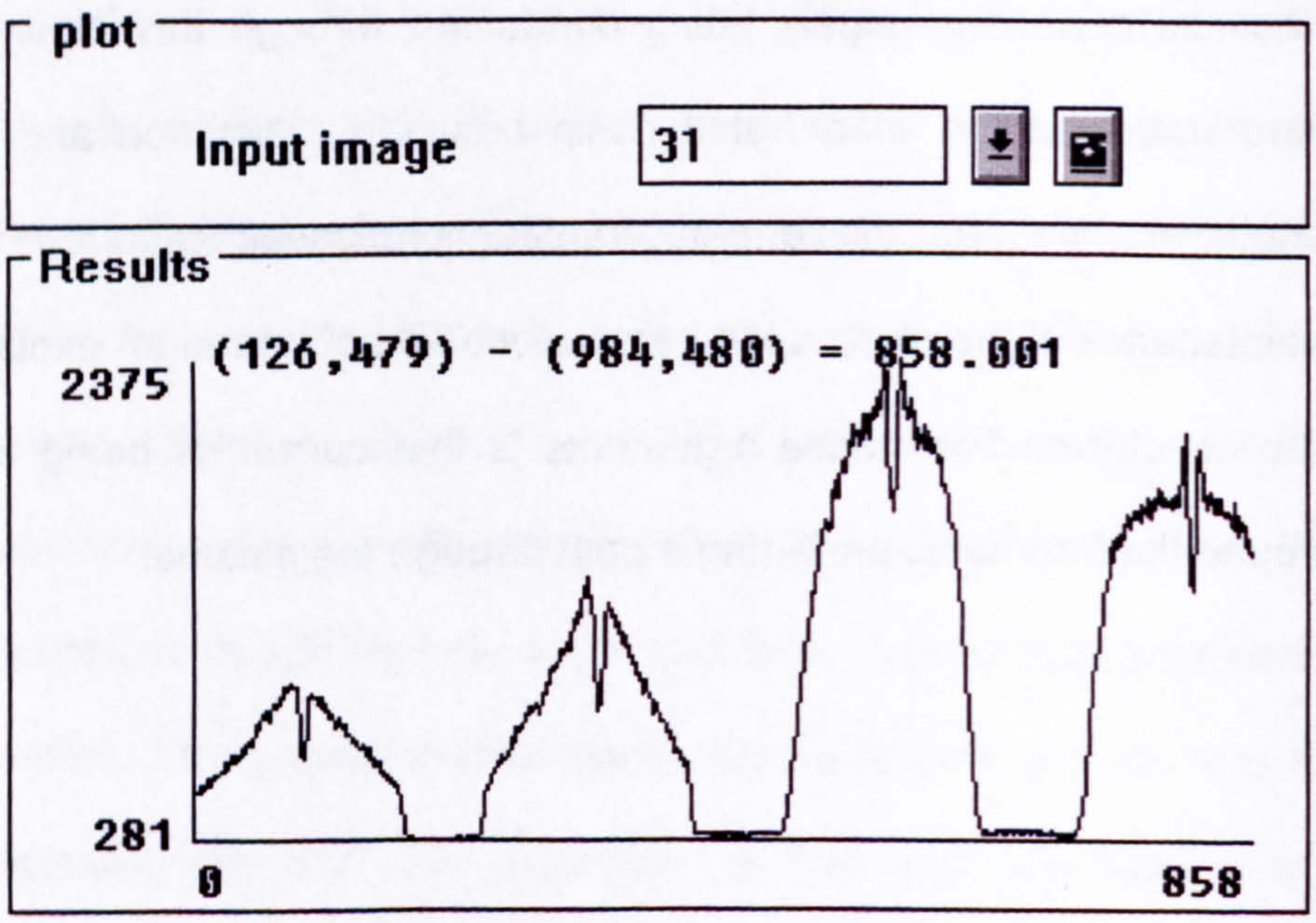

Figure 4.16 Light intensity map along horizontal yellow line in Figure 4.15

2.3 X-radiological studies

2.3.1 Pulsed x-radiological studies were performed to confirm the low condensed mass loss predicted during the wire explosion process from electrical considerations, and to gain further insight into the development of the condensed exploding wire material beneath the plasma sheath [16]. For these exploding wire tests, around 14 kJ of energy were discharged in 0.7 ms, with a peak power of around 120 MW. The wire was held in the balanced field rig and the Ultranac fast-framing camera was again used to compare individual x-radiographs with photographs. Figure 4.17 shows the timings of the flash x-ray pulses relative to the resistance peak; the vertical lines represent times when flash x-radiological images were recorded. The x-radiological images in Figure 4.18 include one pre-test result (first image) and eleven x-radiographs produced from this series of tests. The electrode configuration was changed during the tests due to a lack of component availability. However, the small change in attachment method and length of wire appear to make little difference to the mode of explosion. Electrode separation is around 150 mm with rounded electrodes and 175 mm without.

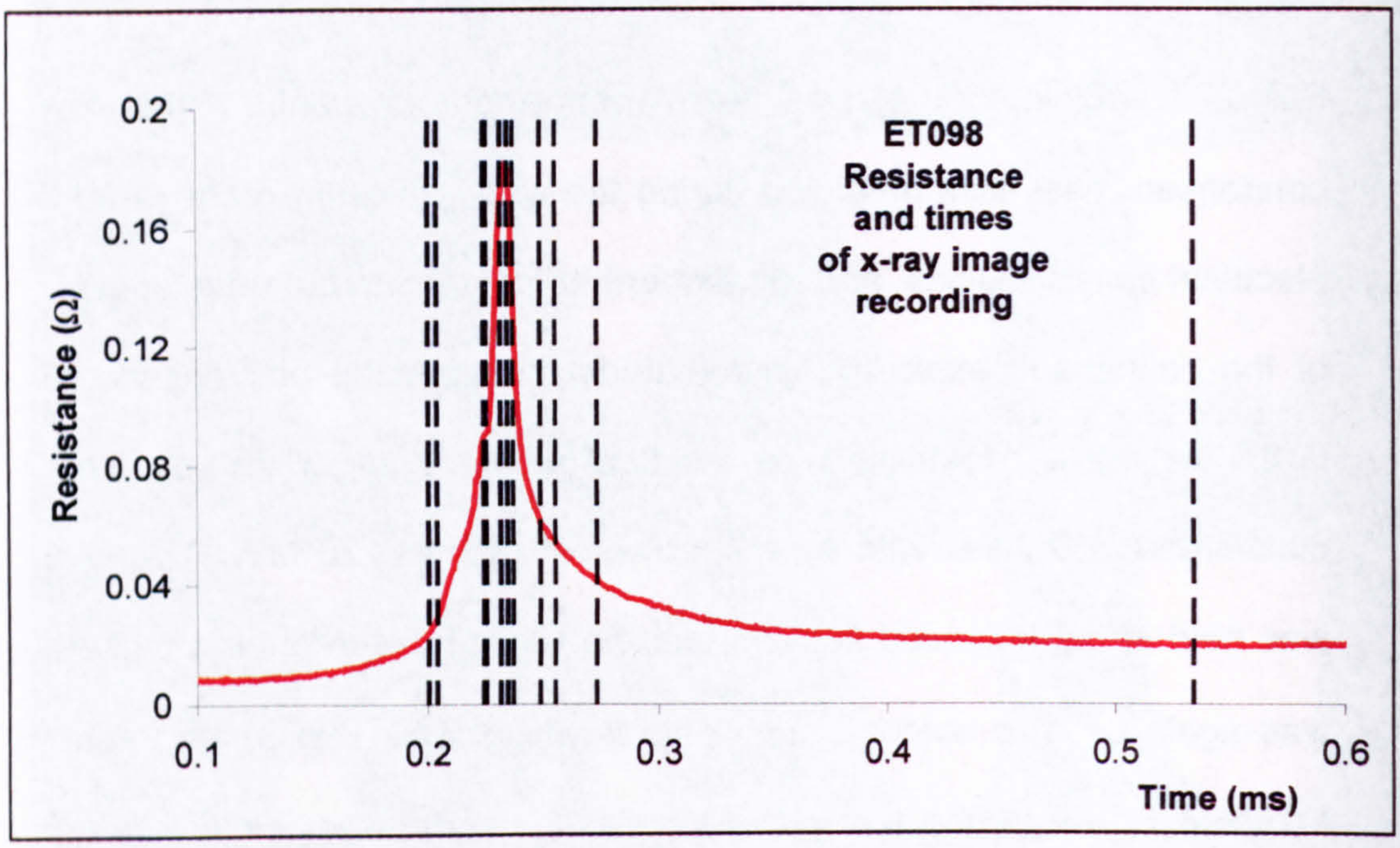

Figure 4.17 Pulsed x-radiological timings with respect to exploding wire resistance

2.3.2 Figure 4.18 indicates that condensed fragments of the wire, several centimetres long, can exist for a period after the peak in resistance (sixth image).

2.3.3 Similar fragmentation was reported throughout the work by Chace and Moore [2], as well as in more recent literature [4 - 6]. Two fragmentation processes seem to be occurring: a coarse process before the peak in resistance (the top row of images in figure 8), and a finer process that appears to occur afterwards. The resolution in these images for condensed copper has been determined at around 100 μm, suggesting that the second process may have been underway before the peak in resistance if the initial breaks were less than 100 μm wide.

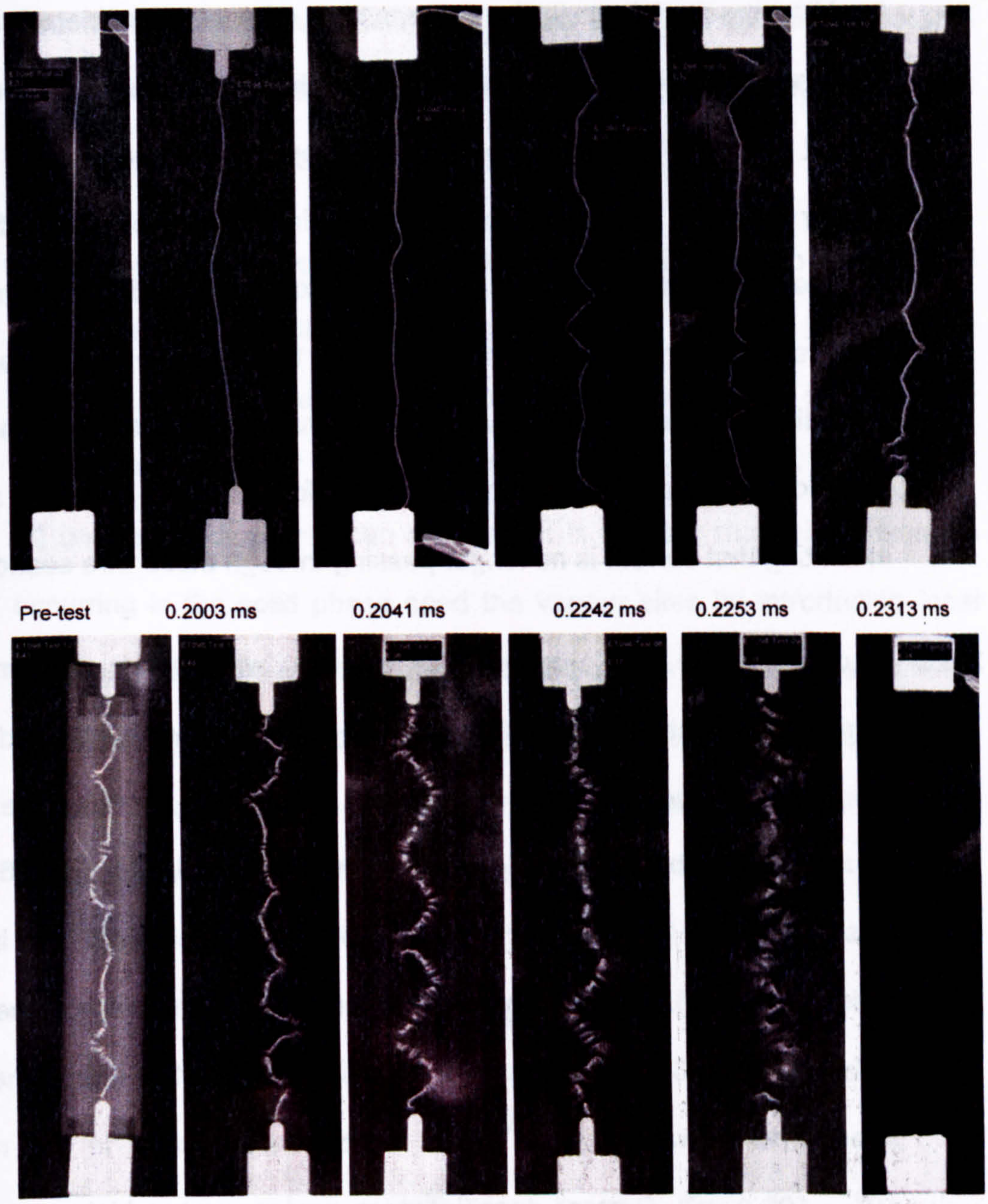

Figure 4.18 X-radiographic images taken at times relating to the exploding wire resistances in Figure 4.17

2.3.4 The coarse process fragments the wire into pieces several centimetres long. The origin of the breaks in the (initially undamaged) wire is associated with kinks established during the buckling of the wire. This

buckling resulted from thermal expansion, originally considered due to the longitudinal confinement of the wire by the electrodes. However, very recent work [17] has shown that freely suspended wires also suffer similar buckling, demonstrating that the wire's own inertia is sufficient confinement. Excess heating at the kink locations leads to premature vaporisation there, whilst further heating at these locations is thought to be radiative once they are covered in plasma. It is shown below that the kink locations are coincident with the formation of plasma spots, indicating that current is no longer passing through these wire sections.

2.3.5 In contrast, the fine process fragments the wire into a random and increasing number of smaller pieces. It has been suggested that thermally-induced stress or other wave phenomena produce the finer structure, possibly while the wire is still in the solid phase [5, 6, 18]. Nasilowski first showed that the wire could fragment whilst still in the solid phase [19], although the experimental conditions were somewhat different. Allen [6] reported that solid phase fragmentation due to thermal stress waves was likely to occur for current densities in the range $10^8 - 10^9$ A m^{-2}. Current densities here are somewhat higher at peak current, but may pass through this range while the wire is still solid. Whether there is sufficient time for solid phase fragmentation to occur is debatable. Shvetsov *et al* [8], among others [2], suggested that the fine structure might be due to 'magnetohydrodynamic (MHD) instabilities of the necking type' [8]. Here, the current flowing through the molten wire causes the metal to flow into a series of globules and necks [19], or

reinforces a similar pre-existing structure [8]. Once established, material flows from the necks to the globules resulting in the fine structure appearance of the wire in Figure 4.18.

2.3.6 Close inspection of the x-radiographs (Figure 4.19) gives no indication of necking associated with the MHD effect. Further, the finer structure first occurs at the kink location once plasma spot development is well under way. Apparent vapour bubbles (showing up as 'smoke-rings' [7] or 'disks' [8] on the x-radiograph) can be seen. It is feasible that micro-fractures occurring in the solid phase seed the vapour sites by introducing local thermal gradients within the solid wire. However, a striated appearance is expected from simple boiling, without the need for invoking solid phase micro-fractures or MHD effects, as the forming vapour bubble is free to expand radially but constrained longitudinally.

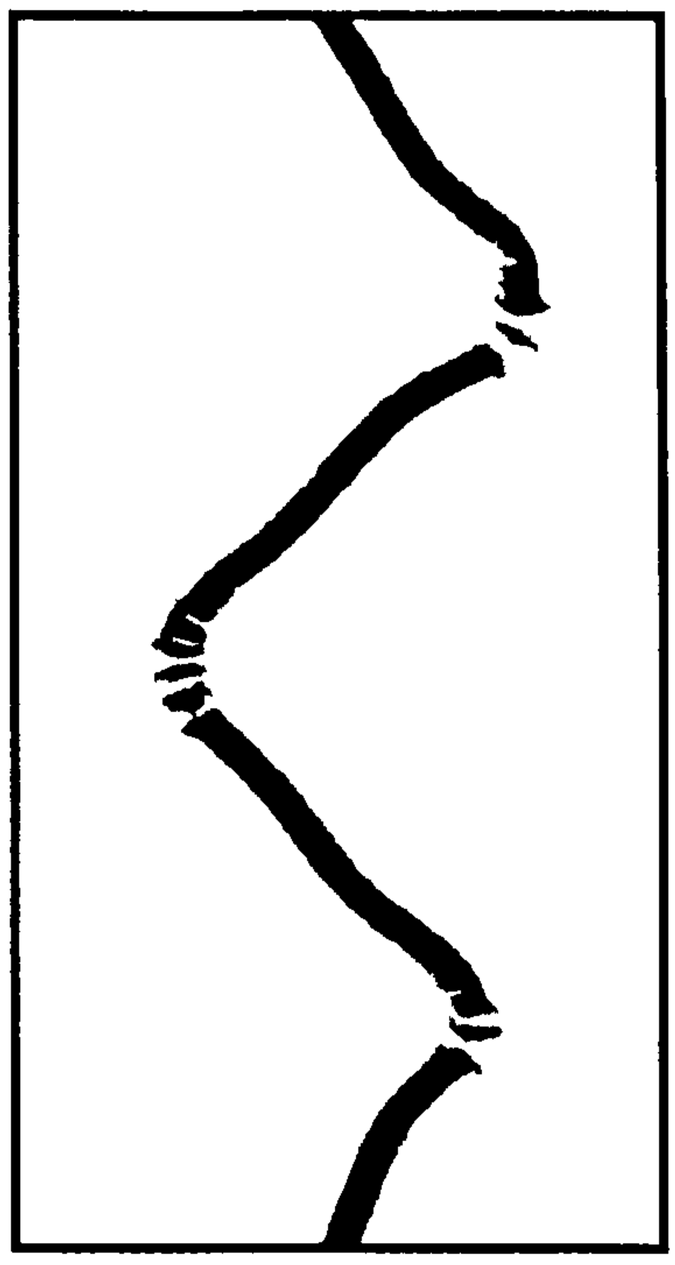

Figure 4.19 Detail from image 4, Figure 4.18 @ 0.2242 ms

2.3.7 The fine structure formed on the inner side of the kink is shown in Figure 4.19. The plasma might be expected to be hotter in the inside of the kink, causing that side of the wire to boil first. Several of the fragments show curvature at their ends, presumably resulting from localised pressure developed during the vaporisation.

2.3.8 Another important finding from images such as those in Figure 4.18 is that condensed material remains essentially in its original location until it has all evaporated away. This indicates that the Lorentz forces associated with the buckled wire are insufficient to drive the condensed fragments from their axial position, adding weight to the argument that little current is being conducted through the fragments. (Lack of Lorentz forces is also cited in reference [7] and x-radiographic images clearly show that it has little significant effect in reference [8]). Further, the confinement of the wire in a capillary (first image, second row of Figure 4.18 @ 0.2344 ms) appears to make little difference as far as the physical mechanisms of the exploding wire are concerned.

2.3.9 Work is in progress to determine if solid phase disintegration is occurring rather than early globule formation in the wire [20]. A thyristor [21] specifically purchased for this task will be connected in parallel with a wire and triggered early in the discharge. This thyristor is capable of diverting the current through itself by reducing its internal resistance to a very low value in several microseconds; such a change to its internal resistance can be triggered externally. This will have the effect of

terminating the wire explosion at a known time, allowing the wire remains to be examined for physical deformation. This will be done repeated at times corresponding to different stages of the process, starting very early in the event before the melt has occurred. The time at which the thyristor needs to be triggered can be determined by the electrical parameters of the initial wire explosion – the melt being easily identifiable through a small rise in resistance, prior to the main resistance rise at the 'wire blow'. This work is due to be completed in the financial year beginning April 2002.

2.3.10 Apart from general visual observations, detailed measurements of the x-radiographs have been made by scanning them electronically using a large digital scanner. Resolution was lost during this process, so it would have been better to enlarge the images photographically and then scan them in, thus preserving the resolution. The digital images were analysed using Image-Pro Plus, a commercially available image analysis software package.

2.3.11 Measuring the length and diameter of the wire allows the volume to be estimated, whilst knowing the linear expansion coefficient for the condensed phases of copper allows the temperature of the wire to be determined from measurements of its length. The length can be determined from the x-radiographs but although the linear expansion coefficient, α_s for solid copper was readily available in materials handbooks [22], the values for liquid copper, α_L had to be calculated from

known values of liquid copper density [23]. For this, a copper cylinder of volume, V_T at initial temperature, T_1 and final temperature, T_2 was considered. Then, from the definition of the linear expansion coefficient given in Equation 4.1, the coefficient multiplied by the temperature change is equal to the fractional increase in the linear dimensions (i.e. diameter and length):

$$\alpha = \frac{\left(\left(\frac{V_{T_2}}{V_{T_1}}\right)^{1/3} - 1\right)}{T_2 - T_1} \qquad \textbf{Equation 4.1}$$

2.3.12 The volume, V_T is calculated from the copper density at T. The values of the linear expansion coefficient for copper used here appear in Figure 4.20.

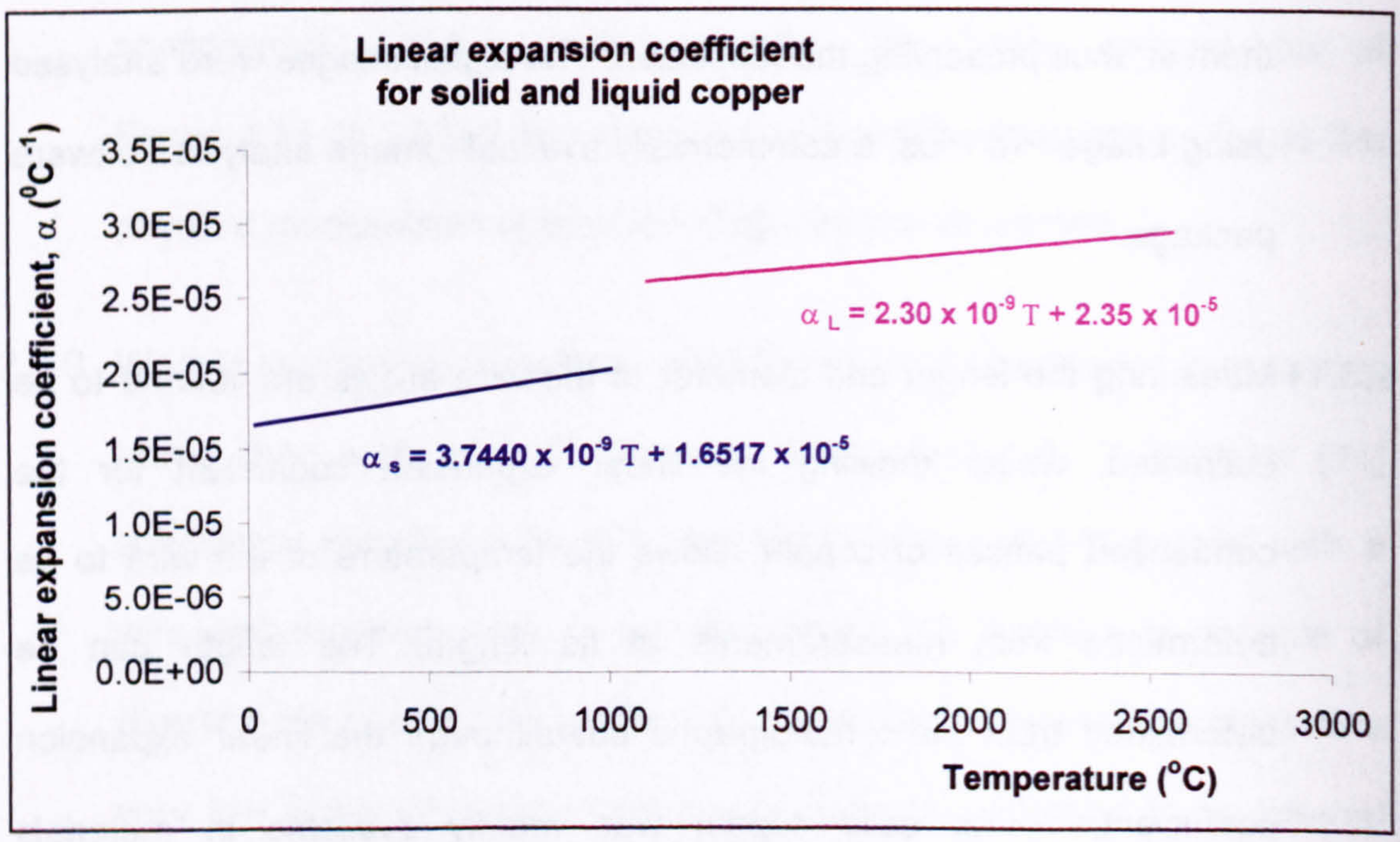

Figure 4.20 Linear expansion coefficient of solid and liquid copper

2.3.13 The length and width of the wire can be determined by using the *manual measurements* facility within the Image-Pro Plus software – see Figure 4.21(a, b and c). This allows the user to measure straight or curved lengths in pixels; photographing a test card allows the measurement to be calibrated in metres (see Appendix B). It was intended to measure the length and diameter of each fragment, calculate the volume of copper in each image and hence determine the evaporation rate of the wire until the wire was completely evaporated. However, as the wire was found to break up into many small pieces, it was difficult to estimate the volume in later stages of the wire explosion process by this method. Measurement of the volume of the longer fragments was straightforward but, as the number of fragments increased, length measurement became increasingly subjective. The methodology involved judgement by eye and addition of a contribution from small fragments together, as shown in Figure 4.21b. The error from this is small as long as the pieces are few, but it becomes very large with many fragments. To determine the wire volume, the diameter of the wire must be known for its entire length. Measurement of the diameter requires the location of the edge of the wire to be determined. Due to the decreasing level of absorption of the x-rays at the edges of the wire where the amount of copper reduces, the edges are fuzzy.

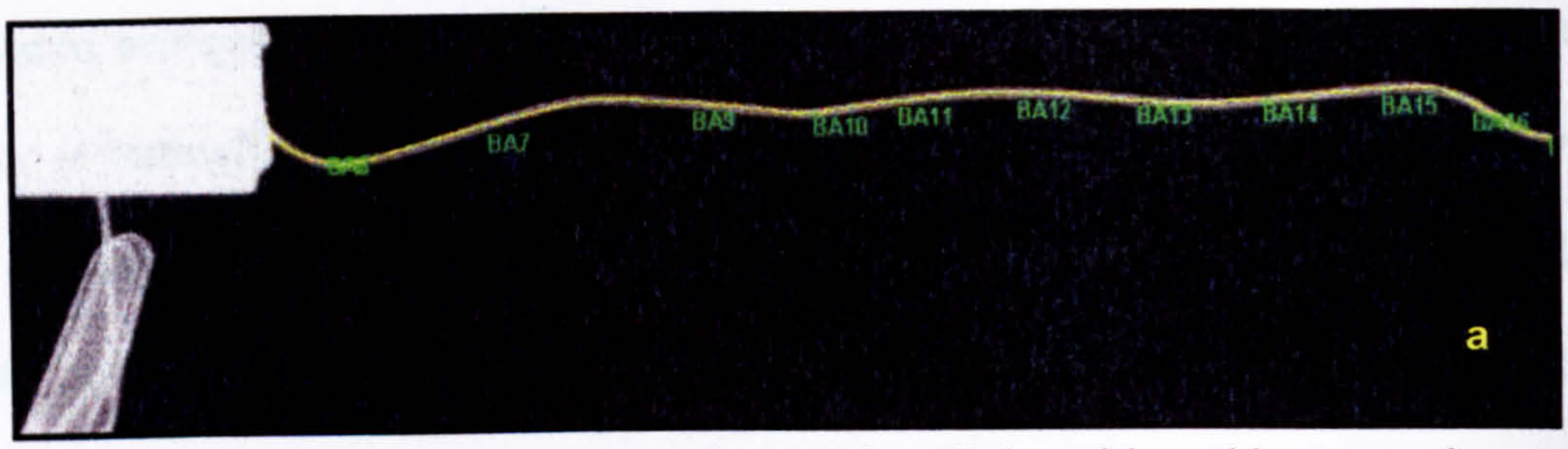

Measurement along a bent but continuous length is achieved by summing small sections

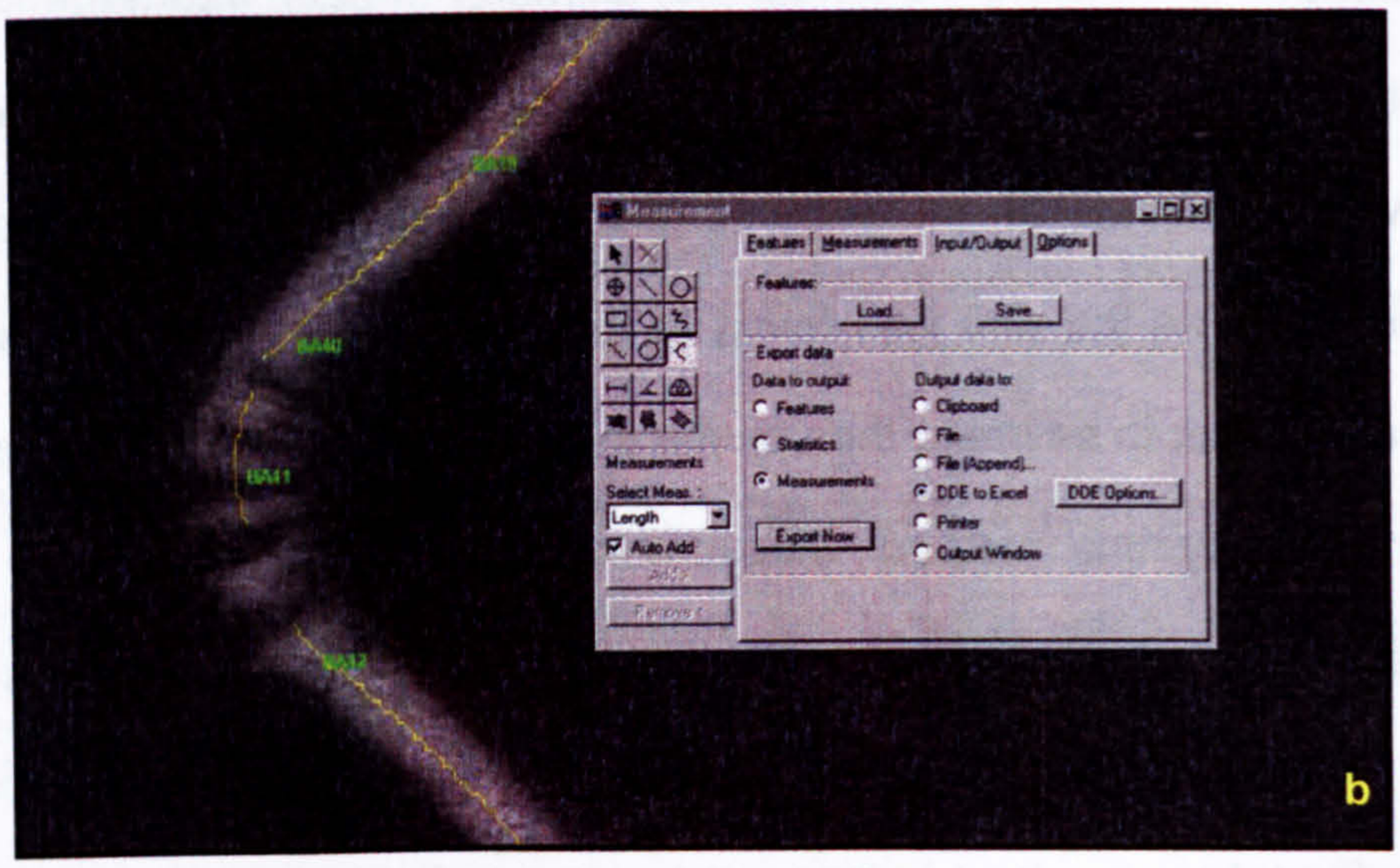

Measurement along a bent non-continuous length estimates the gaps

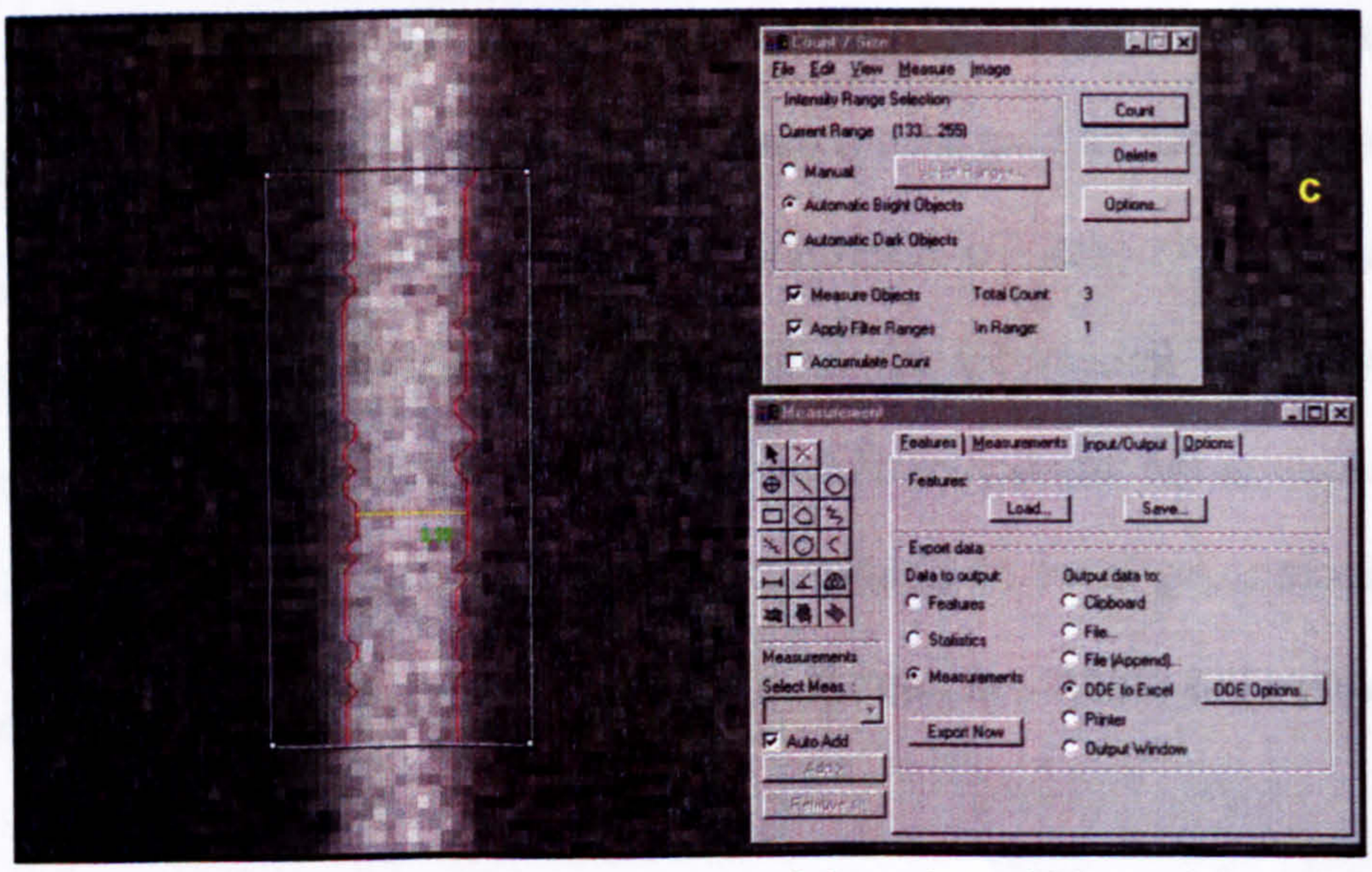

Measurement of the wire width seeks parallel sides

Figure 4.21 Wire length and width determination

2.3.14 To ensure consistency of measurement, the outline of the bright parts of the image can be automatically picked out using the *count/size* menu in Image-Pro Plus (Figure 4.21c). Figure 4.21c shows that the value of the diameter changes by ± one pixel on a local scale, although the diameter along the entire length is remarkably constant. The parts chosen for the measurements were those where the wire is straight for several pixels on each of its sides. Nineteen measurements were made along the length of the wire and statistical methods used to determine the true mean of the wire diameter. The errors in the diameter were of the order of 2 – 3%, whilst the errors in the length were of the order of 0.3%, notwithstanding those arising from the subjective inclusion of the small pieces. The volume was only determined for images up until 0.2344 ms, as after that time the number of gaps became too large to estimate the length with any confidence.

2.3.15 Such measurement of the digitised x-radiograph images was performed using the image analysis software, and the temperatures of these wires were determined: the results appear in Figure 4.22. They confirm again that the bulk of the wire is still a cool liquid for most of the resistance rise. (The error bars are associated with the difficulty in identifying the ends of the wire as it fragments further). Measurements of the axial and radial expansion of the wire confirm that no superheating or rapid radial expansion is occurring.

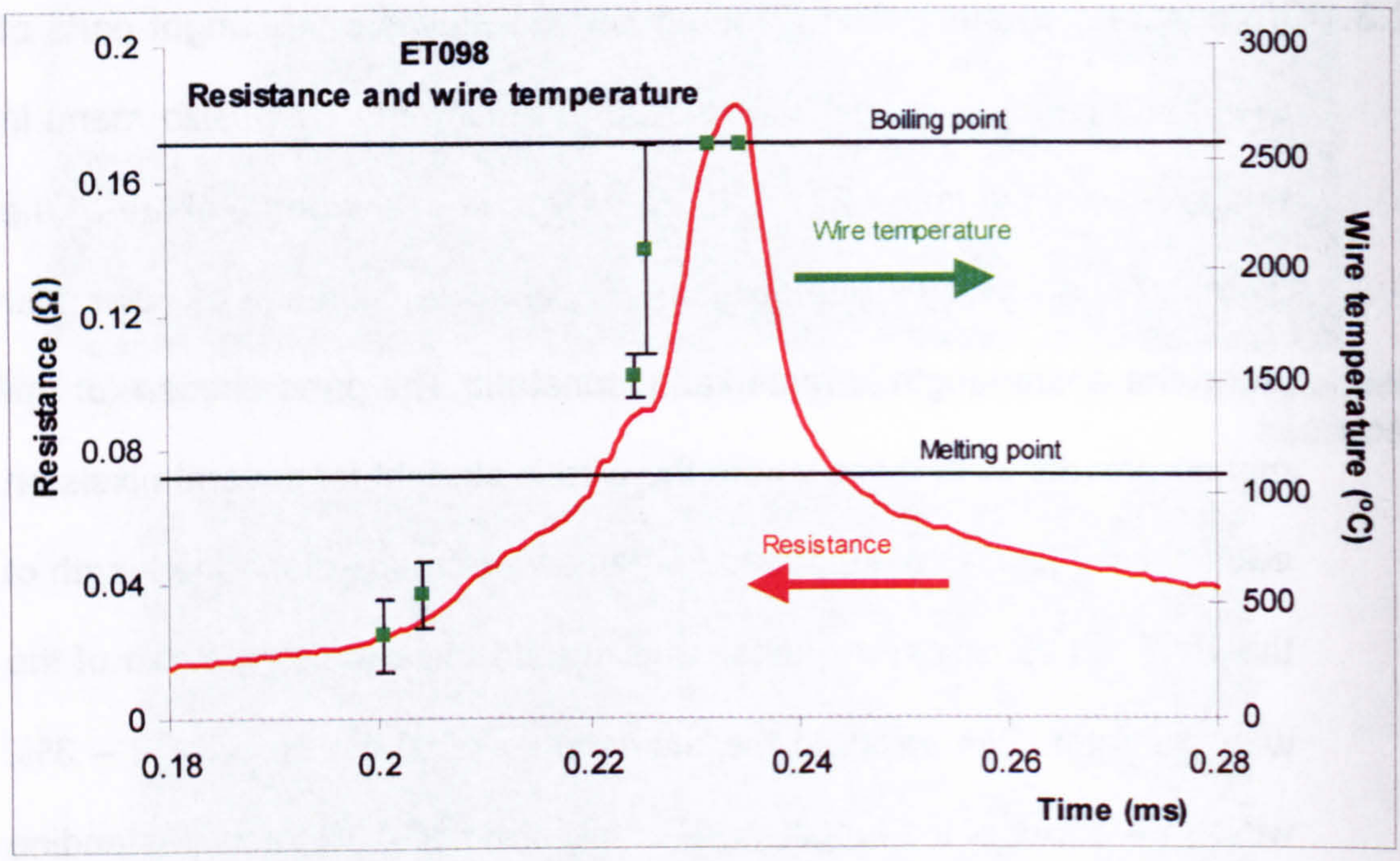

Figure 4.22 Exploding wire resistance and temperature estimation from linear expansion

2.3.16 Examination of the photographic and x-radiographic images of the same event shows the relationship between the plasma development and the fragmentation of the wire. Figure 4.23 comprises six photograph and x-radiograph 'montages' and a further two photographs highlighting intermediate plasma development. The first image is a montage but not of simultaneous images, with the x-radiograph being captured a few microseconds prior to the photograph. The two images that follow are enhanced digital images taken 1 μs apart with an exposure time of 100 ns. The following five images are montages composed of simultaneous x-radiographic and photographic images.

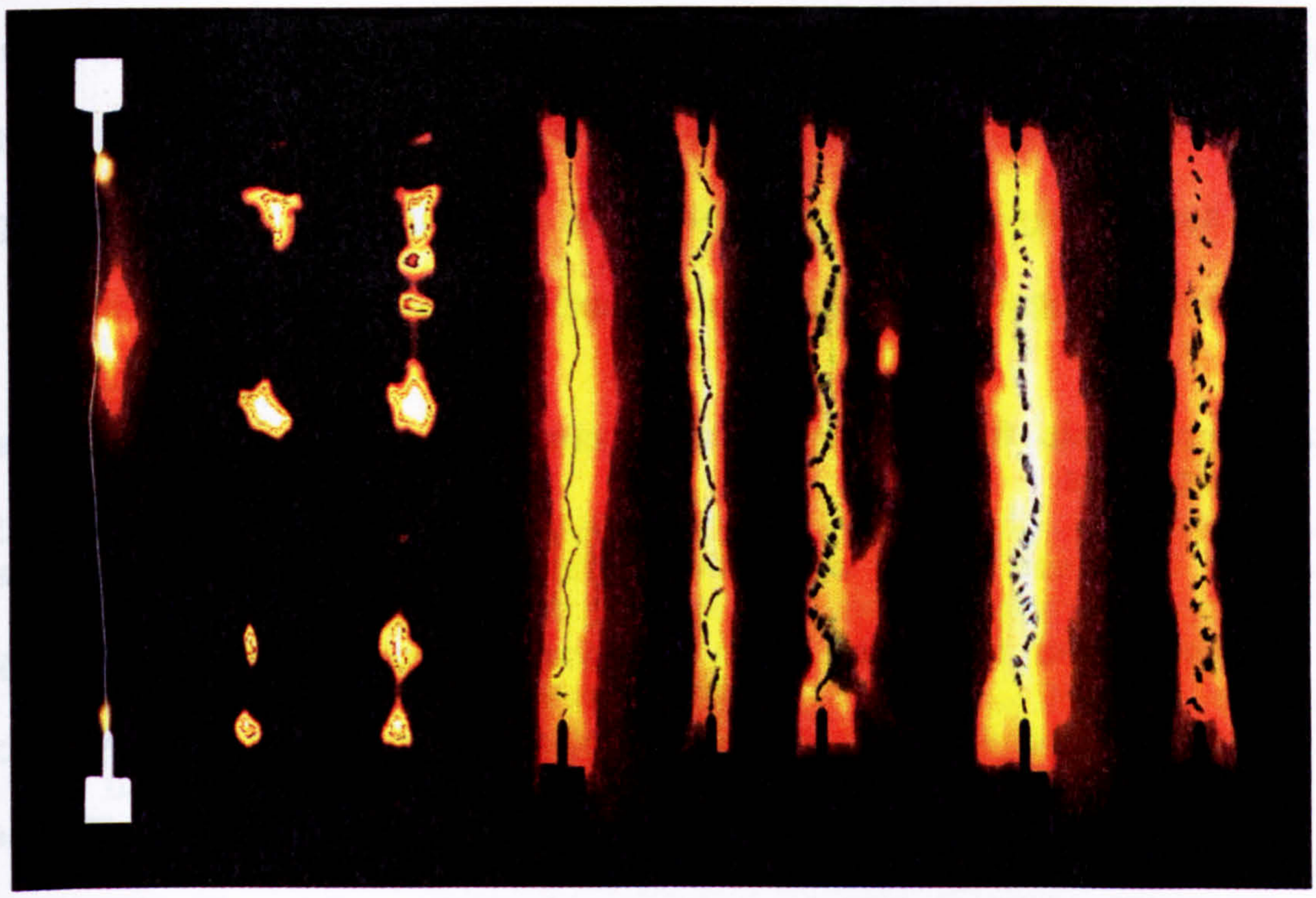

Figure 4.23 X-radiographic and photographic montage

2.3.17 The first image x-radiograph has a developing kink at the location of the subsequent plasma spot, together with the spots at the electrodes. The second and third images show the rapidity of the plasma development, and some interesting but as yet unstudied 'glow' discharges along the length of the wire. The fourth image illustrates the existence of apparently continuous lengths of condensed material several centimetres long, within the plasma. The last four images indicate the slow evaporation of the condensed material and the slow development of the plasma sheath in the radial direction. Also, some interesting plasma flares are seen to break away from the main discharge in the sixth image. These flares developed in brightness over a period of around 30 μs and showed evidence of around 8 mm of motion seemingly

towards (more likely in front of or behind) the wire throughout this time. Such flares could be associated with complex magnetic fields surrounding the plasma. Vlastós [24] reported some quite interesting helical magnetic phenomena during exploding wire studies.

2.4 Hypothesis for the diversion of current around condensed wire fragments

2.4.1 It has been argued above that current is being diverted around the condensed fragments of an electrically exploding wire, necessarily through seemingly higher resistance plasma. This phenomenon was also reported in work conducted for the electric armour programme [7], for aircraft radome lightning segmented divertor strips [5, 25] and segmented strip ETC igniters [26]. Arguments were presented in [7] and [26] on the essentially geometrical nature of the effect, limited to an aspect ratio of gaps and fragments of about unity. In the work described here, the fragment length is at least ten times that of the gap. A physical mechanism that explains current diversion is still needed for these aspect ratios and the Author's following argument attempts to provide one.

2.4.2 It was stated in [5] that the electrical conductivity of the metal vapour under exploding wire conditions was the most difficult aspect of the process to model. Recently published work by Desjarlais [27] has provided experimentally validated electrical conductivity data [28] in the liquid vapour transition region (see Chapter 3 Section 4.4.7) that may help to provide a solution to the current diversion. It is evident how poorly the vapour conducts relative to the cool plasma. It is proposed that an

electrically insulating vapour boundary layer might exist, forming naturally as a result of thermal gradients at the plasma/condensed wire fragment interface (assuming there are no discontinuities in temperature at the interface). This idea is used to explore the current diversion phenomenon.

2.4.3 A simplified model of a copper fragment surrounded by a plasma has a condensed copper fragment of length, l_c diameter, d_c and temperature, T_c located within a copper plasma column of length, l_p diameter, d_p and uniform temperature, T_p. A copper vapour boundary layer of thickness, t and at uniform temperature, T_v surrounds the fragment. Current initially passes into the region of interest through the plasma due to an applied potential across l_p. It then has the option of continuing to conduct through the plasma, or passing through the copper vapour boundary into the condensed fragment. It would then conduct through the condensed fragment and re-enter the plasma by passing back through the vapour boundary layer. The relative resistance of the plasma column and that of the vapour boundary layer together with that of the condensed fragment will determine the relative current density within the plasma and fragment. This problem is shown schematically in Figure 4.24. Apart from the introduction of the vapour boundary layer, the model is similar thus far to Powell's [26].

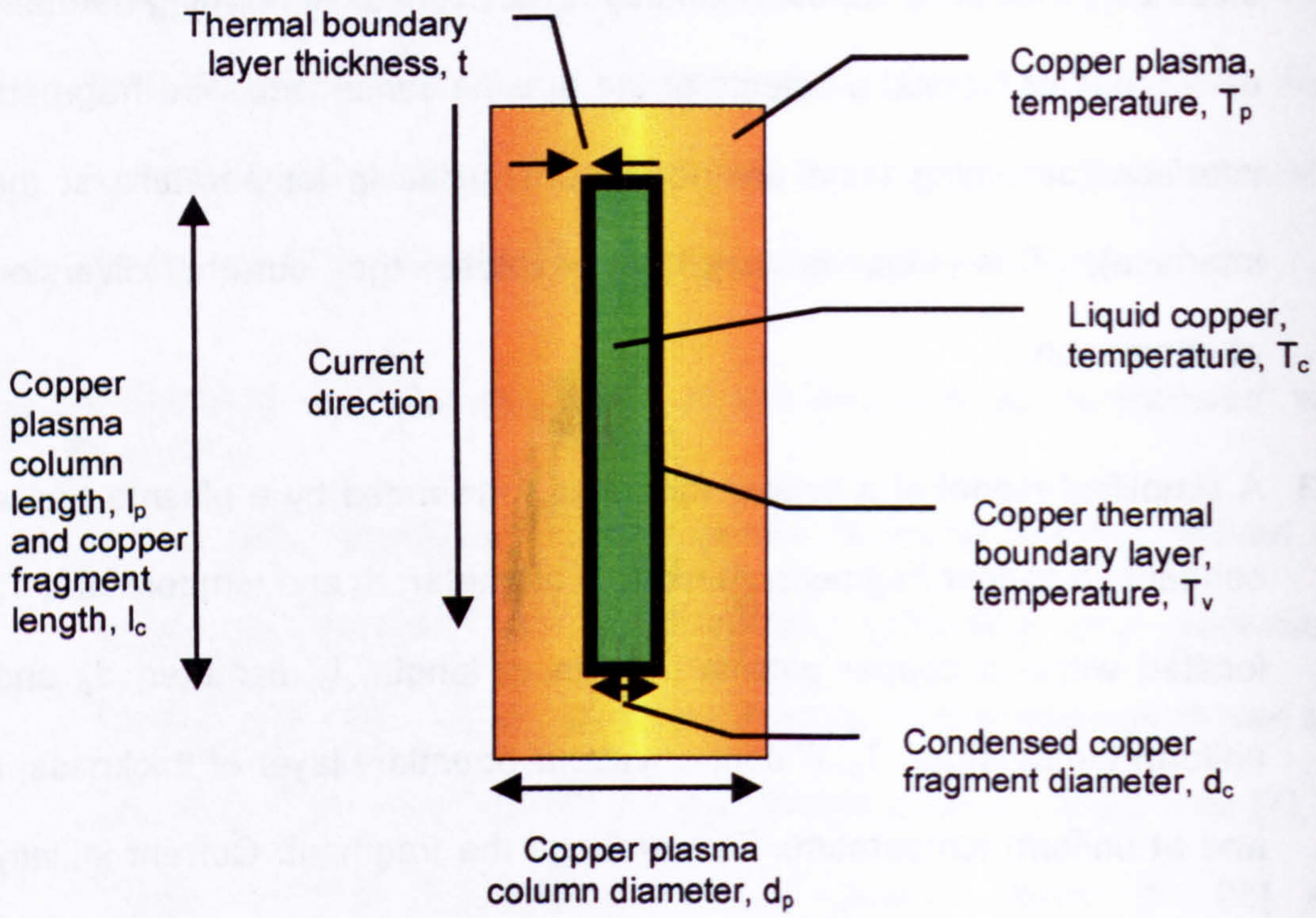

Figure 4.24 Schematic diagram of single copper fragment sheathed in plasma, with a copper vapour boundary layer between them

2.4.4 Powell continued to solve the magnetic diffusion equation, restricted to a limited set of geometrical arrangements, in an attempt to understand the experimentally demonstrable current diversion. Here, current diversion has been explained through a simple resistor network treatment without recourse to specific geometries, by positioning the copper plasma in parallel with a series circuit comprising the copper vapour boundary layer and the condensed copper fragment. The approach imposed a value of resistance on the vapour boundary layer to compel current to favour the route through the plasma. The thickness of the vapour layer, t would be the only variable for a given temperature, T_v that would permit the boundary resistance to be adjusted. The thickness could then be

obtained from the relationship between this imposed resistance and the vapour conductivity given by Desjarlais at T_v.

2.4.5 The level of complexity that was required to model the current density through the vapour boundary along the length of the wire had to be established. It seemed obvious that the current passing through the vapour would not be uniform along the length, l_c but would be concentrated at both ends. Simply treating the entire vapour boundary as two resistors (each with cross-sectional area $\pi d_c l_c / 2$) would probably fail to give a realistic solution for the vapour thickness. A process of mesh refinement was therefore applied to discover an acceptable degree of complexity. This was achieved by modelling the system as an increasing number of parallel and series resistors. Each plasma and condensed copper resistor was connected together by a resistor representing the vapour. The values for each resistor representing plasma and condensed copper were calculated, with a total fragment length, l_c of 50 mm, and diameter, d_c of 1 mm, and a plasma column diameter, d_p of 6 mm. A plasma temperature, T_p of 10 000 K, vapour temperature, T_v of 2850 K and condensed copper temperature, T_c of 2840 K were all assumed. The values of the resistors representing the vapour were varied until sufficiently little total current was flowing through the condensed fragment at the mid-point $l_c / 2$ to be deemed negligible with regard to the lack of experimentally observed effects (such as the Lorentz force). A circuit simulation package was used to determine the current at each point within the resistor network for each case as

complexity increased. By dividing the plasma and condensed copper columns into initially two, then four, eight, twelve and finally sixteen parts it was shown that increasing complexity reduced the thickness of vapour required by smaller increments, and that further complexity would alter the value little. Figure 4.25 is a schematic circuit diagram of the most complex problem solved to date.

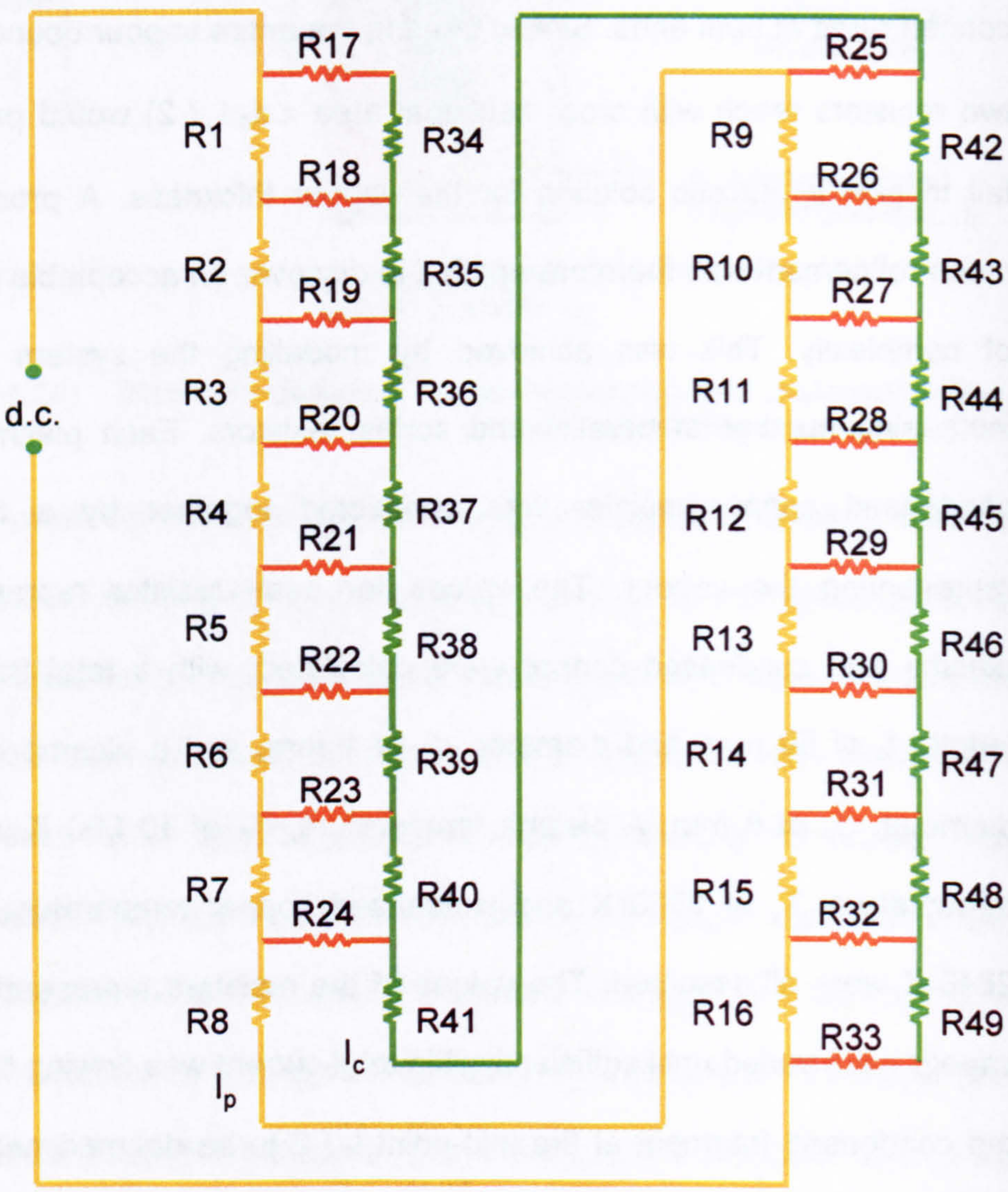

Figure 4.25 Schematic circuit diagram of a shrouded exploding condensed wire fragment

2.4.6 Resistors R1 – R16 represent the plasma; R17 – R33 represent the vapour boundary and R34 – R49 the condensed wire fragment. The resistance values for each section of the sixteen part problem, which constitute around 95% of the total current flowing through the plasma at the mid-point, I_p / 2 (i.e. between resistors R8 and R9 in Figure 4.25) were for the plasma, (R1 – R16) taken as 19 mΩ; for the condensed fragments, (R34 – R49) were 2.47 mΩ and those for the vapour boundary, R_v (R17 – R33) were 12 Ω.

2.4.7 The potential across the wire problem was set to a nominal 300 V. Under these conditions, the value of current in the plasma, I_p between R8 and R9 was 971 A and the current in the condensed fragment, I_c between R41 and R42 was 56 A. The value of the vapour conductivity, (R17 - R33) using the Desjarlais conductivity of copper vapour at temperature 2850 K was 3.83 Ω^{-1} m^{-1}. This gave a boundary layer thickness of around 30 μm, thought to be a reasonable order of magnitude for such a simple model. A more complete model, taking into account radial resistance of the plasma, is expected to reduce the thermal boundary layer thickness requirement significantly.

2.4.8 Sensitivity analysis has shown this model to be insensitive to the condensed-phase temperature (conductivity) but highly sensitive to the plasma-phase temperature (conductivity), with a thinner vapour barrier being required for hotter plasma. This finding of plasma temperature sensitivity may go some way towards explaining why the wire blow is so

similar over a wide range of electrical discharge power levels: a thicker boundary layer is required for a less energetic event resulting from the cooler plasma. However, a thicker boundary layer may naturally form at lower plasma temperatures.

2.5 Experimental evidence for current diversion

2.5.1 Experimental evidence is tentatively presented to support the existence of cool metallic vapour boundary layers under conditions pertinent to those discussed above. Work by the Author has been performed to measure the radiant energy loss from a capillary plasma discharge [10]. As a part of the investigation, a fibre optic input to a spectrograph was placed within the translucent polyethylene capillary liner of a capillary plasma generator, normal to the axis of the capillary and 3 mm from the inner surface. The system was calibrated absolutely in situ (see Appendix A) so that the radiant flux from the plasma incident on the capillary inner surface could be measured. The plasma brightness temperature at the capillary nozzle had been measured at around 12 000 K (see Chapter 5); within the capillary it was expected to be somewhat higher. Figure 4.26 shows the predicted and experimental capillary plasma brightness temperatures at the interface between the plasma and the capillary liner for this test.

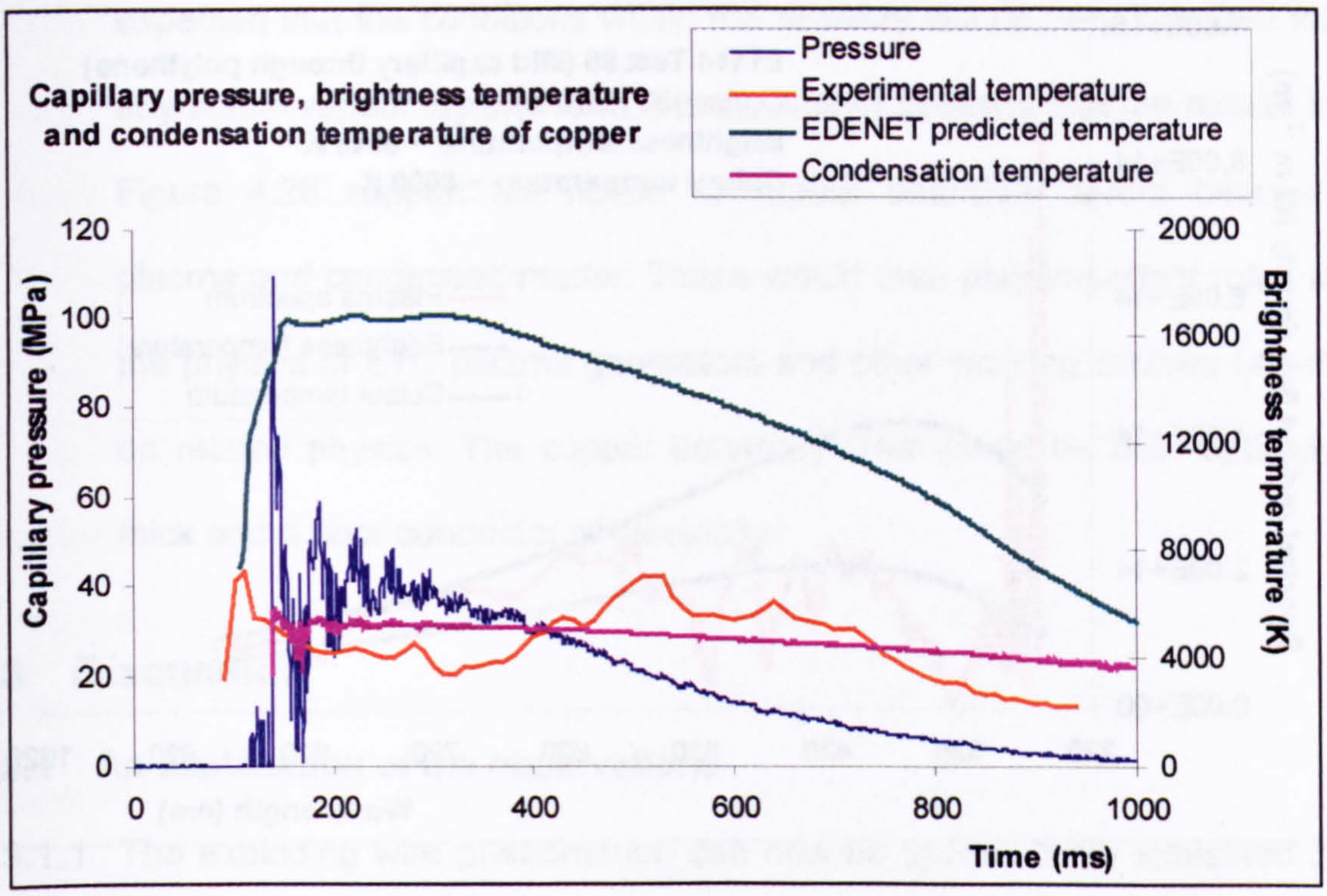

Figure 4.26 Capillary pressure, experimental and predicted brightness temperatures and condensation temperature of copper

2.5.2 The interface temperatures predicted by EDENET between the plasma and the capillary reach around 17 000 K, but the plasma brightness temperature at the capillary interface, measured to be generally at around 4000 K – 5000 K and at most 7000 K, was far less than expected. It was surmised that the brightness temperature of a layer at the molten/vapour phase-change temperature was being measured. Neutral atomic copper strong absorption characteristics in the recorded spectra indicate that the interface has copper associated with it. The spectrum of the hottest curve appears in Figure 4.27, along with the defining brightness and colour temperature blackbody curves. The thermodynamic temperature is around 8000 K. The strong absorption lines shown in the figure are mainly due to copper.

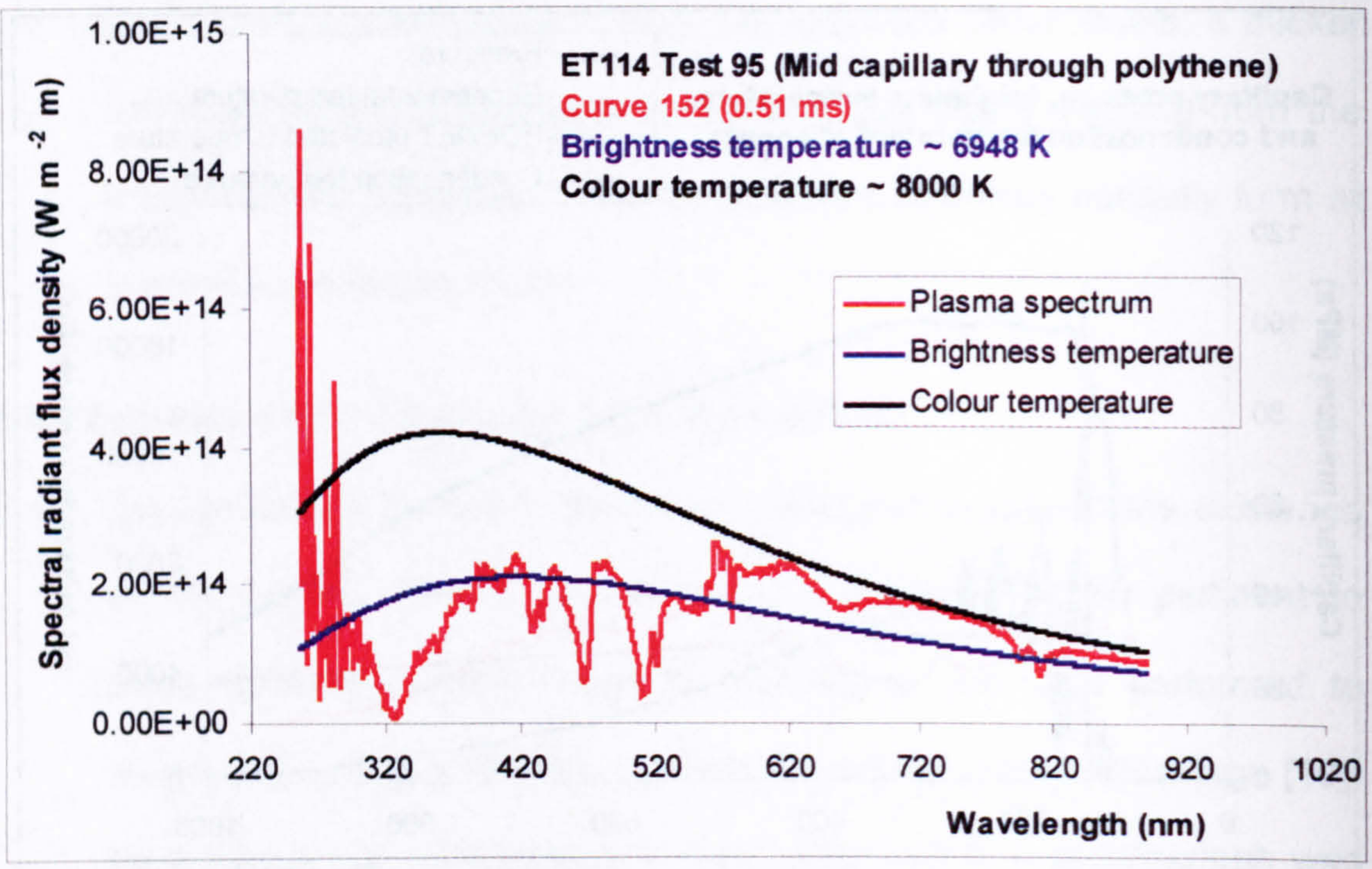

Figure 4.27 Spectrum of hottest recorded capillary plasma, with blackbody curves defining brightness and colour temperatures

2.5.3 Figure 4.26 shows how the experimental brightness temperature varied throughout the test, as well as comparing EDENET's predicted brightness temperature. The large disagreement could be due to an optically thick transition zone underestimated by the physics used in EDENET, which is based upon astrophysical plasmas, (see Chapter 3, Equations 3.4 and 3.5). The nature of this transition zone may be understood in the context of the copper liquid vapour transition, at the pressures within the capillary. The temperature of the transition zone and the pressures recorded also appear in Figure 4.26. The condensation temperature for copper is based upon the GENERA data presented in Chapter 3. It can be seen from the figure that the brightness temperature is close to this transition temperature throughout the entire test. It is

expected that the conditions within the capillary will be very turbulent for any stable vapour layer to form, but the Author believes that the results in Figure 4.26 support the notion of vapour boundary layers between plasma and condensed matter. These would then play important roles in the physics of ETC plasma generators and other working devices based on related physics. The copper boundary later would be both optically thick and a poor conductor of electricity.

3 Discussion

3.1 An explanation of the observations

3.1.1 The exploding wire phenomenon can now be speculatively explained in the following way for the experimental set-up defined earlier. Breaks occur within the wire due to hot spot formation in the condensed phase material. These hot spots occur due to a variety of inhomogeneous factors: magnetohydrodynamic (MHD) instabilities (disturbances in the self-induced magnetic fields within and around the conductor [29]) or ohmic heating, both caused by small deformations within the conductor such as small kinks, nicks, impurities and atomic dislocations, could all be responsible. As the break develops, the resistance and thus the voltage drop across it increase. A point is reached where the voltage attains the Paschen or some similar threshold for electrical breakdown and an arc discharge occurs. At this point the evidence suggests that the condensed portions of the wire are in the liquid phase. The vapour formed by the break expands and the plasma resulting from the arc discharge initially expands quickly to around 8 mm in diameter, and then

more slowly. An energy balance between ohmic heating and radiated (plus other types of) heat loss may determine the expansion rates, rather than magnetic pinch effects which will be small at the current levels used here especially in the low powered tests. Presumably, the plasma will only expand further if there is greater ohmic heating than heat loss. The discharge current, the plasma temperature (resistivity) and spot dimensions will determine the ohmic heating, whilst the plasma temperature (emittance) and the spot dimensions determine the heat loss. Initially, the ohmic heating is far greater than heat loss as the arc will be small, forcing rapid expansion, but once the energy balance approaches equilibrium, the radial expansion slows or even stops. For the range of parameters used in these tests, this initial equilibrium occurs at around 8 mm. This value will probably alter for different wire thickness and possibly different materials.

3.1.2 Current is now forced to leave and re-enter the condensed copper fragments to bridge the break. It has been suggested above that a poorly conducting vapour boundary layer, less than a few tens of microns thick, exists between the plasma and the condensed surface, (see Figure 4.28).

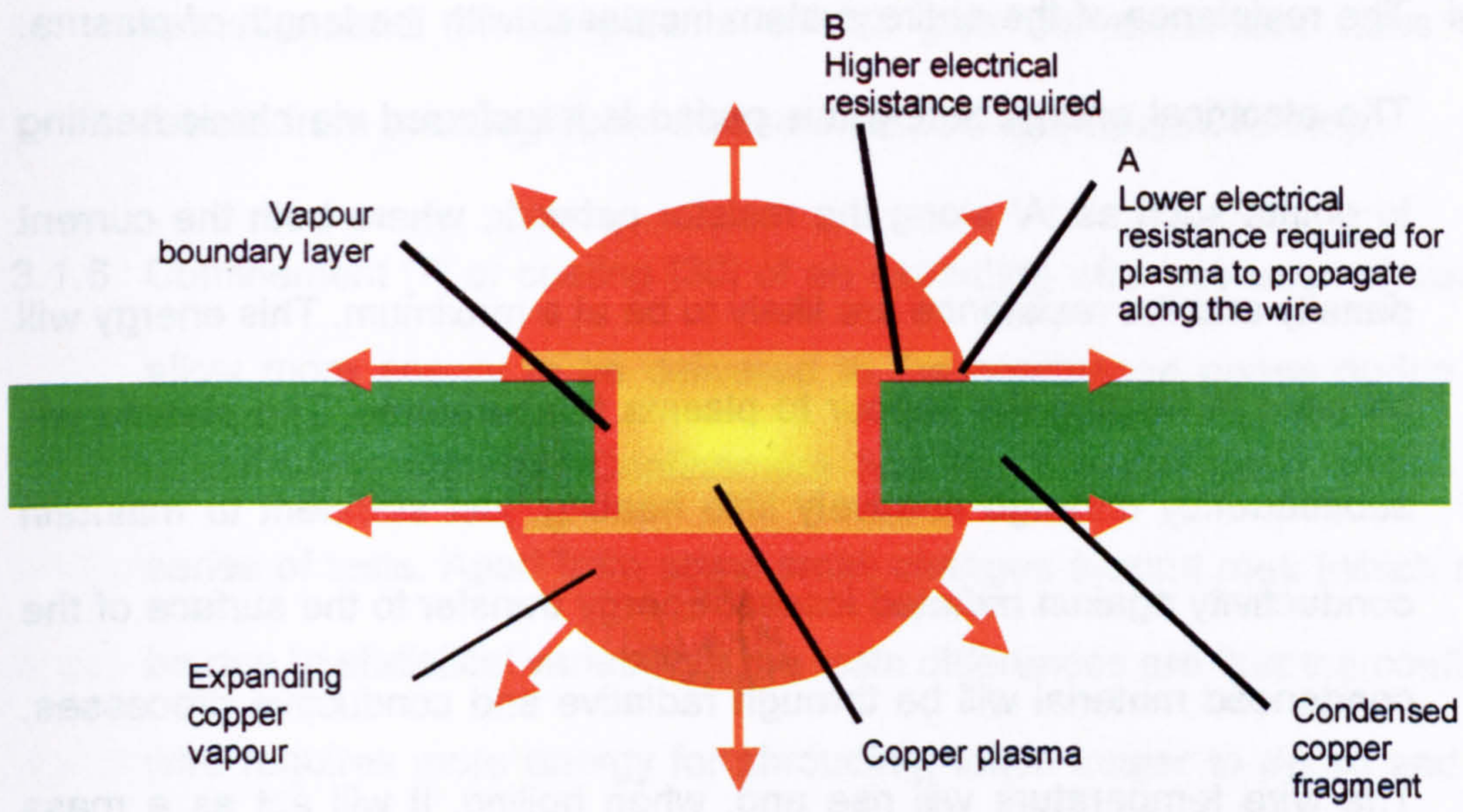

Figure 4.28 Schematic diagram of expanding plasma spot

3.1.3 Vapour from the initial break will expand away from the break through either pressure or momentum. For the plasma to expand longitudinally along the wire, it would be necessary for the current to prefer a path through the boundary layer rather than through the condensed fragment. This preference would necessitate the vapour at the extremity having a lower electrical resistance than that of the vapour boundary along the wire length (sites such as 'B'). This would be the case if the breakdown voltage at 'A' is lower than at 'B', due possibly to a lower plasma density at the former site [5]. As the vapour expands, the plasma sheath would then expand with it, the location of 'A' moving along the wire and electrically insulating vapour boundary layers settling behind it. This would continue until the vapour either stops (or is prevented from) expanding, or meets another contiguous expanding vapour/plasma spot.

3.1.4 The resistance of the entire system increases with the length of plasma. The electrical energy during this period is transferred via ohmic heating to points such as 'A' along the resistor network, where both the current density and the resistance are likely to be at a maximum. This energy will be used in heating the vapour to plasma temperatures. The plasma will subsequently undergo relatively little heating, just sufficient to maintain conductivity against radiated losses. Energy transfer to the surface of the condensed material will be through radiative and conductive processes. The wire temperature will rise and, when boiling, it will act as a mass source for the vapour layer. It has been observed that the wire first boils at locations initially covered in plasma. It is possible (although not necessary) that inhomogeneous heating processes occurring earlier, due to thermally-induced stress or other wave phenomena, cause certain locations to attain boiling point prematurely. The striated appearance of the condensed portions might be the result of such phenomena, or simply indicate random vapour sites.

3.1.5 Once the wire is completely sheathed in conducting plasma, energy distribution along the length of the system is likely to become more uniform, as any high resistance points will either expand or be heated to establish resistance equilibrium. The plasma has been measured to continue expanding radially (acting to reduce the resistance) but at the same time cool (acting to increase the resistance). Because the resistance drops, after the resistance peak (Figure 4.3) the expansion rate must dominate in a wire explosion in free air. Photographic

measurements of the plasma sheath give the expansion rates and results from spectrographic measurements the temperature drop.

3.1.6 Confinement [7] or coating [30] of an exploding wire has been shown to allow more energy to be delivered to the condensed phase during the vaporisation process. Confinement has been investigated within this series of tests. Apart from some small changes around melt (which may be due to statistical variability), the main differences are that the confined wire requires more energy for shrouding, takes longer to do so and (as mentioned above) has a higher resistance for the remainder of the discharge. The discharge is also shorter and more energy is transferred overall in the confined wire explosion (although this is related more to resistance matching of the pulse power supply than the physics of the explosion process itself). The extra energy required for shrouding may either be taken up by the wire and plasma system, or lost to the capillary walls. Previous work [7, 30] suggests the former.

3.1.7 Plasma confinement has also been investigated with EDENET. EDENET has been executed in the axial mode to explore the effects of confinement on plasma properties and is currently being run in radial mode to explore the same effects on the vapour boundary layer [31]. Initial results from the simulations confirm that the confined discharge plasma is hotter (tending to lower the plasma resistance) and more dense (tending to increase the plasma resistance), but with a higher resistance overall than less confined plasmas. In the confined case, an

improved energy transfer efficiency to condensed material may be due both to thinner (less resistant) vapour boundary layers resulting from pressurisation and higher plasma temperature, and a more resistant plasma due to the pressurisation.

3.1.8 In the coated case, the issues are more interesting. The model proposed in Figure 4.28 could involve a coating which would prevent the plasma from spreading with the vapour (assuming it was intact and a good insulator). This is because a coating would not allow conduction through locations such as 'A', thus forcing conduction at the vapour barrier at sites where the coating is damaged, close to the original break. If this were the case, then x-radiographs should show the original break eroding, and photographs would show development of a more spotted plasma sheath.

3.1.9 From the arguments presented here, most of the energy would be transferred to the condensed wire fragments of a tightly constrained wire, where the plasma sheath is prevented from forming altogether. Certain exploding wire applications require energy to be transferred to the condensed phases as efficiently as possible. In the electrothermal-chemical gun, the Author has been proposed that solid propellants ignite through a process of vapour deposition [32]. Here, a metallic vapour generator rather than a plasma generator is required for the efficient ignition of solid propellant. This is discussed further in Chapters 7 - 9.

4 Summary of Chapter 4

4.1.1 In this Chapter, the use of electrically exploded wires to initiate ETC plasma has been explored, along with a brief history and discussion of current applications.

4.1.2 Work conducted by the Author for ETC studies has been described, including electrical, photographic and x-radiographic investigations. It was concluded that electrical current was being diverted around condensed fragments through higher resistive plasma. This effect is not new and reference has been given to other similar observations from workers within the scientific community. However, a new model to explain the current diversion has been introduced by the Author, based on thermal boundary layers proposed to exist between the plasma and condensed copper. This boundary layer supposedly consists of metallic vapour with a very low electrical conductivity. Values of the electrical conductivity of metallic vapour have been published very recently, and using these values the Author has shown that a boundary layer less than a few tens of microns thick would suffice to increase the resistive path through the condensed fragment such that a large proportion of the current, once flowing through the plasma, would continue through it. This model for current diversion has subsequently been incorporated into another model for describing the observed development of a plasma sheath around the exploding wire.

4.1.3 The primary aim of this work was to supply the underlying physics and validating data for the development of a predictive computer model, EDENET. Already, the proposed existence of a metallic vapour layer around the rear capillary electrode has been employed to introduce the concept of resistance in series with the capillary plasma and therefore control of the current decay after the peak current, without recourse to altering the bulk plasma properties (see Chapter 3, Section 4.9.6). However, it is unlikely that the theory will be used to describe the wire explosion itself in a model of a CPG. This would require a lot of costly effort, and an approximation has already been introduced that replicates the observed fragmentation process very well. This approximation introduces small changes in the diameter of the wire. These 'nicks' are natural areas of increased resistance, which cause the wire to fragment (see Chapter 3). Nevertheless, the wire may need to be modelled in detail with some future version of EDENET for other plasma generator designs.

---

1 W. G. Chace, "A Survey of Exploding Wire Progress", Exploding Wires Volume 3, edited W. G. Chace and H. K. Moore, New York: Plenum pp 1-7, 1964

2 Exploding Wires volumes 1-4, edited W. G. Chace and H. K. Moore, New York: Plenum, 1959 - 1967

3 F. D. Bennett, H. S. Burden and D. D. Shear, "Expansion of Superheated Metals", J. Appl. Phys. Vol. 45, 8, pp 3429-3438, 1974

4 P. Graneau, "Wire Explosions", Phys. Lett. 120A, 77-9, 1987

5 Y. Me-Bar and R. Harel, "Electrical Explosions of Segmented Wires", J. Appl. Phys. Vol. 79, 4, pp 1864-1868,1996

6 S. Molokov and J. E. Allen, "The Fragmentation of Wires Carrying Electric Current", J. Phys. D: Appl. Phys. Vol. 30, pp 3131-3141, 1997

7 C. E. Hollandsworth, J. D. Powell, J. Keele and C. R. Hummer, "Electrical Conduction in Exploded Segmented Wires", J. Appl. Phys. Vol. 84, 9, pp 4992-5000, 1998

8 G. A. Shvetsov, A. D. Matrosov, S. V. Fedorov, A. V. Babkin and S. V. Ladov, "Quest of Possibilities for Controlling the Shaped-Charge Effect by Electromagnetic Action", 4th All Electric Combat Vehicle Conference, Noordwijkerhout, Netherlands, 7th – 9th January, 2002

9 D. C. Haugh and M. A. Firth, "UK Electric Gun National Overview", IEEE Transactions on Magnetics, Vol. 37, 1, pp 33-36, 2001

10 M. J. Taylor, "Measurement of the Properties of Plasma from ETC Capillary Plasma Generators", IEEE Transactions on Magnetics, Vol. 37,1, January 2001

11 B. Augsburger *et al*, "DRA 500 kJ Multi-module Capacity Bank", IEEE Transactions on Magnetics, Vol. 31, 1, January 1995

12 M. M. Martynyuk, "Transition of Liquid Metals into Vapour in the Process of Pulse Heating by Current", Int. J. Thermophysics, Vol. 14, 3, pp 457-470, 1993

13 G. T. Dyos and T. Farrell, "Electrical Resistivity Handbook", London: Peter Peregrinus, 1992

14 M. J. Taylor, "ET105 - Photography of an Exploding Wire", DERA unpublished report WSS/WX6/58-ETL/ERD003, January 1999

15 R. A. Marshall, "Properties of Copper and Hydrogen Plasmas", RARDE report R86/216, 1986

16 M. J. Taylor, "ET098 – X-ray Photography of a Length of Copper Wire", DERA unpublished report WSS/WX6/01-ETG/ERD026, June 2001

17 M. J. Taylor and R. J. Gardner, "ET154 – X-ray of Thicker Exploding Wires", DERA unpublished report, May 2001

18 M. L. Coffman, "The First Picosecond in an Exploding Wire", Exploding Wires volume 3, edited W. G. Chace and H. K. Moore, New York: Plenum pp 89-102, 1964

19 J. Nasilowski, "Unduloids and Striated Disintegration of Wires", Exploding Wires volume 3, edited W. G. Chace and H. K. Moore, New York: Plenum pp 295-313, 1964

20 M. J. Taylor, "ET165 – Interruption of Exploding Wires", QinetiQ unpublished report, FST/CDT/58-ETL/ERD025, July 2001

21 ABB thyristor 5STP26N6500 2810A, 650 from ECM Electronics Ltd, Penmaen House, London Road, Ashington, West Sussex.

22 Smithells handbook on metals, 14-3, 2000

23 Smithells handbook on metals, 14-6, 2000

24 A. E. Vlastós, "Restrike Mechanisms of Exploding Wire Discharges", J. Appl. Phys. Vol. 39, 7, pp 3081-3087, 1968

25 Drumm, "Investigations into Segmented Divertor Strips", 23rd ICPL, Firenze (Italy), 23rd – 27th September 1996

26 J. D. Powell and L. D. Thornhill, "Current Distribution and Plasma Properties in Injectors for Electrothermal-chemical Launch", IEEE Transactions on Magnetics, Vol. 37, 1, January 2001

27 M. P. Desjarlais, "Practical Improvements to the Lee-More Conductivity Near the Metal-Insulator Transition", Contributions To Plasma Physics Vol. 41, 2-3, pp 267-270, 2001

28 A. W. DeSilva and J. D. Katsouros, "Electrical Conductivity Measurement in Dense Metal Plasmas: Comparisons of Several Metals", Journal de Physique IV, 10: (P5) pp 209-214, 2000

29 R. J. Goldston and P. H. Rutherford, "Introduction to Plasma Physics", Bristol: Institute of Physics Publishing, 1995

30 D. B. Sinars, T. A. Shelkovenko, S. A. Pikuz, M. Hu, V. M. Romanova, K. M. Chandler, J. B. Greenly, D. A. Hammer and B. R. Kusse, "The Effect of Insulating Coatings on Exploding Plasma Formation", Physics of Plasmas, 7, 2, pp 429-432, 2000

31 C. R .Woodley, "EDENET Run 151 – 153", QinetiQ unpublished report, June 2001

32 M. J. Taylor, "Ignition of Propellant by Metallic Vapour Deposition for an ETC Gun System", Propellants, Explosives, Pyrotechnics, Vol. 26, pp 137 – 143, 2001

Chapter 5 – CPG energy budget

1 Introduction

1.1 Energy Transfers

1.1.1 Subsequent phase changes of the plasma initiation wire material following energy transfers from the PPS were explored in Chapter 4. This Chapter is concerned with how the energy transferred to the capillary of a capillary plasma generator (CPG) is partitioned, and then Chapter 6 goes on to explore other issues relating to the expanding plume.

1.1.2 Central to optimisation of the favourable plasma properties for plasma propellant interactions is the ability to dictate the energy transfer processes through CPG design. This implies the ability to determine where the energy is being transferred within the system, as well as a working knowledge of which of the plasma properties are 'favourable' and how the flow of energy enhances these properties. Being able to measure the energy flows within the system is essential for determining the transfer processes. Estimation of the energy budget for a plasma generator is, to the Author's knowledge, the first experimental attempt in ETC research. No reports have been located of experimental work of this nature on ETC plasmas by other researchers. Public presentation of this work along with informal discussions with other leading workers within the ETC community have led the Author to believe this is the first attempt of its kind. Arguments for the errors and validity of assumptions

associated with this estimation are presented. Comparisons are made with results reported from modelling at the end of Chapter 6.

1.1.3 All work reported within this Chapter is that of the Author unless otherwise stated.

1.2 Experimental arrangement

1.2.1 Electrical energy is transferred to the capillary plasma generator (CPG) at a far greater rate than it is lost from the system, as is evident from the measurements described later. The heated plasma vents under its own pressure from the CPG through the nozzle and continues to do so for the duration of the discharge.

1.2.2 Figure 5.1 is a diagrammatic representation of the experimental design used to determine the radiative energy transfer from the plasma. Figure 5.2 shows a photograph of the components, along with a biro for scaling purposes. In this experiment, the plasma was allowed to expand freely into air at atmospheric pressure [1, 2]. The apparatus used to study the CPG operation and its freely expanding plasma jet comprised a 12 mm diameter, 150 mm long, high density polyethylene capillary fitted with a copper tungsten rear electrode and a steel nozzle (see Appendix A). The capillary was contained within a glass fibre filament-wound body which had three instrumentation ports usually used for pressure transducers. These instrumentation ports lined up with holes within the capillary, two being visible in Figure 5.2. Electrical current was supplied from the PPS via an axial copper rod to a rear

electrode whose tip projected into the rear of the capillary. A length of 0.7 mm diameter tinned copper wire was soldered to the rear electrode tip, it passed along the length of the capillary and was fixed to the front section of the nozzle by being threaded through a small hole. Although the wire was pulled tight, no attempt was made to straighten it perfectly along the capillary axis. Current from the nozzle then returned via eight steel rods to a rear annular copper bracket and hence to the pulsed power supply, completing the circuit. The rods were arranged to be coaxial with the capillary in an attempt to balance the electromagnetic fields within the latter.

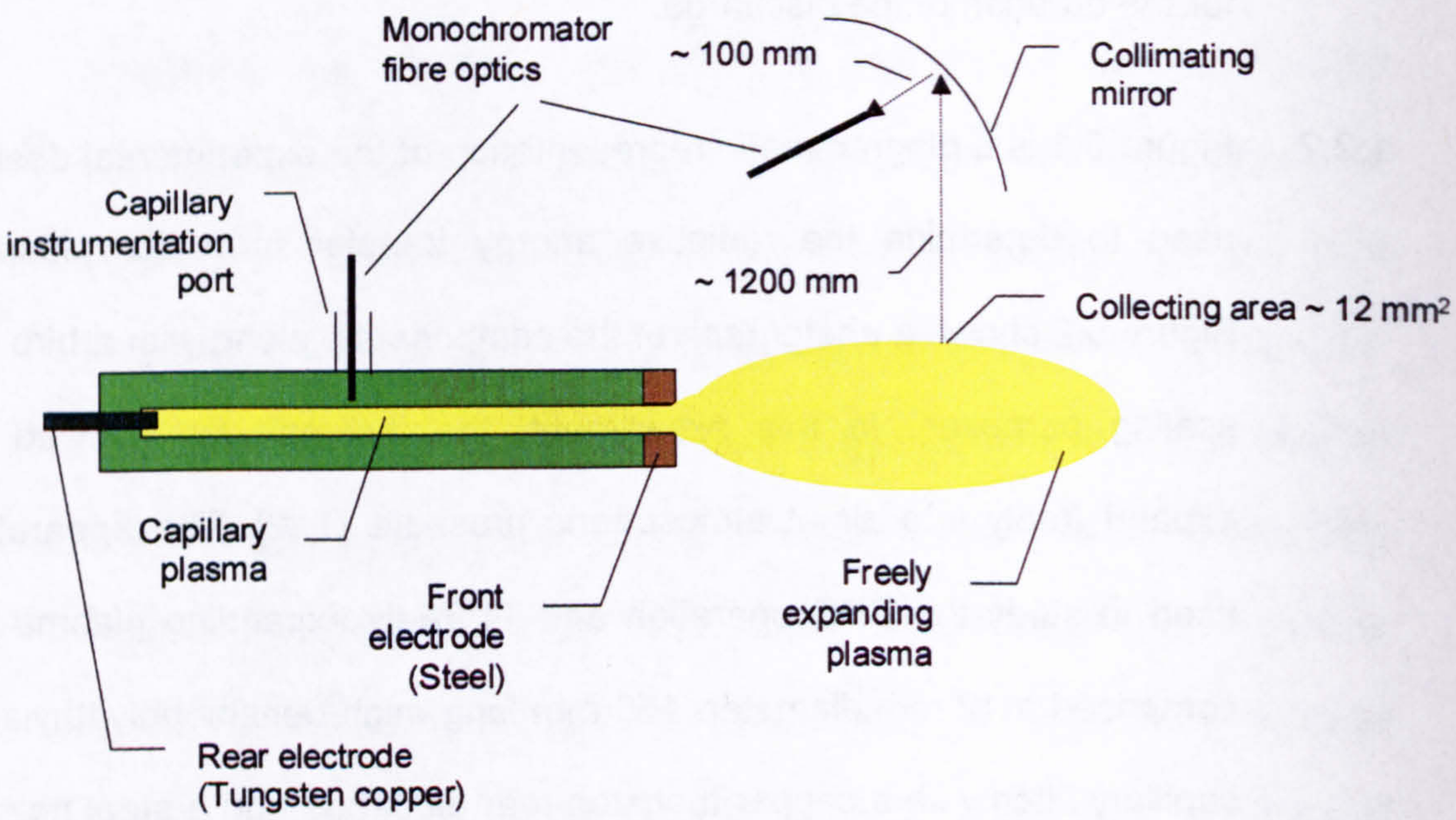

Figure 5.1 Experimental arrangement for collection of plasma spectra

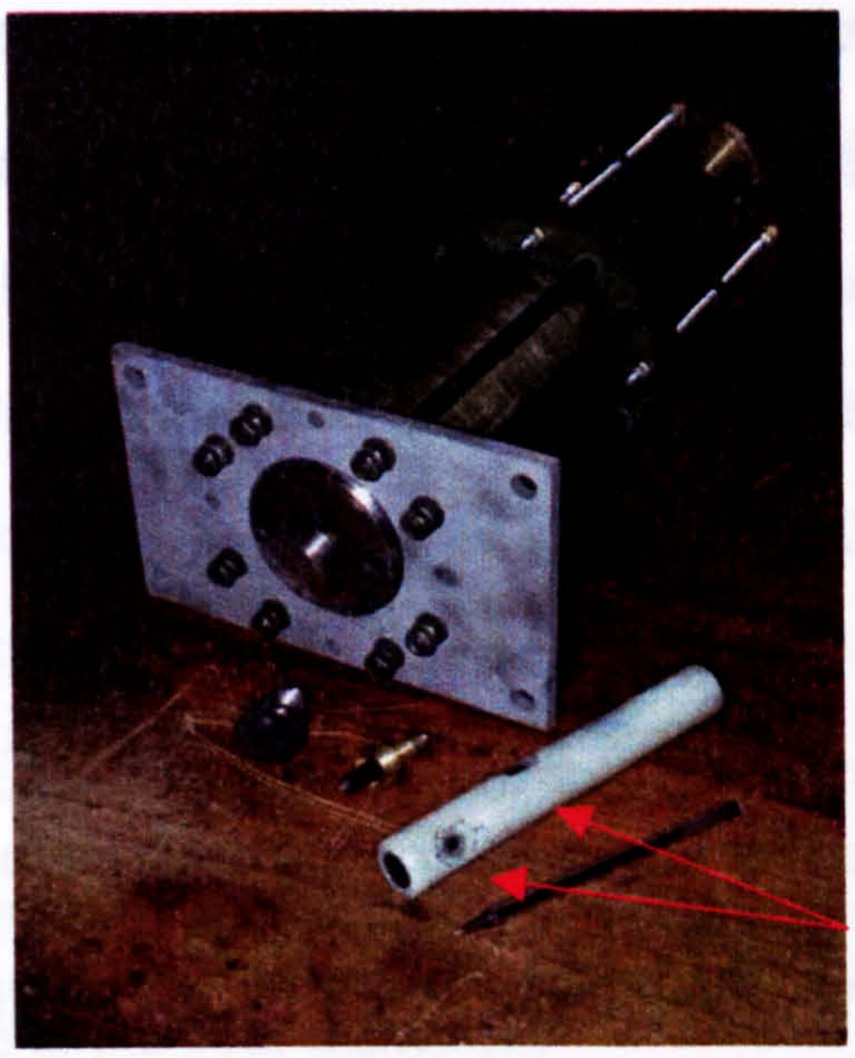

Figure 5.2 Photograph of CPG components

1.2.3 The pulsed power supply used was a single module of a multi-module capacitor bank [3] charged to 10 kV in 11 kV mode and fitted with a (nominally) 26 μH pulse shaping inductor. The stored energy on the capacitor was approximately 40 kJ, with around 30 kJ transferred to the plasma in around 0.8 ms. Measurements were made of the electrical parameters of the plasma at a 10 MHz sample rate using a Rogowski coil for the current and a 3000:1 voltage divider for voltage. The capillary internal pressure was measured using two or three Kistler piezoelectric gauges, depending upon the test.

1.2.4 The expanding plume process was photographed with an intensified fast-framing Ultranac digital camera (see Appendix B), at various exposures (typically 100 ns) and interframe times (typically 100 μs). Plume size measured approximately 0.5 m in length by 0.4 m diameter. Between 8 and 24 images were recorded for any one test, each image

being separately controlled for exposure and interframe time. A Dove prism (see Appendix B) was used to maximise the CCD pixels by rotating the plume image from the horizontal to the vertical aspect. The camera images were calibrated for absolute dimensions by use of a test card (see Appendix B).

1.2.5 Time-resolved spectra of the plasma were recorded (see Appendix A): the grating used for this work had 150 grooves mm^{-1} blazed at 300 nm. The centre wavelength was set at 575 nm, giving a wavelength range from approximately 258 nm to 892 nm with around 0.6 nm resolution. An extra 3.4 μs exposure time was added to the shift time of 6.6 μs, giving a total exposure of 10.0 μs. Up to 250 usable data rows were available in this time resolvable 'kinetics' mode, giving a total time of 2500 μs in which to record the plasma radiant energy.

1.2.6 Light from an area of approximately 12 mm^2 of the plume was collected and transmitted to the spectrograph by a 400 μm diameter 0.22 numerical aperture hydrous quartz fibre optic. (Various pinhole apertures were used to reduce the light levels at some hotter parts of the plasma.) The light was collected via a 50.8 mm diameter, 100 mm focal length surface coated collimating mirror [4]. The 30 m long optical fibre allowed the light to be transmitted to the instrumentation area a safe distance away. The fibre tip to mirror distance was around 100 mm and the mirror to plasma distance around 1200 mm. These distances were determined by shining light from a Class 1 helium-neon

laser backwards through the system, a convenient break in the fibre with suitable SMA connectors being provided for this purpose. (The SMA connections had been tested for changes in their transmission characteristics when disconnected and reconnected. No change above the natural background noise was discernible.) This light was focused through small adjustments to the optical mirror onto white card temporarily placed on the axis of the CPG. (The collimation of the beam was tested by moving the card in and out and checking for no visible change to the spot-diameter.)

1.2.7 Light from the capillary plasma was observed through the translucent capillary wall. The central instrumentation hole in the capillary was not drilled completely through for these tests, with a 4.6 mm thickness of high density polyethylene being left flush with the inner wall. Only two pressure gauges were used for the tests.

1.2.8 Calibration of the spectra is discussed in Appendix A.

1.3 Methodology

1.3.1 The overall approach assumed that a sequence of CPG shots produced similar plasmas. The entire plasma was then divided into two main regions of interest: within and external to the capillary. Due to large thermal gradients, the external plume was sub-divided into seven regions. Measurements of the spectra were made and the spectral radiant flux density (see Appendix A) was averaged from 4 tests within the capillary and 16 tests at each of the seven plume regions, 8 at each

region boundary. (Only two measurements were made for the plume boundary furthest from the nozzle, as the plasma temperature had cooled to below that of condensing copper vapour. Analysis of the measurements stopped when the temperature of the plasma fell below 3000 K, and so a zero reading was taken for this boundary.) Thus, the average time-resolved spectral radiant flux density for each region was determined. Fifty six tests were conducted in this exercise. Two further tests were undertaken to measure the spectral radiant flux density of the expanding plasma plume front face, with the fibre focused along the capillary axis in the direction of the capillary.

1.3.2 Each averaged regional value of time-resolved radiant flux density was multiplied by the time-resolved surface area of that plume region to give the time-resolved radiant flux. The surface area was estimated from the photographic images of the first test for the side profile (see Appendix B) and the first five tests for the front of the expanding plume. The side profiles were cut from the main image. The front expanding face had to be estimated by measuring the plasma front diameter and this was used as the diameter of a flat disk. Visual examination of the expansion images suggests that the flat disk approximation is a reasonable one. It would probably have been far better to average the expansion rates over images from many tests, but each analysis was time-consuming with around ten useful images per test and seven regions per image to examine. This subject is taken further in the discussion on errors, below.

1.3.3 The radiant flux was integrated with respect to time to provide the total radiant energy transferred from each region. The radiant energy density was also obtained by integrating the radiant flux density with respect to time.

1.3.4 Further tests were conducted for a variety of purposes. Twelve tests were undertaken at 200 mm and a further twelve at 100 mm from the nozzle at 45° and 135° angles to the capillary axis in an attempt to spectrally determine the optical depth of the plasma (see below). Four further tests were conducted to identify the effect of the discharge on a Class 1 helium-neon pencil laser in close vicinity, to determine optical thickness. Two tests were used to record plasma spectra 200 mm from the nozzle at different detector centre wavelengths to investigate the plasma properties deeper into the infrared. Twelve (unsuccessful) tests were undertaken to determine the capillary plasma radiant flux density using a sapphire window. Analysis from these twelve tests indicated that the properties of the plasma in the small recess created by the sapphire window port were radically different from those of the plasma in the main capillary chamber. Thus, the translucent properties of the liner wall were used. The first four tests were involved in developing a suitable means of reducing the extreme light levels close to the nozzle, which were saturating the spectrograph CCD detector. Pinholes in card were tried but found to be unreliable due to the card's movement during the discharge. A pinhole in the opaque, rubber dust cover used to protect the fibres during storage worked well, however, with consistent

transmission for many tests. (A 10 cm length of 50 μm fibre has since been purchased to improve upon this improvisation.) In all, 98 tests were conducted for this experiment.

1.3.5 Each set of components was used four times in an attempt to reduce the cost of the experiment and this also allowed the effect of component re-use to be assessed.

2 Error estimation

2.1 Introduction

2.1.1 Estimation of the errors is difficult in the techniques used to measure the radiant energy from the plume. The two largest sources of error are in the estimation of surface area and extrapolation of the radiant flux density over all wavelengths. Further, an assumption is made regarding the optical depth of the plasma that has the potential to introduce further errors.

2.2 Surface area errors

2.2.1 Plume variability was thought to be the most serious risk for surface area errors, as only one test was used in the main analysis. Comparisons of the plumes were made for the first 12 tests through use of proprietary software "Image-Pro Plus version 4" which has the ability to calculate the area (in pixels^2) of a grey scale image, with an intensity threshold value as a free parameter. A value of 300 counts (background subtracted) was chosen for the threshold (see Appendix

B). The first 9 images of the 24 were selected for each test, as these were taken during the electrical discharge. The total surface area of the 2D images was calculated, rather than that of the 3D plume used in radiant flux calculations. Calculating the 3D surface area is rather involved and the error in the 2D images will be proportional to errors in the 3D images. Figure 5.3 demonstrates the results of this analysis. The average area for the first 9 images was around 15 000 pixels^2, with a range of around 3000 pixels^2. Hence, the error in the area measurements due to plume variability is of the order of 10%. The red bars in Figure 5.3 show the tests where new CPG components were used.

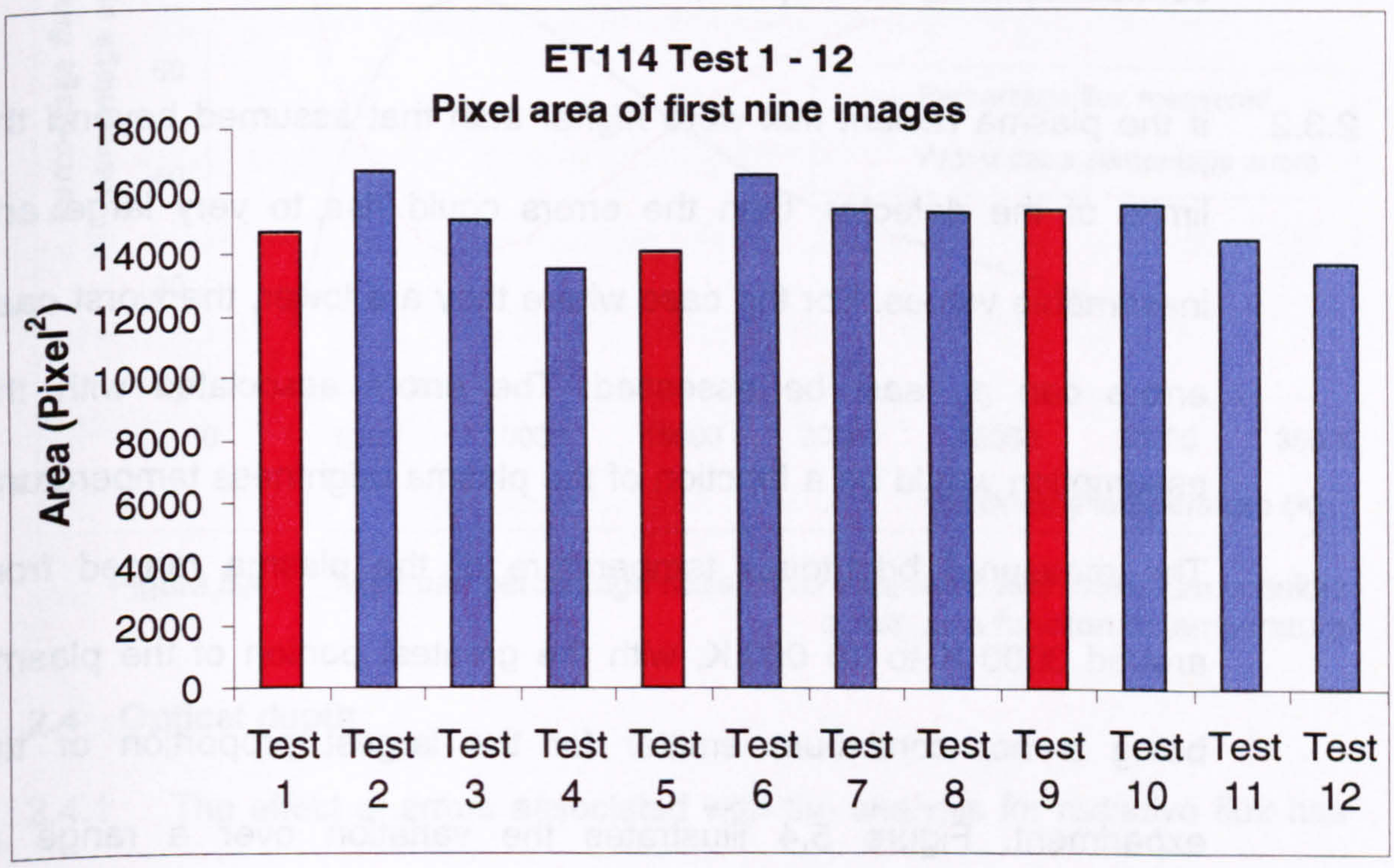

Figure 5.3 Summed plume area for the first 9 images of the first 12 tests

2.3 Radiant flux errors

2.3.1 The errors in the measurements for the radiant flux within the wavelength limits of the experiment were less than 1% (assuming a surface emitter – see below). Extrapolation to all wavelengths from those measured was considered reasonable based upon the agreement between plasma colour and brightness temperatures (see Appendix A). However, the assumption that the plasma spectrum in the measured range is representative of the entire spectrum cannot be easily verified. It is conceivable that the experimental range was entirely unrepresentative, in which case the findings of this work would be invalid. Using a larger wavelength range would increase the confidence in the assumption, however.

2.3.2 If the plasma radiant flux were *higher* than that assumed beyond the limits of the detector, then the errors could rise to very large and inestimable values. For the case where they are lower, the worst case errors can at least be assessed. The errors associated with the assumption would be a function of the plasma brightness temperature. The measured brightness temperature of the plasma ranged from around 3000 K to 10 000 K, with the greatest portion of the plasma being a hot continuum emitter for the largest proportion of the experiment. Figure 5.4 illustrates the variation over a range of temperatures of the ratio of the measured blackbody flux for the experimental wavelength range, to the total blackbody flux for the entire spectrum at that temperature (blue curve). Also shown are the worst

case errors in the flux measurement for this case, which would occur in the unlikely event that emission from the plasma fell to zero beyond the wavelength limits of the experiment (pink curve). This is simply *100 minus the percentage flux measured*. These errors are centred at around 30% for the experimental temperature range, peaking at around 50% at the lower temperatures.

2.3.3 The overall errors of this experiment were thus potentially around 50%.

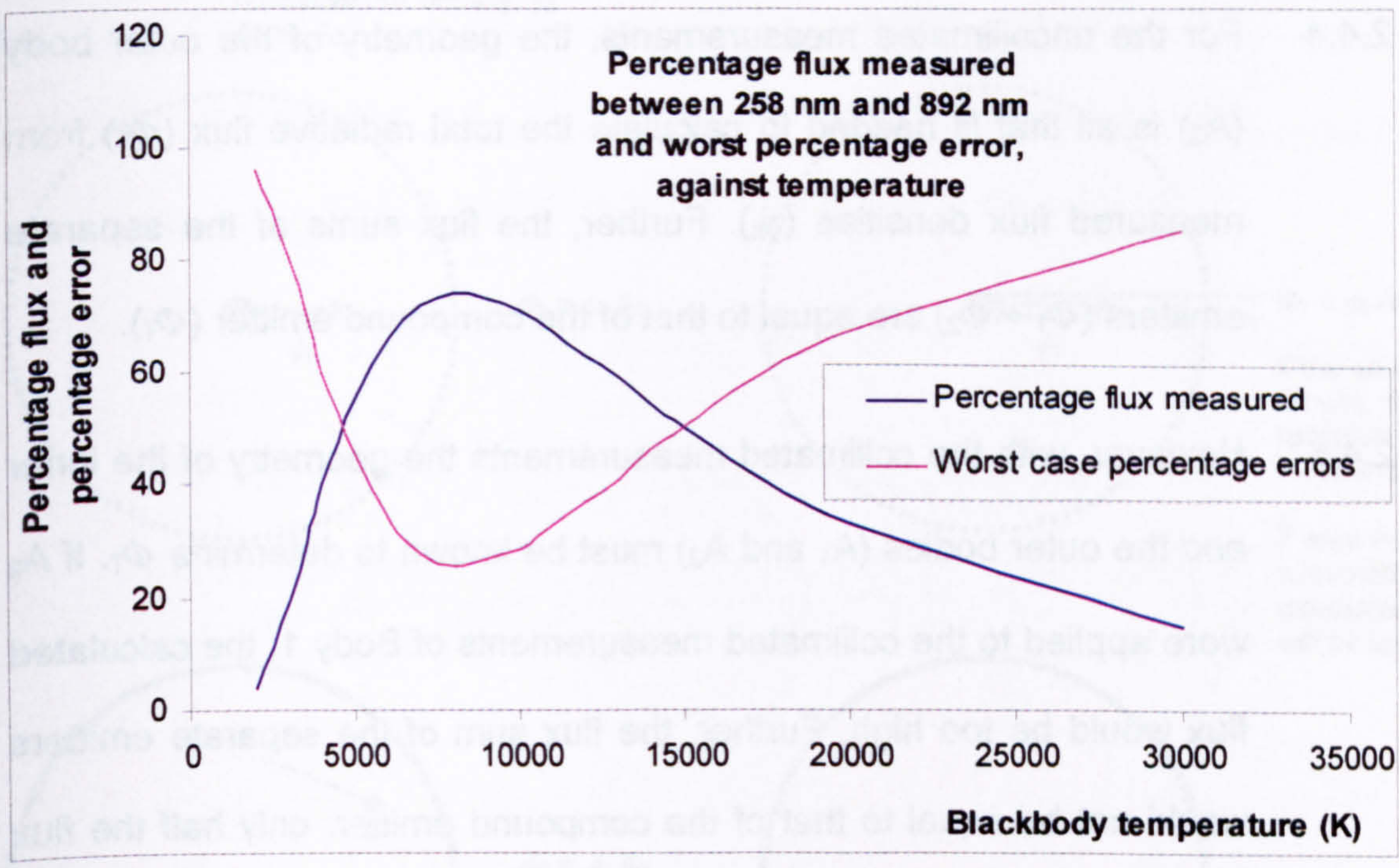

Figure 5.4 Minimum percentage radiant flux measured and maximum possible errors as a function of temperature

2.4 Optical depth

2.4.1 The effect of errors associated with the analysis for radiative flux has been determined by the Author for the case where a surface emitter (or strong scatterer) is wrongly assumed when using a collimated collection technique.

2.4.2 Figure 5.5 demonstrates three scenarios: a hot, optically dense surface emitter (Body 1) centrally located within a volume emitting (non-absorbing) luminous gas (Body 2); the surface emitter alone, and the volume emitter alone.

2.4.3 Measurements of the emissions were considered for a conventional uncollimated device (left group of three in the figure) and a collimated device (right group of three), from a set distance.

2.4.4 For the uncollimated measurements, the geometry of the outer body (A_2) is all that is needed to calculate the total radiative flux (Φ_T) from measured flux densities (ϕ_n). Further, the flux sums of the separate emitters ($\Phi_1 + \Phi_2$) are equal to that of the compound emitter (Φ_T).

2.4.5 However, with the collimated measurements the geometry of the inner *and* the outer bodies (A_1 and A_2) must be known to determine Φ_T. If A_2 were applied to the collimated measurements of Body 1, the calculated flux would be too high. Further, the flux sum of the separate emitters would not be equal to that of the compound emitter: only half the flux from the luminous gas would be measured due to shadowing of the surface emitter.

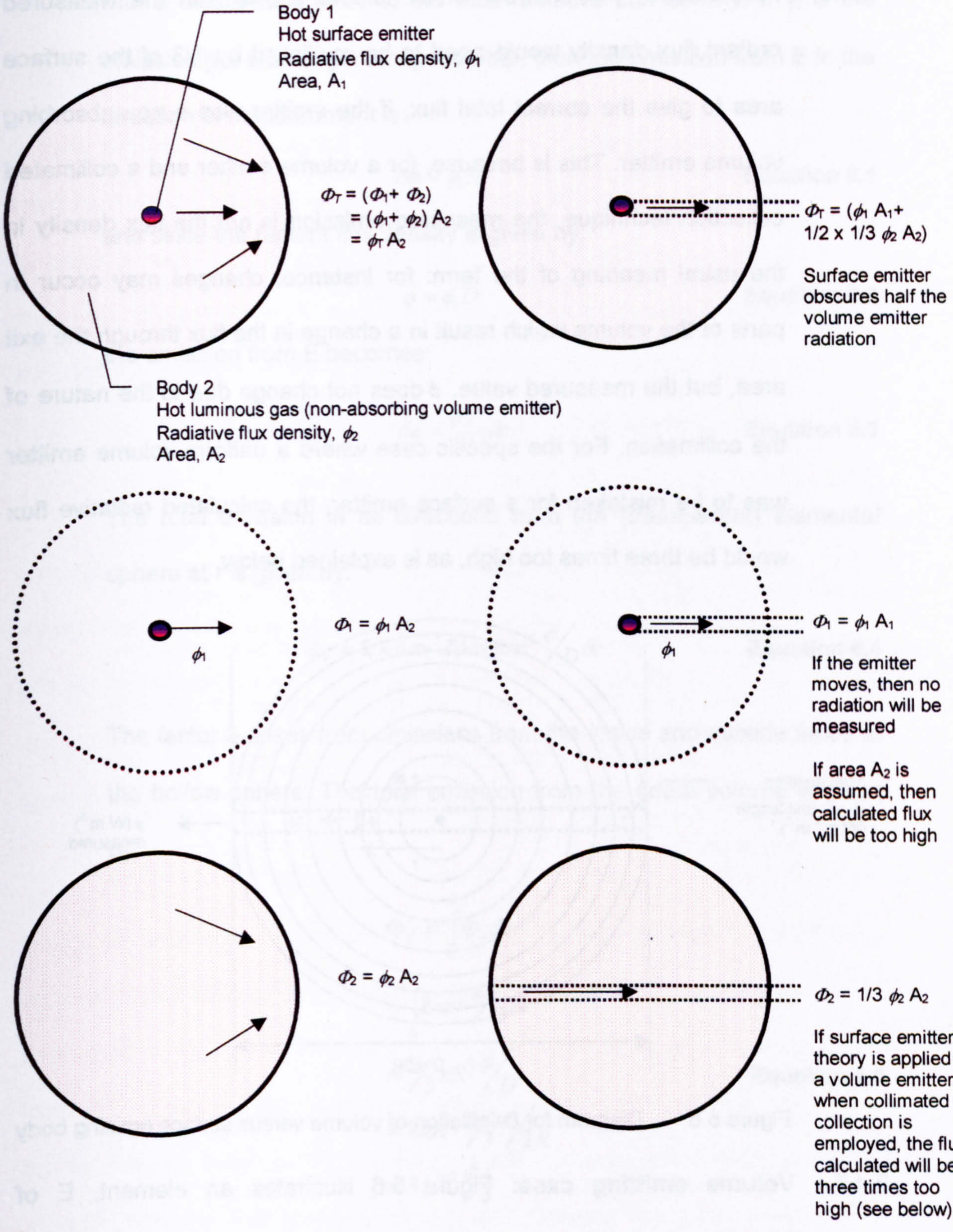

Figure 5.5 Uncollimated (left) and collimated (right) spectrum acquisition

2.4.6 Furthermore, the analysis which follows shows that the measured radiant flux density would need to be multiplied by 1/3 of the surface area to give the correct total flux, if the emitter was a non-absorbing volume emitter. This is because, for a volume emitter and a collimated collection technique, the measured emission is not the flux density in the usual meaning of the term: for instance, changes may occur in parts of the volume which result in a change in the flux through the exit area, but the measured value, ϕ does not change due to the nature of the collimation. For the specific case where a uniform volume emitter was to be mistaken for a surface emitter, the calculated radiative flux would be three times too high, as is explained below.

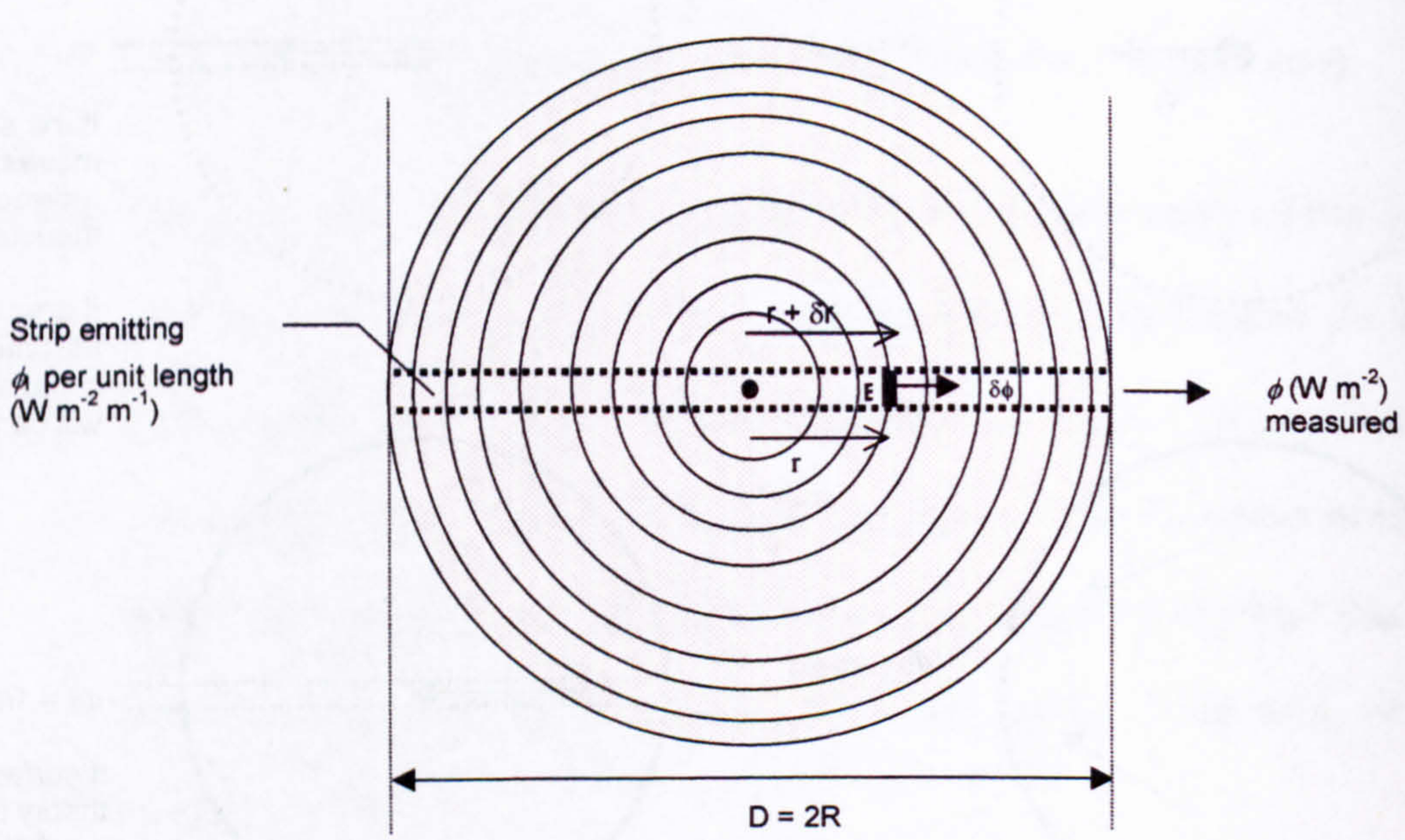

Figure 5.6 Diagram for calculation of volume versus surface emitting body

2.4.7 **Volume emitting case:** Figure 5.6 illustrates an element, E of thickness δr at r from the centre of a uniform, non-absorbing volume emitting sphere of diameter, D emitting in the direction of collimation

with a contribution of $\delta\phi$ to the total radiative flux density. If ϕ_l is the emission per unit length along the strip, then the emission from E in the direction of measurement is:

$$\delta\phi = \phi_l \delta r \qquad \textbf{Equation 5.1}$$

and since the radiant flux density is given by:

$$\phi = \phi_l D \qquad \textbf{Equation 5.2}$$

the emission from E becomes:

$$\delta\phi = {}^{\phi}/_{D}\,\delta r \qquad \textbf{Equation 5.3}$$

The total emission in all directions from the (transparent) elemental sphere at r is given by:

$$\Phi_r = 2 \times 4\pi r^2 \delta\phi = 8\pi r^2 \, {}^{\phi}/_{D}\,\delta r \qquad \textbf{Equation 5.4}$$

The factor 2 arises from emissions from the *inside* and outside faces of the hollow sphere. The total emission from the entire volume is given by:

$$\begin{aligned}\Phi_V &= \int_0^R \Phi_r dr \\ &= \int_0^R 8\pi r^2 \, {}^{\phi}/_{D}\, dr \\ &= {}^{8}/_{3}\,\pi R^3 \, {}^{\phi}/_{D} \qquad \textbf{Equation 5.5} \\ &= 8\pi R^2 \, {}^{R}/_{3} \cdot {}^{\phi}/_{2R} \\ &= 4\pi R^2 \, {}^{\phi}/_{3}\end{aligned}$$

2.4.8 **Surface emitting (or strong scattering) case**: The total emission from the entire volume is simply given by:

$$\Phi_S = 4\pi R^2 \phi \qquad \textbf{Equation 5.6}$$

$$\therefore \Phi_S = 3\Phi_V \qquad \textbf{Equation 5.7}$$

2.4.9 Comparing Equation 5.5 and Equation 5.6 shows that the flux from a perfect homogeneous volume emitter will be three times less than from a surface emitter if a collimated measurement technique is used to determine the radiative flux density. Hence, if this analysis is used on a perfect volume emitter that is mistaken for a surface emitter, the resulting energy transfers will be a factor of three too high.

2.5 Determination of optical depth of ETC Plasmas

2.5.1 Various methods were used in this work to determine whether the plasma resembled a volume or a surface emitter as is described briefly below. However, the analysis of the work was always based on the assumption that the plasma was a perfect surface emitter. Thus, the results are to be taken as maximum values with respect to the energy transfers.

2.5.2 Three methods were considered and two used to determine the optical depth of the plasma plume. The first method considered was to view an intense light source spectrally with the plasma between the source and the spectrograph optics. A Class 1 pen laser was chosen for the task, but this is only good for the case where the recorded intensity of the laser does *not* diminish, i.e. for an optically thin material. This is because a reduction in the recorded intensity might be due to factors other than absorption, such as reflection or refraction. However, this

method proved unsuccessful for an ETC discharge due to the electromagnetic pulse (EMP) from the discharge causing the lasing to cease. This was discovered prior to aiming the laser through the plasma by imaging it into the spectrograph optics behind the CPG during the discharge, where the EMP but not the plasma itself could interfere with the system. Four tests were conducted before the EMP effect was noticed, but clearly, this method could not be used.

2.5.3 The second method involved applying the angular relationship for flux density. For a surface emitting plane imaged with a collimating detector, any viewing angle should return the same result. However, for a volume emitter (especially for one where strong temperature gradients exist throughout the medium) the angle of view can be used to judge the degree of opacity. Looking in the direction of the nozzle, one might expect to record more flux with a volume emitter than when looking radially or away from the nozzle. This method of optical depth measurement was performed at 100 mm and 200 mm from the nozzle, at angles of 45°, 90° (i.e. radially) and 135° to the nozzle. Figure 5.7 shows the analysis of results for the radiant energy density at these distances.

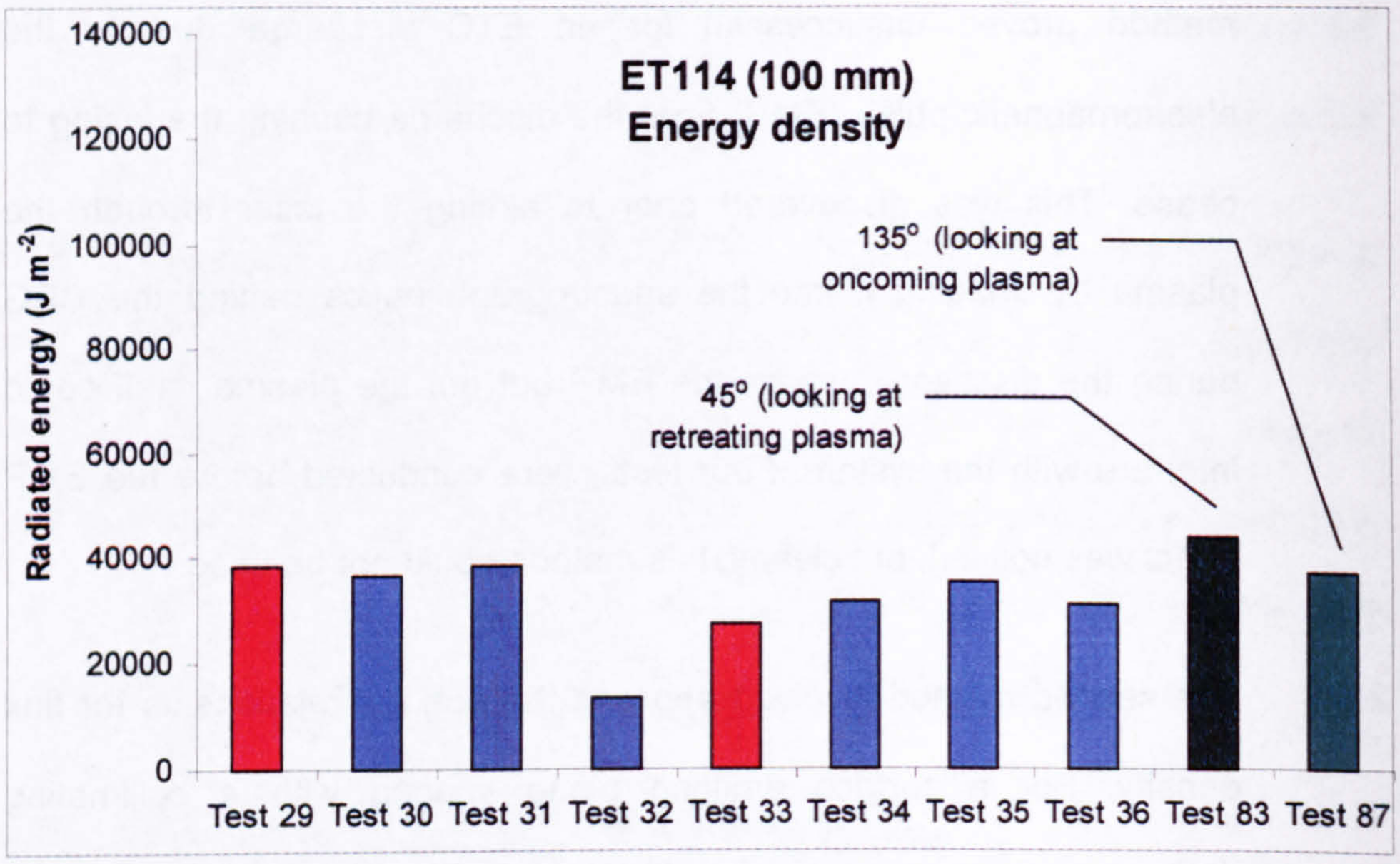

a

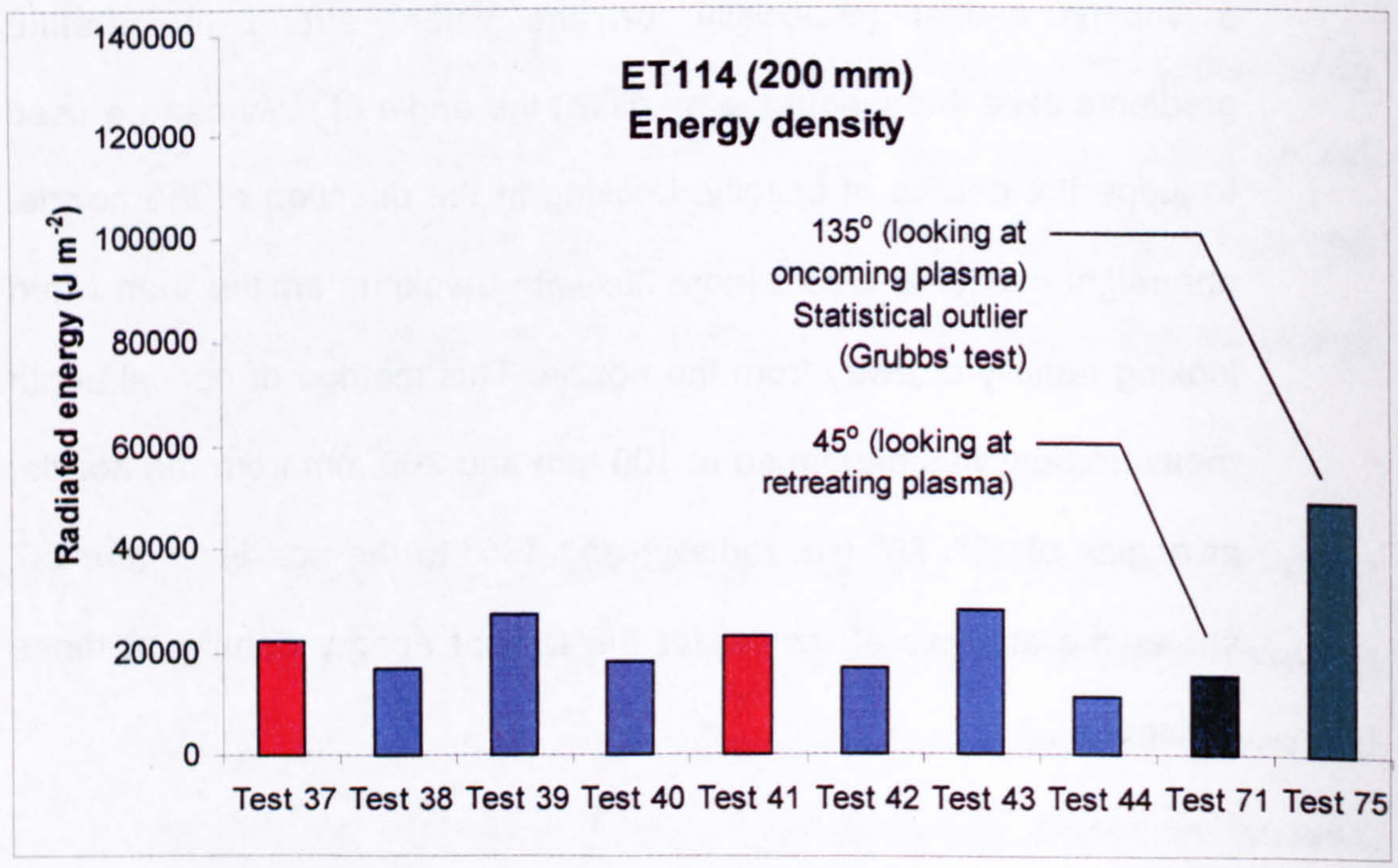

b

Figure 5.7 Radial energy densities at (a) 100 mm and (b) 200 mm

2.5.4 In Figure 5.7, the red bars represent radial energy density results with new components, whilst the radial results with reused components are

shown in light blue. New components and the optics set at 45° to the nozzle (i.e. viewing the retreating plasma) are shown in dark green, and new components viewing the plasma at 135° to the nozzle (i.e. looking at the oncoming plasma) appear in turquoise.

2.5.5 The Grubb's statistical test for a single outlier was performed on the results. There was no measurable difference in the values for the radiant energy density when the plasma is viewed at any of the three angles at 100 mm, with a 95% confidence interval. Therefore, the plasma was confirmed as approximating to an optically thick body and thus a surface emitter at 100 mm.

2.5.6 However, at 200 mm where the plasma had expanded further, a statistical difference was seen for the angle looking at the oncoming plasma, towards the nozzle. The measured radiant energy was far higher at the 95% confidence interval than at the other two angles which are themselves statistically indistinguishable. This implies that the plasma was less optically thick and thus a partial volume emitter. Hence, the results for distances over 100 mm may well be overestimated. That the result for the oncoming plasma is higher, whilst that for the retreating plasma is unchanged may be due to the hotter plasma nearer the nozzle radiating through the expanded cooler plasma.

2.5.7 The third method used the simple technique of placing an opaque object in the centre of the plasma and observing the photographic

digital images visually. The vertical steel bar from a retort stand was placed horizontally along the axis of the capillary, so its blunt end was 200 mm from the nozzle, external to the capillary. The plasma vented over the rod, which did not move during the test. The intensity maps of the images were examined for evidence of a shadow: Figure 5.8 shows one such image.

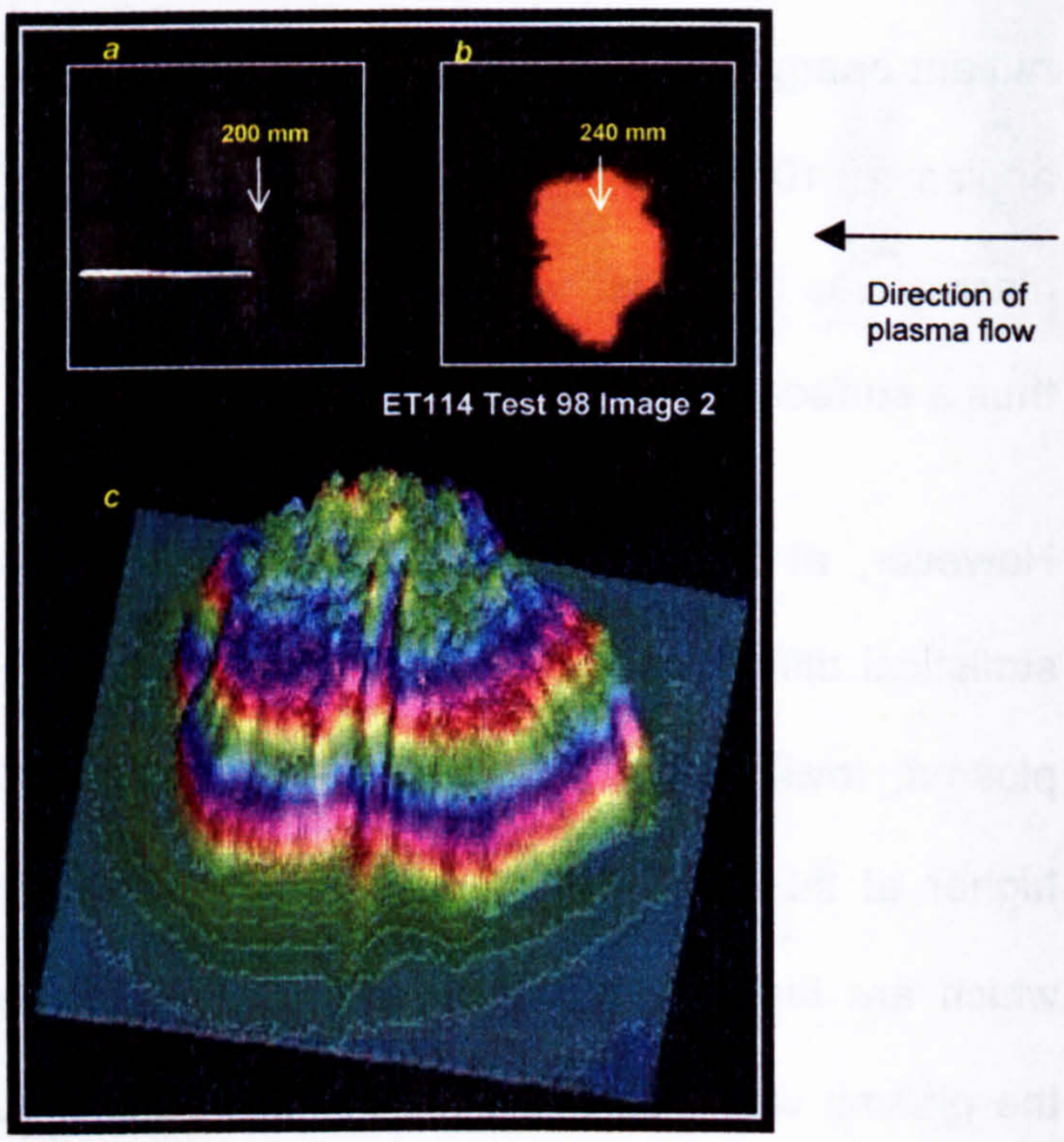

Figure 5.8 Viewing a steel bar through the plasma plume as a test for plasma opacity

2.5.8 Insert *a* shows the location of the steel bar before (and after) the test; insert *b* an image of the plasma venting over the bar, with the latter visible from 240 mm and insert *c* shows a reversed angle intensity map of the same image. The depression in the front of the map is the shadow produced by the bar from 240 mm. This implies that the plasma is thin enough for photons from at least the centre of the image

to propagate through to the edge, from 240 mm and further from the nozzle.

2.5.9 The plasma is therefore concluded to be a good surface emitter up to at least 100 mm from the CPG nozzle. From 240 mm, some photons from near the centre of the plasma can propagate through it without being absorbed. The radiative flux analysis thus gives maximum results for 100 mm onwards, but it will be seen that the fraction of discharged energy emitted from this portion of the plume is very small indeed.

2.5.10 As additional evidence of optical depth, Figure 5.9 images an expanding ETC plasma plume from this experiment, with the capillary nozzle on the right. Surface features are thought to be shadows cast by ripples on the plasma surface. These would not appear on an optically thin volume emitter.

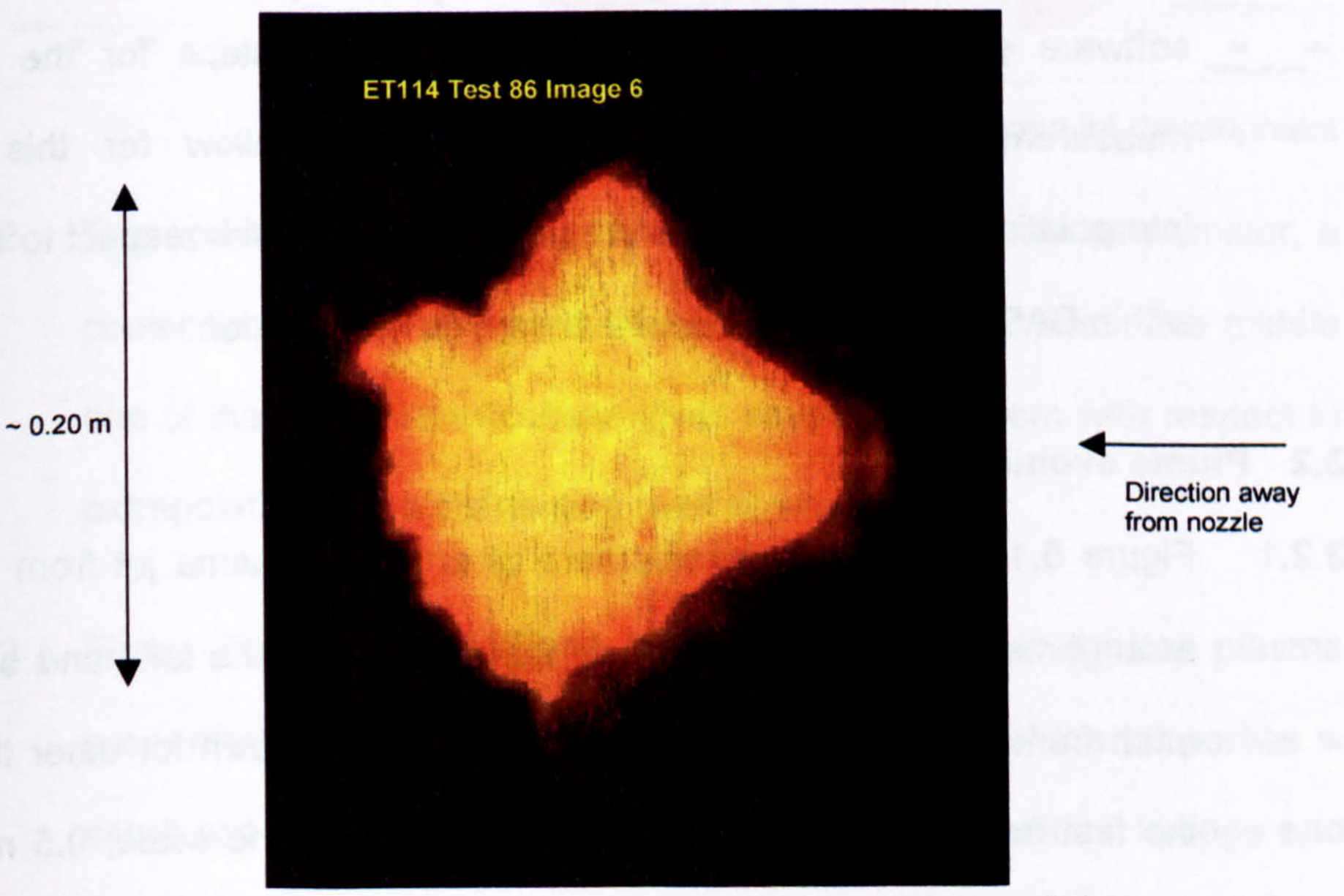

Figure 5.9 Image of plasma at 0.6 ms

2.5.11 Notable in Figure 5.9 is a strong Mach disc, where the flow structure changes from supersonic to subsonic. This feature has been noted in plasma plumes previously [5].

3 Radiative energy transfer results

3.1 Data handling

3.1.1 Results for radiant flux density were averaged to give a time-resolved radiant flux density for each region boundary: at 0 mm, 20 mm, 45 mm, 100 mm, 200 mm, 350 mm and 500 mm from the nozzle; within the capillary and the front expanding plasma face. The boundary results were averaged together to provide each region's estimated radiative flux density.

3.1.2 The process of multiplying the time-resolved radiant flux density by the time-resolved 3D surface area was performed within a data analysis software package, DADiSP. Because the time steps for the two measurements were different, DADiSP could allow for this by interpolation. The resulting flux was also integrated with respect to time within DADiSP to give the radiant energy for each region.

3.2 Plume evolution

3.2.1 Figure 5.10 traces the development of a typical plasma jet from this arrangement. The montage shows the capillary on the left-hand side; each frame starts at the capillary, but this is not shown for other than the first frame. The plume and capillary are shown to scale; 0.5 m is

indicated at the top right of the figure. The current waveform is also shown at the top of the figure: the points on the waveform indicate the timing of the first seven images on the jet expansion montage. Sample plasma spectra are also shown, overlaid with the associated Planckian distribution and displaying the distance from the timing and nozzle (100 mm in each case).

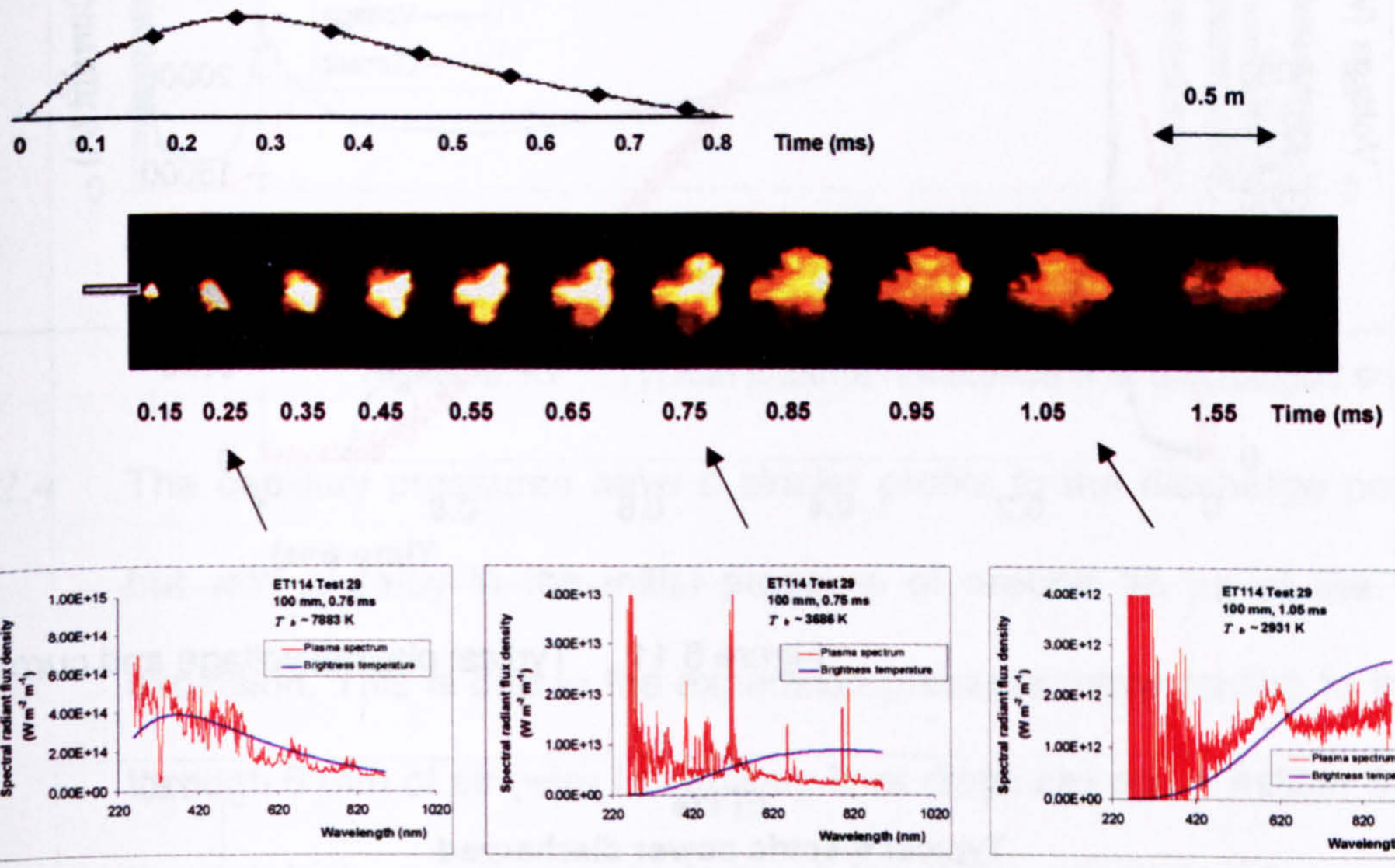

Figure 5.10 CPG plasma jet development

3.2.2 The spectra represent three distinct types: a hot continuum emitter, a cooler line emitter and an even cooler continuum emitter. The middle one of the three classifications gives cause for concern with respect to extrapolation of the distribution over all wavelengths.

3.2.3 Figure 5.11 to Figure 5.13 illustrate some of the typical plasma properties for this test arrangement. The variability of the properties is small and is discussed in some detail below. The electrical voltage and current data have a resolution of 0.1 μs, and some high frequency

ringing on the current trace is noticeable. No analysis has yet been performed on this ringing phenomenon.

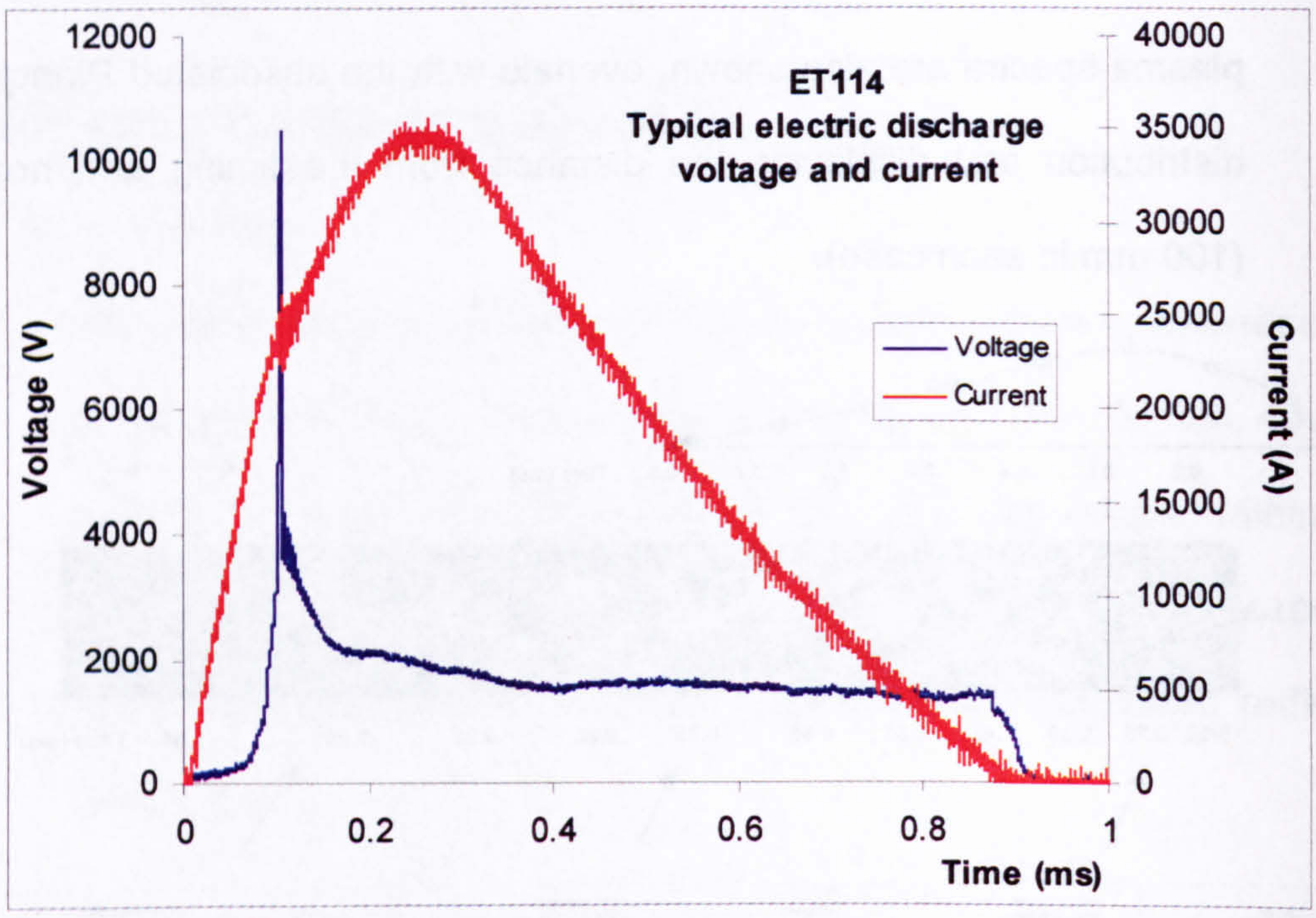

Figure 5.11 Typical plasma voltage and current

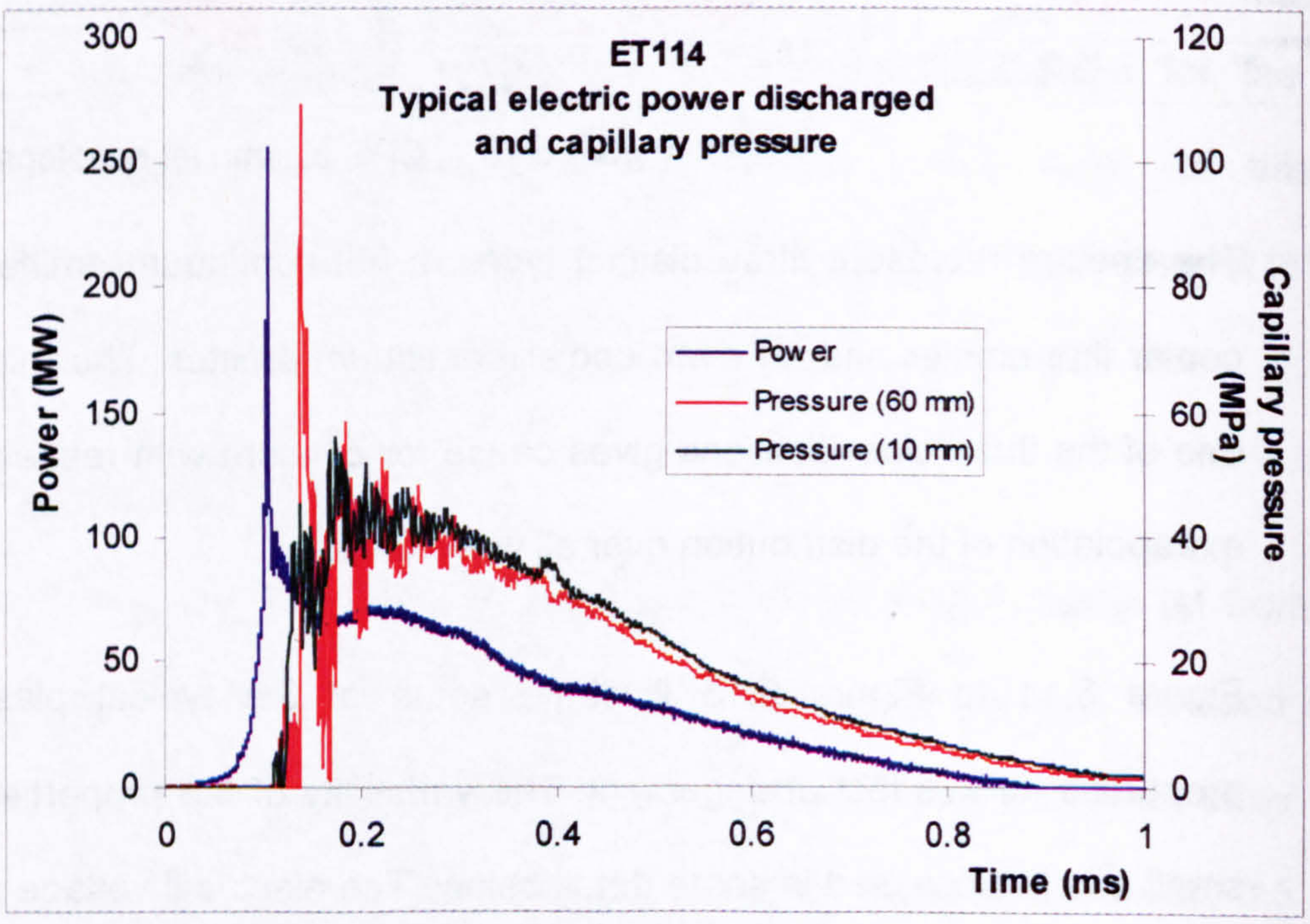

Figure 5.12 Typical plasma discharge power and capillary pressures

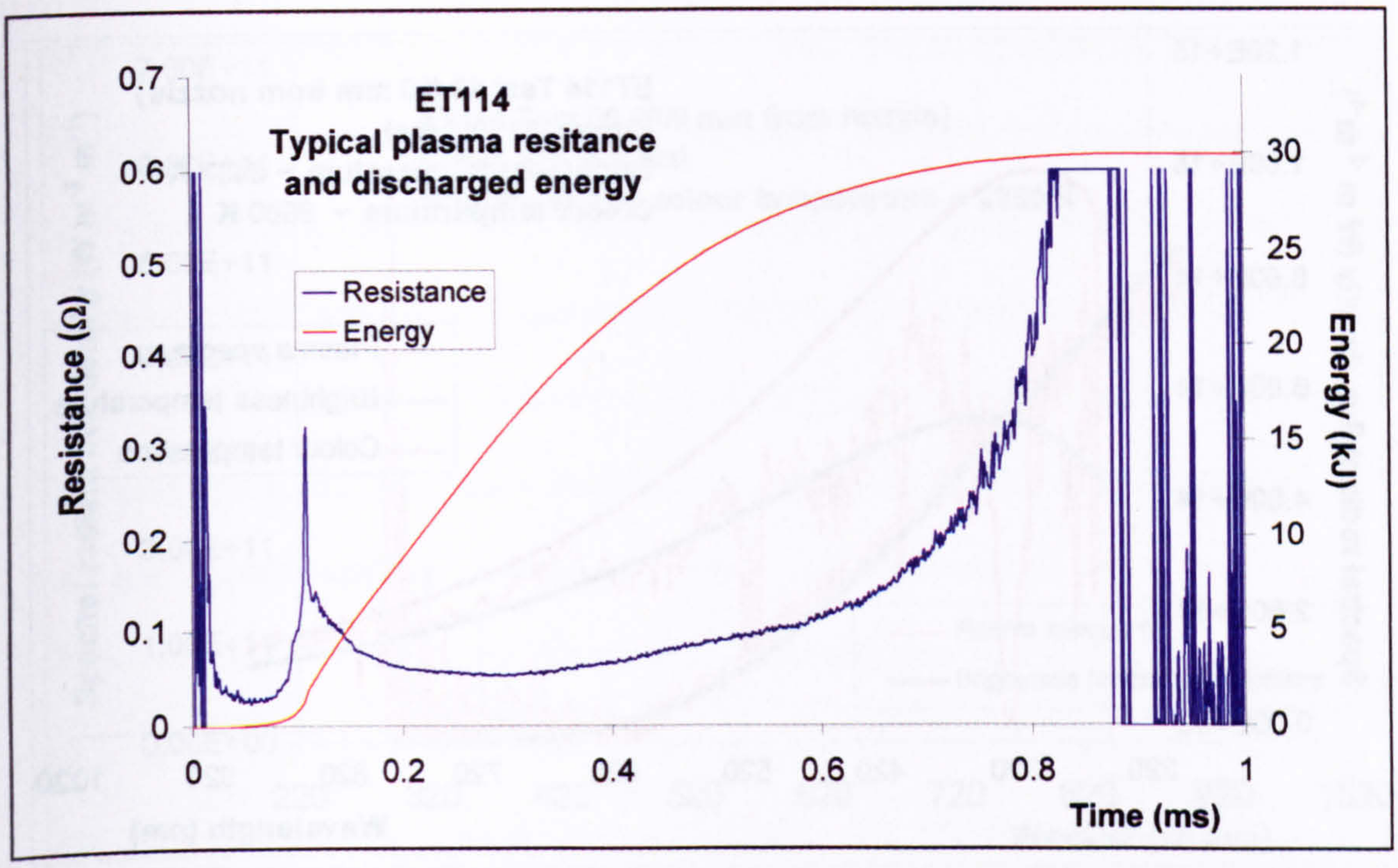

Figure 5.13 Typical plasma resistance and discharged energy

3.2.4 The capillary pressures have a similar profile to the discharge power, but with a delay in the initial pressure of around 35 μs at the wire explosion. This is due to the expansion pressure wave having to travel through 6 mm of air (wire to capillary liner distance) and a further 6 mm through high vacuum grease to reach the Kistler piezoelectric pressure gauge. This actually assists in confirming that the pressure spike is real and is not just due to electrical noise. The plasma resistance can be seen to rise as the power decreases after the initial wire explosion phase. The total electrical energy transferred to the plasma for this series of tests is around 30 kJ.

3.2.5 Examples of the three basic types of plasma spectrum, with brightness and colour temperature profiles fitted, are shown in Figure 5.14 to Figure 5.16.

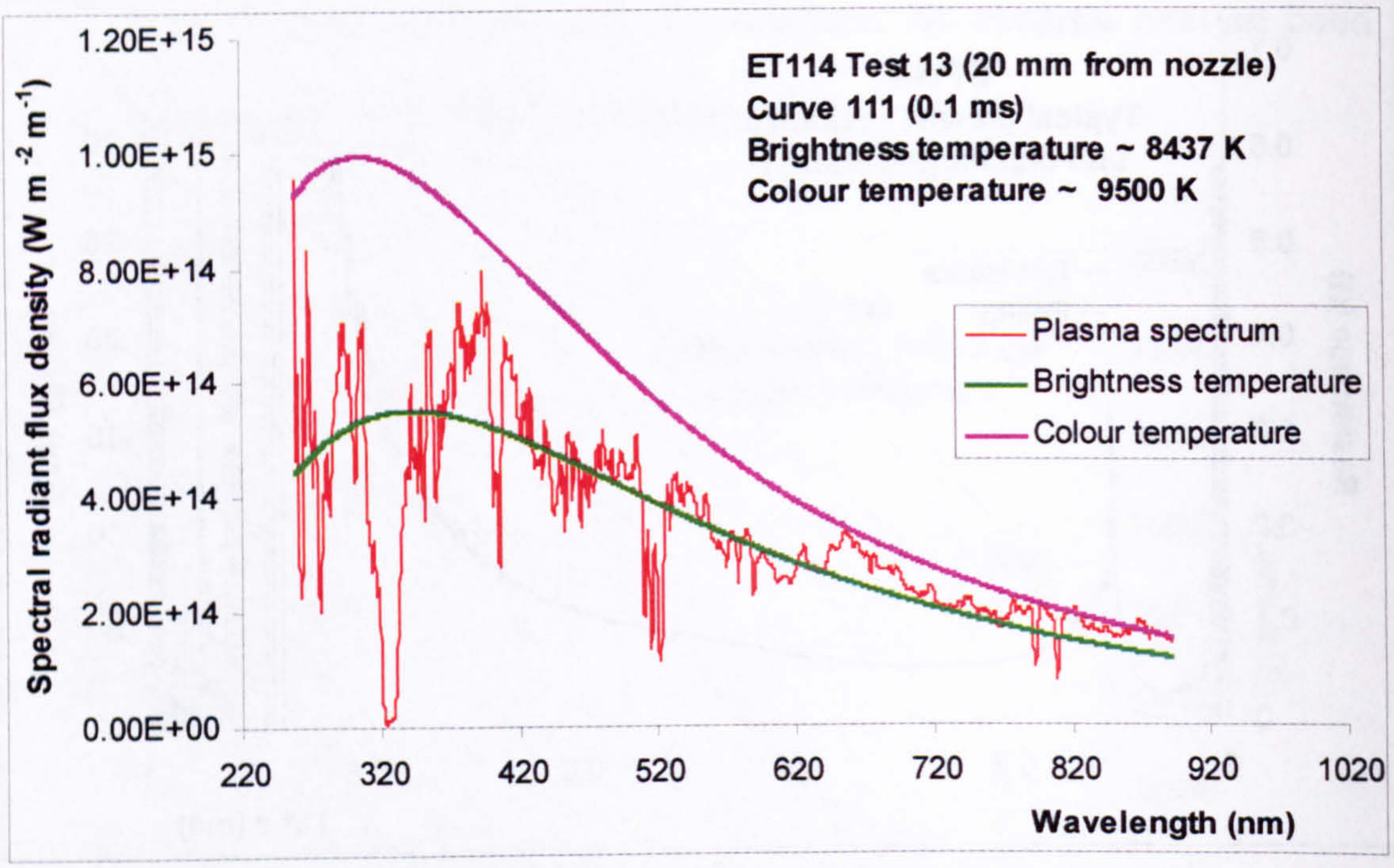

Figure 5.14 Brightness and colour temperature of hot dense plasma

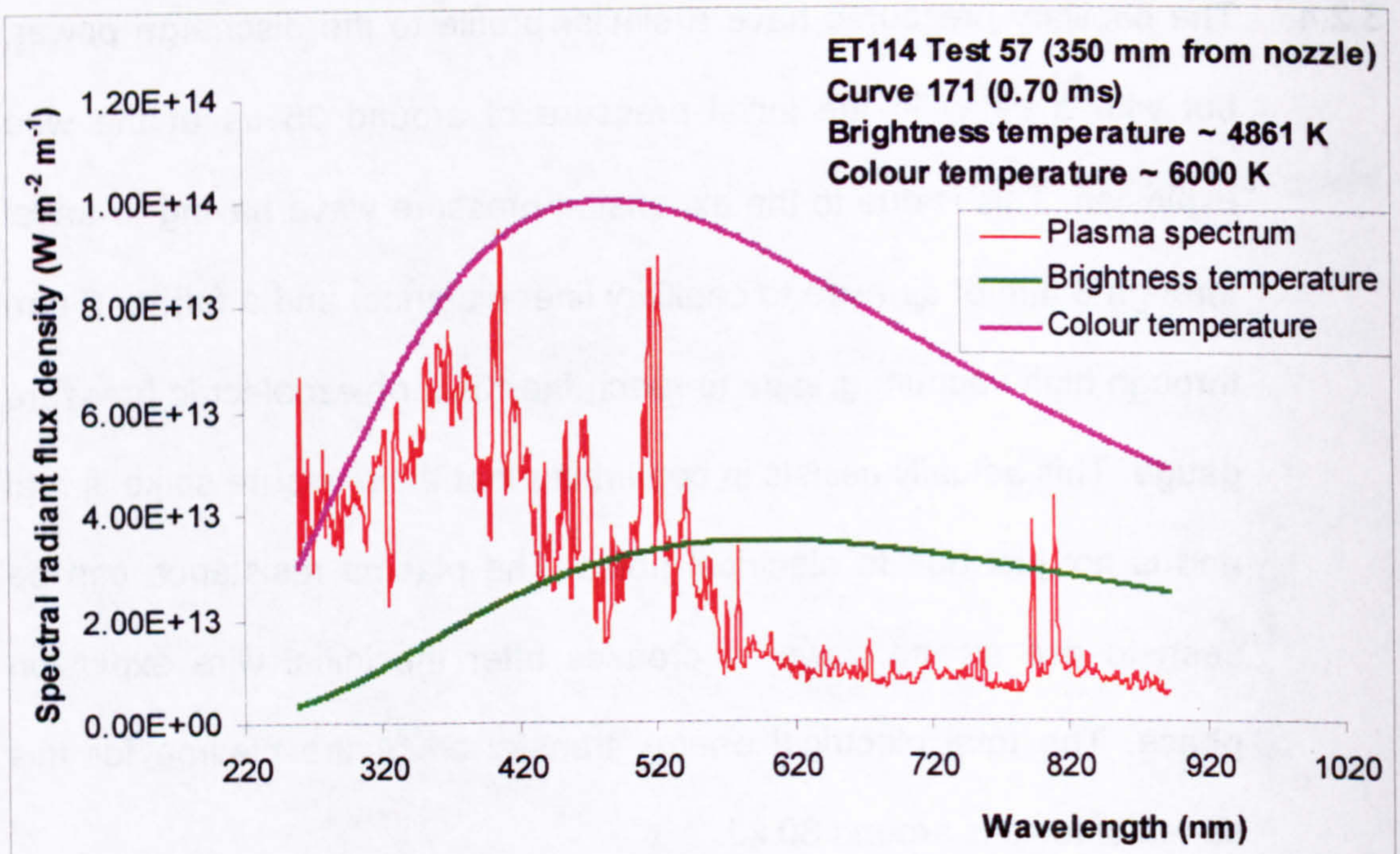

Figure 5.15 Brightness and colour temperature of cooler less dense plasma

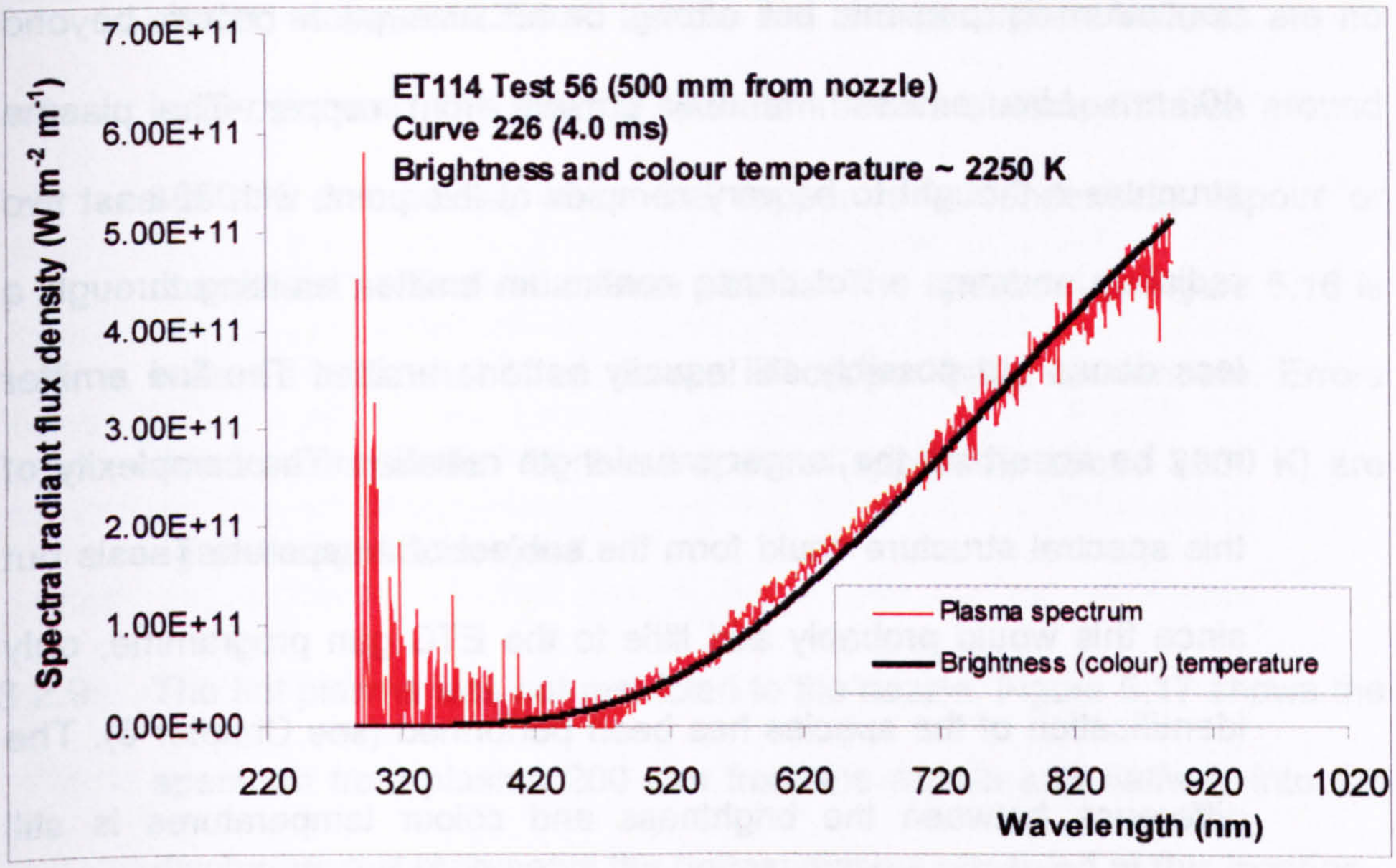

Figure 5.16 Brightness and colour temperature of condensed copper vapour

3.2.6 Figure 5.14 is the spectrum from a relatively hot, dense plasma. This spectrum was obtained at a distance of 20 mm from the nozzle and after 0.1 ms into the discharge. The emission is essentially a continuum but with strong self-absorption due to species – mainly copper – within the plasma. There is around 1000 K difference between the brightness and colour temperatures. The fit for the brightness temperature beyond the wavelength range studied is thought to be good because the plasma spectra agree in general with the Planckian distribution. Therefore, the extrapolation to obtain the radiative flux for all wavelengths is thought to incur only small errors for this type of spectra.

3.2.7 Figure 5.15 demonstrates the spectrum from cooler, less dense plasma, 350 mm from the nozzle and 0.7 ms into the discharge. The

continuum is present, but strong broad absorption occurs beyond 400 nm. Line emission is now present from copper. The plasma structure is thought to be very complex at this point, with at least two radiating sources: a hot dense continuum emitter, emitting through a less dense but possibly still equally hot line emitter. The line emitter may be absorbing the longer wavelength radiation. The complexity of this spectral structure could form the subject of a separate Thesis but since this would probably add little to the ETC gun programme, only identification of the species has been performed (see Chapter 6). The difference between the brightness and colour temperatures is still around 1000 K. Extrapolation to all wavelengths is thought to incur the greatest errors for this type of spectrum as it is not generally Planckian in nature. This experiment benefits in that the contribution to the energy transferred from this type of spectrum is small due to the T^4 relationship with radiated energy and the brevity that this type of spectrum shows. Further, most (around 70%) of the theoretically radiated energy falls within the experimental wavelength range at these plasma temperatures (see Figure 5.4).

3.2.8 Figure 5.16 shows the spectrum of a different characteristic altogether, taken from a distance of 500 mm from the nozzle and around 3.2 ms after the discharge has ended. Noise below around 400 nm can be ignored. This is due to the application of the deuterium calibration curve amplifying a very low signal (examination of the raw data shows no sign of this noise). The brightness and colour temperatures are very

similar, at around 2250 K, but the line and absorption features are no longer present. This form of spectrum occurs at temperatures around 3000 K and below, when the copper is a condensing vapour or condensed aerosol rather than plasma. The spectrum in Figure 5.16 is believed to be that of an aerosol of copper liquid condensate. Errors due to extrapolation for these spectra (applicable above 3000 K) are again thought to be small.

3.2.9 The hot plasma was not restricted to the nozzle. Figure 5.17 shows the spectrum from plasma 200 mm from the nozzle and halfway into the discharge; this represents the hottest plasma observed at this location.

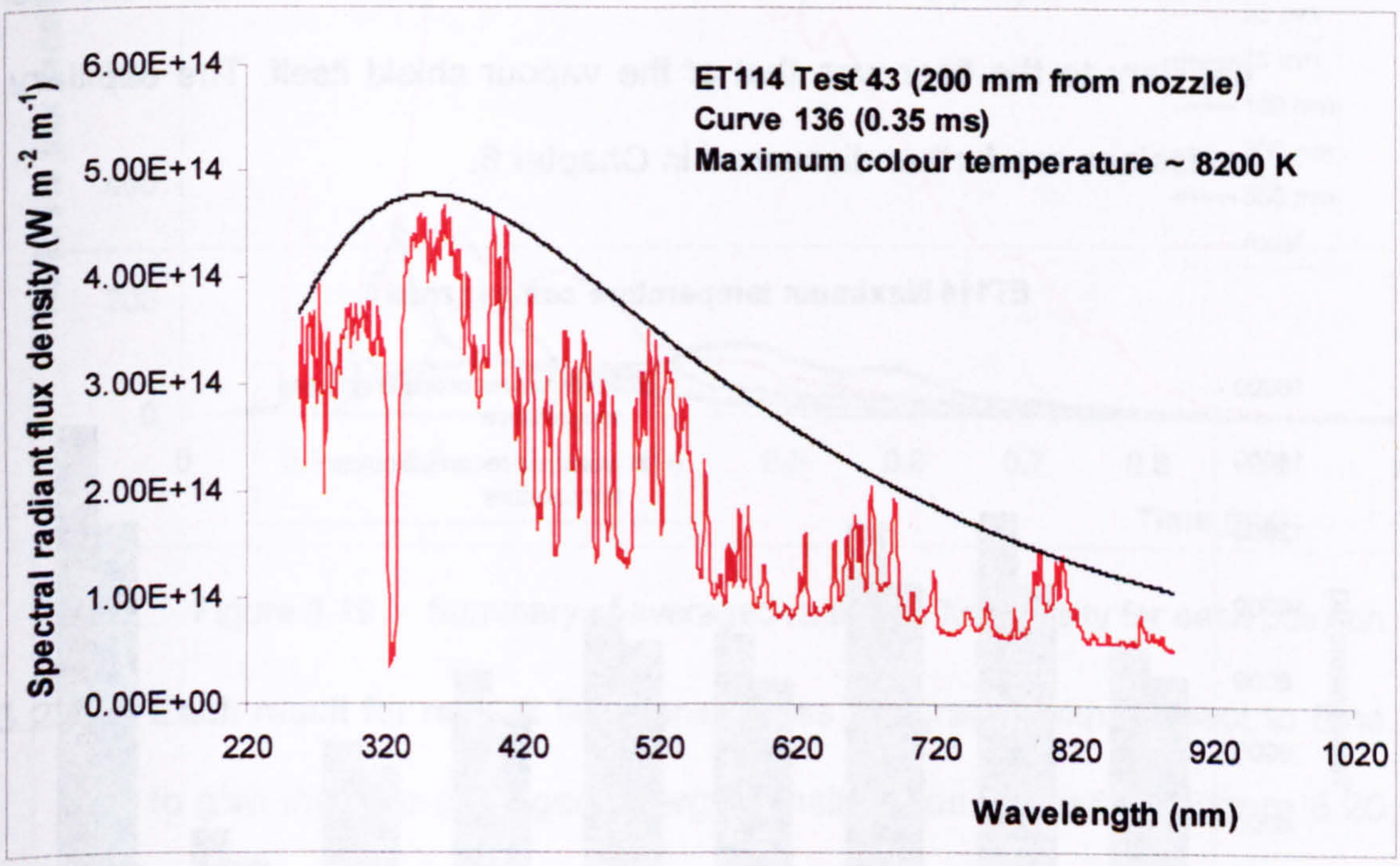

Figure 5.17 Example of hottest plasma at 200 mm

3.2.10 Other locations had similar spectra, although increasingly cooler and of a shorter duration, until at 500 mm where only the cooler (condensing)

type of continuum spectrum was seen. The maximum brightness and colour temperatures for each location appear in Figure 5.18.

3.2.11 The hottest plasma of all was located by looking along the axis of the system towards the capillary; measured temperatures reached around 15 000 K. The temperatures recorded within the capillary were unexpected. It was known that modelling suggested the existence of an absorbing 'vapour shield', which was thought to reduce the radiant energy (i.e. the brightness temperature). Nevertheless, the colour temperature was expected to be that of a hot, strong ultraviolet emitter (i.e. with a high colour temperature). However, the spectra from plasma within the capillary clearly showed that the radiation emitted from the capillary to the liner was that of the vapour shield itself. The capillary emissions are further discussed in Chapter 6.

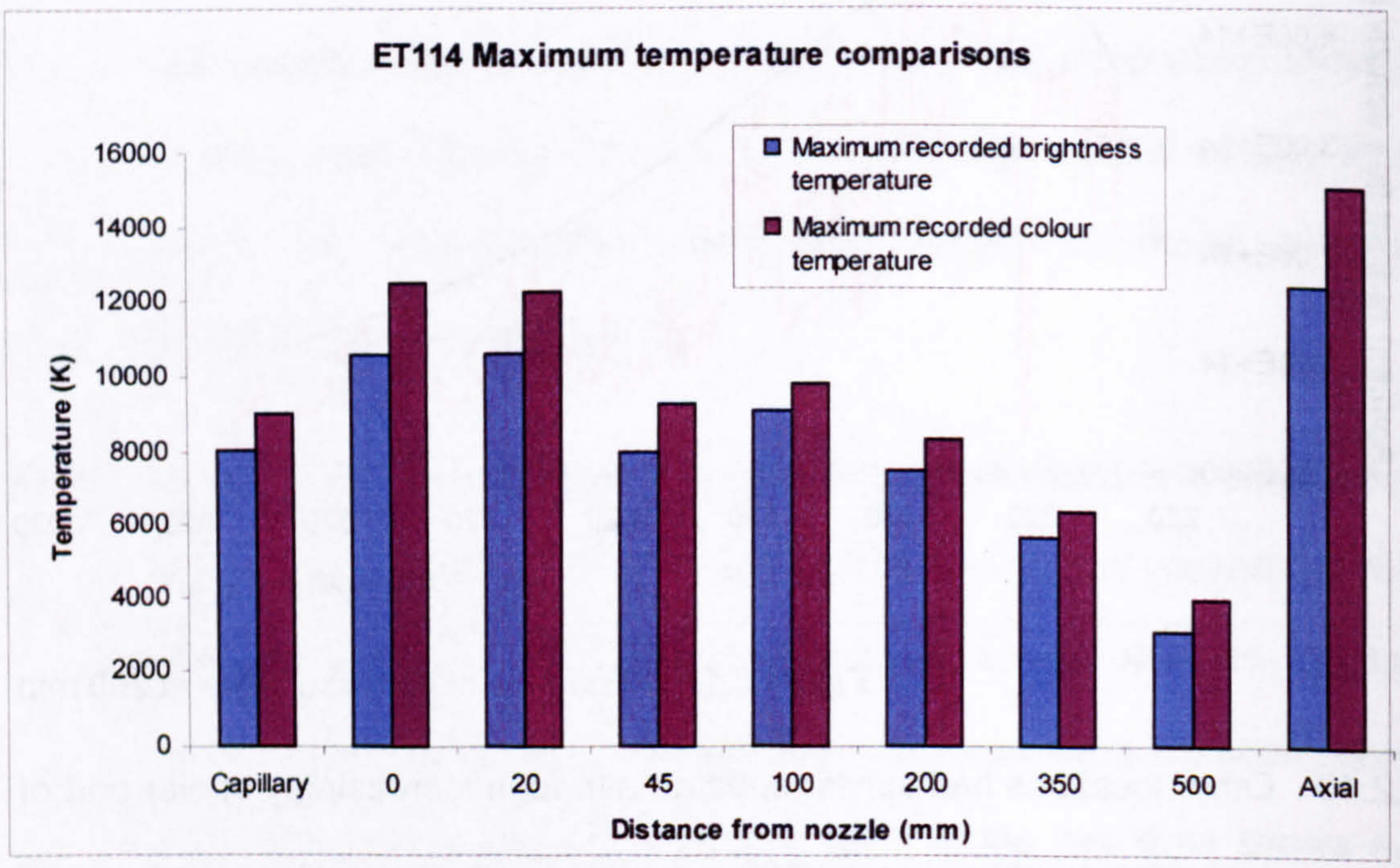

Figure 5.18 Graph of comparisons between the maximum recorded colour and brightness temperatures at each position

3.2.12 Figure 5.19 summarises test-averaged radiative flux density analysis for each position along the plasma. Radiation is dominant along the axis of the plasma. The flux density at 20 mm is greater than at the nozzle for almost half the discharge. At 100 mm, the flux density is also greater than at 45 mm between around 0.2 ms and 0.3 ms. This may be due to the turbulence that occurs beyond the nozzle and is discussed in more depth later.

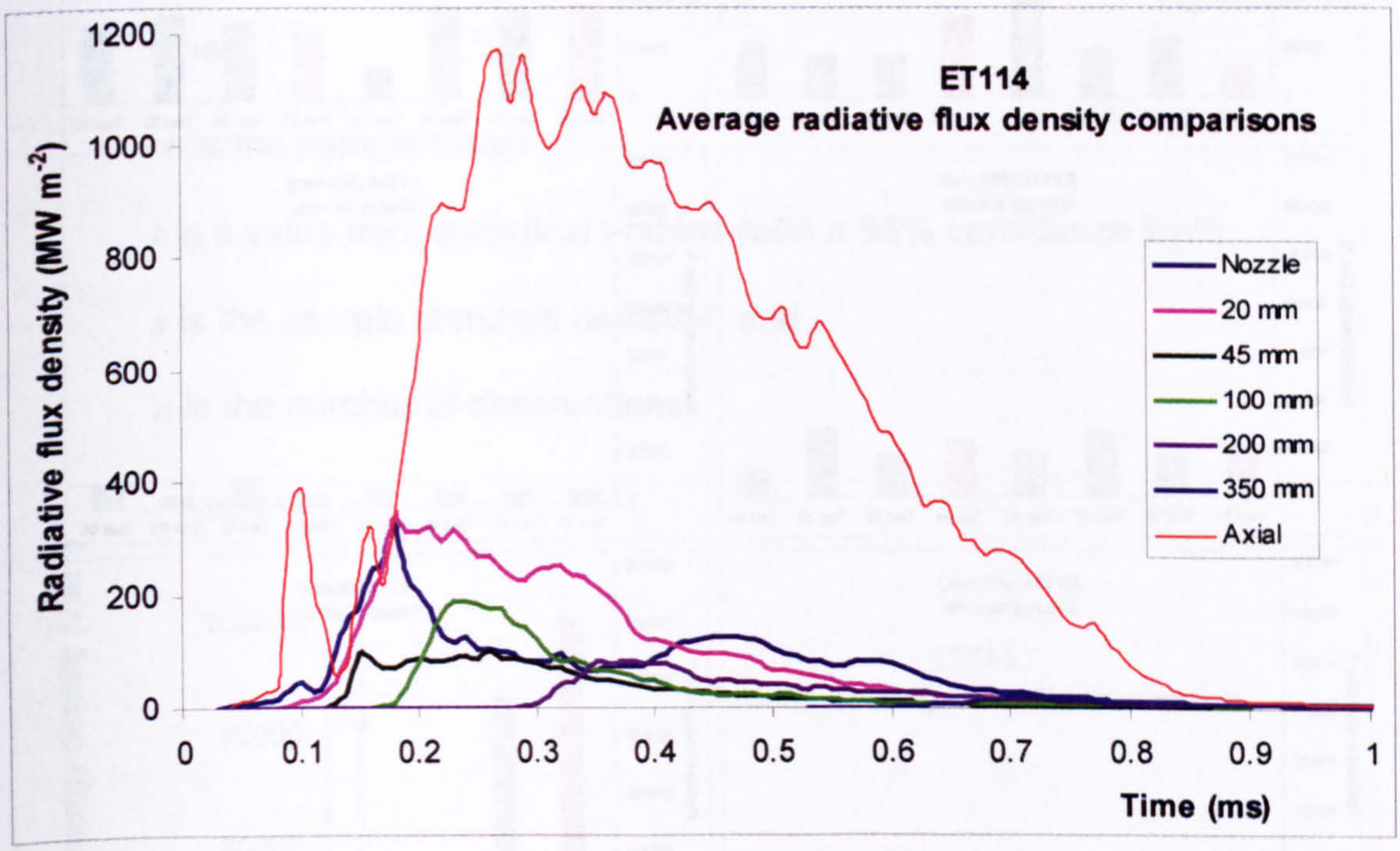

Figure 5.19 Summary of averaged radiative flux density for each position

3.2.13 Each result for radiant flux density was integrated with respect to time to give the time-averaged energy density at each position. Figure 5.20 shows a summary of this integration for each location studied. The tests involving new components are depicted in red and those reusing components are in blue.

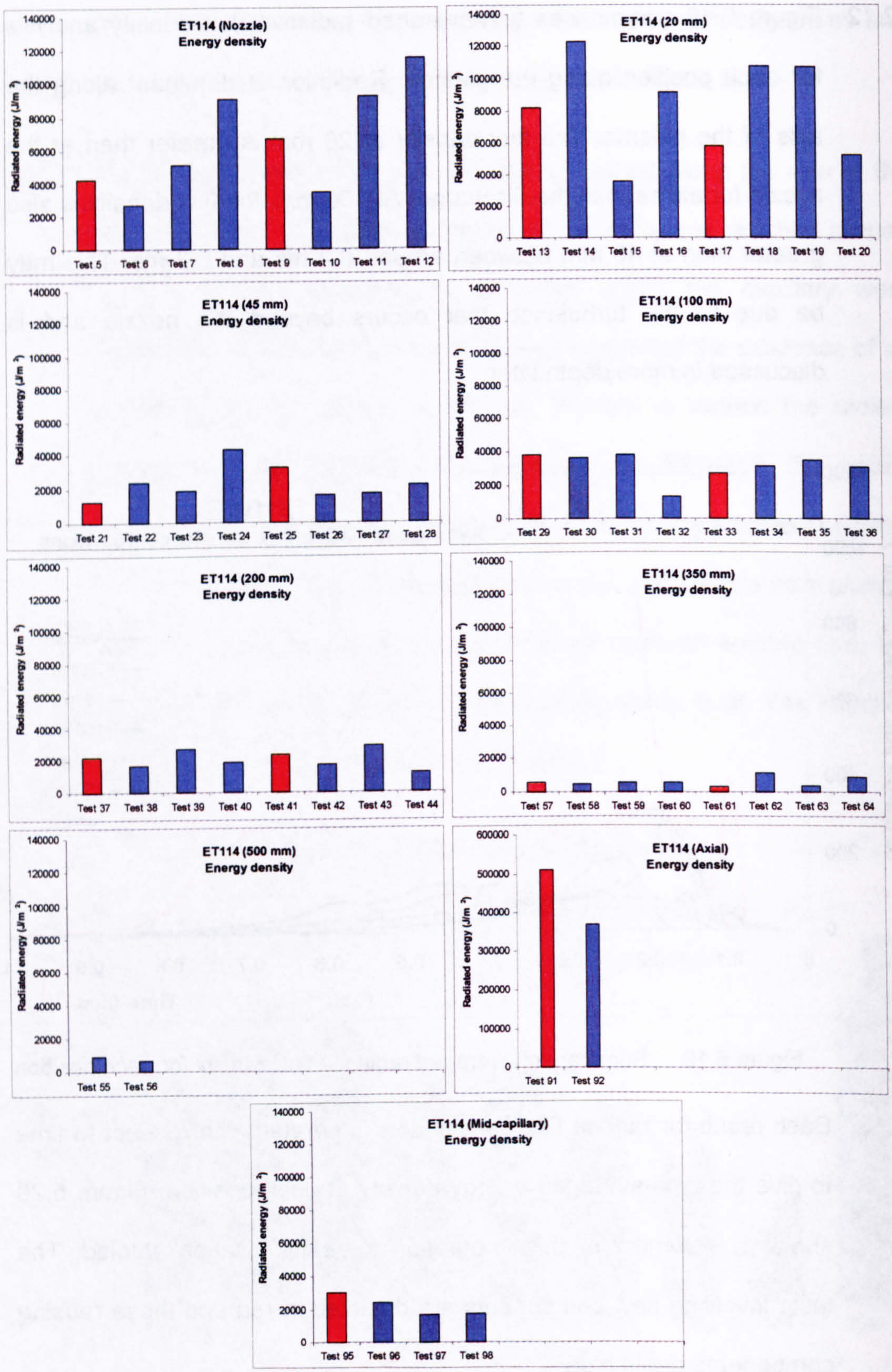

Figure 5.20 Individual test energy densities at positions along the plume

3.2.14 Immediately evident is a high degree of test to test variability, independent of how many times a component has been used (up to four times). The degree of variability makes assessment of the data difficult; statistical methods were employed therefore to clarify the assessment. Figure 5.21 shows the 'true mean' radiated energy density for each position viewed from the radial direction (including viewing the capillary plasma through the wall). The true mean is defined as:

$$\bar{x} \pm ts/\sqrt{n} \qquad \textbf{Equation 5.8}$$

where

$\bar{x}$ is the sample mean

t is a value from statistical t-tables (with a 95% confidence limit),

s is the sample standard deviation and

n is the number of observations.

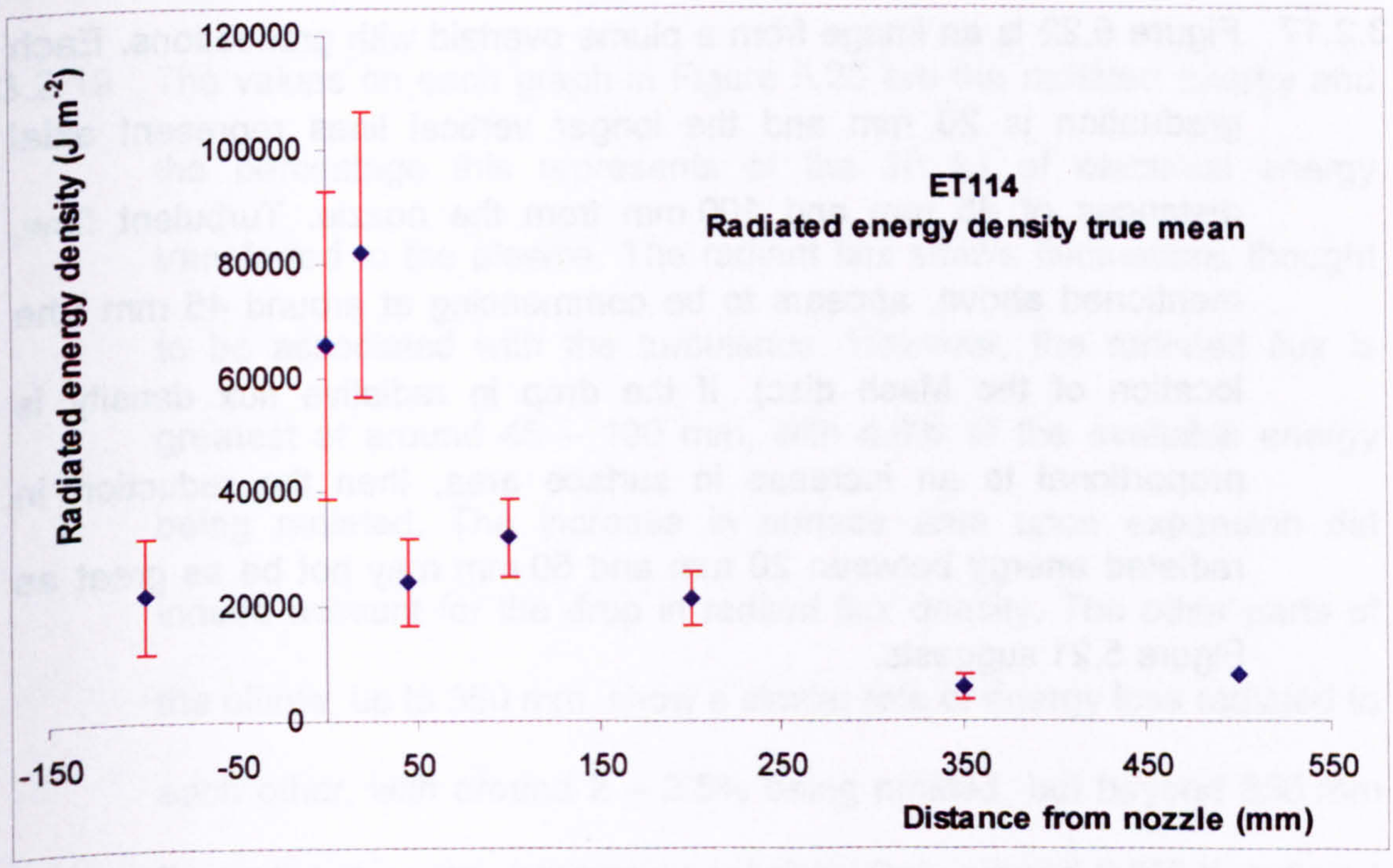

Figure 5.21 True mean of the time averaged energy density for each position along the plume

3.2.15 The 500 mm energy density true mean gave a nonsensical return due to being based only on two available tests for the analysis (having a small value of n and a large value for t), with significant variation between the two tests (a large value for s). Hence, the sample mean is indicated in the figure with no error bars.

3.2.16 It is clear that the highest radiated energy densities (in the radial direction) come from the first 20 mm of the plasma plume. By 50 mm, the value has significantly reduced, possibly due to cooling or surface area increase as the plume expands. The energy density remains reasonably constant between the distances 50 mm and 200 mm. By 350 mm, the value has fallen to very low levels but, again, increases in the surface area could offset some of this reduction.

3.2.17 Figure 5.22 is an image from a plume overlaid with graduations. Each graduation is 20 mm and the longer vertical lines represent axial distances of 45 mm and 100 mm from the nozzle. Turbulent flow, mentioned above, appears to be commencing at around 45 mm (the location of the Mach disc). If the drop in radiative flux density is proportional to an increase in surface area, then the reduction in radiated energy between 20 mm and 50 mm may not be as great as Figure 5.21 suggests.

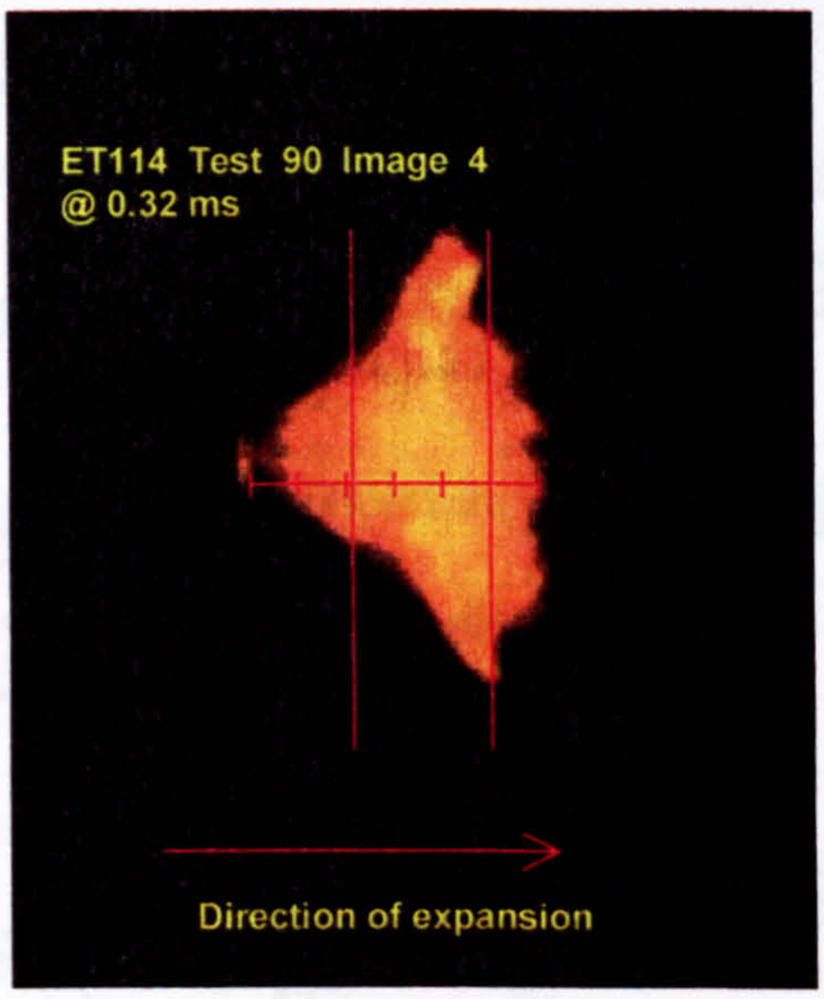

Figure 5.22 Image of the plasma plume

3.2.18 Figure 5.23 provides the results of the radiated flux and energy from the plasma plume, where the surface area expansion has been taken into account, for each segment studied. (The methodology leading to the calculation of surface area is set out in Appendix B.)

3.2.19 The values on each graph in Figure 5.23 are the radiated energy and the percentage this represents of the 30 kJ of electrical energy transferred to the plasma. The radiant flux shows fluctuations thought to be associated with the turbulence. However, the radiated flux is greatest at around 45 – 100 mm, with 4.6% of the available energy being radiated. The increase in surface area upon expansion did indeed account for the drop in radiant flux density. The other parts of the plume, up to 350 mm, show a similar rate of energy loss radiated to each other, with around 2 – 2.5% being emitted, but beyond 350 mm the radiated energy becomes negligible. Only around 0.5% is radiated to the capillary wall, a far lower level than expected (see Chapter 6).

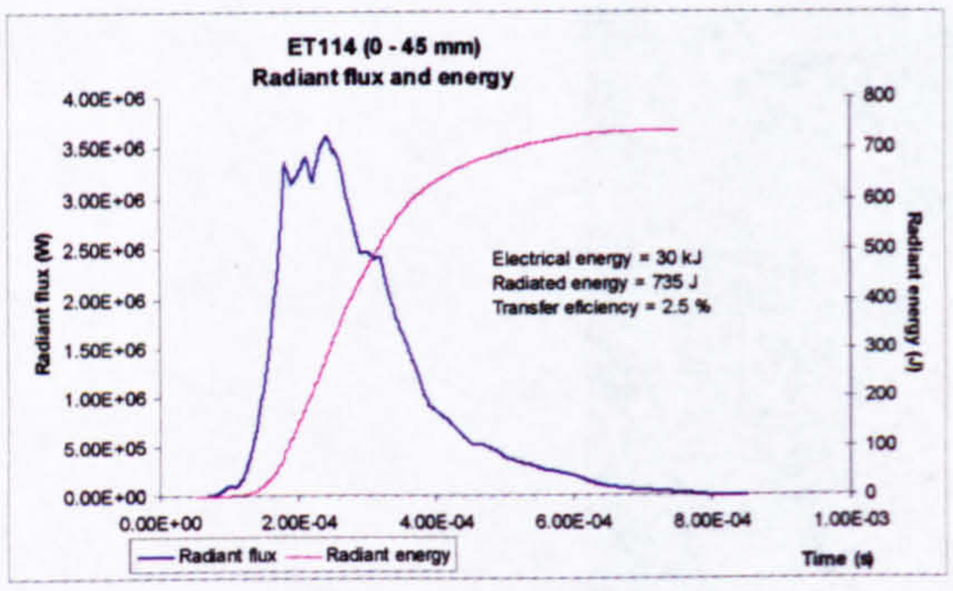

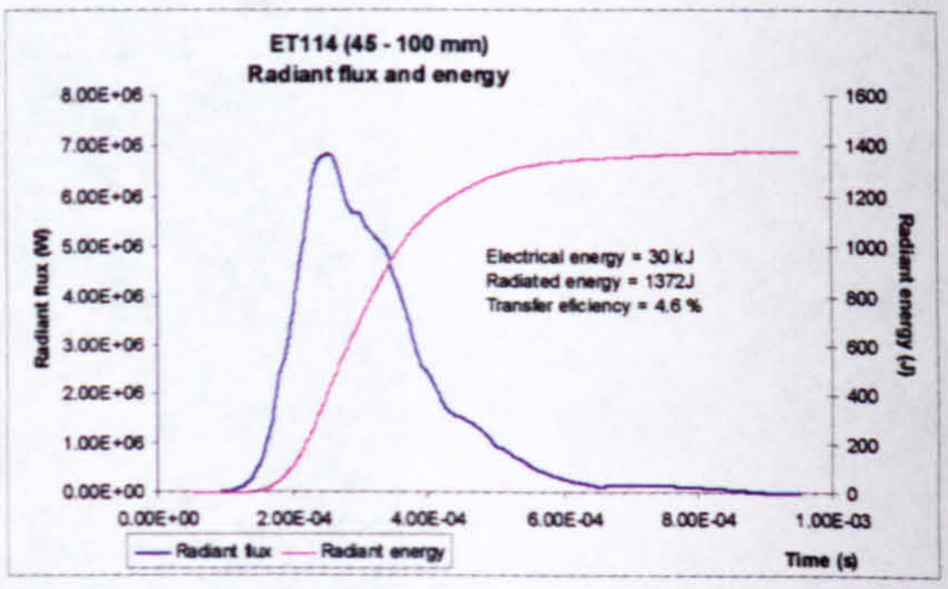

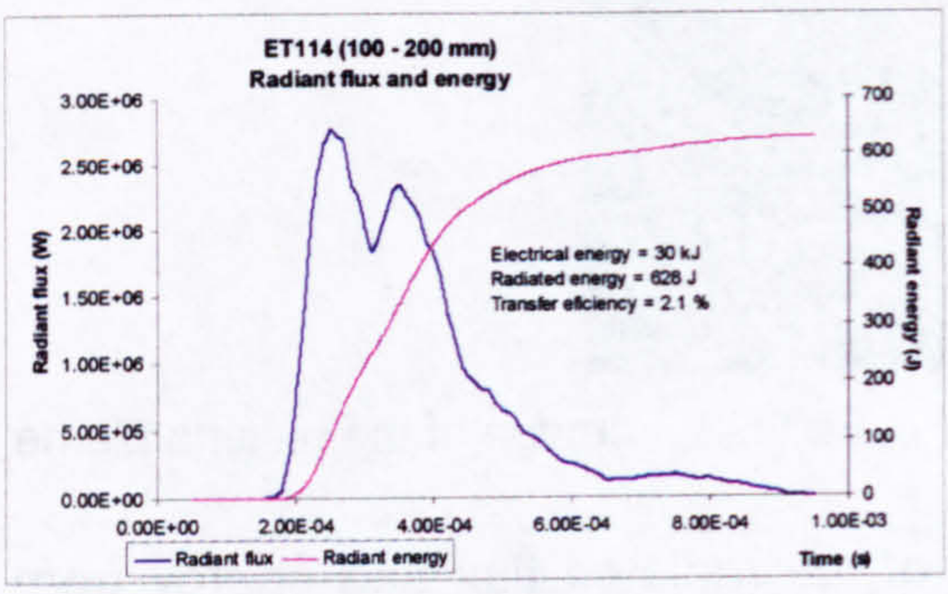

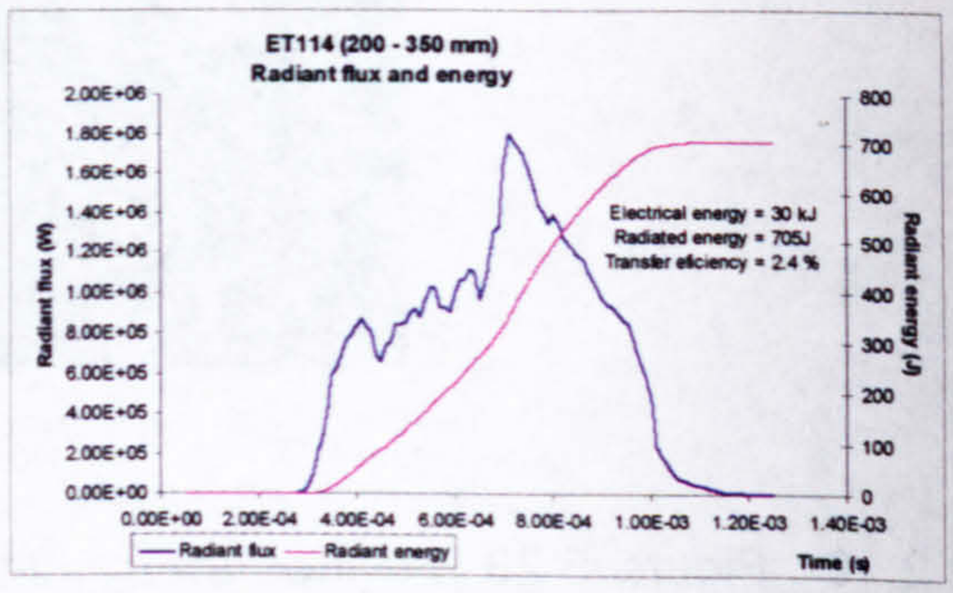

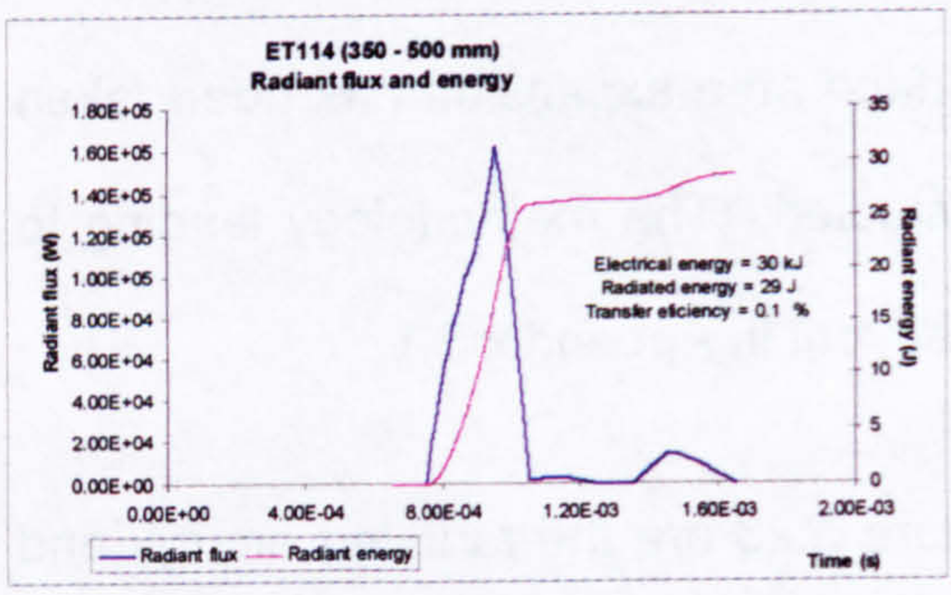

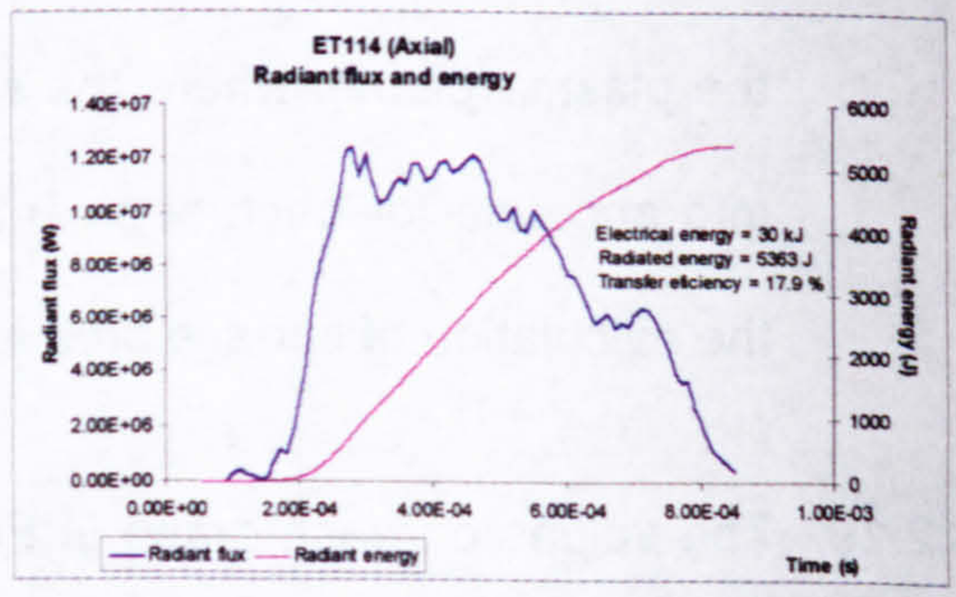

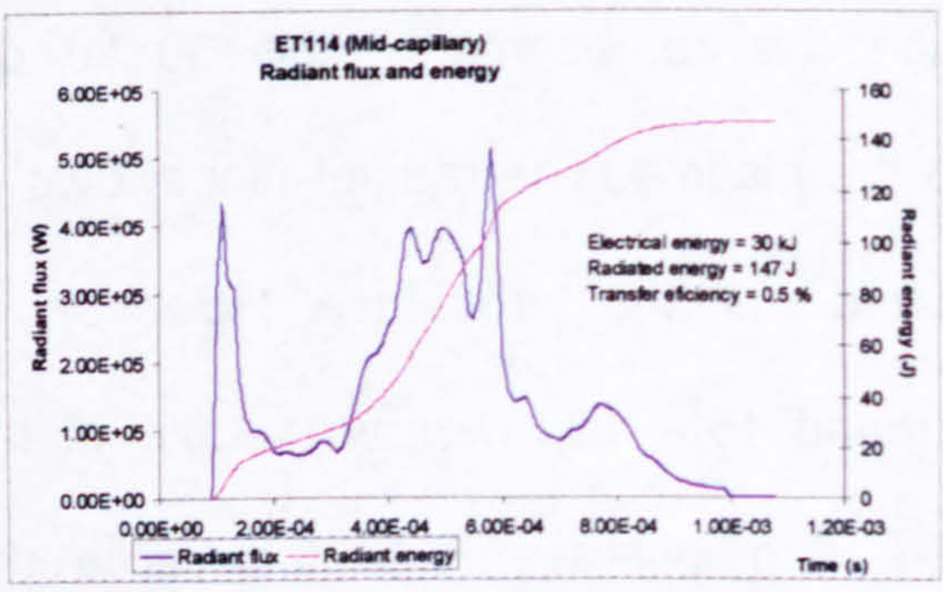

Figure 5.23 Averaged regional radiative flux and radiative energy summary

3.2.20 The 17.9% of energy radiated forward in the axial direction is thought to be an overestimate, due to use of the radiant flux density from the centre of the plume face to the entire face area. This is thought to be an unreasonable assessment and work has now been completed

(awaiting full analysis) indicating that strong temperature gradients exist across the face. The percentage radiated forward has been initially re-estimated at around 5%, rather than 17.9%.

3.2.21 Further discussions are detailed in Chapter 6 on why so little radiative energy is measured in the radial direction.

4 Non-radiative energy transfer results

4.1 Plume expansion velocity

4.1.1 Two tests have been analysed for velocity. The position of the luminous plasma front can be determined from the Ultranac digital images, since the time of each image is accurately known. The leading edge had to be defined in terms of pixel intensity, and a value of 300 counts was chosen as the standard. This has been demonstrated as equivalent to a plasma temperature of 3000 K in these tests (see Appendix B). Figure 5.24 illustrates the distance-time curve for Test 1. The general relationship at first sight appears to be logarithmic, but when the velocity of the plasma front is calculated from numerical differentiation of the distance-time data, the plasma is clearly expanding in an erratic manner, characteristic of turbulent flow.

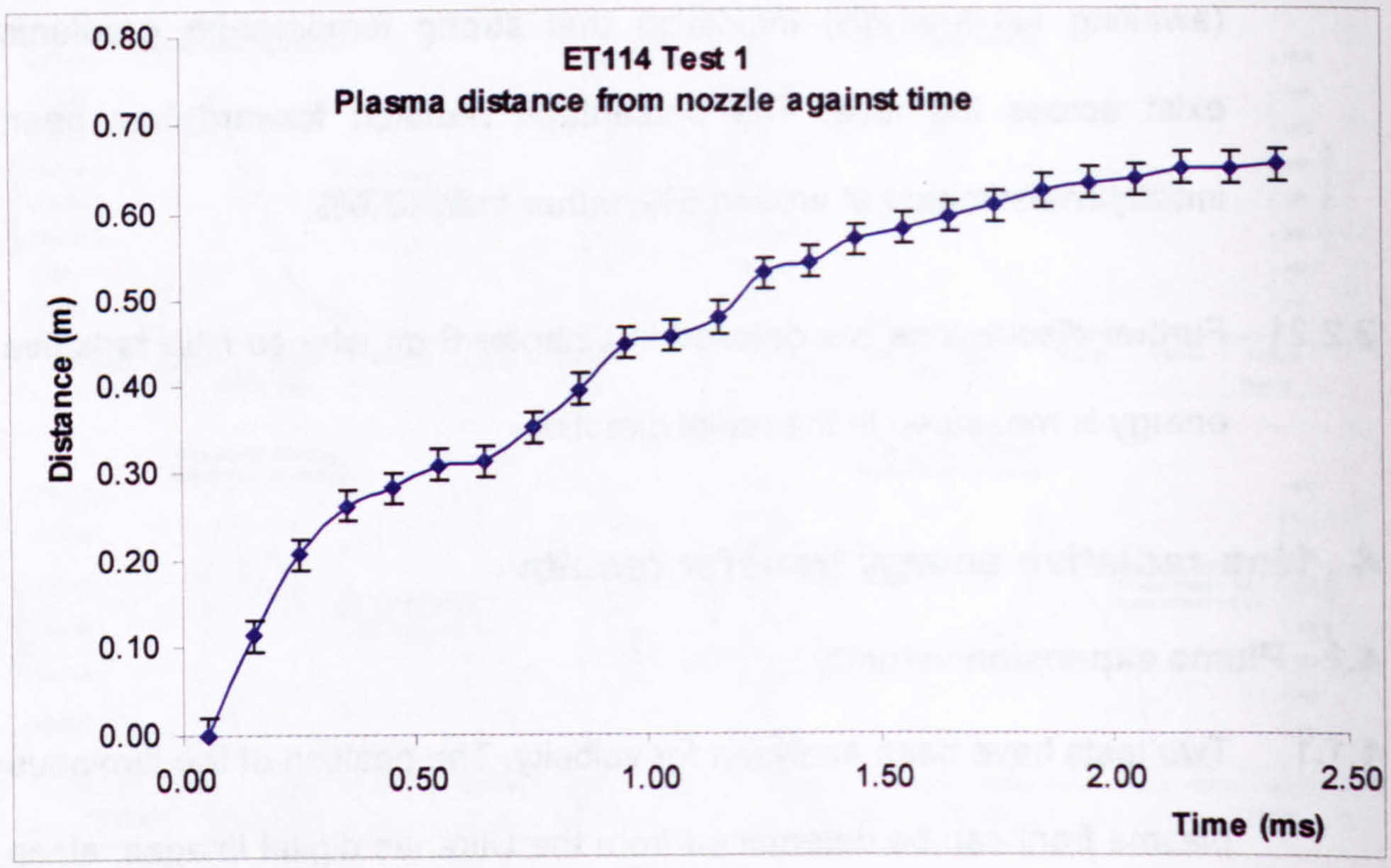

Figure 5.24 Distance-time profile of expanding plasma front

4.1.2 Figure 5.25 is the velocity-time curve for Tests 1 and 4; the measured nozzle velocity is initially around 1100 ms^{-1}. An attempt was made to model this in 1D using EDENET, although the codes have not been validated for plume expansion, by changing the cross-sectional area of the cells with position. The initial cone half-angle of expansion from the parallel nozzle used was determined from photographs as being 45°. Modelling was successful for angles up to around 10°, but unsuccessful at 20° due to the excessively small time-intervals (down to 9 ns by 0.15 ms into the discharge and decreasing at a rate of 0.17 femtoseconds per time step). The problem appeared to be associated with the acceleration of the plasma to supersonic velocity through a diverging nozzle. However, the result from the 10° modelling has been incorporated into Figure 5.25.

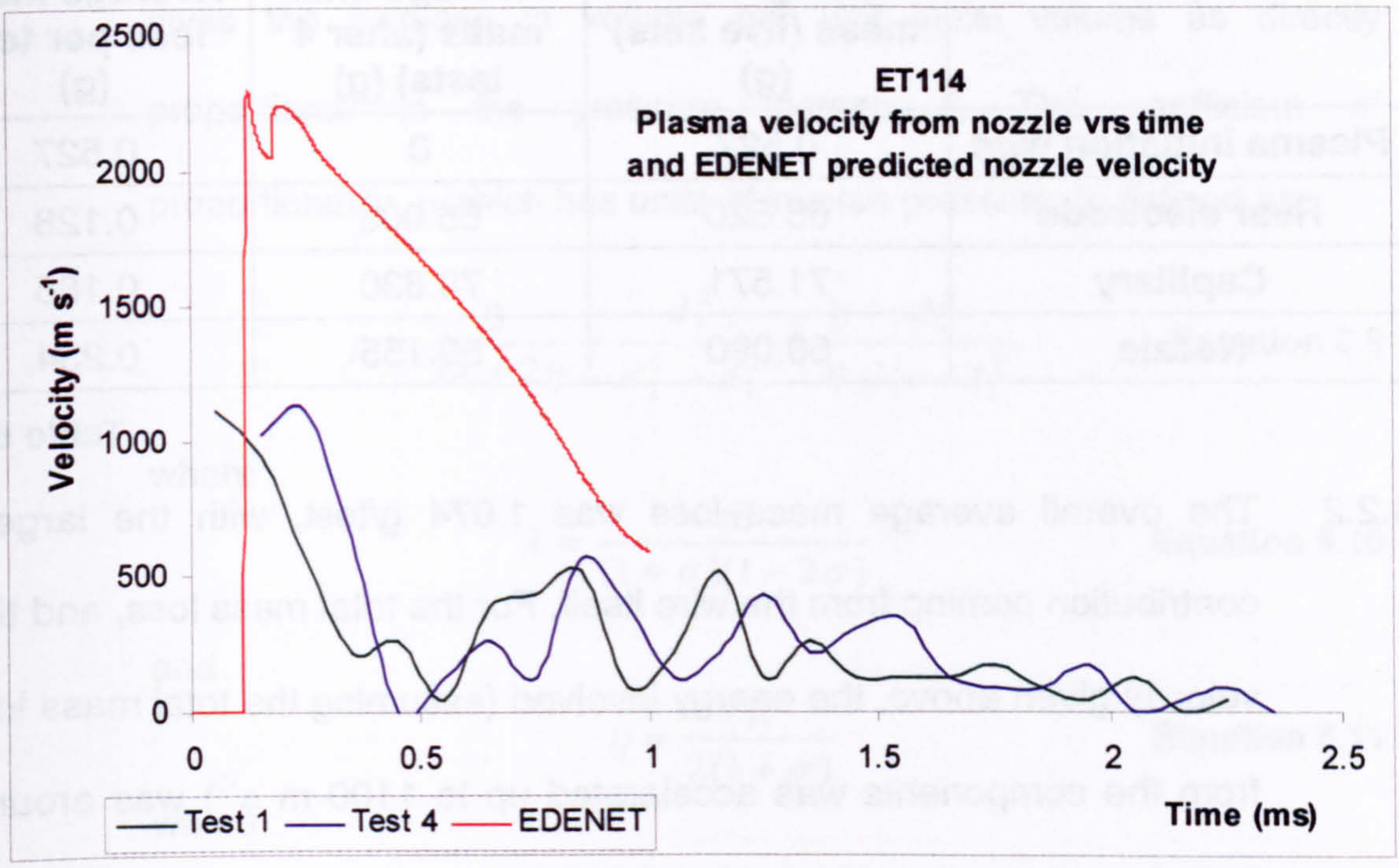

Figure 5.25 Velocity-time profile of expanding plasma front

4.1.3 Further modelling of the expansion velocity has been attempted with a different gas expansion code, PLUME (detailed in Chapter 6). Finally, although EDENET did not succeed in reproducing the result, its successor EDEN-IB will need to do so.

4.2 Component mass loss

4.2.1 Component mass loss was measured in a number of tests. Table 5.1 shows the component mass loss breakdown for five sets of CPG components, each of which had been used four times.

Component	Average initial mass (five sets) (g)	Average final mass (after 4 tests) (g)	Average mass loss per test (g)
Plasma initiation wire	0.527	0	0.527
Rear electrode	66.520	66.008	0.128
Capillary	71.571	70.830	0.185
Nozzle	60.090	59.155	0.234

Table 5.1

4.2.2 The overall average mass loss was 1.074 g/test, with the largest contribution coming from the wire itself. For the total mass loss, and the velocity given above, the energy involved (assuming the total mass lost from the components was accelerated up to 1100 m s^{-1}) was around 650 J, representing about 2% of the energy discharged. Figure 5.24 and Figure 5.25 suggest that this energy may have been transferred to the surroundings within the first 300 mm of travel.

4.3 Capillary compression

4.3.1 The internal pressure within the capillary peaks at around 50 MPa, as shown in Figure 5.12. This will cause the capillary liner to compress, as discussed in Chapter 3. The work done to compress the liner will cause energy loss to the system, energy which will be transferred mostly into heat within the high density polyethylene liner upon relaxation, with some energy causing permanent plastic deformation and some effecting a decrease in the rate of depressurisation of the plasma. It is assumed here that all energy used to compress the material is lost to the system. If a closed cylinder with internal and external diameters of d_1 and d_2 and initial volume, V_0 is pressurised, standard elasticity theory

gives the increase in volume per unit initial volume as directly proportional to the pressure increase, P. The coefficient of proportionality, ρ which has units of inverse pressure, is defined as:

$$\rho = \frac{3}{3\lambda + 2\eta} + \frac{d_1^2}{d_2^2 - d_1^2} + \frac{1}{\eta}\frac{d_2^2}{d_2^2 - d_1^2} \qquad \textbf{Equation 5.9}$$

where

$$\lambda = \frac{\sigma E}{(1+\sigma)(1-2\sigma)} \qquad \textbf{Equation 5.10}$$

and

$$\eta = \frac{E}{2(1+\sigma)} \qquad \textbf{Equation 5.11}$$

where

E is Young's modulus for the cylinder material and σ is Poisson's ratio.

The total work done in expansion per unit initial volume is:

$$E_* = \frac{1}{2}\rho p^2 \qquad \textbf{Equation 5.12}$$

and hence the total work done during the expansion process is:

$$\frac{1}{2}\rho p^2 V_o \qquad \textbf{Equation 5.13}$$

* See figure 5.12

4.3.2 Table 5.2 shows results for the high density polyethylene capillary used in this test; the filament-wound vessel is treated as being made from high density polyethylene. A maximum of around 200 J of energy is predicted to be used during the expansion process, which represents around 0.7% of the energy discharged. It is difficult to assess the errors associated with this figure due to the transient nature of the expansion

process, and the small energy transferred makes any further effort difficult to justify.

Young's modulus, E (Pa)	1.E+09
Poisson's ratio, σ	0.4
Pressure increase, p (Pa)*	6.E+07
Capillary inner diameter, d_1 (m)	1.40E-02
Capillary outer diameter, d_2 (m)	2.70E-02
Filament wound outer diameter, d_2 (m)	2.00E-01
Capillary length (m)	0.15
Capillary volume (m^3)	2.31E-05

λ (Pa)	1.4E+09	4.0E+08
η (Pa)	3.6E+08	3.6E+08
ρ (Pa^{-1})	4E-09	3E-09

Total work done on expansion (J)	
Capillary	168
Capillary and filament wound	117

[6]

* See figure 5.12

Table 5.2

4.4 Retained energy

4.4.1 The analysis for radiative heat transfer was halted at 3000 K. The analytical method used would be very unreliable at these low temperatures mainly due to the problem of defining the vapour (aerosol) edge, and thus its surface area. Some energy would be retained by the material in the form of latent and specific heat after the analysis was halted.

4.4.2 Table 5.3 shows the energy breakdown involved in heating the material (assumed to be 1 g copper) and hence energy retained by the uncondensed vapour.

Thermodynamic properties of condensed copper		
Temperature, θ (K)		$\Delta\theta$
Room	293	
Melting point	1356	1063
Boiling point	2840	1484
Specific heat capacities (J kg^{-1} K^{-1})		
Solid, c_s	385	
Liquid, c_l	500	
Specific latent heats (J kg^{-1})		
Melt, L_m	205000	
Boil, L_v	4796000	
Mass of copper evaporated (kg)	0.001	**Percentage of energy discharged**
Energy required to heat to melt (J)	409	1.36
Energy required to melt (J)	205	0.68
Energy required to heat to boil (J)	742	2.47
Energy required to boil (J)	4796	16
Total energy required (J)	**6152**	**20.5**

Table 5.3

4.4.3 The total energy involved here is 6.2 kJ, representing 20.6% of the discharged. There is a small error involved due to the presence of iron, carbon and hydrogen. The iron is more likely to be melted than vaporised. Examination of the nozzle clearly shows grooves, and video footage of the discharge indicates a shower of slowly moving sparks.

These sparks have been interpreted as molten iron. Other species within the plasma are dealt with fully in Chapter 6.

5 Energy Budget

5.1 Results

5.1.1 An estimate of the CPG energy budget can now be attempted for this particular 30 kJ plasma discharge. Figure 5.26 illustrates the energy budget breakdown. The overall plasma energy transferred as radiation is lower than shown, as the energy radiated forward is known to be an overestimation (a more thorough analysis has since been performed showing this figure to be in the region of 5%). The energy shown in green will be transferred to the surroundings over a long time-scale with respect to the duration of the discharge.

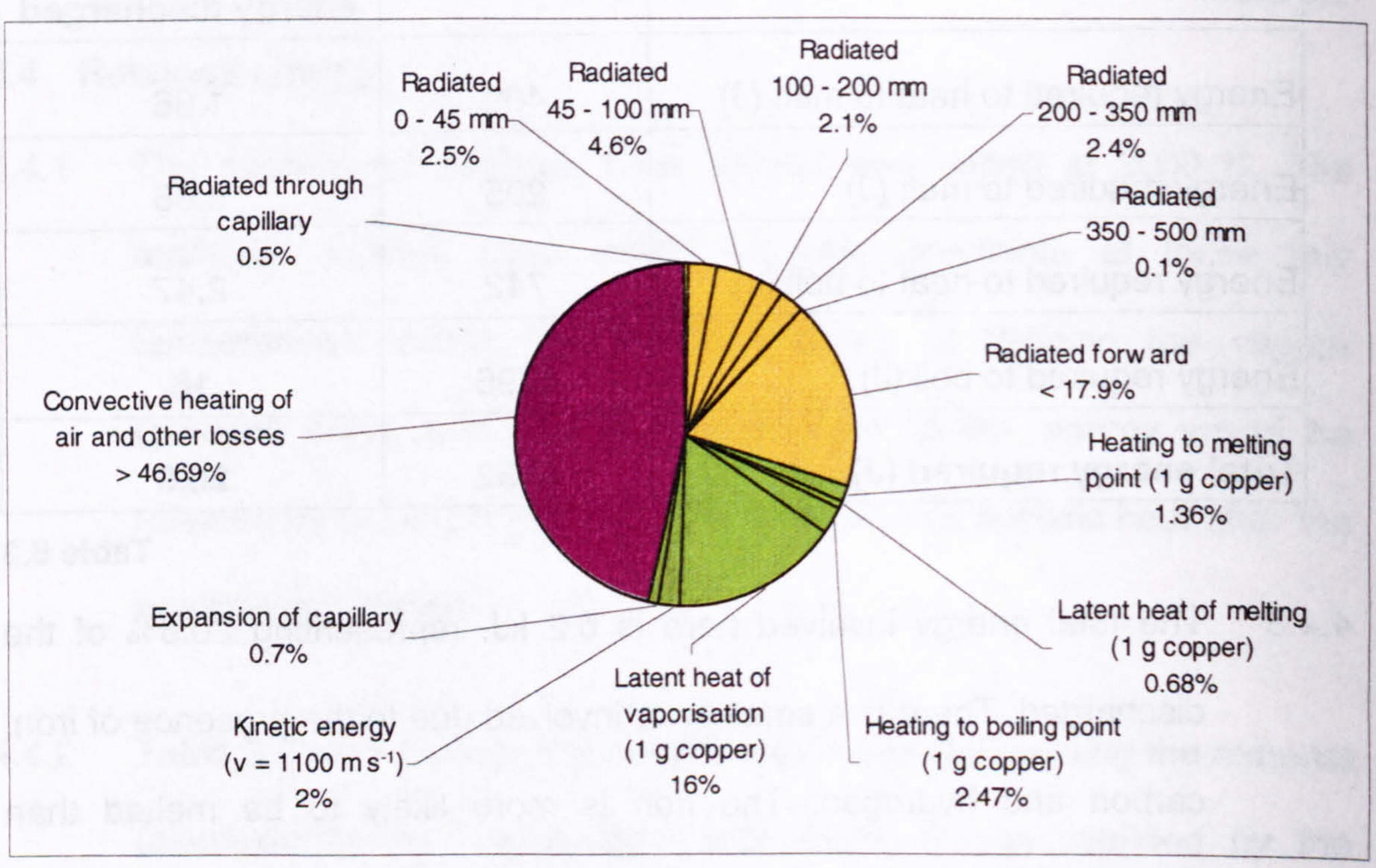

Figure 5.26 CPG experimental energy budget summary

5.2 Remaining energy

5.2.1 The 47% or so of energy remaining has been assigned to convective heating of the air as it mixes with the plasma. Inspection of images such as those in Figure 5.10, which can be merged into short video sequences with Image Pro-Plus version 4, shows the lobes to be rolling backwards as the centre of the plasma thrusts forward. Air will become entrained in the turbulence and heated. The convective heating of the air has since been measured and is discussed in Chapter 6. Exothermic oxidation reactions which occur after this analysis has been halted will also be discussed.

6 Summary of Chapter 5

6.1.1 This Chapter has detailed work conducted by the Author aimed at obtaining an estimate for the energy partition of a typical capillary plasma generator. Arguments for the errors and validity of assumptions associated with this estimation have been presented. This work is wholly original, with no previous experimental estimation of its kind known to the Author. The work can be used to validate and improve EDENET, and its anticipated successor EDEN-IB.

6.1.2 The main finding from this study has been the small fraction of energy radiated from both the capillary plasma (to the translucent capillary liner) and from the expanding plume itself. Arguments to explain this are presented in Chapter 6. Chapters 7 – 9 go on to discuss the

implications for energy transfer to the propellant, along with more experimental evidence supporting this initial energy budget.

---

1 M. J. Taylor, "ET114 – Estimation of Radiant Energy from a Plasma Jet", DERA internal document WSS/WS4/58-ETL/ERD008, Experiment No. ET114, February 2000

2 M. J. Taylor, "Measurement of the Properties of Plasma from ETC Capillary Plasma Generators", IEEE Transactions on Magnetics, Vol. 37, 1, January 2001

3 B Augsburger et al, "DRA 500 kJ Multi-module Capacity Bank", IEEE Transactions on Magnetics, Vol. 31, 1, January 1995

4 Newport Ltd. 20 D C200 ER.1 100 mm focal length, 50.8 mm diameter surface coated mirror

5 J. M. Kohel, L. K. Su, N. T. Clemens and P. L. Varghese, "Emission Spectroscopic Measurements and Analysis of a Pulsed Plasma Jet", IEEE Transactions on Magnetics, Vol. 35, 1, January 1999

6 Mechanical data from Goodfellow, Cambridge Science Park, England

Chapter 6 – CPG plasma properties

1 Introduction

1.1.1 This Chapter is concerned with the plasma that forms within, and vents as a plume from, the capillary. The energy partition was discussed in detail in Chapter 5, and this Chapter looks at some of the possible explanations for the main findings, as well as describing other aspects of the plume properties.

1.1.2 The main purpose of this work is code development and validation for EDENET and its successor, EDEN-IB (see Chapter 3). As such, work is focussed towards this end. All work reported within this Chapter is that of the Author, unless otherwise stated.

2 Initial plasma

2.1 Formation

2.1.1 As the plasma initiation wire is heated by the electrical discharge, it vaporises preferentially at the electrodes (see Chapter 4) due to contact resistance and possibly other magnetic boundary effects. Around 25 mm of wire material within the CPG nozzle design is used for this experiment, and this is thought to vaporise before the main wire length within the capillary. The plasma within the nozzle will be subject to Lorentz force acceleration out of the nozzle. An initial plasma plume that precedes the main plume was identified when photographic investigations of the nozzle region at the time of the voltage spike were made [1]. Figure 6.1 shows this initial plasma. It detaches from the nozzle (Figure 6.1 images 5 – 11) and, being isolated from the

electrical discharge cools due to expansion and convective heat transfer to the surrounding air. This small mass (around 0.1 g) of copper and undetermined mass of nozzle material (steel) has a velocity of around 500 ms^{-1} and brightness temperature, which peaks at around 11 000 K.

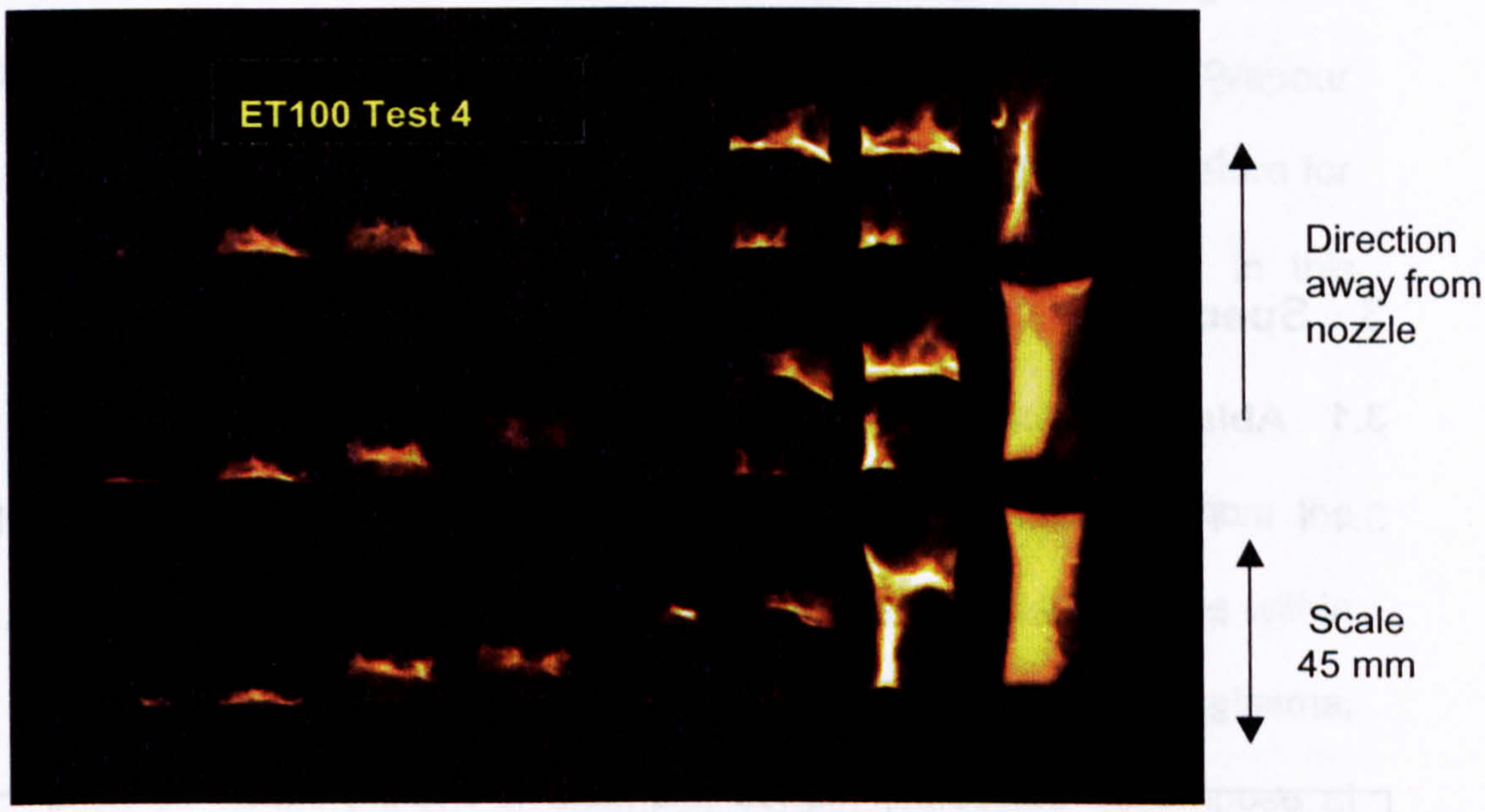

Image	**1**	**6**	**7**	**12**	**13**	**18**	**19**	**24**
Time (μs)	83.14	98.64	101.74	117.24	122.34	147.84	152.94	498.44
Image	**2**	**5**	**8**	**11**	**14**	**17**	**20**	**23**
Time (μs)	86.24	95.54	104.84	114.14	127.44	142.64	158.04	248.34
Image	**3**	**4**	**9**	**10**	**15**	**16**	**21**	**22**
Time (μs)	89.34	92.44	107.94	111.04	132.54	137.64	168.14	198.24

Figure 6.1 Formation of initial plasma plume

2.1.2 In some tests, including this one, the initial plasma cools entirely (Figure 6.1 images 12 – 14) before being influenced by the main plasma jet (Figure 6.1 image 15 - 21). This appears to re-heat the

vapour through some unknown energy transfer mechanism – possibly magnetic in a similar manner to solar prominence heating, or through compression (image 15 is concurrent with the arrival of a pressure wave at the nozzle, as measured by pressure transducers within the capillary). The initial plasma is eventually engulfed by the main plasma jet (Figure 6.1 image 21) whose velocity is in excess of 1000 ms^{-1}. In other similar tests, the initial plasma was seen to be engulfed before it had entirely cooled.

3 Species

3.1 Ablated species

3.1.1 The atomic constituents in a typical CPG plasma have been calculated from measured component mass losses (see Chapter 5, Table 5.1): a summary of the constituents appears in Table 6.1.

Plasma constituent	Number of atoms in plasma	Percentage of total
Hydrogen	15.9E+21	48.9
Carbon	7.96E+21	24.4
Copper	6.17E+21	18.9
Iron	2.52E+21	7.8

Table 6.1

3.1.2 The capillary liner material contributes the greatest number of particles to the plasma, in contrast with mass. The mass is shown dominated by the initiator wire for this particular experimental set-up. Ionisation potentials for these materials are 13.6 eV for hydrogen; 11.3 eV for

carbon; 7.7 eV for copper and 7.9 eV for iron. The ionisation of the hydrogen and carbon would be minimal at 8000 K. (1 eV equates to a temperature of around 11000 K). At 8000 K, 16 % of copper but only 0.2 % of hydrogen atoms would be singularly ionised [2]. However, the material will be available for oxidation reactions, allowing energy to be released as the plasma mixes with the air. This provides a significant amount of extra energy to the system, allowing the expanded (vapour and aerosol) plume to maintain a higher than expected temperature for tens of milliseconds. This issue is explored in detail later in this Chapter.

3.1.3 The main constituents of the plasma plume will be formed from the available constituents of the CPG and air. Evidence of species within the plasma spectra gives clues as to other properties of the plasma, such as temperature. For example, certain molecules decompose at certain temperatures and the presence of such molecules indicates the maximum temperature of the plasma at that location. Much more work could be conducted with species determination, but it is debatable as to applicability to the ETC gun project of spending more time on this aspect.

3.2 Species (Initial plasma)

3.2.1 From emission spectroscopic investigations, the composition of the initial plasma would appear to be mainly metallic copper, copper II oxide (CuO) and iron II oxide (FeO). Figure 6.2 shows the spectrum

from ET114 Test 91 looking at the oncoming initial plasma plume and shows clear evidence of these species. (Evidence for ionised copper is unconvincing as strong Cu^+ lines are either missing completely or coincident with the metal oxide lines.)

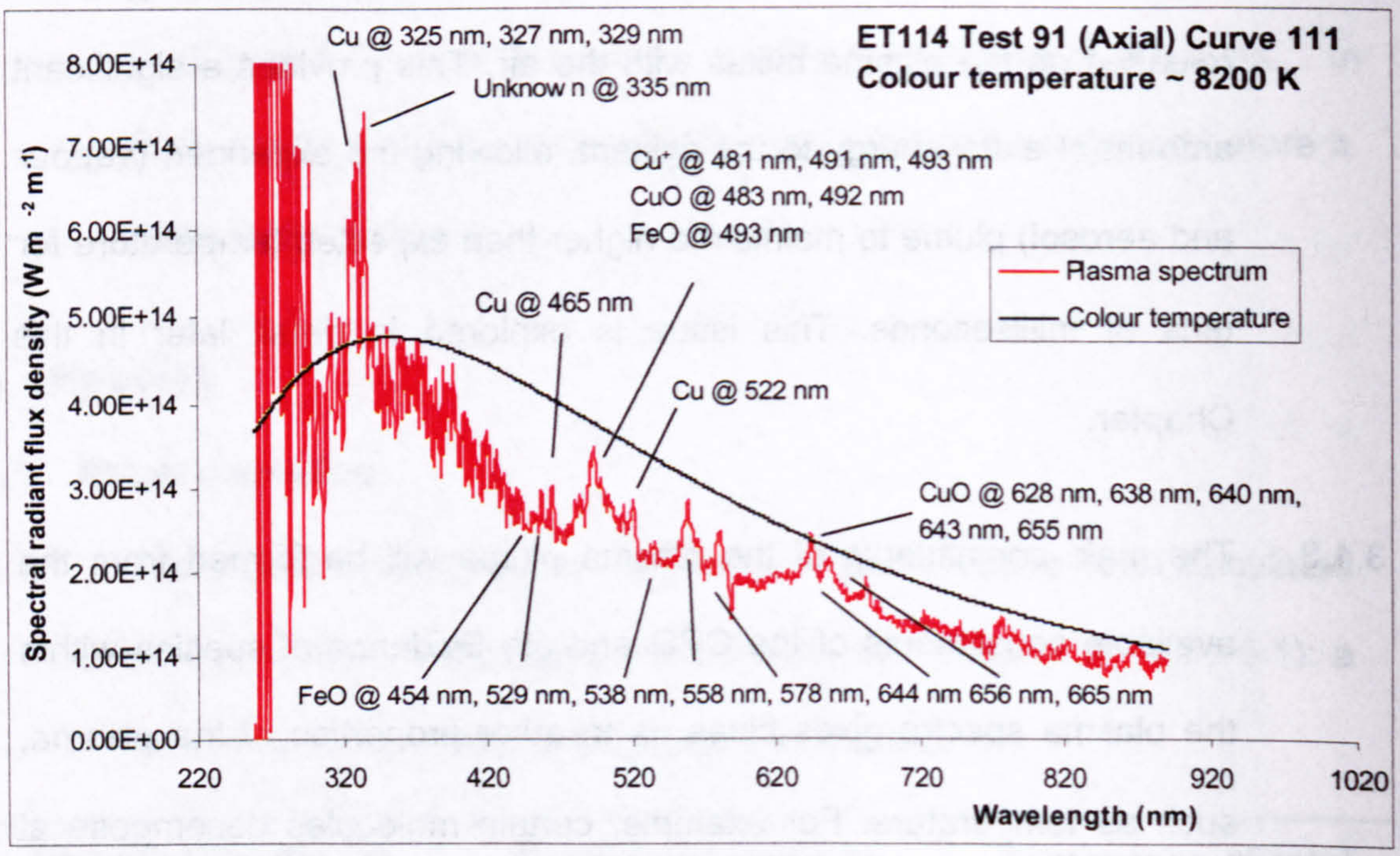

Figure 6.2 Axial spectrum from initial plasma plume showing various species present

3.2.2 The temperature has been determined from the spectrum (see Appendix A) as 8200 K. This is thought to be too hot for the oxides to exist: it is believed that cooler line emitters (a rarefied metallic and metallic oxide mix) are superimposed upon a hotter continuum emitter of neutral and ionised metals as would be expected if the front edge of this plasma were cool. The copper at 325 nm – 329 nm and unknown species at 335 nm would appear to be at around 9000 K, hotter than the main plasma species themselves. The reason for this is unknown. It

seems, however, that local thermal equilibrium conditions do not exist in this initial plasma plume.

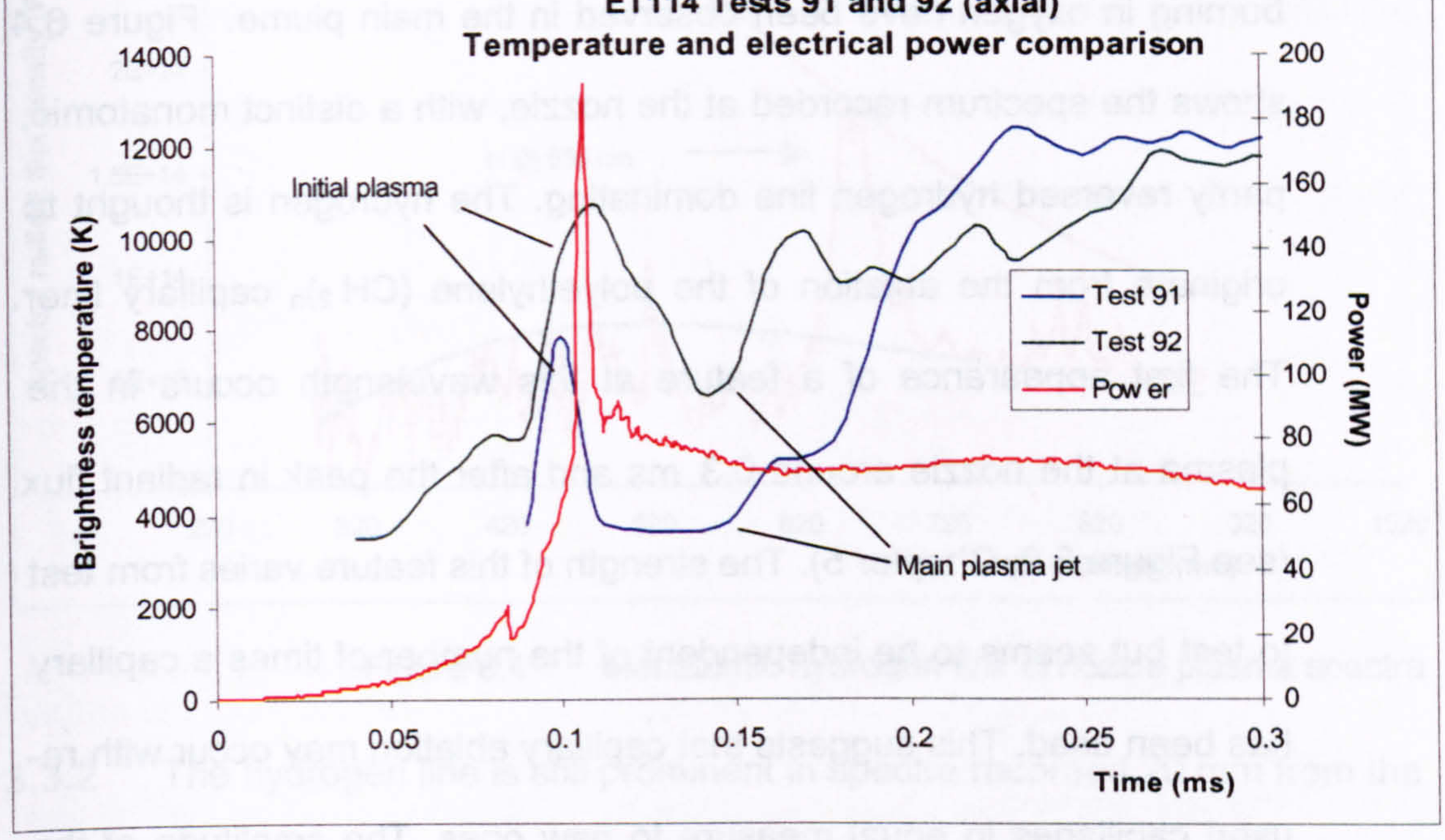

Figure 6.3 Comparison between input electrical power and brightness temperature for the first part of the discharge

3.2.3 Figure 6.3 compares two tests that recorded the plasma from along the axis of the expanding plume. The brightness temperatures are shown with respect to the electrical power discharged within the capillary. In both tests the initial plasma is a peak in the temperature, with Test 91 seemingly cooling in a similar way to the plasma shown in Figure 6.1, whilst Test 92 shows the initial plasma being engulfed by the main plasma jet before it has cooled to condensation temperature (around 3000 K).

3.3 Species (Main plume)

3.3.1 Exothermic reactions and exotic species have been observed in the main plasma discharge. The spectra of atomic hydrogen and hydrogen burning in oxygen have been observed in the main plume. Figure 6.4 shows the spectrum recorded at the nozzle, with a distinct monatomic, partly reversed hydrogen line dominating. The hydrogen is thought to originate from the ablation of the polyethylene $(CH_2)_n$ capillary liner. The first appearance of a feature at this wavelength occurs in the plasma at the nozzle around 0.3 ms and after the peak in radiant flux (see Figure 5.9, Chapter 5). The strength of this feature varies from test to test but seems to be independent of the number of times a capillary has been used. This suggests that capillary ablation may occur with re-used capillaries in equal measure to new ones. The amplitude of the line is often far greater than the plasma brightness temperature, suggesting that the hydrogen is hotter than other species within the plasma. The example in Figure 6.4 gives the hydrogen to be 2000 K hotter than the average plume temperature. It is possible that the number of collisions the hydrogen has incurred, with a small collisional cross-section, has not enabled it to attain local thermal equilibrium.

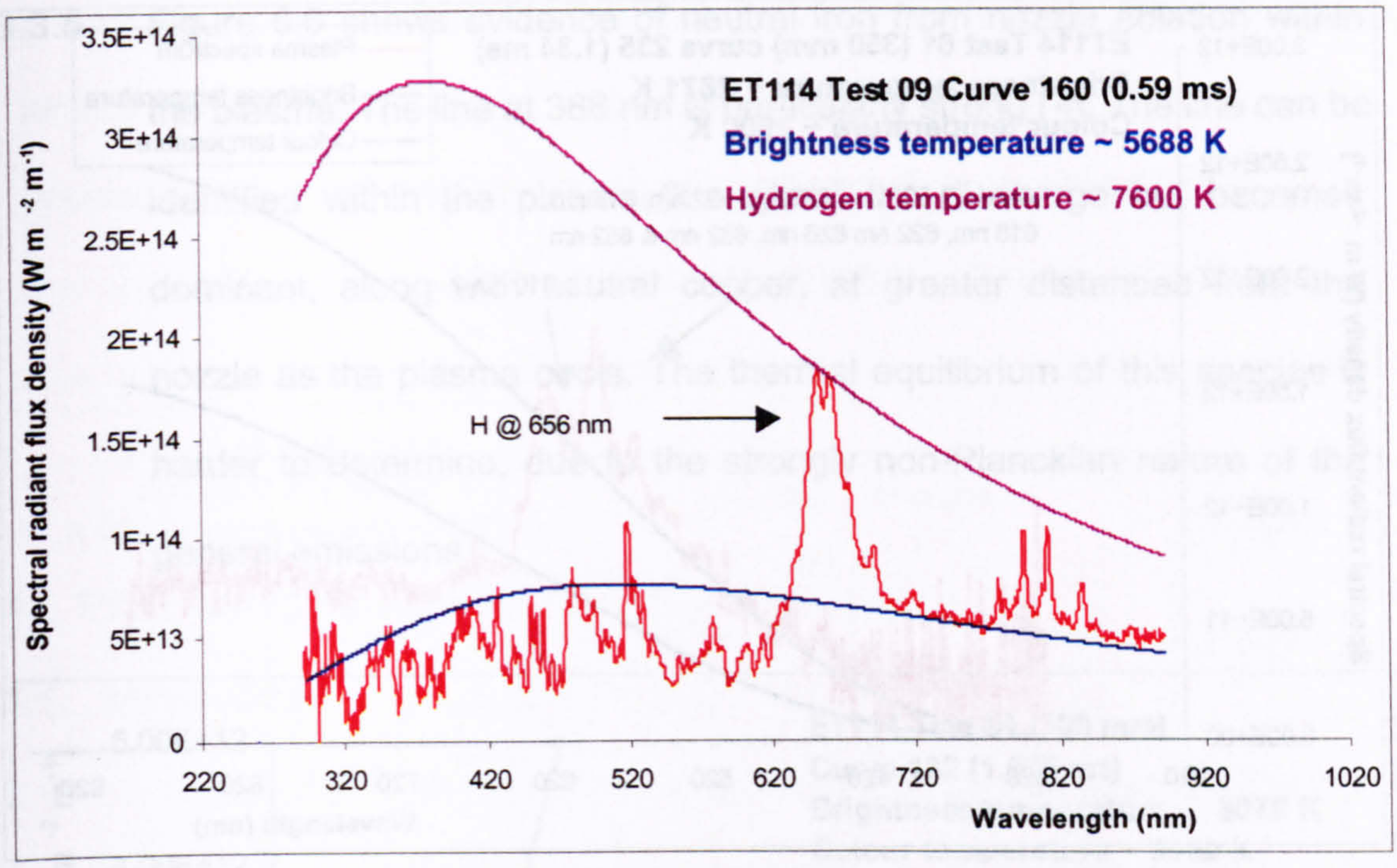

Figure 6.4 Monatomic hydrogen line in nozzle plasma spectra

3.3.2 The hydrogen line is still prominent in spectra recorded 20 mm from the nozzle, but no longer dominant. The appearance of the hydrogen line is concurrent with its appearance at the nozzle, although much cooled at a colour temperature similar to those of the other species. This could indicate that the species are more or less in thermal equilibrium at 20 mm from the nozzle. At other distances the hydr ogen line continues to be prominent for most of the duration of the discharge.

3.3.3 Another interesting feature is that of water formation, superimposed upon the blackbody profile as the plasma cools after the end of the electrical discharge (see Figure 6.5). This emitting species seems to be at a temperature 100 K or so above that of the surroundings.

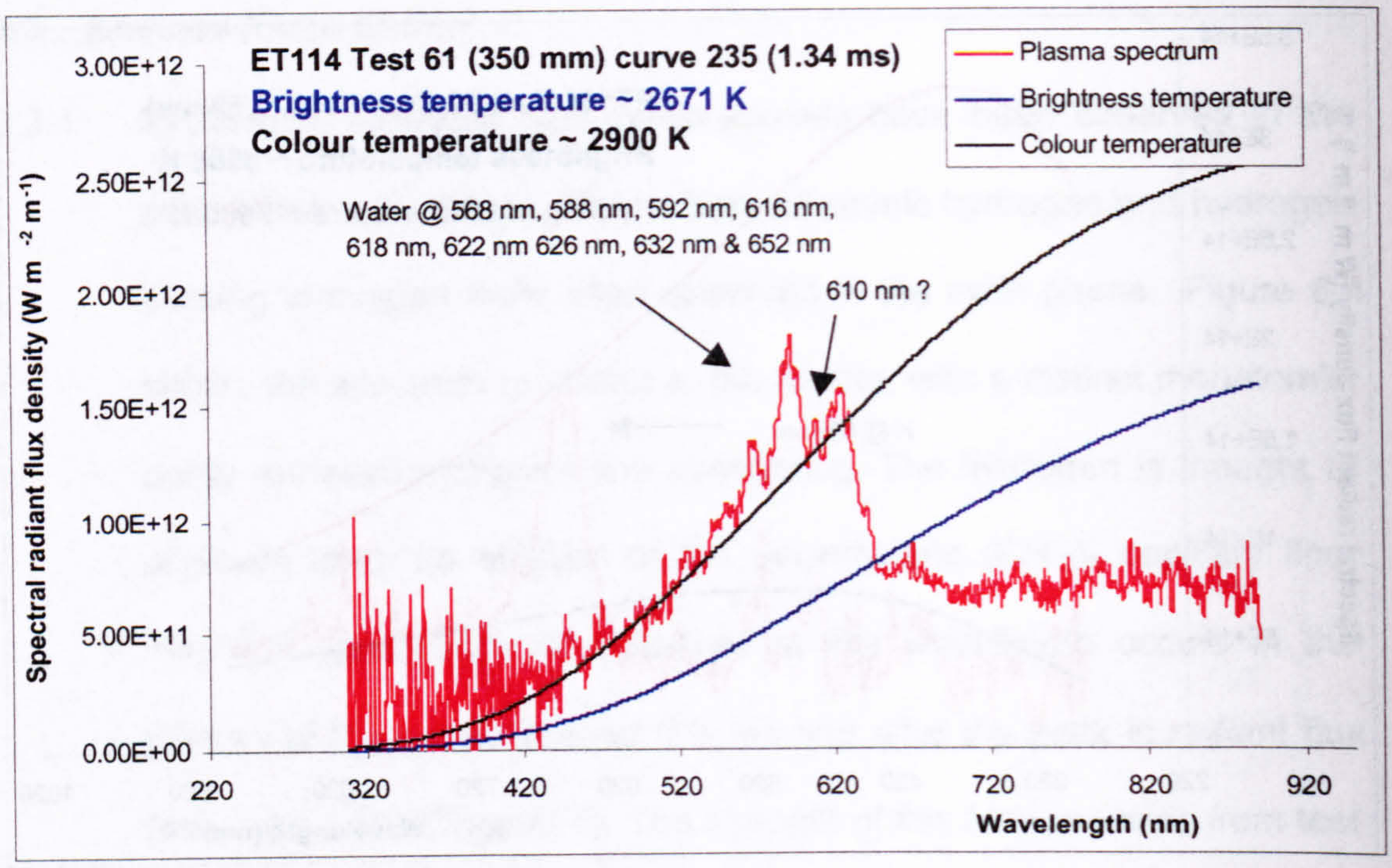

Figure 6.5 Vibration-rotation band structure of water from plasma spectrum at 350 mm from the nozzle

3.3.4 The specific peaks are known (Pearse & Gaydon [3]) to be part of the vibration-rotation band structure of water – a weak structure given best by a flame of oxygen burning in hydrogen. The source of this hydrogen is probably ablated capillary products associated with the strong hydrogen line (Figure 6.4) which, in the presence of oxygen from mixing with air, is now exothermically reacting – hence the higher temperature. There are still several peaks of unknown origin, notably the peak at 610 nm. It is possible that this is also water, as Pearse & Gaydon proclaim this band structure as complex and not very definite: certainly the band heads do come and go from one spectrum to the next. The cause of the strong, broad absorption at longer wavelengths is unknown, but again may be associated with the formation of water.

3.3.5 Figure 6.6 shows evidence of neutral iron from nozzle ablation within the plasma. The line at 386 nm is particularly strong [4]. The line can be identified within the plasma throughout the discharge but becomes dominant, along with neutral copper, at greater distances from the nozzle as the plasma cools. The thermal equilibrium of this species is harder to determine, due to the strongly non-Planckian nature of the general emissions.

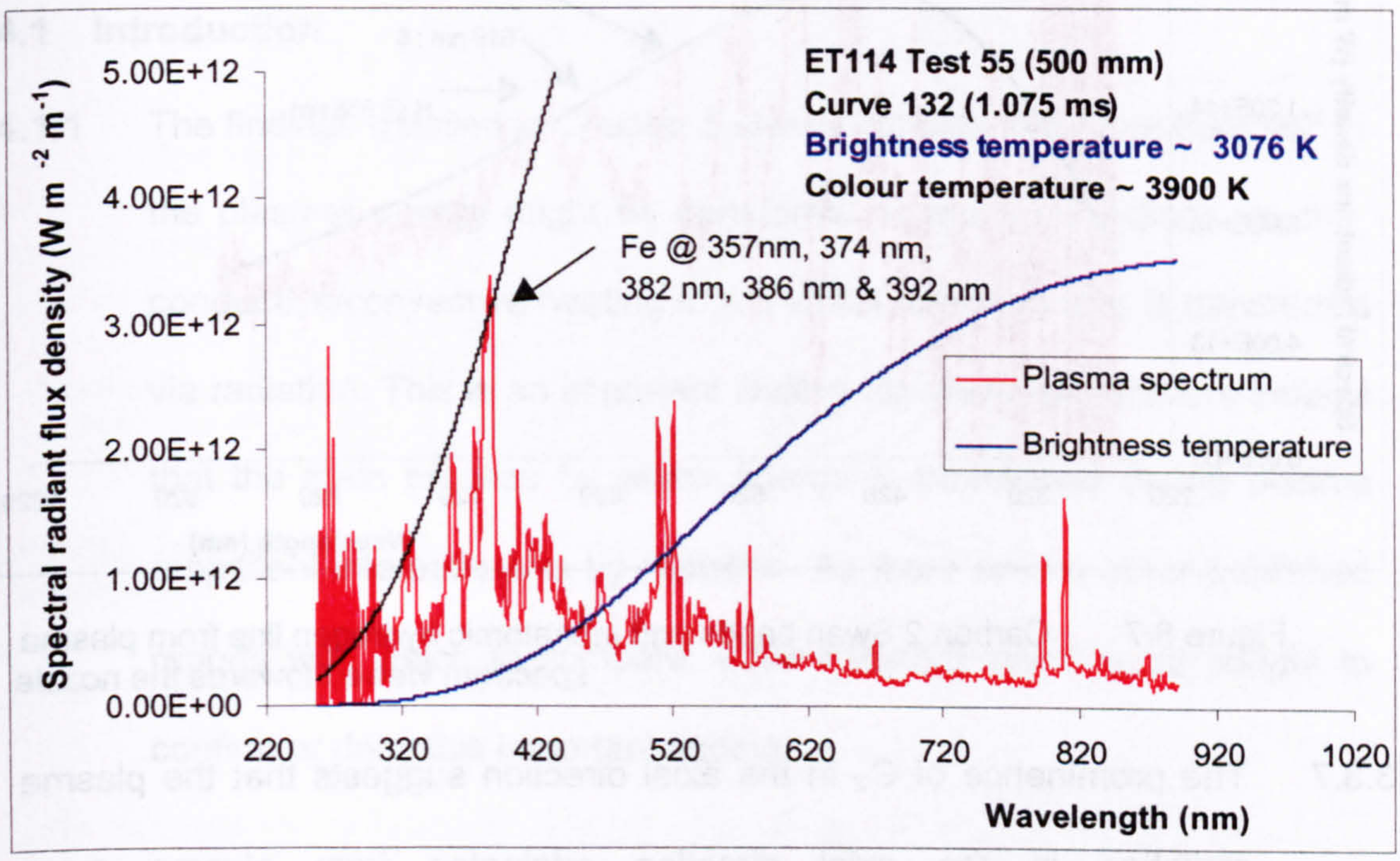

Figure 6.6 Iron lines from plasma spectrum at 500 mm from the nozzle

3.3.6 One interesting species observed in spectra emitted from the plasma front in the axial direction (and weakly at 20 mm from the nozzle in the radial direction) is diatomic carbon (C_2). This unstable and highly reactive molecule is regularly observed within comet heads [5] and by American ETC spectroscopists [6]. Figure 6.7 shows the C_2 spectral bands known as the Swan bands together with the presence of atomic

hydrogen in the axial plasma spectrum. The wavelengths at which the Swan band structure occurs are shown, as are the reported number of band heads; each band head can be clearly identified in the spectrum. (The band heads are 'shaded' towards the red).

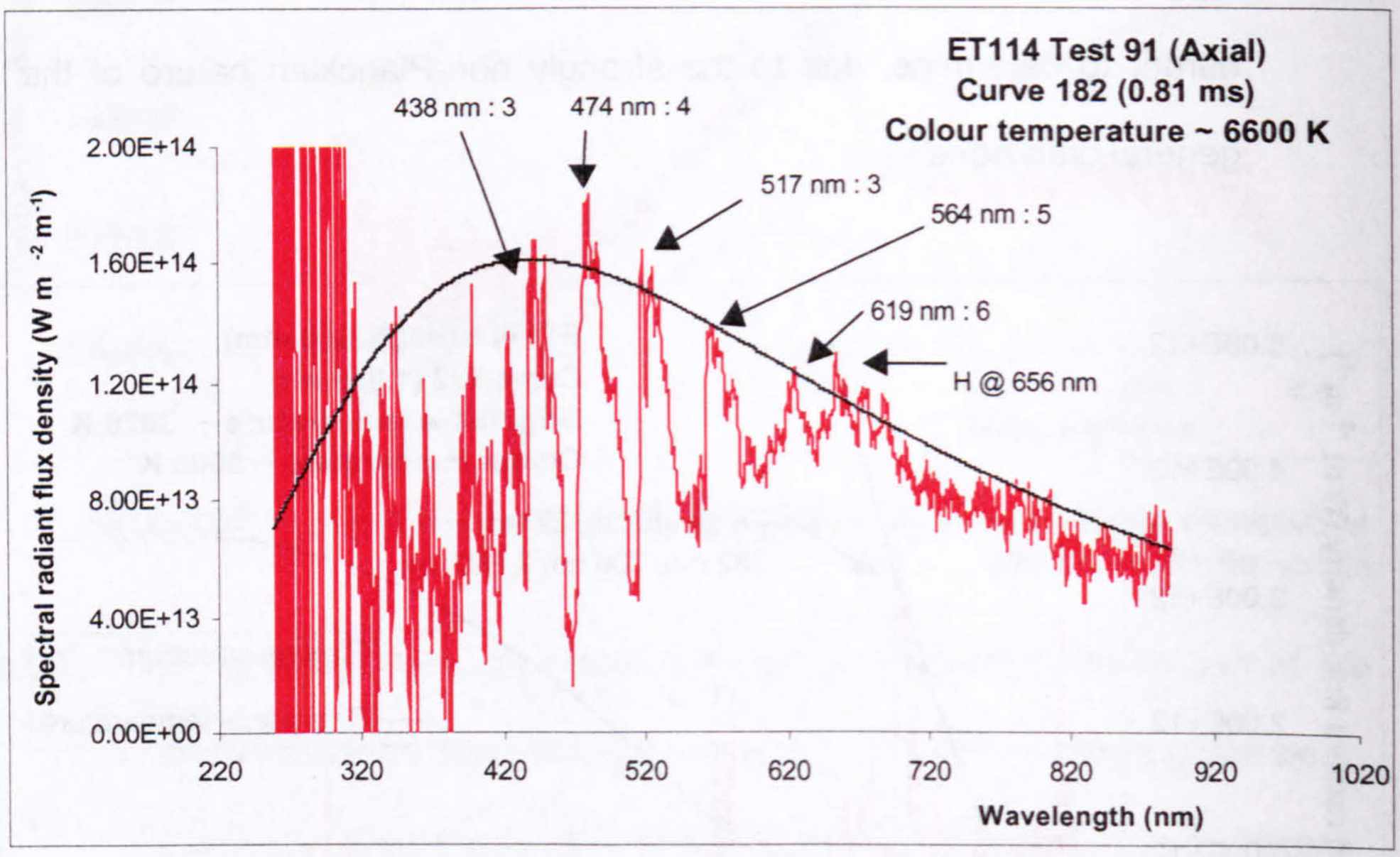

Figure 6.7 Carbon 2 Swan bands and monatomic hydrogen line from plasma spectrum viewed towards the nozzle

3.3.7 The prominence of C_2 in the axial direction suggests that the plasma radiation in the axial direction originates from plasma more representative of that from the core, while the plasma seen from the sides (not exhibiting C_2 characteristics) is from a cooler, optically thick boundary layer obscuring the core plasma. The core plasma from the capillary is seen to be pushing its way through the plasma plume until it reaches the quiescent air in front of the plume. It then decelerates quickly (possibly with the liberation of kinetic energy converting into

thermal energy) and is subsequently pushed to one side from the following core plasma. This would explain a number of observations, including the large fraction of energy transferred to the air through turbulence, the hot plasma with very reactive species from the capillary line at the plume leading edge and the much cooler plasma with no strong indication of such reactive species at the sides of the plume.

4 Post-analysis vapour cloud

4.1 Introduction

4.1.1 The findings detailed in Chapter 5 clearly indicate that more than half of the plasmas energy might be transferred to the surroundings via the conductive/convective heating of air, whilst relatively little is transferred via radiation. This is an important finding, as many researchers believe that the main process by which energy is transferred during plasma propellant interactions is by radiation. As there are no other published reports with which to compare, other methods need to be sought to confirm or deny this important finding.

4.1.2 Around 30 kJ of electrical energy are provided to the CPG as the capacitors discharge. This would correspond to the release of up to 15 kJ to the air. The heating effect on the air is used here in an attempt to verify this figure. An experiment was designed to record the temperature of the air and plasma species mixture, and together with photographs of the plume, an estimation made of the thermal energy contained within the cooled plume.

4.1.3 Figure 6.8 shows an Ultranac image montage of a hot plasma plume emitted from an experimental plasma generator design, along with the cooling vapour cloud. The montage was produced by the Author from two similar tests, but with different exposure times. It clearly shows how an expanded cloud develops, and it was the energy associated with such clouds that the Author has attempted to estimate.

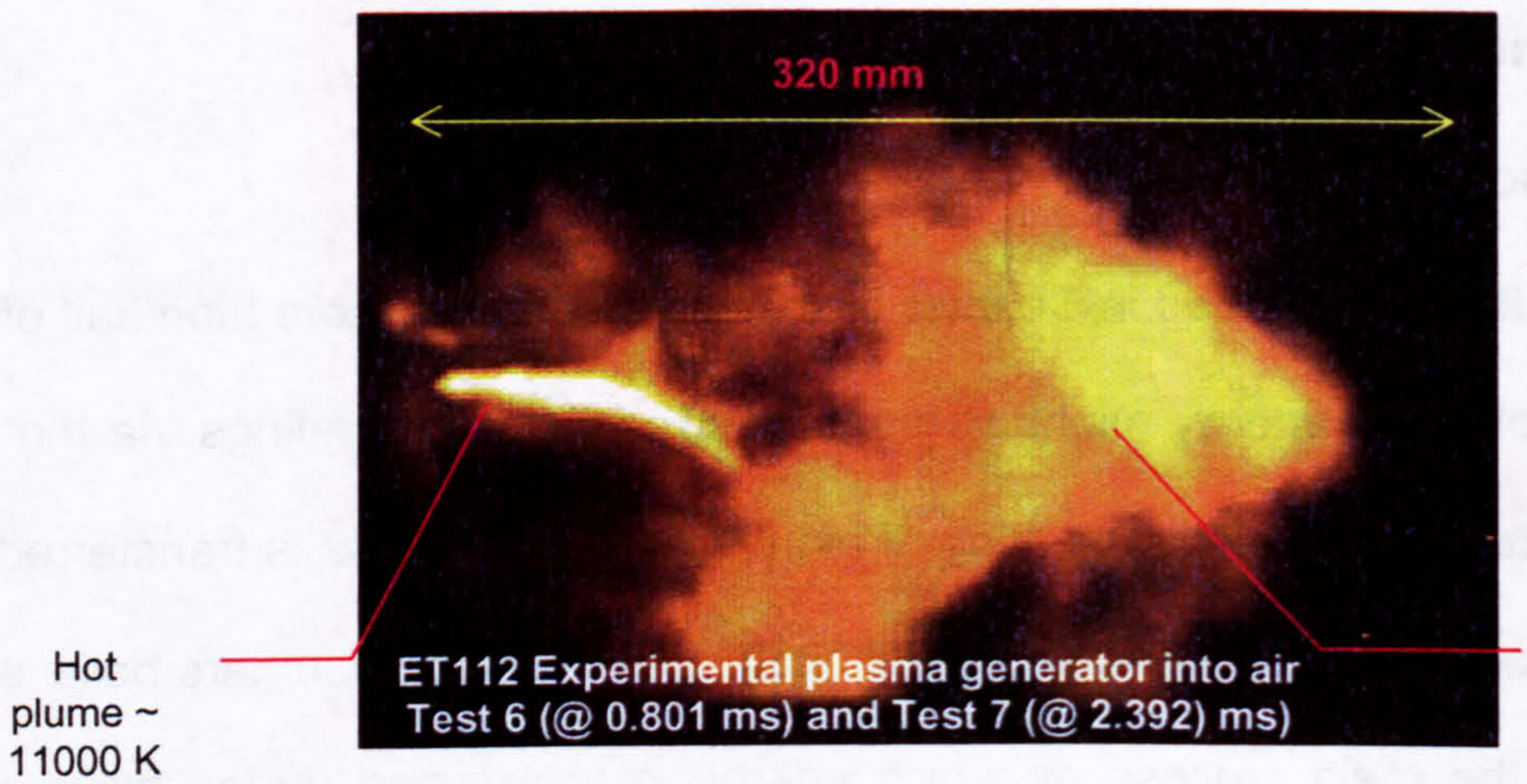

Figure 6.8 Hot plume and cooling vapour cloud from an experimental plasma generator

4.2 Experimental set-up to estimate the percentage energy transferred to air

4.2.1 Once the electrical discharge has ended, the plasma plume cools and can be seen in standard video frames to drift slowly away from the plasma generator in a cloud-like manner. The cloud remains radiant for several tens of milliseconds. The CPG components and electrical discharge parameters used to study this cloud were as in the energy budget and related work described in Chapter 5.

4.2.2 It was planned to measure the cloud temperature with an infrared thermal imaging digital camera. The camera would produce a time-resolved 2D spatial map of cloud temperature. Knowing the constituents of the cloud, the specific heats could be used to estimate the thermal energy of the cloud. However, due to concerns over the harsh environment that the thermal imaging camera would experience, the owner of the equipment declined to allow its use for the experiment. Hence, it was decided to try calibrating the Ultranac camera as a temperature measuring device and the methodology used is given in Appendix B. Essentially, the spectrograph was used to calibrate the digital photographs for brightness temperature, and since the cloud radiated as a Planckian emitter, the thermal temperature of the cloud was assumed to be equal to its brightness temperature.

4.3 Results

4.3.1 Much effort was expended on the positioning and correct exposure time of the Ultranac and spectrograph. ET133 Test 15 [7] gave the best result out of 16 tests, and was chosen for analysis. Figure 6.9 shows a false colour image acquired from the Ultranac camera for 9.6 ms. The concave mirror used to collimate the collection area for the spectrograph can be seen silhouetted in the foreground. The red arrow shows the spectrograph view location and the red line shows where the spectra would have been acquired as the cloud drifted past. The plasma generator is on the right. The drift velocity of the cloud was

difficult to determine from these images, because the leading edge was cooling faster than the cloud was moving.

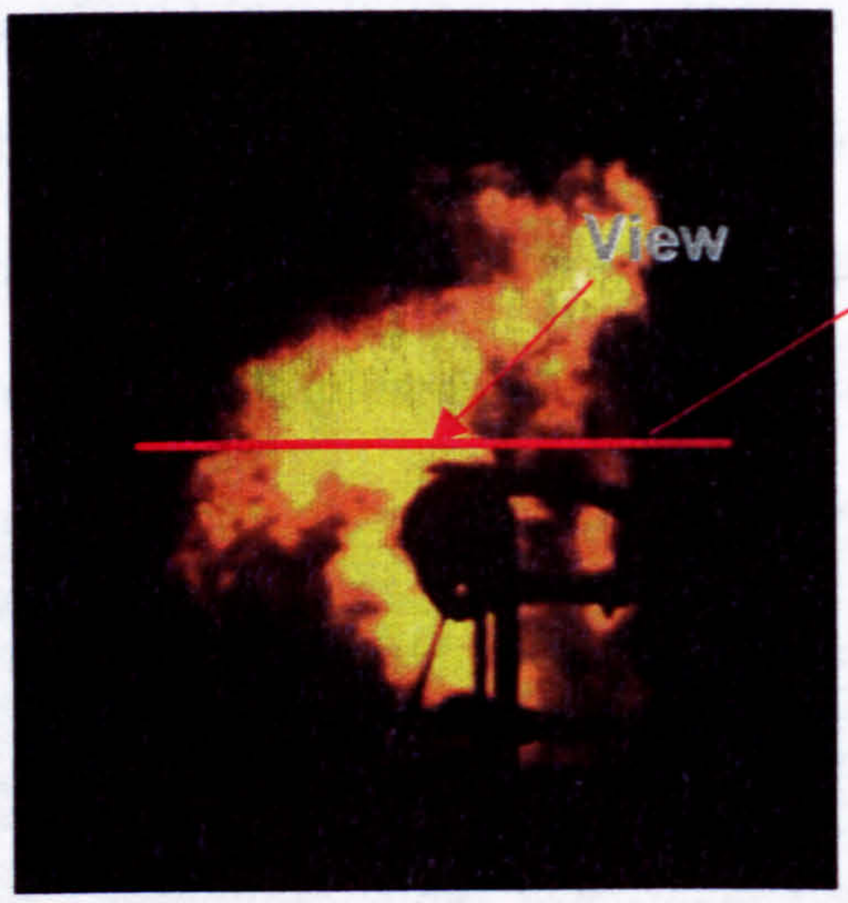

Figure 6.9 Image of vapour cloud for ET133 Test 15 @ 9.6 ms

4.3.2 Figure 6.10 shows the thermal temperature analysis results from the spectrograph. The horizontal dashed line represents the boiling point for copper. The vertical dashed lines represent the time frame over which Ultranac images were obtained for this test. The spectra below were taken at the times indicated. The error bars correspond to the establishment of thermal temperature from the spectrum colour and brightness temperatures (see Appendix A).

4.3.3 The earliest temperature corresponds to the plasma seen on the left-hand edge of Figure 6.9, although at a time earlier than this image was captured. It is apparent that at the hottest point in the centre of the cloud, exothermic reactions of hydrogen burning in oxygen (producing water) were occurring. The conspicuous characteristic emission feature centred on 600 nm provides evidence for this. The cloud temperature

peaks where this is occurring, at a little above the boiling point of copper (2840 K), but most of the cloud appears to be at a temperature consistent with liquid copper (i.e. an aerosol of copper).

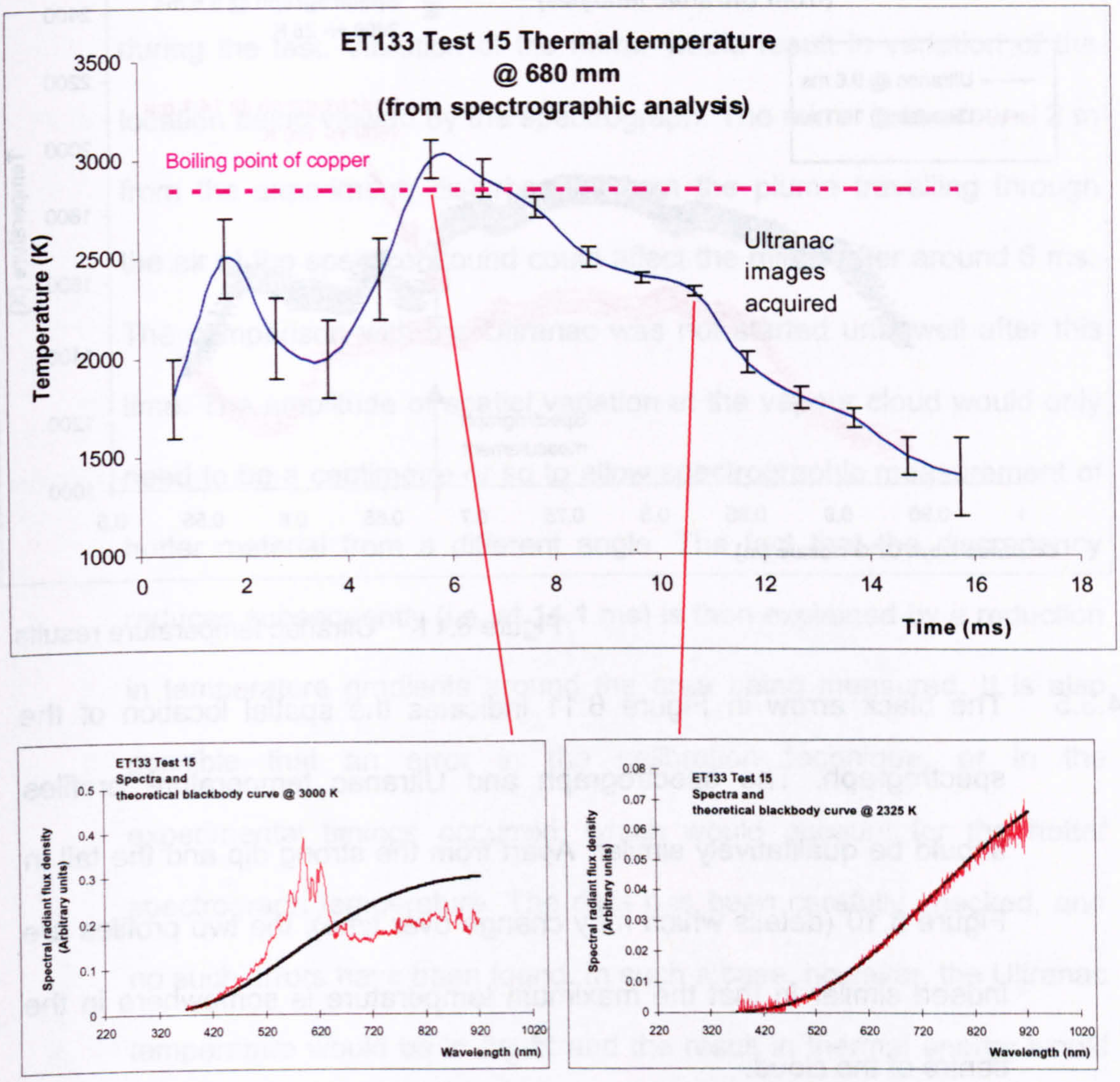

Figure 6.10 Temperature results from the spectrograph

4.3.4 The Ultranac results for the same line profile (Figure 6.9) as the spectrograph results appear in Figure 6.11. (Note that the abscissa in Figure 6.11 has been reversed to ease interpretation for the reader.) A

2 % error has been assigned to the Ultranac temperatures, due to the error in the calibration constant (see Appendix A).

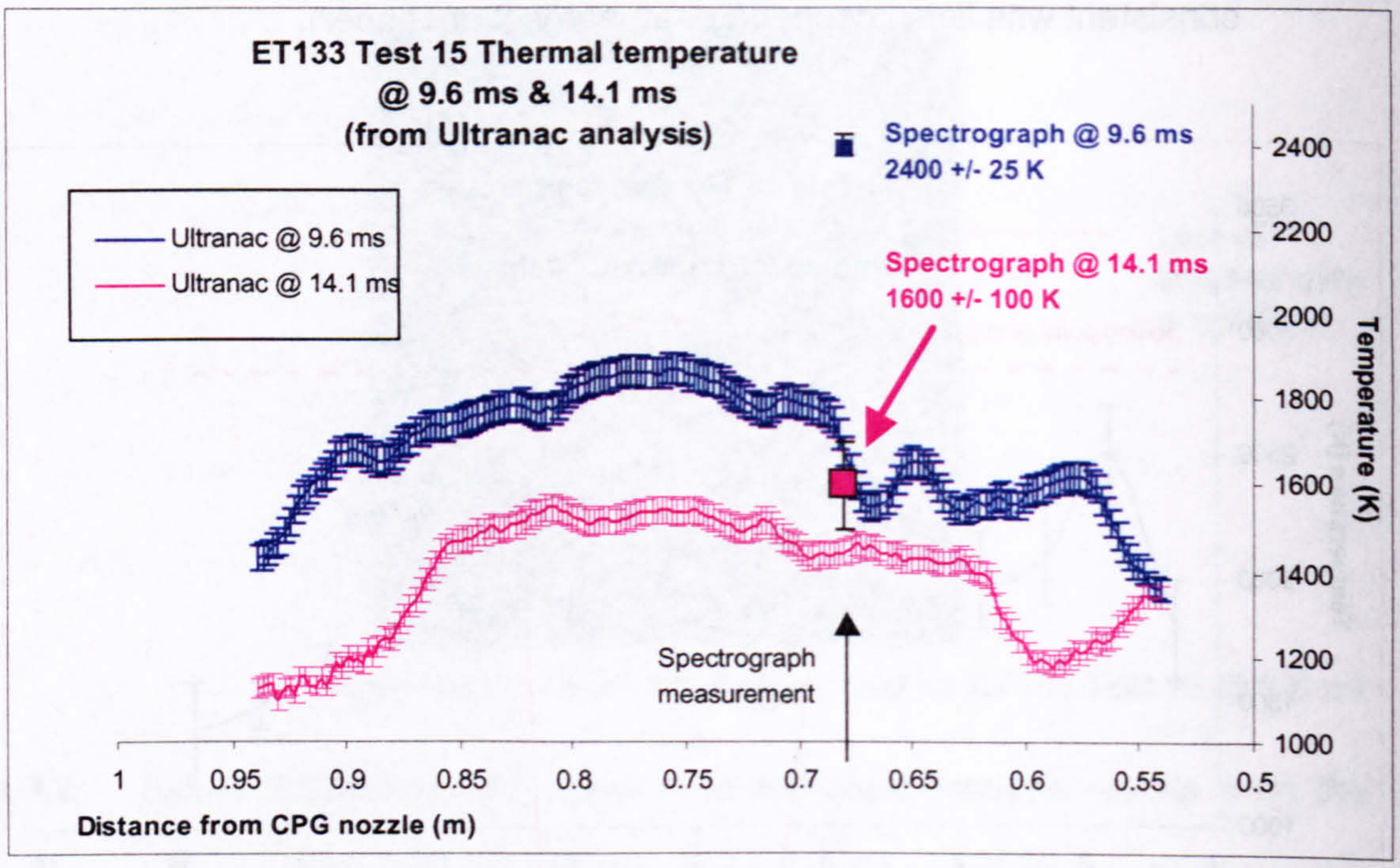

Figure 6.11 Ultranac temperature results

4.3.5 The black arrow in Figure 6.11 indicates the spatial location of the spectrograph. The spectrograph and Ultranac temperature profiles should be qualitatively similar. Apart from the strong dip and the tail in Figure 6.10 (details which may change over time), the two profiles are indeed similar in that the maximum temperature is somewhere in the centre of the cloud.

4.3.6 There is a significant difference is in the absolute values of temperature, however. The spectrograph recorded temperatures of 2400 +/- 25 K and 1600 +/- 100 K at 9.6 ms and 14.1 ms respectively, given by the square data point markers in Figure 6.11. The

temperatures from the Ultranac are around 1750 +/- 90 K and 1450 +/- 75 K for these same times and at the same location. The differences cannot be accounted for by analytical errors. The most likely explanation is vibration of the spectrograph collimating mirror during the test. Vibration of the mirror would result in variation of the location being viewed by the spectrograph. The mirror was around 2 m from the experiment; disturbances from the plume travelling through the air at the speed of sound could affect the mirror after around 6 ms. The comparison with the Ultranac was not started until well after this time. The amplitude of spatial variation at the vapour cloud would only need to be a centimetre or so to allow spectrographic measurement of hotter material from a different angle. The fact that the discrepancy reduces subsequently (i.e. at 14.1 ms) is then explained by a reduction in temperature gradients around the area being measured. It is also possible that an error in the calibration technique, or in the experimental timings occurred, which would account for the hotter spectrograph temperature. The data has been carefully checked, and no such errors have been found. In such a case, however, the Ultranac temperature would be in doubt and the result in thermal energy would then be under-estimated.

4.3.7 The maximum temperatures recorded by the Ultranac camera are shown in Figure 6.12. The standard 2 % error has been applied. Figure 6.13 shows the temperature map of the plume at 9.6 ms (Figure 6.9).

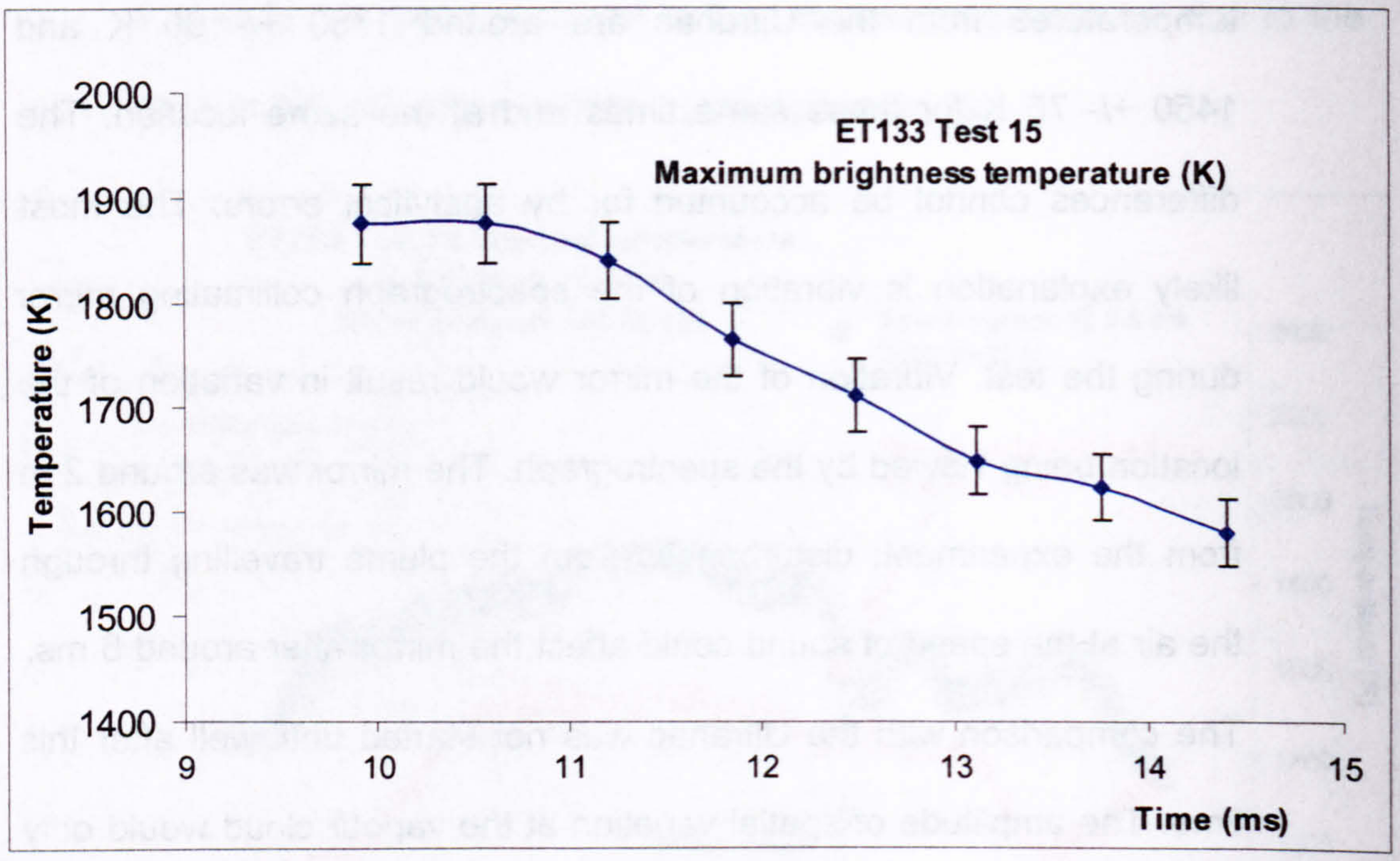

Figure 6.12 Ultranac temperatures

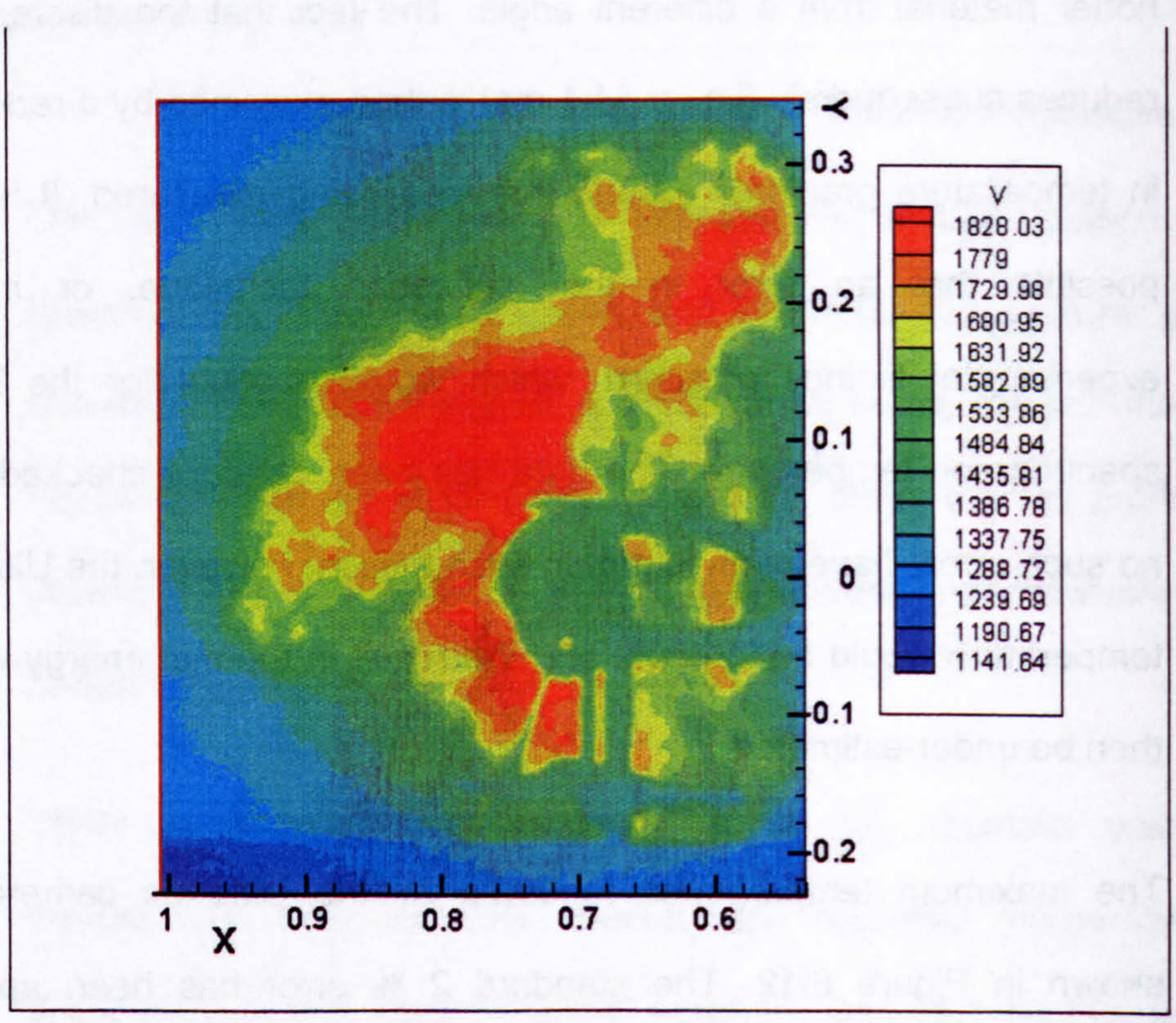

Figure 6.13 Thermal temperature profile at 9.6 ms

4.3.8 An estimation of the energy within the plume can now be made. Ideally, the spatial temperature plot of images from this work could be used to accurately determine this, by using computing power to produce a 3D temperature map from the 2D plot. However, as a first approximation, the volume of the plume has been taken to be that of a sphere of 0.4 m diameter containing air at atmospheric pressure at a temperature of 1800 K. The size and temperature have been estimated from the Ultranac temperature at 9.6 ms (Figure 6.13). The mass of air is obtained from the volume and density, and energy from the specific heat capacity (SHC). Air density and SHC at 1800 K have been extrapolated from the CRC Handbook data [8]: this extrapolation is shown in Figure 6.14.

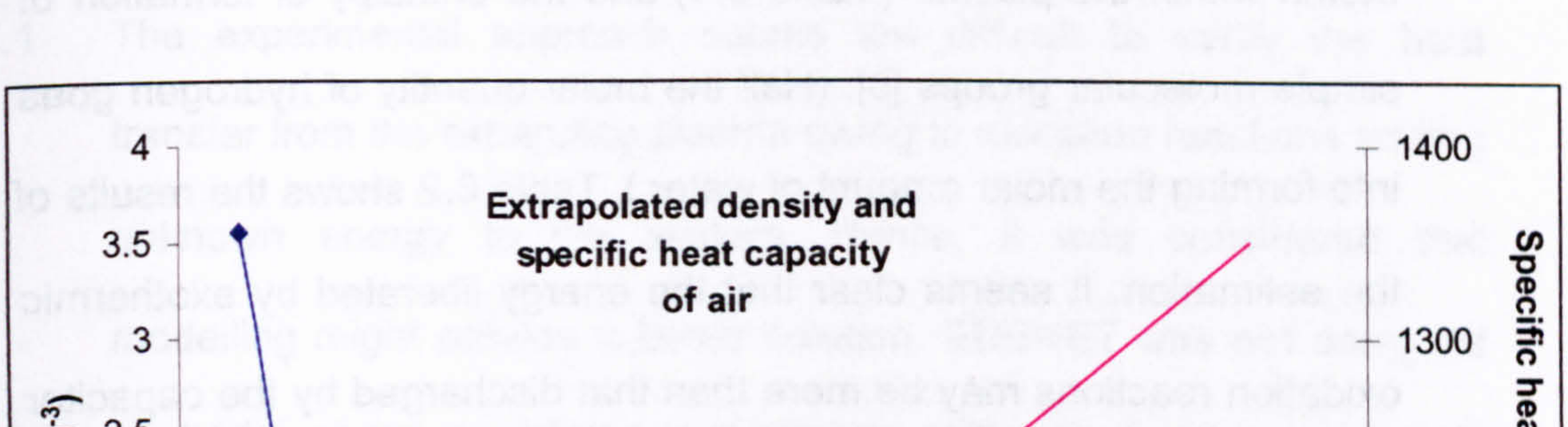

Figure 6.14 Properties of air at 1800 K

4.3.9 Then, the energy within the cloud (i.e. needed to raise its temperature above ambient) would be around 13 kJ, representing around 43% of the electrical energy discharged. This is thought to be an underestimation, as no account has been taken of the other species – especially water – within the cloud. Further, if an error in the calibration technique or timing occurred, this may again increase this figure. Hence, the result of 43% is in reasonably good agreement with the estimate of 50% (minimum) transferred from the energy budget as described in Chapter 5.

4.3.10 However, the energy released during exothermic reactions also has not been taken into account. This can be estimated from the number of atoms within the plasma (Table 6.1) and the enthalpy of formation of simple molecular groups [9]. (Half the molar quantity of hydrogen goes into forming the molar amount of water.) Table 6.2 shows the results of the estimation. It seems clear that the energy liberated by exothermic oxidation reactions may be more than that discharged by the capacitor bank. Obviously at the time the above estimation was performed, an unknown proportion of the plasma constituents had oxidised or otherwise reacted. Nonetheless, the results in this table suggest that the estimation of the percentage of electrical energy transferred to the air by this method will have very large and inestimable errors associated with it.

Plasma constituent	Amount of constituent in plasma (mol)	Standard molar enthalpy (heat) of formation at STP (kJ mol^{-1})	Energy liberated on formation (kJ)
Water	0.14	-241.8	34
Carbon dioxide	0.13	-393.5	51
Copper (II) oxide	0.10	-175.3	18

Table 6.2

4.3.11 This experiment seems, therefore, to have been inadequate in indicating that the air-mixing figure is reasonable. An alternative means has thus been explored to obtain a more representative result.

4.4 Modelling route to verify the percentage energy transferred to the air

4.4.1 The experimental approach seems too difficult to verify the heat transfer from the expanding plasma owing to oxidation reactions adding unknown energy to the system. Hence, it was considered that modelling might provide a better solution. EDENET was not designed to model plume expansion in particular, although there is an in-built capability for varying the capillary or nozzle diameter. However, this has never been validated against experiment and an attempt to adjust the nozzle to mimic the early expansion processes was not very successful (see Chapter 5).

4.4.2 Hence, the Author made an approach to co-workers from the field of rocketry, with expertise in the expansion of hot gaseous plumes. They suggested use of a company, S & C Thermofluids [10], who specialise

in this field. S & C Thermofluids have modelling capability for such situations, although this had never been tested for such hot gases. The model does not include radiative energy transfer, but fortunately, this was just what was needed. The radiative energy transfer had been measured at such a low level that to a first approximation it could be ignored. If the plume could be modelled to behave in a manner predictable with low radiative heat loss with exothermic reactions occurring later in the plume development, then the energy partition detailed in Chapter 5 would be verified. A contract was thus set up between the Author and S & C Thermofluids [11].

4.4.3 S & C Thermofluids' model PLUME was seen as the best way forward and input data for the model, mass and energy flux were obtained from EDENET exit conditions. The main features were that the plasma flow lasted for 1 ms and reached a peak pressure of 28.8 MPa, a peak temperature of 15 700 K and a peak velocity of 2240 m s^{-1} in 0.18 ms. These values then decayed rapidly. Figure 6.15 shows the plasma pressure and velocity, and Figure 6.16 the plasma density and temperature. The plasma is composed of copper. Initially the PLUME software was used without any modifications for this work, but problems with convergence were encountered early on. It was felt that the coefficients used in the calculation of constant pressure specific heat, C_p might have been inappropriate for the levels of temperature in the plasma. A separate fluid dynamics model was therefore

constructed from scratch in order to simplify and control some of the physical properties. Eventually, a solution was obtained.

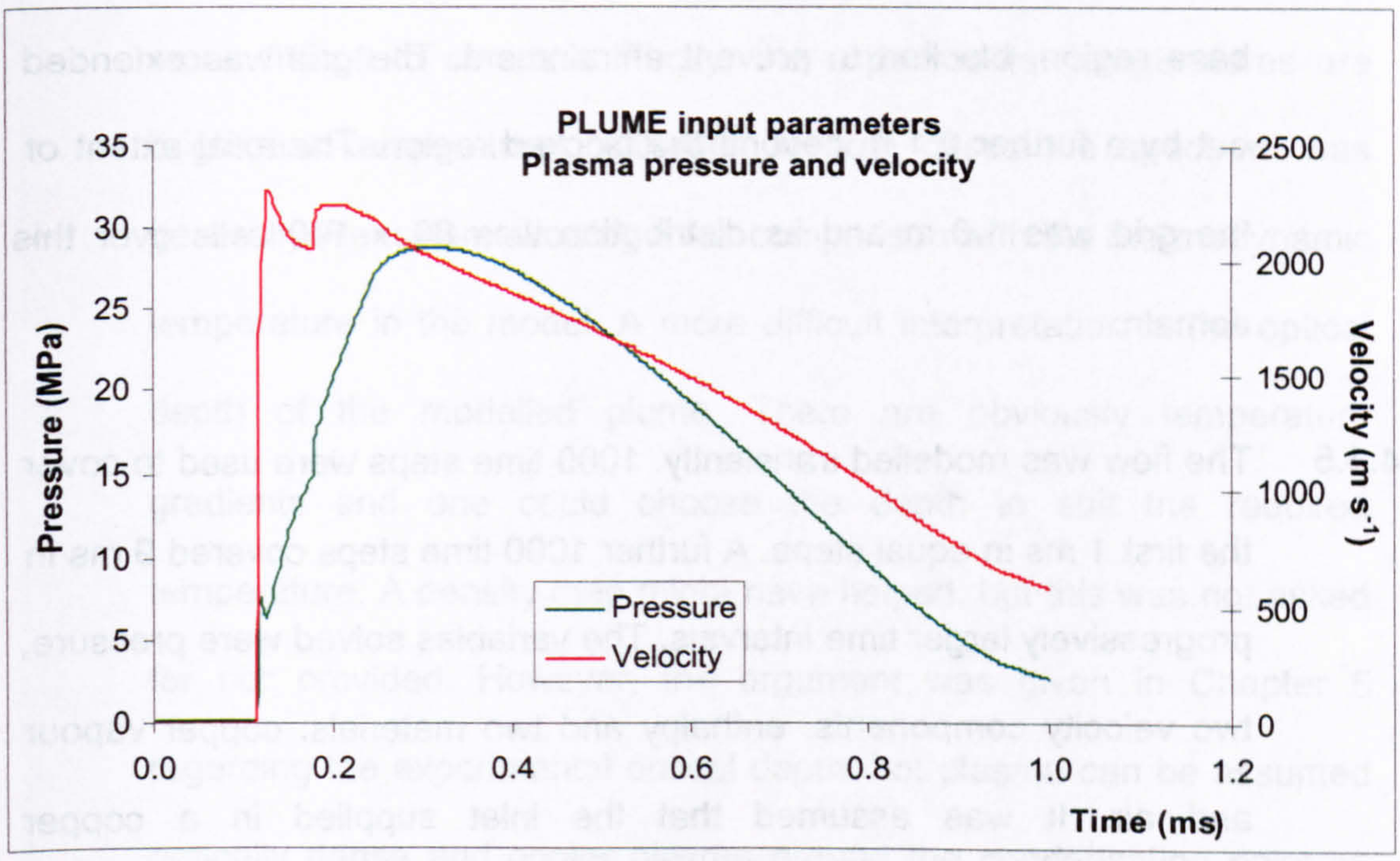

Figure 6.15 Input parameters for PLUME: plasma pressure and velocity

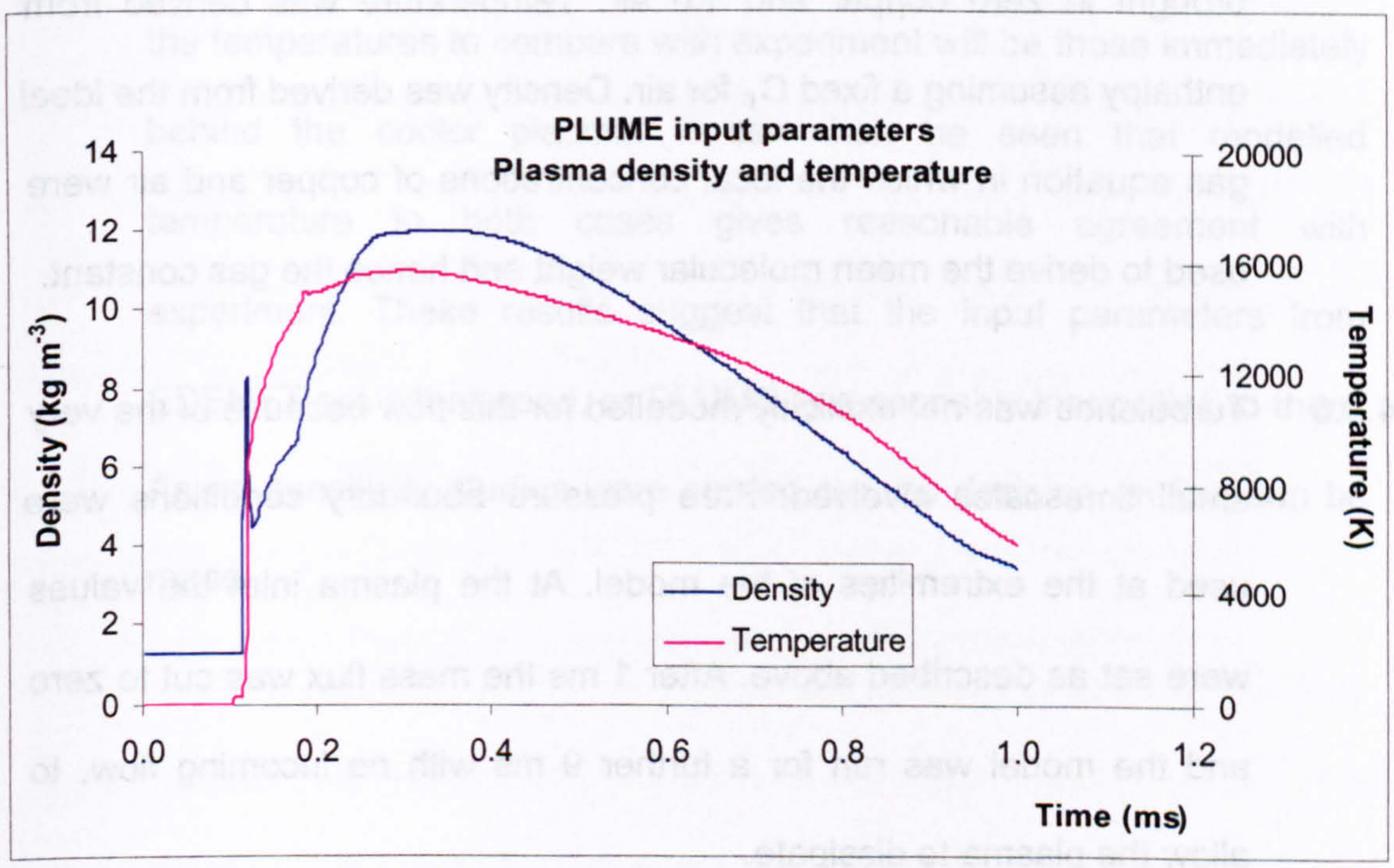

Figure 6.16 Input parameters for PLUME: plasma density and temperature

4.4.4 The model geometry was 2D, axisymmetric using a polar co-ordinate system. The flow enters the domain through a hole 14 mm in diameter into an unbounded region. This was surrounded by a 300 mm diameter base region, blocked to prevent entrainment. The grid was extended out by a further 0.1 m beyond the blocked region. The axial extent of the grid was 1.0 m and its distribution was 80 x 100 cells over this domain.

4.4.5 The flow was modelled transiently. 1000 time steps were used to cover the first 1 ms in equal steps. A further 1000 time steps covered 9 ms in progressively larger time intervals. The variables solved were pressure, two velocity components, enthalpy and two materials: copper vapour and air. It was assumed that the inlet supplied in a copper concentration of 1.0 and no air and that the free stream boundaries brought in zero copper and 1.0 air. Temperature was derived from enthalpy assuming a fixed C_p for air. Density was derived from the ideal gas equation in which the local concentrations of copper and air were used to derive the mean molecular weight and hence the gas constant.

4.4.6 Turbulence was not explicitly modelled for this flow because of the very small timescales involved. Free pressure boundary conditions were used at the extremities of the model. At the plasma inlet the values were set as described above. After 1 ms the mass flux was cut to zero and the model was run for a further 9 ms with no incoming flow, to allow the plasma to dissipate.

4.4.7 Figure 6.17 shows the comparison between modelling (left) and experiment (right) during the discharge and immediately afterwards. Agreement on spatial distribution is excellent. Temperatures are a little more difficult to compare. Firstly, the experimental temperatures are brightness temperatures, although in both cases the spectrum was generally Planckian, allowing a fair comparison with the thermodynamic temperature in the model. A more difficult interpretation is the optical depth of the modelled plume. There are obviously temperature gradients and one could choose the depth to suit the required temperature. A density map might have helped, but this was not asked for nor provided. However, the argument was given in Chapter 5 regarding the experimental optical depth: hot plasma can be assumed optically dense and cooler plasma around the condensation point as optically thin. Applying this argument to modelled results suggests that the temperatures to compare with experiment will be those immediately behind the cooler plasma. It can then be seen that modelled temperature in both cases gives reasonable agreement with experiment. These results suggest that the input parameters from EDENET are either good, or PLUME is reasonably insensitive to them. As no sensitivity studies were carried out, no decision on this can be made.

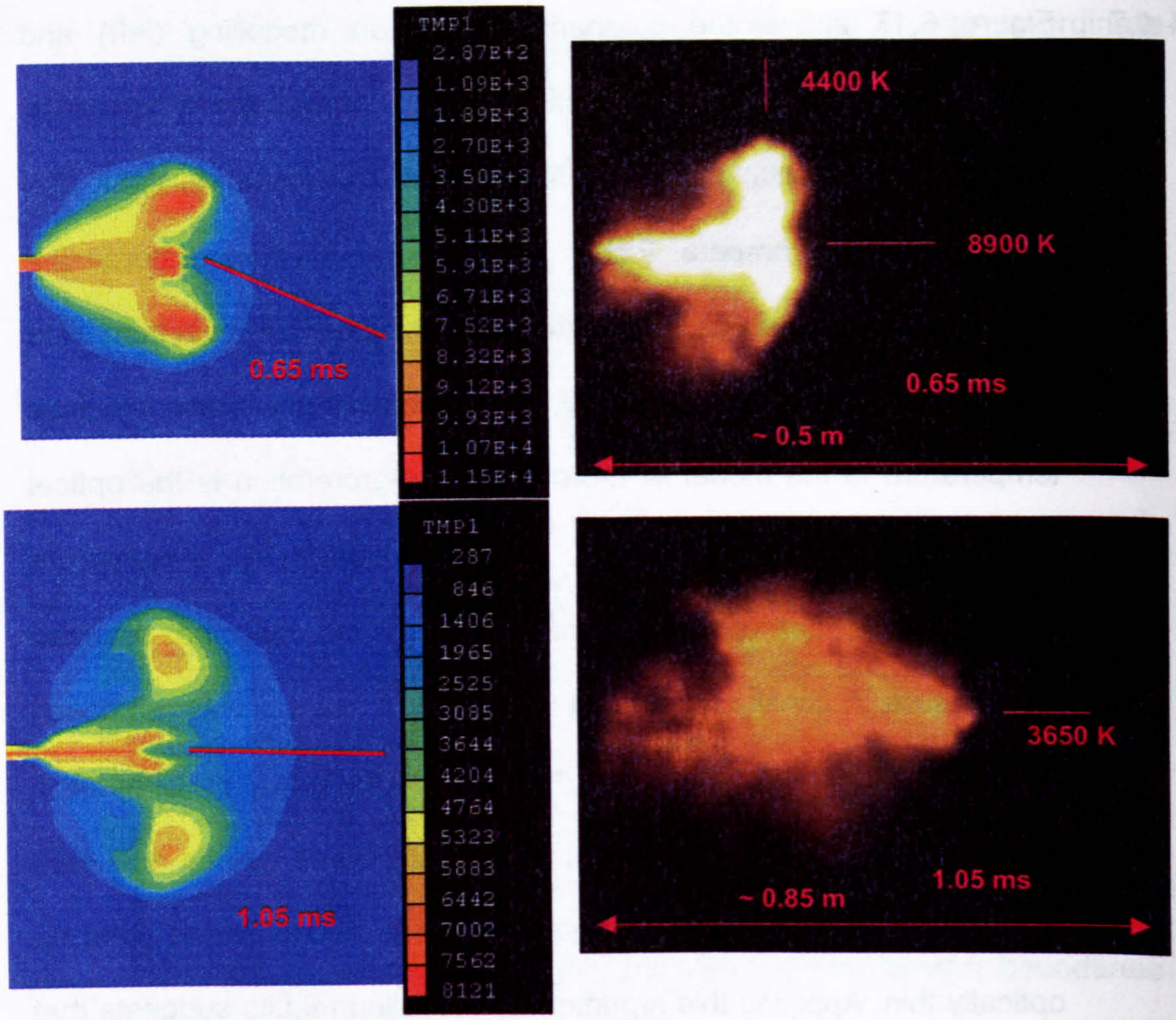

Figure 6.17 PLUME expansion modelling (left) and experimental comparison (right)

4.4.8 It has been argued here that the modelling of plume expansion agrees reasonably well with experimental results for the duration of the discharge. This assumed no radiative energy transfer to the surroundings, and so the low radiative energy transfer measured from experimentation is thus tentatively confirmed. Further, the assumption of air mixing as the prime energy transfer mechanism is also confirmed, as no other energy loss mechanism was introduced into the model.

4.4.9 The PLUME expansion modelling work has also been compared to experiment at the later time of 10 ms. Figure 6.11 shows that the

temperature of the plasma peaks in the region of 1900 K and not below 1400 K. Figure 6.18 shows that PLUME calculates lower temperatures.

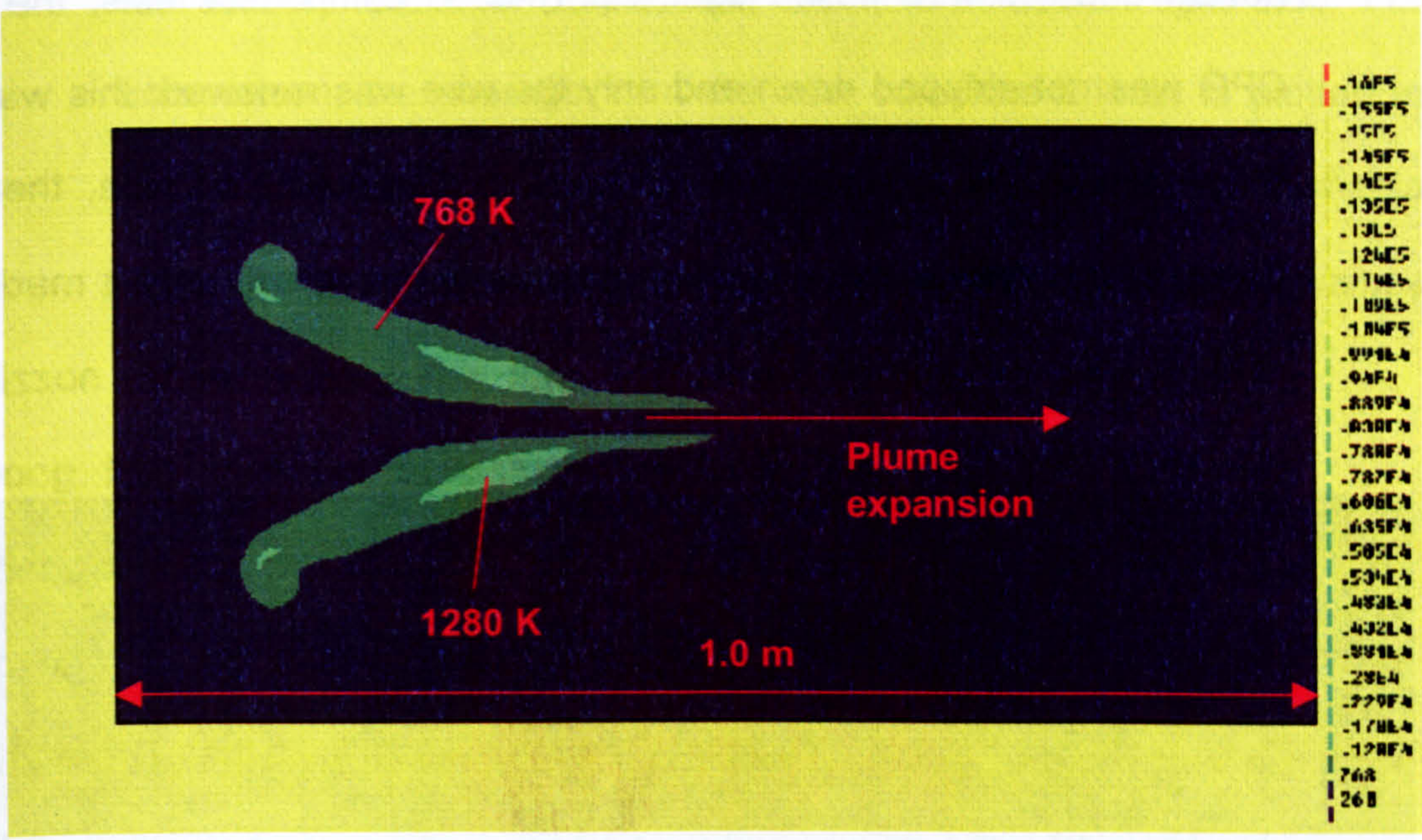

Figure 6.18 PLUME expansion modelling at 10 ms

4.4.10 It seems clear that the discrepancy at later times is due to the chemistry (i.e. the exothermic reactions) occurring within the expanded plume. Thus, doubting the validity of the experimental estimation (Paragraph 4.3.11) of the energy originating from the electrical discharge remaining within the cooled vapour cloud from its temperature has been ratified.

5 Component Re-use

5.1 Plasma voltages

5.1.1 The plasma voltages, discharge duration, energy input, radiated energy density and plasma expansion have been briefly investigated with respect to re-use of CPG rear electrode, capillary and nozzle electrode.

For new component tests, the CPG was stripped down and each component replaced; a new wire was threaded through a hole in the nozzle and the wire pulled tight. For re-used component tests, the CPG was not stripped down and only the wire was renewed: this was done by winding a small coil in one end of a length of wire, then inserting this coiled end into the capillary via the nozzle until it made contact with the rear electrode. The wire was secured to the nozzle electrode with tape. An ohmmeter was used to check that good electrical contact was achieved between the rear and front electrodes. Figure 6.19 shows the new component test voltages; the average of these tests is shown in red and the individual tests in yellow. There are variations of around 12% in the plateau values and around 6% in the duration of the discharge.

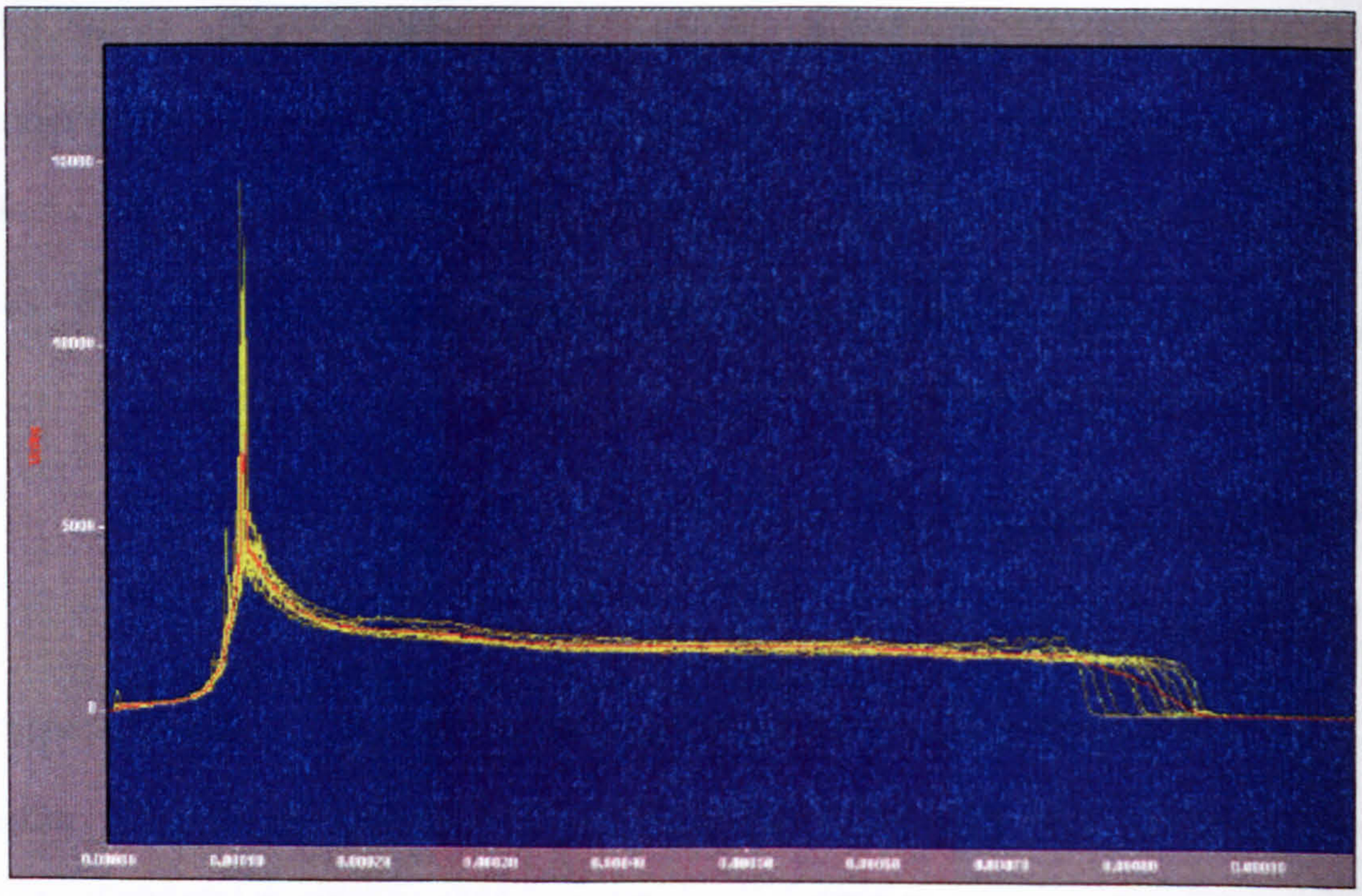

Figure 6.19 Voltages in new component tests (average in red)

5.1.2 Figure 6.20 shows the re-used component test voltages. The average is shown in yellow, the voltages with the first re-use in green, those with the second re-use in purple, and the third re-use in light blue. For comparison, the average from the new component tests is plotted in red. The variations between the test voltages with re-used components were similar to those with new components, but the absolute values differed.

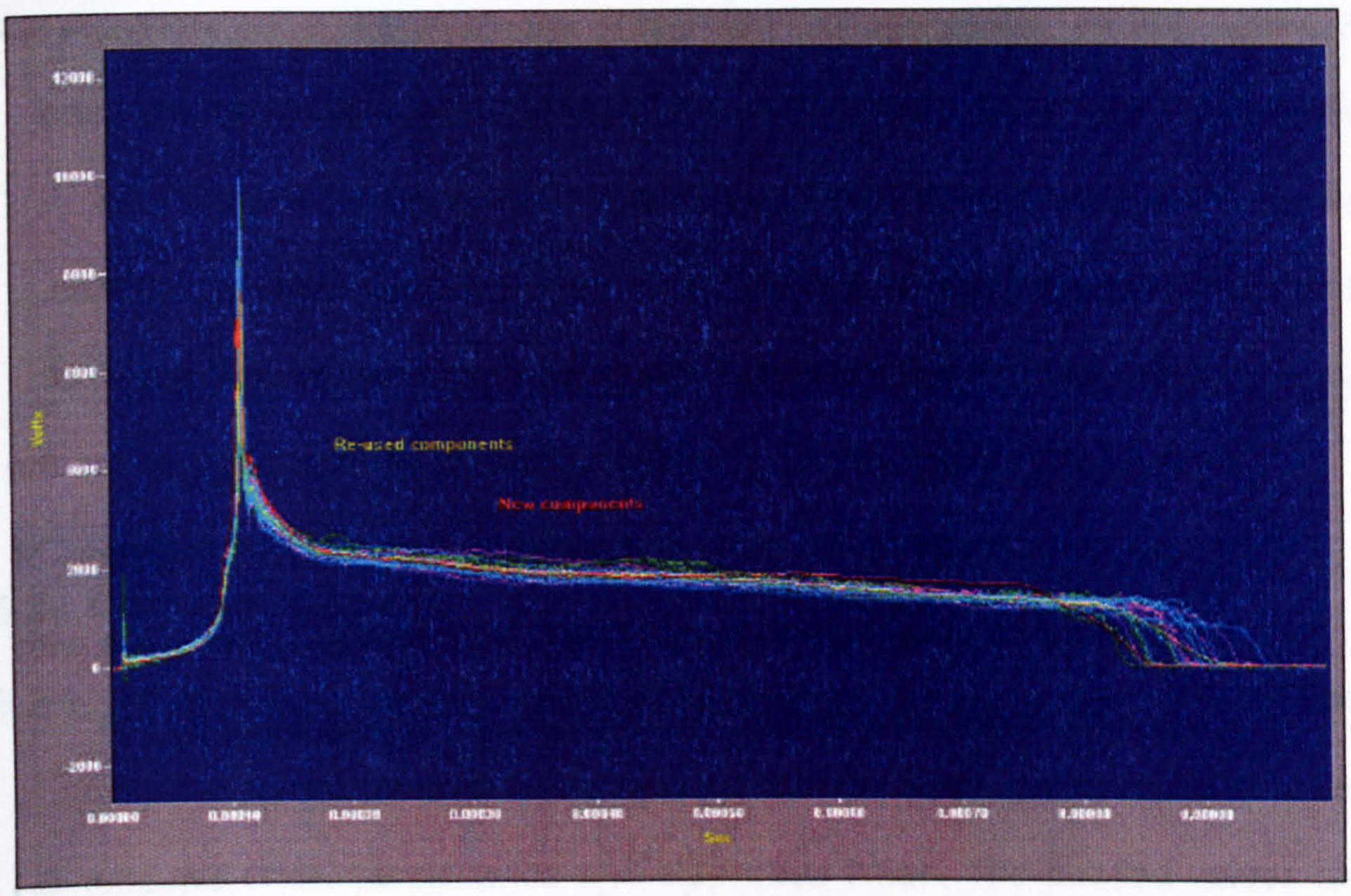

Figure 6.20 Voltages from re-used component tests (re-used component average in yellow; new component average in **red**)

5.1.3 The graphs are confusing and difficult to interpret clearly. One way to compare the absolute values for the voltages is to study the integrated voltage with respect to time. Table 6.3 is a summary of the statistical analysis of integrating the voltage with respect to time.

Test type	Mean integrated voltage ($V\ s^{-1}$)	Comparison between	Test value, t	Difference?
New'	1.48	New & 1	1.56	No
1'	1.46	New & 2	2.72	Yes
2'	1.45	New & 3	3.74	Yes
3'	1.44	1 & 2	1.06	No
		1 & 3	1.81	No
		2 & 3	0.49	No

Table 6.3

5.1.4 The comparison is between 'new' parts and parts that were re-used once, '1' parts re-used twice, '2' and parts re-used three times, '3' The two-sample 't-test' is a significance test for comparing two means. Twelve 'new' test voltages were integrated and averaged, and seven of each of the others, giving seventeen degrees of freedom (*df)* for the mean comparison with new components and twelve degrees of freedom for all other comparisons. This test compares a test value with a value from statistical tables. The test value, t is calculated by:

$$t = \frac{\left|\overline{x}_A - \overline{x}_B\right|}{S\sqrt{\frac{1}{n_A} + \frac{1}{n_B}}} \qquad \textbf{Equation 6.1}$$

where

x_A and x_B are the means of groups A and B

n_A and n_B are the number of data points in groups A and B and

S is a combined standard deviation of the two data groups, where

$$S = \sqrt{\frac{\sum(df \times sd)^2}{\sum df}} \qquad \textbf{Equation 6.2}$$

This assumes that the standard deviation, *sd* is the same for both data sets.

5.1.5 The statistical table value is given as 2.11 at a 95 % confidence level with 17 *df.* If the test value, *t* is less than the statistical table value, then there can be said to be no difference between the test means. There would seem to be a significant difference between the new part tests and the tests where parts are re-used two and three times. However, there is a trend in the integrated voltage value means towards decrease with use, supported by a trend to increase in the Test values between new and re-use. This suggests that small differences occur in the capillary plasma properties as the parts become worn. The fact that the Test value between 2 & 3 is lower than that between 1 & 2 may suggest that the difference with continued re-use is decreasing.

5.2 Discharge duration

5.2.1 Figure 6.21 shows the averaged voltages for each type of test. The curve in red represents the new component tests, green represents re-used once, purple twice and blue three times. The plateau values for re-using the parts falls around half-way through the discharge with respect to new parts, and re-using the parts seems to suggest that the discharge lasts progressively longer.

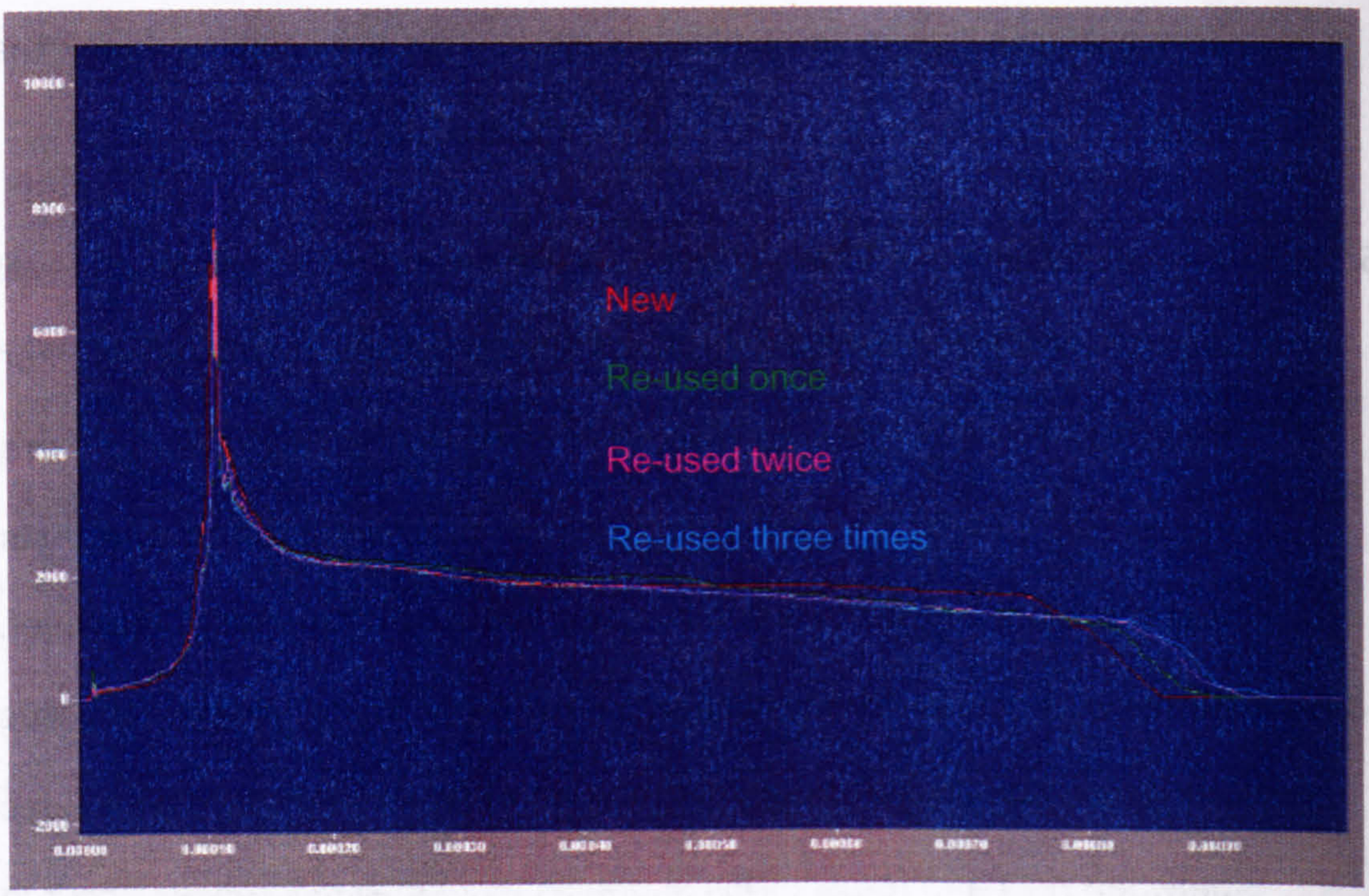

Figure 6.21 Average voltages from tests re-using components

5.2.2 Table 6.4 is a summary of the same statistical analysis on the means of the discharge duration. There is a statistical difference in the duration of the discharge when parts are re-used, with a similar trend as above, that continued re-use results in progressively less difference. The overall increase in discharge length from new compared to three re-uses of components is around 10 %. The increase in discharge duration as parts are re-used is possibly due to lower plasma resistivity, reducing the rate at which energy is transferred to the plasma.

5.2.3 Figure 6.22 shows the averaged discharge duration as a function of re-use, and emphasises the point that continued re-use results in less of a difference. A possible explanation for this is that the plasma resistivity reduces due to extra capillary material ablated from a pitted rear copper tungsten electrode, with the remaining tungsten preventing

increased ablation with continued re-use. Another possibility is that material remaining within the capillary from previous firings (perhaps condensed on the capillary wall) acts as the source of such material. Further experimentation would be required to determine the cause of this.

Test type	Mean discharge duration (μs)	Comparison between	Test value, *t*	Difference?
New'	832.17	New & 1	3.06	Yes
1'	873.43	New & 2	4.79	Yes
2'	899.57	New & 3	5.50	Yes
3'	908.43	1 & 2	1.98	No (borderline)
		1 & 3	2.74	Yes
		2 & 3	0.64	No (strong)

Table 6.4

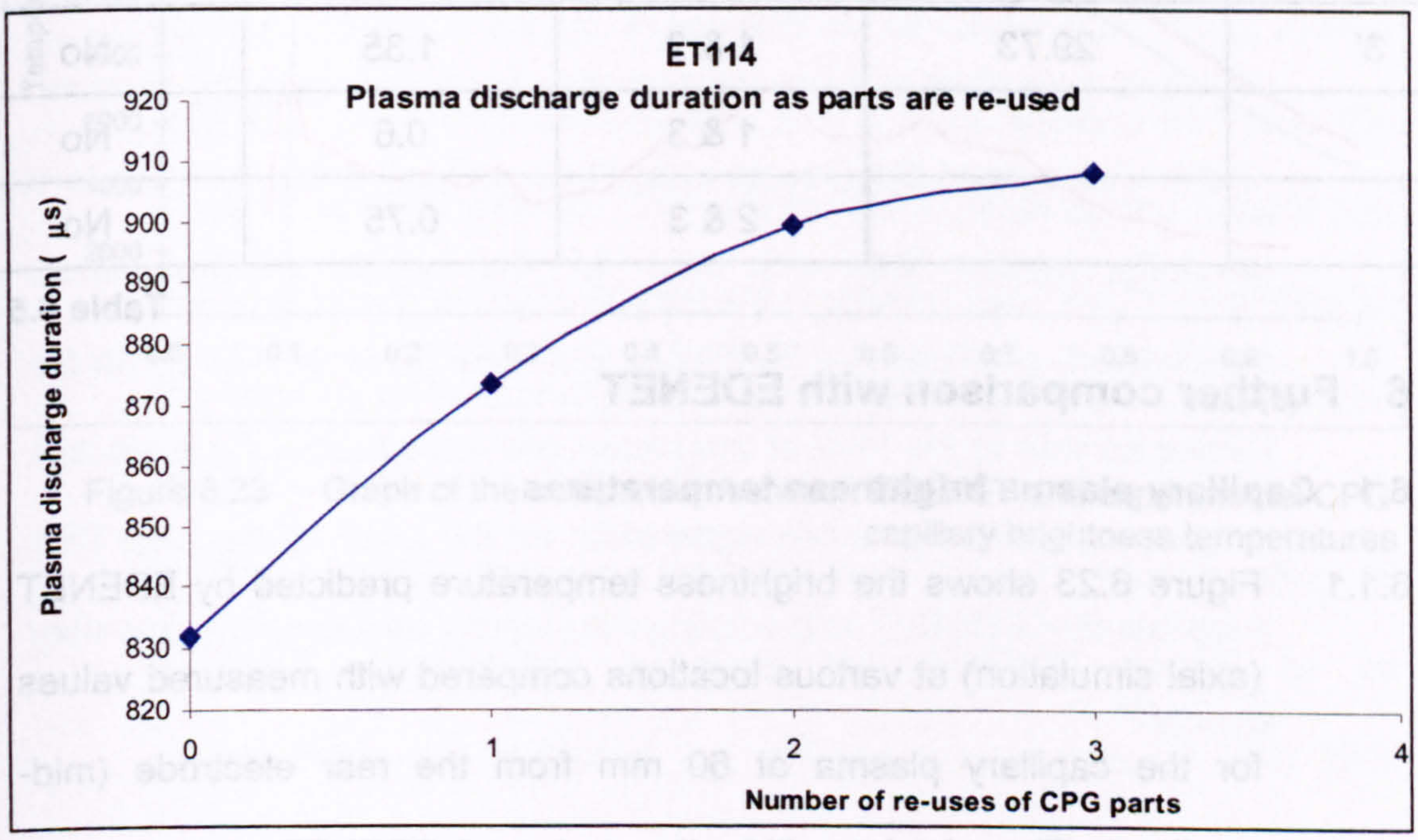

Figure 6.22 Graph to show discharge duration as components are re-used

5.3 Electrical energy transfer

5.3.1 Table 6.5 summarises statistical analysis of the electrical energy transferred to the capillary plasma. There is a statistical difference in the electrical energy transferred during the discharge when parts are re-used compared to when parts are new, although no difference when re-use continues. The decrease in electrical energy transferred due to component re-use is around 3 %. These finding provide another means to validate EDENET. To date, no attempt has been made to investigate this.

Test type	Mean discharged electrical energy (kJ)	Comparing	Test value, *t*	Difference?
New'	30.48	New & 1	2.68	Yes
1'	29.83	New & 2	3.73	Yes
2'	29.60	New & 3	3.05	Yes
3'	29.73	1 & 2	1.35	No
		1 & 3	0.6	No
		2 & 3	0.75	No

Table 6.5

6 Further comparison with EDENET

6.1 Capillary plasma brightness temperatures

6.1.1 Figure 6.23 shows the brightness temperature predicted by EDENET (axial simulation) at various locations compared with measured values for the capillary plasma at 60 mm from the rear electrode (mid-capillary). The physics within the codes of EDENET suggests the

formation of an optically thick boundary layer at the plasma-capillary interface with a brightness temperature significantly lower than the core (see Chapter 3). However, the temperature of this layer may be significantly lower than currently predicted. This issue has been discussed already in Chapter 4. The explanation for the temperature variations shown in Figure 6.23 could be that an optically thick layer of copper vapour/condensate is forming at the capillary liner surface. Figure 6.24 shows a spectrum of the hottest plasma recorded in this test, containing strong evidence of copper absorption lines.

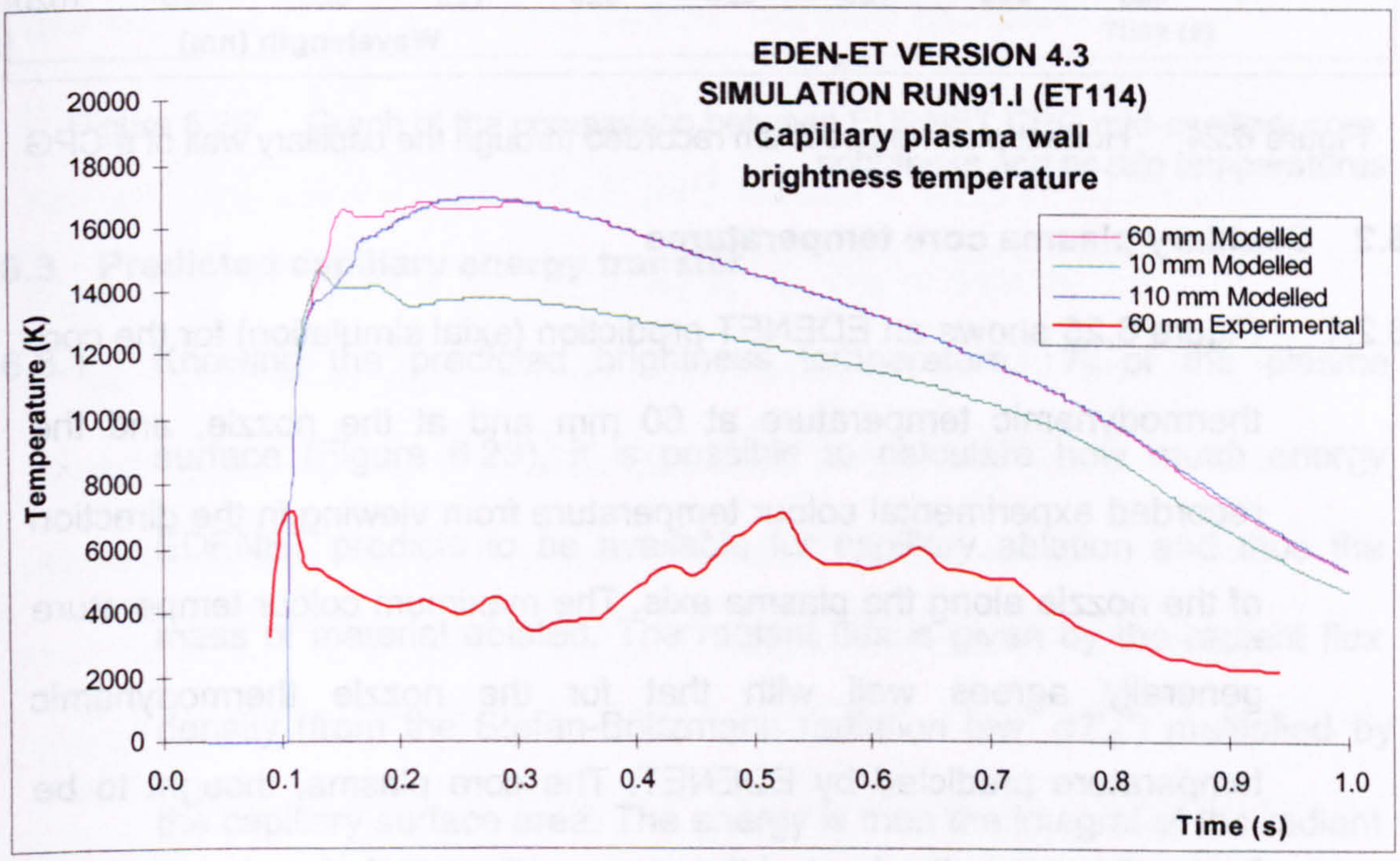

Figure 6.23 Graph of the comparison between EDENET and experimental CPG capillary brightness temperatures

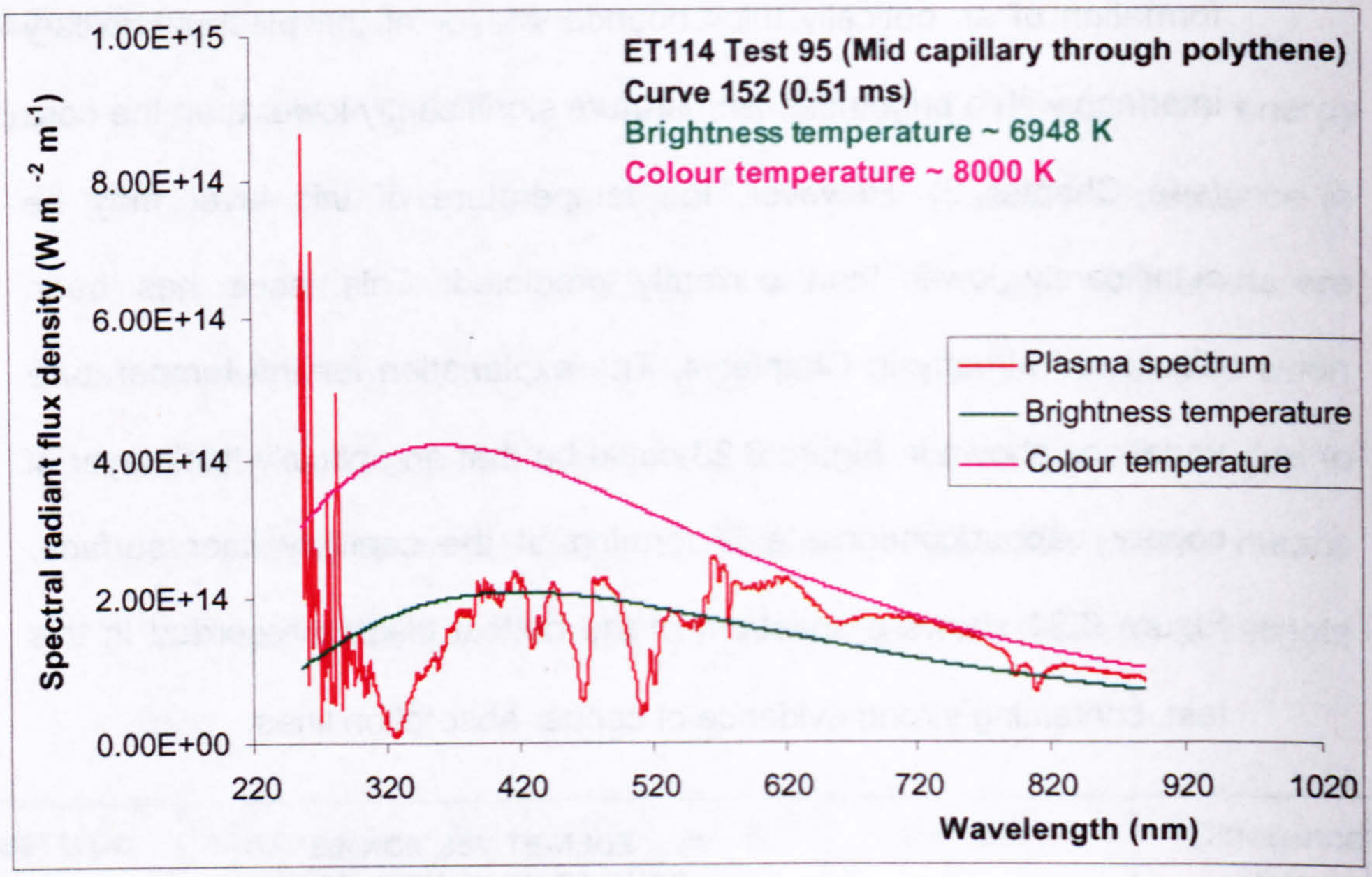

Figure 6.24 Hottest plasma spectrum recorded through the capillary wall of a CPG

6.2 Capillary plasma core temperatures

6.2.1 Figure 6.25 shows an EDENET prediction (axial simulation) for the core thermodynamic temperature at 60 mm and at the nozzle, and the recorded experimental colour temperature from viewing in the direction of the nozzle along the plasma axis. The maximum colour temperature generally agrees well with that for the nozzle thermodynamic temperature predicted by EDENET. The core plasma, thought to be forcing its way to the front of the plume, will nevertheless be expected to cool, providing a possible explanation for the small differences. This suggests that EDENET is predicting the plasma core temperatures very closely.

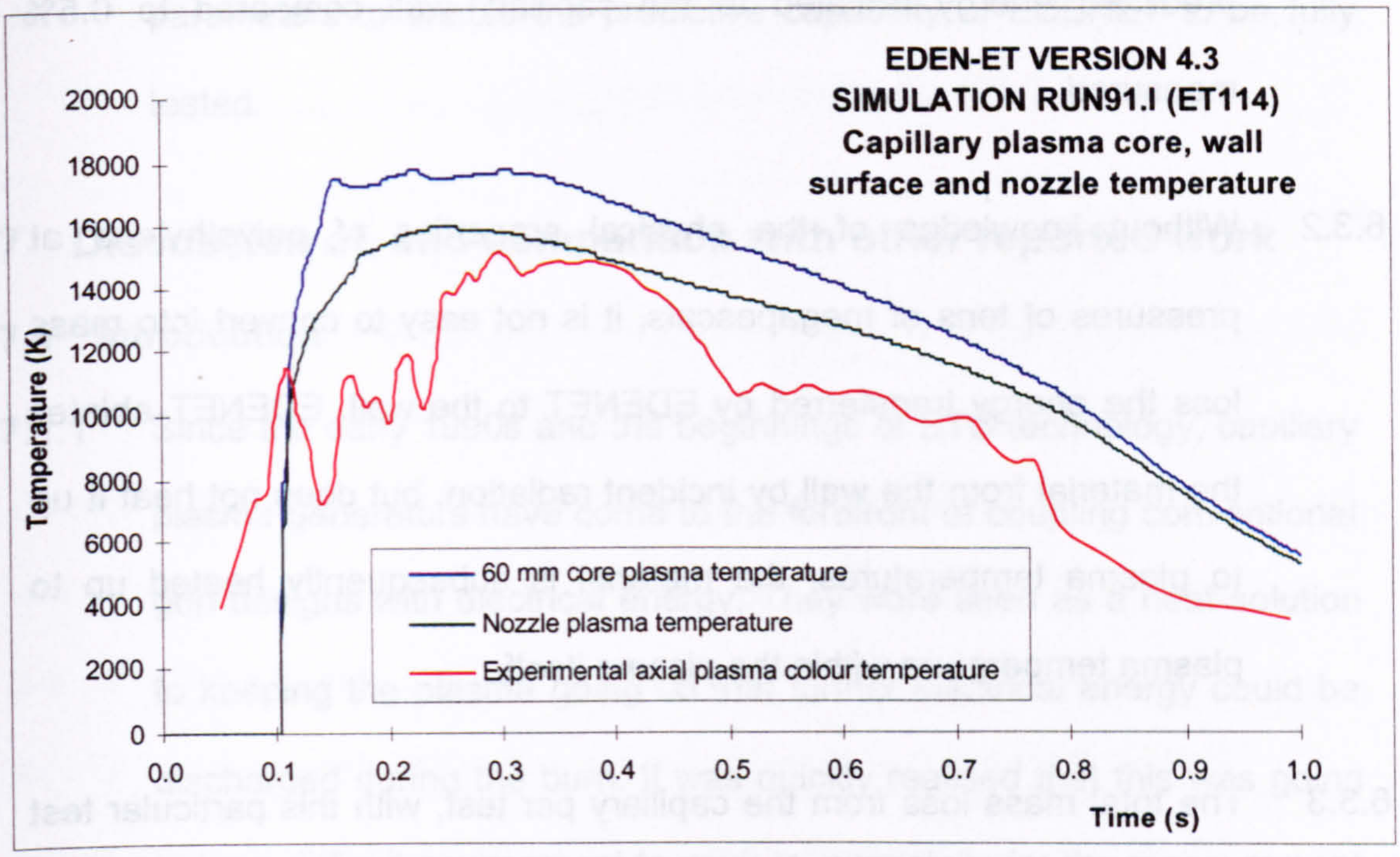

Figure 6.25 Graph of the comparison between EDENET CPG mid-capillary core, brightness and nozzle temperatures

6.3 Predicted capillary energy transfer

6.3.1 Knowing the predicted brightness temperature, T_b of the plasma surface (Figure 6.23), it is possible to calculate how much energy EDENET predicts to be available for capillary ablation and thus the mass of material ablated. The radiant flux is given by the radiant flux density (from the Stefan-Boltzmann radiation law σT_b^4) multiplied by the capillary surface area. The energy is then the integral of the radiant flux with respect to time. The results of this analysis using the brightness temperature from the latest version (at the time of writing) of EDENET (Version 6.0) suggests that EDENET seems to be considerably over-predicting the radiated energy transfer, with 20%

predicted energy radiated to the capillary wall compared to 0.5% measured.

6.3.2 Without knowledge of the physical properties of polyethylene at pressures of tens of megapascals, it is not easy to convert into mass loss the energy transferred by EDENET to the wall. EDENET ablates the material from the wall by incident radiation, but does not heat it up to plasma temperatures; the material is subsequently heated up to plasma temperature within the plasma itself.

6.3.3 The total mass loss from the capillary per test, with this particular test set-up, is around 0.2 g (see Chapter 5, Table 5.1). EDENET can report how much material is ablated from the capillary components. For this test, the ablated mass of polyethylene is 0.23 g, in very good agreement with experiment. This has seemingly required 20 kJ to ablate, as the capillary is treated as opaque. The high energy results from the high specific heat capacity of polyethylene – around 30 times greater than that of copper [12].

6.3.4 Hence, although the brightness temperature is very high, the energy is returned to the plasma and the reported ablation is correct for this particular test. The mass and energy flux exiting the capillary may still be correct even if it is aided by ablation occurring through the wrong energy transfer process. This is supported by the good agreement with both experiment (Figure 6.25) and other modelling work (Figure 6.17). However, this aspect will require more work over a range of discharge

parameters to enable the predictive capability of EDENET to be fully tested.

7 Discussion of, and comparison with other reported work

7.1 Introduction

7.1.1 Since the early 1990s and the beginnings of ETC technology, capillary plasma generators have come to the forefront of coupling conventional gun designs with electrical energy. They were seen as a neat solution to keeping the plasma going so that further electrical energy could be discharged during the burn. It was quickly realised that this was going to be a difficult environment to work in, especially for the measurement of mass and energy flux from the capillary nozzle. So computer models were constructed, but little experimentation for validating some of the CPG operations was performed. Many of the assumptions made then still hold now. For instance, Mohanti and Gilligan [13] and Hsiao, Phillips and Su [14] stated in 1993 that the main energy transfer mechanism to the capillary wall would be radiative, just as EDENET and other researches [15] show at present. As discussed in following Chapters, similar assumptions for radiated energy transfer apply for plasma propellant interactions.

7.1.2 Another difficulty arises with comparing results from different models in that the CPG design and discharge parameters differ greatly from one report to another. This is partly due to the application specific nature of the work in this area, as different organisations historically have

different gun designs. However, some of the general findings with respect to CPGs are discussed below.

7.2 Plasma composition

7.2.1 CPG devices have been referred to as ablation stabilised arcs'plasma generators [16, 17], due to an assumption that the metallic elements within the capillary plasma generator play an insignificant role in contributing to the plasma global properties. As mentioned earlier in the Thesis, it is thought by some that the capillary liner is central to the ablated material that sustains the plasma within the capillary [17, 18, 19, 20, 21, 22]. However, published plasma spectra from these same devices show the presence of metallic species [6, 23] and even the use of dominating metallic spectral lines to calculate the plasma temperature [21]. On the other hand, other researchers describe their plasma in terms of metal vapour [24, 25].

7.2.2 That the plasma composition is described in such different terms may be due to differences in the plasma generator, but more likely differences in the bias placed on species within the plasma. The Author has shown that, by mass, the plasma is dominated by metal (Chapter 5, table 5.1), but dominated atomically by hydrocarbons (Table 6.1). However, the Author would wish to describe the plasma as *metallic*, due to the large role played by the metal vapour in propellant ignition (see Chapters 7 – 9). Those who hold that the plasma radiation is

dominant appear to describe the plasma as comprising high electrical resistance, hot hydrocarbons.

7.3 Capillary erosion and the vapour shield

7.3.1 One interesting assumption made early in CPG code development from as early as 1980 was that of the existence of a vapour shield between the capillary liner and the plasma. Powell and Zielinski [17] implied the existence of a thin boundary, δ at the interface but they take the limit as $\delta \rightarrow 0$ for their calculations. They cite Ibrahim in reference [26] who suggested this boundary being a possible reason for poor agreement between measured and calculated capillary plasma pressure. Mohanti and Gilligan [13] explicitly used such a boundary layer to reduce the heat flux reaching the capillary wall, thus reducing the ablation of the liner due to excessive radiation. This vapour boundary layer acted as a neutral-density optical filter – i.e. the brightness temperature of the plasma was given by the Stefan-Boltzmann radiation law at the temperature that of the hot core plasma, but reduced with an emissivity of around 0.3. Experimental measurements of ablation rates were later performed and an estimated 5 % of incident radiation was thought to be reaching the liner [27]. The vapour shield allowed a negative feed-back mechanism to control ablation rates: the ablation rate increased with plasma temperature, but this served to thicken the boundary layer and thus reduce the effect of the radiation. However, it has now been experimentally shown by the Author that the vapour shield acts as an optically dense material through which radiation from the core is not

transmitted. The brightness temperature at the plasma capillary liner interface is in fact that of the boundary itself (Figure 6.24). Further, it is argued by the Author (Chapter 4 Figure 4.26) that the temperature of the boundary layer is consistent with that of condensing copper at the capillary plasma pressures measured.

7.3.2 Edwards, Bourham and Gilligan [27] used the concept of a vapour shield in the context of radiation shielding of propellant during plasma propellant interactions. They cite this as being responsible for an angular dependence upon plasma propellant interaction test results [28]. The formation of optically thick boundary layers at the propellant surface is further explored by the Author in later Chapters, where flux incident upon the propellant surface has been measured in a similar fashion to that incident upon the capillary liner, using translucent propellant as a window.

7.3.3 Silvestre, Hensel and Darèe [29] used the *wall-stabilised arc* argument with radiation being the dominant ablation mechanism, although ablation rates were tied to the plasma exit velocity. Their argument is that, in the limiting case of zero exit velocity, the radiation reaching the wall and the radiation ablation will be at a maximum; as the plasma exit velocity increases, radiation is prevented from reaching the wall because it heats material ablated by other processes. The plasma flow velocity is said not to be able to exceed (pressure / density) $^{0.5}$ [30].

7.3.4 Jacob, Bouquet and Tortel [31] considered the mechanism involved in the radiation ablation process. They believed that the Planckian radiation destroys the carbon-carbon bonds in the polyethylene $(CH_2)_n$ chains to produce CH_2 radicals which subsequently heat up in the plasma. The binding energy of the carbon bonds is given as 3.6 eV. They suggest that the energy difference between the radiant energy incident upon the liner and the cool ablated material is lost in the dissociation process to the thermal component of the energy balance. The lack of any melting is offered as evidence for 'cold' ablation. Such specific action by the radiation must be through a process of photon absorption/excitation acting upon these bonds. The required photons would need to have energy of around 3.6 eV, and this corresponds to a wavelength of 340 nm. Figure 6.24 shows this to be the position of the peak radiation for the hottest plasma temperatures assuming a perfect Planckian emitter. However, there is a broad, strong copper absorption feature centred on 329 nm (Figure 6.2) that significantly reduces the energy available for such ablation by this method. Jacob, Bouquet and Tortel did not consider these aspects of their mechanism.

7.3.5 Hsiao, Phillips and Su [14] reported that their model, BISON, initially used radiation as the dominant heat transfer mechanism for the plasma-wall interaction. However, initial modelling was reported to show that such transfer was small to low temperature working fluids, used for the electrothermal liquid propellant concept. No reason was given for why it should be dominant in one case but small in another.

7.3.6 One interesting paper, by Hewkin and Figura [32], considered the plasma to be initially metallic from the exploding wires, but then ablation of polyethylene from the capillary liner sustained the discharge. However, this paper decided that the main energy transfer to the capillary liner was convective rather than radiative, in line with the Authors findings. This paper was based upon work done for Royal Ordnance by FGE. Ironically, this work was the forerunner to EDENET which now bases ablation upon radiative energy transfer! Powell and Zielinski [17] also suggested the possibility that the main erosion mechanism might be other than radiative, and proposed turbulent convection.

7.4 Magnetohydrodynamic pressure

7.4.1 Magnetic pinch and other effects are considered negligible for the plasma current typically used by ETC CPGs [14, 17, 33] since the peak current is usually less than 100 kA.

7.5 Energy budget

7.5.1 As stated at the beginning of Chapter 5, there is no reported work (to the Authors knowledge) concerning the experimental measurement of energy partitioning of CPG plasma, but some published work examines various CPG models.

7.5.2 In 1993, Mohanti and Gilligan [13] included in their model, USIBD, heating effects of friction as plasma accelerates along the capillary length. They suggested that friction provides as much as 6 % of the

plasma heating. Thus, the process would appear to play some role in changing the energy flux of plasma venting from the capillary, with kinetic energy being transferred into thermal energy. This effect is not included in EDENET as initial calculations suggested it to have a negligible effect on the CPG operation.

7.5.3 In the same paper, Mohanti and Gilligan suggested that the capillary plasma contained 69% of the discharged energy in the form of internal energy, with the remaining 31% comprising work done (11%) and radiation losses (20%). Oberle *et al* [34] gave similar figures from the same source model in 1997. This compares to with Authors estimation of 98.8% as internal energy and 1.2% as losses with calculated work done (0.7%) and measured radiation (0.5%). It would thus appear that the Authors' CPG is very efficient in comparison, or otherwise certain assumptions are incorrect. It would certainly appear that Mohanti and Gilligans' use of a vapour shield as a neutral-density optical filter could be open to question.

7.5.4 For the expanding plume, Katulka and White [35] used the model by Powell and Zielinski [17]. They suggested that approximately 70% of the energy would be transferred from the plume in the form of radiation, with the remainder being kinetic (no other forms were considered). The plasma was treated as a blackbody emitter. Such high estimations of radiative energy transfer were likely to have been due to estimations of plasma temperature, possibly based on the Boltzmanns' Plot method of

relative line intensity without recourse to the plasma emissivity (see Appendix A).

8 Summary of Chapter 6

8.1.1 This chapter has explored further the properties of capillary plasma generator plasma plumes. The existence of an initial plasma plume, small and transient compared to the main discharge plume, has been identified and studied. It is believed to originate from the premature evaporation of a small length of wire within the capillary nozzle and be subject to Lorentz forces, due to the asymmetrical magnetic fields at the nozzle. The species within this and the main plume that soon engulfs it have been studied through examination of the plasma spectra.

8.1.2 An attempt was made to measure experimentally the energy content of the expanded, cooled vapour/aerosol cloud. This was to confirm the findings from Chapter 5 that the losses due to radiative energy transfer are small, and the main process of energy transfer to the surroundings is via convective air mixing. However, although the attempt did successfully measure the energy content and good agreement was found with findings from Chapter 5, the results were invalidated by the Authors own argument that a secondary energy source had been overlooked: that of exothermic chemical reactions occurring during the air mixing phase. Evidence was presented in the form of spectra of both reactive species and products. It was argued that the chemical

energy available exceeded that discharged from the capacitor banks. As no qualitative estimation of the amount of reactants left at the time of the measurement could be made, the results were considered invalidated.

8.1.3 A second attempt was made to confirm the findings of Chapter 5. This time, modelling considered only convective energy transfer. The results of this both confirmed the findings of Chapter 5 and vindicated the rejection of the previous experimental attempt. The predicted expanded plume temperature and geometry were in excellent agreement immediately post discharge, but too cool later. This was interpreted as being due to the exothermic energy source omitted by the model. This is an important finding for future ETC modelling of energy transfers within the gun chamber, as it indicates both the importance of exothermic reactions and also the likely timescale for their consideration.

8.1.4 The re-use of CPG components was considered. Small but statistically significant trends were observed as the use of components increased. Such trends are likely to be due to capillary liner and rear electrode wear, and can be used to validate EDENET. It is interesting to note from Chapter 5 that no differences were detected in the external plasma properties with re-used components. This is a useful discovery as, since that time, components have been reused where possible during ETC experiments on the assumption that the plasma plume

properties were unaffected. This has considerably reduced the cost of some inert (i.e. inert propellant) ETC studies.

8.1.5 Further comparisons were made with findings from EDENET. It was reiterated that the predicted brightness temperature of the capillary plasma was too high, but then argued that this may not in fact be as important as first thought. Initially, the worry was that too much material would be ablated from the capillary components. However, the component ablation is well predicted for this experimental set-up, probably because other aspects of ablation are not considered (especially convective heat transfer). That the model returns the energy, and the mass loss is correct means that the predicted mass and energy flux exiting from the capillary may still be correct. Ideally the model would be investigated for improvement and a wider parameter range experimentally explored, but the resources need to be available.

8.1.6 Finally, a paper study was included for the CPG operation. This explored the issues of:

- plasma composition
- capillary erosion and a vapour shield concept
- magnetic effects and
- a survey of other energy partition analysis.

1 M. J. Taylor, "ET105 - Photography of an exploding wire", DERA unpublished report WSS/WX6/58-ETL/ERD003, January 1999

2 R. A. Marshall, "Properties of Copper and Hydrogen Plasmas", RARDE report R86/216, 1986

3 Pearse & Gaydon: Identification of Molecular Spectra, Chapman and Hall Ltd publishers, 1950

4 79th CRC Handbook of Chemistry and Physics, 10-34

5 Herzberg: Molecular Spectra and Molecular Structure I. Spectra of Diatomic Molecules, 2nd Edition, Princeton: Van Nostrand publishers, 1950

6 James M. Kohel, Lester K. Su, Noel T. Clemens and Philip L. Varghese, "Emission Spectroscopic Measurements and Analysis of a Pulsed Plasma Jet", IEEE Transactions on Magnetics, Vol. 35, 1, January 1999

7 M. J. Taylor, "ET133 – Estimation of the Energy Transferral from a Plasma Jet to the Surrounding Air", DERA unpublished report DERA/WSS/WS4/58-ETL/ERD009, April 2000

8 79th CRC Handbook of Chemistry and Physics, 6-1

9 79th CRC Handbook of chemistry and physics, 5-5

10 The Old Tannery, Kelston, Bath, BA1 9AN

11 DERA, Fort Halstead / S & C Thermofluids Plumes software enhancement and application Contract WSS/X4103 Modelling of a Plasma Flowfield – task 13

12 J. D. Dunnett and D. C. Swift, "Capillary Plasma Generator Modelling using EDENET: Final report on Phase 3 of Contract WSS/R6991", DERA internal report, May 2000

13 R. B. Mohanti and J. G. Gilligan, "Time Dependent Simulation of the Plasma Discharge in an Electrothermal Launcher", IEEE Transactions on Magnetics, Vol. 29, 1, January 1993

14 C. C. Hsiao, G. T. Phillips and F. Y. Su, "A Numerical Model for ETC Gun Interior Ballistics Aapplications", IEEE Transactions on Magnetics, Vol. 29, 1, January 1993

15 R. Alimi, C. Goldenburg, L. Perelmutter, D. Melnik and D. Zoler, "The Effect of External Pressure on the Plasma Parameters in Ablative Capillary Discharges", IEEE Transactions on Magnetics, Vol. 35, 1, January 1999

16 A. W. Williams and K. J. White, "Plasma-Propellant Interactions Studies: Measurement of Heat Flux Produced by Hydrocarbon Ablation-Supported Plasmas", IEEE Transactions on Magnetics, Vol. 35, 1, January 1999

17 J. D. Powell and A. E. Zielinski, "Capillary Discharge in the Electrothermal Gun", IEEE Transactions on Magnetics, Vol. 29, 1, January 1993

18 W. F. Oberle and G. P. Wren, "Further Studies Concerning the Energy Distribution in the ETC Closed Chamber And The Impact On Observed Propellant Burn Rate", IEEE Transactions on Magnetics, Vol. 37, 1, January 2001

19 M. J. Nusca, M. J. McQuaid and W. R. Anderson, "Development and Validation of a Comprehensive Model of the Plasma Jet Generated by an Electrothermal-Chemical Igniter", 19th International Symposium of Ballistics, Interlaken, Switzerland, May 2001

20 L. Perelmutter, M. Sudi, C. Goldenberg, D. Kimhe, Z. Zvi, S. Arie, M. Melnik and D. Melnik, "Temperature Compensation by Controlled Ignition Power in SPETC Guns", 16th International Symposium on Ballistics, San Francisco, CA, September 1996

21 J. Caillard, C. delzarra and L. Brunet, "Experimental Assessment of a 1 kJ Electro-pyrotechnic Device Ignited in the 300-1000 V Range for ETC Studies", IEEE Transactions on Magnetics, Vol. 37, 1, January 2001

22 J. Ashkenazy, "The Effect of the External Pressure on the Internal Conditions Inside the Discharge Tube", IEEE Transactions on Magnetics, Vol. 29, 1, January 1993

23 R. Alimi, A. Borenstein, C. Goldenberg, L. Perelmutter, A. Pokryvailo, N. Shafir, S. Wald, E. Weiss, D. Zoler and M. Shapira, "ETC Research at Soreq NRC, Israel, IEEE Transactions on Magnetics, Vol. 37, 1, January 2001

24 A. A. Bogomaz, A. V. Budin, V. A. Kolikov and Ph. G. Rutberg, "Powerful Pulse Generator of Dense Plasma with High Concentrations of Metal Vapour", Int. J. Impact Engng. 17, pp 93-98, 1995

25 L. L. Raja, P. L. Varghese and D. E. Wilson, "Modelling of the Electrothermal Igniter Metal Vapour Plasma for Electrothermal-chemical Guns", IEEE Transactions on Magnetics, 33, 1, January 1997

26 E. Z. Ibrahim, "The Ablation Dominated Polyethylmethacrylate Arc", J. Phys. D:Appl. Phys., 13, p 2045, 1980

27 C. M. Edwards, M. A. Bourham and J. G. Gilligan, "Experimental Studies of the Plasma-propellant Interface for Electrothermal-chemical Launchers", IEEE Transactions on Magnetics, Vol. 31, 1, January 1995

28 M. A. Bourham and J. G. Gilligan, "Analysis of Solid Propellant Combustion Behaviour under Electrothermal Plasma Injection for ETC Launchers", IEEE Transactions on Magnetics, Vol. 33, 1, January 1997

29 N. Silvestre, D. Hensel and K. Darèe, "A Comprehensive, Numerical Model of Electro-thermal Propulsion", IEEE Transactions on Magnetics, Vol. 29, 1, January 1993

30 P. Kovitya and J. J. Lowke, "Theoretical Predictions of Ablation-stabilised Arcs Confined in Cylindrical tubes", J. Phys D, 17, pp 1197 – 1212, June 1984

31 E. Jacob, S. Bouquet and B. Tortel, "A Global Theoretical Approach for the Electrothermal Gun: Scaling Laws and a 0-D Time-dependent Model", IEEE Transactions on Magnetics, Vol. 31, 1, January 1995

32 D. Hewkin and E. Figura, "Fundamental Research and Numerical Modelling of the Ballistics of Electrothermal Chemical Guns", IEEE Transactions on Magnetics, Vol. 29, 1, January 1993

33 D. A. Benson and S. N. Kempka, "Studies of Confined High-pressure Discharges in an Electrothermal Capillary", IEEE Transactions on Magnetics, Vol. 29, 1, January 1993

34 G. L. Katulka, W. F. Oberle, G. P. Wren, J. Okamitsu and N. A. Messina, "Pulsed-power and High Energy Plasma Simulations for Applications to Electrothermal-chemical Guns", IEEE Transactions on Magnetics, Vol. 33, 1, January 1997

35 G. L. Katulka and K. J. White, "Characterisation of High-energy Plasma for the Electrothermal-chemical Propulsion Concept", 16th Internal Symposium on Ballistics, San Francisco, CA, 23-28th September, 1996

Chapter 7 – Plasma propagation and ignition studies: Theory and initial experimentation

1 Introduction

1.1.1 Chapters 5 and 6 were mainly concerned with the expansion of a plasma plume in free air. The CPG, however, is designed to vent into a gun chamber packed with gun propellant. The energy transfer mechanisms studied so far may be useful for code validation, but may be very different from those occurring within a propellant bed in a gun chamber.

1.1.2 This and the remaining Chapters mainly aim to investigate the nature of energy transfers occurring as the plasma expands into a densely packed propellant bed with initial conditions at STP. Inert material was used as an energetic propellant substitute in much of the work described in these Chapters to simplify measurement techniques and experimental apparatus.

1.1.3 This Chapter introduces the Author's hypothesis that the prime energy transfer process from the plasma to the solid propellant leading to propellant ignition is via a mechanism of metallic vapour deposition. The experiments described in this and following Chapters to test the hypothesis used small quantities of solid propellant both in open air and within closed vessels. The use of translucent propellant has allowed the radiative flux incident on the surface of propellant grains to be determined, and enabled estimations to be made of the heating effect on the grains. Measurements of deposition thickness, together with estimations of condensation rates have allowed the same to be done

for vapour deposition. Thus, the effects of metallic vapour deposition and radiative energy transfer on grain heating are compared quantitatively. In addition, experimental measurements have been made of the radiative flux from conventional igniters. The theory and ideas leading up to the hypothesis for ignition by metallic vapour deposition are described in this Chapter. Some experimentation and calculations have been included to show how such a process of ignition compares with that of a standard gunpowder igniter.

1.1.4 Again, all work within this Chapter is original and was undertaken by the Author, unless stated otherwise.

2 Early propagation studies

2.1 Open air studies

2.1.1 In the early stages of the Author's studies into ETC energy transfers, residual deposition was noticed occurring on plasma generator components and test equipment following ETC plasma discharges. Further, close inspection of displays from other researchers in the field at symposia both in the past [1] and more recently [2] showed the same types of residue. Direct vapour deposition has been used successfully by Kevin E Moran [1] to record the plasma event on paper. Figure 7.1a shows a photograph of his wire exploding against white paper card and Figure 7.1b provides the result. Note the radial geometry of the plasma in Figure 7.1a and how this is recorded on the paper in Figure 7.1b.

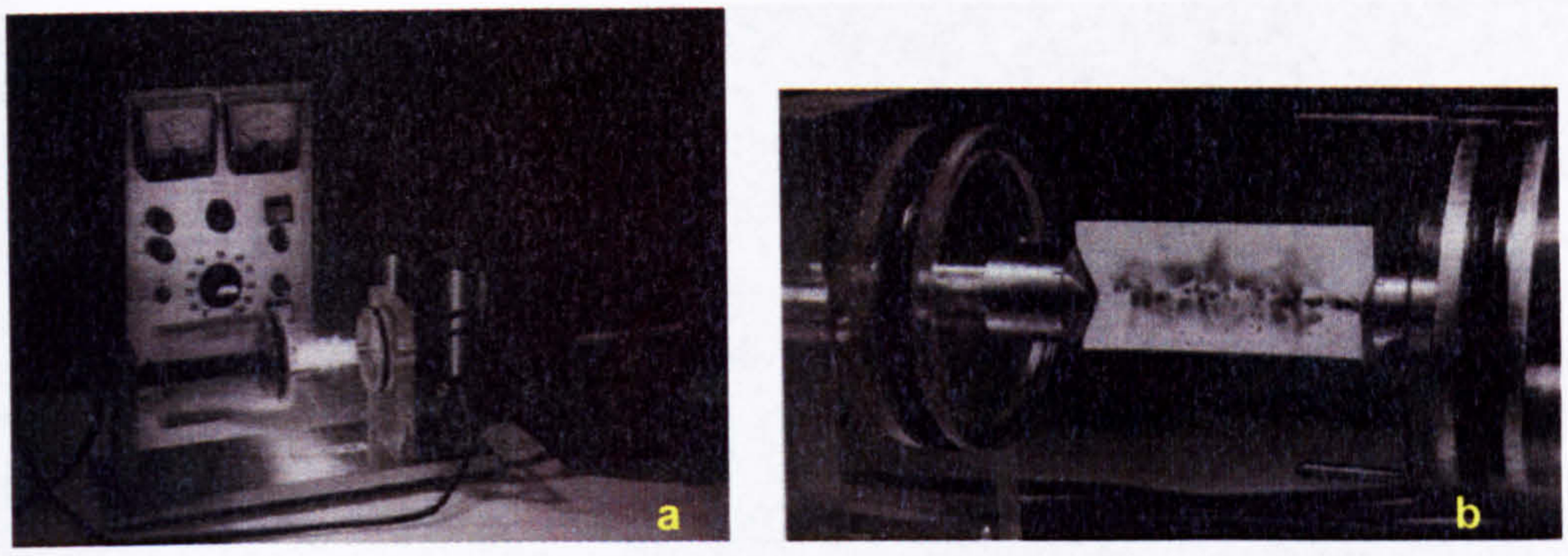

Figure 7.1 Record of plasma by direct vapour deposition (K E Moran [1])

2.1.2 In response to questions on the nature of this residue, the answer invariably has been it consisted of sooty carbonised deposits. However, this answer was inapplicable to plasma deposits from exploding wire experiments in open air, with deposition on metallic components because no carbon was involved. To the Author, the deposits seemed to be oxides of copper similar in appearance to carbon. It became clear that such deposits might be useful not only in the study of plasma propagation but could transfer considerable energy to surfaces during the condensation phase.

2.1.3 Initial tests of plasma propagation used large sheets of white card held close to plasma generators. Figure 7.2 illustrates the results from one such test. The plasma generator in this case consists of a pair of vertical poles around 150 mm apart, with a 0.7 mm diameter copper wire strung between them. The card was placed in a vertical plane, 75 mm behind the wire. Drawn on the card is the approximate location of the poles and wire. The left pole was the cathode and the right the anode: a small hole at the top of the anode through which the wire was strung is also depicted. The multi-coloured deposit can be clearly seen.

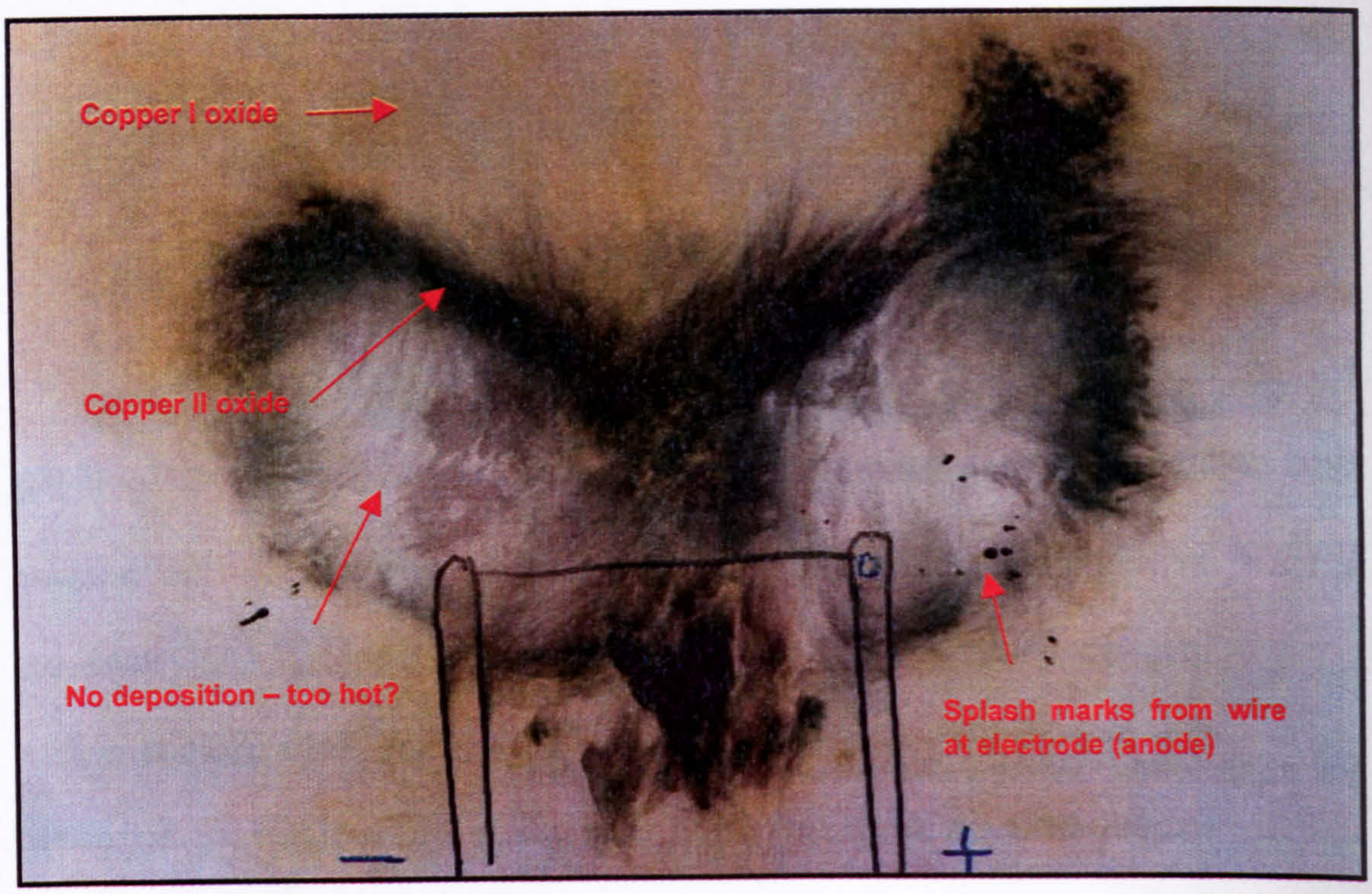

Figure 7.2 Plasma residual deposition from an exploding wire in air on card

2.1.4 Analysis of this deposition material is discussed later, but it was found to be metallic. Further deposition onto a glass plate clearly showed that metallic copper lay beneath the oxide deposits. A residual coating composed of black copper II oxide (CuO) and red/brown copper I oxide (cuprous oxide, Cu_2O) can be seen in Figure 7.2. Copper II oxide is the more stable of the two compounds but copper I oxide would be expected to form preferentially in an oxygen-deficient environment. Further, copper I oxide decomposes at around 2000 K [3], whilst copper II oxide exists at higher temperatures. Hence, the boundary between the black and red/brown oxides could mark a temperature boundary within the cooling, oxygen-deficient vapour cloud, the red/brown copper I oxide forming preferentially but only when the ambient temperature falls below 2000 K. Also noticeable in these tests

was the absence of a deposit close to the exploding wire. This might be due to the plasma being too hot and turbulent for condensation to occur.

2.1.5 When rubbed, some of the deposit is removed very easily but some remains firmly coated to the surface. Later work with polyethylene discs required mechanical skimming to remove this firm coating. The initial deposition is thought to occur through vapour condensation, with a secondary loose coating from an aerosol. In Figure 7.2, the black copper II oxide was found to be mainly firm, whilst the copper I oxide was much looser. The metallic nature of the coating immediately in contact with the surface, as shown by the glass plates, suggests that oxidation of the initial coating occurs after deposition. The loose nature of some of the copper II oxide and most of the copper I oxide suggests that the secondary coating is already oxidised, at least on the liquid drop surface.

2.1.6 Also of interest in Figure 7.2 is the appearance of splash marks. These are burns from larger liquid copper droplets, thought to originate at the electrodes. Several turns of copper wire are wrapped around the electrode and then twisted together, and it is believed that material from this wire is ejected from the vicinity of the electrodes through Lorentz or other forces. Video clips show sparks emanating from the wire connections to electrodes. Figure 7.3 is an x-radiograph image capturing one such piece of wire in the process of ejection [4].

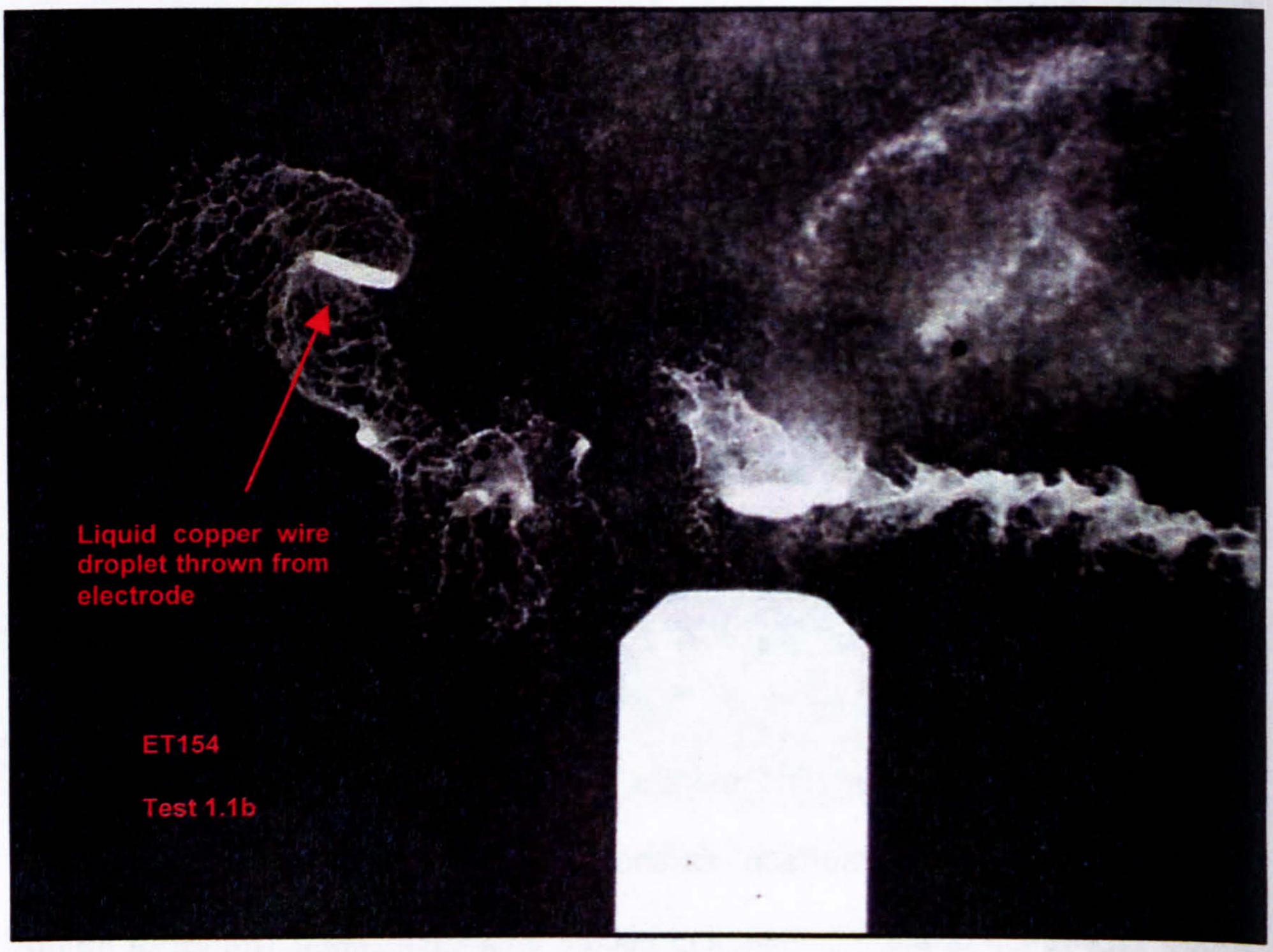

Figure 7.3 X-radiograph of exploding wire in air, capturing ejected liquid copper

2.1.7 The method of deposition onto card has been used to study the propagation of plasma in air not only for wires on vertical poles but also for capillary plasma generators and discharge rods. Besides details of the plasma propagation, it also shows the potential for damage to components close to the plasma generators from the various plasma discharges. Figure 7.4 shows the destruction of a card for a distance of around 120 mm when held close to the nozzle of a CPG [5]. No such damage occurs with other types of plasma generator because the plasma is pressurised within the capillary and builds up a high exit velocity, focused onto one small area. This does not occur with other plasma generators, for which the plasma velocity is not necessarily

lower but the kinetic energy spreads over a much wider area. The damage caused to the card by plasma jets gave an early indication of the potential damage to propellant within a gun chamber.

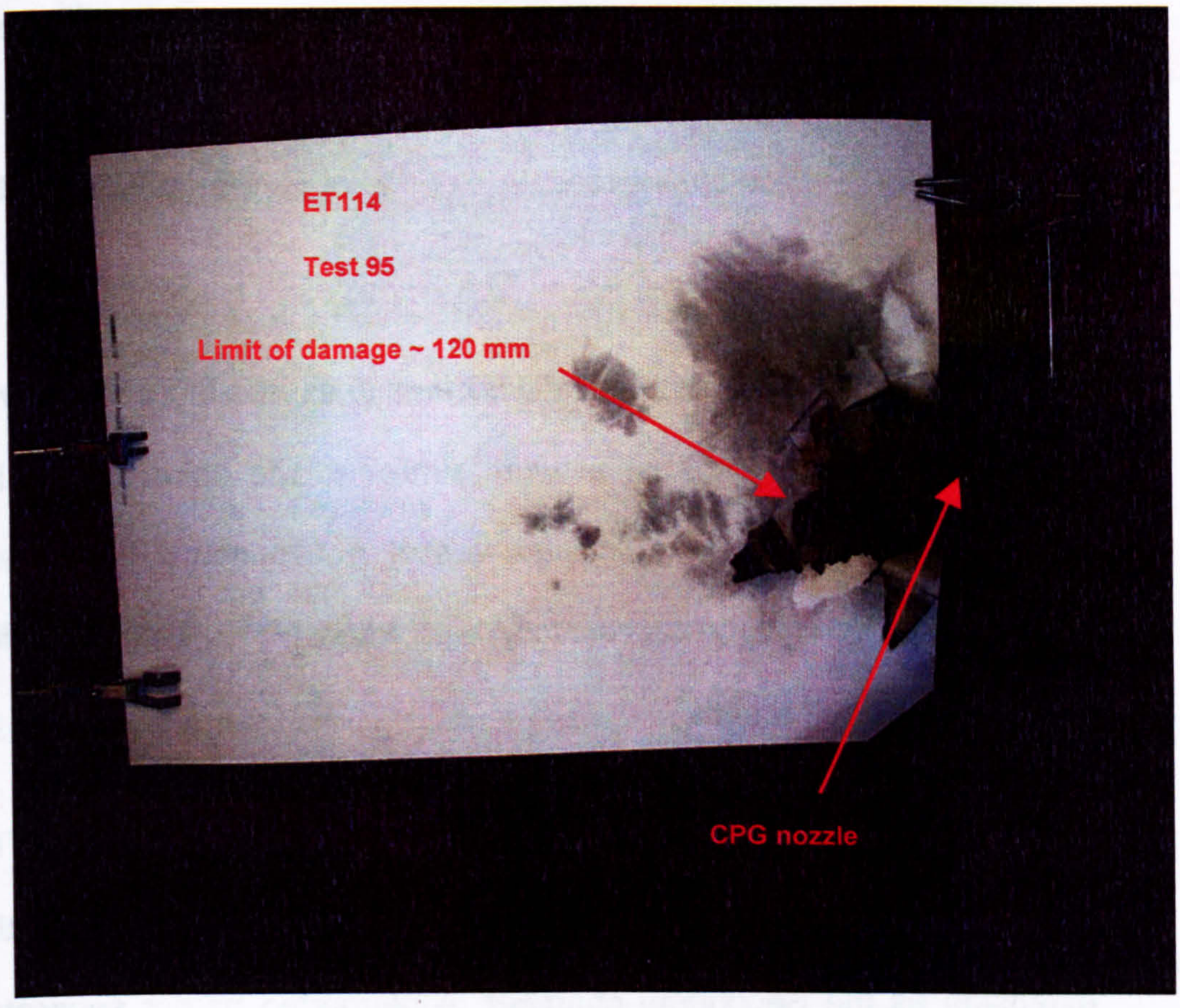

Figure 7.4 Damage to card from plasma jet originating from a CPG

2.2 Closed chamber studies – ignition energy transfer mechanisms

2.2.1 Following the success of the open air deposition studies, some closed vessel work was undertaken in the Universal vessel (a chamber with a volume of around 400 cm^3, used for much of the small-scale ETC studies). This chamber is designed to link up with capillary plasma generators, discharge rods, 'current injection' exploding wires, as well as a number of conventional powder igniters. It can be used as a closed bomb, in which pressure is released slowly, or as a vented

vessel with a thin fitted disc designed to rupture at a given pressure and quickly depressurise the chamber. Further, this vessel can have a 30 mm gun barrel fitted to permit small calibre ETC gun firings. Ports around the vessel allow access for various instrumentation (e.g. pressure transducers), powder igniter initiators and vent plugs. In addition, an extension chamber is available to double the volume of the Universal vessel.

2.2.2 The aim of this early closed vessel work was to assess the possibility of conducting plasma propagation work similar to the open air studies described above but in a closed vessel environment. Work was performed at STP very successfully, but extension to pressurisation failed to give good results.

2.2.3 The experimental arrangement is depicted in Figure 7.5 [6]. The Universal chamber is labelled as the Primary chamber, with the extension as the Secondary chamber. A perforated barrier separates the two to prevent the wedge and propellant from entering into the Secondary chamber, whilst allowing gas and plasma to propagate freely between the chambers.

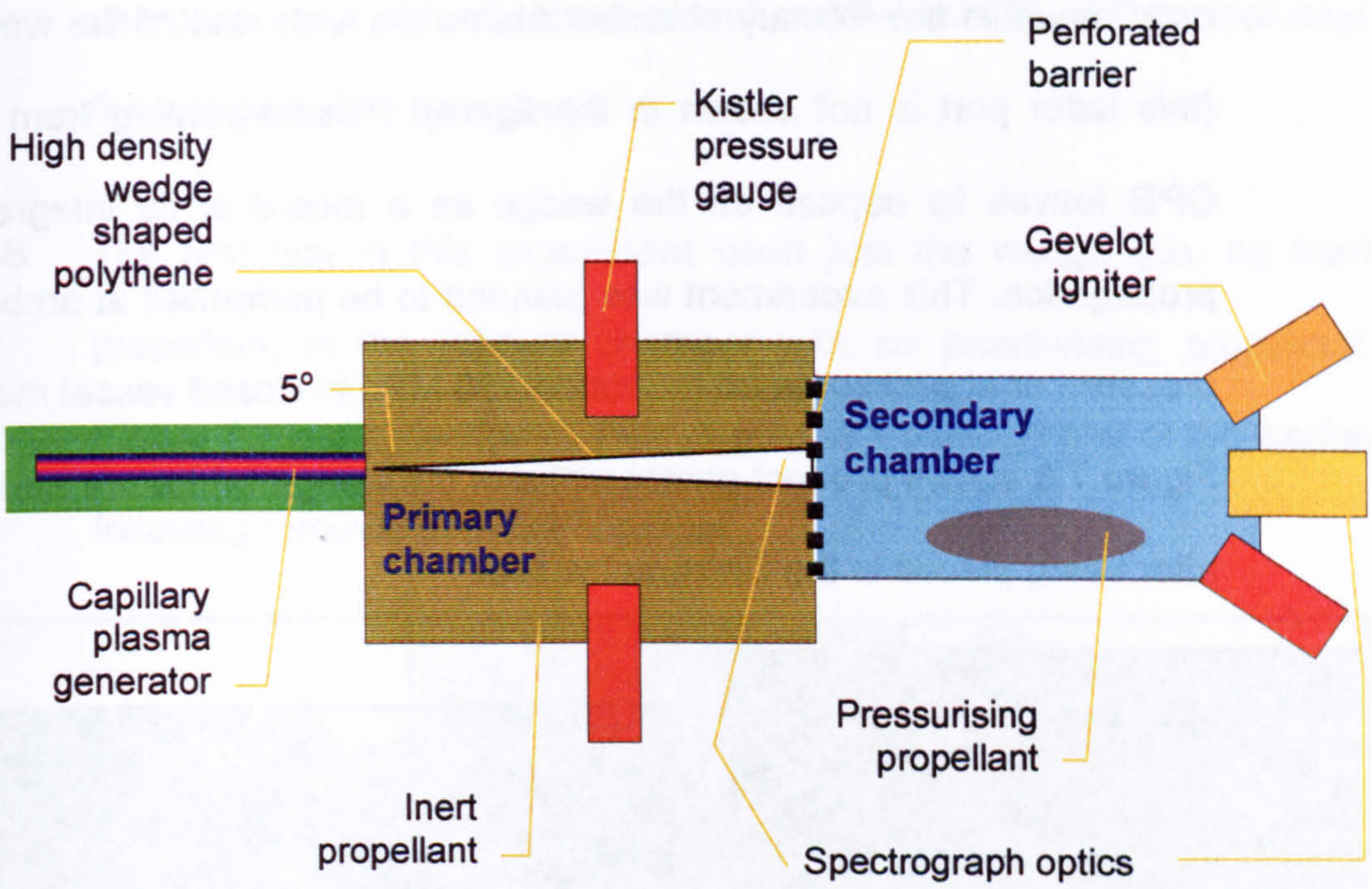

Figure 7.5 Experimental arrangement for early closed vessel propagation studies

2.2.4 Inert propellant is packed tightly into the Primary chamber around a polyethylene wedge (the wedge has a 5° angle). The narrow end of the wedge fits into a slot in the CPG nozzle, whilst the wide end of the wedge is pressed against the perforated barrier between the two chambers. The secondary chamber contains pressurising energetic propellant (optional) that can be ignited by a 'Gevelot' gunpowder percussion ignition system (the percussion is initiated by a small precursor gunpowder charge, set off in turn by a heated electric element). Three 'Kistler' quartz pressure transducers record the pressure at two co-planar positions in the primary chamber and at one position in the secondary chamber. Finally, the spectrograph can record time-resolved spectra through a sapphire window fitted into the Secondary chamber (with the instrumentation port shown in the figure)

or from within the Primary chamber above the wide end of the wedge (this latter port is not shown in the figure). Plasma venting from the CPG leaves its deposit on the wedge as a record of its integrated propagation. This experiment was planned to be performed at ambient pressure or at pressures up to around 150 MPa in closed vessel mode. Figure 7.6 shows pre-test photographs of the wedge (a) before and (b) after being placed in the Universal vessel.

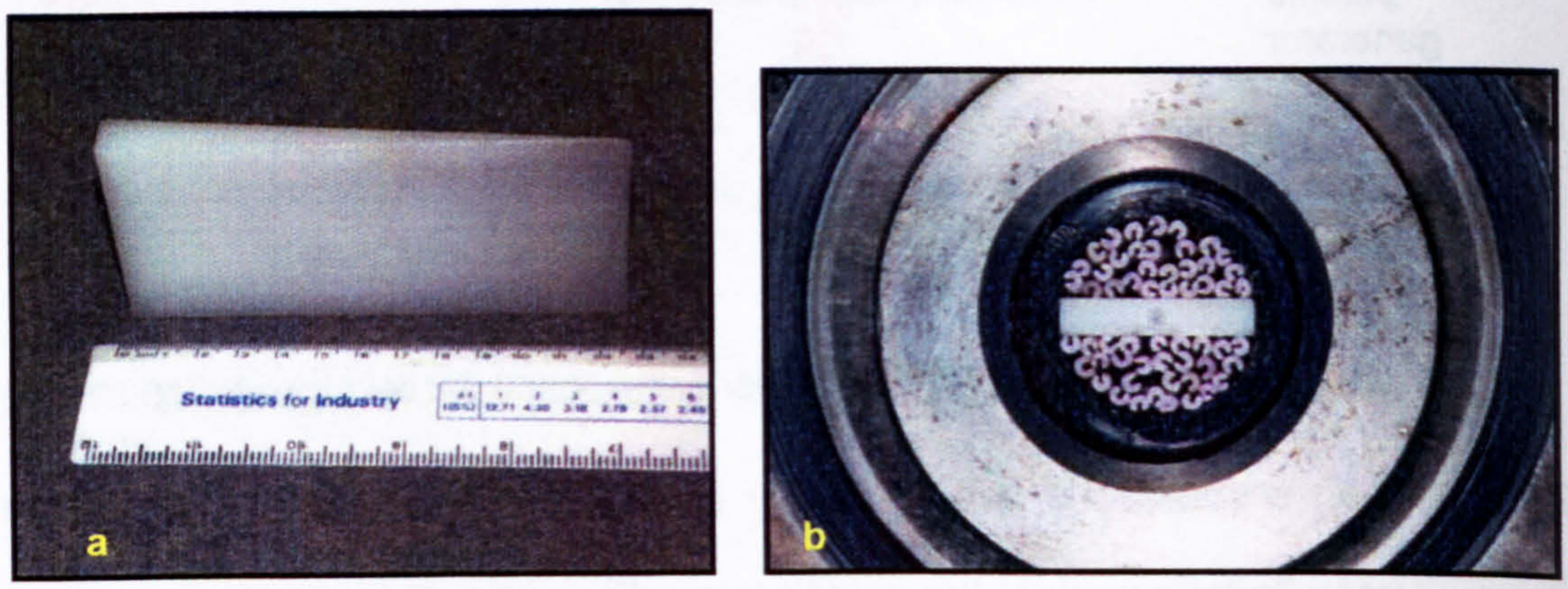

Figure 7.6 Polyethylene wedge (a) before and (b) after insertion into the inert propellant bed

2.2.5 The inert slotted stick propellant can be seen in Figure 7.6b along with the wide end of the wedge prior to the Secondary chamber being fitted. The number and location of inert sticks in the Primary chamber was controlled in these tests, but no effort was made to align the slots in the propellant or reproduce their orientation from test to test. (The instrumentation port for spectroscopy in the Primary chamber is located to the right of the wedge, hidden by the wedge in Figure 7.6b, and around 1 cm into the chamber.) The wedges were unintentionally made around 3 mm too long, so each had to be cut down at the sharp end when loaded into the chamber. This worked well because the original

sharp end was actually too thin and malleable. Figure 7.6a indicates the wedge before being cut.

2.2.6 The first test in this experiment used just the wedge (i.e. no inert propellant) in the Primary chamber with no pressurising propellant. Figure 7.7 is a collection of various post-test photographs of the wedge following removal from the chamber.

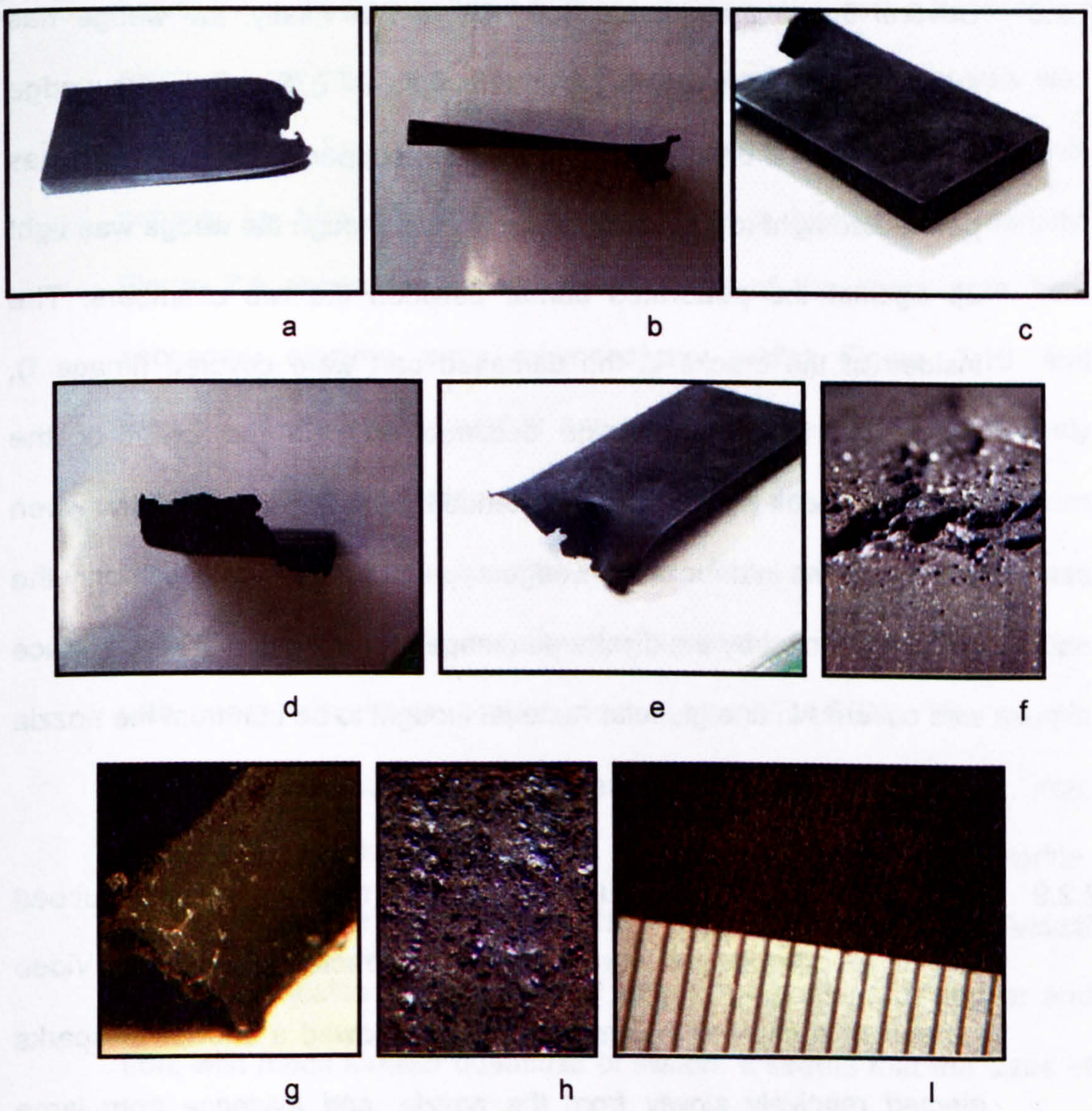

Figure 7.7 Photographs of post-test wedges with no inert or pressurising propellant

2.2.7 The CPG and discharge parameters were reasonably similar to those defined in Chapters 5 and 6, i.e. a 10 mm diameter, 150 mm long polyethylene capillary with a 0.7 mm diameter tinned copper wire. One module of the capacitor bank was fitted with a 26 μH inductor and charged to 10 kV: around 30 kJ of electrical energy were discharged in 0.8 ms.

2.2.8 Several things are notable from Figure 7.7. Firstly, the wedge has suffered damage at the nozzle end (images a – f). Secondly, the wedge is covered in a uniform coating of black copper (II) oxide, which has permeated right to the back (image c) even though the wedge was tight up against the perforated barrier between the two chambers. The insides of the cracks in the damaged part were covered (image f), suggesting that the damage occurred early in the event or the deposition took place over an extended period of time. Thirdly, when cut in two, the interior of the wedge appeared unchanged, with only the surface affected by the discharge (image g). Finally, the wedge surface was covered in fine globular material thought to be iron from the nozzle (images h and I show a 0.5 mm scale up against the surface).

2.2.9 The CuO coating was difficult to remove, but the larger globules rubbed off with a soft cloth and were found to be attracted to a magnet. Video footage of a capillary plasma jet into air showed a shower of sparks ejected relatively slowly from the nozzle, and evidence from large calibre gun firings has shown that nozzle erosion causes the barrel

diameter to reduce. These globules, sparks and the barrel diameter reduction are all linked to molten iron ablated from the iron nozzle. The solution to this ablation has been an extension of the high density polyethylene capillary to the nozzle exit, with an external annular electrode. (It is interesting to note that modern Israeli ETC CPGs use the same technique, possibly for the same purposes [7].)

2.2.10 Figure 7.8 is a high resolution atomic number image from a backscatter electron x-ray microanalysis of the wedge sample. This analysis was performed at Fort Halstead under the Author's instruction but not actually by him. The bright objects have a high atomic density. Figure 7.9 shows the topographical image of the same area from secondary electron x-ray microanalysis, whilst Figure 7.10 and Figure 7.11 are atomic number and topographical images respectively taken at a lower resolution. The 10 μm and 50 μm reference lines can be seen on each respective image. The wedge sample was qualitatively analysed for metals using a scanning electron microscope with energy dispersive x-ray microanalysis (SEM-EDX). The sample comprises a background predominantly of carbon, with copper, iron, silicon and much smaller quantities of potassium, sulphur and chlorine. Oxygen cannot be detected using this equipment. Analysis of individual globules indicates the presence of varying proportions of copper and iron, with much smaller quantities of silicon. It seems that the sizes of the globules range down to the sub-micron level (the limit of the detector).

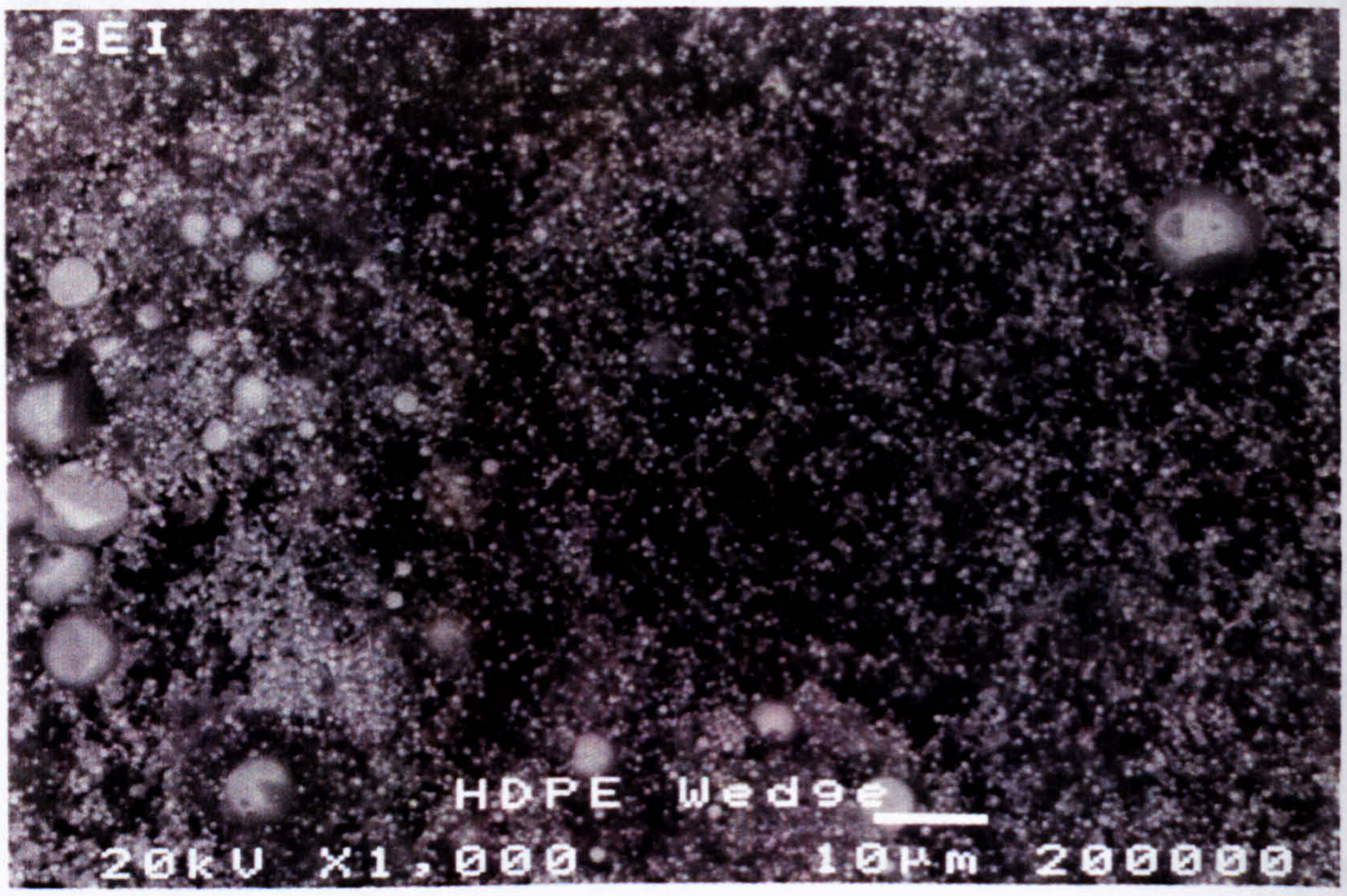

Figure 7.8 High resolution atomic number image of post-test wedge surface

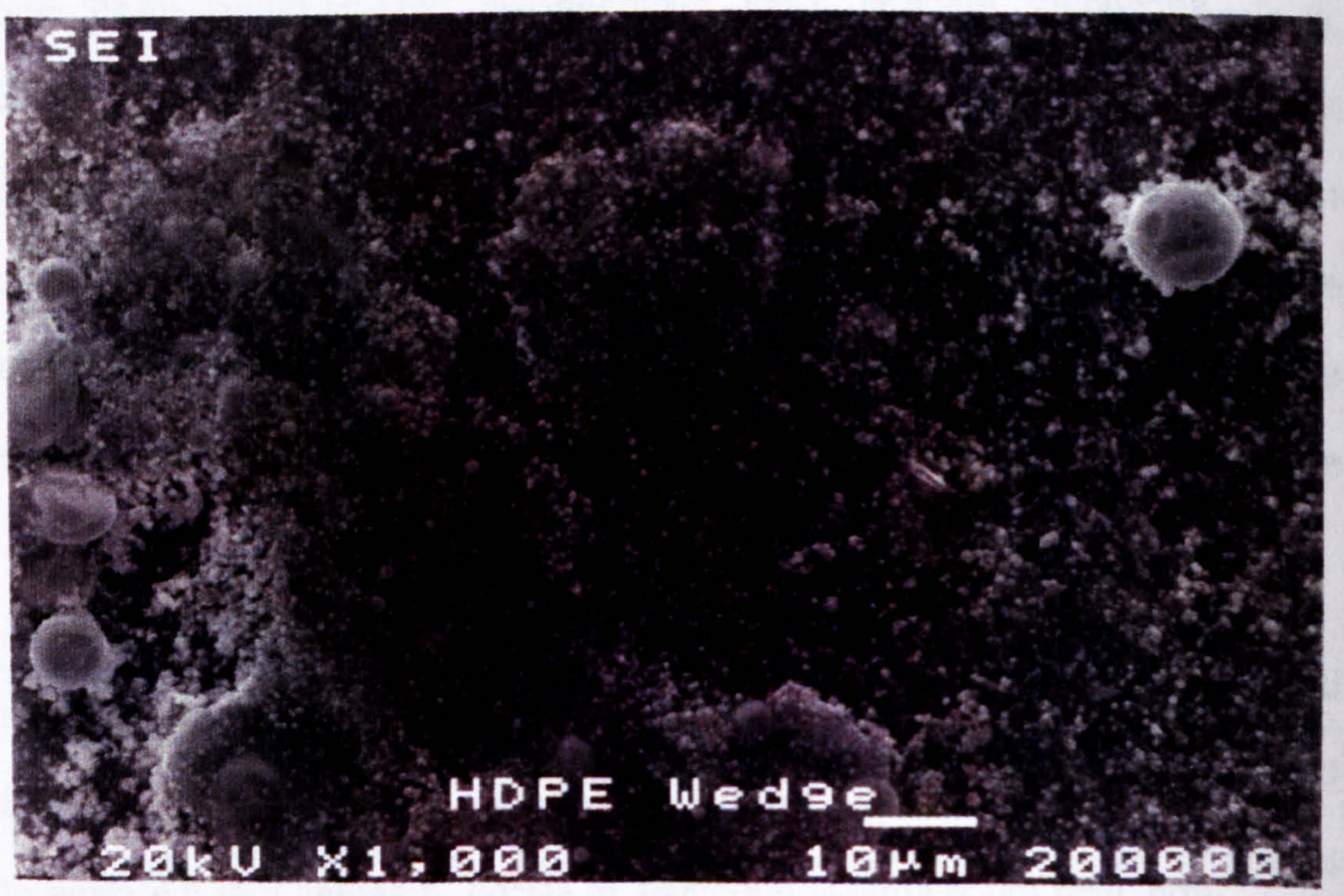

Figure 7.9 High resolution topographical image of post-test wedge surface

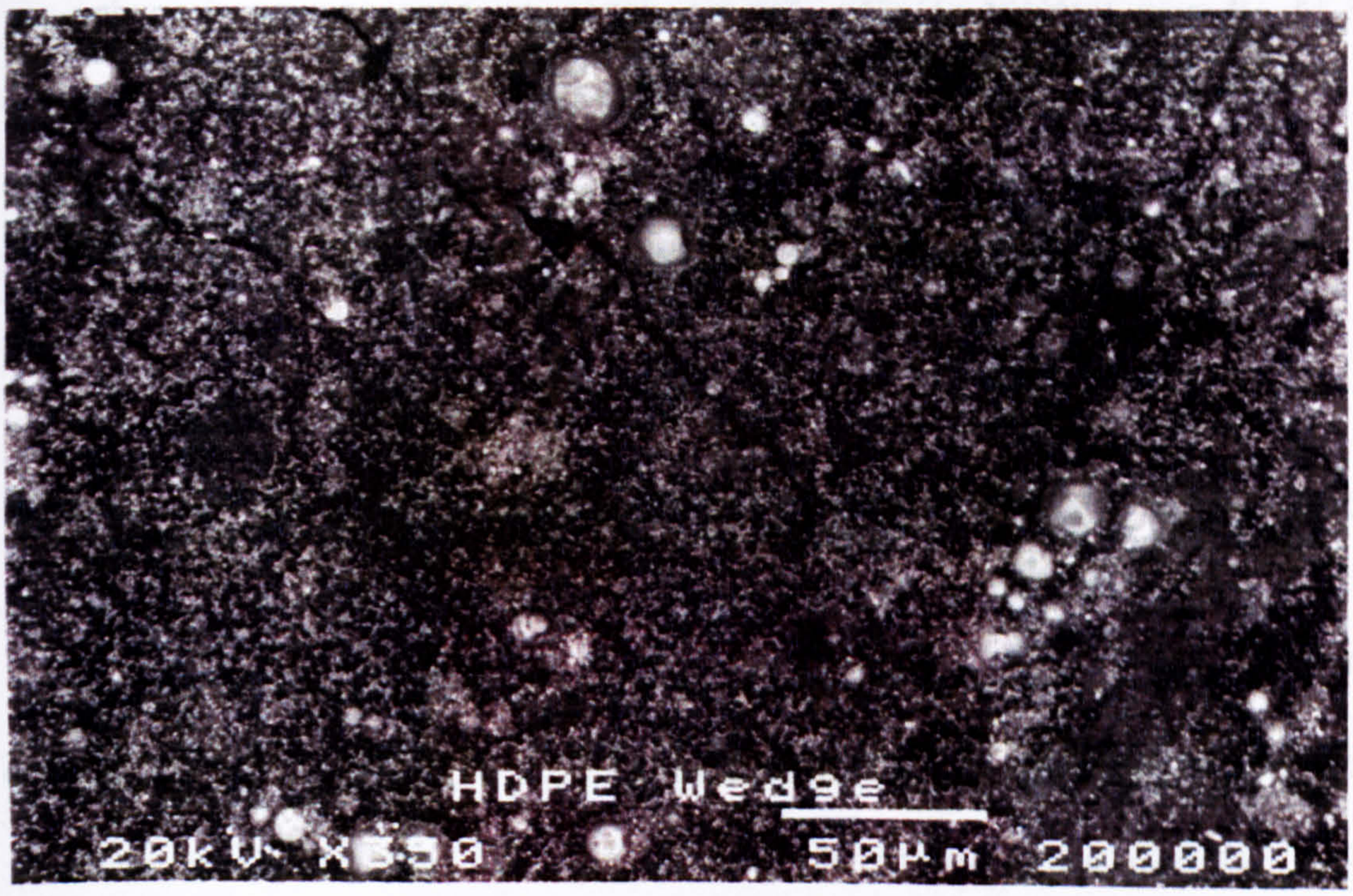

Figure 7.10 Low resolution atomic number image of post-test wedge surface

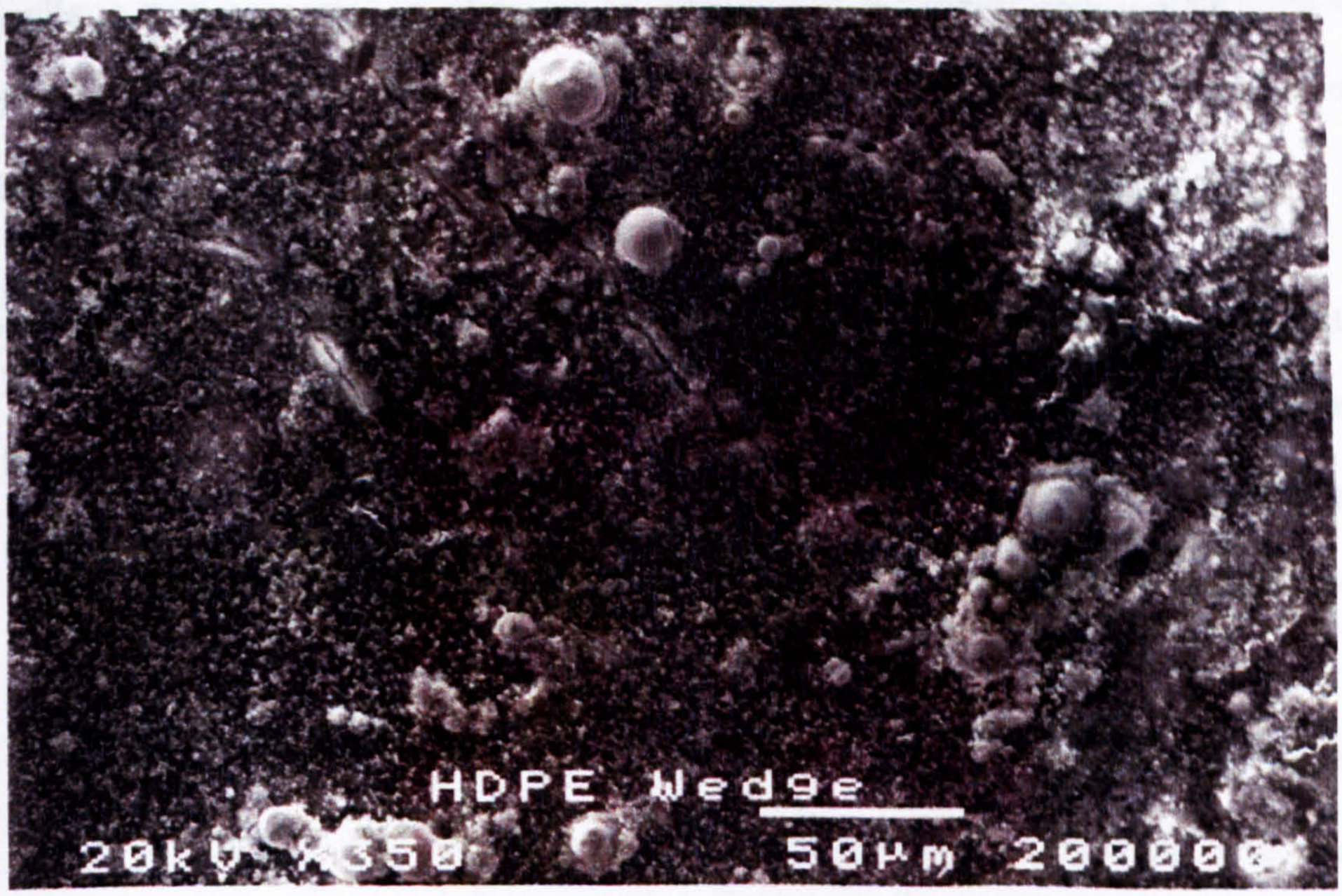

Figure 7.11 Low resolution topographical image of post-test wedge surface

2.2.11 It was unclear whether the condensation process was dropwise or filmwise, or if the globules originated from the nozzle and then ended up upon the condensed layer of filmwise condensed copper. The latter would tally with the drops moving at a much slower pace than the capillary copper plasma.

2.2.12 In the second test, 56 sticks of inert slotted stick propellant were packed around both a new wedge and the plasma from the CPG. When the chamber was opened after the test, the wedge and sticks had not moved from their original positions. A coating of plasma residue was apparent on the rear face of both the grains and the wedge, which had been pressed against the perforated barrier. Upon dismantling, the wedge appeared to be uniformly covered in a coating of copper (II) oxide, apart from some stratification where inert propellant had probably been pressed hard to the surface. The end of the wedge closest to the CPG was again damaged: Figure 7.12 shows the wedge with the stratification and damage at the thin end. The damage was less severe than in Test 1, probably due to the support from the inert propellant. Some of the propellant sticks were also damaged around the nozzle area.

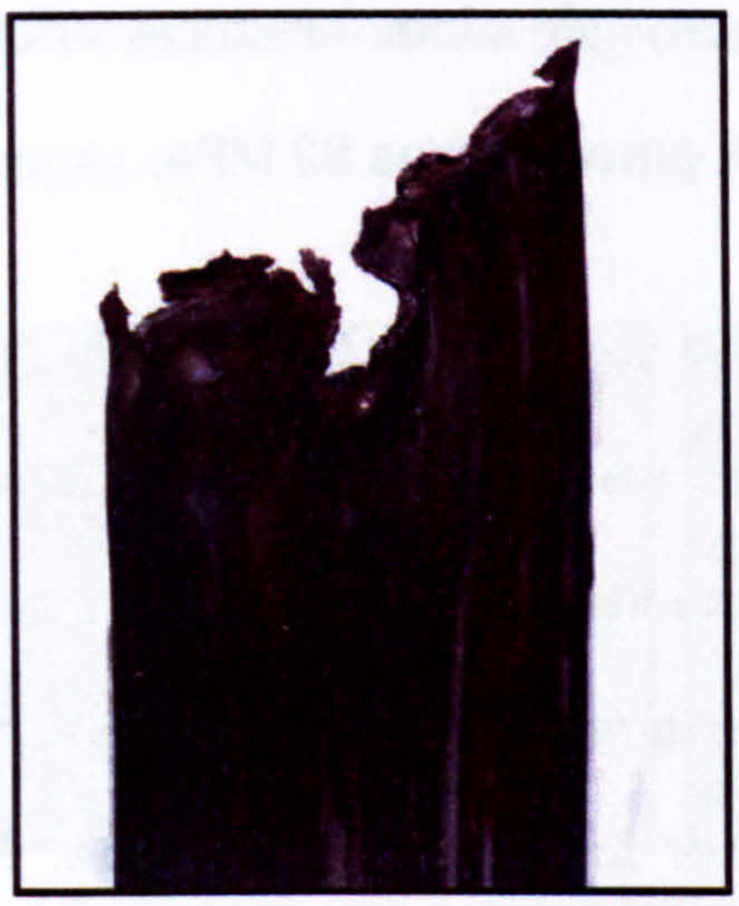

Figure 7.12 Wedge after Test 2

2.2.13 The next test was designed to investigate the situation when the chamber was pre-pressurised, and involving new inert propellant and a new wedge. 50 g of standard gun propellant was chosen and placed into the Secondary chamber, together with a further 1 g of gunpowder to aid ignition. Even so, the propellant failed to ignite and a mis-fire drill was carried out.

2.2.14 Test 4 was a repeat of the mis-fired Test 3, this time with 3 g of gun powder to aid ignition. Care was taken to heap the propellant around the igniter within the secondary chamber and the propellant successfully ignited in this test. Inspection of the pressure data shows that pressure did not start to rise until around 55 ms, remaining at 1 MPa for some time. 10% peak pressure (a standard figure for measuring ignition delay) was achieved after a further 65 ms. The initial rise of 1 MPa at 55 ms is taken to mark gunpowder ignition in the chamber; the pressure appears along with Test 14 results in

Figure 7.20. Nearly 30 kJ of electrical energy were discharged at 65 MPa and peak pressure was 82 MPa.

2.2.15 On dismantling the vessel after the test, care was taken to keep intact the integrity of the wedge and inert propellant. Figure 7.13a indicates the condition of the inert propellant with the wedge still inserted into it. The sticks were charred and there was no sign of copper (II) oxide on either the sticks or the side of the wedge. Figure 7.13b shows the wedge with the top portion of the inert propellant removed. The black residue comprised large loose particles, thought to be carbonised deposits. No firm copper deposits were visible on brushing the wedge, but there was damage to its nozzle end similar to that in Test 2, indicating that plasma had discharged.

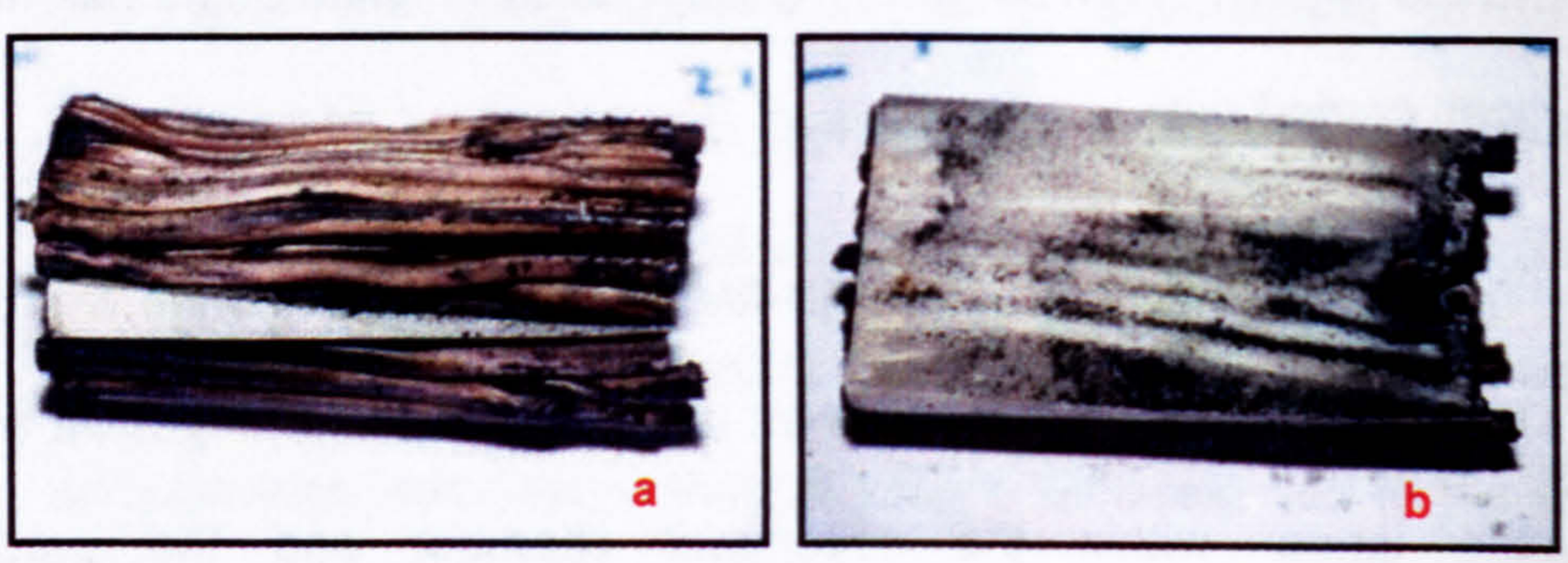

Figure 7.13 Wedge and inert propellant after Test 4

2.2.16 Figure 7.14a illustrates the nozzle after Test 4. As indicated, the nozzle has been closed at some moment during the test, but it is unclear whether it became closed before, during or after the discharge. Figure 7.14b shows a deposit sample found loose within the capillary and Figure 7.14c shows the bisected capillary. A widening of the

capillary diameter near to the nozzle suggests that a blockage formed during the discharge.

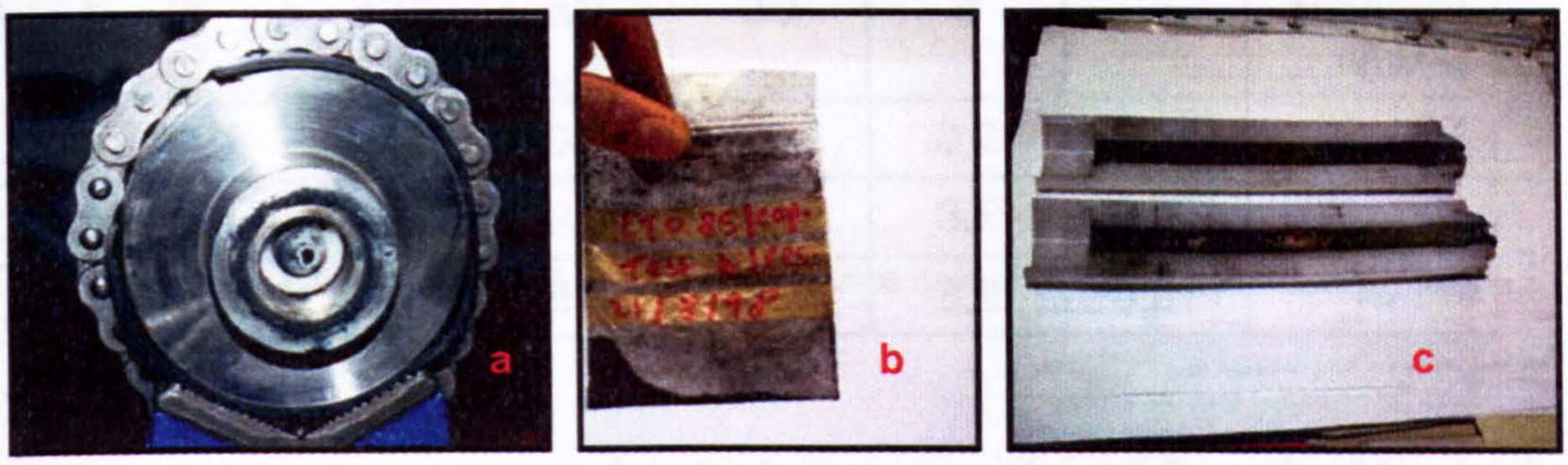

Figure 7.14 Dismantling Test 4 components after discharge at 65 MPa

2.2.17 The sample in Figure 7.14b was qualitatively analysed for metals using scanning electron microscopy with energy dispersive x-ray microanalysis (SEM-EDX). Copper, (Cu) potassium, (K) calcium, (Ca) tungsten, (W) and iron, (Fe) were identified in the sample. A Leco CS344 measured the amount weight by weight (w/w) of carbon and sulphur present in the sample and an ARL 3410 inductively coupled plasma atomic emission spectrometer (ICPAES) was used to quantify Cu, K, Ca, W, S and Fe. These quantitative analyses were carried out in duplicate. Again, this work was instigated by the Author, but carried out by Fort Halstead staff.

2.2.18 Table 7.1 contains the results of this analysis. The poor reproducibility between the duplicate analyses A and B for some elements indicates that the sample was not homogeneous. Insufficient time was available to determine the oxygen content, the density or to examine the sample for discrete particles. However, 82.3% w/w of the sample had been accounted for with the missing 17.7% w/w possibly oxygen. If the

metals detected were present as CuO, CaO, WO_2, K_2O and FeO, the theoretical oxygen content would be 17.5% w/w.

Analysis % w/w	C	S	Cu	Ca	Fe	W	K
A	16.4	2.6	50.1	10.07	1.61	0.21	2.68
B	15.5	2.6	46.7	10.96	1.97	0.17	3.20
Mean	16.0	2.6	48.4	10.52	1.79	0.19	2.94

Table 7.1

2.2.19 Whether all the plasma was ejected from the capillary during this test was uncertain. Certainly, the current from the discharge was irregular, as Figure 7.15 indicates. Typical discharges were approximately half-sinusoidal. This discharge had a sharp dip at 136.1 ms, indicating that the plasma's resistance increased sharply at this moment. Figure 7.15 also shows the resistance, and the increase is clearly visible. This increase may have been the wire explosion occurring later than expected in the discharge. It is speculated that the wire became dislodged from the nozzle end of the capillary during the initial pressurisation, or a piece of inert propellant stick could have been rammed into the capillary. The discharge could have created an arc through the high resistant propellant gases at the nozzle end, which would have heated up and softened the polyethylene. When the wire eventually exploded, the material would then be prevented from venting into the chamber. The propellant gases at the nozzle end may have been ejected at high velocity, causing damage to the wedge. The material within the capillary appears mostly composed of copper oxide. The carbon may have originated from the capillary or the propellant

gases, whilst the calcium hydroxide and potassium are trace elements within propellants containing nitrocellulose as well as the inert propellant. Tungsten was part of the rear electrode and steel (iron) was ablated from the nozzle.

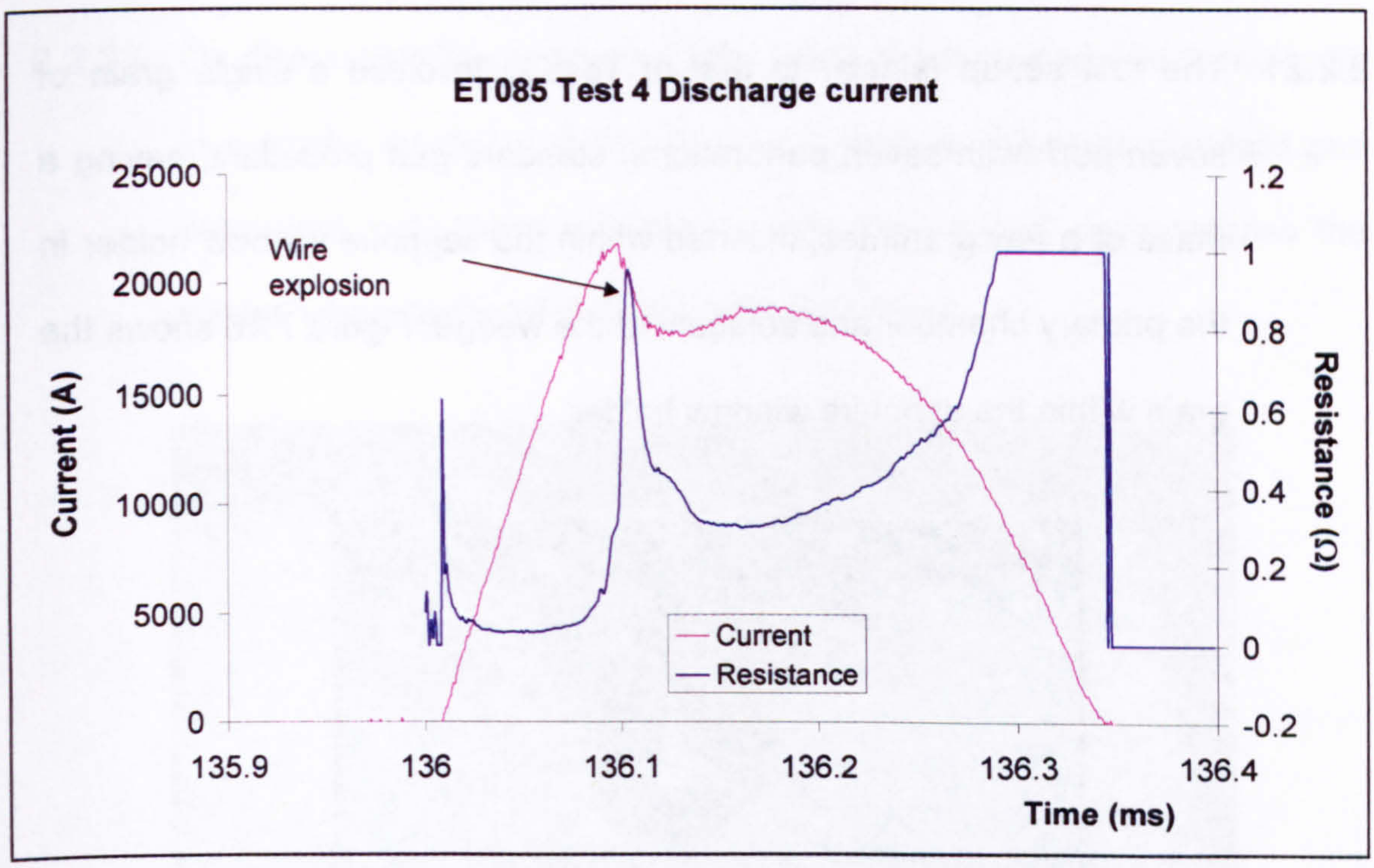

Figure 7.15 Current from plasma discharged into 65 MPa pressure

2.2.20 The wedge could have become coated in a plasma deposit which was subsequently burnt off by the hot propellant gases. During consultation on the experiment with a colleague, it was suggested to the Author that a small piece of energetic propellant could be inserted into the chamber along with the inert propellant to determine whether it would ignite. This idea was considered and it was felt that this would form an opportunity for the newly established spectral radiant flux analytical technique (Appendix A) to determine the nature of the plasma during ignition. It had by now occurred to the Author that one of the main energy transfer

mechanisms for ignition might in fact result from the latent energy transferred during condensation of the copper residue. Hence, the experiment was extended by a test to determine the effect of the plasma on a grain of live propellant.

2.2.21 The test set-up (similar to that of Test 2) involved a single grain of seven perf (with seven perforations) standard gun propellant, having a mass of a few grammes, inserted within the sapphire window holder in the primary chamber and adjacent to the wedge. Figure 7.16 shows the grain within the sapphire window holder.

Figure 7.16 Grain of 7 perf standard gun propellant set within the sapphire window port

2.2.22 The grain was firmly wedged in place with a piece of plastic, which can be seen in the photograph below the grain. The holder was placed into the Primary chamber location indicated in Figure 7.5 and the spectrograph measured the time-resolved spectra in the region of the propellant sample. If the propellant ignited and high radiation temperatures were not measured, then radiative energy transfer would

be known to play only a minor role in the ignition energy transfer mechanisms. The time of ignition would be recorded by either the spectral signatures of the propellant grain's trace elements or from other changes in the spectra.

2.2.23 On dismantling the equipment after the test, the wedge was found to be in a similar condition to that in Test 2, and the piece of standard gun propellant had ignited and burnt away. Figure 7.17 demonstrates the wedge when removed from the inert propellant.

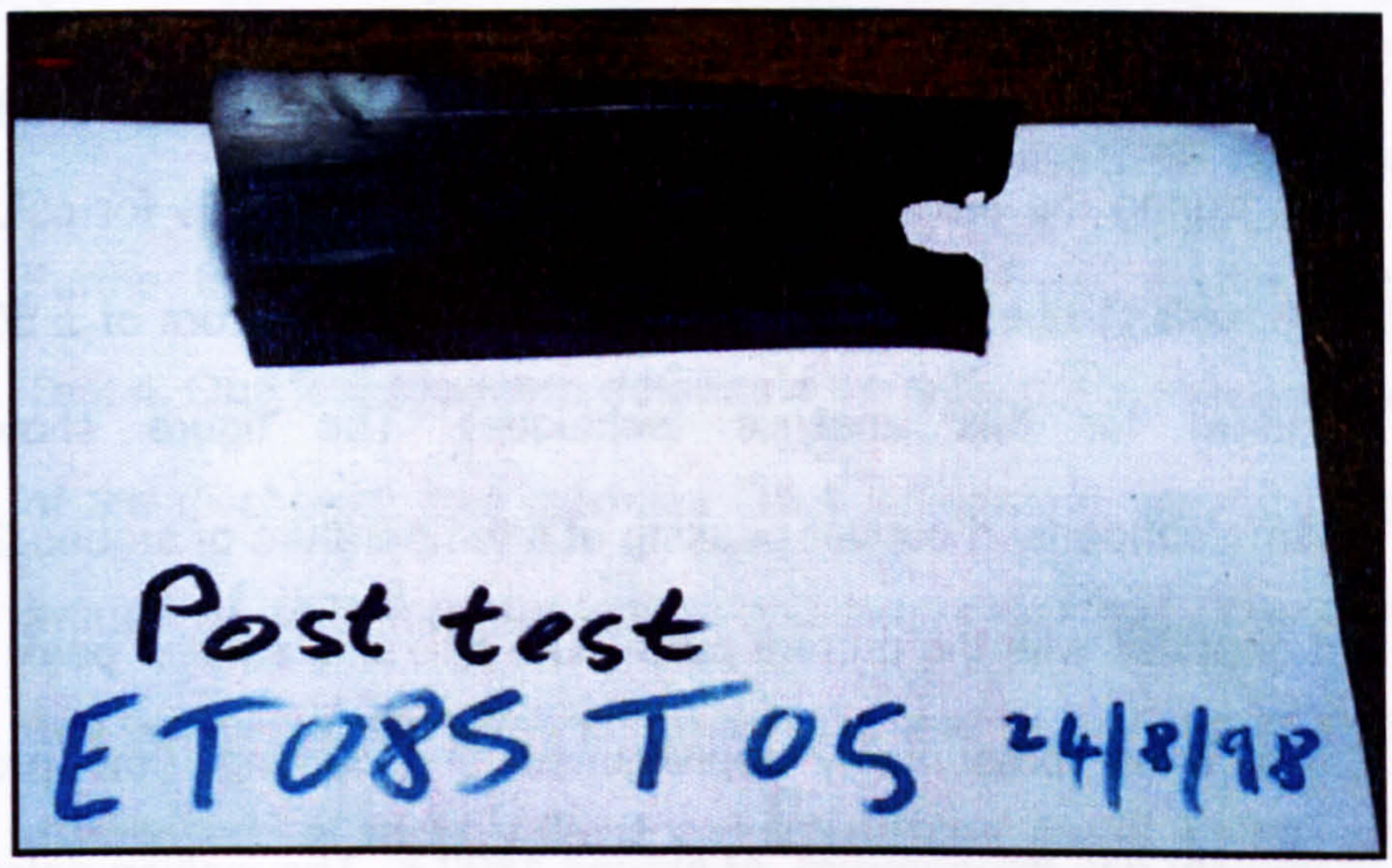

Figure 7.17 ET085 Wedge after Test 5

2.2.24 Both the stratification and the damage were as in Test 2. However, the wedge also had an area of less pronounced copper oxide deposit than elsewhere. This coincided with the vicinity of the standard gun propellant grain: the deposit was thought to have been burnt away by the ignited grain, suggesting that it had occurred before or during the grain burn.

2.2.25 Examination of the spectra showed supposed signatures of the propellant grain's trace elements (sodium and potassium) right from the start of the spectral record and so these could not be used to identify when the propellant started to burn. It was thought that the inert propellant may contain the same trace elements as the energetic propellant, and that these were being mixed with the plasma during ablation near the CPG nozzle. The same trace elements were indeed detected in the inert propellant by burning some of it in air and recording the spectral output.

2.2.26 Figure 7.18 shows the thermal temperature profile of the locality of the grain during the test as given by the spectral analysis for colour and brightness temperatures (detailed in Appendix A; errors of ± 50 K are standard for this analysis technique). The figure shows the plasma/condensed copper peaking at a temperature of around 2700 K, out of phase with the current pulse. The following smaller peak around 2 ms later, presumably represented the burning (low pressure) propellant gas temperature, at around 1800 K. The ignition delay (here defined as the time from the start of the discharge to the first sign of ignition) is estimated at 1.5 ms. The temperature of the copper being below its boiling point suggests that, if the vapour deposition ignition hypothesis is assumed, condensation must have occurred via the passage of the vapour around the grain, to the rear where the temperature was measured. The copper would have been a metallic aerosol possibly in the process of oxidation.

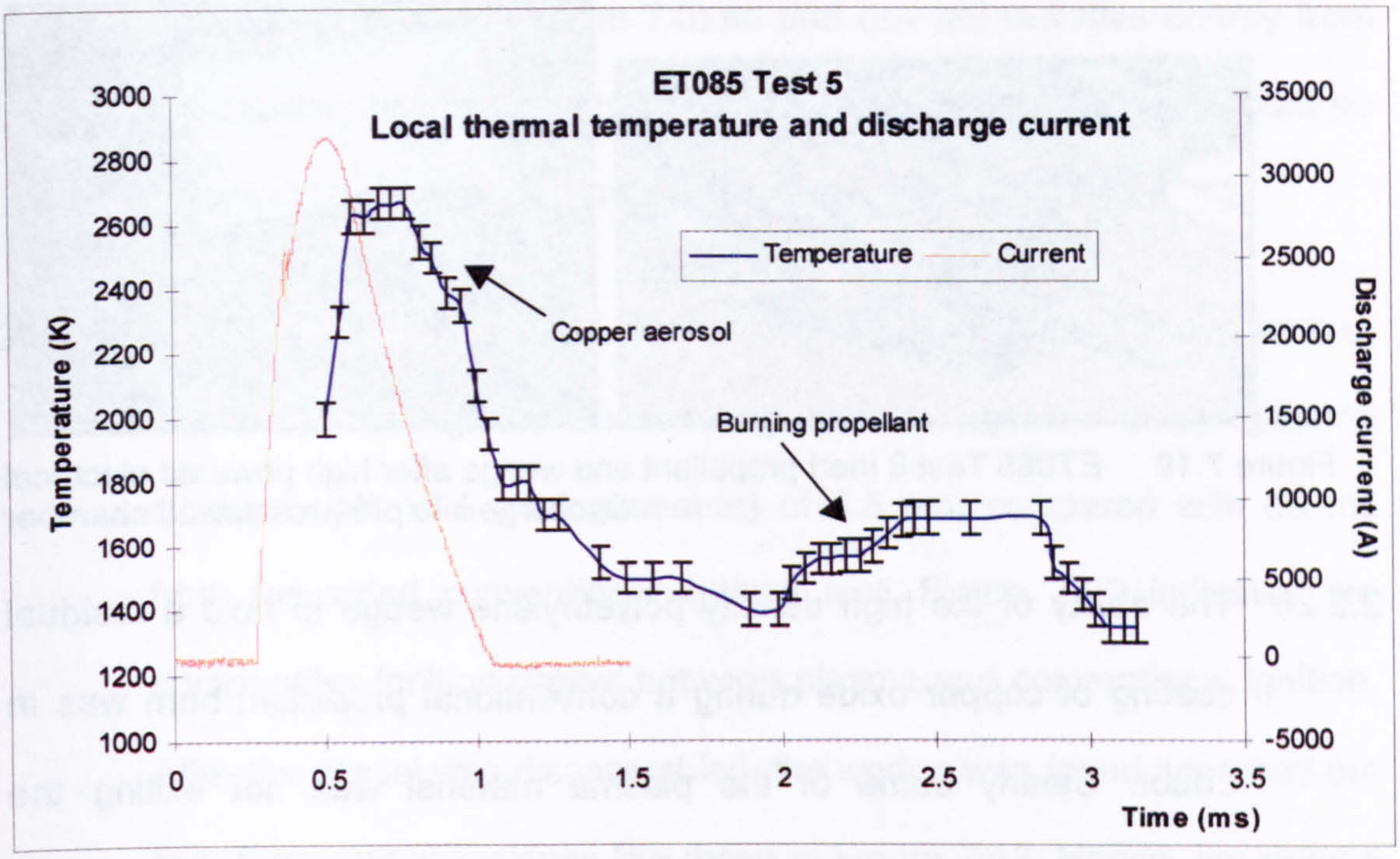

Figure 7.18 Test 5 temperature close to the sapphire window

2.2.27 Further tests in pre-pressurised chambers suffered similar problems to Test 4. One test sought to determine the effect of increasing the power of the discharge: four modules (79.1 kJ energy) were discharged at around 35 MPa into the wedge and inert propellant. The CPG failed and propellant gas washed through the rear of it. When the CPG was dismantled, a stick of inert propellant was found to have become lodged in the capillary, probably during the pressurisation sequence. No damage was observed to the wedge and there was no deposit coating it. Figure 7.19a shows the inert propellant as extracted from the capillary: the offending stick can be clearly seen. Figure 7.19b illustrates the cleanliness of the wedge. It is thought that no plasma was discharged from the capillary into the chamber but instead it had been discharged out through the rear of the CPG.

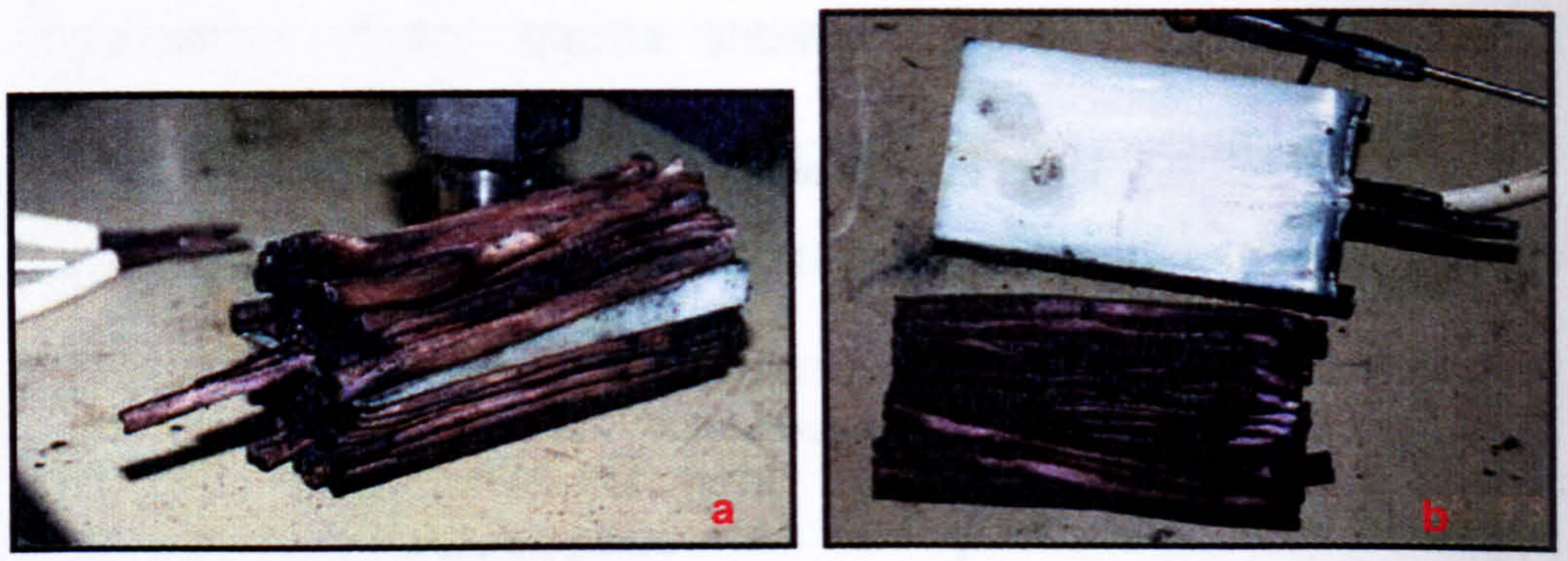

Figure 7.19 ET085 Test 8 inert propellant and wedge after high powered electrical discharge into pre-pressurised chamber

2.2.28 The ability of the high density polyethylene wedge to hold a residual coating of copper oxide during a conventional propellant burn was in doubt. Clearly some of the plasma material was not exiting the capillary, but it was thought that some could be and this in turn was being burnt from the wedge by the hot pressurising combustion gases.

2.2.29 To check for this, a test was performed in which one capacitor module was discharged at time zero (known from Tests 2 and 5 to produce a uniform coating of copper deposit). The Primary chamber was loaded with a wedge and inert propellant similar to Tests 2 and 5, but around 50 g of standard gun propellant were placed in the secondary chamber. The idea was that the plasma would vent from the capillary, coating the wedge prior to igniting the propellant. Post-test examination of the wedge would confirm whether the hot propellant gases were burning the residue off the wedge.

2.2.30 A second objective of this test was to measure the plasma temperature spectrally as the plasma moved into the Secondary chamber. The sapphire window was located in the end pressure port of the

Secondary chamber (Figure 7.5) so that any hot radiative energy from the capillary plasma, which might be responsible for ignition, would be recorded by the spectrograph optics.

2.2.31 Around 32 kJ of electrical energy were discharged into the chamber. The propellant ignited successfully with an ignition delay (plasma initiation until 10% peak pressure) of 6.5 ms, compared with 65 ms from the aided conventional ignition test. Figure 7.20 indicates the comparative ignition delays between plasma and conventional ignition. After the vessel was disassembled, the wedge was found scorched but free from copper residues like those in Figure 7.13. Hence, the reason for the lack of copper material on the wedges is thought partly to be because it has been burnt off by the hot propellant combustion gases.

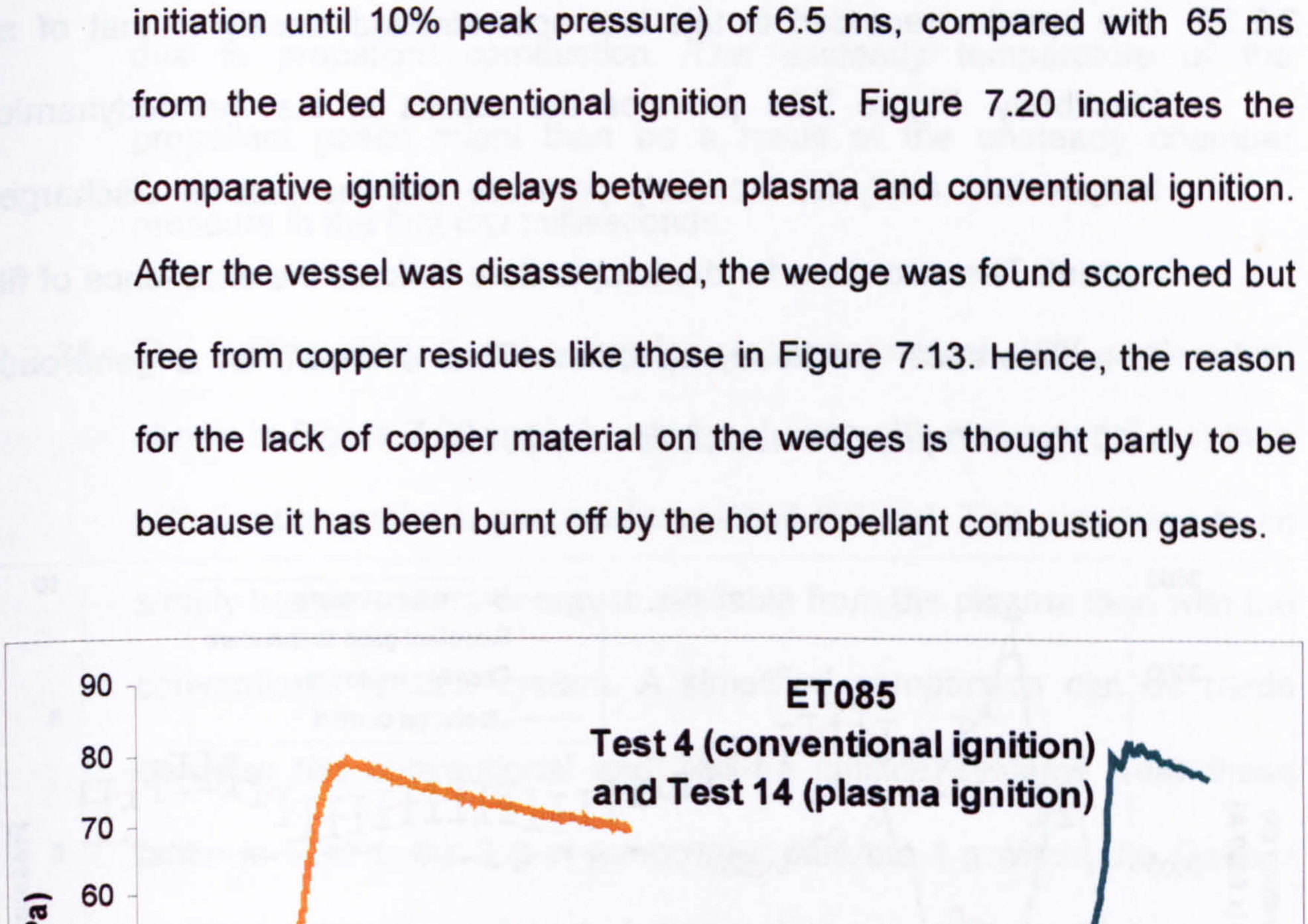

Figure 7.20 Comparison of Test 4 (conventional) and Test 14 (plasma) ignition delays

2.2.32 This method was considered therefore of no further use in plasma propagation tests with a pressurisation system using hot propellant gases and polyethylene wedges. Some other wedge material such as aluminium oxide or some cold pressurisation system might give improvements, but this was never investigated.

2.2.33 The spectra recorded in this test approximated closely to that of a blackbody. Figure 7.21 provides the results of the thermodynamic temperature analysis, the early pressure and the plasma discharge current. The error bars for the temperature indicate the excellence of fit to a theoretical blackbody spectrum. This is shown as a generous ± 50 K, but in practice was closer to ± 20 K.

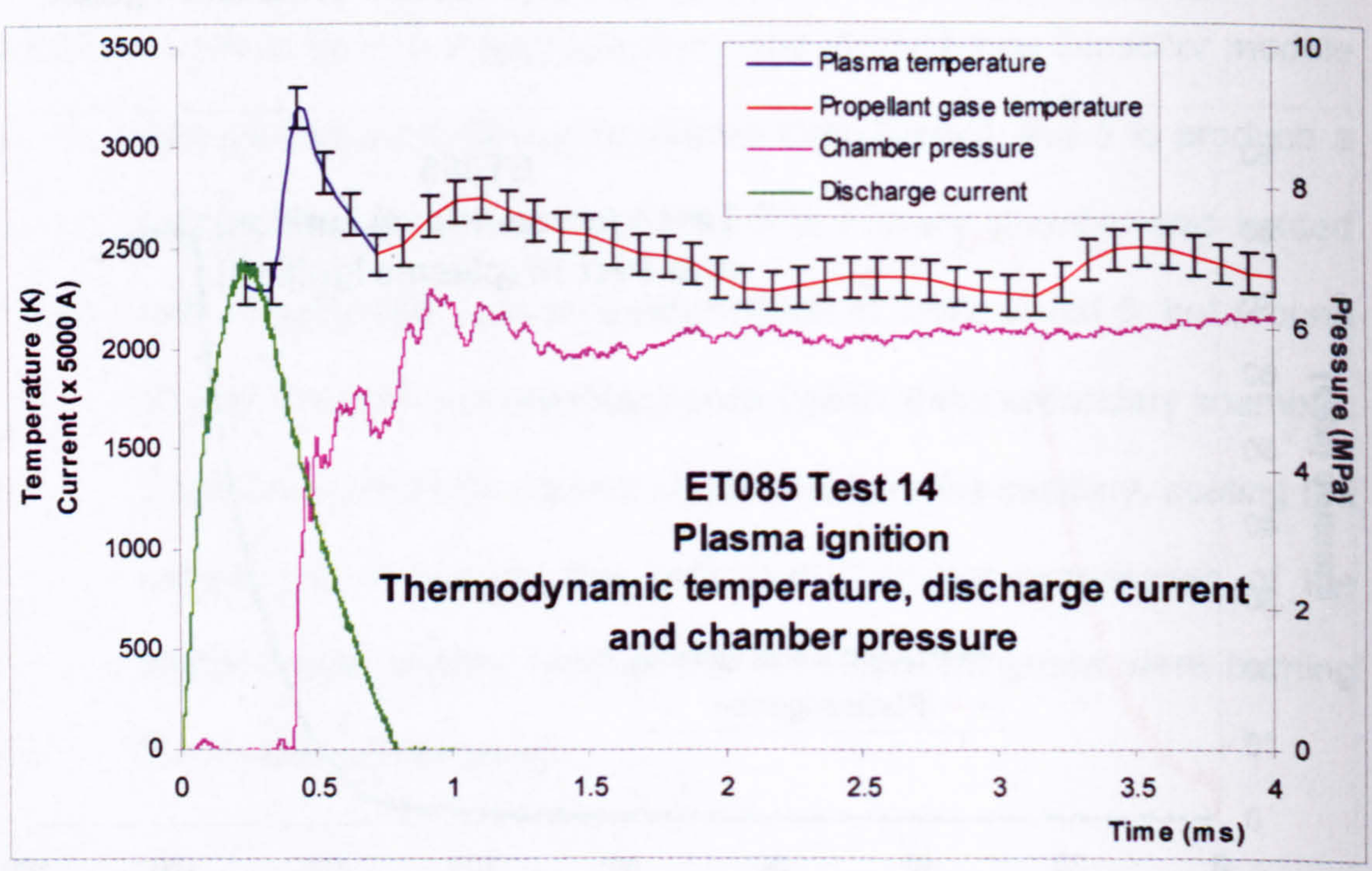

Figure 7.21 ET085 Test 14 results showing discharge current, chamber pressure and chamber brightness temperature

2.2.34 The chamber species reached the temperature of copper vapour and cooled to below its condensation temperature in less than 1 ms, so it was speculated to be copper. The temperature of these species (blue) was out of phase with, but otherwise similar to, the current (and power) and would have continued to fall if no propellant was present. This suggests that the subsequent rise in species temperature (red) was due to propellant combustion. The unsteady temperature of the propellant gases might then be a result of the unsteady chamber pressure in the first few milliseconds.

2.2.35 The ignition delay (i.e. the time for pressure to reach 10% peak value) shown in Figure 7.20 is obviously far shorter with plasma (6.5 ms) than with the conventional gunpowder method (65 ms). This may have been simply because more energy is available from the plasma than with the conventional ignition system. A simplified comparison can be made between the conventional and plasma ignition systems from these tests. In Test 4, the 3 g of gunpowder plus the 1 g within the Gevelot igniter provides around 4 kJ of chemical energy available for transfer to the propellant. Obviously, only a small percentage of this would in fact be transferred to the propellant, with the remainder being transferred to the chamber. In Test 5, the electrical energy discharged was around 30 kJ, but the plasma had to pass through a densely packed inert propellant bed where it lost an unknown amount of energy. An estimation of the thermal energy available for transfer to the propellant can be made by assuming that 1 g of copper vapour entered into the

Secondary chamber. Then, the plasma would contain around 6 kJ energy, 5 kJ of which would be available for transfer during condensation; the remaining 1 kJ would be unavailable because the temperature remained close to the boiling point of copper. The same argument of transfer to the chamber would apply as mentioned in the conventional ignition case above. Hence, there would appear to be little difference in the available energy.

2.2.36 The difficulty with this seemingly straightforward comparison occurs when the pressures are examined. In the conventional case, the pressure rises by 1 MPa, but in the plasma case it rises by 4 MPa. The relative effect of this increased pressure rise on the ignition delay is difficult to quantify with little study done to date. However, FHIBS internal ballistics code (see Chapter 3) was used tentatively to explore this issue. The ignition delay incurred by increasing the ambient pressure with a constant ignition stimulus was studied and the effects of pressure on the delay appear in Figure 7.22. There would appear to be a linear relationship, with the ignition delay reducing by a factor of two for pressure increases from 1 MPa to 4 MPa. The reduction in ignition delay from conventional compared with plasma ignition is more than a factor of eight. Hence, the conclusion is that the flux linkage from the igniter material to the propellant has increased significantly for plasma ignition over conventional ignition, even with the differences in test conditions taken into account.

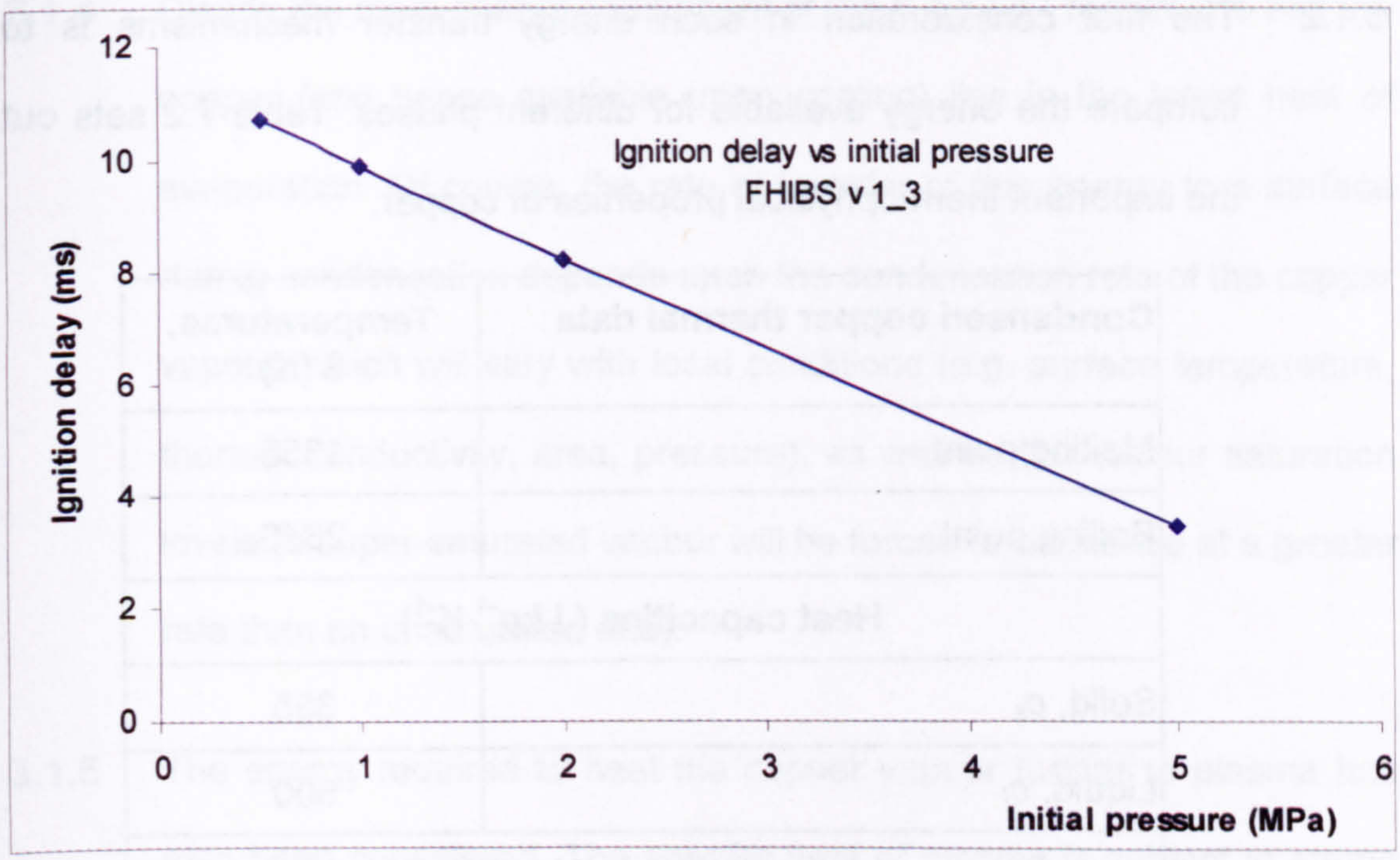

Figure 7.22 Effect on ignition delay of increasing the ambient pressure with a constant ignition stimulus

3 Ignition by metallic vapour deposition

3.1 Introduction

3.1.1 The success of the early experimental work detailed above encouraged the Author to use the spectroscopic method for plasma propellant interaction studies in the area of ignition. However, before that work is described in the following Chapters, the hypothesis of propellant ignition by metallic vapour deposition will be outlined. This mechanism will be compared with conventional ignition systems. The theoretical modelling was performed shortly after the closed vessel tests described above, as some energy transfer mechanism other than radiation was clearly dominating plasma ignition.

3.1.2 The first consideration in such energy transfer mechanisms is to compare the energy available for different phases. Table 7.2 sets out the important thermophysical properties of copper.

Condensed copper thermal data	**Temperatures, θ (K)**
Melting point	1356
Boiling point	2840
Heat capacities (J kg^{-1} K^{-1})	
Solid, c_s	385
Liquid, c_l	500
Latent heats (J kg^{-1})	
Melt, L_m	205000
Boil, L_v	4796000

Table 7.2

3.1.3 The energy available for thermal transfer in each phase is given by the energy required to traverse each phase – for 1 g mass of copper in Table 7.3.

Available thermal energy for copper (kJ g^{-1})	
Energy to elevate from room temperature to melting	0.4
Energy to melt	0.2
Energy to elevate from melt to boiling	0.7
Energy to boil	4.8
Total energy required to evaporate from room temperature	**6.1**

Table 7.3

3.1.4 Clearly the main energy component of the 6.1 kJ g^{-1} required to boil the copper (and hence available upon cooling) lies in the latent heat of evaporation. Of course, the rate of transfer of this energy to a surface during condensation depends upon the condensation rate of the copper vapour, which will vary with local conditions (e.g. surface temperature, thermal conductivity, area, pressure), as well as the vapour saturation levels (a super-saturated vapour will be forced to condense at a greater rate than an unsaturated one).

3.1.5 The energy required to heat the copper vapour further to plasma has also been considered. The specific heat of plasma is subject to strong variations resulting from ionisation processes at given temperatures. Data from Marshall [8] were used; the specific heat of copper is shown in Figure 7.23. With these values and assuming no losses, 4.8 kJ g^{-1} (the latent heat required to boil copper) will heat the vapour from boiling point to a plasma at just over 8000 K; the energy required to heat copper vapour to 12 000 K is 17.4 kJ g^{-1}.

3.1.6 Another consideration was the way conventional ignition systems deposit gunpowder particles onto the surface of propellant, burning and transferring energy directly to the surface through convection and conduction. The energy is then transferred to the propellant sub-surface region through conduction. Radiative energy transfer would be negligible at these temperatures. Thermal contours about spherical gunpowder particles will in turn have spherical symmetry: in contrast,

plasma and hot gas ignition has a linear geometry and thus linear thermal contours.

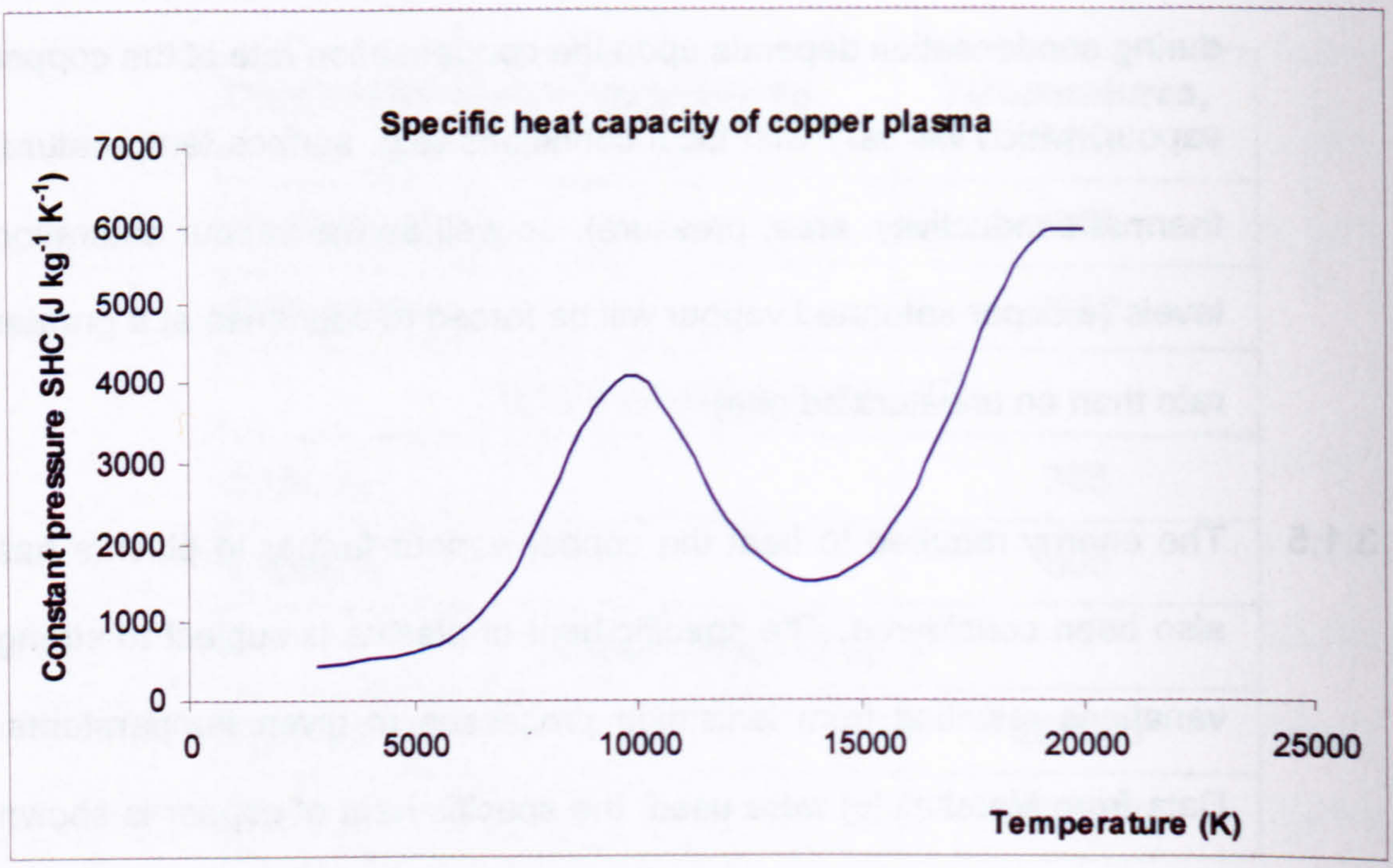

Figure 7.23 Specific heat capacity of copper plasma (Marshall [8])

3.1.7 Figure 7.24 illustrates 200 K and 400 K thermal contours for both a conventional particulate and plasma/hot gas scenario. The time taken to initiate self-sustaining combustion would, in the conventional particulate case, depend on the density of gunpowder grains producing separate spot ignition sites and in both cases be dependent on the rate of heat transfer from source to the surface of the propellant. For any given ignition criteria and equal heat flux, plasma ignition would be more efficient due simply to the increased surface area over which heat energy can transfer.

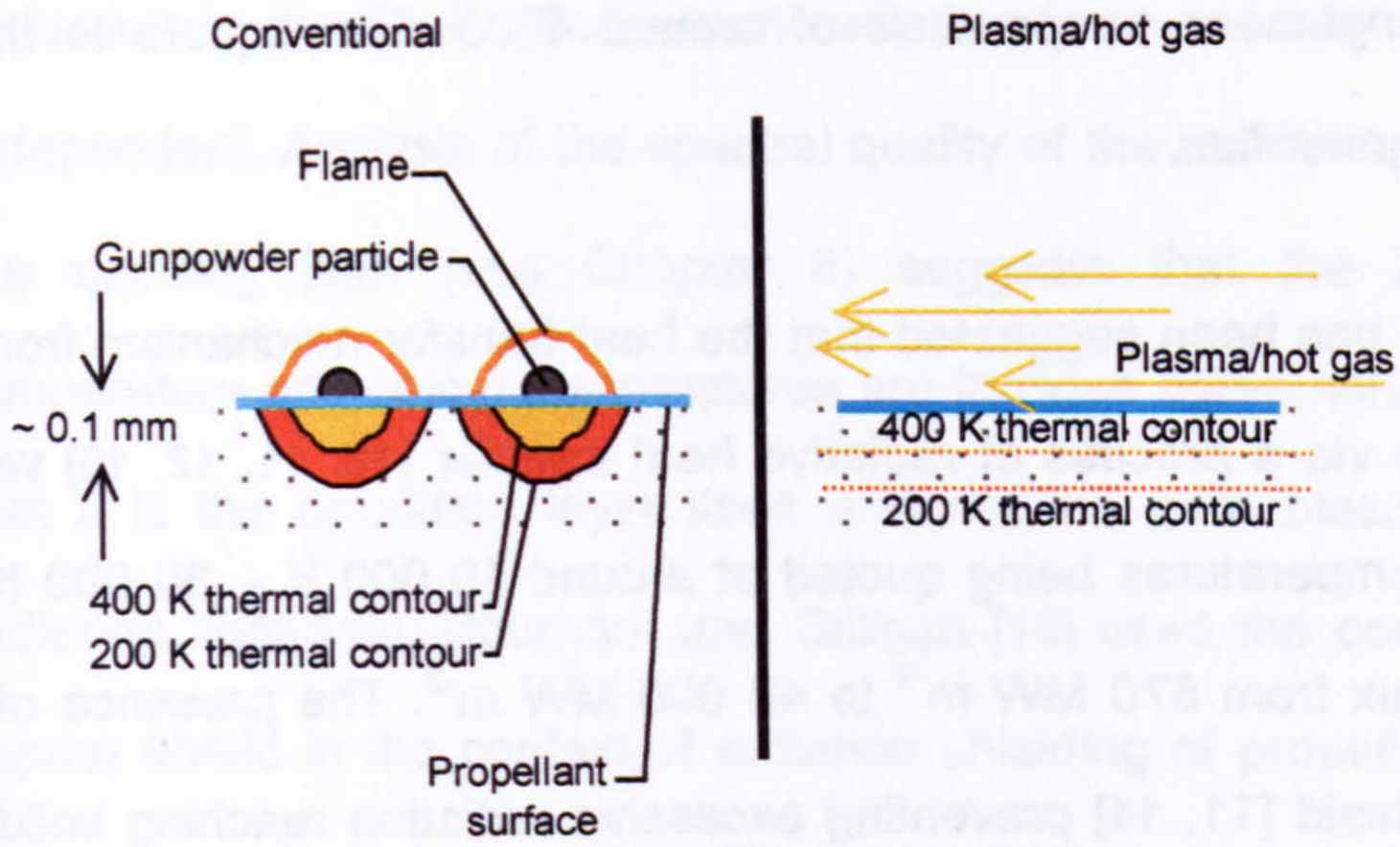

Figure 7.24 Thermal contours of conventional particular ignition systems and plasma/hot gas ignition systems

3.2 Conventional heat transfer – Gevelot igniter

3.2.1 The heat transferred during conventional ignition with a Gevelot gunpowder igniter has been estimated and will be compared below with plasma ignition by radiative energy transfer and metallic heat transfer. The constant flux for the Gevelot igniter is calculated as 20 MW m^{-2}. This is assuming a constant convection heat transfer coefficient over the entire propellant surface, calculated at 0.01 MW m^{-2} K^{-1} and a gas temperature of 2000 K [9].

3.3 Plasma heat transfer – radiation

3.3.1 The radiative heat flux is given by the Stefan-Boltzmann radiation law (see Appendix A) along with an appropriate emitter and absorption emissivity. The emitter emissivity is unity if the brightness temperature is used and for simplicity, the emissivity of the propellant has been taken as unity. In this situation, the emitter would need to have a

brightness temperature of around 4300 K to equate to the Gevelot igniter flux.

3.3.2 It has been suggested that the heat transfer mechanism from plasmas is via a process of radiative heat transfer [10, 11, 12, 13] with plasma temperatures being quoted at around 10 000 K – 30 000 K (giving a flux from 570 MW m^{-2} to 48 000 MW m^{-2}. The presence of a vapour shield [11, 14] preventing excessive radiation reaching solid surfaces, however, suggests that the effective temperature may be less. Radiation is still thought by some to play an important role not only in ignition but also in the initiation, control and optimisation of all plasma/propellant interaction processes [13, 15, 16].

3.3.3 The experimental results discussed in Chapters 4, 5 and 6 for inert surfaces suggest that the radiative energy transferred to energetic propellant surfaces during a plasma/propellant interaction may be less than expected [5, 17]. Absolutely calibrated spectroscopic measurements show that only around 0.5% of the total electrical energy discharged within the capillary itself was incident on the CPG liner, whereas EDENET suggests 20%. The measured brightness (blackbody equivalent) temperature of the plasma/liner boundary was far less than expected from the modelling, which suggested a brightness temperature of around 17 000 K for these tests.

3.3.4 As discussed earlier, one explanation for this might be the vapour shield effect. However, Mohanti and Gilligan [11] proposed that the

reduction in the Stefan-Boltzmann radiation law would be frequency independent. Analysis of the spectral quality of the radiation emitted to the capillary liner (see Chapter 6) suggests that the brightness temperature and colour temperatures are in close agreement, showing that it is the boundary layer itself and not the core plasma that is radiating. Edwards, Bourham and Gilligan [18] used the concept of a vapour shield in the context of radiation shielding of propellant during plasma/propellant interactions. They cite this as responsible for an angular dependence on plasma propellant interaction test results [19].

3.3.5 Another explanation is that a thin boundary layer of optically thick liquid metallic copper is forming on the condensed surface. In this situation, insufficient radiative energy would be available to initiate self-sustaining combustion within the timescale of experimental plasma ignition tests. The only way to demonstrate this would be to measure the radiative energy incident upon the propellant surface. This has been performed by the Author as described in the following Chapters, but it can be stated here that the amount of radiative energy transfer during ignition is negligible.

3.4 Plasma heat transfer coefficients – copper vapour deposition

3.4.1 The latent heat from condensing propellant igniter material has been previously proposed in connection with practical ignition systems [20]. Here it was quoted that black (gun) powder contained 8.7% condensable elements and a new composition Primer mixture 953

based on boron and potassium nitrate contained 72.2% condensable elements at the propellant isobar flame temperature. Copper vapour/plasma contains 100% condensable elements available for heat transfer. The latent heat transferred from a condensing copper vapour to a cold propellant surface has been modelled by the Author [6, 21], and the resultant temperature of the propellant estimated as a function of depth and time. This has been compared with the temperature profile expected from a typical Gevelot gunpowder igniter.

3.4.2 The heat transfer coefficient, h for copper vapour condensing onto a cylindrical surface can be expressed as [22; 23]:

$$h = 0.73 \sqrt[4]{\frac{g\rho_L^2 L_V K_L^3}{\mu_L \Delta T d}} = 23.7 \Delta T^{\frac{1}{4}} MWm^{-2}K^{-1} \qquad \textbf{Equation 7.1}$$

where

g is the gravitational field strength, 9.81 N kg^{-1}

ρ_L is the liquid copper density, 6800 kg m^{-3} (at 2840 K) [24]

L_v is the latent heat of vaporisation for copper, 4.796 MJ kg^{-1} [26]

K_L is the thermal conductivity of liquid copper, 1184 W m^{-1} K^{-1} at 2840 K [25]

μ_L is the viscosity of liquid copper, 1.09 mN s m^{-2} at 2840 K [24]

ΔT is the temperature difference between the condensing copper and the propellant surface below saturation temperature, T_{sat} (T_{sat} = 2840 K [26]) and

d is the propellant diameter, 3 mm.

This gives the flux for copper condensate as a function of temperature of:

$$F = 23.7\Delta T^{-\frac{1}{4}}\Delta T = 23.7\Delta T^{\frac{3}{4}}\ MWm^{-2} \qquad \textbf{Equation 7.2}$$

3.4.3 In the case of copper condensing onto a propellant grain, the temperature difference ΔT will be at least about 2000 K, giving a flux of around 7 GW m^{-2}. Equation 7.1 was written for steady-state condensation of steam onto copper cooling pipes, hence the inclusion of gravity and viscosity. The process of copper condensing onto propellant is far from steady-state and thus Equation 7.2 is likely to be a gross simplification. No work has been undertaken to establish whether this is an over- or underestimation, although the magnitude of the flux suggests the former. Work is in hand to formulate a more appropriate expression for condensing copper than Equation 7.1.

3.4.4 Figure 7.25 demonstrates the results of modelling [27] the temperature rise of a propellant grain using the 7 GW m^{-2} flux from condensing copper compared with the 20 MW m^{-2} flux from a gunpowder (GP) Gevelot igniter. The figure shows how the temperature of a propellant grain subsurface would be expected to rise after 0.1 ms when the heat fluxes given above are applied. The advantage of copper condensation over a conventional ignition process is apparent, although probably exaggerated. The condensate heats the grain at least an order of magnitude faster than by the conventional method, even though the latter has two distinct advantages: the flux has been held constant,

whereas it would actually diminish proportionally to ΔT, and it has been treated to act over the entire propellant surface, whereas in reality spot heating is more likely to occur.

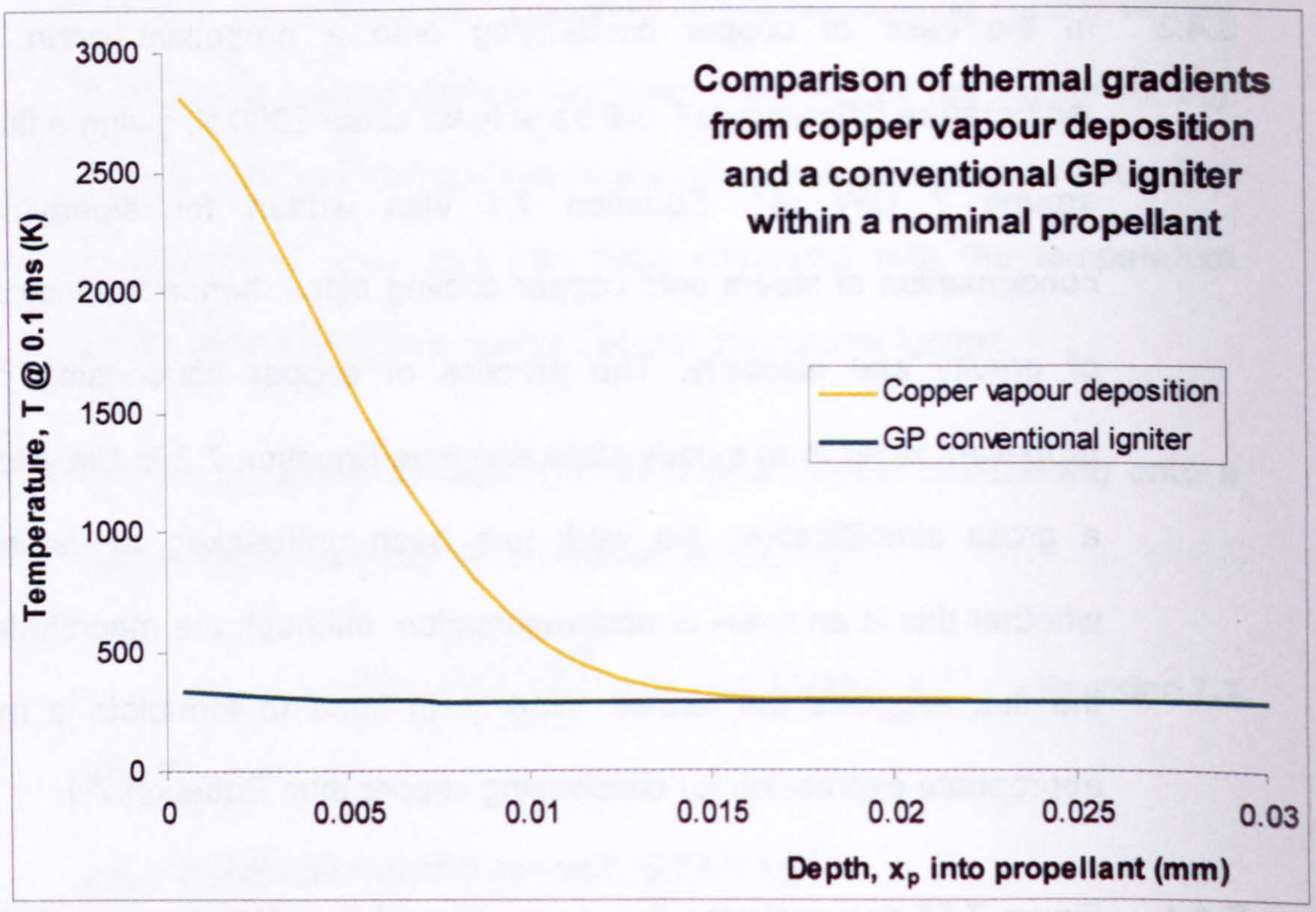

Figure 7.25 Results of modelling thermal gradients from Equation 7.2 for condensing copper and a Gevelot gunpowder (GP) igniter

3.5 Mass of propellant ignitable by metallic vapour condensation

3.5.1 When metallic (copper) vapour condenses onto cold propellant, the liberated latent heat energy will be transferred to the surface of the grain and this heat will in turn conduct into the grain. The total propellant charge mass that one gramme of copper vapour might ignite can be estimated without recourse to equation 7.1 with some simplifying assumptions. To perform an accurate calculation of this type requires knowledge of the temperature gradient and pressure

relationship for initiating self-sustaining combustion reactions. These relationships for achieving self-sustained ignition are not well defined in the conventional case, quite apart from that of a transient (<< 1 ms) ignition stimulus. Also, details of the heat impulse (condensation rate and duration) and local pressure from the copper vapour are required, besides the condensation temperature and pressure relationships. (The Author has undertaken measurements of the heat impulse and pressure in the vicinity of the propellant surface of a dense propellant bed (see Chapter 9), as well as obtaining the relevant condensation information (see Figure 3.6, Chapter 3) during the work for this Thesis.)

3.5.2 The simplified model assumes that the temperature increase to a skin depth, x_p is uniform; a suitable ignition criterion can then be defined which expresses a given temperature at this depth. The mass of heated propellant, m_x can be calculated from the known total energy transferred, the specific heat of the propellant and the given temperature rise for that propellant. This mass can then be assigned to any given skin depth, x_p for estimating the total charge mass, M of propellant that might be ignited. The thinner the heated skin depth required, the greater the total charge mass that can be ignited: the model appears in Figure 7.26. The figure shows a cord of propellant with length, ℓ and radius, R. Copper vapour is deposited onto the surface such that a thickness of the propellant, x_p is uniformly heated and a central core radius r is unaffected.

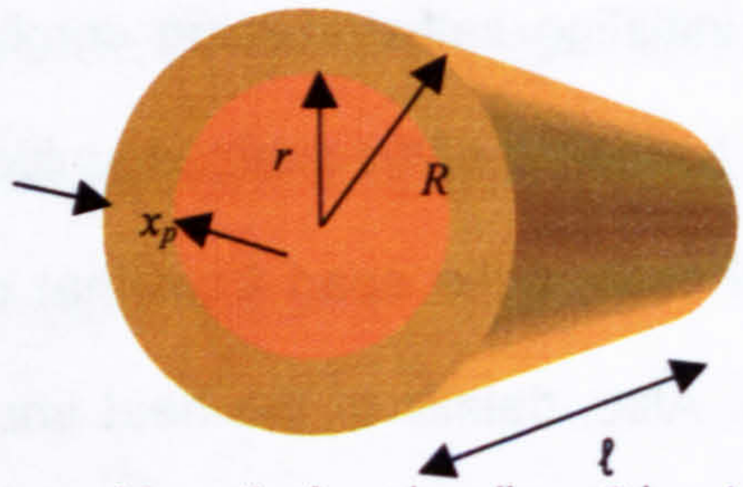

Figure 7.26 Propellant cord length, ℓ and radius, R heated to a skin depth, $x_p = R - r$

3.5.3 From the definition of density, the mass of heated propellant is:

$$m_x = \pi \ell \rho (R^2 - r^2) \qquad \textbf{Equation 7.3}$$

where ρ is the propellant density. The total charge mass of the propellant chord is:

$$M = \pi \ell \rho R^2 \qquad \textbf{Equation 7.4}$$

and therefore the relationship between the total charge mass, M and heated mass, m_x in terms of r and R is:

$$M = m_x / (1 - r^2/R^2) \qquad \textbf{Equation 7.5}$$

But

$$x_p = R - r \qquad \textbf{Equation 7.6}$$

Therefore, the relationship between charge mass M and heated skin depth x_p is:

$$M = m_x R^2 / x_p (2R - x_p) \qquad \textbf{Equation 7.7}$$

3.5.4 As an example, a standard gun propellant (NQ) grain at a bulk temperature of 20 °C was examined. The criteria have been simplified such that ignition is pressure independent and will occur when the propellant surface has been heated to 500 °C. Data appear in

Table 7.4 and results of applying the data to Equation 7.7 shown in Figure 7.27.

Propellant specific heat capacity of NQ at 80 °C (J g^{-1} K^{-1})	1.4
Energy from condensing copper vapour (J g^{-1})	4800
Temperature rise of propellant surface for ignition (K)	500
∴Affected mass, m_x (g)	6.86
Cord radius, R (mm)	1.50

Table 7.4

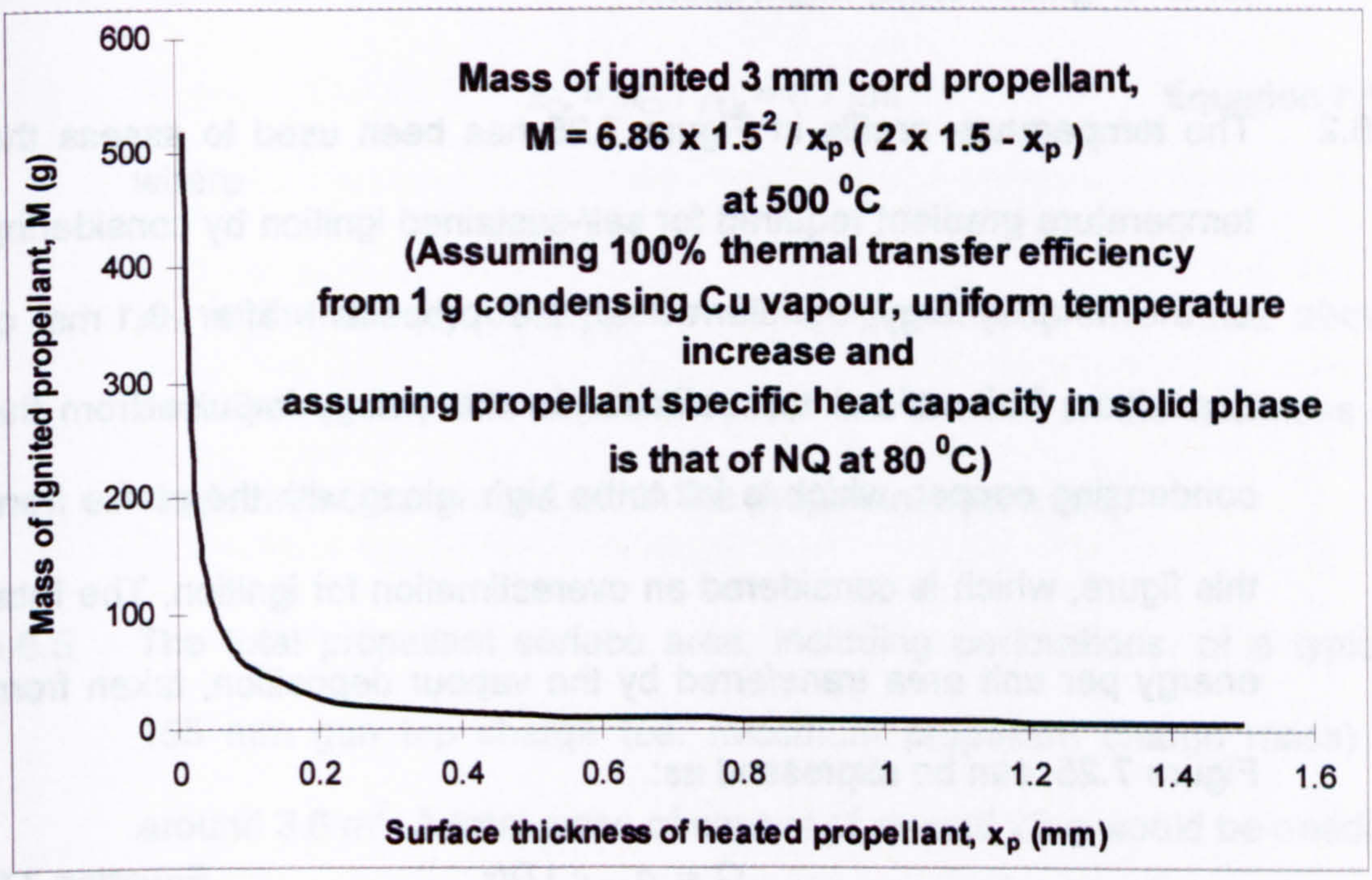

Figure 7.27 Relationship between skin depth and total mass of propellant that can be heated to ignition by 1 g condensing copper

3.5.5 The total charge mass of ignitable propellant rises steeply with the reduction in the surface thickness of propellant heated to 500 °C is reduced. If the heated thickness required for sustainable burning was around 100 μm, then around 50 g of propellant could be simultaneously ignited for each gramme of copper condensed: if the thickness was

around 10 μm, then the total charge mass would be around 500 g per gramme of copper condensate.

3.6 Copper thickness required for self-sustained combustion

3.6.1 As an alternative to the above calculation, the thickness of copper, x_{Cu} required to initiate self-sustained ignition can be estimated from given ignition impulses. The estimated thickness can then be used to determine the mass of propellant that 1 g of copper (the typical amount for ETC ignition tests) might ignite.

3.6.2 The temperature profile in Figure 7.25 has been used to assess the temperature gradient required for self-sustained ignition by considering of the total energy transferred to the propellant after 0.1 ms of deposition. This utilises the estimate for the energy impulse from the condensing copper, which is felt to be high, along with the profile from this figure, which is considered an overestimation for ignition. The total energy per unit area transferred by the vapour deposition, taken from Figure 7.25, can be expressed as:

$$Q = \rho_{NQ} c \int T dx_p \qquad \textbf{Equation 7.8}$$

where

ρ_{NQ} is the density of solid NQ propellant (at 80 °C) = 1670 kg m^{-3} and

c is the specific heat capacity of solid NQ propellant (at 80 °C) = 1.4 J g^{-1} K^{-1}.

3.6.3 This is transferred from a given mass of condensing copper, the mass per unit area, m_{Cu} of which is given by:

$$m_{Cu} = \frac{\rho_{NQ} c}{L_v} \int T dx_p = 6.5\, gm^{-2} \qquad \textbf{Equation 7.9}$$

where

L_v is the specific latent heat of copper = 4.796 MJ kg^{-1}.

3.6.4 The thickness of deposited copper required for the profile in Figure 7.25 is thus:

$$x_{Cu} = m_{Cu} / \rho_{Cu} = 0.7\ \mu m \qquad \textbf{Equation 7.10}$$

where

ρ_{Cu} is the density of copper = 8960 kg m^{-3} [26]. The value above describes a very thin deposition layer but is close to the thickness of single molecular groups within the propellant matrix [28].

3.6.5 The total propellant surface area, including perforations, of a typical 155 mm gun top charge (i.e. maximum propellant charge mass) is around 3.6 m^2. A total mass of copper of around 23 g would be needed to produce the temperature profile of Figure 7.25 uniformly in each grain. However, line ignition may be obtained on the surface of a propellant charge adjacent to a perforated central ullage tube. If the tube were of radius 20 mm and length 0.8 m then around 1 g of copper would be required and in this case only around 5 kJ energy would be needed for ETC ignition of the propellant charge. This energy

requirement, valid for metals other than copper, is similar to results from large calibre plasma ignition tests from Germany [29].

3.6.6 This theory has been applied to a more realistic ignition case study [30] since the above estimation was first made. In their paper, Alimi et al presented the results of ignition modelling with ETC plasma discharges, based on radiative and convective/conductive energy transfer mechanisms, but not vapour deposition. However, most useful to the current discussion are their heat wave penetration (read from the graph in reference [30] and reproduced in Figure 7.28).

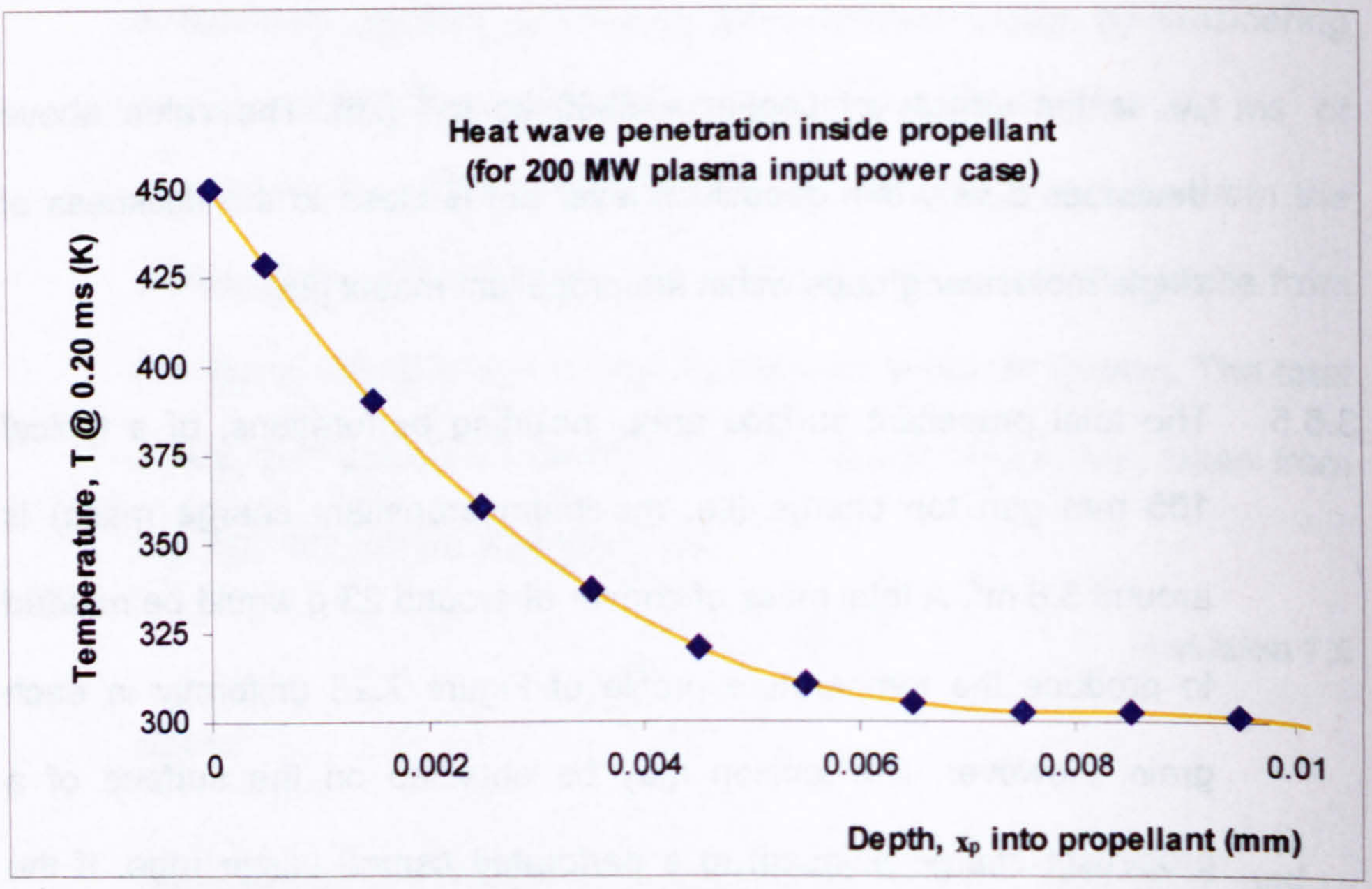

Figure 7.28 Heat wave penetration into propellant at the moment of ignition (Alimi et al [30])

3.6.7 These results are given at the moment of ignition. Application of this temperature profile in Equation 7.9 leads to a copper thickness of

0.2 μm, which represents an even thinner layer of copper and a proportional decrease in the theoretical minimum energy required to ignite a large calibre charge. The effect of the fast rate of energy transfer from vapour deposition may bring even more beneficial decreases. Measurements of the actual thickness obtained during a typical discharge onto a cold plastic-like surface have been made, and are discussed in Chapter 9.

3.7 Forced condensation and the ignition timescale

3.7.1 A typical ETC discharge currently used for large calibre ignition lasts for around 2 ms, but the time over which condensation occurs for ignition may be very short and the flux linkage will depend upon the rate of condensation. A pressure increase of several megapascals is noticed during typical large calibre and small-scale closed chamber ETC ignition discharges and is believed to aid ignition. The rate at which the deposition occurs is currently unknown but this will be influenced by the increase in chamber pressure resulting from the phase changes as copper vaporises (copper evaporation occurs throughout the ETC discharge due to rear electrode ablation). The condensation temperature of copper is known to be a function of pressure (see Chapter 3): as the pressure rises, the boiling point increases. With a relatively small increase in pressure, any vapour just above the normal boiling point will become supersaturated and forced to condense on any surface, transferring energy more rapidly than normal to the propellant grains onto which it condenses. The influence of the

pressure oscillations is unlikely to be easily understood through experiment alone, so modelling may be required to elucidate the significance of these effects.

---

1 K. E. Moran, Exploding Wires Vol. 3 p285 Proc. 3rd Conference On Exploding Wires Phenomenon, edited W. G. Chace and H. K. Moore (New York: Plenum), 1964

2 G. L. Katulka, K. J. White, W. F. Oberle, P. Kaste, R. Pesce-Rodriguez and M. Leadore, "Experimental Characterisation of Plasma Effects on Energetic Materials for Electrothermal-Chemical Launch Applications," IEEE Transactions on Magnetics, Vol. 35, 1, January 1999

3 CRC handbook 79th edition; 4-55

4 M. J. Taylor and R. Gardner, "ET154 - X-rays of Thicker Exploding Wires", unpublished DERA report LWS/WS4/58-ETL/ERD017, March 2001

5 M. J. Taylor, "ET114 – Estimation of Radiant Energy Emission from a Plasma Jet", DERA unpublished report WSS/WS4/58-ETL/ERD008, February 2000

6 M. J. Taylor, "ET085 - Recording the Time Integrated History of a Plasma Jet Through a Pressurised Bed by Direct Vapour Deposition", QinetiQ unpublished report WSS/WX6/01-ETG/ERD021, June 2001

7 R. Alimi et al, 'ETC Research at Soreq NRC, Israel", IEEE Transactions on Magnetics, Vol. 37, 1, January 2001

8 R. A. Marshall, Editor "The Properties of Copper and Hydrogen Plasma", Classified RARDE report 86/2163

9 C. Woodley, QinetiQ, private communication

10 C. C. Hsiao, G. T. Phillips and F. Y. Su, "A Numerical Model for ETC Gun Interior Ballistics Applications," IEEE Transactions on Magnetics, Vol. 29, 1, January 1993

11 R. B. Mohanti and J. G. Gilligan, "Time Dependent Simulations of the Plasma Discharge in an Electrothermal Launcher," IEEE Transactions on Magnetics, Vol. 29, 1, January 1993

12 J. D. Powell and A. E. Zielinski, "Capillary Discharge in the Electrothermal Gun," IEEE Transactions on Magnetics, Vol. 29, 1, January 1993

13 K. Kappen and U. H. Bauder, "Simulation of Plasma Radiation in Electrothermal-Chemical Accelerators," IEEE Transactions on Magnetics, Vol. 35, 1, January 1999

14 M. A. Bourham, J. G. Gilligan and W. F. Oberle, "Analysis of Solid Propellant Combustion Behaviour Under Electrothermal Plasma Injection for ETC Launchers," IEEE Transactions on Magnetics, Vol. 33, 1, January 1997

15 K. Gruber, K. Kappen, A. Voronov and H. Haak, "Radiation Absorption of Propellant Gas," 10th Electromagnetic Launch Symposium, San Francisco, California, 25th – 28th April 2000

16 K. Kappen and U. H. Bauder, "Calculation of Plasma Radiation Transport for Description of Propellant Ignition and Simulation of Interior Ballistics in ETC Guns," IEEE Transactions on Magnetics, Vol. 37, 1, January 2001

17 M. J. Taylor, "Measurement of the Properties of Plasma from ETC Capillary Plasma Generators," IEEE Transactions on Magnetics, Vol. 37, 1, January 2001

18 C. M. Edwards, M. A. Bourham and J. G. Gilligan, "Experimental Studies of the Plasma-propellant Interface for Electrothermal-chemical Launchers", IEEE Transactions on Magnetics, Vol. 31, 1, January 1995

19 M. A. Bourham and J. G. Gilligan, "Analysis of Solid Propellant Combustion Behaviour under Electrothermal Plasma Injection for ETC Launchers", IEEE Transactions on Magnetics, Vol. 33, 1, January 1997

20 H. Penner, "Ignition of High-performance Gun Ammunition", 66th (B) Specialist Meeting, AGARD, Propulsion and Energetics Panel, Interior Ballistics of Guns, Florence, Italy, 9th – 11th September 1985

21 M. J. Taylor, "Ignition of Propellant by Metallic Vapour Deposition for an ETC Gun System", Propellants, Explosives, Pyrotechnics, 26, pp 137 – 143, August 2001

22 F. J. Bayley, J. M. Owen and A. B. Turner, "Heat Transfers", Nelson 1972, pp. 347-352

23 W. Nusselt, "The Filmwise Condensation of Steam", Z. Ver. Dt. Ing. 60, (1916)

24 7th Smithells Metals reference Book 14-6

25 Extrapolated from 7th Smithells Metals reference Book 14-11

26 Goodfellow Cambridge Ltd. catalogue 1996/97

27 C. Woodley, DERA, private communication, March 2000

28 P. Kaste et al, "Analysis of Burning Rate Phenomena and Extinguished Solid Propellant From an Interrupted Closed Bomb with Plasma Igniter", IEEE Transactions on Magnetics, Vol. 37, 1, January 2001

29 Thomas Weise, "German Nation Overview", IEEE Transactions on Magnetics, Vol. 37, 1, January 2001

30 R. Alimi, C. Goldenberg, L. Perelmutter, D. Melnik and D. Zoler, "A Solid Phase Model for Plasma Ignition of Solid Propellant", Proc. 1st International Symp. On Chemical Propulsion, Stockholm, Sweden, May 1996

Chapter 8 – Plasma propagation and ignition studies: Small-scale ETC ignition experiments

1 German small-scale ETC ignition experiments

1.1 Introduction

1.1.1 As stated previously, the two main contenders for energy transfer from ETC plasma to propellant leading on to propellant ignition are radiation and (the Author's hypothesis) metallic vapour deposition. In this chapter, a critique is provided of open and closed vessel plasma ignition experimentation performed by other groups, along with the Author's own investigations into that work. It further describes an experiment designed to quantify the effect of radiant energy upon propellant during the ignition phase from an ETC plasma discharge.

1.1.2 Plasma ignition experiments have been jointly conducted by the Fraunhofer-Institut für Chemische Technologien (ICT) and Technologiezentrum Nord (TZN) for the German Government [1, 2, 3, 4, 5, 6], using opaque (standard) and translucent (modified) forms of a similar propellant composition (JA2) in a small-scale closed chamber (volume 96 cm^3). This work compared the effects of plasma (radiation) on opaque and translucent propellant. The only difference in the composition was that the opaque propellant contained a small percentage by mass (0.05%) of graphite as parts of the standard composition to turn the naturally translucent propellant opaque. In particular, the translucent formulation exhibited enhanced gas generation rates (EGGR) due to plasma ignition in tests conducted in closed vessels. Tests in the open air showed that significant damage

was being done to the translucent formulation when exposed to plasma that would produce increased surface area when burnt. The aim of the work was to tailor a propellant whose burn-rate could be enhanced by an ETC plasma discharge. The effects were claimed to be due to plasma radiation, although no measurements of the incident flux were made to support this claim.

1.1.3 In the work conducted by the Author, measurements were made of the radiative flux incident on a translucent propellant surface of similar composition to JA2, both during open air and closed vessel tests with plasma and conventional ignition [7]. Damage to translucent propellant was found to occur, but it was limited to aluminium plasma with much greater discharge energy densities than reported by ICT. No conclusive correlation was found between measured incident radiative flux and the damage to the propellant grain. Closed vessel tests showed no enhanced burn of translucent propellant with plasma ignition, so the conclusions reached by ICT and TZN were not valid for conditions at Fort Halstead.

1.1.4 Some calculations have been performed by the Author to determine the temperature rise of propellant compositions from incident radiative flux measurements during an ETC plasma discharge. The temperature rise of the translucent propellant surface would be as little as a few kelvin, and for opaque compositions the surface temperature rise would be less than one hundred kelvin. Plasma ignition by radiative energy

transfer is thus very unlikely in QinetiQ ETC plasmas. However, the ignition delay in conventional ignition tests increased twelve-fold with respect to plasma ignition tests at comparable energy.

1.2 Closed vessel test results – ICT and TZN

1.2.1 Closed vessel results from ICT and TZN appear in Figure 8.1 [1, 5]: they indicate that there is no difference between opaque and translucent compositions with conventional powder (1 g mass of B/KNO_3) ignition. It was claimed [5] that the gas generation rate for plasma ignition, of the standard opaque JA2 composition at a given pressure was found to be similar to that ignited conventionally. However, the gas generation rate of translucent propellant was faster with plasma ignition.

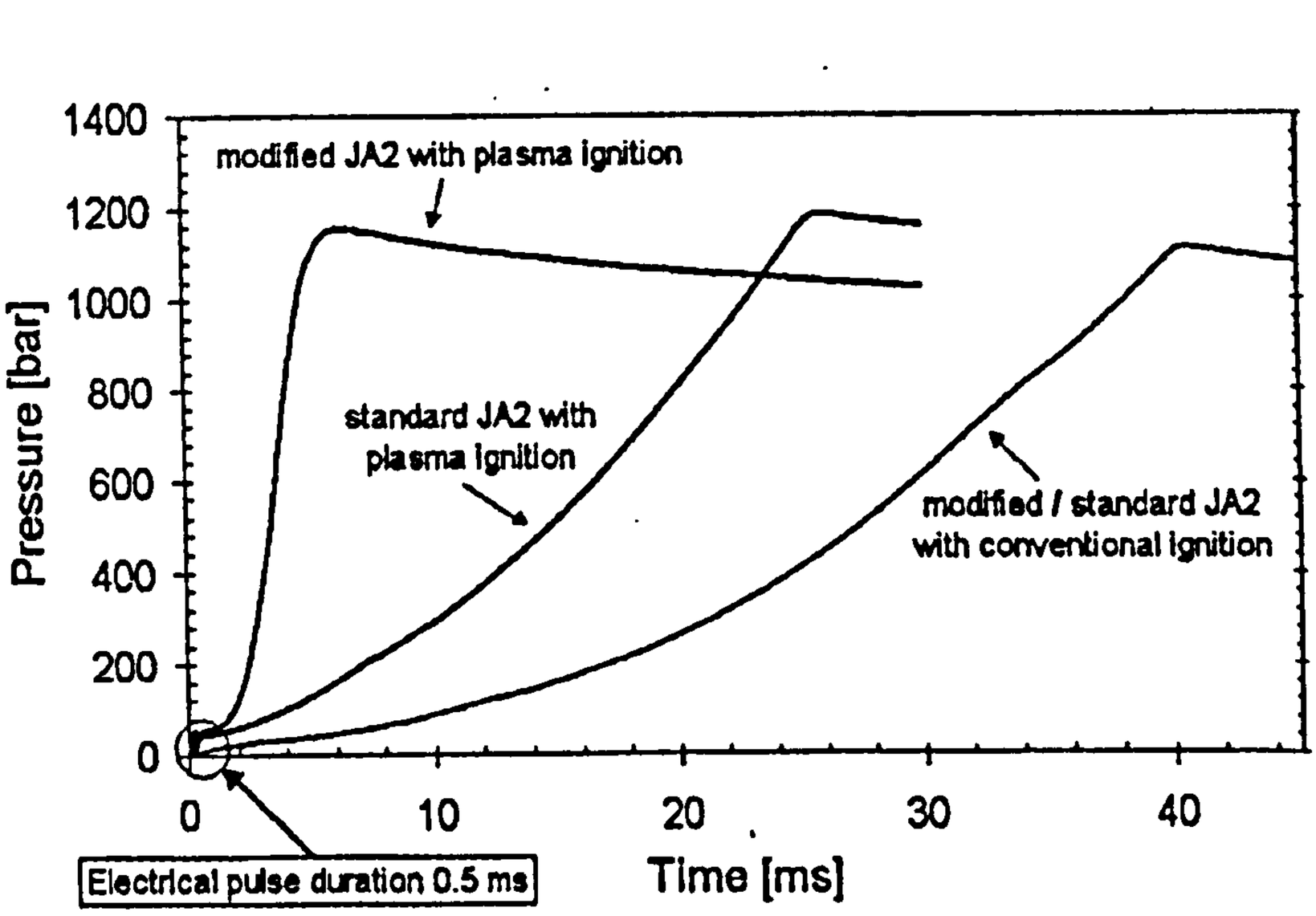

Figure 8.1 Results with conventional and plasma ignition of opaque and translucent JA2

1.2.2 The conclusion reached by ICT and TZN from this work, with some supporting experimental evidence from interrupted burn tests and using

lasers as a radiation source [2], is that radiative energy from the plasma penetrates the translucent propellant and causes physical damage within the bulk grains. This allows for a greater gas generation rate during the burn arising from the increased surface area. The plasma generator employed by ICT and TZN was a current injection type using aluminium wire, with the propellant in the form of a tube that fitted into the cylindrical vessel. The plasma initiation wire was around 17 mm from the propellant surface [8]. It was the Author's opinion that the closed chamber tests should be repeated with different types of plasma generator to test the generality of the results to all types of plasma generator, or if they were plasma generator specific. The Author has attempted to do this with a CPG and copper initiation wire. Some of ICT and TZN's original work has also been reproduced (as far as possible) by the Author but with a composition other than JA2.

1.2.3 The plasma ignition energy used in the study by Koleczko et al [3] was around 2 kJ with a pulse duration of 0.5 ms. The temperature the plasma attained was not reported, and without detailed knowledge of the plasma generator, no estimations of the temperature can be made. However, this energy is only sufficient to vaporise around 0.3 g of metal, quite apart from attaining any reasonable plasma temperature. The results from Voronov et al in supporting confirmation laser tests [2] were performed under conditions far from those of the plasma ignition tests [1, 3]. The radiant energy used for the supporting laser experiments was monochromatic laser radiation (wavelength,

λ = 1053 nm), with a total energy, ε of 0.5 J discharged in a pulse duration, τ of 20 ns and over an area, A of 7.9 X 10^{-7} m^2. This gave an incident radiant flux density, Φ of 3.2 x 10^{13} W m^{-2} onto monolithic propellant grains. Using the Stefan-Boltzmann radiation law, a blackbody emitter at a (brightness) temperature, T_b of around 150 000 K would be required to reproduce this flux. The propellant was damaged to a depth of around 5 mm [2]. Knowing the absorption coefficient of the propellant, a threshold energy value, ε_t for radiation damage was given as 2.3 x 10^5 J m^{-2}. This gives a threshold flux density of 1.15 x 10^{13} W m^{-2} and a blackbody equivalent threshold temperature of around 120 000 K for the 20 ns pulse, thus representing an excessively hot and short-lived ETC plasma. Small-scale ETC plasma ignition discharges occur more typically over around 0.5 ms. If the same energy density were to be delivered in 0.5 ms rather than 20 ns, this would give an incident flux density of 13 x 10^8 W m^{-2}, requiring a plasma with a more likely brightness temperature of around 12 000 K. The threshold flux density would then be 4.6 x 10^8 W m^{-2}, requiring a plasma with a threshold brightness temperature of 9 500 K. These temperatures are far more reasonable than those in the hundreds of thousands of kelvin, especially with such low discharge energies. The various strands of the above argument are summarised in Figure 8.2.

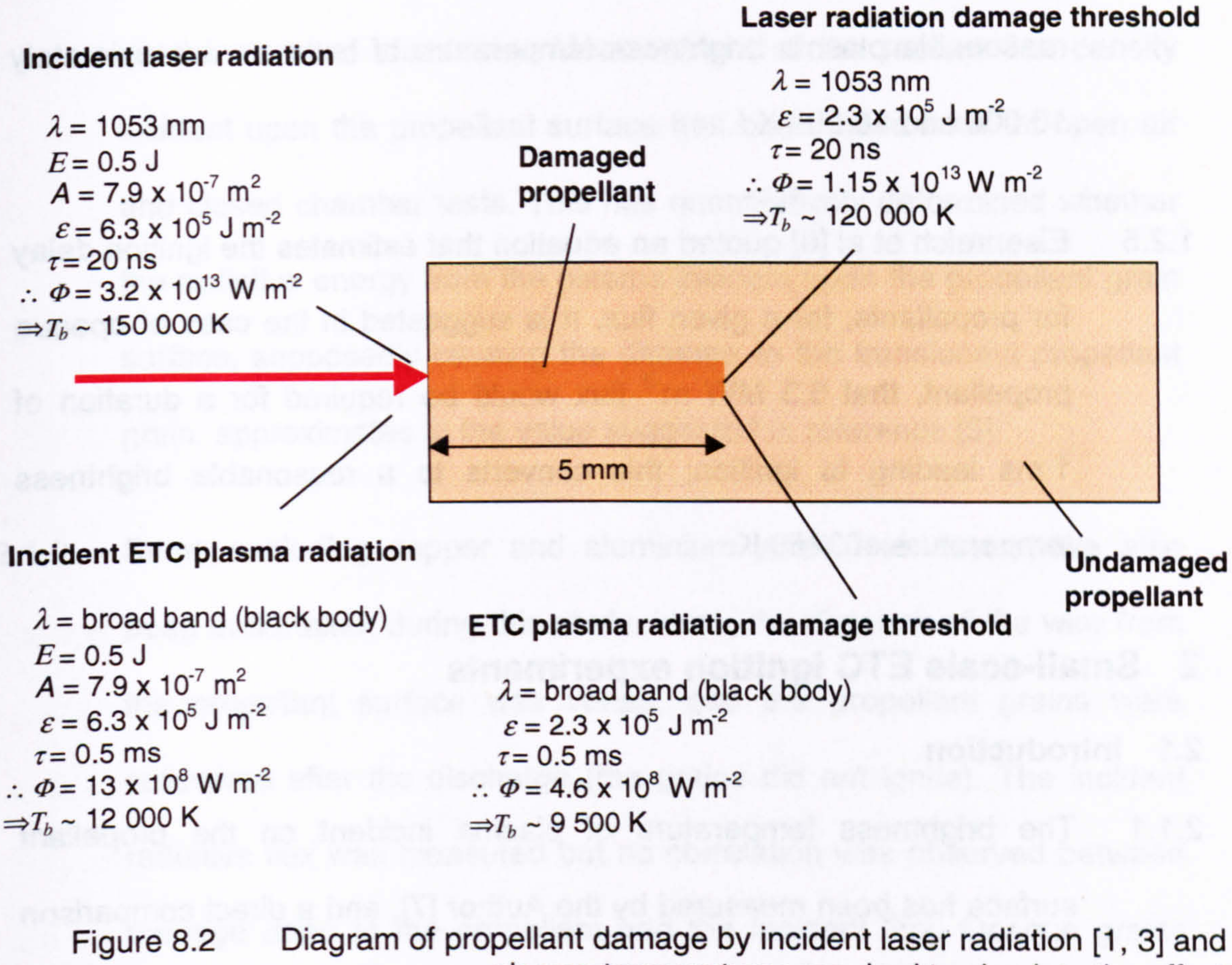

Figure 8.2 Diagram of propellant damage by incident laser radiation [1, 3] and plasma temperatures required to simulate the effect

1.2.4 It is generally the power and not the energy that is important in radiation damage and so the laser tests detailed in reference [2] were concluded as unrepresentative due to the excessively high power density. Detailed in reference [5] are the results of other estimates from ICT for the power density transferred from plasma to propellant. These estimates are based on closed vessel gas generation rate values of the *opaque* JA2, subjected to plasma pulses. Radiation supposedly incident upon and absorbed by the propellant surface caused burning rates to increase leading to quoted values of incident power density. The estimated power density is given as between 7.5×10^8 W m^{-2} and 35×10^8 W m^{-2} during a typical ETC discharge. This corresponds to a

reasonable plasma brightness temperature of between approximately 10 000 and 16 000 K.

1.2.5 Eisenreich et al [6] quoted an equation that estimates the ignition delay for propellants, for a given flux. It is suggested in the case of opaque propellant, that 6.3 MW m^{-2} flux would be required for a duration of 1 ms leading to ignition; this converts to a reasonable brightness temperature of 3250 K.

2 Small-scale ETC ignition experiments

2.1 Introduction

2.1.1 The brightness temperature of plasma incident on the propellant surface has been measured by the Author [7], and a direct comparison made with the values quoted above. Hence, the conclusion that the physical damage is due to radiative effects has been challenged for a CPG-type plasma generator.

2.1.2 The experiment described here attempted to repeat the conventional and plasma ignition closed vessel experiments with translucent and opaque propellant in references [1 & 3]. An exact replication was not the aim: these tests attempted to indicate whether the results of gas generation rate enhancement from plasma ignition of translucent propellant as reported by ICT and TZN were generally reproducible. A capillary plasma generator was used rather than a current injection type plasma generator, with seven solid cylindrical propellant grains rather than single tubes. Copper was the plasma initiation wire material

used instead of aluminium. Measurement of the radiant flux density incident upon the propellant surface has been made both for open air and closed chamber tests. This has quantitatively determined whether the radiative energy from the plasma incident upon the propellant grain surface, supposedly causing the damage to the translucent propellant grain, approximates to the value suggested in reference [5].

2.1.3 Some exploding copper and aluminium wires-in-air tests have also been undertaken during this study. Here, the distance of the wire from the propellant surface was varied, and the propellant grains were recovered after the discharge (the grains did not ignite). The incident radiative flux was measured but no correlation was observed between damage done to the propellant and the incident flux. Opaque grains suffered no damage, but far greater damage was observed in translucent grains from aluminium rather than copper wires so shock is speculated as responsible for the damage. This would require the graphite to alter the attenuation of the shock front in such a way to prevent damage being done.

2.1.4 With the set-up described below for the closed vessel tests, the plasma can be assumed fairly uniform where the propellant is located at a distance greater than around 100 mm from the nozzle. Each grain can then be assumed to receive a similar ignition impetus. The moment that ignition occurs can thus be determined from the presence of spectral lines of the propellant trace elements sodium and potassium. An

estimation has been made of the incident radiative flux contributing to the plasma ignition of propellant.

2.2 Set-up for closed vessel tests

2.2.1 Translucent and opaque (with 0.05% graphite) double-base NG/NC

propellant grains, similar in composition to JA2, have been obtained [9]. The geometry of this propellant is cylindrical, with a diameter of 15 mm and length of around 25 mm. Seven of the translucent samples were glued to the end plate of the Universal vessel, providing a propellant mass of around 50 g. They were ignited both by a plasma from a CPG located opposite the end plate at the far end of the chamber, and also conventionally ignited in a second test by use of a puffer bag also located opposite the end plate. These tests were repeated with the opaque propellant samples. Pressure/time data were acquired for each test and the four sets of tests were compared with the results from references [1] and [3]. The entire test sequence was repeated to check for variability.

2.2.2 An additional diagnostic technique was UV/vis/NIR time-resolved

spectroscopy (see Appendix A). The radiant flux density incident upon the grain surface could be measured by inserting a sacrificial optic fibre through the end plate and into a propellant grain, followed by absolute calibration of the spectrograph system *in situ*. Figure 8.3 is a schematic diagram of a propellant grain and the arrangement of the seven grains

on the end plate of the Universal vessel; the fibre is inserted into the central grain.

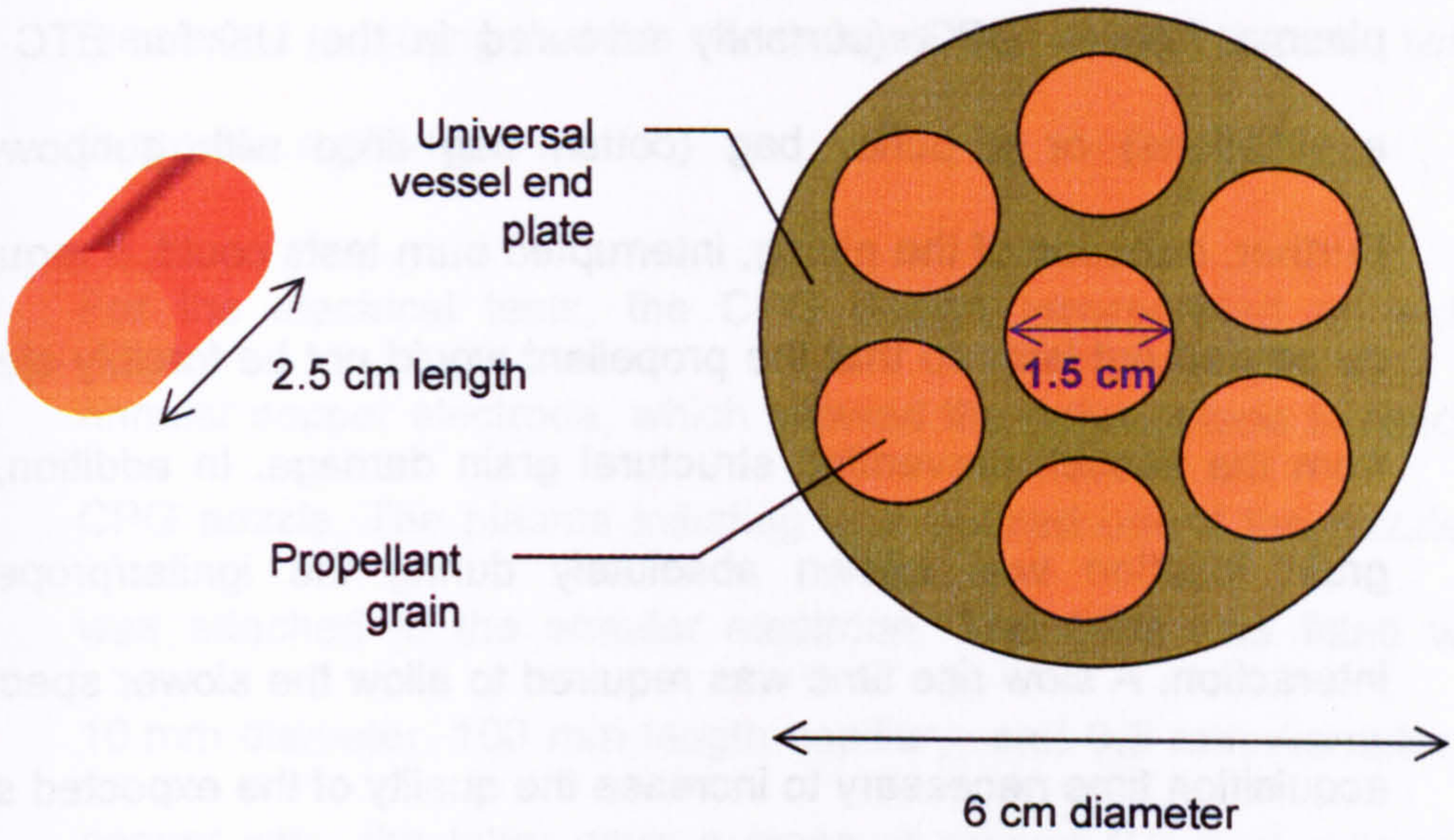

Figure 8.3 Propellant geometry for closed vessel plasma ignition tests

2.2.3 Figure 8.4 shows the pressure/time rise predicted [10] for this propellant composition, mass and geometry in the Universal vessel. The long rise time results from the large surface area of the propellant.

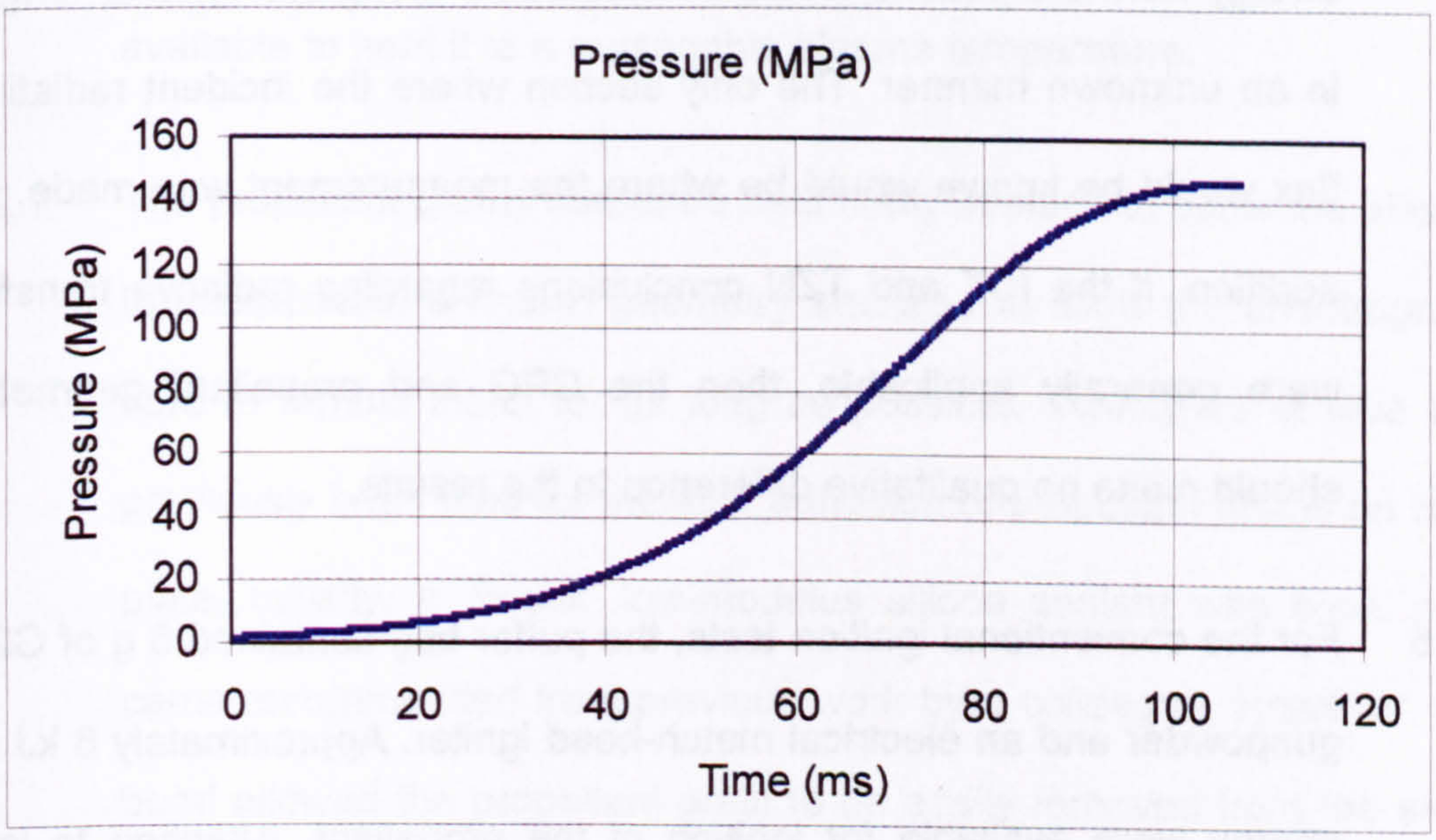

Figure 8.4 Pressure rise expected for this propellant composition

2.2.4 Much deliberation had gone into the design of the propellant grain geometry. A versatile arrangement was needed that could be ignited by plasma from a CPG (currently favoured in the UK for ETC gun applications) or a puffer bag (cotton bag filled with gunpowder). Further, because of the gluing, interrupted burn tests could, if required, be carried out later so that the propellant would not be forcibly ejected from the vessel, preventing structural grain damage. In addition, the grain location was known absolutely during the igniter/propellant interaction. A slow rise time was required to allow the slower spectrum acquisition time necessary to increase the quality of the expected small amplitude spectra of low temperature plasma/vapour. The work carried out by ICT and TZN used a hollow cylindrical grain the length of the chamber, with current injection for plasma ignition. However, the hollow cylinder would not be satisfactory with a plasma jet from a CPG, as the energy from the plasma would be distributed along the cylinder length in an unknown manner. The only section where the incident radiative flux would be known would be where the measurement was made. In addition, if the ICT and TZN conclusions regarding radiative transfer were generally applicable, then the CPG and propellant geometry should make no qualitative difference to the results.

2.2.5 For the conventional ignition tests, the puffer bag contained 6 g of G20 gunpowder and an electrical match-head igniter. Approximately 6 kJ of energy were available for ignition of the propellant. Attached to low voltage ignition electrodes the leads to the puffer bag passed through

the instrumentation port nearest the far end plate, where it was secured by a screw to the electrodes. The electrodes were then screwed into the vessel (ensuring that the match-head lead did not become twisted) to provide a gas-tight seal.

2.2.6 For the electrical tests, the CPG design incorporated an external annular copper electrode, which allowed the polyethylene to reach the CPG nozzle. The plasma initiating wire passed out of the nozzle and was attached to the annular electrode. The CPG was fitted with a 10 mm diameter, 100 mm length capillary, and 0.5 mm diameter pure copper wire: the latter gave a mass of around 0.2 g of copper. The capacitor bank was fitted with a 150 μH inductor, and charged to 43% in 11 kV mode. This discharged around 6 kJ of energy, similar to the conventional ignition stimuli. Only around 1.2 kJ of this energy were required to evaporate the copper; the remaining 5 kJ or so were available to heat it to a reasonable plasma temperature.

2.2.7 The propellant grains had to be held firmly in place to allow the plasma to interact with a known geometry and also to allow the spectrograph fibre to remain intact for as long as possible. Two types of glue had previously been tried for the safe adhesion of propellant grains on steel plate. Initially, a 'Bostik' low-modulus silicon sealant was tried, as it came recommended from previous work by a colleague. However, this bond allowed the propellant grain to be easily removed from the steel. 'Araldite' was then tried and this held fast against as much force as

could be applied by hand. The glued propellant sample has been subsequently stored safely in a fume cupboard for several days to test for any possible chemical reactions. When the grain was inspected, no sign of any reaction could be detected at the glue/grain interface. Thus, Araldite was used to glue the propellant to the end face of the Universal vessel.

2.2.8 A total of 30 tests was carried out for this experiment, many of which were simply exploding wire tests for determining the damage mechanisms involved with the translucent propellant.

2.3 Spectrograph calibration problem

2.3.1 As already explained in Appendix A, the same experimental geometry must be used or copied for certain parts of the spectrograph calibration process. For this experiment, radiation incident upon the surface of a propellant grain was the prime interest. The emitter (plasma) was expected to be in intimate contact with the propellant and the spectra were acquired from within a translucent propellant grain. Thus, ideally, the objective end of the spectrograph fibre optics would be inserted into the propellant grain and the full calibration routine carried out, with the heated graphite calibration sources against the propellant grain. Unfortunately, this was impractical since the propellant would ignite, so the graphite acquisition had to be performed without the propellant *in situ*. Further, the spectrograph detector charge shifting idiosyncrasy alluded to in Appendix A, required the tungsten irradiance calibration

lamp spectra to be acquired in kinetics mode. The low intensity of this lamp, together with the absorption by the translucent propellant grain, ensured that this had to be done without the propellant grain in situ if excessively long exposure times (of around eight hours!) were to be avoided. Thus, the tungsten acquisition also had to be performed without the propellant in place.

2.3.2 A procedure for calibrating the system in such instances has been devised by the Author. It involves measuring the spectral transmittance, '$k\ (\lambda)$' where $k \leq 1$, of the propellant sample and dividing the experimental spectra by this so that a 'perfectly transparent' propellant is used throughout. Then, the graphite and tungsten acquisition can be accomplished without the propellant in situ. The transmittance of the propellant sample is measured by acquiring spectra of the tungsten lamp (with the spectrograph detector in standard mode) with and without the propellant. If the spectrum acquired without propellant records '$\phi\ (\lambda)$' counts per second, and that with the propellant records '$\phi\ (\lambda)\ k$' counts per second, then the transmittance, k, can be obtained simply by dividing '$\phi\ k$' by 'ϕ'. The experimental data, $\phi_\varepsilon\ (\lambda)\ k$ are divided by k to give $\phi_\varepsilon(\lambda)$: the propellant then becomes 'perfectly transparent'. To ensure k does not change between its measurement and the test, the graphite, tungsten and '$\phi\ (\lambda)$' spectra are all acquired before the spectrograph fibre is placed into the propellant and then

'$\phi(\lambda)\ k$' spectra are acquired afterwards. The propellant can then stay, glued to its mount, for the test.

2.3.3 Figure 8.5 represents an example of the values of k for translucent propellant in Test 19 of this experiment, ET163. This value is test specific in that it depends upon: (i) the depth of the hole drilled (or of the propellant sample thickness if using a slice as a window); (ii) the degree of polishing on the propellant surface and (iii) the finish within any drilled hole. Where the finish within the hole was good and a polished surface was being used, the value of k was far greater than shown in Test 19 (Figure 8.5). As long as k was measured for each test where absolute calibration was required, and the sample was not removed from the spectrograph objective fibre once calibration had been performed the variation of k mattered little from test to test.

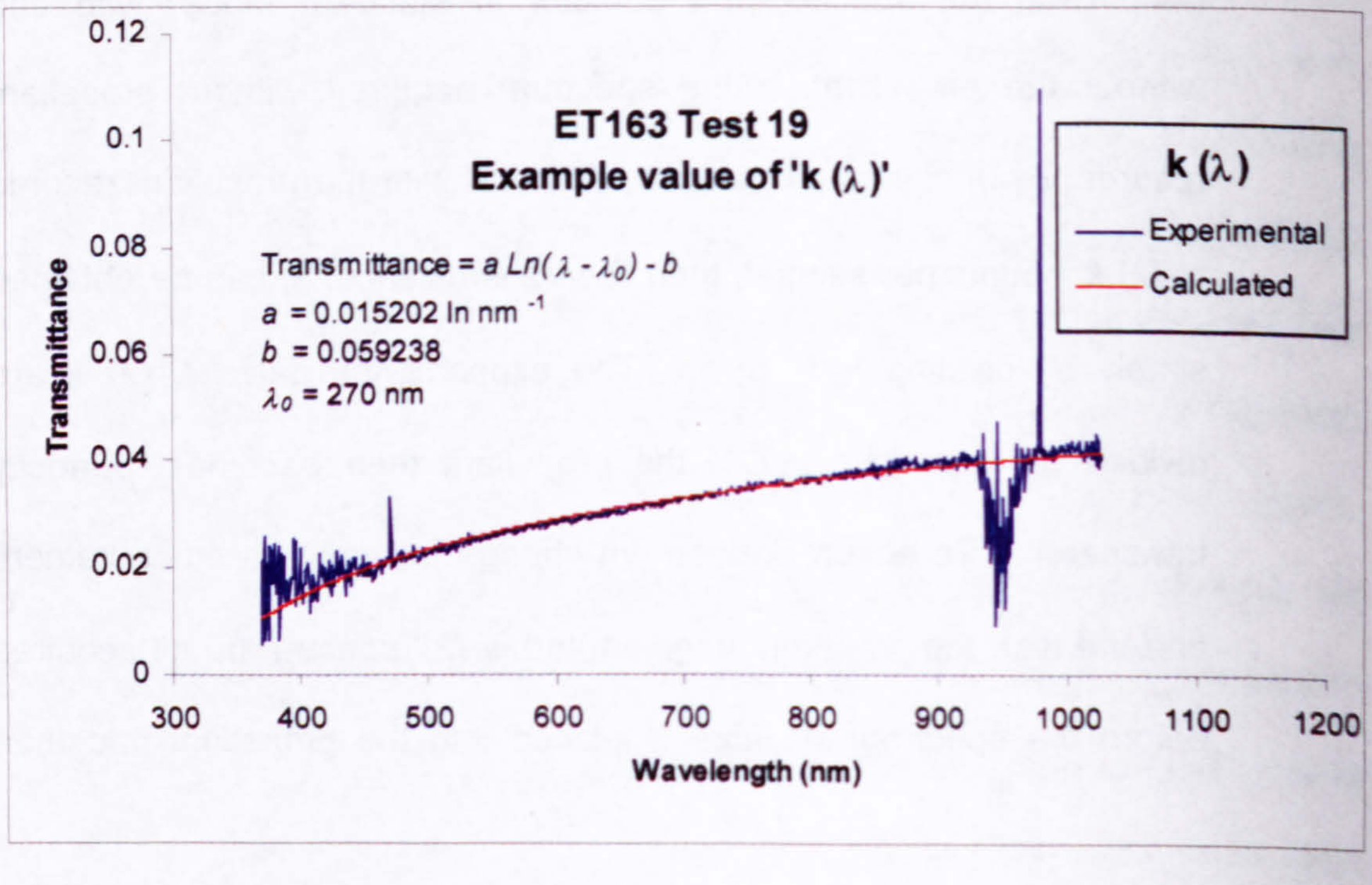

Figure 8.5 Example of transmittance, k for translucent propellant

2.3.4 A further improvement in the application of *k* has been made. This is based on the fact that *k* smoothly varies with wavelength. A fit has been made to the experimental data to eliminate the spectral noise and such an example appears in Figure 8.5. From various fitting schemes, a logarithmic fit to '$a\ ln\ (\lambda - \lambda_0) - b$' was the most appropriate. This required knowledge of the wavelength, λ_0 where the transmittance would tend to zero. In practice, this was obtained from a method of minimising the sum of the squares of the differences between the experimental data and the fitted curve and involving the 'solver' routine within Microsoft Excel to adjust the three constants, *a*, *b* and λ_0. Only the reliable portion of the curve was used for this fitting process. The dip in the experimental data at around 950 nm was due to excessive absorption by the 40 m length silicon objective fibre, noise at the lower wavelengths not being included in the fitting routine. It is interesting to note that, with this propellant, significant transmittance seems to occur into the near-ultraviolet with a cut-off at around 270 nm: the propellant transmittance reported by ICT showed a distinct cut-off at around 425 nm.

2.3.5 However, during this experiment, each test was subjected to a brief analysis at the end of the day's work, so that the progress of the experiment could be gauged. In addition, if any new ideas were worth following up based upon that day's results, then arrangements could be made accordingly. However, a mistake was made in the application of *k* during the daily analysis which went unnoticed at the time because

the results were so convincingly good (i.e. fitting to a theoretical blackbody). It only came to light afterwards during consideration of the multistep calibration process.

2.3.6 During the daily analysis between tests, the *graphite* data were mistakenly divided by *k*. No application of *k* should have been made to these graphite data, however, as the objective fibre was not embedded within the propellant sample during the graphite spectra acquisition. The results still gave excellent fitting of blackbody curves to experimental data. Later, upon correct application of *k*, it was discovered that the *experimental spectra* needed to be divided by a constant to obtain such an excellent fit. The value of this constant changed from test to test, between 1 and 30. The experimental spectra should not have needed any division by a constant unless something had changed the experimental geometric constant, Λ (see Appendix A). The successful (although incorrect) application of a constant could only be explained if this division were countering some other error. The last test in this experiment, 'methodology check', was designed to check the calibration procedure to determine whether some subtle aspect could account for the successful application of *k* to the graphite spectra, or otherwise requiring the experimental data to be divided by a constant. In this methodology check test, the ignition source used was the graphite sample. As this ignition source was well understood, (i.e. the temperature and emissivity were well known), any problems associated with the method could be easily identified.

2.3.7 As it transpired, the problem was tracked to the use of unpolished propellant: scattering on the unpolished face of the propellant sample artificially increased the effective collection area of the fibre. This was not accounted for in the calculation of Λ, as the sample was not located on the fibre for the graphite spectral acquisition. The greater the degree of roughness, the greater the collection area and subsequent divisor. Two unpolished faces actually existed: the external propellant face and an internal face produced by drilling a 1 mm diameter hole into the propellant, into which the spectrograph fibre was inserted. Those tests where the divisor constant, c = 1 had spectra recorded through the *smooth* curved face of the propellant (i.e. ET163 Tests 14 – 17). This indicated that it was the outer face that required polishing, to cut down the resulting scatter. Indeed, when light was shone backwards through the fibre, the scattering effect could be clearly seen on unpolished faces. Polishing the propellant has since been performed using 30, 12, 5 and 1 μm fibre optic linnishing paper, with alcohol as a wetting agent.

2.3.8 The fact that dividing the graphite by *k* gave almost precisely the same flux as dividing the spectrum by a constant was not easy to understand. On further investigation, it was discovered that the graphite temperature as determined by blackbody fitting was around 100 K hotter in the case where the graphite spectrum was inadvertently divided by *k*. The fit was equally good in both cases. This was only possible because the shape of the absorption curve, *k* was very similar

to the shape of the *change* that occurs to a blackbody spectral profile as it is heated by around 100 K.

2.3.9 Figure 8.6 attempts to explain the problem. Figure 8.6a shows the theoretical blackbody spectrum fitted to that of graphite, which had (correctly) not been divided by *k*. This fit indicated that the temperature of the graphite was 1816 K. Figure 8.6b shows the theoretical blackbody spectrum fitted to that of graphite, which *had* been divided by *k*. This fit showed the temperature of the graphite was 1914 K. Figure 8.6c compares the division of the two blackbody curves, with the division again by 13. The profile shape and magnitudes of the blackbody curve ratio and *k* are almost identical: this is a staggering coincidence, as the two curves are totally independent. The factor 13 is the constant by which the experimental spectra needed to be divided to obtain sensible answers, when the proper analysis was undertaken. This meant that 13 times more light was collected as a result of scattering from the unpolished propellant faces; dividing the graphite curve by *k* coincidentally compensated for that fact. If *k* had been any other shape then the error would have been picked up quickly, because a reasonable fit of experimental data to a theoretical blackbody curve would not have resulted.

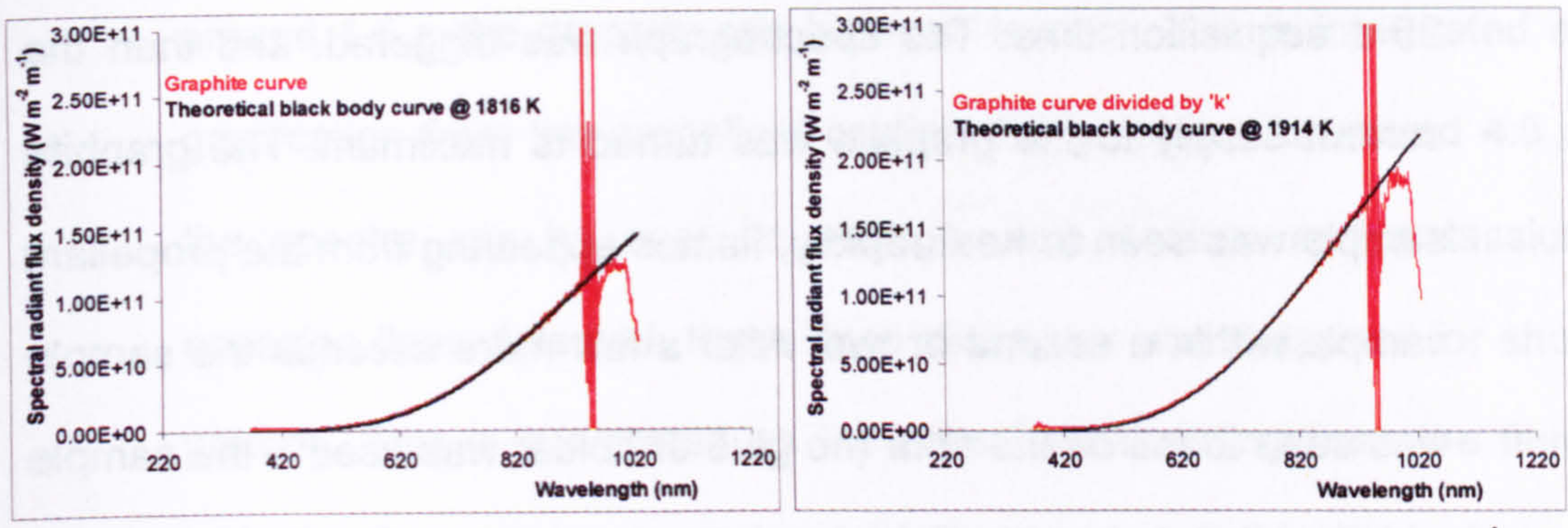

Figure 8.6 Origin of error resulting from division of graphite spectra by *k*

2.4 Methodology check test

2.4.1 Besides helping to resolve the (rather difficult) arguments presented above regarding the problem associated with the calibration procedure, this test gave some very useful data on the spectral criteria for ignition.

2.4.2 Figure 8.7 shows the arrangement for this test. The spectrograph was calibrated absolutely. The propellant sample, with the spectrograph fibre loosely inserted, was placed so as to touch the graphite sample. The spectrograph exposure time was set to 100 ms per curve, giving a

25 s acquisition time. The spectrograph was triggered, and then the current supply to the graphite was turned to maximum. The graphite sample was seen to heat rapidly, flames appearing from the propellant sample within a second or two. After a few more seconds the sample was seen to fall off the fibre (no glue or holder was used – the sample was just left in position over the fibre), and the power supply was promptly turned off.

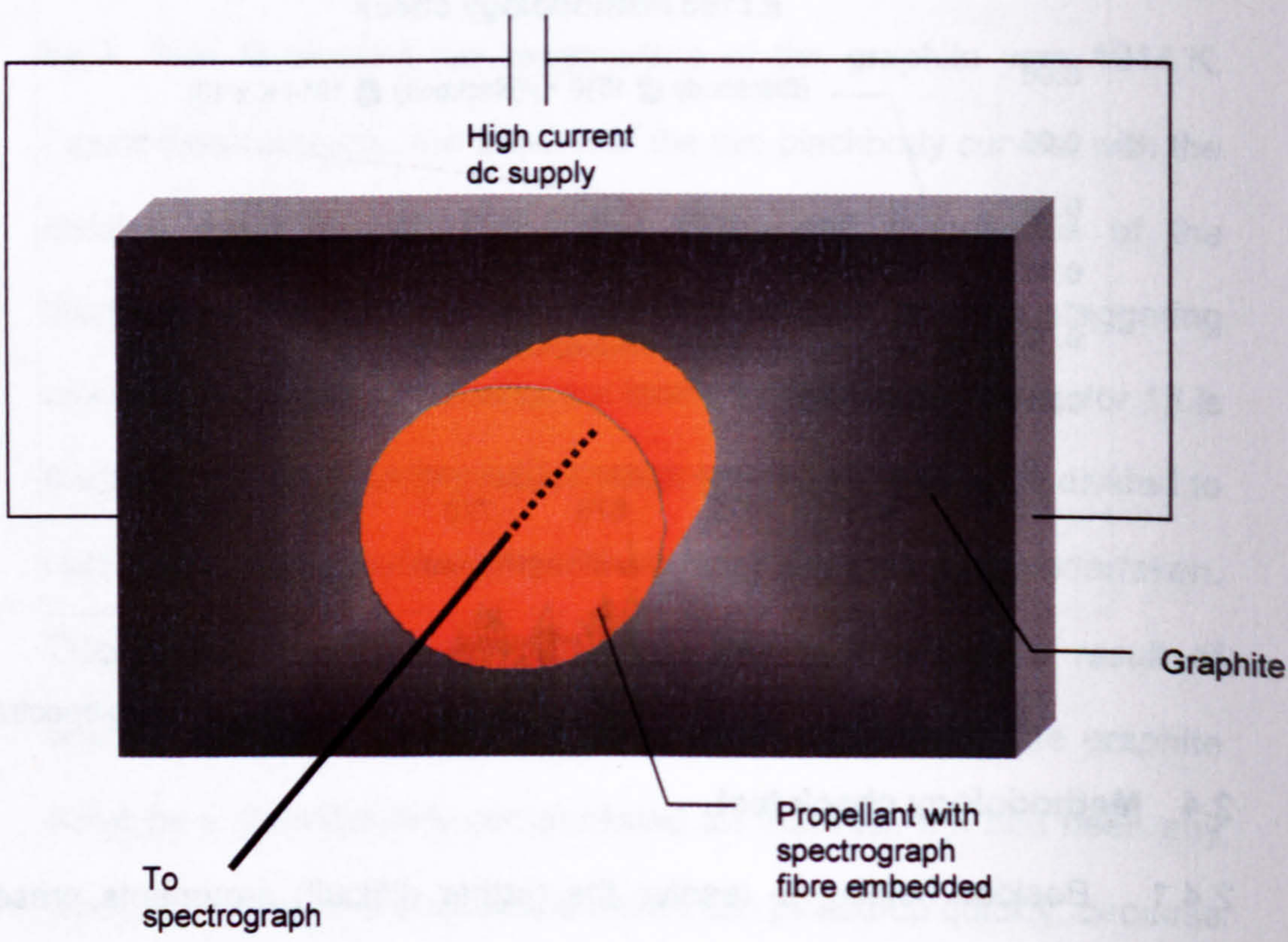

Figure 8.7 Methodology of ignition set-up

2.4.3 The calibrated spectra were analysed to determine the thermodynamic temperature of the graphite. Figure 8.8 shows the results from the spectrographic data. Initially, the graphite can be seen to heat up: left to itself, it would continue to heat until it burnt away. However, after

around 1.5 s the graphite can be seen to cool. This is interpreted as gasification from the propellant cooling the graphite. At around 4.5 s, the spectra can be seen to change, with sodium and potassium emission lines detected: these lines disappear and reappear for short periods. This is interpreted as the propellant tumbling from the fibre, with the flame going in and out of the spectrographic field of view. Finally, at around 8.5 s the graphite begins to cool, once the graphite power supply has been turned off.

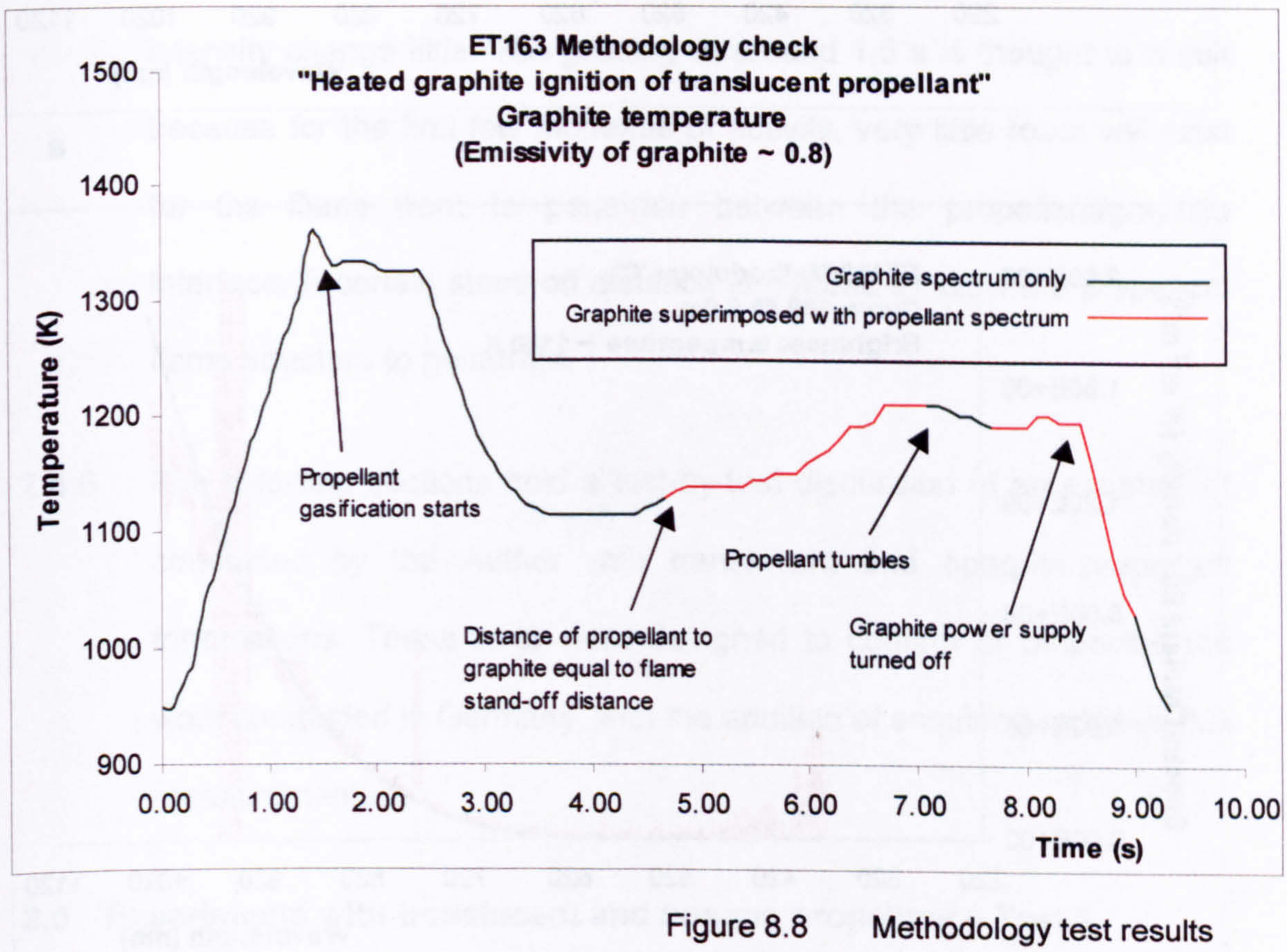

Figure 8.8 Methodology test results

2.4.4 Figure 8.9 has sample calibrated spectra and theoretical blackbody curves from the methodology test.

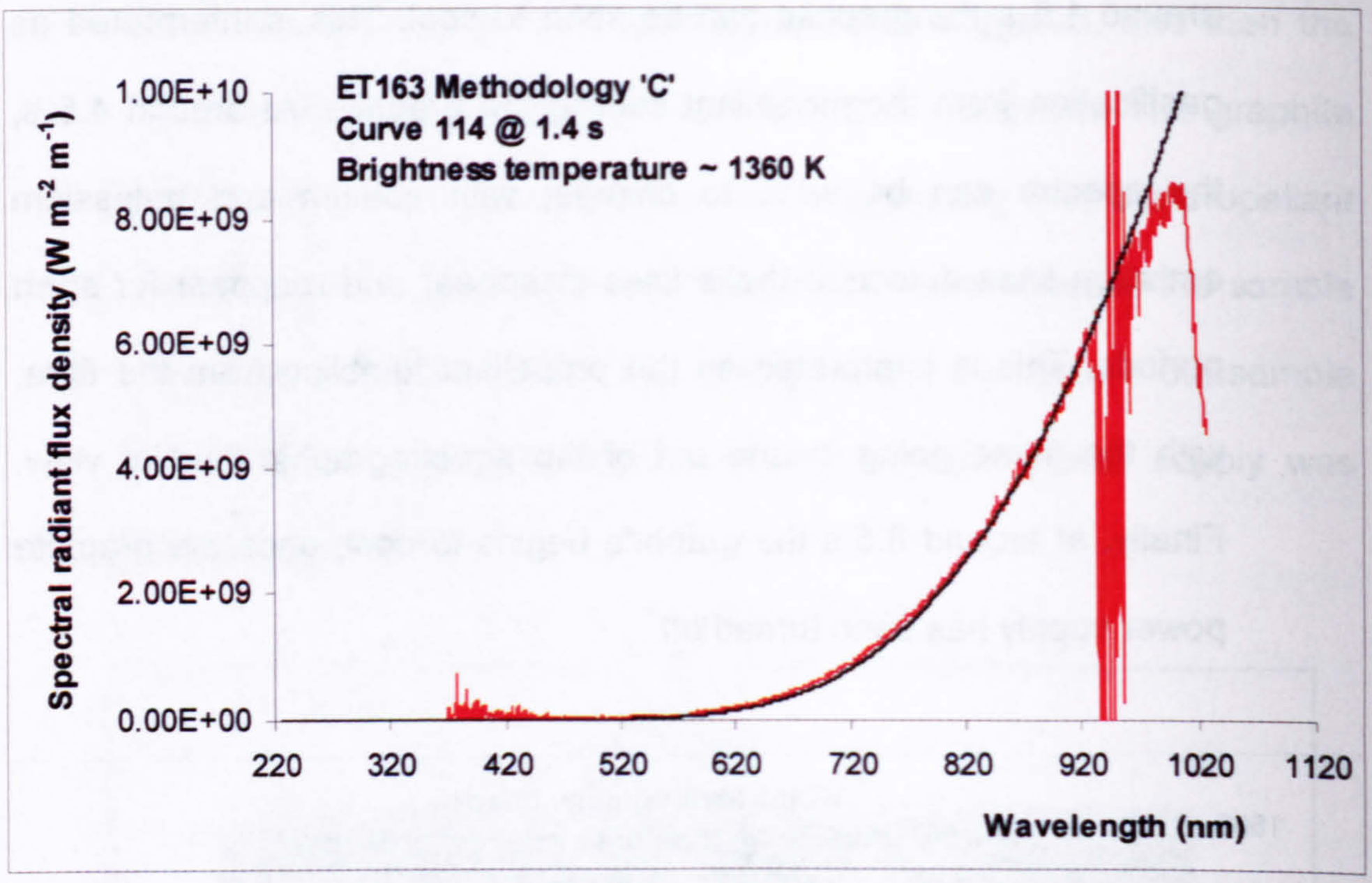

a

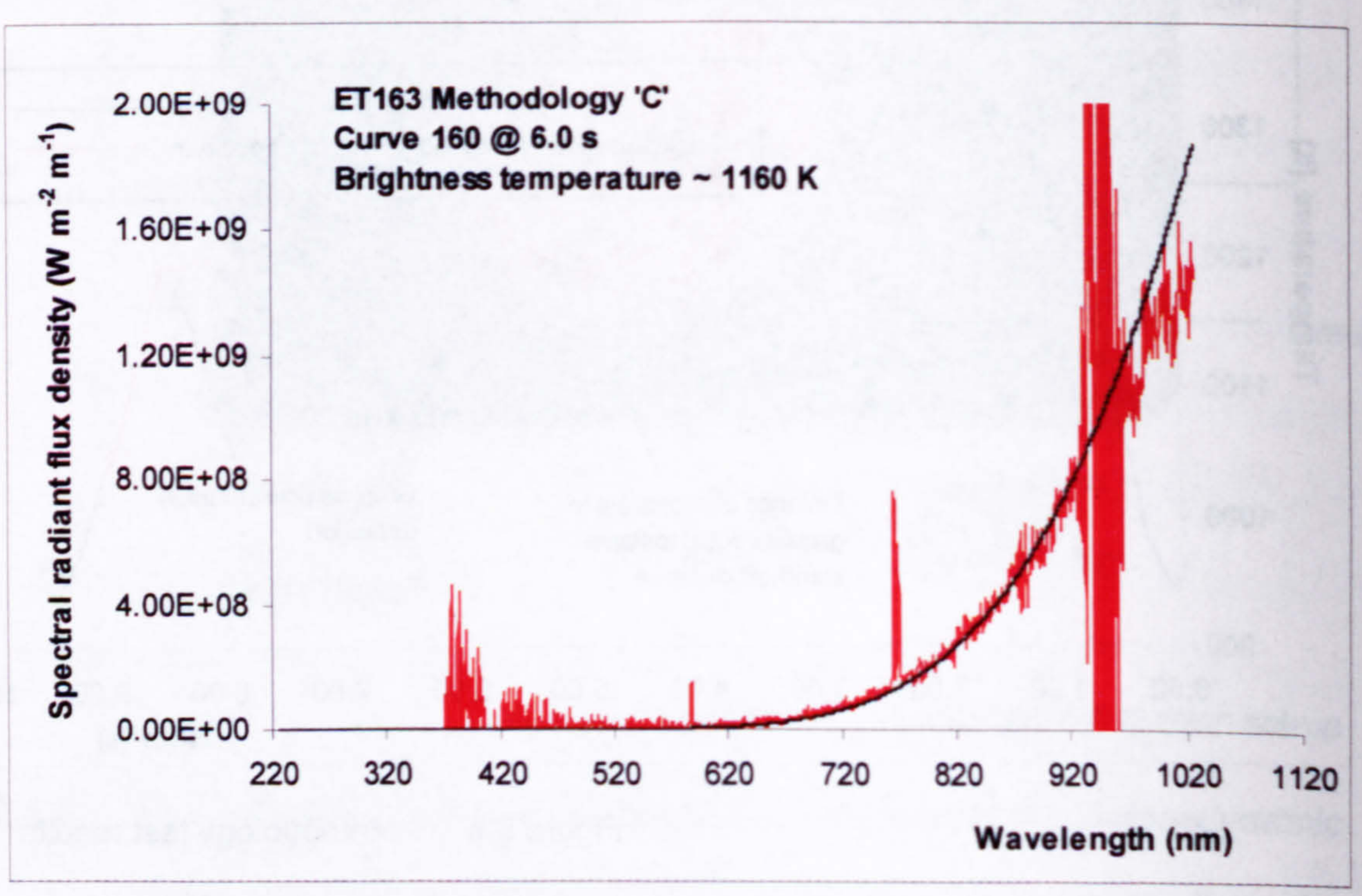

b

Figure 8.9 Example spectra from methodology test

2.4.5 The spectrum in Figure 8.9a was acquired at 1.4 s, when the graphite spectrum was hottest. The feature lying between 920 nm and 1000 nm was calibration noise due to strong absorption in the spectrograph objective fibre, and this occurs on all spectra during the experiment. The spectrum in Figure 8.9b was acquired at 6.0 s, where the sodium and potassium lines are superimposed upon the graphite continuum. The propellant flame at atmospheric pressure emits very little apart from the trace element wavelengths: this implies that the gas will be very transparent at all but these wavelengths, and so the graphite intensity change little. The gassing at around 1.5 s is thought to result because for the first few moments of activity, very little room will exist for the flame front to penetrate between the propellant/graphite interface. A certain stand-off distance is needed to allow the propellant flame structure to penetrate.

2.4.6 The following sections hold a test-by-test discussion of an experiment conducted by the Author with translucent and opaque propellant formulations. These tests were designed to confirm or otherwise the work conducted in Germany, with the addition of acquiring radiative flux measurements.

2.5 Experiments with translucent and opaque propellant – Test 1

2.5.1 Test 1 was designed to investigate the light levels expected for plasma ignition. The propellant was held in the open air. If the plasma was hot (i.e. tens of thousands of kelvin), then the spectrograph parameters

(e.g. exposure time, fibre diameter) had to be different to those needed for a cooler plasma (i.e. just a few thousand kelvin). The open-air location alters the plasma temperature slightly, but the test could be repeated several times, quickly and cheaply, for optimisation of the spectrograph system. Figure 8.10a shows how the fibre was inserted into the propellant for this test, with the propellant glued to a wooden rod. This simple assembly was held within the Universal vessel by retort stands and clamps in the same location as in closed vessel mode (as shown in Figure 8.10b). Unfortunately, at one point during the test the venting plasma caused the propellant to become detached from the rod, breaking the fibre. The propellant sample was recovered, whereupon no damage or other visible changer to the propellant was found. Spectroscopic results from this test were disregarded, therefore.

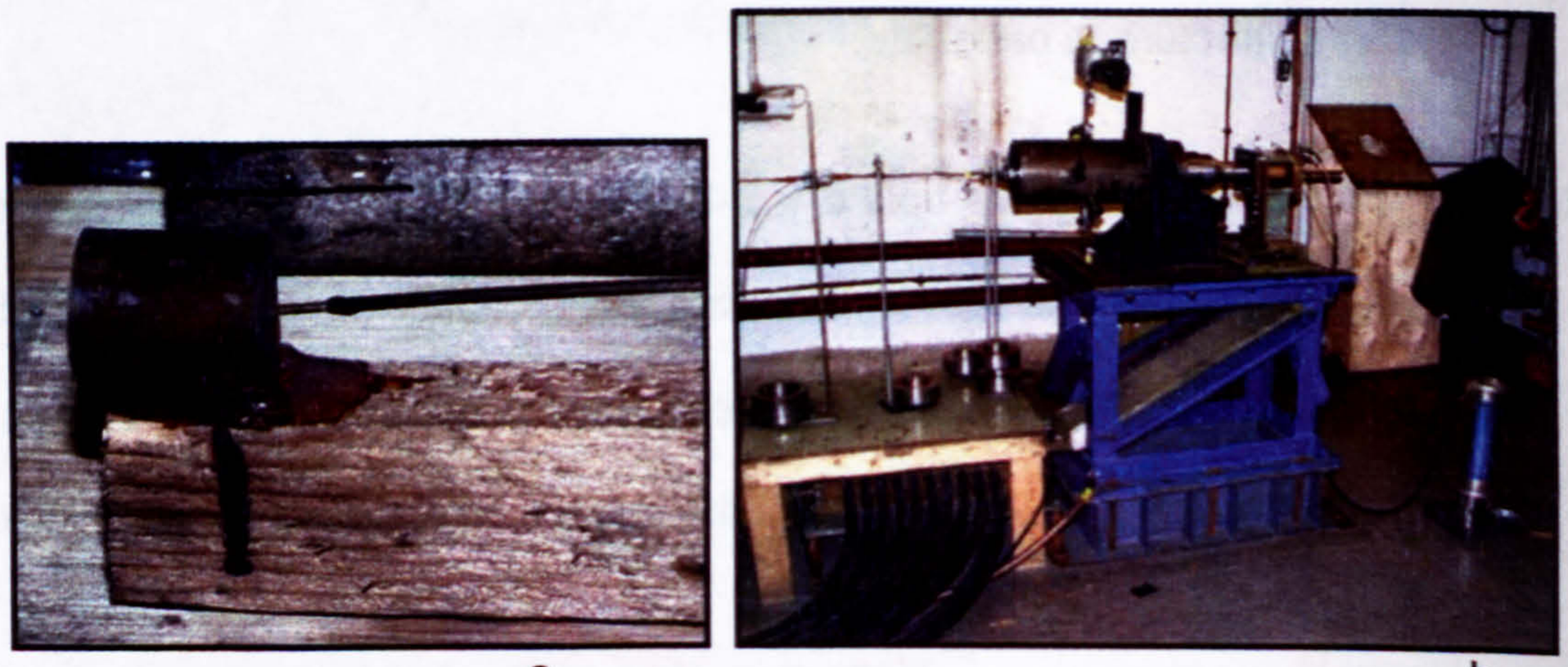

a b

Figure 8.10 Test 1 equipment

2.6 Experiments with translucent and opaque propellant – Test 2

2.6.1 This test had the same aim as its predecessor. To prevent the fibre from breaking under the force of the plasma discharge, use was made

of the fibre optic mount designed to fit into the instrumentation port of the Universal vessel for closed vessel tests. This increased the surface area of the glued propellant. The spectrograph fibre was threaded through the small hole running through the mount (Figure 8.11a) and into a translucent propellant grain with a hole drilled into it. The hole was made using a 1.18 mm drill bit, stopping 2 mm from the propellant grain surface. The plastic coating on the fibre was stripped away to the depth of around 16 mm to ensure a snug fit. The propellant was then glued to the mount to secure it (Figure 8.11b). The mount was held with retort clamps so as to locate the propellant grain relative to the plasma generator, but without the end-plate being fitted to the Universal vessel. Electrical energy was then discharged and the spectra recorded.

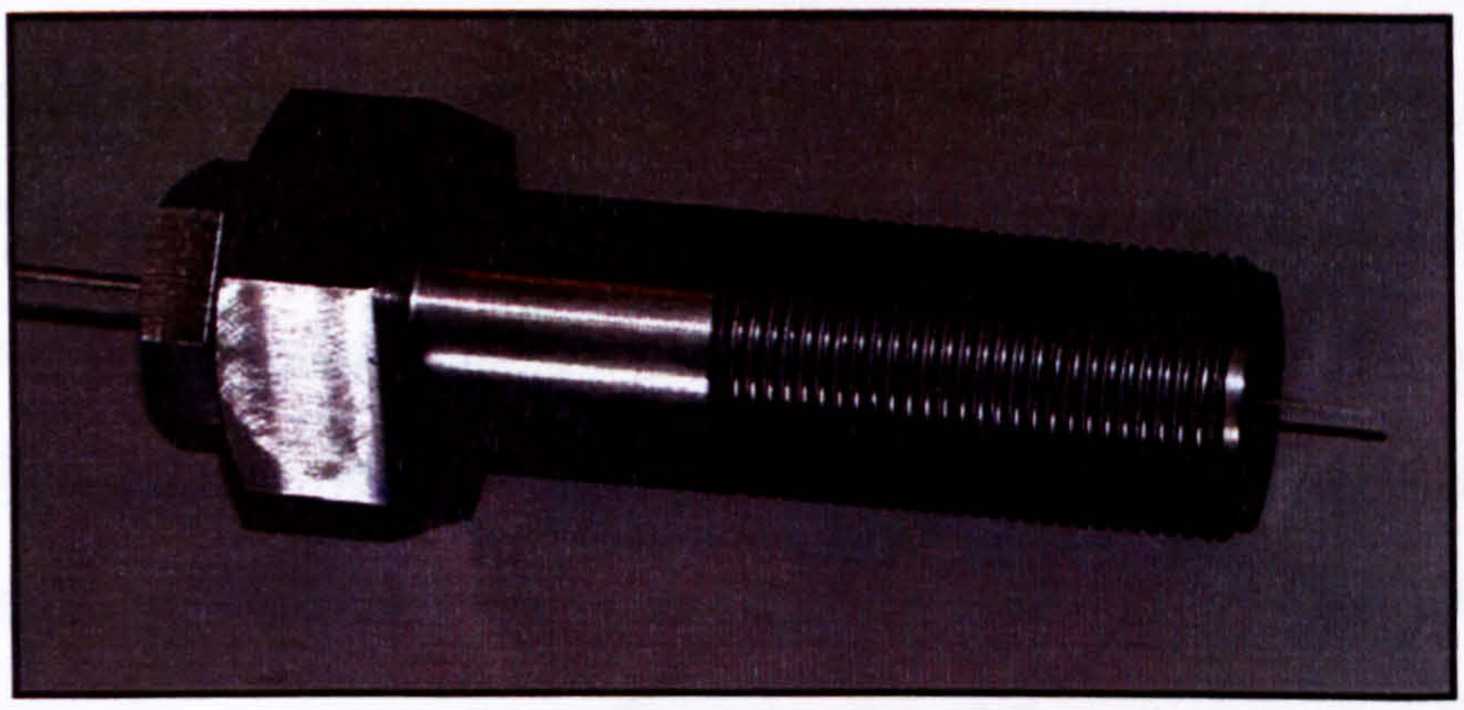

a

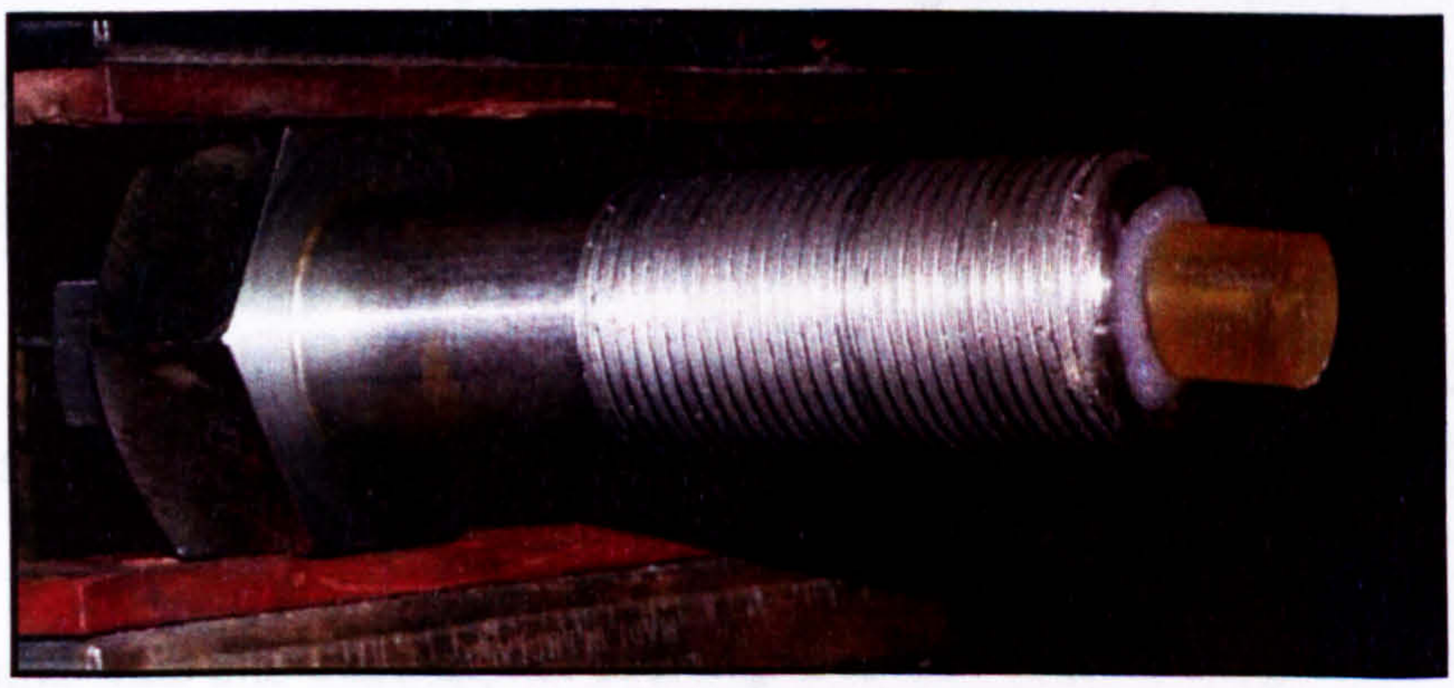

b

Figure 8.11 Fibre optic mount with (a) fibre and (b) propellant

2.6.2 This test was successful. Figure 8.12 shows the plasma brightness temperature recorded, and Figure 8.13 the radiant flux density (radiant power per unit area, σT_b^4), both plotted with electrical discharge power. The peak in plasma temperature is around 5000 K, whist the peak radiant flux density of around 35 MW m^{-2} compares with the convective heat transfer of 20 MW m^{-2} for a conventional gunpowder igniter [11]. The peak in radiant power lags behind the electrical discharge power by 0.45 ms. Assuming that the peaks in radiant power and discharge power within the capillary occur simultaneously, over the 120 mm or so distance the plasma needs to travel it has an average plasma velocity of around 920 m s^{-1} (in good agreement with the earlier plasma velocity measurement).

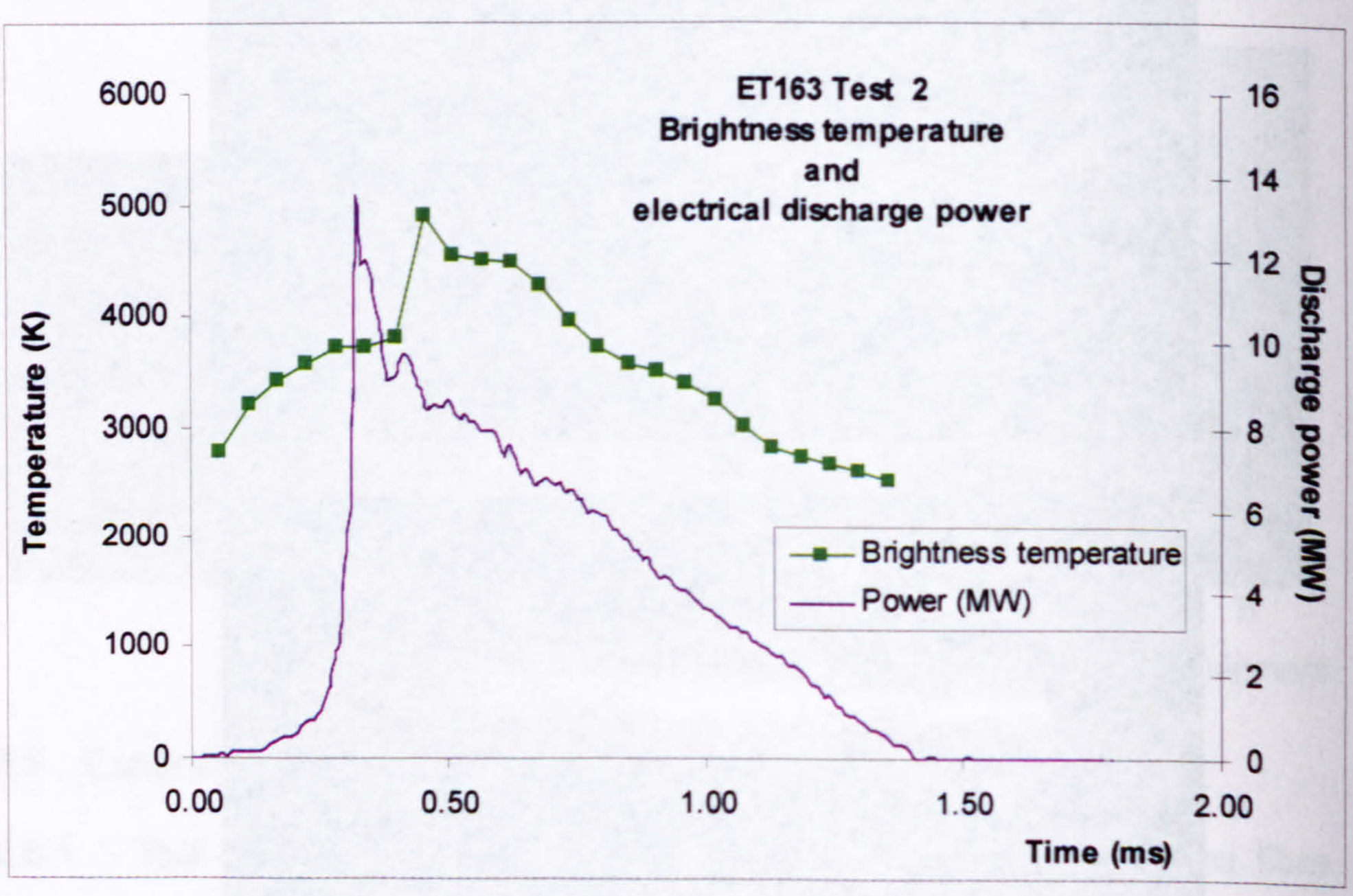

Figure 8.12 Test 2: brightness temperature and discharge power

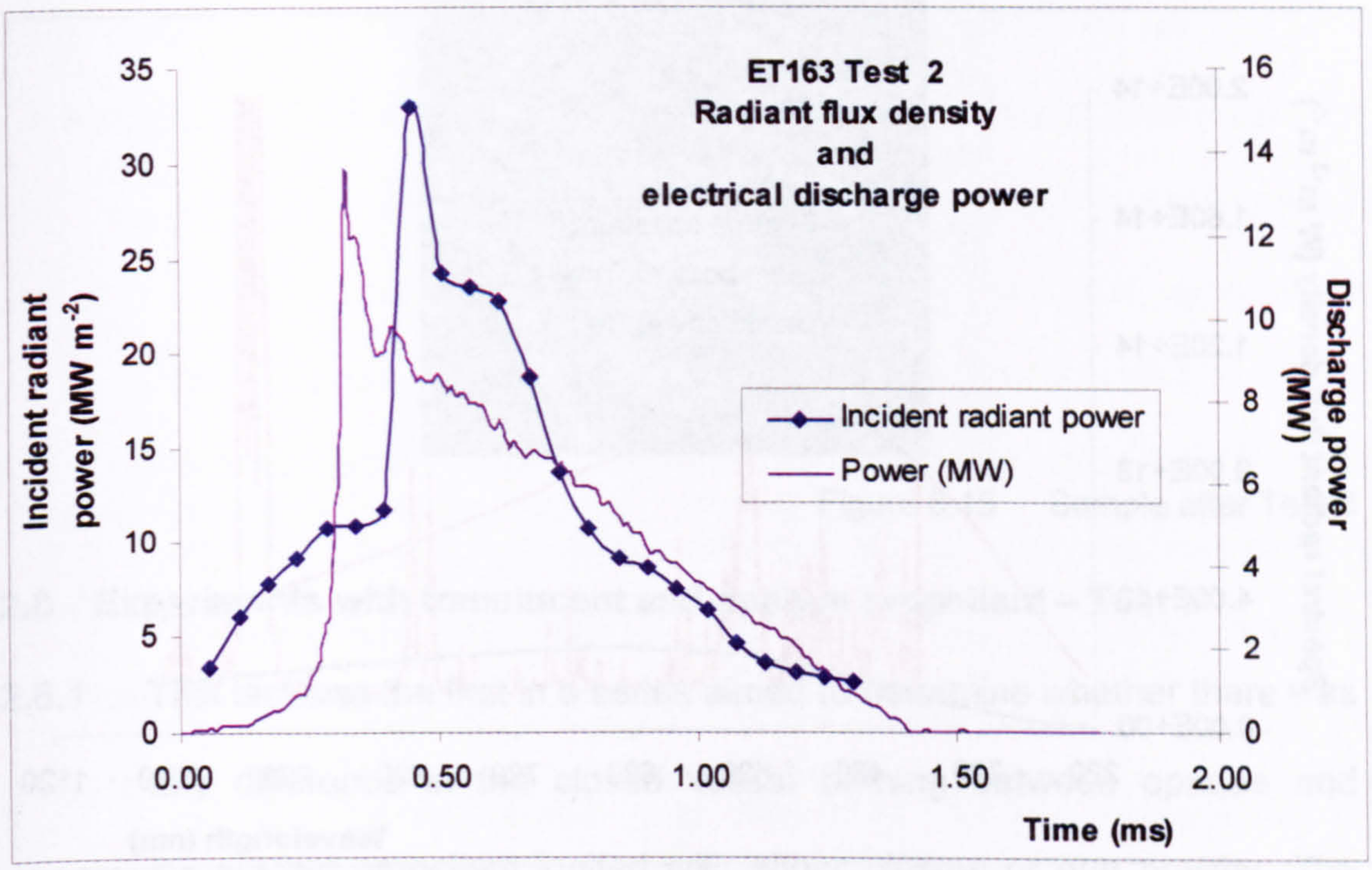

Figure 8.13 Test 2: incident radiant flux and discharge power

2.6.3 The spectrum for the hottest plasma appears in Figure 8.14: this is a complex mix of continuum and line emission. Also plotted in Figure 8.14 are blackbody curves representing the brightness temperature (at 4550 K) and colour temperature (at around 6000 K). The plasma has an emissivity of around 0.3, suggesting a spectrum emitted probably from low density, fully expanded plasma. The propellant sample did not ignite and on inspection, no physical change had occurred. The plasma temperature was well below that required for radiation damage, as cited by ICT [5].

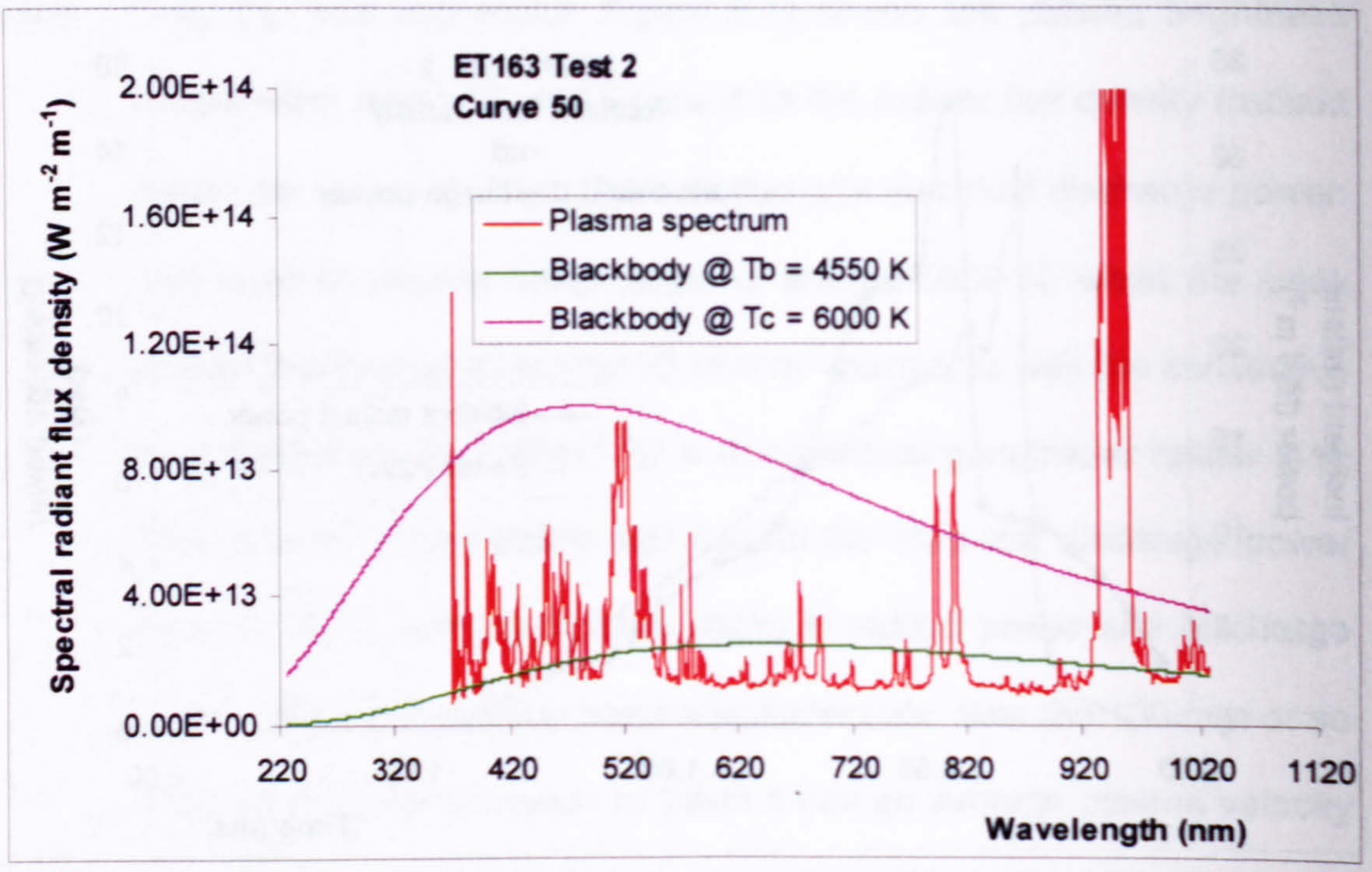

Figure 8.14 Test 2 Hottest plasma spectra

2.7 Experiments with translucent and opaque propellant – Tests 3 & 4

2.7.1 Tests 3 and 4 were repeats of Test 2, but using opaque rather than translucent propellant. These tests were added to the experiment to determine mainly whether the opaque propellant would ignite under open-air plasma conditions. This was a response to information from ICT that their opaque cylinders ignited under open-air conditions [4], presumably because the effects of radiation absorption at the surface caused the samples to heat to ignition. Figure 8.15 illustrates the sample after the plasma discharge in Test 3; the sample did not ignite in either Tests 3 or 4.

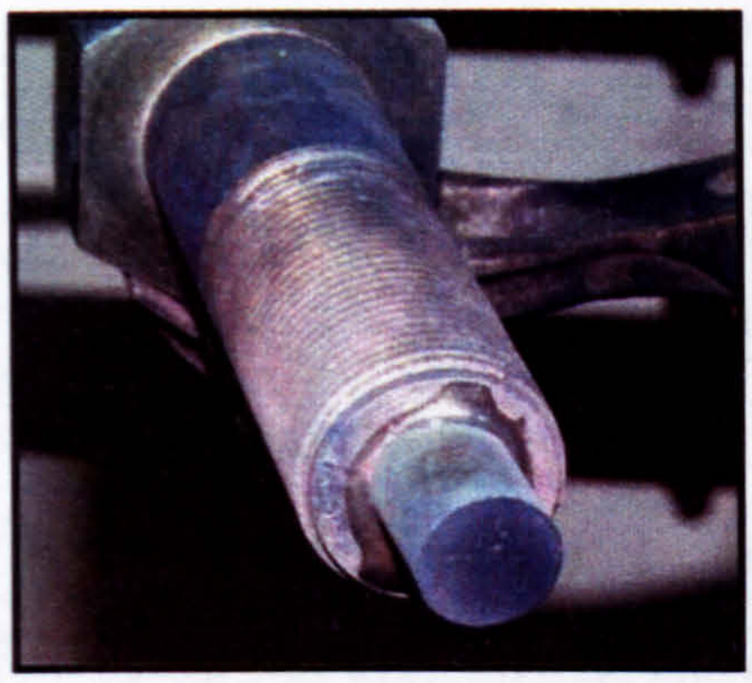

Figure 8.15 Sample after Test 3

2.8 Experiments with translucent and opaque propellant – Test 5

2.8.1 This test was the first in a series aimed to determine whether there was any difference in the closed vessel burning between opaque and translucent propellant ignited with either plasma or gun powder. The ICT work detected a significantly enhanced gas generation rate with plasma ignition of translucent propellant, which was explained by internal radiation damage increasing the surface area of the grains.

2.8.2 Figure 8.16 indicates the way the propellant was laid onto the end plate, opposite the CPG. Note that the centre grain, which would be instrumented in tests using translucent propellant, was recessed. This was not planned, but arose from an oversight regarding to the holder design. The distance from the CPG was around 12 cm to the central grain and 10 cm to the rest. Conclusions are drawn later based upon measurements taken from the location of the centre grain. It is assumed that the plasma properties experienced by the central grain would be similar to those of its neighbours.

Figure 8.16 Opaque propellant closed chamber test

2.8.3 The propellant ignited, but in this test, the contents of the vessel leaked through the capillary plasma generator. This was due to capillary design changes, having weakened one of the seals. The vessel was damaged during this test and so part of the experiment was postponed until the vessel could be repaired and a redesign undertaken for the capillary seal.

2.9 Experiments with translucent and opaque propellant – Tests 6 - 17

2.9.1 An e-mail discussion between Andreas Koleczko of ICT and the Author over his published results revealed details not reported in papers on the ICT open-air test set-up. Koleczko said the wire used was aluminium with a diameter of 0.5 mm and length of 45 mm. The propellant sample's surface was 17 mm from the wire. The power supply, similar to the R13 bank, used a 20 μH inductor; for a 2 kJ discharge, the energy per unit wire length was around 45 J mm^{-1}. The duration for their discharge has been reported as around 0.5 ms. It was decided to investigate a similar test set-up, while repairs to the vessel were underway.

2.10 Experiments with translucent and opaque propellant – Test 6

2.10.1 Figure 8.17 shows the layout for Test 6: two grains of propellant were used, one translucent (forward in the figure) and one opaque (towards the back in the figure). The grains were glued to pieces of wood and the wood clamped in by retort stands. A 0.5 mm diameter aluminium wire was simply attached to vertical electrodes on top of the CPG feed assembly. The spectrograph objective optical fibre was inserted into the translucent grain and the capacitor bank was charged to 45%. 4 kJ of energy were discharged in 1.5 ms with a peak power of around 80 MW. The wire length used here was 142 mm (dictated by the vertical electrode separation), around three times longer than that used by ICT. This gave an energy density of around 30 J mm^{-1}, three quarters of the ICT amount. The power densities used in the test and at ICT cannot be compared without details of their discharge power, but the ICT peak power density would have greatly exceeded that used in this test, as the wire and discharge duration were both three times longer in this case.

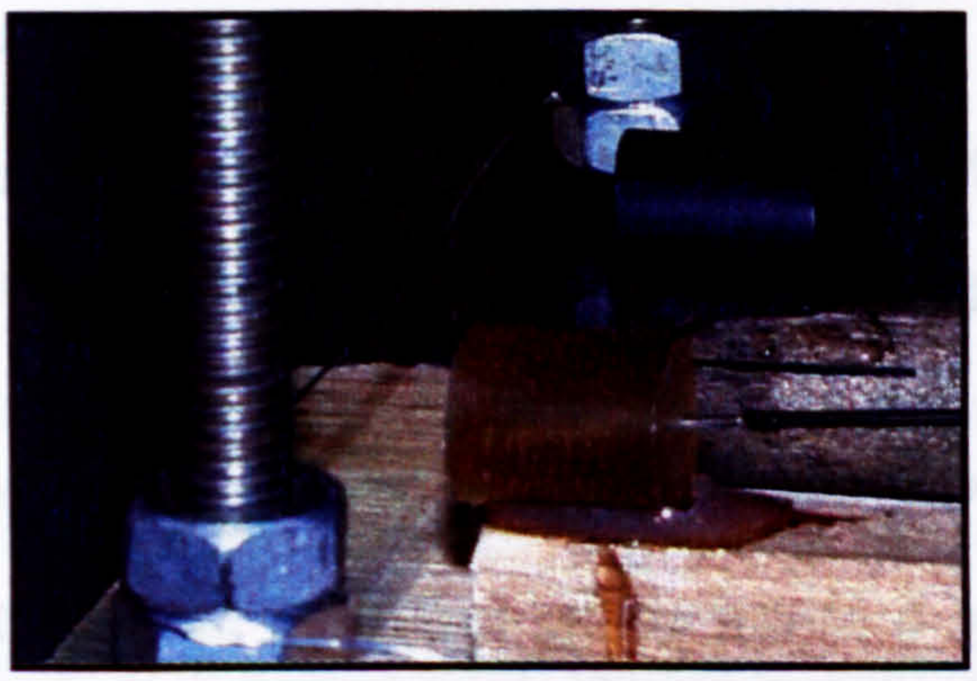

Figure 8.17 Location of propellant for Test 6

2.10.2 Figure 8.18 is the spectrum calibrated absolutely from the hottest plasma in Test 6, with a brightness temperature of around 4850 K. It is clear that the continuum radiation dominates indicating that the spectrum was from a dense, under-expanded plasma. It also enables the radiation flux to be determined with confidence (as applying σT_b^4 implies the continuum could be extrapolated to all wavelengths).

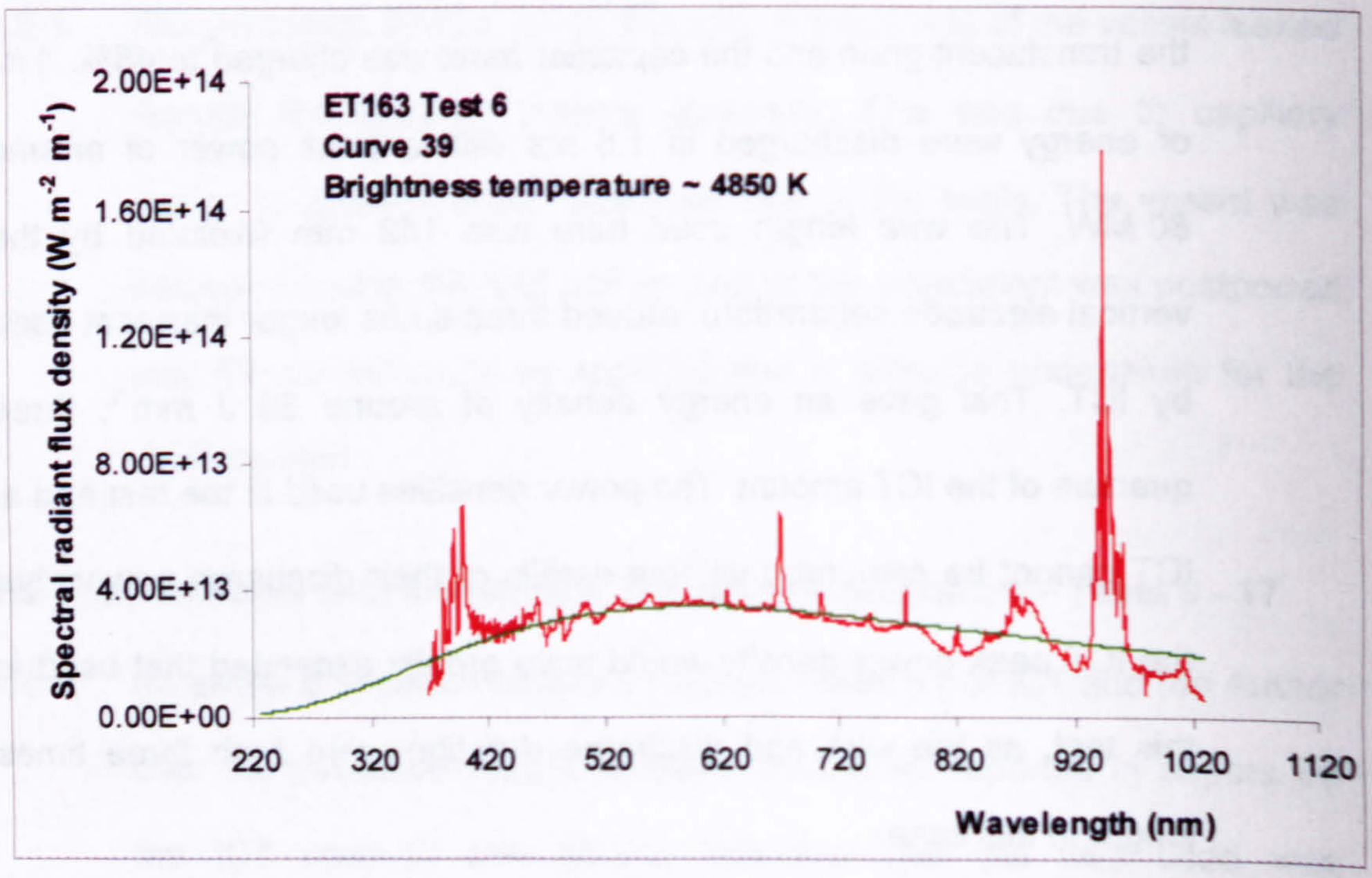

Figure 8.18 Hottest plasma spectrum from Test 6

2.10.3 None of the grains ignited, nor was damage observed within the transparent sample.

2.11 Experiments with translucent and opaque propellant – Test 7

2.11.1 Test 7 used a similar set-up to Test 6, but with the bank charged to 90% to see whether an increase in the power (and energy) density would elicit damage/ignition to the samples. As the samples from Test

6 appeared unaffected, it seemed an efficient management of resources to reuse them. The energy discharged was around 16 kJ over a period of 2 ms, with a peak power of around 230 MW. The energy density in this case was over 110 J mm^{-1}, more than double that used by ICT, but again no comparison for the peak power density with ICT can be made.

2.11.2 The propellant failed to ignite, but upon inspection there was some damage, similar to the crazing described by ICT within the transparent sample. Around ten individual sites were counted deep inside the grain, well away from the propellant face; they also appeared to be aligned parallel with the axis of the cylindrical grain. This feature had also been reported by ICT [4], where the crazing was aligned parallel with the rolling direction of their cylinders. Oddly, no damage was seen at or very close to the propellant surface. If the damage had been due to radiation, the bulk would be expected occur close to the surface where the radiation had the greatest power density (absorption being non-negligible). No damage was observed on the outside surface of the opaque grain.

2.11.3 Figure 8.19 is the spectrum from the hottest plasma in this test. The spectra were similar to those of Test 6, but from a plasma peaking around 1000 K hotter. This temperature is still very low (considering the T_b^4 relationship to radiated power) compared with ICT calculations [5].

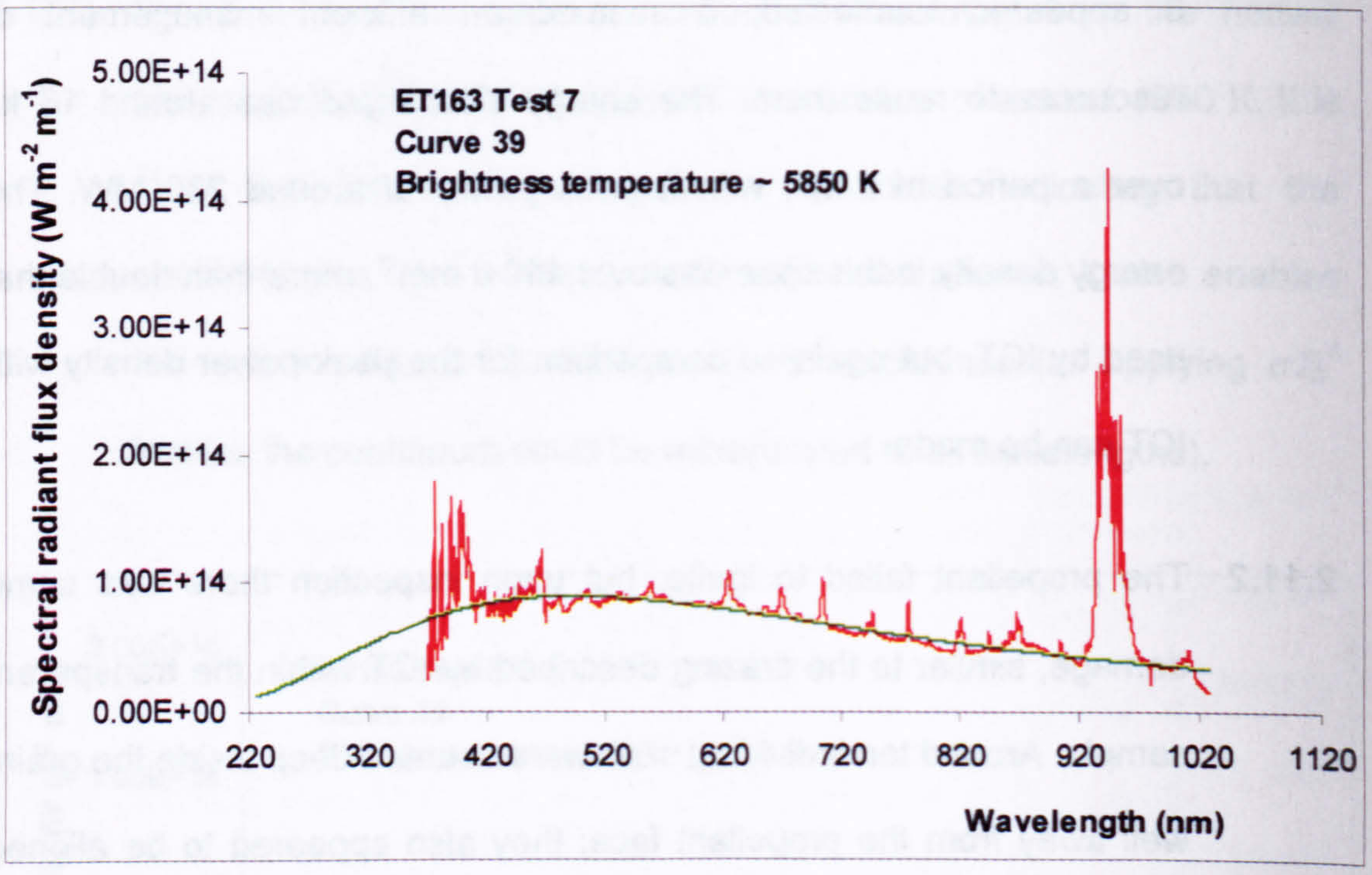

Figure 8.19 Hottest plasma spectrum from Test 7

2.12 Experiments with translucent and opaque propellant – Test 8

2.12.1 This test was used to explore the crazing phenomenon further, now that it had been detected at Fort Halstead. Three new transparent samples were used: two located 17 mm from the exploding wire, and one 35 mm from the wire. The centre sample (17 mm from the wire) had black insulation tape glued to its *rear* face (i.e. that part of the grain facing away from the exploding wire) to prevent radiation entering the rear of the sample if it became engulfed in plasma. No spectrograph data were acquired in this test.

2.12.2 A discharge similar to that in Test 7, resulted in the sample 17 mm from the wire without tape on its rear face showing a comparable degree of crazing within the grain to the sample from Test 7, demonstrating a

certain degree of reproducibility. The crazing, comprising around 10 cracks of 1 mm in length, was estimated to reach depths greater than 5 mm from any surface but again no damage was seen at or very close to the surface. The taped sample 17 mm from the wire acquired one small damage site at a depth of around 2 mm from the front face (i.e. that closest to the wire). The sample at 35 mm suffered two small damage sites at a depth of around 1 mm from the front face.

2.13 Experiments with translucent and opaque propellant – Test 9

2.13.1 For Test 9 three new transparent samples were placed at the same distance from the wire as in Test 8, but they were set upright (i.e. their polished cylindrical faces were towards the exploding wire). Tape was again employed for the central grain (17 mm from the wire), but on this occasion a vertical window facing the wire was all that remained exposed. This window was around 4 mm in width and ran for the whole length of the cylindrical face. Again, no spectrograph was used for this test.

2.13.2 Discharge parameters were as in Test 7. This time, the uncovered grain 17 mm from the wire showed a far greater degree of crazing lending support for the radiation damage theory. Two large 'laminated' cracks were clearly visible within the grain, running parallel to the axis for several millimetres. These cracks were about midway between the surface and the central axis of the grain. A number of smaller crazing sites were located throughout the grain, concentrated at the top and

front. The grain with the window showed no sign of crazing whatsoever, seemingly in contradiction of the radiation damage theory. The uncovered grain 35 mm from the wire had three very small crazing sites a few millimetres within it on the wire facing side.

2.14 Experiments with translucent and opaque propellant – Test 10

2.14.1 In Test 10, one new transparent propellant sample was placed centrally to the wire. This grain was taped cylindrically leaving a 4 mm window running around its cylindrical face; it was then set upright with the window 17 mm from the wire. The wire thus ran parallel to the length of the window. Discharge parameters were as in Test 7 and no damage occurred to the sample. No spectra were recorded for this test.

2.15 Experiments with translucent and opaque propellant – Test 11

2.15.1 Test 11 used three new transparent samples; each was located 17 mm from the wire, upright with a 0.5 mm aluminium wire midway along their cylindrical faces. One sample was covered with a transparent plastic bag. This arrangement appears in Figure 8.20 and discharge parameters were similar to Test 7; the results are demonstrated in Figure 8.21. No spectra were recorded for this test. Upon inspection after the test, the uncovered sample (furthermost left in Figure 8.21) was found to be excessively crazed throughout. This sample appeared to be darker in colour than others in this test (there would appear to be a variation in the optical properties from grain to grain). The central sample was lightly damaged, apart from one very large laminated crack

central to it and in the lower half. This crack nearly spanned the entire sample, but did not reach as far as the cylindrical surface. The sample covered with a transparent bag had no damage whatsoever, but it should be noted that the bag had blown off at some point during the test. Assuming the velocity of the plasma was around 1 km s^{-1}, it would take around 20 μs for the physical blast from the discharge to reach the sample and an unknown time interval for the bag to overcome its inertia. No conclusion could therefore be reached on whether the bag was fitted or not during the discharge itself.

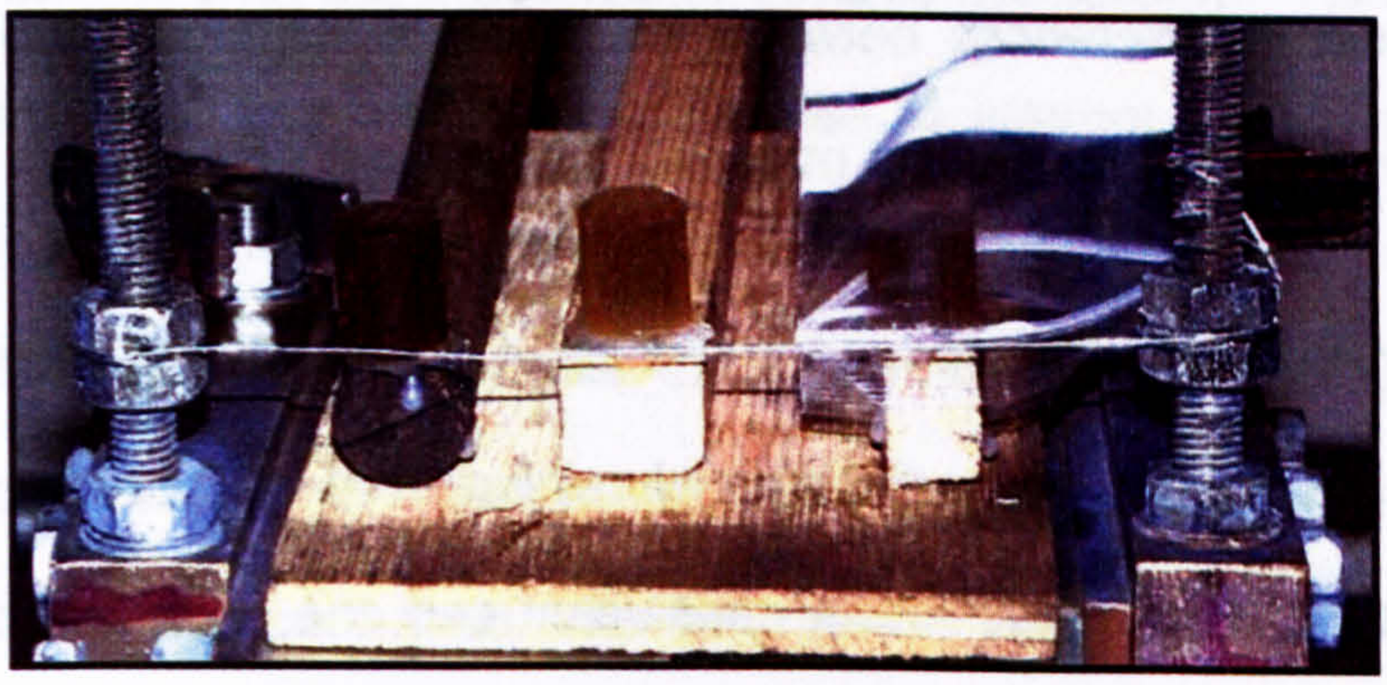

Figure 8.20 Test 11 arrangement

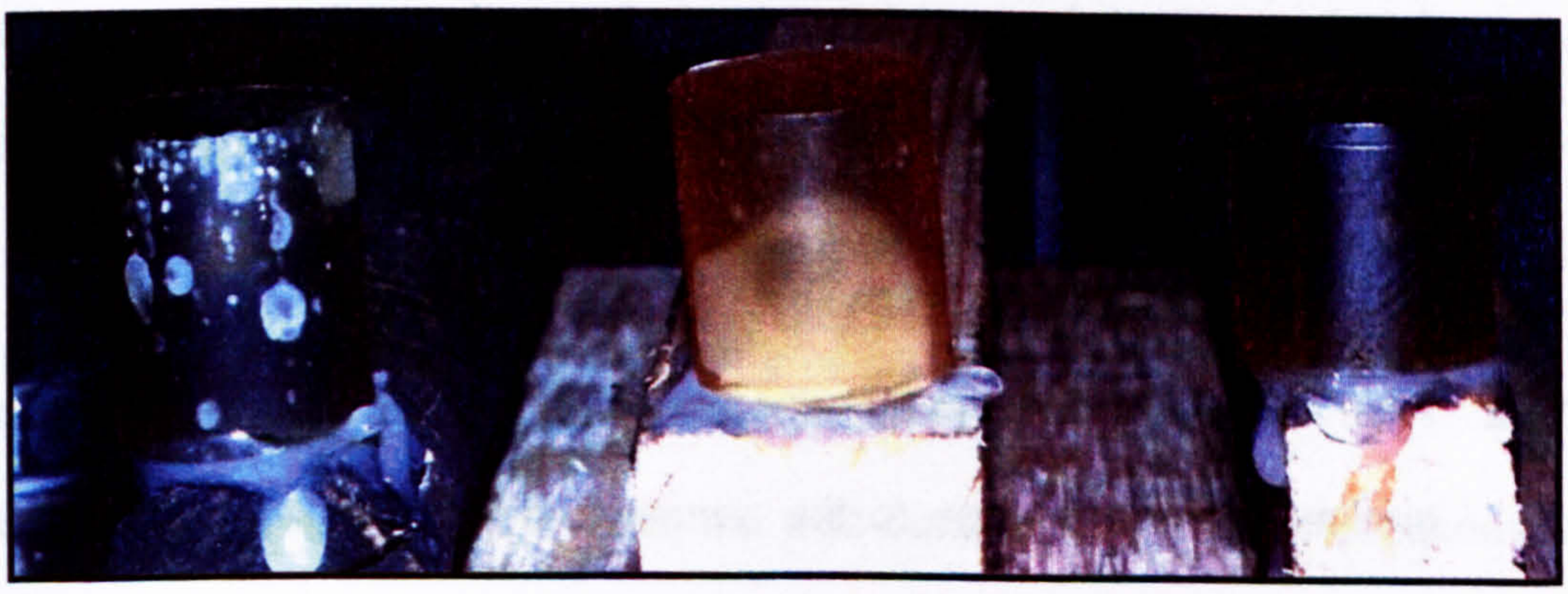

Figure 8.21 Results from Test 11

2.16 Experiments with translucent and opaque propellant – Test 12

2.16.1 Test 12 repeated Test 11, but used 0.5 mm diameter copper wire rather than 0.5 mm aluminium wire. Around 20 kJ of electrical energy were discharged in Test 12, with a peak discharge power of around 200 MW, compared to just over 16 kJ and a discharge peak power of around 150 MW in Test 11. Again, the bag came off the covered sample and only very light damage was recorded for any sample, with only one or two specks of crazing to be seen overall. This indicates possible differences between the types of damage to the propellant caused by different wire materials initiating the plasma.

2.17 Experiments with translucent and opaque propellant – Test 13

2.17.1 In Test 13, 0.5 mm diameter aluminium wire was used with two new propellant samples – one translucent and one opaque. Both samples were held upright, 8 mm from the wire and positioned at either end of it (similar to the left and right grains in Figure 8.20). The aim of this test was to see whether the opaque sample suffered internal damage. Discharge parameters were as in Test 7.

2.17.2 After the test, it was readily apparent that the transparent sample had similar internal damage to the central grain in Test 11 (Figure 8.21). The grains were carefully sliced with a scalpel blade after being warmed in hot water (which softened them). Figure 8.22 shows the degree of damage to the translucent sample had been mainly confined

within the interior of the grain. No damage was evident with the opaque sample, which appears to further support the radiation damage theory.

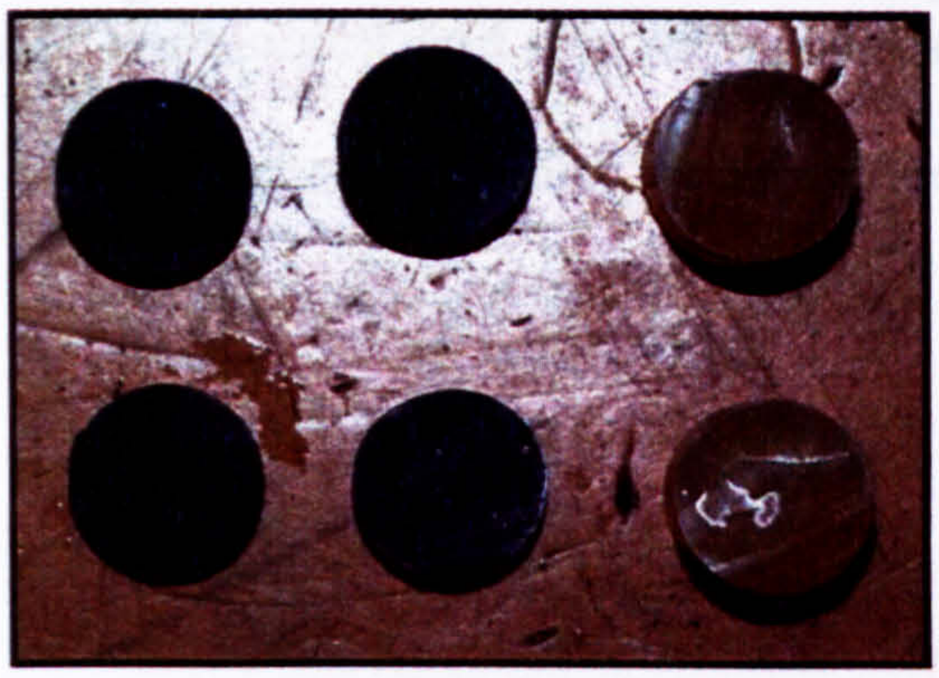

Figure 8.22 Sliced propellant after exposure to plasma

2.18 Experiments with translucent and opaque propellant – Tests 14 – 17

2.18.1 A series of four tests was completed to attempt a correlation of the incident radiation with the degree of crazing. One grain had a hole drilled into the cylindrical face through which the spectrograph objective optical fibre was inserted. Absolute calibration for spectrographic analysis was performed. The tests varied grain location and wire type as follows: Test 14 had the grain 100 mm from a 0.5 mm diameter aluminium wire; Test 15 had the grain 100 mm from a 0.5 mm diameter copper wire; Test 16 had the grain 50 mm from a 0.5 mm diameter aluminium wire; Test 17 had the grain 17 mm from a 0.5 mm diameter aluminium wire. Discharge parameters were as in Test 7.

2.18.2 The grain at 100 mm from the wire suffered no damage whatsoever in the case of either wire type; that at 50 mm using aluminium wire suffered very light crazing and that at 17 mm with aluminium wire suffered rather more damage (as did the sample in Test 7). Because

the amount of damage from 50 mm was so light and not in the locality of the fibre optic, it seemed reasonable to continue with use of the same sample at 17 mm, thus reducing effort on spectrograph calibration.

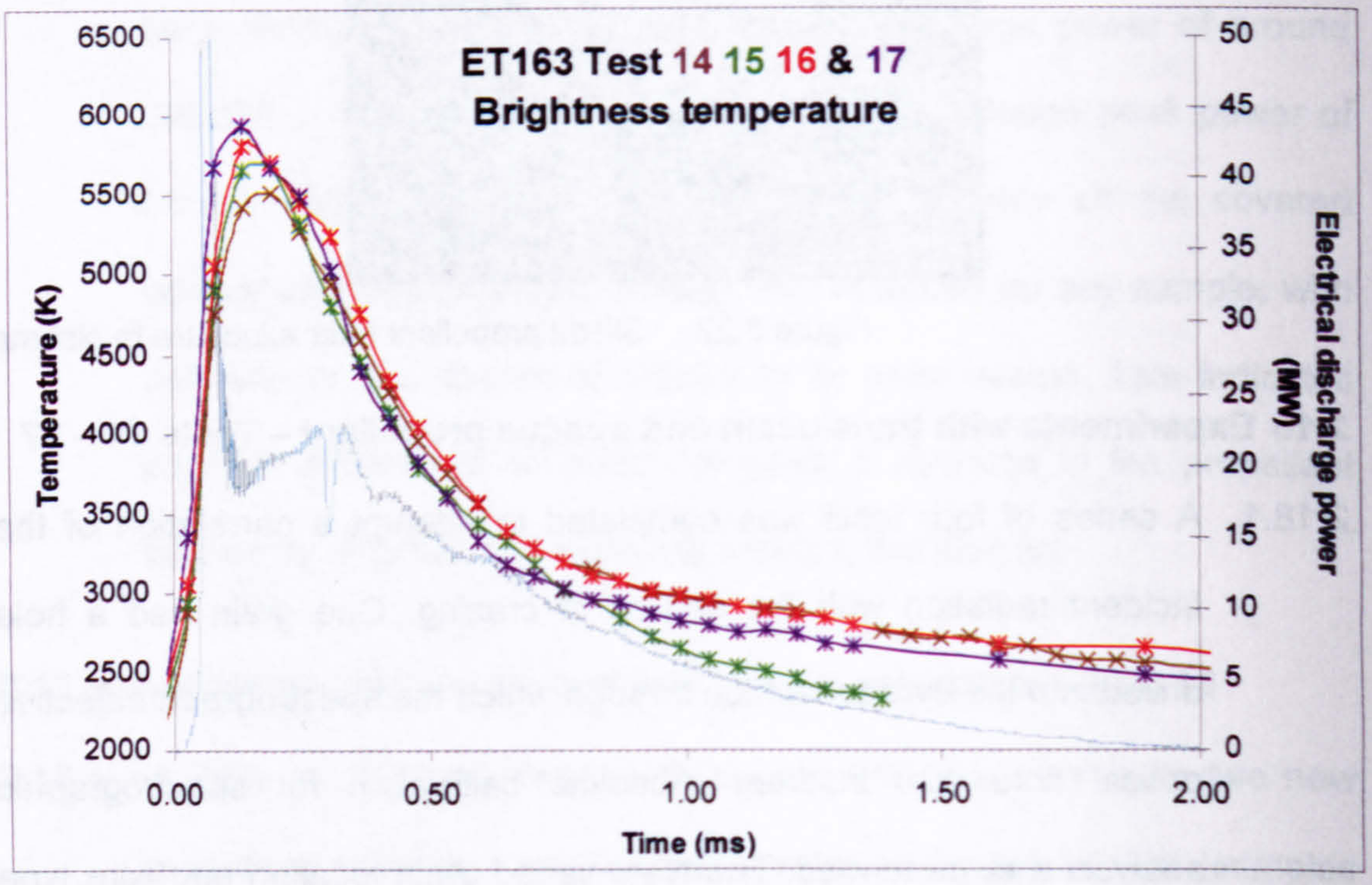

Figure 8.23 Brightness temperatures in Tests 14 – 17

2.18.3 The results from analysis of the radiant energy entering the sample at each location were surprising. Figure 8.23 shows the brightness temperature for each test of this wire-in-air series: plasma 100 mm from the wire was only 500 K cooler than that 17 mm from the wire. This represents a very small change in the incident radiant flux, with a significant change in the degree of damage observed. The dense, under-expanded plasma allowed blackbody curve fitting, giving a good

degree of confidence in the radiant flux density analysis. This finding contradicts the radiation damage theory.

2.19 Experiments with translucent and opaque propellant – Tests 18 – 27

2.19.1 This series of tests completed the aims of the experiment, since pressure time profiles were recorded for around 50 g of opaque and transparent propellant in closed vessel mode, under plasma and conventional ignition.

2.20 Experiments with translucent and opaque propellant – Test 18

2.20.1 Test 18 was a repeat of Test 5, to determine the gas generation rate of opaque propellant within a closed chamber under plasma ignition. The test was successful and good data were recorded.

2.21 Experiments with translucent and opaque propellant – Test 19

2.21.1 Test 19 was designed to determine the gas generation rate of transparent propellant within a closed chamber and with plasma ignition. An optical fibre was inserted into the vessel through the centre of the end plate and into the central propellant grain (see Figure 8.24). The propellant mount is the same as in Figure 8.11b and the layout of the grains as shown in Figure 8.16. During the test, the gas leaked through the optical fibre instrumentation port, and the pressure data were therefore untrustworthy. However, the spectrographic data pertinent to the ignition phase were deemed to be acceptable, as the leak was thought not to have occurred until significant pressurisation had been reached.

2.21.2 Results from further analysis are given below in the section on Test 22.

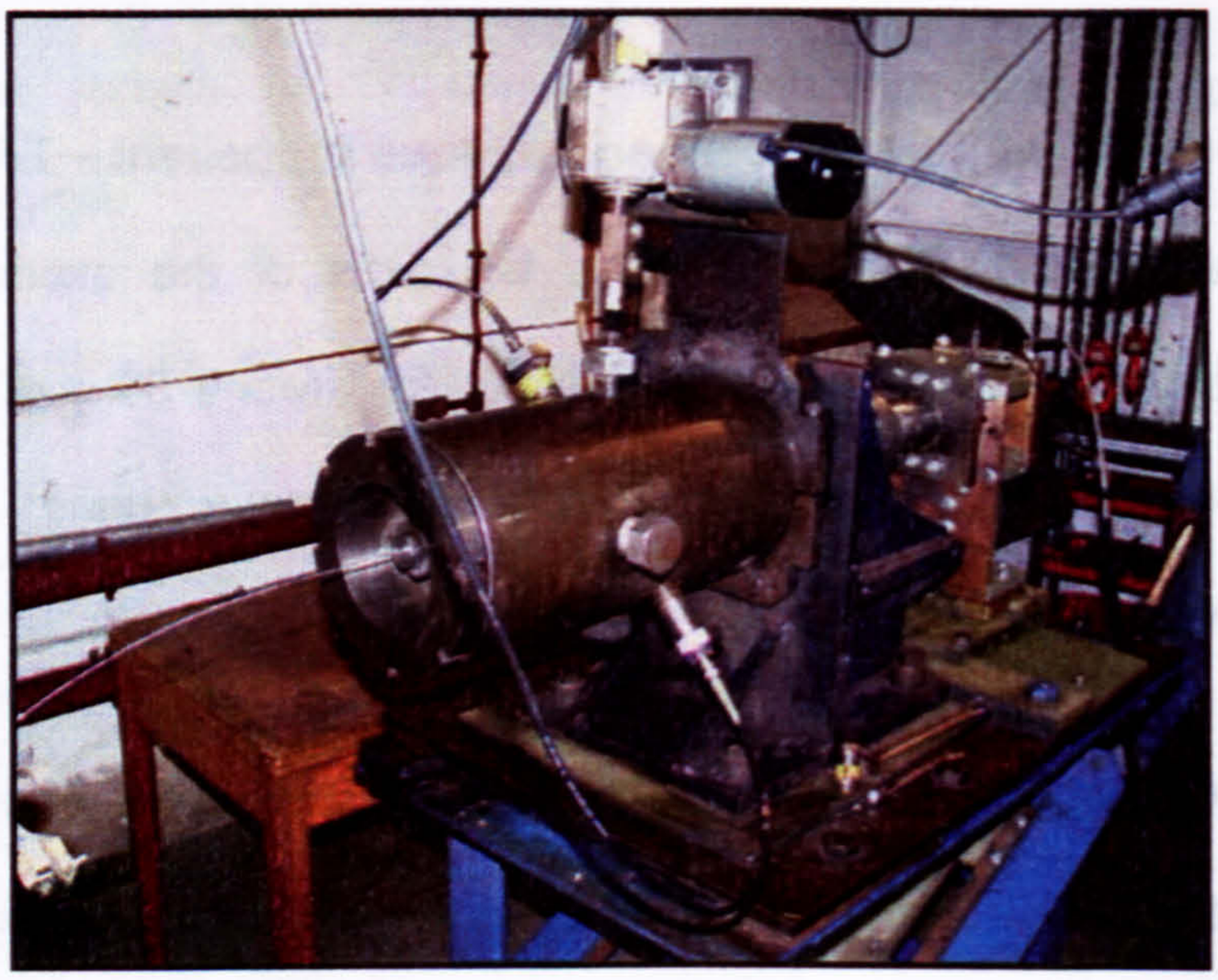

Figure 8.24 Universal vessel with spectrograph fibre inserted

2.22 Experiments with translucent and opaque propellant – Test 20

2.22.1 Test 20 was a fill-in test while components were being assembled to better withstand the pressure in the closed vessel when optic fibres were used, and was a repeat of Test 2. Translucent propellant with the spectrograph objective optical fibre inserted was held securely on the mount without the end plate assembled, in a location relative to the CPG used in closed-vessel firing. Plasma was discharged and the incident radiant energy recorded. The test was successful and results were similar to those in Figure 8.12 and Figure 8.13, indicating a certain degree of reproducibility.

2.23 Experiments with translucent and opaque propellant – Test 21

2.23.1 Test 21 was a repeat of Test 19, with plasma igniting translucent propellant in a closed vessel, but no spectrograph fibre was used. The test was successful and good pressure data were recorded.

2.24 Experiments with translucent and opaque propellant – Test 22

2.24.1 Test 22 was a repeat of Test 19, using plasma to ignite translucent propellant in a closed vessel. A fibre mount designed for the purpose of withstanding these pressures, with a good fit for the 1 mm diameter sacrificial spectrograph objective optical fibre, relied on super glue to secure the fibre. This test was successful, with good spectra and pressure data recorded.

2.24.2 Figure 8.25 demonstrates the plasma brightness temperature and electrical discharge power from the open air Tests 2 and 20, compared with data from the closed vessel ignition Tests 19 and 22. Also plotted is the electrical discharge power for Test 2. The open air and closed vessel firings have some important differences; the most obvious is that the brightness temperature remains above 3000 K beyond the end of the electrical discharge in closed vessel firings. Interrogation of the spectra produces evidence for neutral atomic potassium from quite early stages (orange plots), indicating that propellant gases are burning with an incandescent flame. The moment the 'propellant' spectra are first seen can be defined as the point of ignition; the maintenance of the temperature is due to energy released from burning propellant.

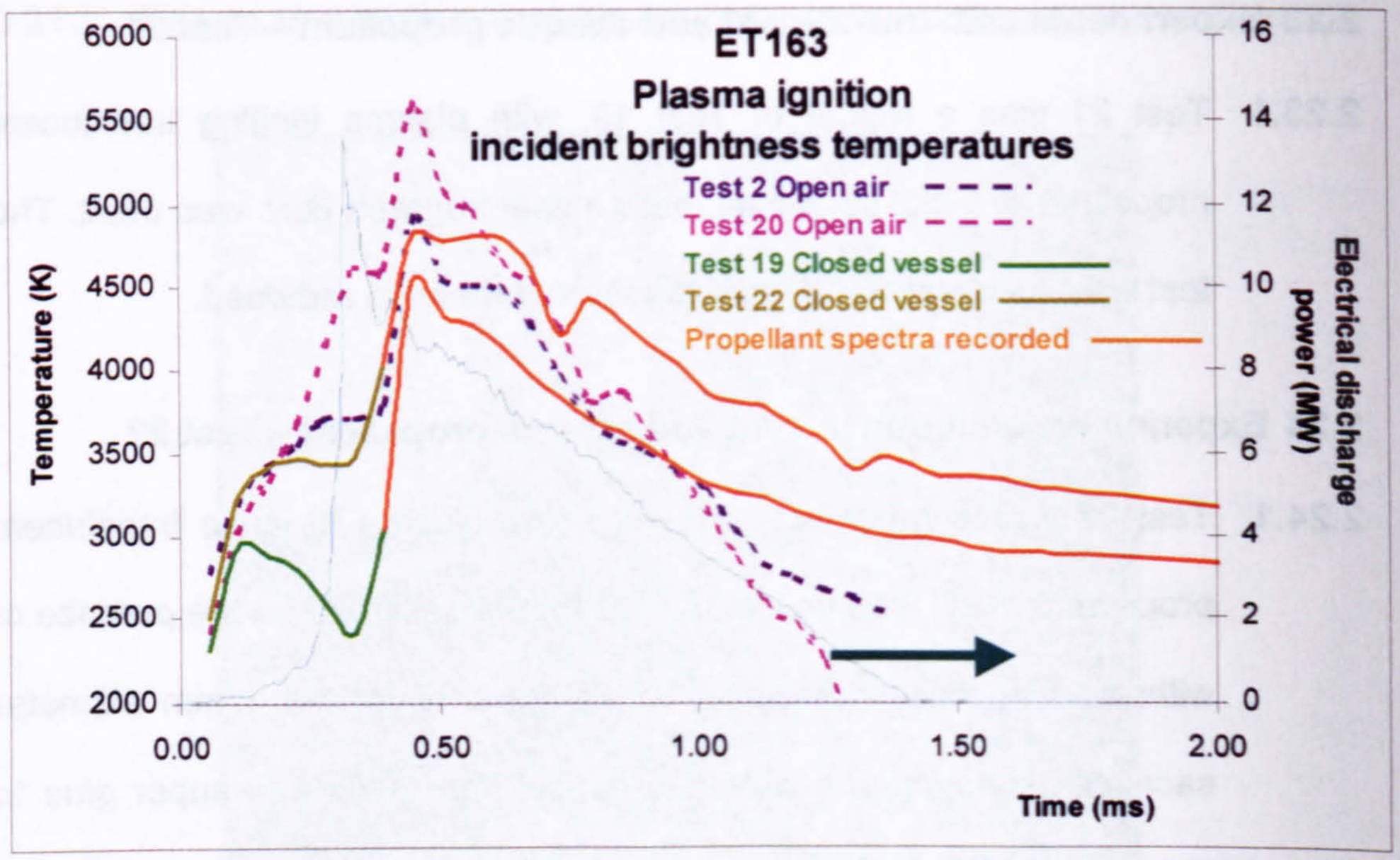

Figure 8.25 Open air and closed vessel ignition tests

2.24.3 Plasma ignition can be seen to occur in less than 400 μs. This is very much a maximum because it is unclear exactly when the igniting flux was incident upon the propellant. The 'plasma' temperature can be seen to rise initially to a peak, then fall and rise again to its maximum. This is especially clear in Test 19 where the initial 'plasma' temperature just reaches that of copper vapour (3000 K), then cools again to 2500 K, before rising to a peak of 4500 K. This initial peak could be due to the initial plasma plume discussed in Chapter 6. This plasma originates from the small piece of wire connected to the annular front electrode, which has been seen to explode before the main wire length and be expelled from the nozzle region, possibly through Lorentz forces. The initial plume will be very low in mass and may not contain enough copper vapour to instigate ignition. However, this is purely

speculative, and so it is assumed here that ignition has occurred after 400 μs of the igniting flux being incident on the propellant.

2.24.4 Chapter 7 (Section 2.2.31) reported that the ignition delay, defined as the time for pressure to reach 10% peak value, was 6.5 ms for plasma. In that experiment there was no reasonable way to determine the precise moment of ignition. Spectral lines, however, provided a very precise definition and so time can be related to the ignition event. Later, this new definition and measurement technique are used with a conventional igniter and a comparison made with plasma ignition.

2.25 Experiments with translucent and opaque propellant – Test 23

2.25.1 Test 23 was a repeat of Test 18, using opaque propellant under plasma ignition. The test was successful and good pressure data recorded.

2.26 Experiments with translucent and opaque propellant – Test 24

2.26.1 Test 24 was the first test in this study to employ conventional ignition. Opaque propellant was ignited by 6 g of G20 gun powder in a puffer bag together with an electrical match-head. The puffer bag and match-head were located at the far end of the vessel chamber away from the propellant. The test was successful and good pressure data were obtained.

2.27 Experiments with translucent and opaque propellant – Test 25

2.27.1 Test 25 conventionally ignited translucent propellant. The spectrograph objective optical fibre was inserted into the central grain via the

instrumentation port. The port for this was similar to the one used in Test 19, rather than the fibre mount in Test 22, because these better-designed plugs were not immediately available: two other plugs used in previous experiments needed reconditioning. Thus, the vessel was expected to leak and did so, leading to unusable pressure data, but the conventional ignition spectral data were deemed good. Results appear below along with those from Test 28.

2.28 Experiments with translucent and opaque propellant – Test 26

2.28.1 Test 26 attempted to obtain a good pressure record for conventionally ignited translucent propellant. The spectrograph was not used, to increase the chance of success, but due to a worn copper seal in a blanking plug replacing the optical fibre mount, the vessel leaked again and the results were unusable.

2.29 Experiments with translucent and opaque propellant – Test 27

2.29.1 This was a repeat of Test 26 with conventionally ignited translucent propellant. The test was successful and good pressure data were recorded.

2.30 Experiments with translucent and opaque propellant – Test 28

2.30.1 Analysis of the spectral data from the conventional ignition Test 25 demonstrated the difficulty in distinguishing between the spectra of gunpowder and propellant. It would appear that the trace element potassium was present in both gunpowder as well as propellant, because the characteristic lines were present from the start of the

spectral data acquisition. However, a sodium line appeared in Test 25 only after several milliseconds, suggesting that sodium might not be present in the G20 gunpowder and that the presence of sodium in the spectrum was indicative of propellant ignition. It was therefore important to obtain the spectrum of G20 on its own. Hence, Test 28 was designed to acquire absolutely calibrated spectra of a puffer bag being ignited. Figure 8.26 illustrates how this was achieved.

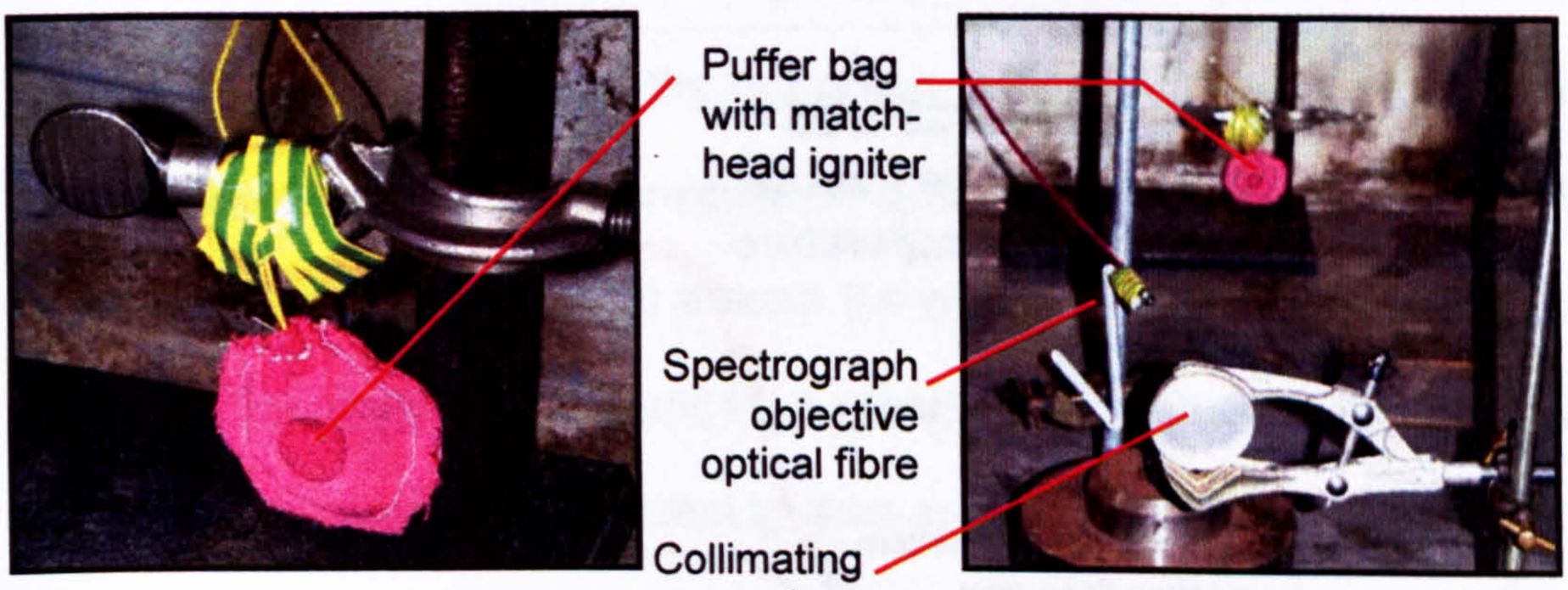

Figure 8.26 Acquisition of G20 gunpowder spectra

2.30.2 Figure 8.26a shows the puffer bag, and Figure 8.26b the location of the spectrograph fibre with respect to the bag and a collimating mirror. The mirror focused the field of view of the spectrograph onto the centre of the puffer bag. The test was successful and spectra were acquired with similar brightness and colour temperatures. Inspection of the spectra shows that potassium is present and sodium is absent from the gunpowder.

2.30.3 A comparison is summarised in Figure 8.27 between the G20 gunpowder Test 25 (closed vessel with propellant) and Test 28 (open

air without propellant). Figure 8.27 indicates that the contents of the puffer bag reach a peak temperature of around 1750 K, which compares favourably with thermochemical codes suggesting that gunpowder burns at 1700 K. The figure also shows that there is an inflection during Test 25, the propellant test, with a definite departure in temperature from Test 28, the gunpowder-only test. This could be interpreted as the point of ignition of the propellant.

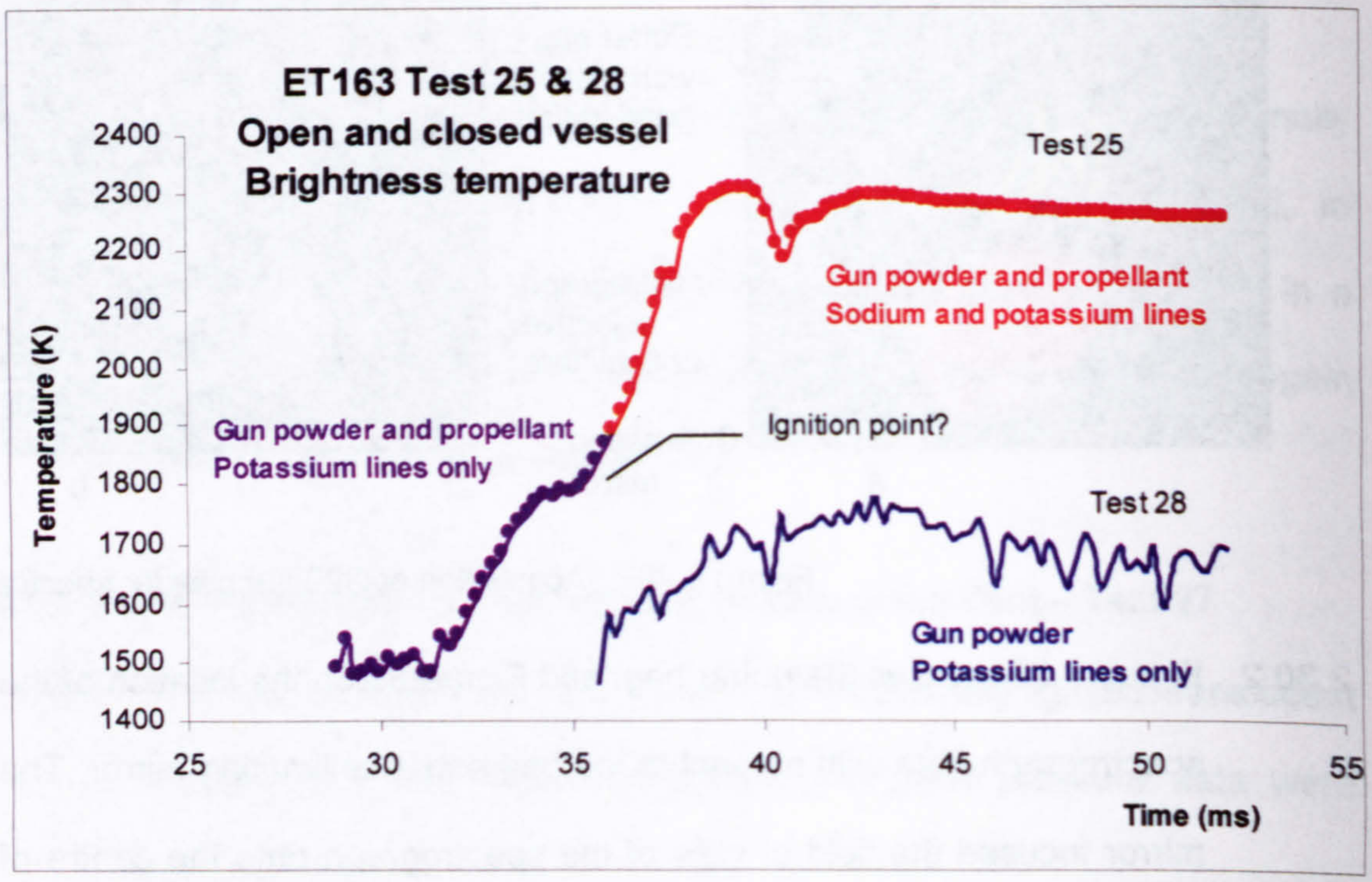

Figure 8.27 Comparison between brightness temperatures of G20 gunpowder and G20 with translucent propellant

2.30.4 The moment that a sodium line was seen in the spectrum has also been depicted in Figure 8.27 by the mauve to red colour change for Test 25. This occurs shortly after the point of inflection in temperature. Three spectral curves were recorded (i.e. 0.7 ms) between the time of inflection and the time of arrival of a noticeable sodium presence. This

may indicate that the use of trace element spectral characteristics is not a trustworthy measure of the exact point of ignition, or it could indicate that propellant grains other than the one being looked through might have ignited. It may also indicate that exothermic gasification occurs with no flame structure – the propellant could be smouldering.

Figure 8.27 also illustrates an inherent ignition delay in the production of gases from the puffer bag of around 30 ms and that this time varies from test to test. If ignition delay is defined as the time between the energy being incident on the propellant surface and the first sign of propellant ignition, then conventional ignition gives an ignition delay of around 5 ms, compared to around 0.4 ms for plasma ignition (Figure 8.25). This means there could be a greater than twelve-fold increase in ignition delay with conventional ignition over plasma ignition.

2.30.5 The gunpowder-only Test 28 spectra show that potassium (not sodium) is present, and also that the G20 gunpowder is a good blackbody emitter (probably due to the presence of carbon particles as soot). Figure 8.28 compares spectra acquired just prior to the first indication of sodium (taken as gunpowder only) with spectra acquired around 15 ms later, when there is thought to be a mixture of sooty gunpowder products and smokeless products from the propellant. (Noise centred on 960 nm has been removed for clarity.) The gunpowder spectrum is a continuum emitter, approximating closely to a blackbody with a self-absorption potassium line. The mixture spectrum is more akin to propellant burning in air, with a complex mix of line and continuum

emitters. The continuum component is far stronger than when burnt in air, however. The spectrum of the burning propellant also reveals the presence of molecular calcium hydroxide, which does not appear until around 2 ms after the sodium. This lag between sodium and calcium hydroxide has been noticed previously and may be due to a temperature effect (i.e. the calcium hydroxide requiring a higher temperature before molecular rotation occurs). This further emphasises that care needs to be exercised in using such features as ignition indicators. It is considered that the trace elements sodium and potassium are related to the manufacturing processes of either RDX or HMX and that calcium hydroxide arises from the production of nitrocellulose. The propellant safety sheet that accompanied the translucent propellant stated RDX was present.

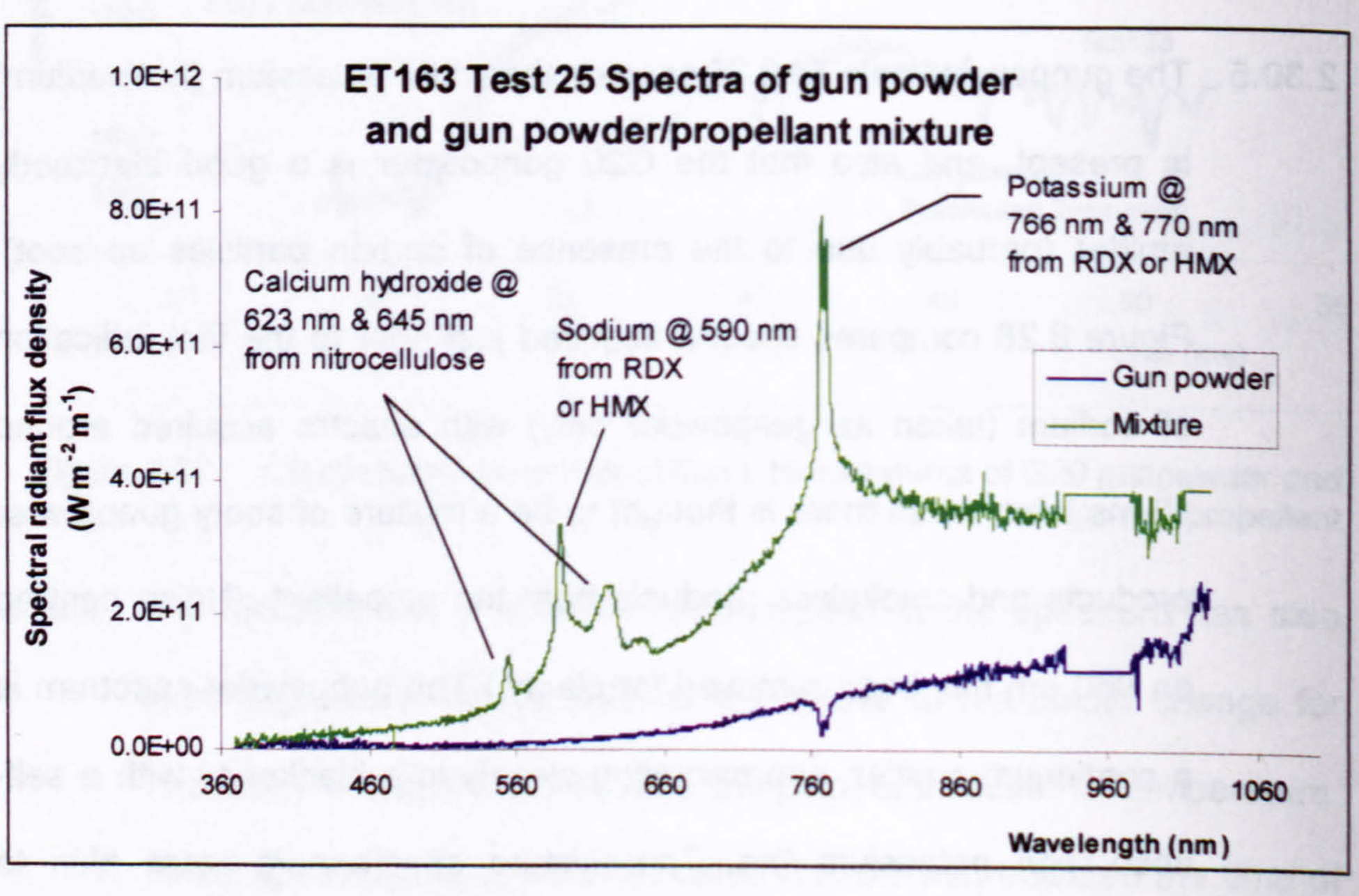

Figure 8.28 Spectra from gun powder only and gunpowder/propellant mixture

3 Discussion on small-scale ETC ignition experiments

3.1 Chamber pressure analysis

3.1.1 Figure 8.29 shows the chamber pressures and Figure 8.30 the burn rate analysis results for the closed vessel tests conducted during this study. Ignition delays were removed from the conventional tests for this plot, to allow an overlay of the pressure rise in Figure 8.29. For Test 24, 24 ms were removed from the time-base, whilst 18 ms were removed for Test 27. It is clear that opaque and translucent propellants have different burn characteristics, although the only physical difference is 0.03% by weight of carbon added to the composition to make it opaque. The opaque propellant appears to have a higher burn rate than its transparent counterpart. The translucent propellant has an energy content of 5234 J g^{-1} and the opaque propellant 5096 J g^{-1}, so the carbon appears to reduce the propellant energy by 2.5%. A reduction in energy is unlikely to be responsible for the increased burn rate, all else being equal, so an alternative explanation must be sought. The energy radiated from the burning propellant flame will be absorbed on the surface of opaque propellant, and within the bulk of the translucent variety. This energy absorbed at the surface may be sufficient to increase the propellant surface temperature and hence instigate the various reactions affecting the burn rate.

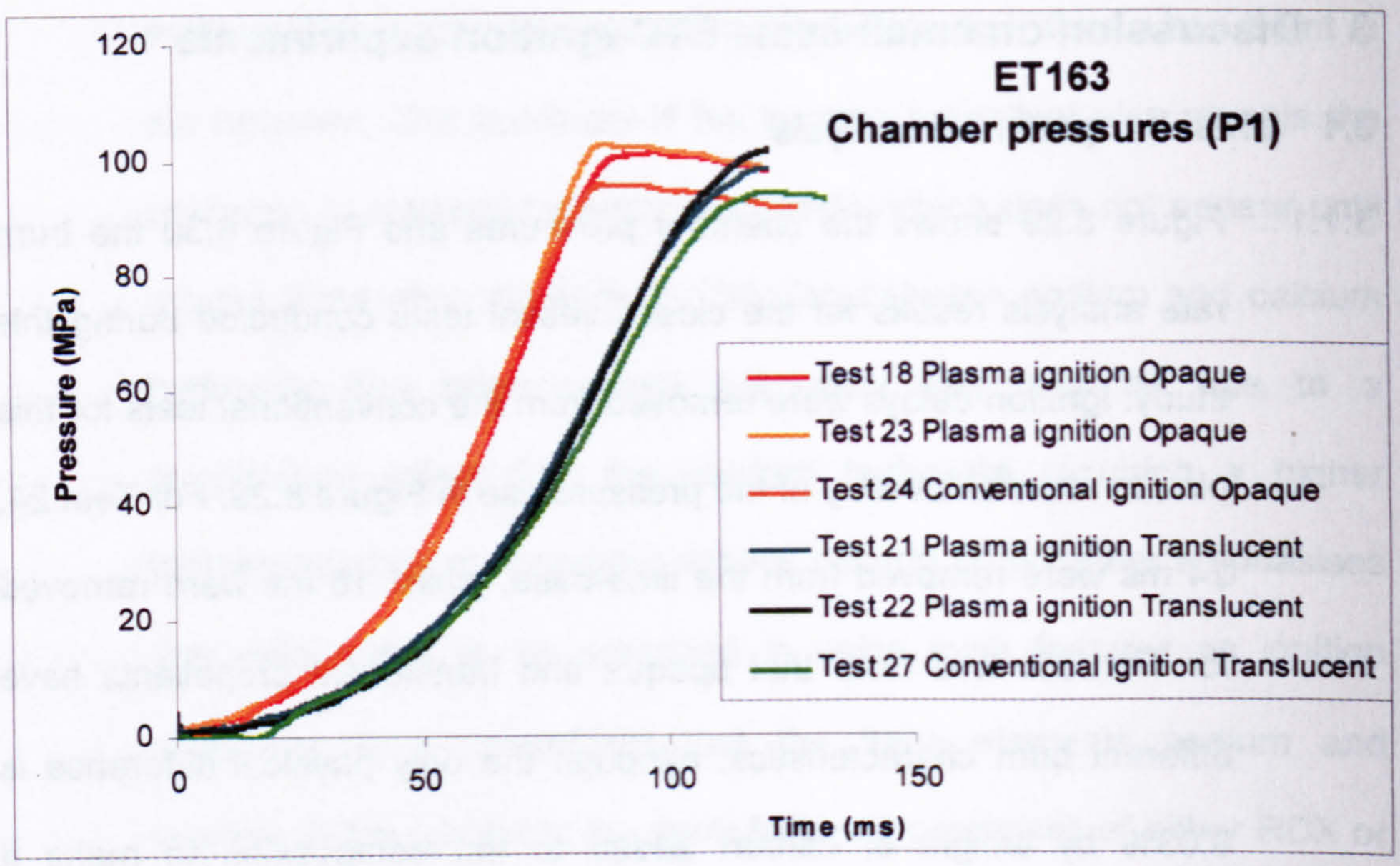

Figure 8.29 ET163 Pressures in closed chamber tests

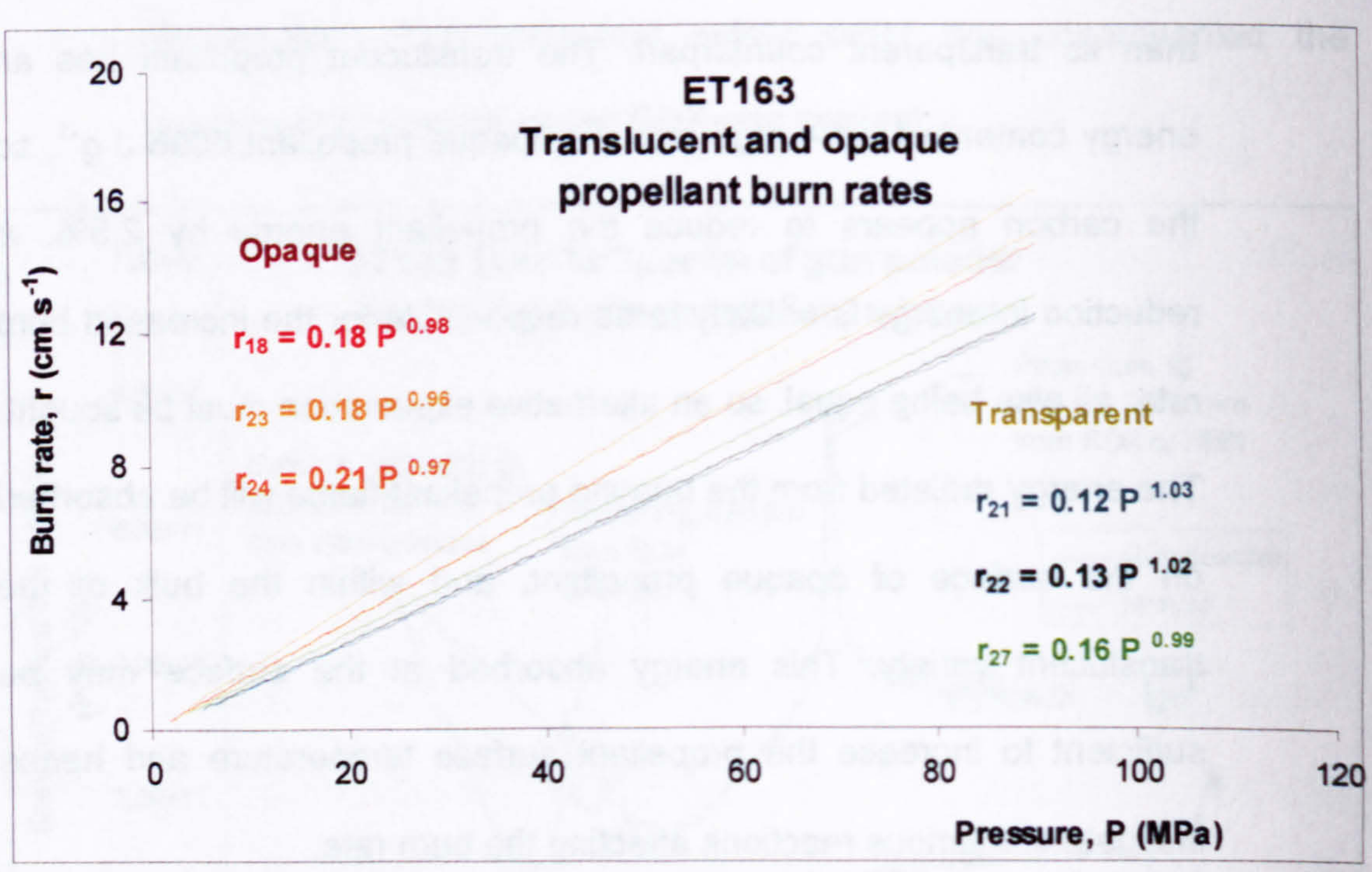

Figure 8.30 ET163 Burn rate analysis

3.1.2 The ignition method appears to have resulted in no measurable difference to the gas generation rate between the propellant types. No

enhancement to the gas generation rate is obtained with plasma ignition – a result contrary to that reported by ICT. However, this is expected from the earlier tests conducted with plasma discharges from CPGs in an open environment in this experiment, where no damage to the recovered propellant was observed. It is also expected that if the experimental set-up of ICT and TZN were more closely followed, with an aluminium plasma initiation wire exploding 17 mm from the propellant surface, discharge parameters similar to Test 7 (Section 2.11) and the same propellant geometry as in these tests, then measured gas generation rate enhancements would be similar to those shown in Figure 8.1. This is because the plasma properties would then be such that internal damage would have occurred to the translucent, but not the opaque propellant, as indicated in the tests described earlier.

3.2 Radiant energy analysis

3.2.1 One theory for the ignition of propellant by plasma involves the radiation from the discharge heating up the propellant surfaces to temperatures exceeding an ignition threshold [12, 13, 14, 15]. These same theories suggest that in-grain heating occurs (with translucent propellant) which might alter the gas generation rate characteristics of plasma ignited propellant. A calculation has thus been performed based on measured values of incident flux due to the discharge, to determine the temperature of a rectangular propellant slab as a function of depth. This was an attempt to determine the actual effect of

the measured incident radiation. The calculation assumed no heat conduction to the surface or within the interior of the grain during the 1.2 ms or so over which the radiant energy was significant. As the propellant is a thermoplastic, considering it a thermal insulator over such a short time-frame is felt to be justified.

3.2.2 The calculation performed by the Author assumed an absorption coefficient, α estimated from work performed by ICT [4]. In the ICT paper is a graph of the transmission characteristics of a polished sample of transparent JA2 propellant, with a thickness of 3 mm. Their data suggest all radiation below 425 nm is absorbed and transmission increases smoothly. α is given up to a wavelength of 1100 nm. The transmission profile is similar in some respects to that of *k* in Figure 8.5, apart from the magnitude (the magnitude for *k* included absorption and scattering by unpolished surfaces). The ICT data have been extrapolated to a wavelength of 10 μm, the extrapolated being estimated to give a smoothly varying spectral profile. The extrapolation was performed to provide an estimation of the absorption over a more significant portion of the infrared spectrum.

3.2.3 The results of the published and extrapolated data appear in Figure 8.31. It should be noted that at plasma temperatures of around 5000 K, only half the radiation emitted from a perfect (blackbody) emitter will be within the wavelength range quoted by ICT and the extrapolation will have further reduced significance at higher

temperatures. A curve from a theoretical blackbody emitter at 5000 K also appears in Figure 8.31 to emphasise this point.

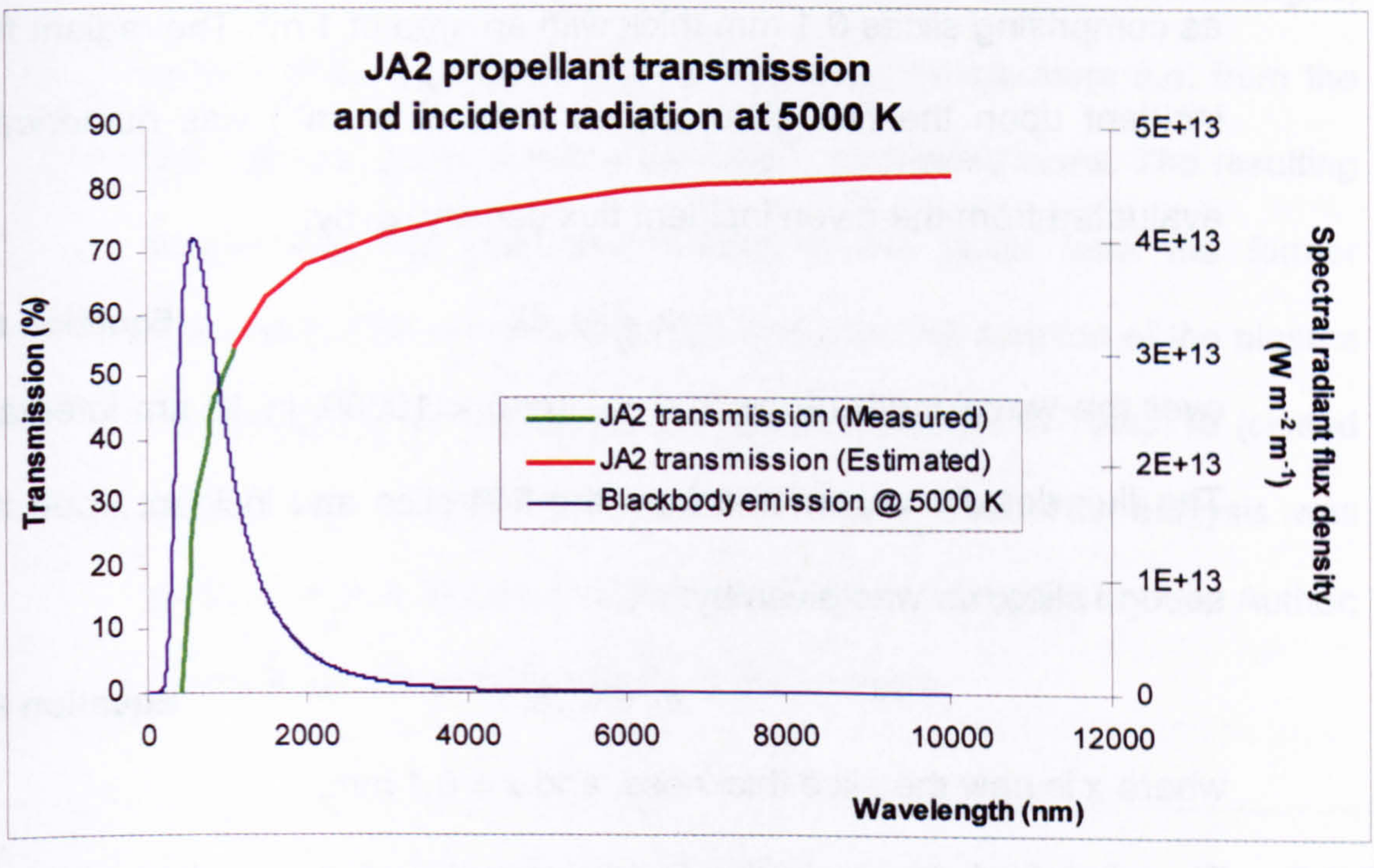

Figure 8.31 Transmission characteristics of JA2 propellant

3.2.4 The absorption coefficient in units of mm^{-1} is obtained from the transmission data via the relationship:

$$\alpha = (-1/x) \ln (\phi_T/\phi_0) \qquad \textbf{Equation 8.1}$$

where

x is the sample thickness, and x = 3 mm

ϕ_T is the radiation transmitted through the 3 mm sample

ϕ_0 is the measured incident spectral radiation flux density.

3.2.5 The measured incident spectral radiant flux density provided by a theoretical blackbody at plasma brightness temperature, T_b was mathematically applied to the translucent propellant through the

absorption coefficient supplied by Equation 8.1. This assumes that the plasma emissivity for this extended wavelength range is close to the value for the measured wavelength range. The propellant was treated as comprising slices 0.1 mm thick with an area of 1 m^2. The radiant flux incident upon the first slice, Φ_0 (in units of W m^{-2}) was numerically evaluated from the given incident flux density, ϕ_0 by:

$$\Phi_0 = \int \phi_0 \, d\lambda \qquad \textbf{Equation 8.2}$$

over the wavelength range $200 < \lambda\,(nm) < 10000$, in 10 nm intervals. The flux density transmitted from the first slice and incident upon the second slice, Φ_1 was given by:

$$\Phi_1 = \Phi_0 \, e^{-\alpha x} \qquad \textbf{Equation 8.3}$$

where x is now the slice thickness, and $x = 0.1$ mm.

3.2.6 The absorbed energy in the first rectangular slice was then obtained from the difference between the incident and transmitted fluxes, multiplied by the time over which the flux was applied; this period was the exposure time of the spectrograph, which recorded the incident flux. The temperature rise of the first slice was then obtained from dividing this energy by the slice mass and the propellant specific heat capacity. The propellant mass was calculated from a rectangular propellant slice with an area of 1 m^2, thickness 0.1 mm and density 1630 kg m^{-3}, and the propellant specific heat capacity being taken as 1300 J kg^{-1} K^{-1}.

3.2.7 The temperature rise in subsequent slices was calculated using the incident radiant flux density, Φ_n transmitted from the previous slice, Φ_{n-1}. The incident spectral radiant flux density, ϕ_0 was then changed, subject to the change in plasma brightness temperature (i.e. from the next spectral curve) and the calculation performed anew. The resulting temperature rise was then added to the value from the former calculation. This process was repeated over the duration of the plasma discharge, for the brightness temperature profiles of Tests 19 (closed vessel) and 20 (open-air) shown in Figure 8.25. The analysis was performed in a Microsoft Excel spreadsheet compiled by the Author; Figure 8.32 provides the results of the analysis.

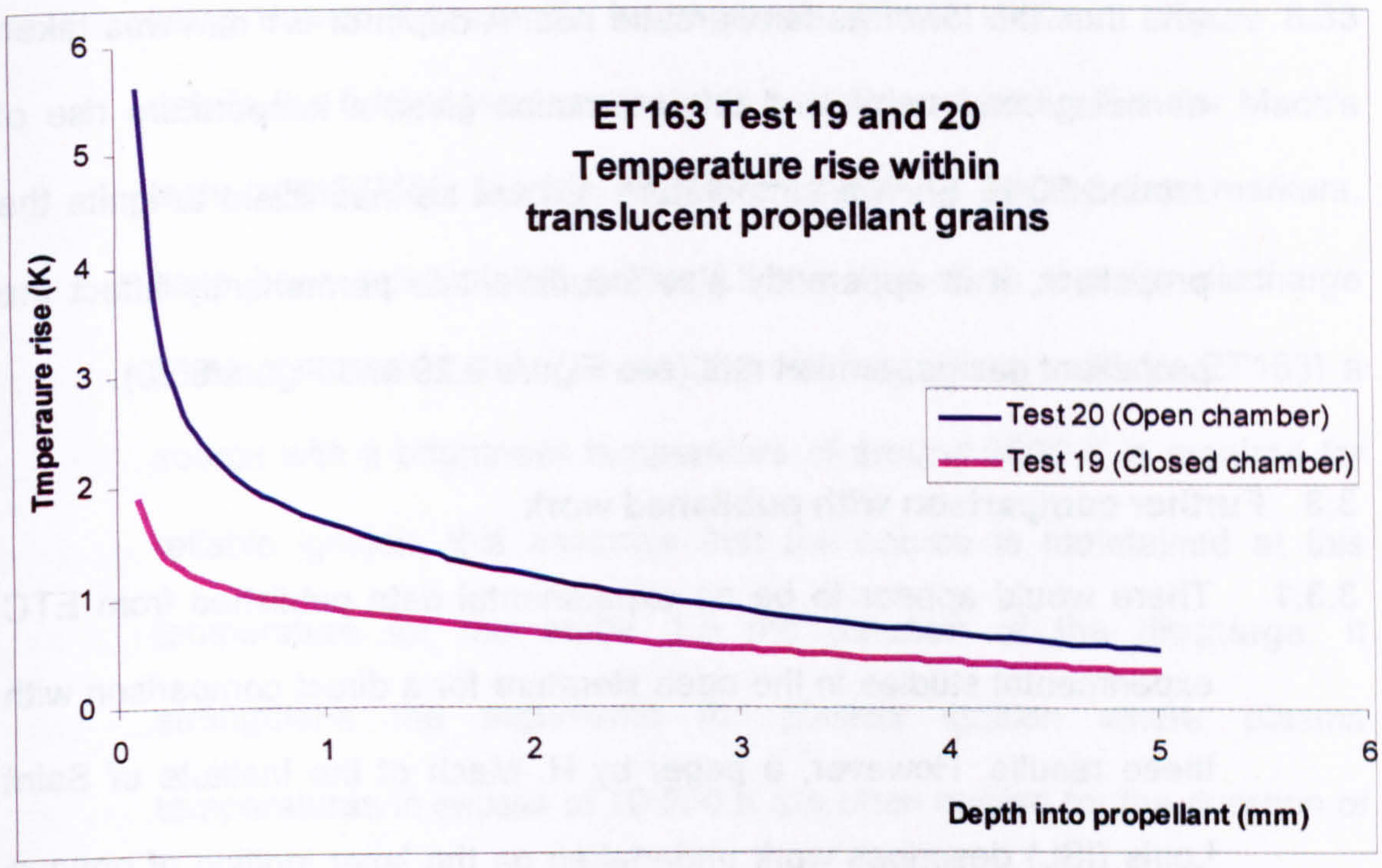

Figure 8.32 Temperature rise within translucent grain due to incident plasma radiation

3.2.8 As can be seen from Figure 8.32, there is a difference between performing the test in the open air and in a closed chamber. However, the temperature rise is only a few degrees for the first millimetre or so of propellant in both tests, and then it decays to below a degree. This temperature rise is small due to the relatively low plasma temperature of a few thousand kelvin; the deduced temperature rise is considered too low to have any measurable effect on the propellant, whether for ignition or other thermally induced damage.

3.2.9 The effect of this incident flux on opaque propellant can be estimated by considering the energy to be absorbed within a reasonable skin depth; the thicker the depth, the greater the mass of propellant heated and thus the lower its temperature rise. A depth of 0.1 mm was taken as being reasonable and this estimation gives a temperature rise of around 90 K. Such a temperature rise will be insufficient to ignite the propellant, it is apparently also insufficient to permanently affect the propellant gas generation rate (see Figure 8.29 and Figure 8.30).

3.3 Further comparison with published work

3.3.1 There would appear to be no experimental data published from ETC experimental studies in the open literature for a direct comparison with these results. However, a paper by H. Mach of the Institute of Saint Louis (ISL) describes work undertaken on the laser ignition of opaque single-based solid propellants B19T98 and BTU85, and opaque double-based propellant JA2 [16]. This paper enables a comparison of

sorts to be made with the radiant flux recorded for the experiment described here, given certain assumptions.

3.3.2 In his paper, Mach describes many tests in which laser energy with a spot diameter of 8 mm was incident on a propellant grain in a closed vessel. The duration and incident power of the laser pulse were varied until a statistically reliable (95% probability) ignition occurred, providing a value for the threshold energy required for reliable ignition. The quoted values of radiant flux density have been converted by the Author to brightness (blackbody equivalent) temperatures. This conversion assumed the ignition could be ascribed to thermal processes arising from the absorption of radiation, rather than anything being due to the specific laser wavelength of 1060 nm. Figure 8.33 details the brightness temperatures and the pulse duration for Mach's tests with BTU85. Mach's results, indicated by the red data markers, have been extrapolated below 3.5 ms and show that for discharge times of approximately 1.5 ms (the discharge time used for ET163) a source with a brightness temperature of around 9000 K is required for reliable ignition; this assumes that the source is maintained at this temperature for the entire 1.5 ms duration of the discharge. It strengthens the arguments for plasma ignition where plasma temperatures in excess of 10 000 K are often quoted for the duration of the discharge. Such high temperatures are assumed, however, rather than measured.

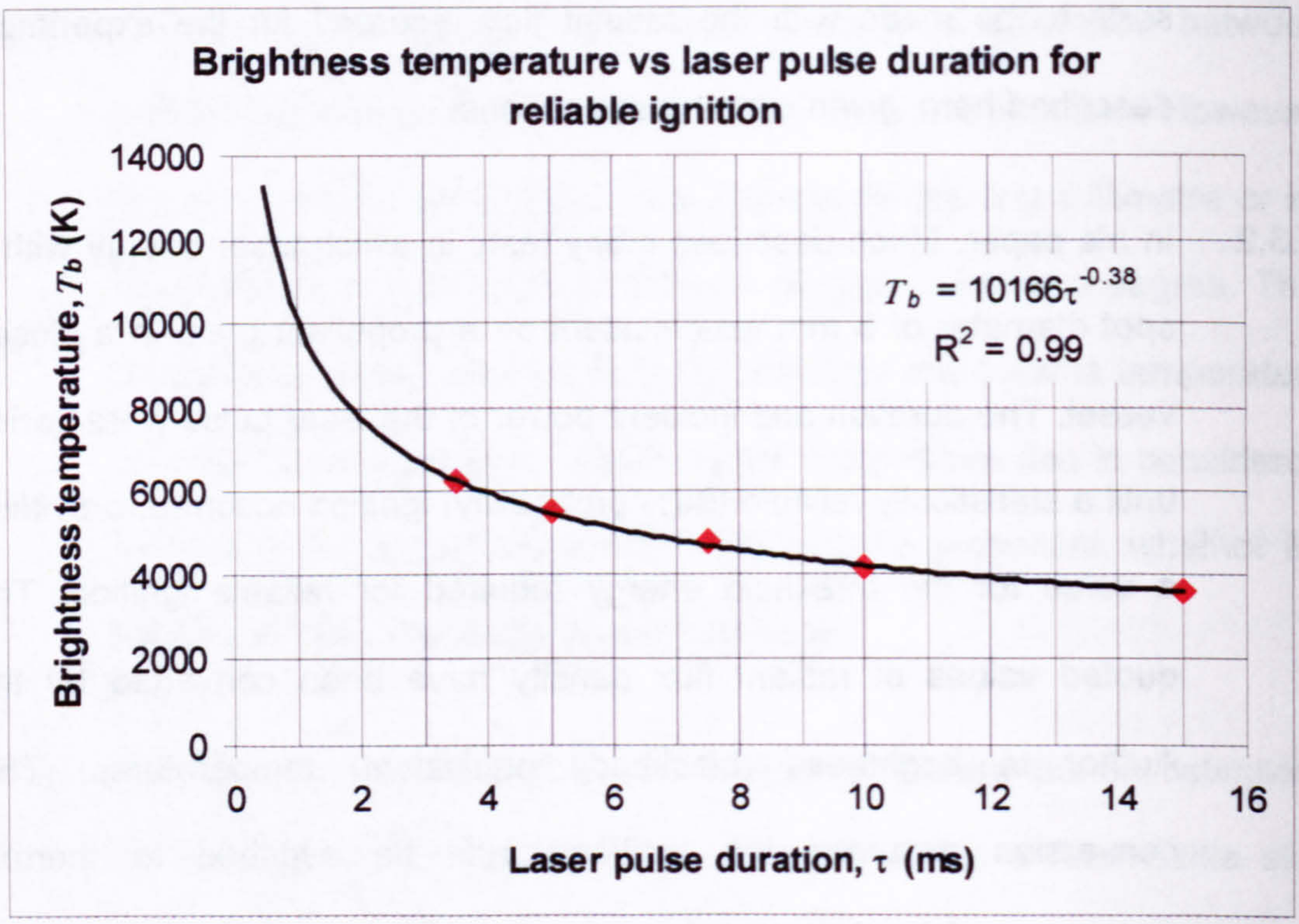

Figure 8.33 Brightness temperatures and pulse duration for Mach's tests with BTU85 single-based propellant

3.3.3 A comparison was made between prediction of the radiant energy required for ignition based upon Mach's results and the radiant energy measured from typical ETC plasmas (ET163 Test 20) – see Figure 8.34. With a plasma discharge, thirty times less energy is incident on the propellant surface than the predicted requirement for radiant ignition and yet plasma ignition still occurs with sub-millisecond ignition delay times. For radiation ignition of opaque propellant in less than 0.4 ms, a plasma with a brightness temperature greater than 15000 K would be required. These results further strengthen the Author's arguments for ETC plasma ignition by some means other than radiation energy transfer.

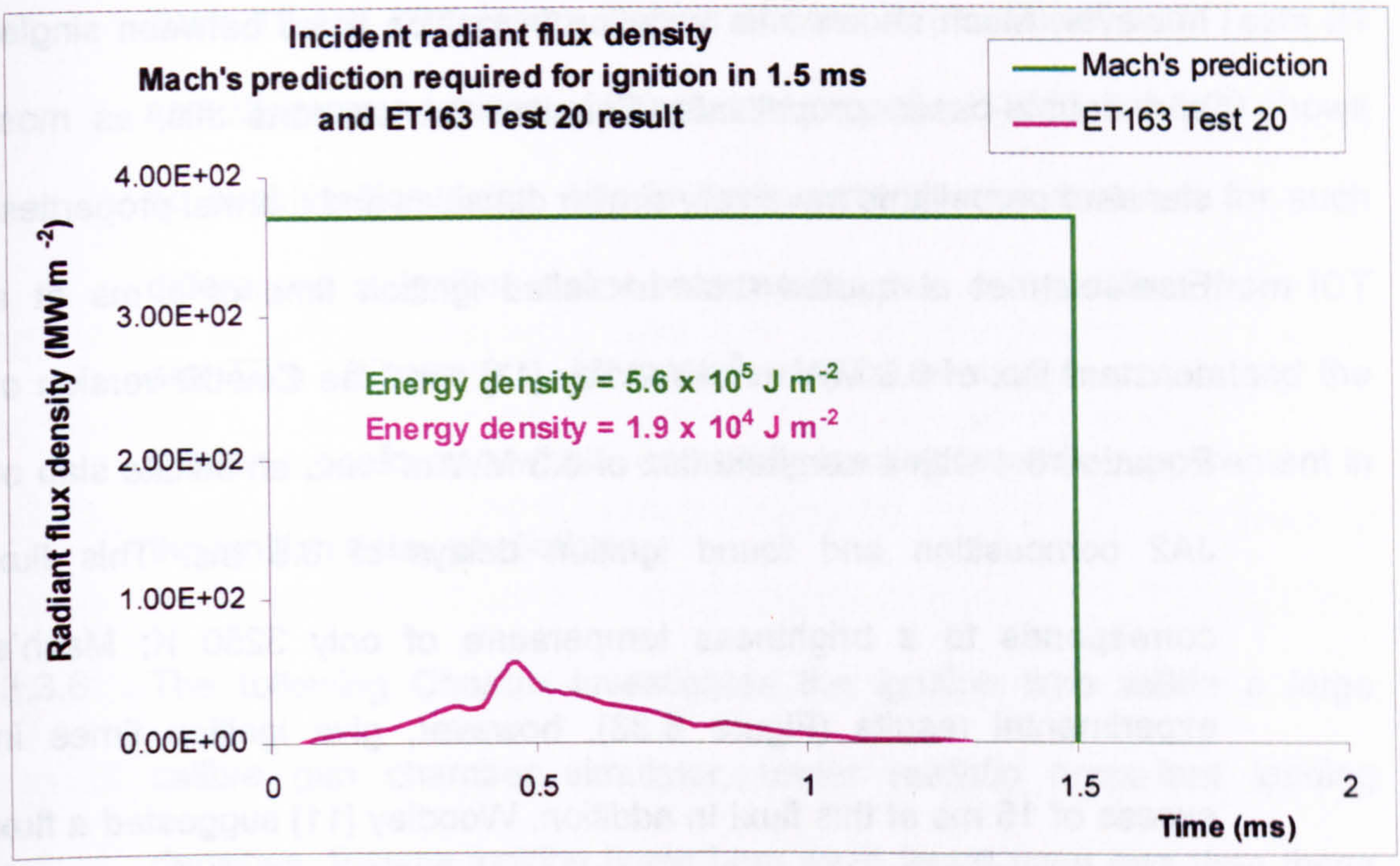

Figure 8.34 Comparison between radiant energy required for ignition (Mach) and typical radiant energy from an ETC discharge

3.3.4 Interestingly, Eisenreich et al [6] have shown that the times for ignition of an infinite propellant slab, t_{ign} can be predicted by:

$$t_{ign} \approx \pi \lambda \rho c (T_s - T_\infty) / 4 Q_0^2 \qquad \textbf{Equation 8.4}$$

where

λ is the thermal conductivity

ρ is the propellant density

c is the propellant specific heat capacity

T_s is the burning propellant surface ignition temperature

T_∞ is the propellant bulk temperature before ignition and

Q_0 is the total heat flux absorbed by the surface.

3.3.5 Equation 8.4 predicts a far shorter ignition delay than that quoted by Mach, although this could be partly explained by a dependency on propellant composition (i.e. frequency dependent opacity). In his paper,

however, Mach shows little variation in ignition times between single- and double-based propellants. Equation 8.4 supports this, as most standard propellants have very similar densities and thermal properties. Eisenreich et al quoted their modelled ignition time of 1 ms at a constant flux of 6.3 MW m^{-2}. Woodley [17] used the QinetiQ version of Equation 8.4 with a constant flux of 6.3 MW m^{-2} and an infinite slab of JA2 composition and found ignition delays of 0.5 ms. This flux corresponds to a brightness temperature of only 3250 K; Mach's experimental results (Figure 8.33), however, give ignition times in excess of 15 ms at this flux! In addition, Woodley [11] suggested a flux of 20 MW m^{-2} for a conventional gunpowder igniter and Figure 8.27 clearly shows that the ignition times for such a system is 4 ms; this is three times *more* flux and an ignition delay four times *longer* than predicted by such ignition delay equations. The assumption behind Equation 8.4 and other similar formulae is that there is no distinction between conductive and radiative energy transfer processes leading to ignition; the flux of one would have an effect equal to the flux from the other. This may be true for perfectly opaque propellants and supports the Author's use of Mach's laser ignition work at a narrow wavelength, in evaluation of the broadband (Planckian) brightness temperatures required to simulate his results. However, this argument also implies that translucent propellant should have a longer time to ignition than the opaque variety because of the lower amount of radiation absorbed on the surface of the former type of propellant. Comparison of ET163

Tests 18 and 23 (plasma ignition of opaque propellant) with Tests 21 and 22 (plasma ignition of translucent propellant) in Figure 8.29 shows no such ignition delay. Nor is there currently any evidence for such differences in ignition delay between the two compositions from ICT and TZN (Figure 8.1). More work may be needed to understand the ignition process as a whole, especially leading towards improvement in the ignition delay predictions.

3.3.6 The following Chapter investigates the ignition time within a large calibre gun chamber simulator, under realistic propellant loading densities. Plasma ignition times here were found even less than those for the small-scale chamber, due to the more precisely defined time-of-arrival of the ignition flux in these large calibre tests.

4 Conclusions from small-scale ignition experiments

4.1 EGGR from plasma ignition:

4.1.1 No measurable difference was detected in gas generation rates between conventional and plasma ignition of translucent or opaque propellants determined in closed vessel tests (Figure 8.29). However, if an aluminium plasma initiation wire 17 mm from the propellant surface had been used in the Author's experiments, rather than copper plasma from a CPG 10 – 12 cm from the surface, with a 16 kJ discharge and a peak power of 230 MW over a period of 2 ms, there could well have been significant differences in gas generation rate enhancement. This is because under such conditions in the Author's work damage was

found to occur to the translucent propellant that would increase the surface area during burning. This increase in burning area would then correspondingly increase the gas generation rate of the propellant.

4.1.2 The gas generation rate of opaque propellant was greater than for the translucent formulations (Figure 8.30). It is suspected that this could be due primarily to the radiant energy from the reaction zone (i.e. the propellant flame) being absorbed on the propellant surface of opaque compositions, but transmitted to the propellant body (i.e. lost to the system) in the translucent variety. ICT detected no difference in the gas generation rate between opaque and translucent propellants at low pressures (< 30 MPa), but Figure 8.30 seems to indicate that there is a difference in gas generation rates in the work conducted by the Author at these pressures.

4.2 Radiation damage to propellant:

4.2.1 Work conducted by ICT and TZN suggests a minimum plasma temperature of 9500 K sustained for 0.5 ms to produce surface radiation damage. From the Author's work reported in this Chapter, the maximum brightness temperature measured was around 6000 K, sustained for much less than 0.5 ms (Figure 8.23). However, these discharges still produced significant grain damage: the radiation damage theory is thus not upheld.

4.2.2 No significant damage to translucent propellant occurred from the use of copper plasma initiation wires, but significant damage did result to

the same propellant from exploding 0.5 mm diameter aluminium wires under similar discharge parameters as in the copper wire study (Figure 8.21). No significant difference was measured between the incident radiant flux from copper and aluminium wires (Figure 8.23). Again, this finding does not support the notion of radiation damage.

4.2.3 Locating propellant samples further from the wire significantly reduced the damage to the grain, but the incident radiative flux reduced only marginally (Figure 8.23). Further, the use of optical windows (formed from black masking tape) appeared to prevent damage to translucent propellant grains. These results also do not support the radiation damage notion.

4.2.4 A polished propellant surface rather than an unpolished one seems to produce a greater degree of damage. This supports the radiation damage theory. Covering the translucent propellant sample with a plastic bag also appears to prevent damage, which might support the radiation damage theory if the bag absorbs significant radiant energy (in the UV). However, these tests were inconclusive as no measurements were made of the incident radiation, or of the moment the bags were displaced. In addition, a lack of damage to opaque compositions appears to contradict rather than support the radiation damage conclusion.

4.2.5 On the strength of these arguments, it has been concluded that damage to translucent propellant in these tests is not caused via a

radiative mechanism: it may result from a shock-initiated mechanism instead. The 0.03% graphite within the opaque composition, tape on the propellant, a non-smooth propellant surface and covering the propellant with a plastic bag would then have to change the attenuation or other properties of the shock front.

4.3 Thermal effects of plasma radiant energy for propellant ignition:

4.3.1 The Author has found that opaque propellant does not ignite under the stimulus of plasma in an open-air environment, unlike in the jointly reported work by ICT and TZN. Indeed, estimations with measured incident radiative flux indicate a maximum temperature rise of 90 K can be expected. With translucent propellant, the temperature increase decays as a function of depth, with a maximum temperature rise of a few degrees kelvin at the surface.

4.3.2 In closed vessel tests, ETC plasma is shown to ignite propellant at least twelve times faster than a conventional gunpowder igniter of comparative energy. This supports the notion that some mechanism other than radiative produces significant energy flux for ignition to the surface of the propellant.

4.3.3 Comparison with a study of the ignition of propellant by laser radiation, based on the assumption that the energy transfer process is purely thermal, has allowed the brightness temperatures required for such an ignition process to be examined. This comparison concluded that a blackbody emitter at 9000 K for 1.5 ms would be required to ignite a

standard propellant composition. This is thirty times more radiant energy than was measured over the entire duration of ETC discharges for a similar timescale, and yet plasma ignition has been shown to occur on a sub-millisecond timescale. Radiation is again not the prime energy transfer mechanism for plasma ignition in these tests.

4.3.4 Formulae that predict ignition delay have been discussed with regard to incident flux. Such formulae have been found lacking when compared with experiments involving gunpowder and laser ignition systems, assuming the origin of the flux is divided equally between conductive and radiative sources. The ignition times predicted by such formulae would appear to be far shorter than experimental evidence suggests.

5 Recommendations and further work

5.1.1 A propellant exchange has been proposed by the Author with ICT, to allow an investigation into each other's sample compositions. This will enable both parties to repeat each other's work more closely so that each set of conclusions can be verified. This would be the first step in determining which parameters are important for the two studies.

5.1.2 A more rigorous investigation needs to be undertaken with regard to the damage done by aluminium wires, with a more thorough system measuring the damage. Experiments need to be devised to test other candidate mechanisms for damage formation. Advice needs to be sought regarding shock damage to propellants: there may be some overlap between this work and detonics.

5.1.3 Finally, more work in general needs to be undertaken towards an understanding ignition processes as a whole.

---

1 K. Kappen and U. H. Bauder, "Calculation of Plasma Radiation Transport for Description of Propellant Ignition and Simulation of Interior Ballistics in ETC guns", IEEE Transactions on Magnetics, Vol. 37, 1, January 2001

2 A Voronov, A Koleczko, H Haak, T Weise and N Eisenreich, "Energy Criteria for Combustion Control in a Large Calibre Gun", IEEE Transactions on Magnetics, Vol. 37, 1, January 2001

3 A. Koleczko, N. Eisenreich, H. Schmid and K. Kappen, "Plasma-propellant Interaction in ETC Applications – Part 1: Experimental Results and Propellant Characteristics", Submitted for publication.

4 A. Koleczko, W. Ehrhardt, S. Kelzenberg and N. Eisenreich, "Plasma Ignition and Combustion", Propellants, Explosives, Pyrotechnics, Vol. 26, pp 75 – 83, 2001

5 A. Koleczko, W. Ehrhardt, H. Schmid, S. Kelzenberg and N. Eisenreich, "Plasma Ignition and Combustion", 19th International Ballistics Symposium, Interlaken, Switzerland, May 2001

6 N. Eisenreich, W. Eckl, T. Fischer. V. Weiser. S. Kelzenberg, G. Ianger and A. Baier, "Burning phenomena of the Gun Propellant JA2", Propellants, Explosives, Pyrotechnics Vol. 25, pp 143 – 148, 2000

7 M. J. Taylor, "ET163 – Investigation of Plasma Ignition of Opaque and Translucent Propellant", Unpublished QinetiQ internal report FST/CDT/58-ETL/ERD023, December 2001

8 A. Koleczko, private communication

9 QinetiQ internal memo 0201, file DRA/WX6/5/4/7/19

10 C. R. Woodley, Simulation reference *mtdx03.in* BRLCB code, private communication

11 C. R. Woodley, 'Convective heat flux.xls', Private communication, May 2000

12 M. Jung, Reinmetall Ordnance Ltd, "ETC – Gun Technologies for Main Battle Tank Weaponisation", CEPA16 Workshop, November 2001

13 K. Kappen and U. H. Bauder, "Simulation of Plasma Radiation in Electrothermal-Chemical Accelerators," IEEE Transactions on Magnetics, Vol. 35, 1, January 1999

14 K. Gruber, K. Kappen, A. Voronov and H. Haak, "Radiation Absorption of Propellant Gas," IEEE Transactions on Magnetics, Vol. 37, 1, January 2001

15 K. Kappen and U. H. Bauder, "Calculation of Plasma Radiation Transport for Description of Propellant Ignition and Simulation of Interior Ballistics in ETC Guns," IEEE Transactions on Magnetics, Vol. 37, 1, January 2001

16 H. Mach (ISL), 'Measurement of the threshold energies for reliable ignition of solid propellants using a pulsed Nd-glass laser', 14th International Symposium on Ballistics Quebec, Canada, 26th – 29th September 1993

17 C. R. Woodley, QinetiQ, private communication, February 2002

Chapter 9 – Plasma propagation and ignition studies: Large-scale ETC ignition experiments

1 Introduction

1.1.1 The previous two chapters have described work conducted in the open air and at small scale to understand ETC plasma propagation and plasma/propellant energy transfer mechanisms. This chapter looks at how ETC plasmas develop in the large-scale 155 mm calibre gun environment. All work described has been conducted by the Author, unless stated otherwise.

1.1.2 The chapter will cover work conducted in a 155 mm calibre acrylic vessel with small amounts of live propellant distributed within an inert propellant bed.

2 155 mm acrylic vessel inert propellant tests

2.1 Experimental aims

2.1.1 This experiment [1] sought to measure the radiant flux density incident upon propellant grain surfaces during plasma ignition of a representative 155 mm gun charge and loading density. Ignition times were determined from the unique spectra of trace elements within the propellant. Further, the work aimed to investigate whether a correlation existed between the plasma vapour deposition and propellant ignition. The thickness of the coating was measured and the flux estimated assuming a suitable time interval over which deposition occurred. The flux from the deposition was compared with that from radiant energy measurements and conventional gunpowder igniters. The pressure local to the propellant grains was also obtained.

2.1.2 Capillary pressures and time-resolved spectroscopic measurements were recorded of the capillary plasma and plume expanding along the central ullage. The Ultranac camera was used to measure the plasma propagation velocity. This study was designed to validate QinetiQ's capillary plasma generator code EDENET and its successor EDEN-IB.

2.2 Test arrangement

2.2.1 A 155 mm simulator test rig was used for this experiment, comprising a cylindrical acrylic chamber, 165 mm in diameter and 1035 mm in length, with steel end plates. This is shown complete with polyethylene discs in Figure 9.1.

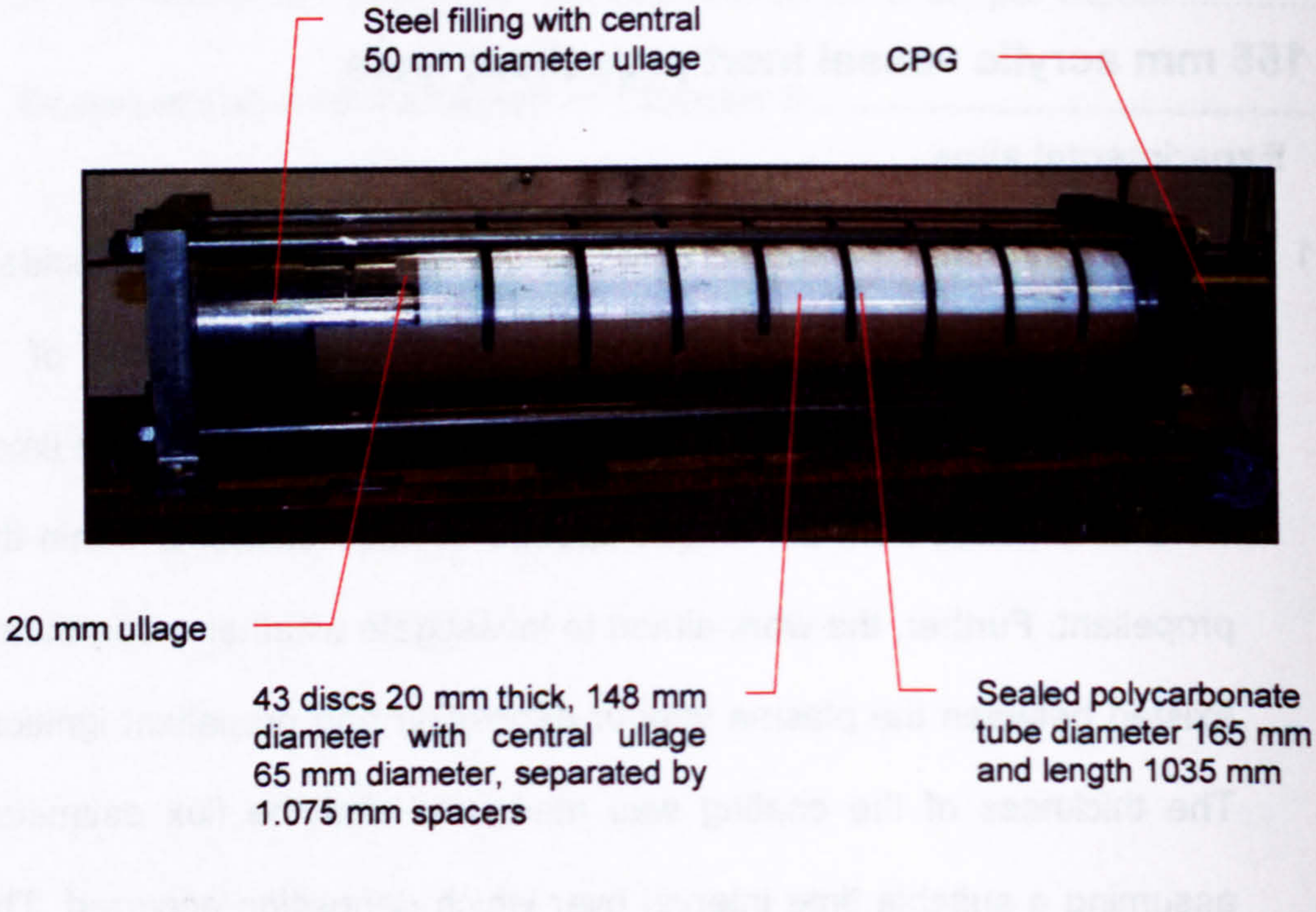

Figure 9.1 155 mm simulator test rig loaded with polyethylene discs

2.2.2 The vessel walls were 36 mm thick, designed to withstand dynamic pressures up to 18 MPa and hence the vessel could be used for

ignition tests with small amounts of live propellant. It has also been used as a sacrificial vessel in tests with several kilogrammes of propellant (not discussed in this Thesis due to space restrictions). The rig has been designed to couple with a CPG as used in the 155 mm ETC gun. Vent bolts are provided in the steel endplates at either end of the rig to release any pressure built up during tests. For some of the tests, the vent bolt at the opposite end of the rig to the CPG was replaced by an acrylic window to allow for emission spectroscopy measurements.

2.2.3 The test rig was attached to a filament-wound CPG body based on the contemporary capillary plasma generator design (100 mm long and 10 mm in diameter). The capillary was fitted with 0.9 g pure copper plasma initiation wire made from a single strand 1 mm in diameter and 125 mm in length (the only exception being Test 7, when 0.4 g wire was used). 25 mm of the wire formed the connection to the external annular electrode, held in place with sticky tape. This small length of wire was similar to that giving the initial plasma plume (discussed in Chapter 4). The wire simply touched the rear electrode: electrical continuity was checked before the rig assembly was completed. The arrangement appears in Figure 9.2.

2.2.4 A total of 43 polyethylene discs, 20 mm thick with 148 mm outer diameter and a central ullage 65 mm diameter was inserted into the cylinder (illustrated in Figure 9.1). Discs represent a generic propellant

geometry useful in fundamental ETC studies. The Author had heard of reports of such experimental disc geometry being used in Germany [2] and the USA and realised their relevance for these studies.

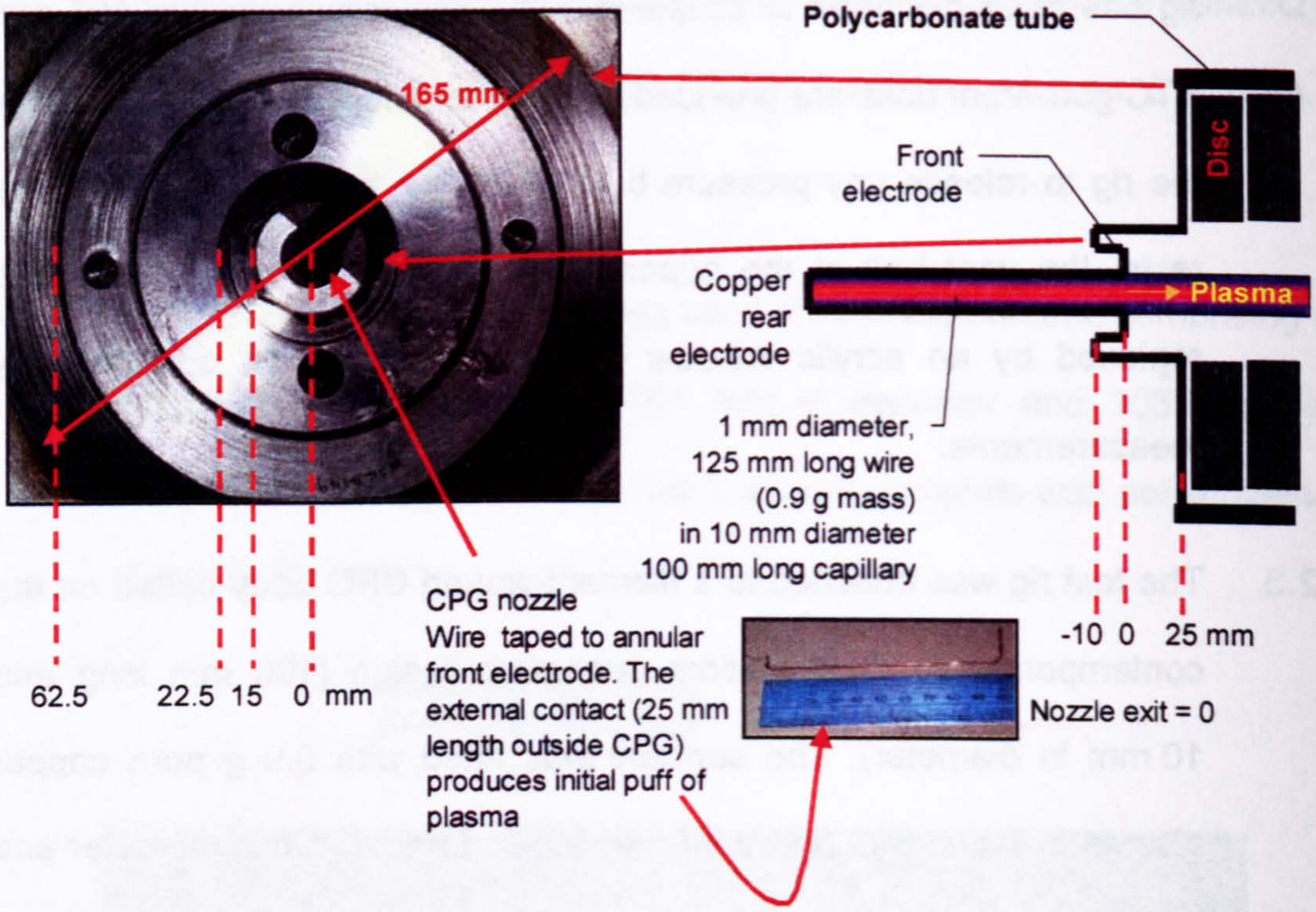

Figure 9.2 Details of CPG and rig endplate

2.2.5 Discs were numbered from 1 to 43 with Disc 1 being closest to the CPG; hence, disc location and orientation were known. Disc spacing was achieved using three 0.7 mm diameter copper wires, wound around every other disc, but because the wires did not lie exactly flat against the discs, and the latter were not pressed tightly together in the vessel, disc separation actually was greater than 0.7 mm. The exact separation was important in modelling work, so the average disc separation of 1.075 mm was calculated by measuring the distance to the front face of the fourth disc and every subsequent fifth disc (where

black tape was laid as indicated in Figure 9.1). This separation was given by the gradient, as shown in Figure 9.3. No ullage was left unfilled at the 'projectile' end of the rig: the ullage was filled with steel filling rings (as in Figure 9.1).

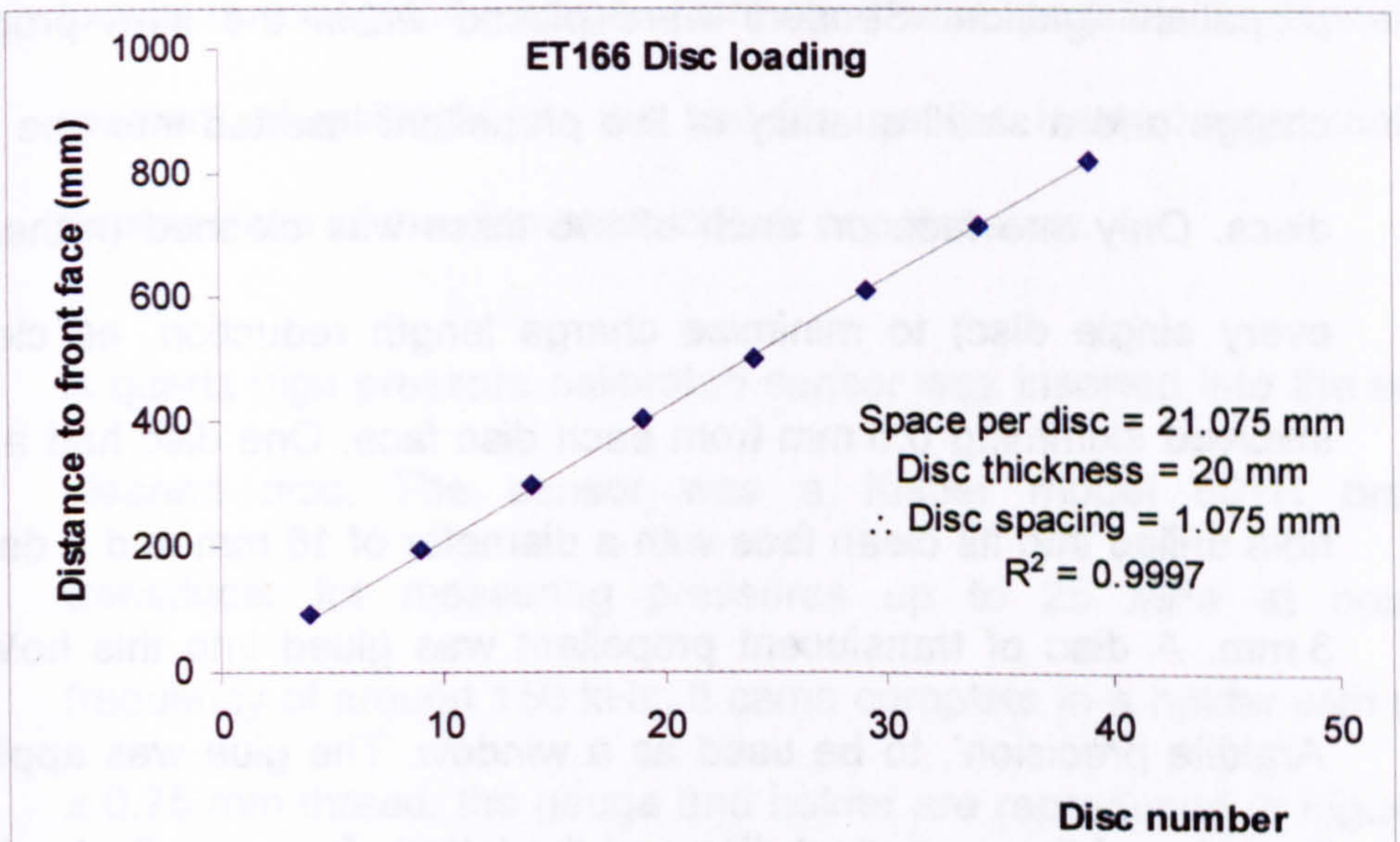

Figure 9.3 Calculation of average disc spacing

2.2.6 Capacitor bank parameters were such as to give a similar discharge power to that used in 155 mm ETC ignition tests. Four modules (two in Test 7) fitted with a 255 μH inductor were used, with the capacitor bank charged to 60%. When the discharge occurred, copper plasma vented from the capillary and cooled plasma constituents condensed onto the discs. The pressure at the disc surface increased temporarily and radiant energy was transferred to the discs. Both the pressure and the transferred radiant energy were measured at a number of locations along the inert charge.

2.2.7 In the first test, the discs were new. This test measured the deposition along the charge, since some discs were removed and saved for analysis later. The second and successive tests measured plasma/vapour properties along the charge length, to correlate with the propellant ignition. Sensors were placed within the inert propellant charge and a small quantity of live propellant inserted into one of the discs. Only one face on each of two discs was cleaned (rather than every single disc) to minimise charge length reduction, as cleaning involved skimming 0.5 mm from each disc face. One disc had a small hole drilled into its clean face with a diameter of 16 mm and a depth of 3 mm. A disc of translucent propellant was glued into this hole with 'Araldite precision', to be used as a window. The glue was applied to the *edge* of the propellant disc and the latter's face was flush with the face of the inert disc. Another hole with a diameter of 1.1 mm was drilled all the way through the centre of the first hole to the reverse side of the disc. A sacrificial optical fibre was then threaded through this smaller hole and made contact with the propellant.

2.2.8 The propellant had been polished on both sides so that it could act as a window through which to measure the radiative flux incident on its front surface. Four discs in turn had a 2 mm slot cut all the way through to the central ullage, to allow the fibre to be led out of the vessel without the application of too great a bend radius. The acrylic chamber had a 2 mm hole drilled through at an appropriate location to allow the fibre to pass out of the chamber. The hole was then back-filled with resin to act

as a gas seal. When assembled, the spectrograph was attached to the sacrificial fibre and calibrated absolutely *in situ* in the manner described in Appendix A. In this way, the radiant energy from the plasma discharge was recorded as an ignition stimulus at a number of locations along the charge. Further, it was possible to identify the moment of ignition from the spectra, as the inert charge contained neither trace of the elements sodium or potassium.

2.2.9 A quartz high pressure calibrated sensor was inserted into the second cleaned disc. The sensor was a Kistler model 601H pressure transducer for measuring pressures up to 25 MPa at operating frequency of around 150 kHz. It came complete in a holder with an M7 x 0.75 mm thread: the gauge and holder are reproduced in Figure 9.4. The disc required a hole to be cut through it and tapped with M7 x 0.75 mm pitch threads. The pressure sensor was inset 1 mm from the clean face of the disc, so that some high vacuum grease could be used to protect the gauge head from the copper vapour. This may have altered the readings by a negligible amount, but the risk to the gauge (at £1500 each) if unprotected from the plasma was otherwise too high. A further disc required a slot to be cut into it. This was to allow for the holder (longer than the 20 mm disc thickness) and the microdot lead to be taken through a second 2 mm hole drilled into the acrylic vessel wall. This hole was also back-filled with resin.

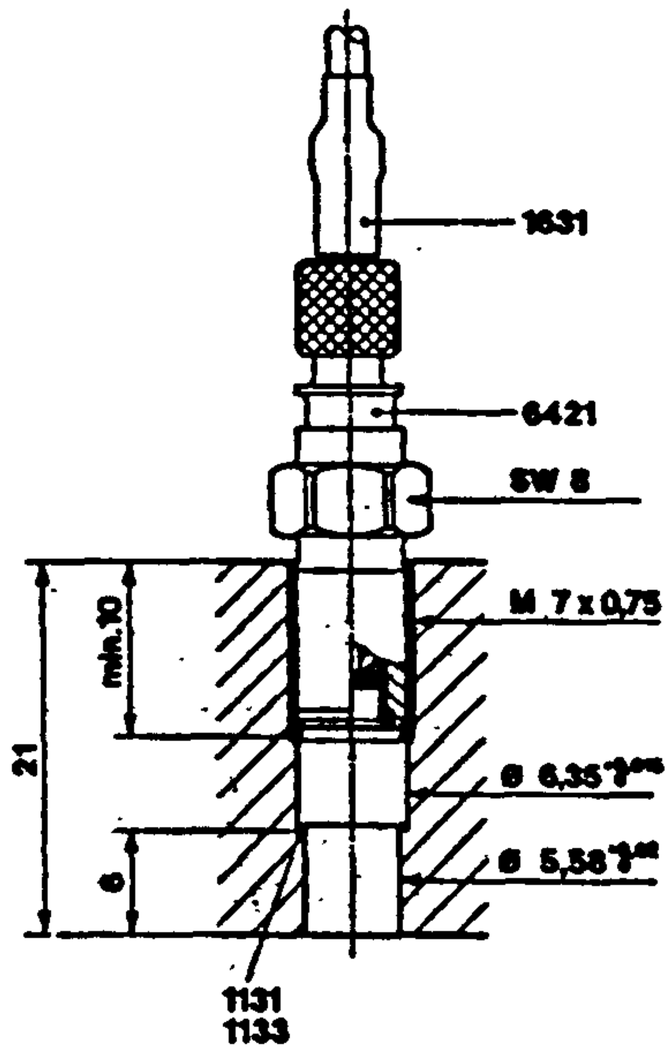

Figure 9.4 601H Kistler gauge and holder

2.2.10 Figure 9.5 is a schematic diagram of the instrumented part-inert charge set-up. The disc with the pressure sensor and that with the live propellant were opposite one another.

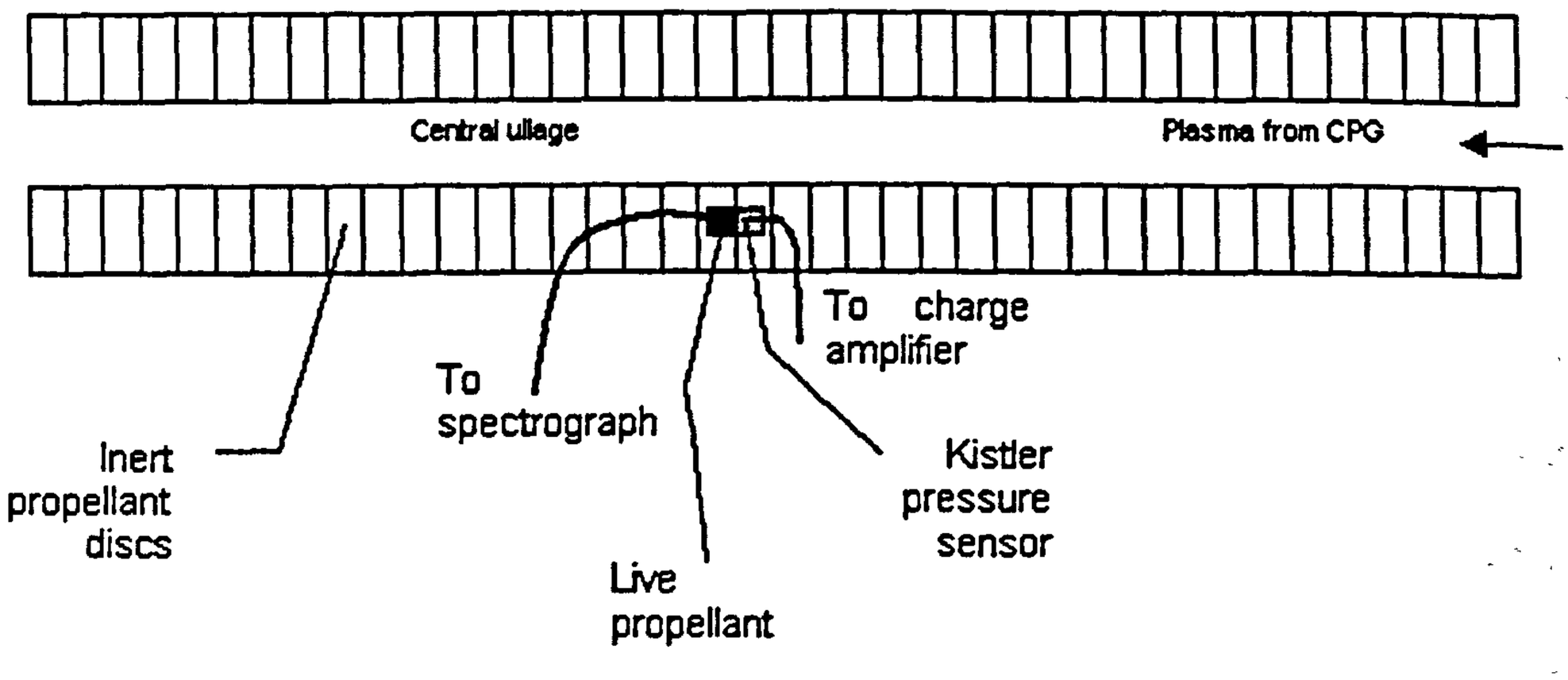

Figure 9.5 Instrumentation within inert polyethylene disc charge

2.2.11 After each test, the fibre and lead were cut either side of the acrylic vessel wall and left fixed within the vessel. (At the operating pressures for this test it was thought extremely unlikely that the vessel would fracture as a result of the weaknesses arising from this activity.)

2.2.12 Three locations were chosen from which to acquire spectroscopic and pressure measurements. In the event, some repeat tests were performed to increase confidence in the results, and give some indication of the tests' repeatability. Ideally, more tests should have been performed, but they were very time-consuming (and therefore expensive) to execute.

2.2.13 For this experiment, seventeen tests were conducted. Test 1 – 8 and 11 – 13 were plasma discharges into the chamber, fully loaded with polyethylene discs. Tests 14 – 15 had a partially loaded chamber with discs only at the 'projectile' end, away from the capillary. Tests 9 – 10 and Tests 16 – 17 were open-air firings and used the Ultranac camera to measure the plasma expansion velocity into the open air. Tests 16 – 17 were also used to verify seemingly anomalous capillary pressure gauge readings.

2.3 Test results – Capillary measurements

2.3.1 Component re-use was studied in detail earlier in the Thesis (see work reported from experiment ET114 [3], in Chapter 6), although at a much lower power density (5 MW cm^{-3} peak power density in ET114 compared with 10 MW cm^{-3} for this experiment). The conclusion was

that statistically, no effect from re-using components up to four times could be measured on external plasma properties. Hence, to reduce costs, capillary tubes and electrodes were re-used a number of times in these tests. The assumption was that each test resembled the next for a similar experimental arrangement.

2.3.2 Figure 9.6 and Figure 9.7 show the mean voltage and current, with discharge power and energy for this series of tests. The tests were included in the averaging regardless of being conducted in open air or into a closed vessel, except for Test 7 which involved different test parameters. Figure 9.8 illustrates how the test-averaged capillary pressure varied with time at three locations. These were adjacent to the rear electrode (twelve tests), mid-capillary (fourteen tests) and a few millimetres short of the nozzle (two tests). Only two pressure gauges were used at any one time due to availability, so a complete set of pressures for one single test was not possible. The rear gauge was the first to respond to the plasma pressure, and the effect moved along the capillary towards the nozzle. This was similar to the findings with ET114 [3]. Peak pressure was around 80 MPa, so compared with 50 MPa for the ET114, consistent with an increase in discharge power density. The test to test variability was again high, but seemingly anomalous behaviour in the capillary gauge readings was noted at peak pressure. Normal behaviour in a single-ended venting capillary (including a gun chamber) would suggest that a constant pressure gradient should exist, with pressure peaking at the closed end.

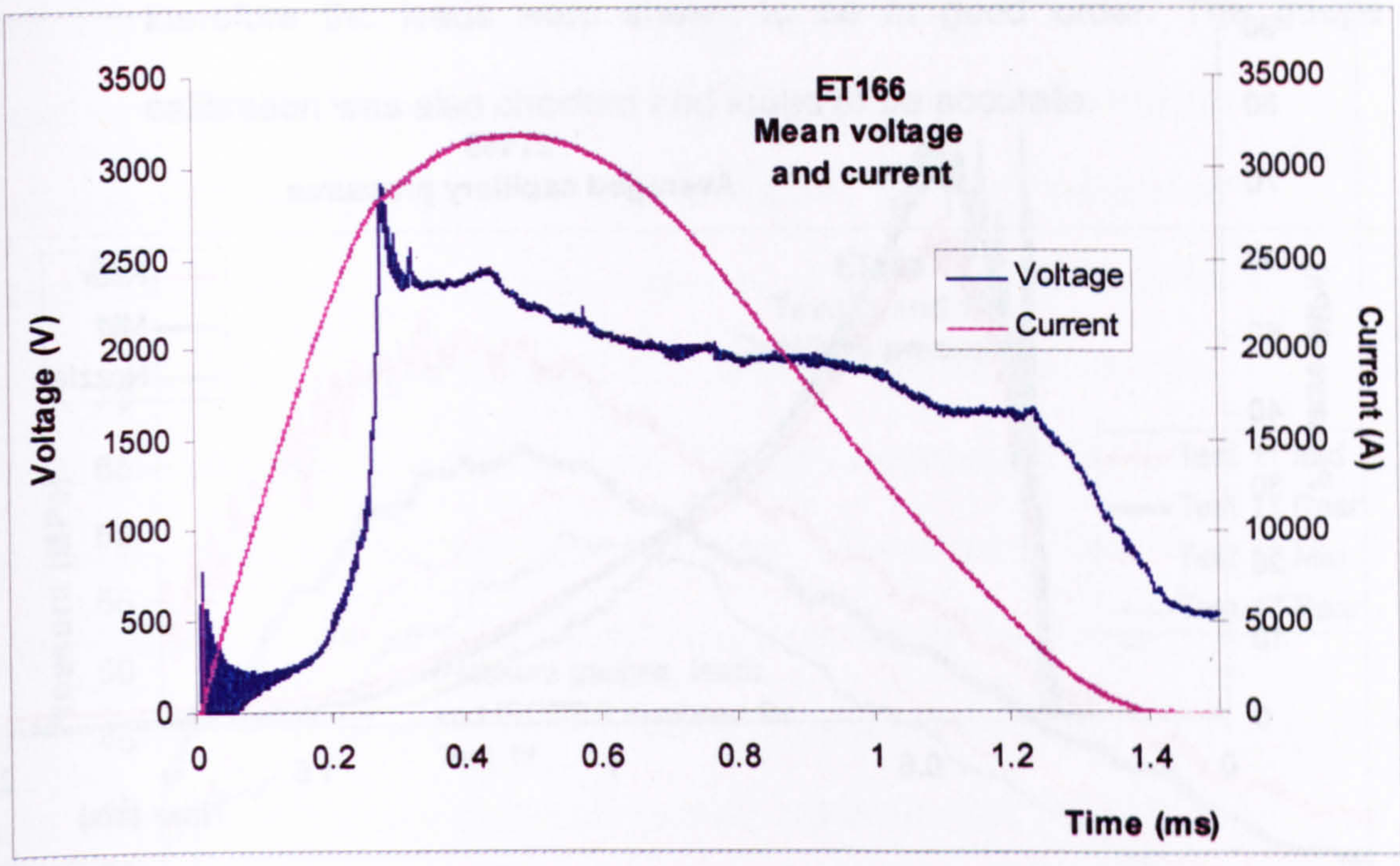

Figure 9.6 ET166 Mean discharge voltage and current

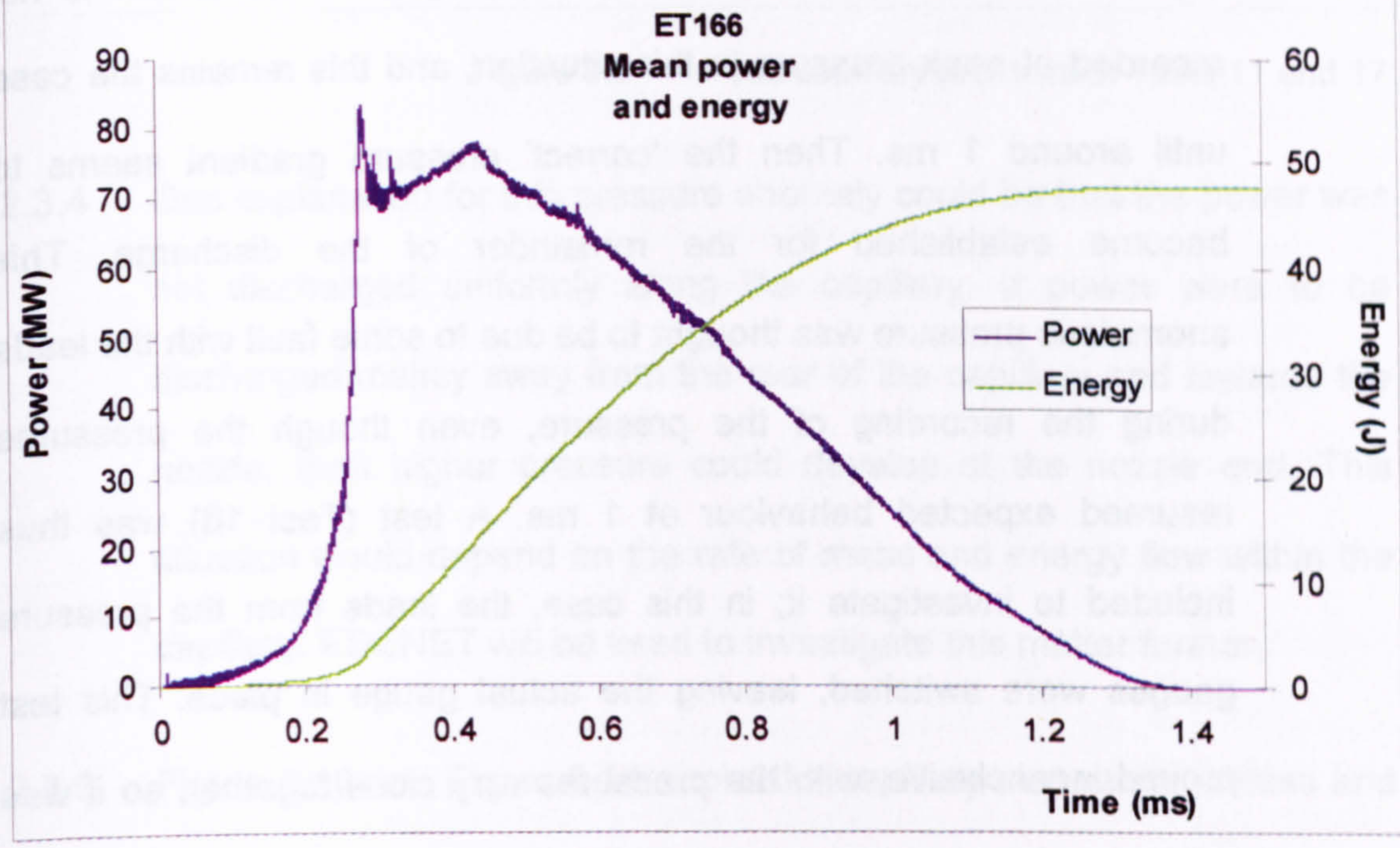

Figure 9.7 ET166 Mean power and energy of discharge

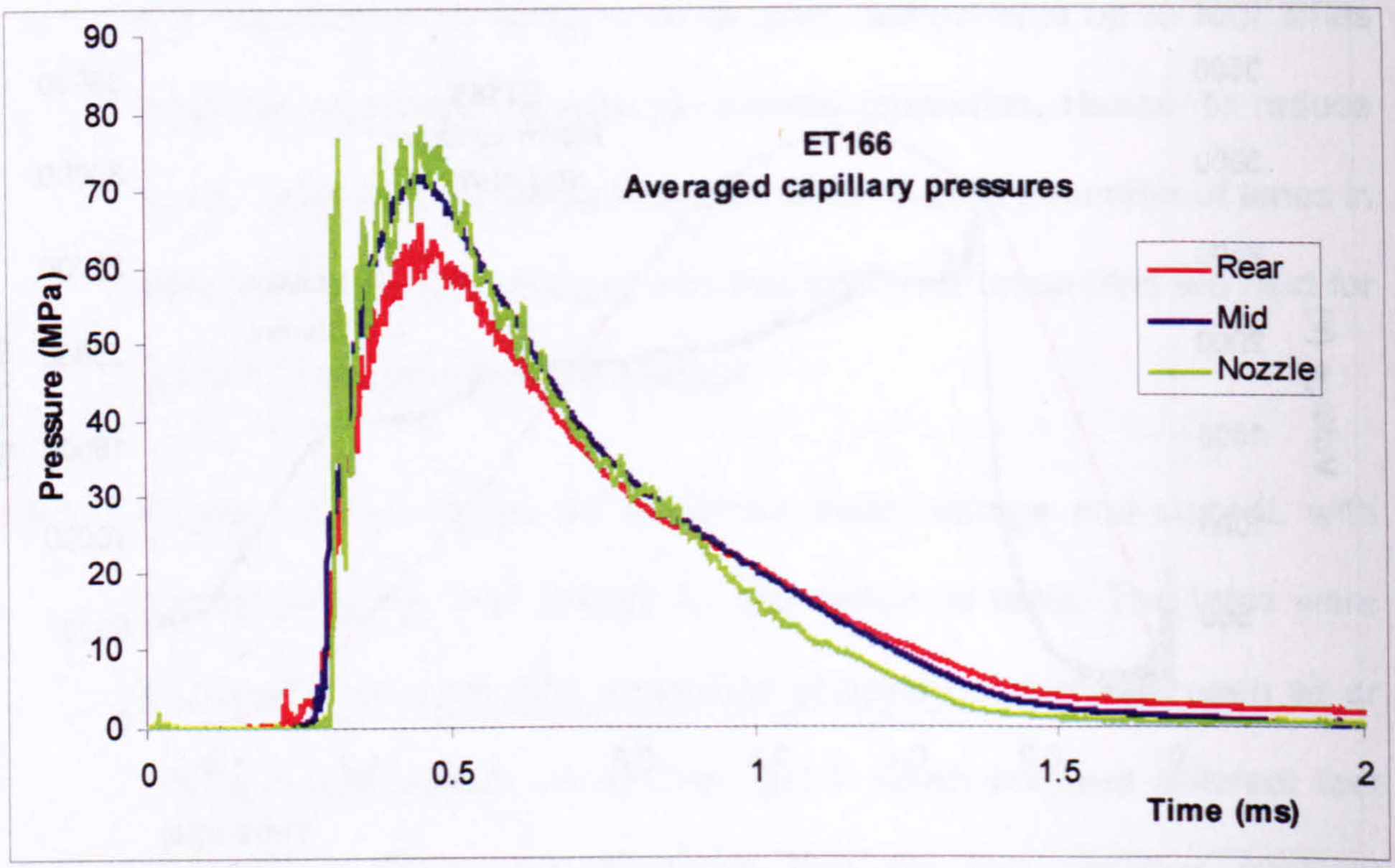

Figure 9.8 Capillary pressure

2.3.3 Figure 9.8 indicates that normal pressure gradient behaviour is not recorded at peak pressure in this situation, and this remains the case until around 1 ms. Then the 'correct' pressure gradient seems to become established for the remainder of the discharge. This anomalous pressure was thought to be due to some fault with the leads during the recording of the pressure, even though the pressures resumed expected behaviour at 1 ms. A test (Test 16) was thus included to investigate it; in this case, the leads from the pressure gauges were switched, leaving the actual gauge in place. This test proved inconclusive, with the pressures very close together, so it was repeated (Test 17). Figure 9.9 shows the result of Test 17 peak pressure along with another good example, Test 11. The pressure gradient is clearly seen to be reversed at peak pressure for both tests,

therefore the leads were shown to be in good order. The gauge calibration was also checked and found to be accurate.

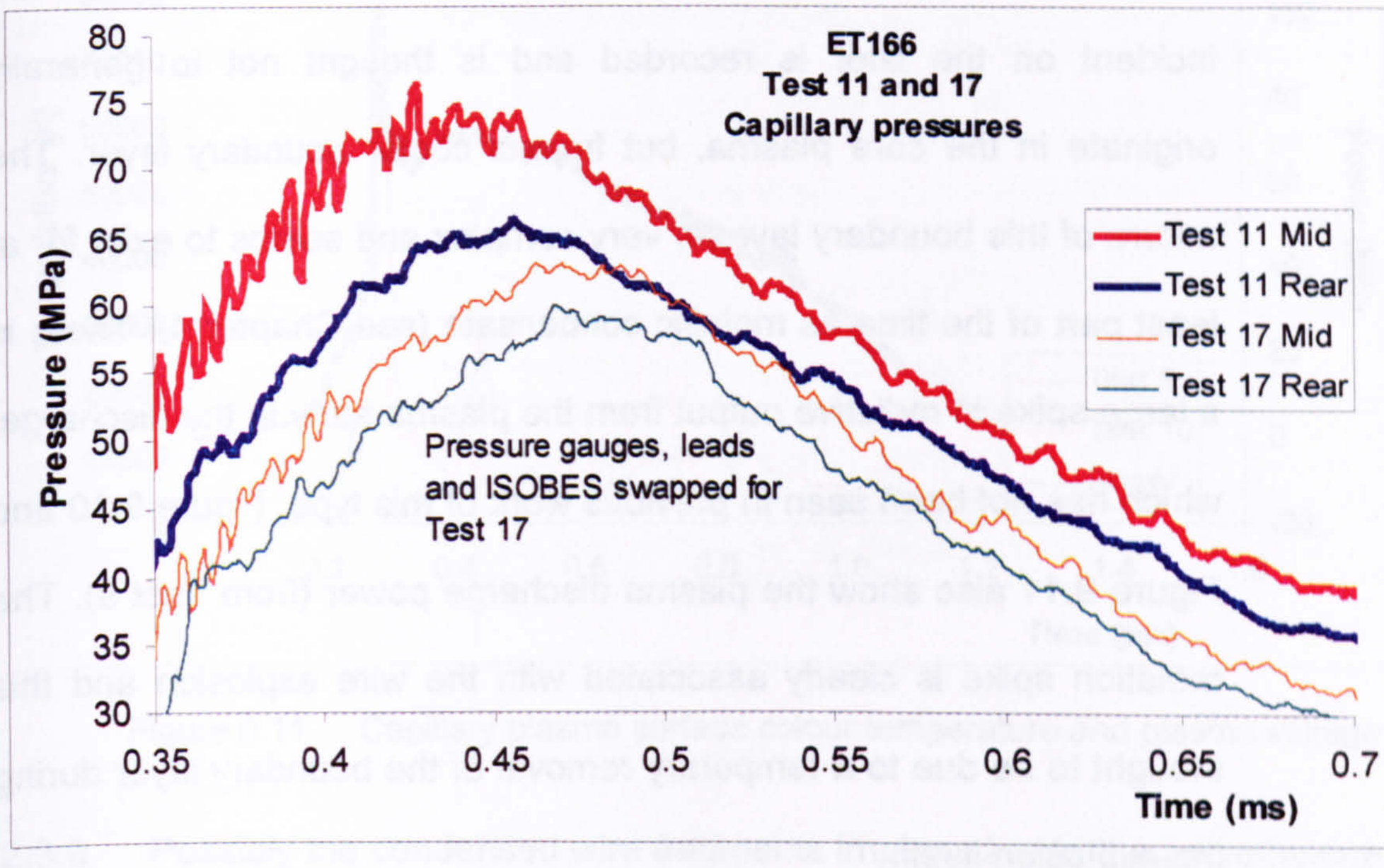

Figure 9.9 Peak capillary pressure in Tests 11 and 17

2.3.4 One explanation for this pressure anomaly could be that the power was not discharged uniformly along the capillary. If power were to be discharged mainly away from the rear of the capillary and towards the nozzle, then higher pressure could develop at the nozzle end. This situation would depend on the rate of mass and energy flow within the capillary. EDENET will be used to investigate this matter further.

2.3.5 Figure 9.10 and Figure 9.11 depict the capillary plasma brightness and colour temperatures respectively, for two tests where the spectra were recorded within the capillary. The spectra were obtained by inserting the spectrograph optical fibre into the translucent capillary wall, leaving

2 – 3 mm of liner acting as a window. The spectrograph system was calibrated absolutely in situ, so the absorption effects of the liner were accounted for. This process is detailed in Appendix A. The radiation incident on the liner is recorded and is thought not to generally originate in the core plasma, but from a cooler boundary layer. The nature of this boundary layer is very complex and seems to exist for at least part of the time as metallic condensate (see Chapter 4). There is a large spike in radiative output from the plasma early in the discharge, which has not been seen in previous work of this type. Figure 9.10 and Figure 9.11 also show the plasma discharge power (from Test 9). The radiation spike is clearly associated with the wire explosion and this thought to be due to a temporary removal of the boundary layer during the explosion itself.

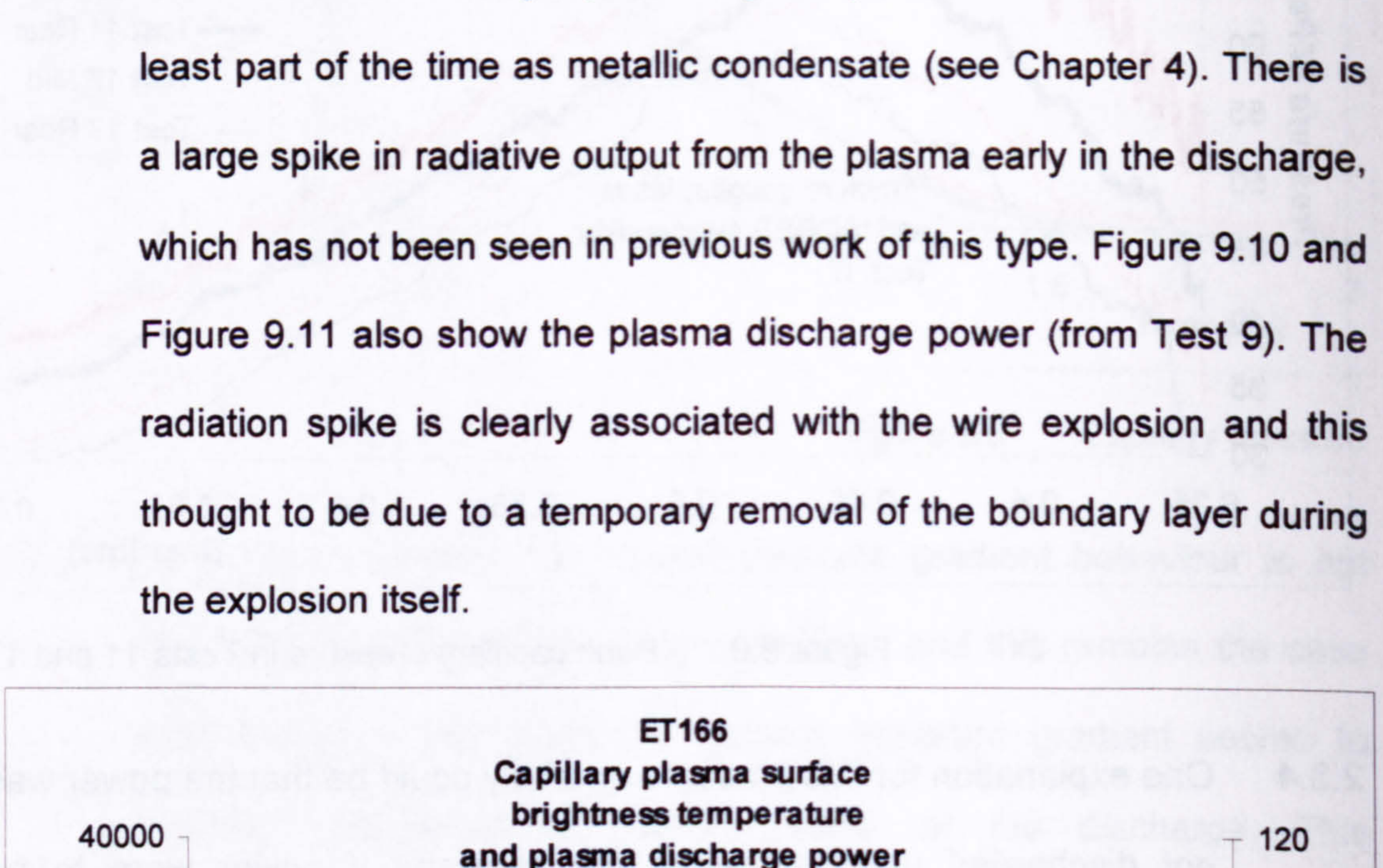

Figure 9.10 Capillary plasma surface brightness temperature and plasma voltage

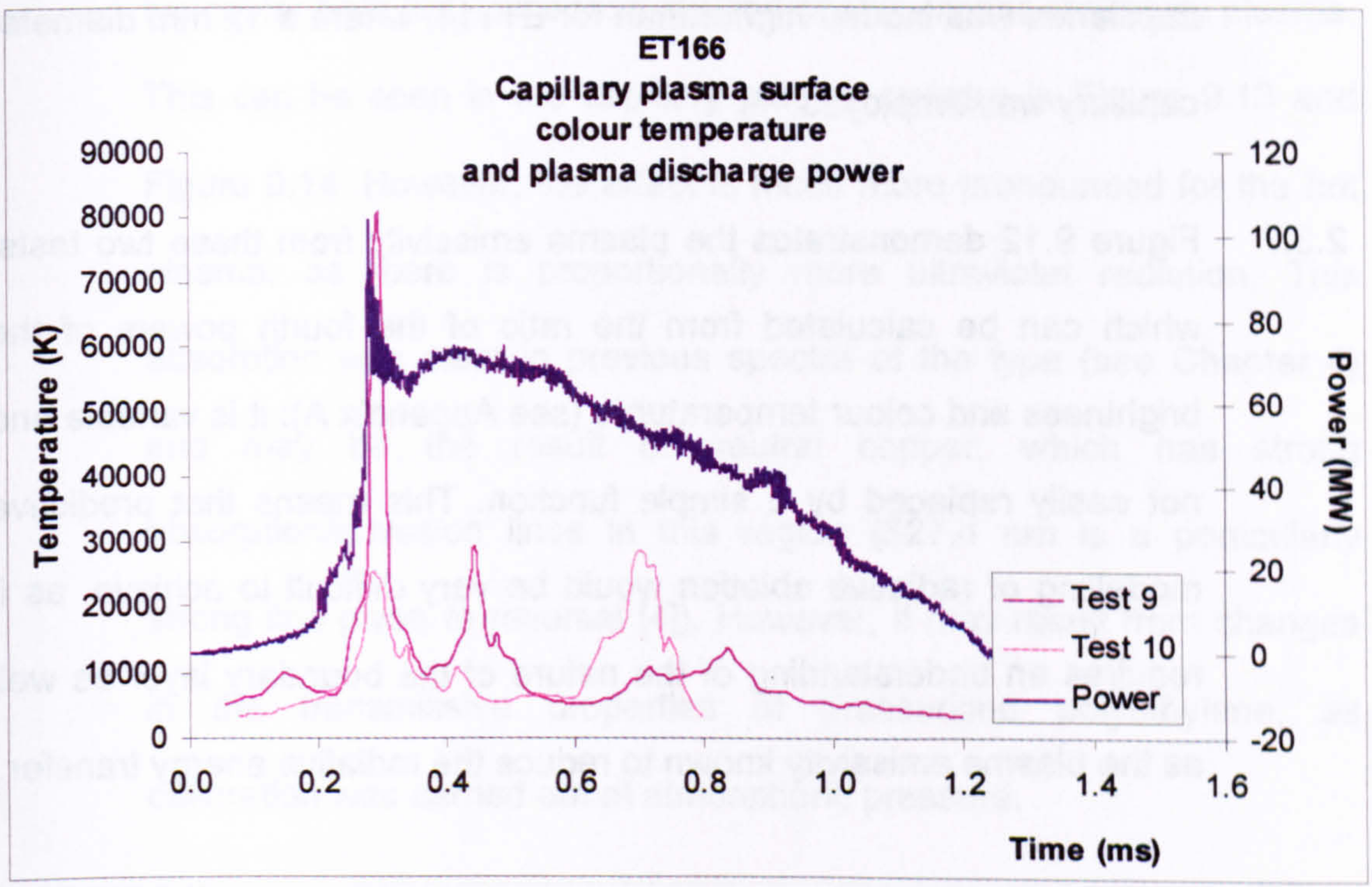

Figure 9.11 Capillary plasma surface colour temperature and plasma voltage

2.3.6 Possibly the condensed wire fragments impinged onto the polyethylene liner during the wire explosion, exposing it to the surrounding plasma discharge. Although this is speculation, x-radiographs of the wire fragments within a 12 mm diameter capillary (Figure 4.17, Chapter 4) clearly show this contact occurring, and inspection of the capillary liner after discharge often reveals lines scored into the liner from the hot wire. This effect may well become more important as the capillary diameter reduces. The test to test variability in electrical discharge parameters may be partially explained in this way. The discharge may become more sensitive to initial conditions at higher power density because of the interaction of the condensed fragments with the liner. The test to test variability for this experiment using 10 mm diameter

capillaries was indeed higher than for ET114, where a 12 mm diameter capillary was employed.

2.3.7 Figure 9.12 demonstrates the plasma emissivity from these two tests, which can be calculated from the ratio of the fourth powers of the brightness and colour temperatures (see Appendix A): it is variable and not easily replaced by a simple function. This means that predictive modelling of radiative ablation would be very difficult to achieve, as it requires an understanding of the nature of the boundary layer as well as the plasma emissivity known to reduce the radiative energy transfer.

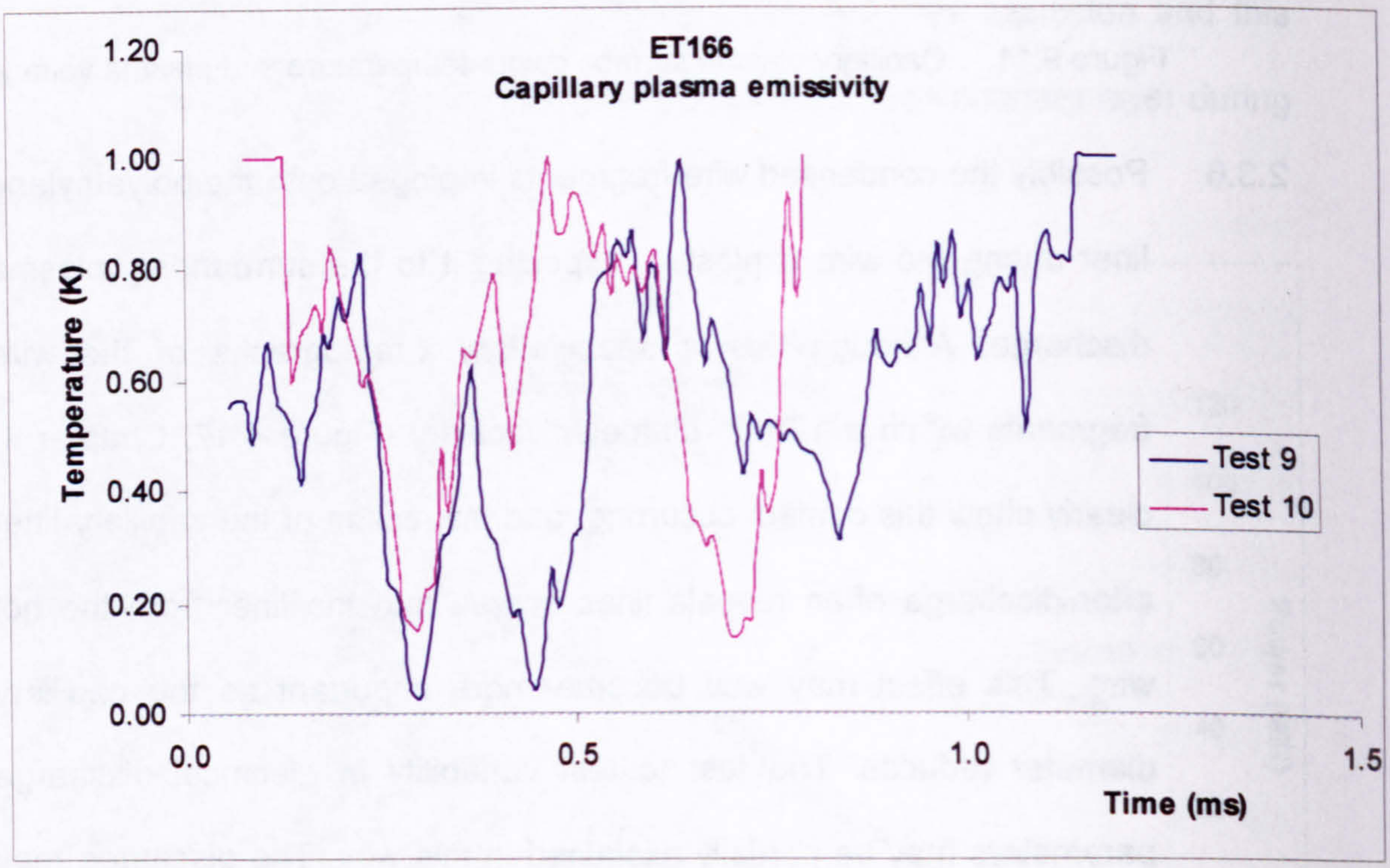

Figure 9.12 Capillary plasma emissivity

2.3.8 The plasma emissivity (in the wavelength range measured) seems to be dominated by absorption below around 500 nm, which appears

typical for both hot, low emissivity and cooler, higher emissivity plasma. This can be seen in the capillary plasma spectra in Figure 9.13 and Figure 9.14. However, the effect is much more pronounced for the hot plasma, as there is proportionally more ultraviolet radiation. This absorption was clear in previous spectra of the type (see Chapter 4) and may be the result of neutral copper, which has strong absorption/emission lines in this region (327.4 nm is a particularly strong line given to reversal [4]). However, it may result from changes in the transmissive properties of pressurised polyethylene, as calibration was carried out at atmospheric pressure.

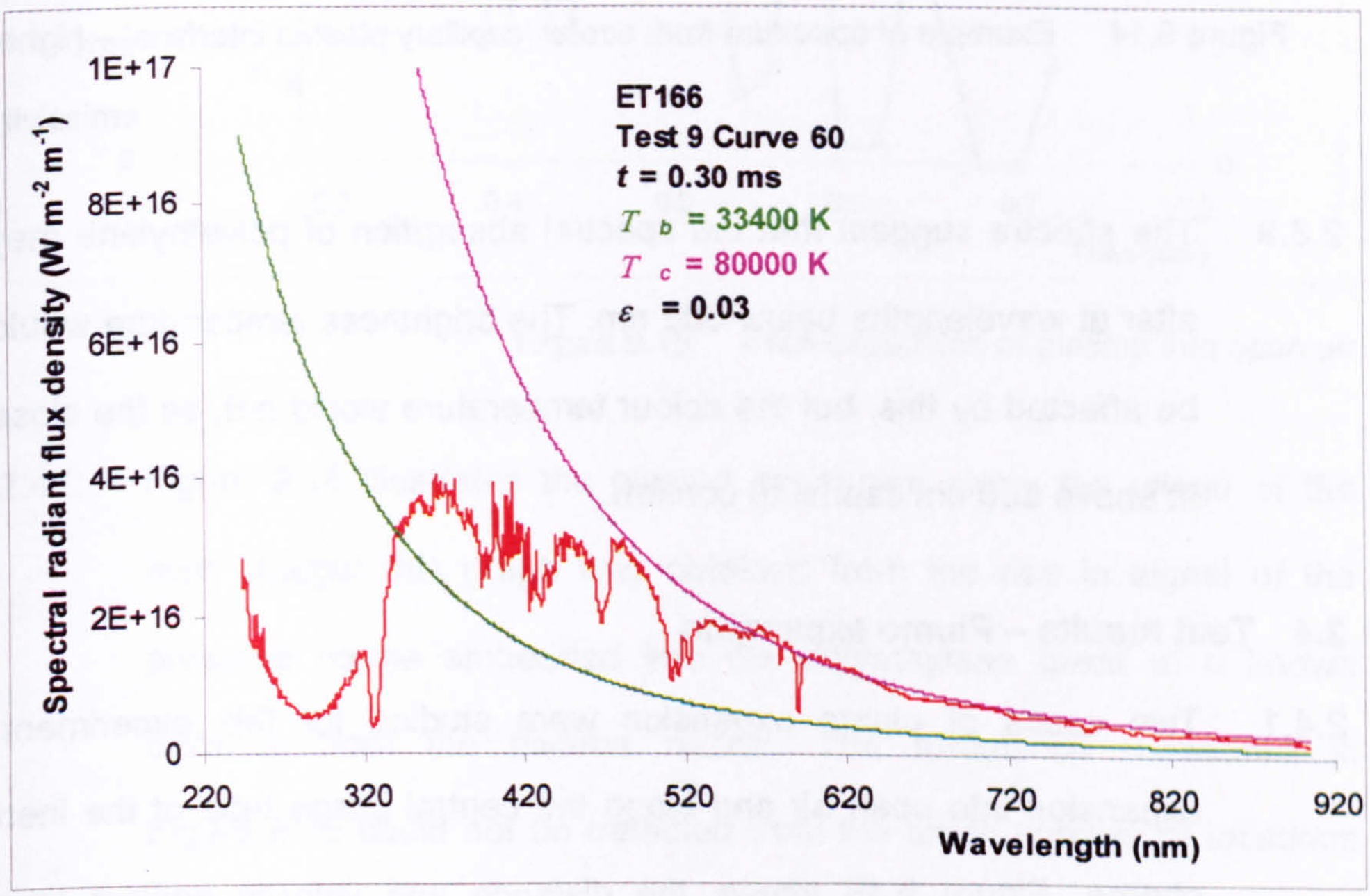

Figure 9.13 Example of spectrum from hot 'capillary plasma interface' – low emissivity

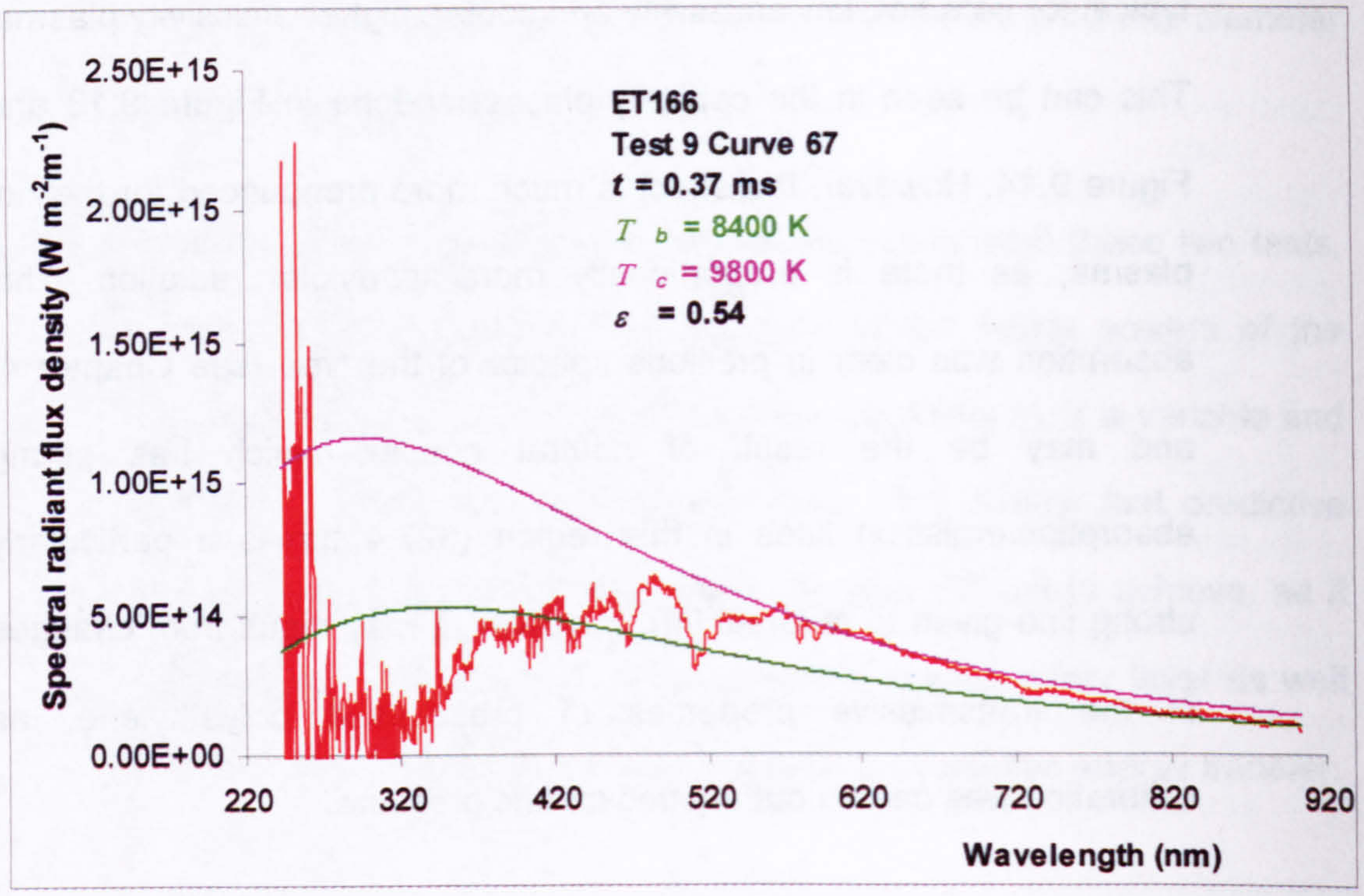

Figure 9.14 Example of spectrum from cooler 'capillary plasma interface' – higher emissivity

2.3.9 The spectra suggest that the spectral absorption of polyethylene may alter at wavelengths below 500 nm. The brightness temperature would be affected by this, but the colour temperature would not, as the close fit above 500 nm seems to confirm.

2.4 Test results – Plume expansion

2.4.1 Two cases of plume expansion were studied for this experiment: expansion into open air and along the central ullage tube of the inert charge. Figure 9.15 shows the distance and velocity against time curves for open air expansion in experiment ET166. The velocity was calculated by differentiation of the distance/time data and the results are similar to those from ET114 (see Chapter 5), especially regarding

the presence of turbulence. The initial velocity here is around 400 m s^{-1} faster than given by the ET114 experiment – to be expected with the higher power density in this case.

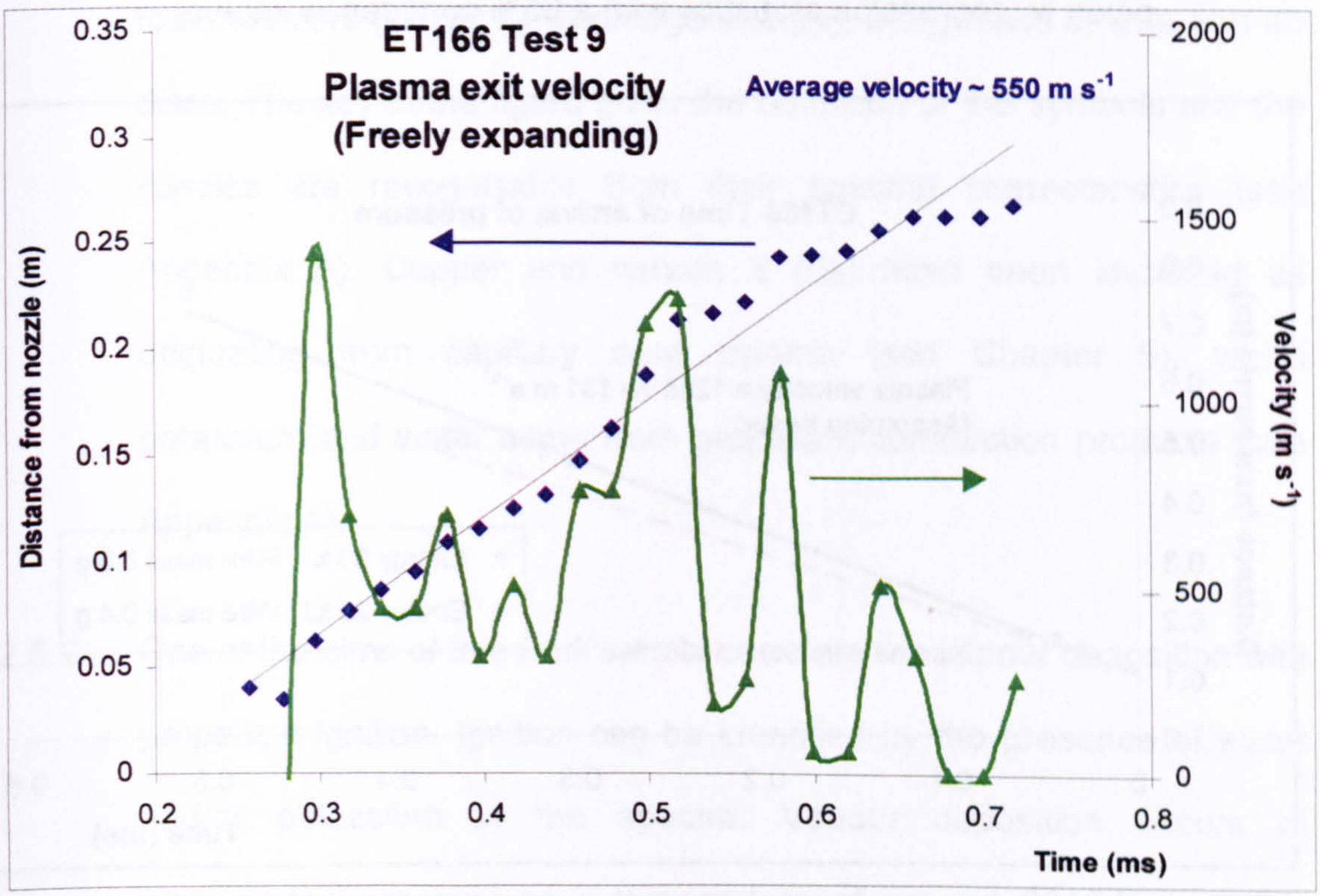

Figure 9.15 Free expansion of plasma into open air

2.4.2 Figure 9.16 illustrates the plasma expansion along the ullage of the inert charge: this graph was obtained from the rise in signal of the pressure gauge embedded into the polyethylene discs at a known distance from the plasma nozzle. The turbulence measured in Figure 9.15 could not be detected from the small number of locations studied, so an average velocity was determined: in the open air tests, this average was found to be around 550 m s^{-1}. In the case of confined expansion, the expansion rate was enhanced to around 1200 m s^{-1}: this is to be expected, as the energy density for its confined counterpart

is far higher than for a free expansion. In Figure 9.16 an error of ± 0.5 mm was assumed in each disc thickness (due to the removal of some material from them during cleaning), and the error in velocity was given by regression statistics with a 95% confidence interval.

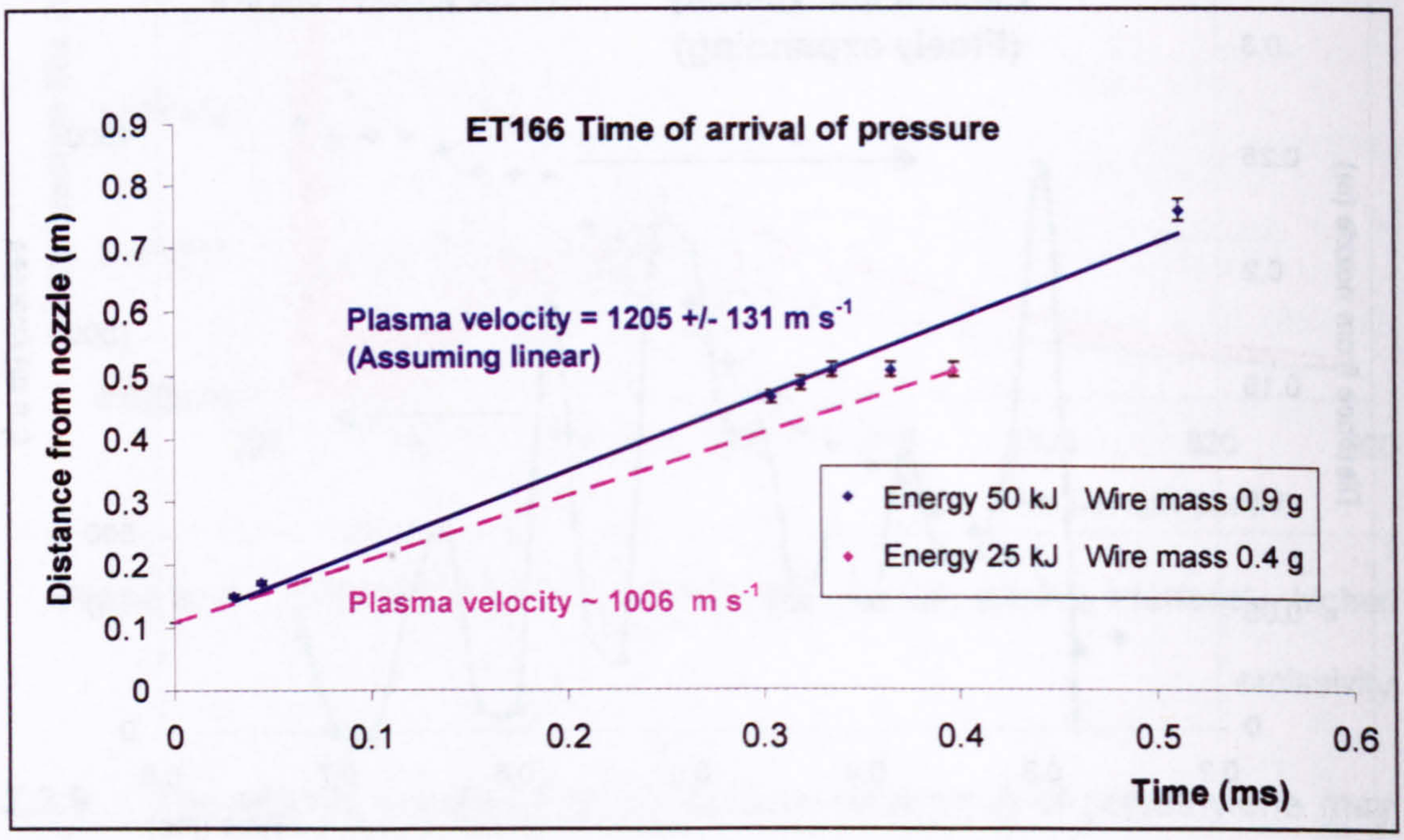

Figure 9.16 Constrained expansion along ullage tube

2.4.3 The plasma would appear to originate from a location 0.1 m in front of the nozzle, which can be explained if the initial plasma velocity was greater than its average between around 0.15 m and 0.75 m. This is reasonable, as the plasma velocity in open air is subject to an extreme initial deceleration. Test 7 used half the wire mass and half the discharge energy of the other tests: the velocity for Test 7 was 200 m s^{-1} slower than in the other tests, and is shown in Figure 9.16. The same initial velocity was assumed as in all other tests and so the same ordinate intercept was used for the linear average.

2.5 Test results – Local pressure and temperature

2.5.1 Figure 9.17 illustrates the local pressure and temperature at the disc face for certain locations along the charge, with the test set-up using four inductors (i.e. 50 kJ discharge energy), 0.9 g mass of wire and 43 discs. The key in the figure gives the definition of the symbols and the species are recognisable from their spectral characteristics (see Appendix A). Copper and carbon 2 (C_2) have been identified as originating from capillary core plasma (see Chapter 6), whilst potassium and water come from propellant combustion products (see Appendix A).

2.5.2 One of the aims of this work was to correlate the vapour deposition with propellant ignition. Ignition can be identified by the presence of water and/or potassium in the spectra. Vapour deposition occurs at atmospheric pressure at a temperature of around 2840 K, and this temperature is indicated in the figure by a dashed horizontal line. The experimental temperatures in Figure 9.17 are the brightness temperatures, but for all cases of temperature below around 4500 K, the brightness and colour temperatures are very similar and the brightness temperature can be taken as synonymous with the thermodynamic temperature below this value. It is then clear that ignition occurs when the plasma/vapour temperature reaches that of copper vapour.

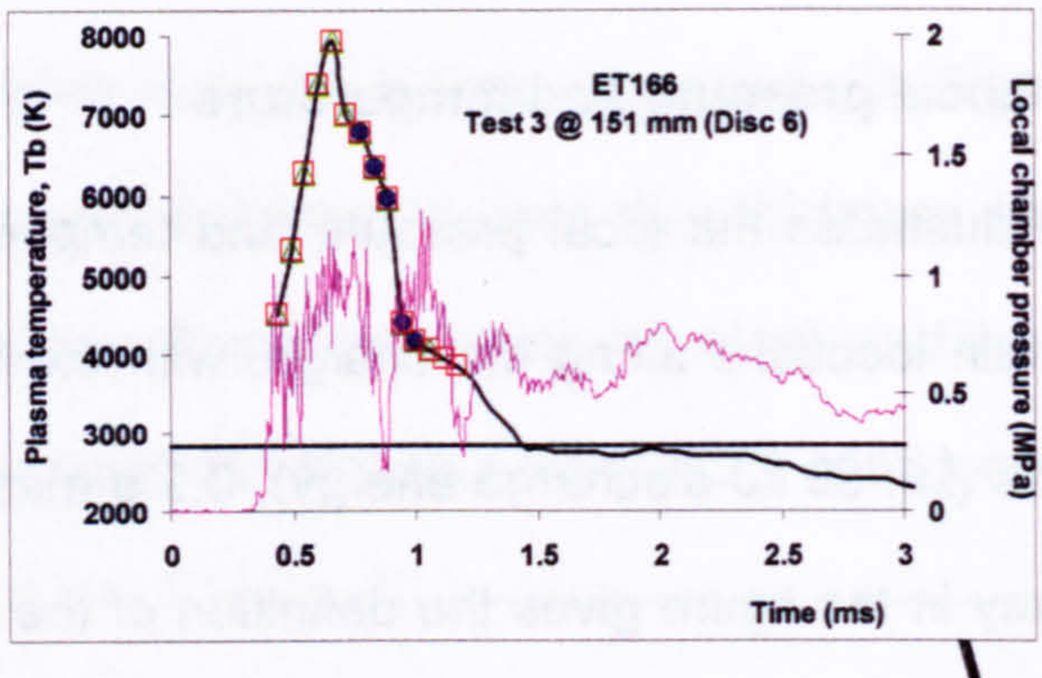

Species:
Copper
Potassium
Carbon 2 (C_2)
Water

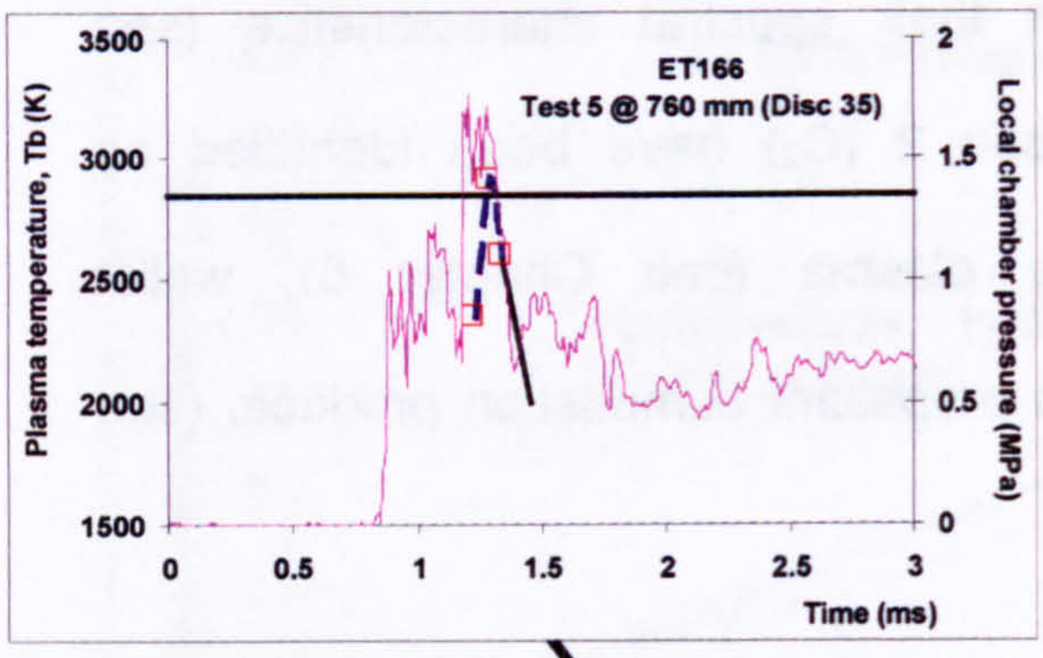

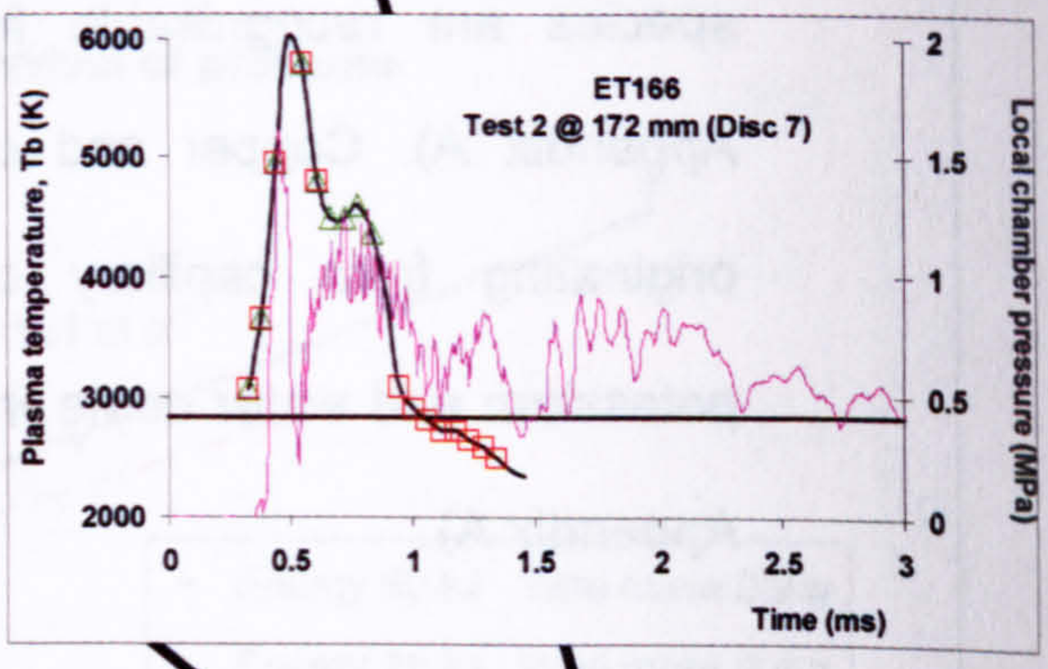

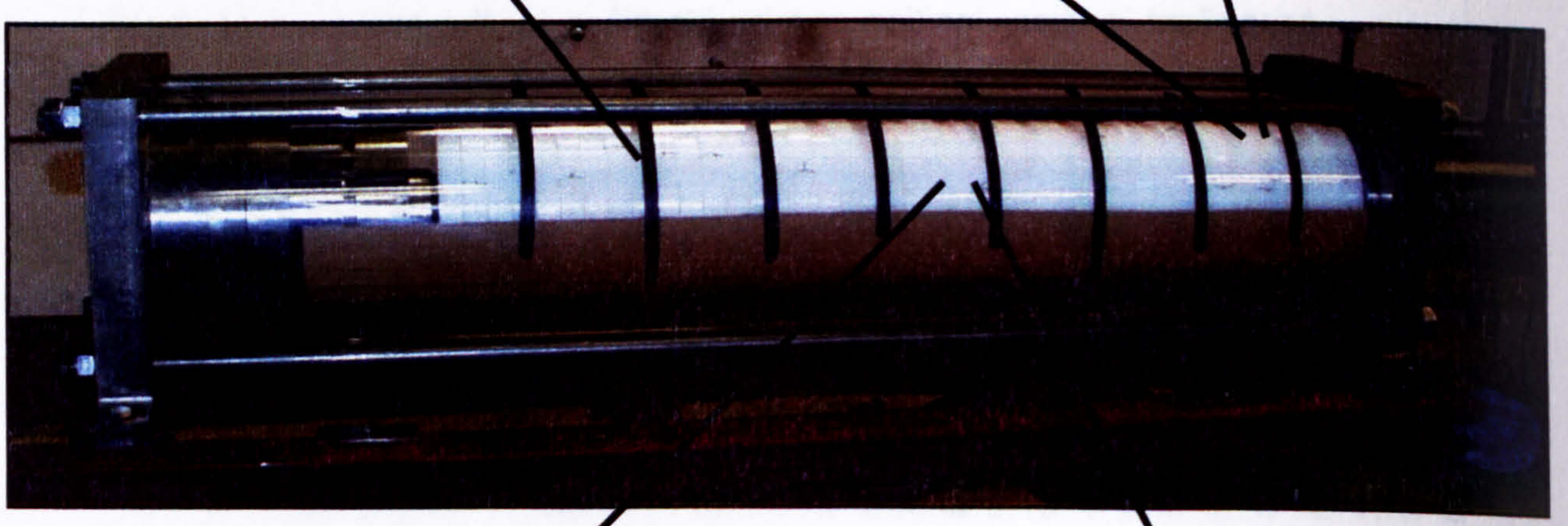

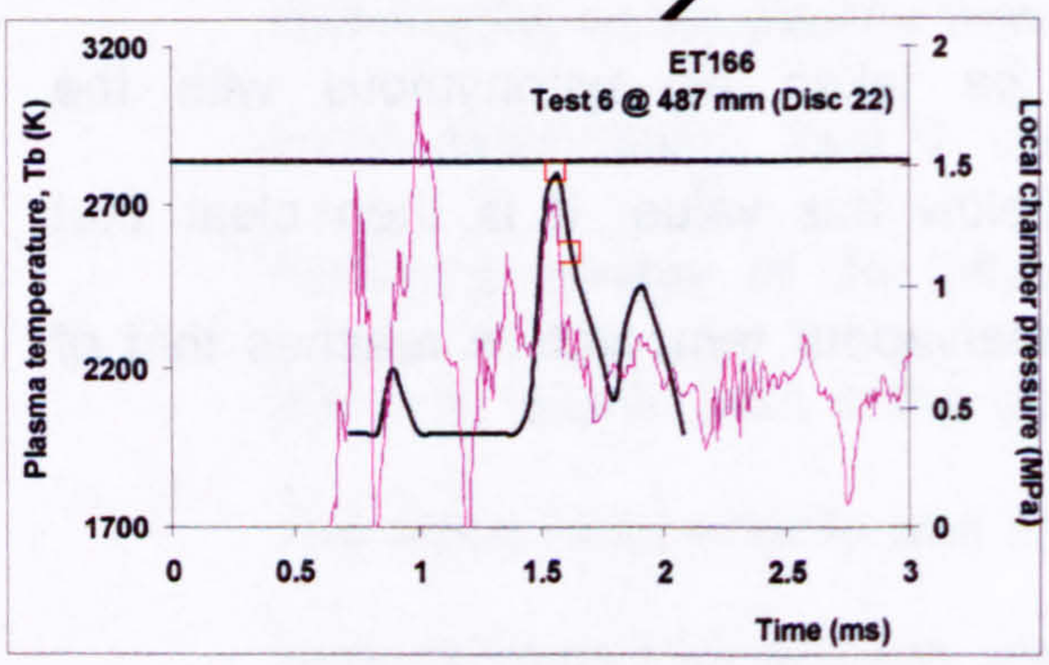

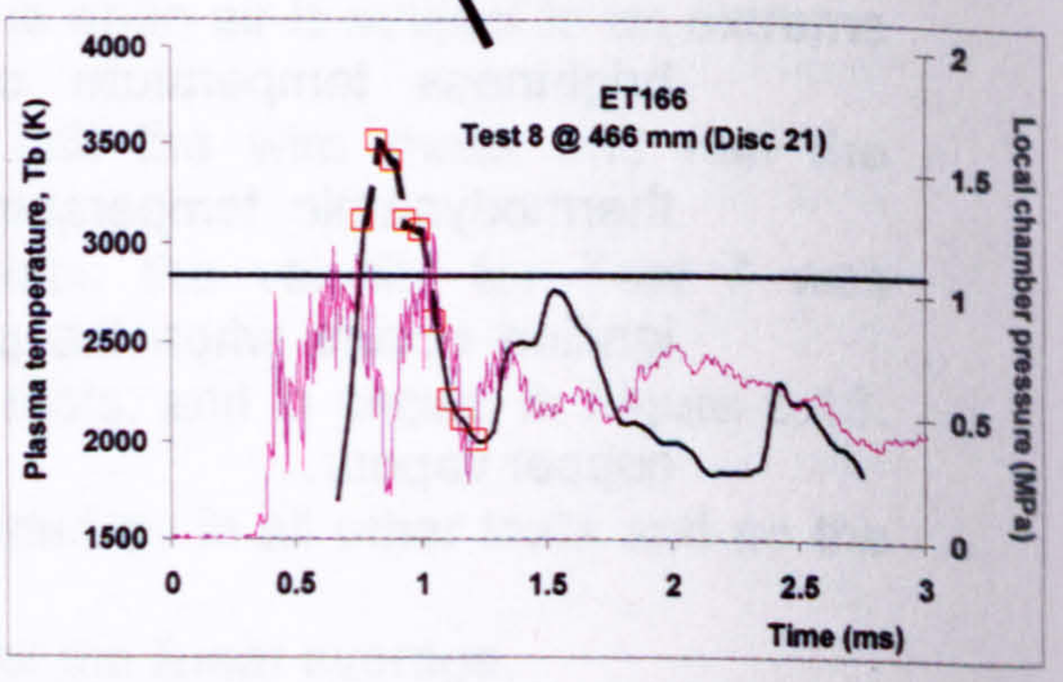

Figure 9.17 Local pressure and temperature for the 'standard' test set-up

2.5.3 For tests closest to the plasma generator (Tests 2 & 3), clear indication of ignition can be observed in the first spectrum. In the centre of the charge (Tests 6 & 8) ignition occurs as the temperature reaches that of boiling copper and not before. With the test farthest from the plasma generator, the spectrum obtained immediately prior to reaching the temperature of copper vapour shows a very weak sign of potassium. However, there is an error in this means of obtaining one spectrum, as the acquisition and thus the temperature are integrated over the exposure time (0.0565 ms for these tests). If the temperature rises and ignition characteristics become pronounced at the end of that time-period, a low temperature and a weak ignition signal may well be recorded.

2.5.4 This interpretation would imply that the start of vapour deposition and combustion was virtually instantaneous. An alternative explanation that ignition occurred due to *droplets* of molten copper from an aerosol might require ignition before vapour temperature was achieved (in Tests 6 & 8): there was an aerosol present prior to the vapour and ignition characteristics.

2.5.5 Small cylinders of propellant were used as 'windows' for these tests: each had a mass of around 1.3 g. These windows were found in place after the test and an example of one such post test propellant window appears in Figure 9.18 – it was from Disc 6 from Test 3.

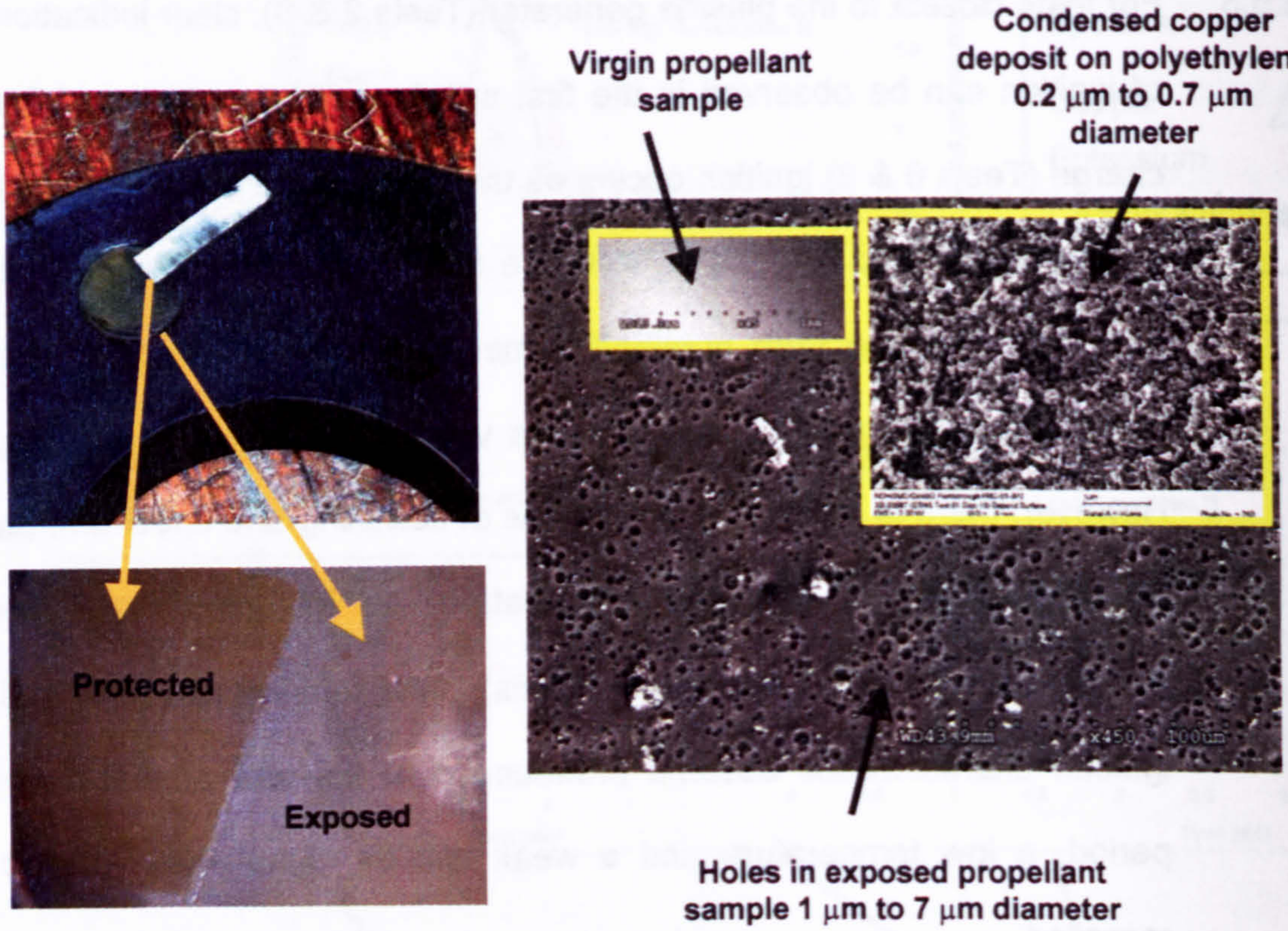

Figure 9.18 Disc with propellant 'window' after the test (top left); propellant after the test with tape removed (bottom left); SEM of propellant surface post-test, plus virgin sample (left inset) with post-test polyethylene disc (right inset)

2.5.6 It was assumed prior to the experiment that the propellant would ignite and combust completely if the deposition exceeded a given thickness, so the aim was to correlate deposition thickness with ignition. The first test was intended to measure the deposit thickness as a function of distance along the chamber. However, the plan to correlate thickness with ignition of propellant was ill-conceived for two reasons. Firstly, the deposition was found to vary: from Figure 9.19 it is clear that the coverage on individual discs was uneven. This unevenness was sharp enough for a clear demarcation to occur regularly across the propellant

sample. Secondly, the propellant failed to combust to completion and so a clear 'go no-go' ignition definition was not possible.

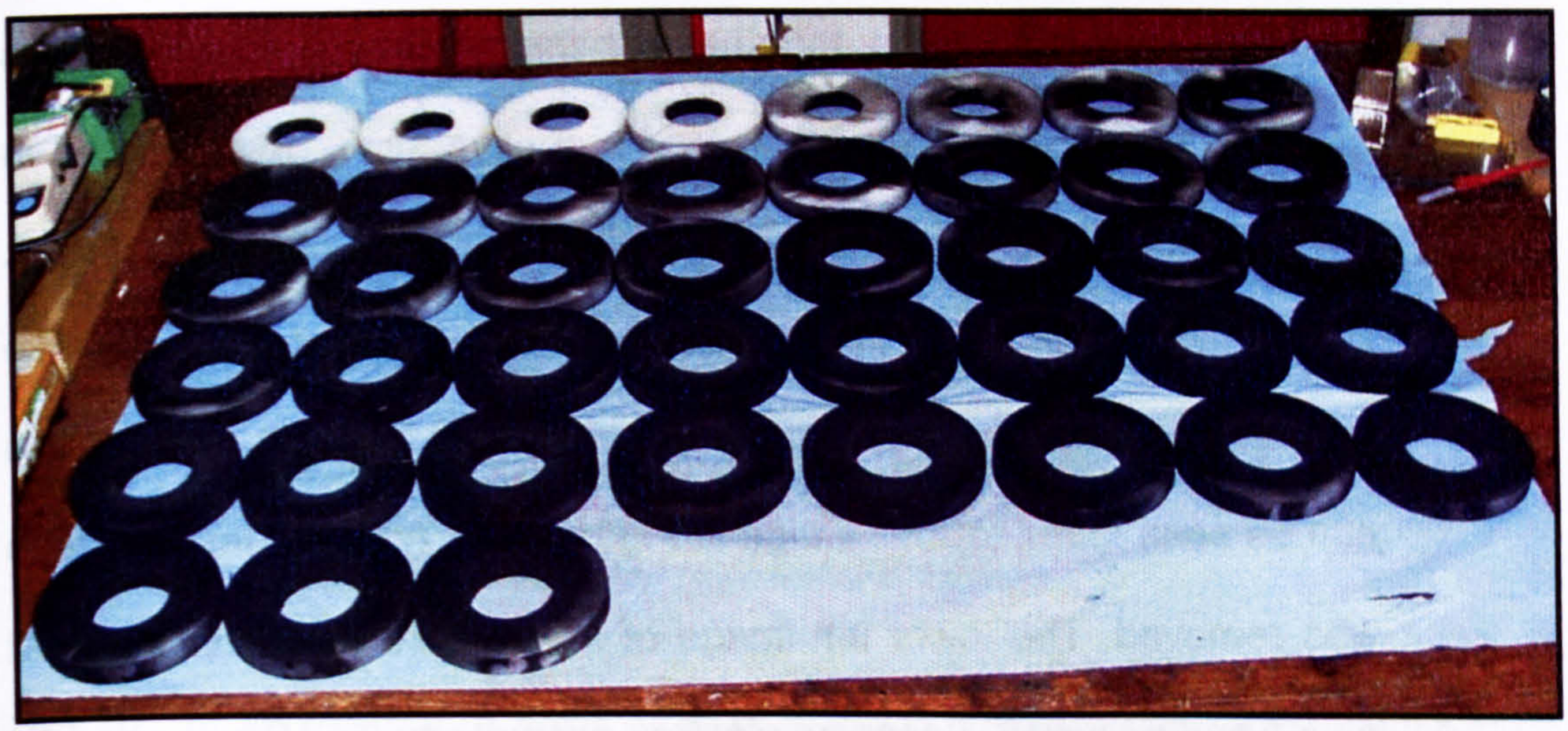

Figure 9.19 Discs from ET166 Test 1 on display after the test (Disc 1, closest to the CPG, is in the foreground on the right; discs then run numerically from right to left)

2.5.7 It is believed the amount of propellant was too small to permit self-sustained combustion. That combustion products were so clearly seen in the spectra was a strong indication of the start of combustion, although not conclusive proof that this would have been sustained given more propellant. Combustion products could well have been liberated all the time an ignition energy flux was present. Once the flux was removed, however, the magnitude of the heat loss to the surroundings, together with the turbulence within the chamber removing reactants from the immediate vicinity of the propellant grain, prevented sufficient flux linkage with the propellant from its own

combustion reactions for combustion to be sustained. Hence, combustion ceased.

2.5.8 Evidence for this scenario, together with the spectroscopic evidence, is provided by inspecting the recovered propellant grain. It was noted in the first propellant test (Test 2) that the recovered grain was pitted. Hence, from Test 3 and in all subsequent tests a small piece of white masking tape was used to protect the propellant from the plasma: this can be seen in the top left image in Figure 9.18. After the test this tape was removed. The lower left image of Figure 9.18 clearly shows that pitting had occurred. Scanning electron microscopy (SEM) was used [5] to examine the surface of the propellant, and it was discovered that these pits, in the right-hand image of Figure 9.18, were around 1 - 7 μm in diameter. Virgin propellant from beneath the tape showed no such pitting, as can be seen in the left hand inset of the right hand image in Figure 9.18.

2.5.9 A scattering of small globules of solidified copper several tens of micrometers in diameter were seen on the exposed propellant surface – illustrated in the right hand image of Figure 9.18. These globules appeared to make no significant difference to the propellant surface. Crystals of condensed copper 0.2 – 0.7 μm in diameter were very evident on the polyethylene disc immediately next to the propellant (these crystals can be seen in the right hand inset in the right-hand image of Figure 9.18). However, no trace of copper crystals was visible

on the exposed surface of the recovered propellant. The interpretation for this was that the propellant combustion gases venting from the surface scrubbed away the condensed copper vapour deposit, but the globules were too heavy or arrived later. In the scenario described here, the copper condensed in a dense drop-wise fashion, creating individual ignition sites that would ordinarily grow together to form a linear burning front. However, this process stops without continued flux linkage to the combustion surface, leaving pits around ten times the diameter of the original crystal condensate.

2.5.10 In an attempt to force ignition to occur, Test 8 introduced significantly more propellant into the chamber. Care had to be exercised not to be too generous with the mass used, as the acrylic vessels were very costly, and it was planned to drill holes and prepare for instrumentation in only one of them. For this test the translucent propellant window had a reduced thickness of 2 mm, with a mass of 0.8 g. A further 6.5 g of standard (opaque) cord propellant was glued into a slot specially bored into the facing disc. This is shown in the left-hand photograph of Figure 9.20; the pressure gauge can be seen in the top of the disc. The discs were loaded so that the spectrograph could record emitted light from the combusting cord propellant, but even with this mass of propellant neither the translucent nor the cord propellant ignited. The right-hand photograph of Figure 9.20 illustrates the propellant after the test.

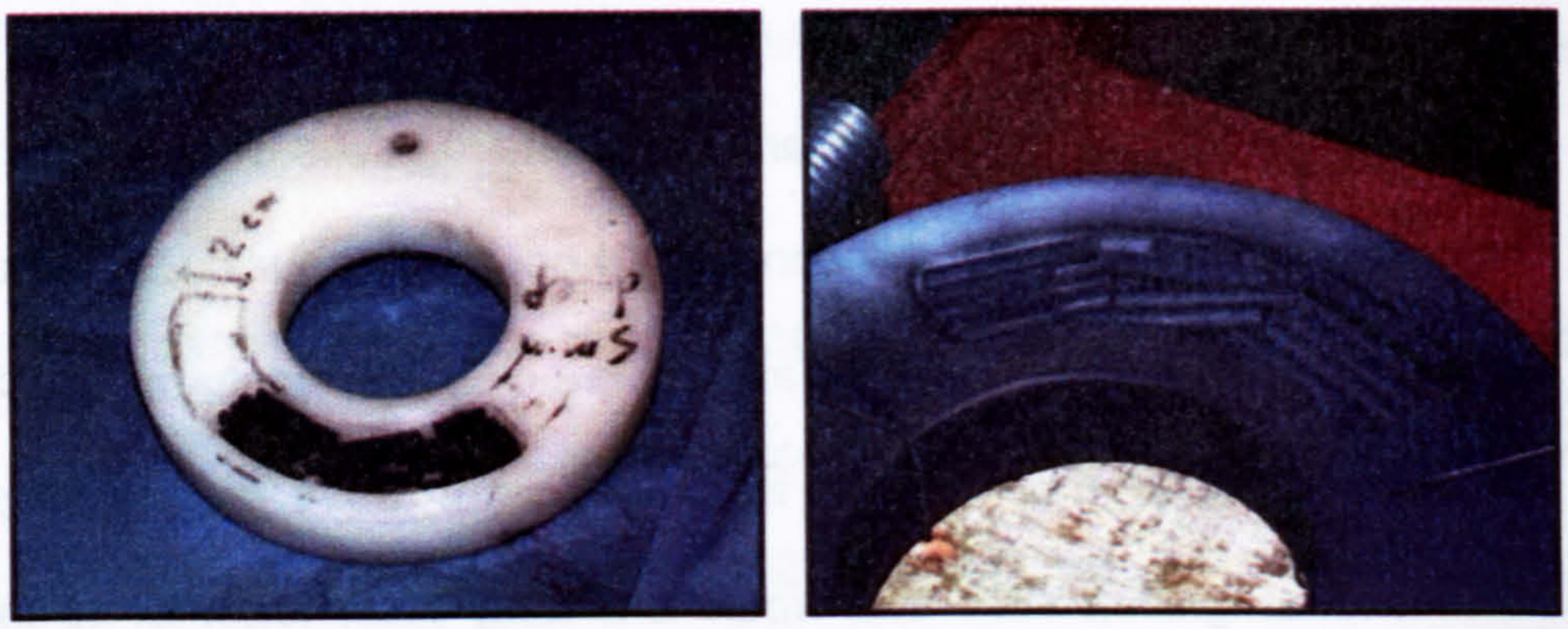

Figure 9.20 ET166 Test 8 Standard propellant in polyethylene disc (left) prior to and (right) after the test

2.5.11 The spectra from the combustion products were very strong, an example appears in Figure 9.21. No further increase in charge mass was attempted, since it was feared that the cylinder might explode upon propellant ignition.

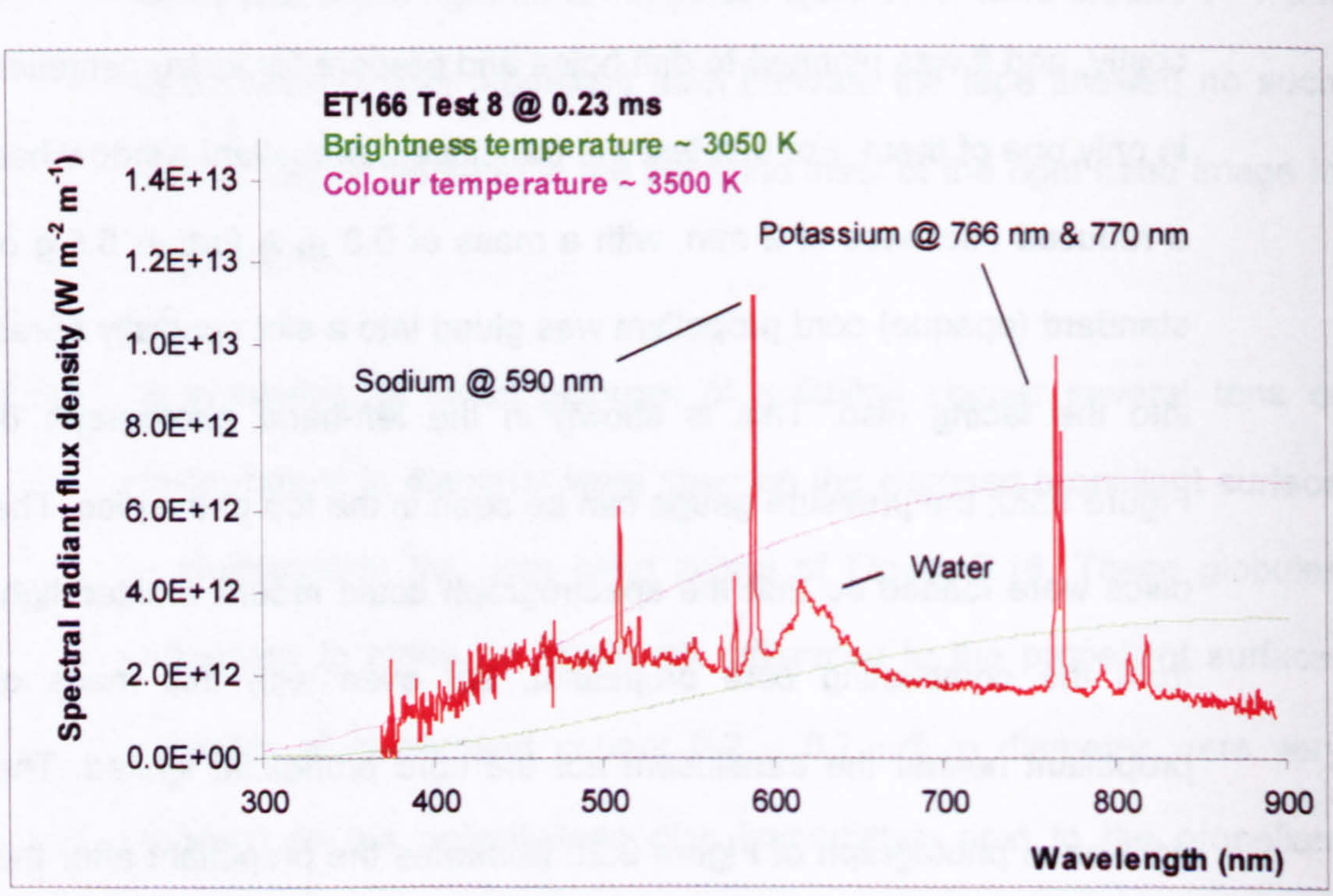

Figure 9.21 Spectrum with potassium, sodium and water from combustion of propellant in Test 8

2.6 Test results – Ullage plasma temperature

2.6.1 Four tests were included in the experiment to measure the temperature of the plasma as it expanded down the axis of the chamber. Previous tests with a freely expanding plume (see Chapter 5) found the hottest plasma to be at the plume expansion front. Tests 12 and 13 used 43 polyethylene discs (i.e. a fully loaded chamber) whilst Tests 14 and 15 used only seven discs at the far end of the chamber from the CPG. This gave a 710 mm length of empty chamber in which the plasma could expand. Two co-planar pressure gauges were included in the face of the disc closest to the CPG for Tests 14 and 15: the idea in these two tests was to provide validating data for EDEN-IB for an empty chamber scenario. This would then provide a full suite of data of increasing complexity: for free expansion into the open air; for expansion into an empty vessel and finally expansion into a loaded vessel. Figure 9.22 shows the arrangement for Tests 14 and 15; that for Tests 12 and 13 was similar apart from the number of discs. Light from the plasma parallel to the chamber axis was collected and recorded in these tests by the inclusion of an acrylic window in the end plate farthest from the CPG. A collimating mirror focussed the light into the spectrograph optical fibre. The spectrograph was calibrated absolutely in the manner described in Appendix A.

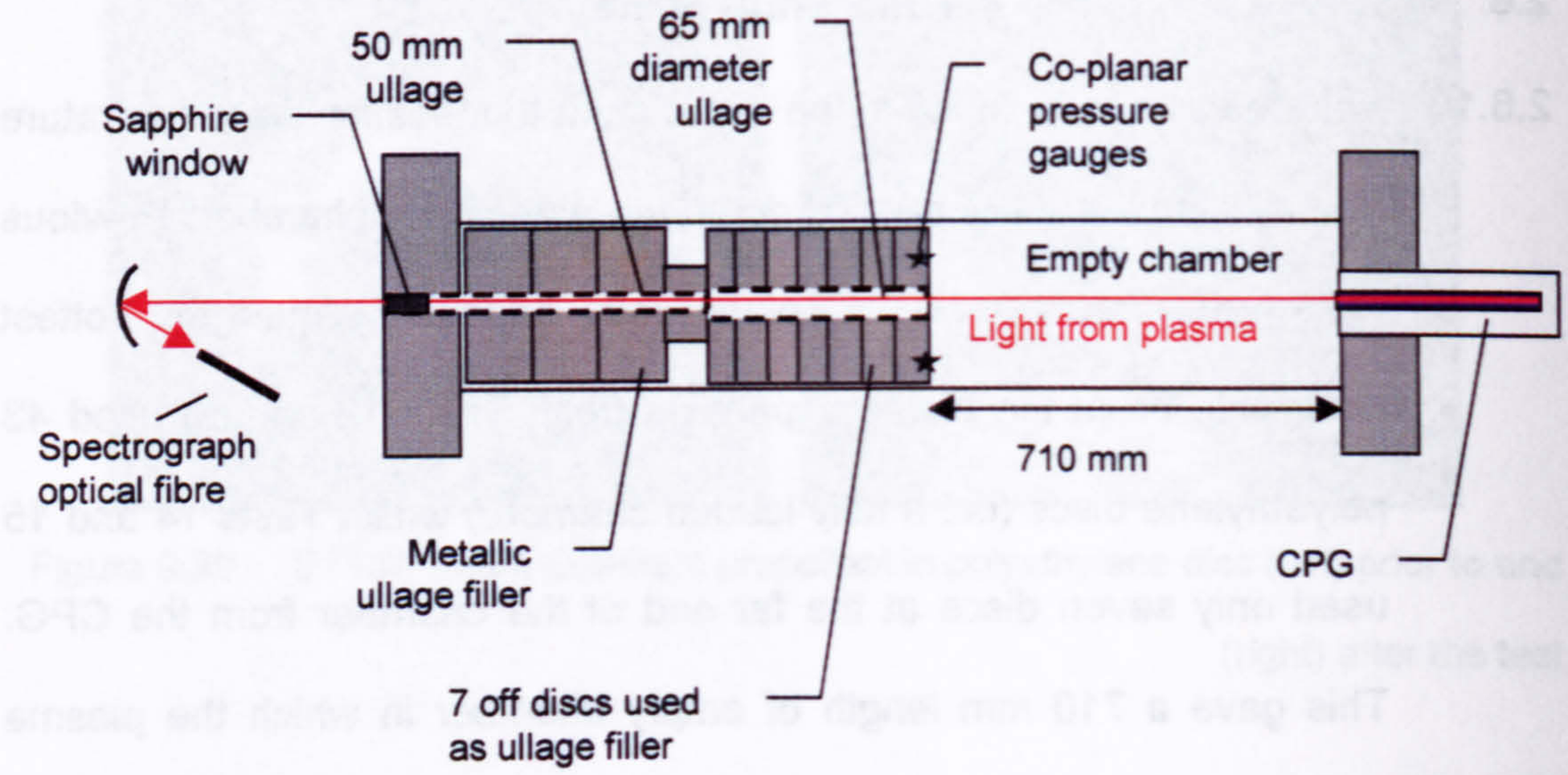

Figure 9.22 Experimental set-up for Test 14 and 15

2.6.2 Figure 9.23, Figure 9.24 and Figure 9.25 show the plasma brightness temperature, colour temperature and emissivity of the expanding plume plotted against time for both the loaded and empty chambers. Figure 9.26, Figure 9.27 and Figure 9.28, however, illustrate the plasma brightness temperature, colour temperature and emissivity of the expanding plasma plotted against distance for the loaded chamber only. The plots of distance could not be provided for the empty chamber, as the expansion rate here was unknown. Comparison of these graphs indicates that the plasma expanding into an empty chamber is far more turbulent since the temperature plots are far noisier. Also, interestingly, the cooling rate is similar in both cases, at around 6300 K ms^{-1}. (This was estimated by fitting a straight line subjectively through the data in Figure 9.23 and calculating its gradient. The same process for the temperature-distance plot is shown in Figure 9.26: a spatial cooling of around 7000 K m^{-1} resulted.)

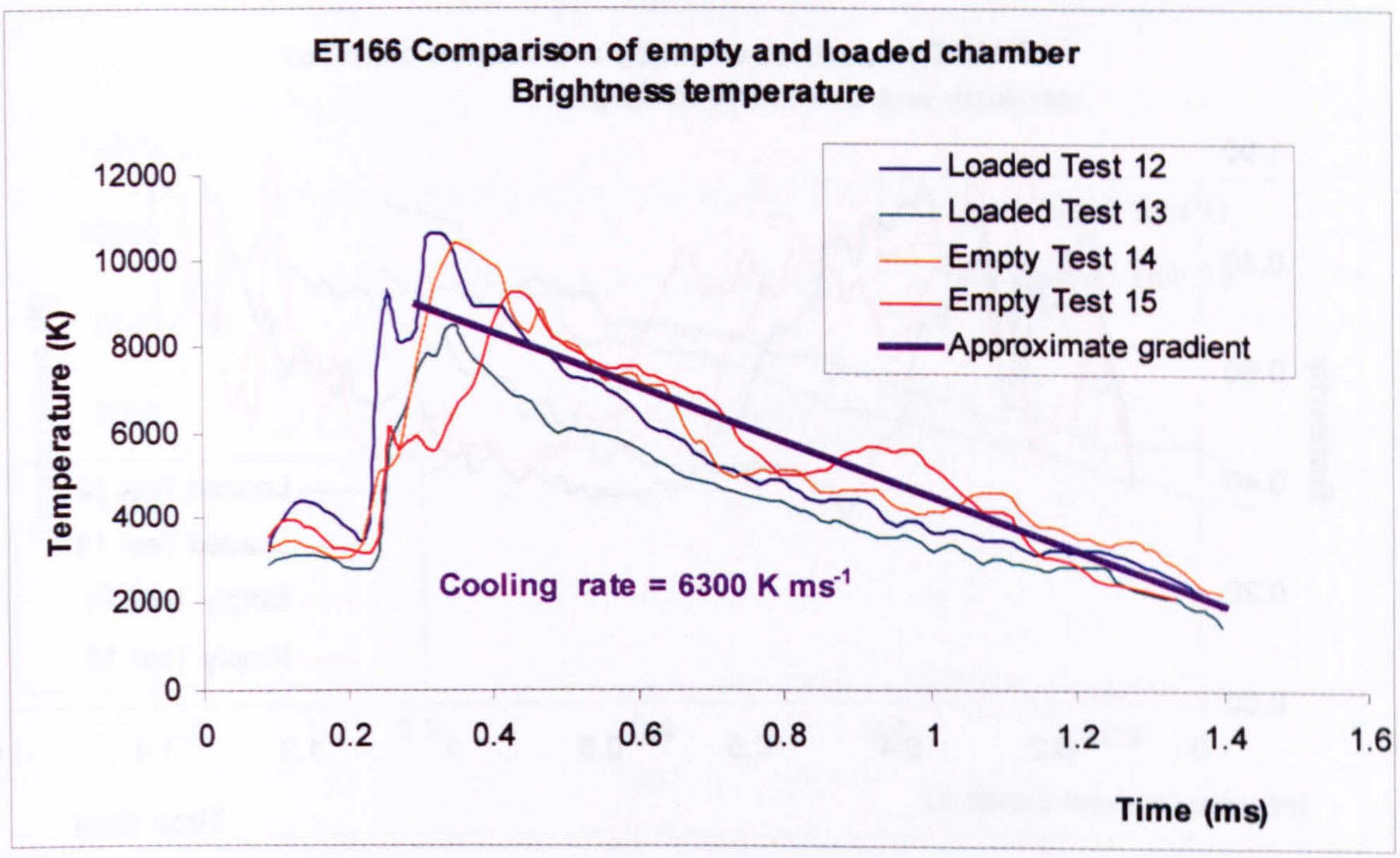

Figure 9.23 ET166 Empty and loaded chamber: brightness temperature and time

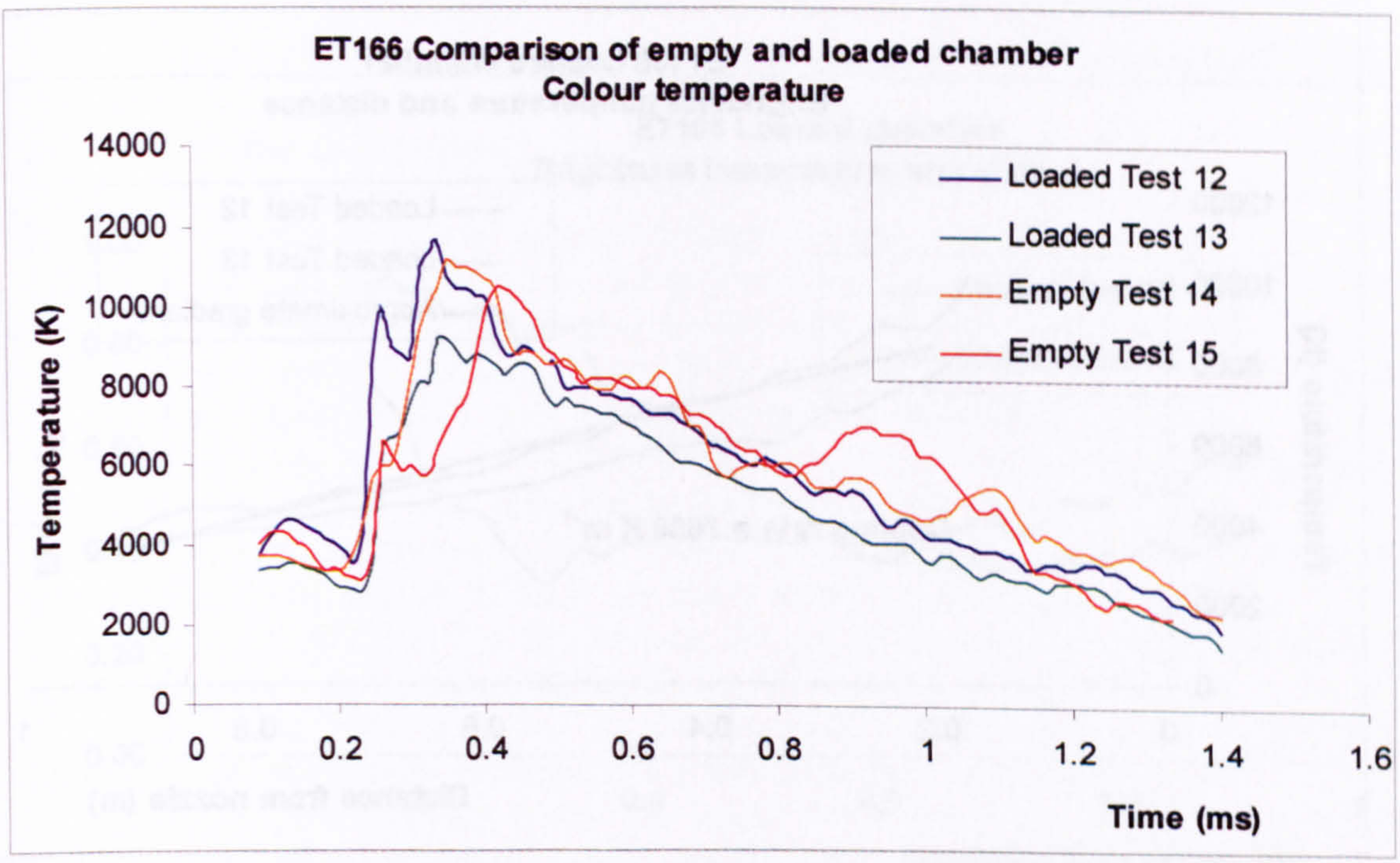

Figure 9.24 ET166 Empty and loaded chamber: colour temperature and time

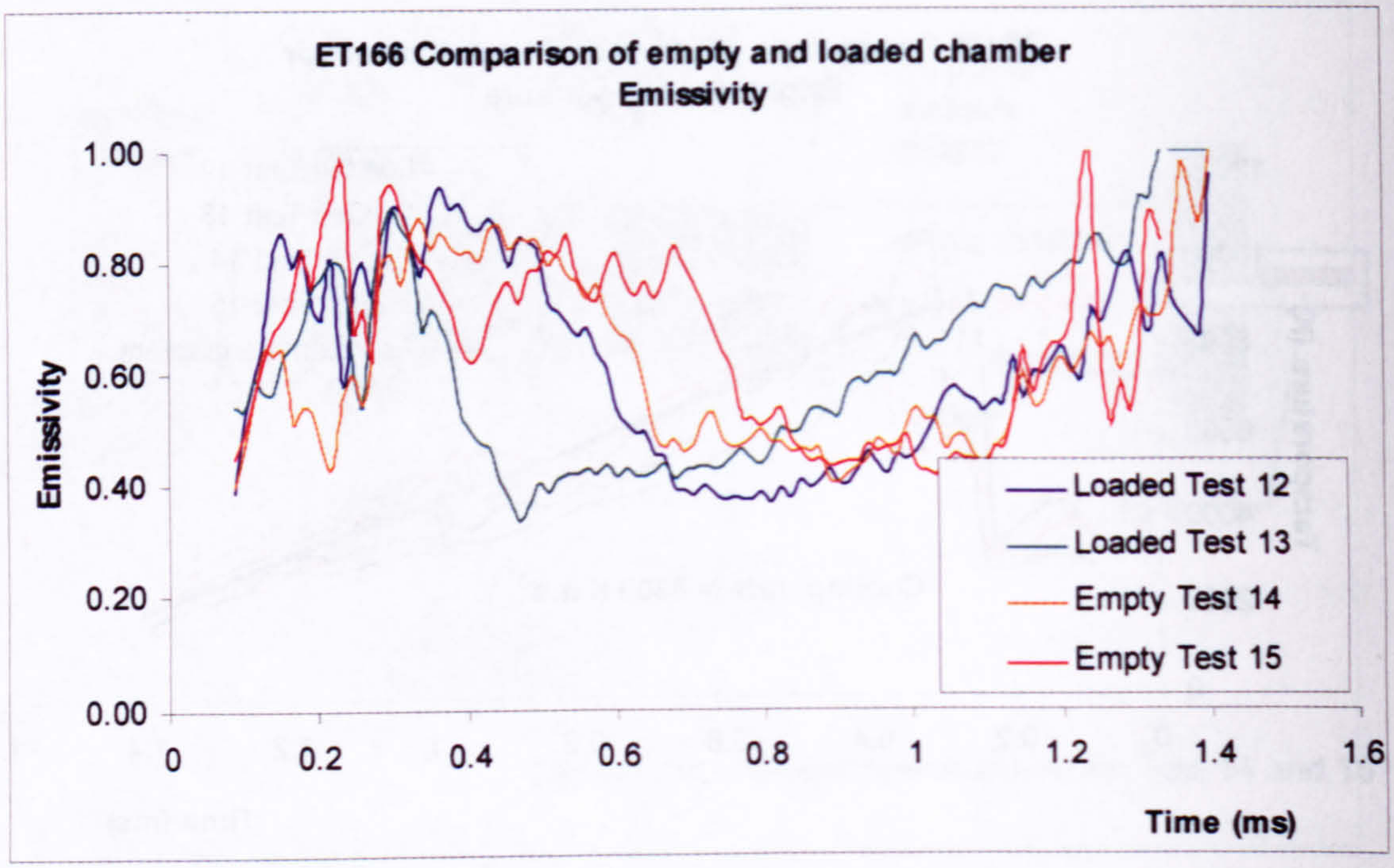

Figure 9.25 ET166 Empty and loaded chamber tests: emissivity and time

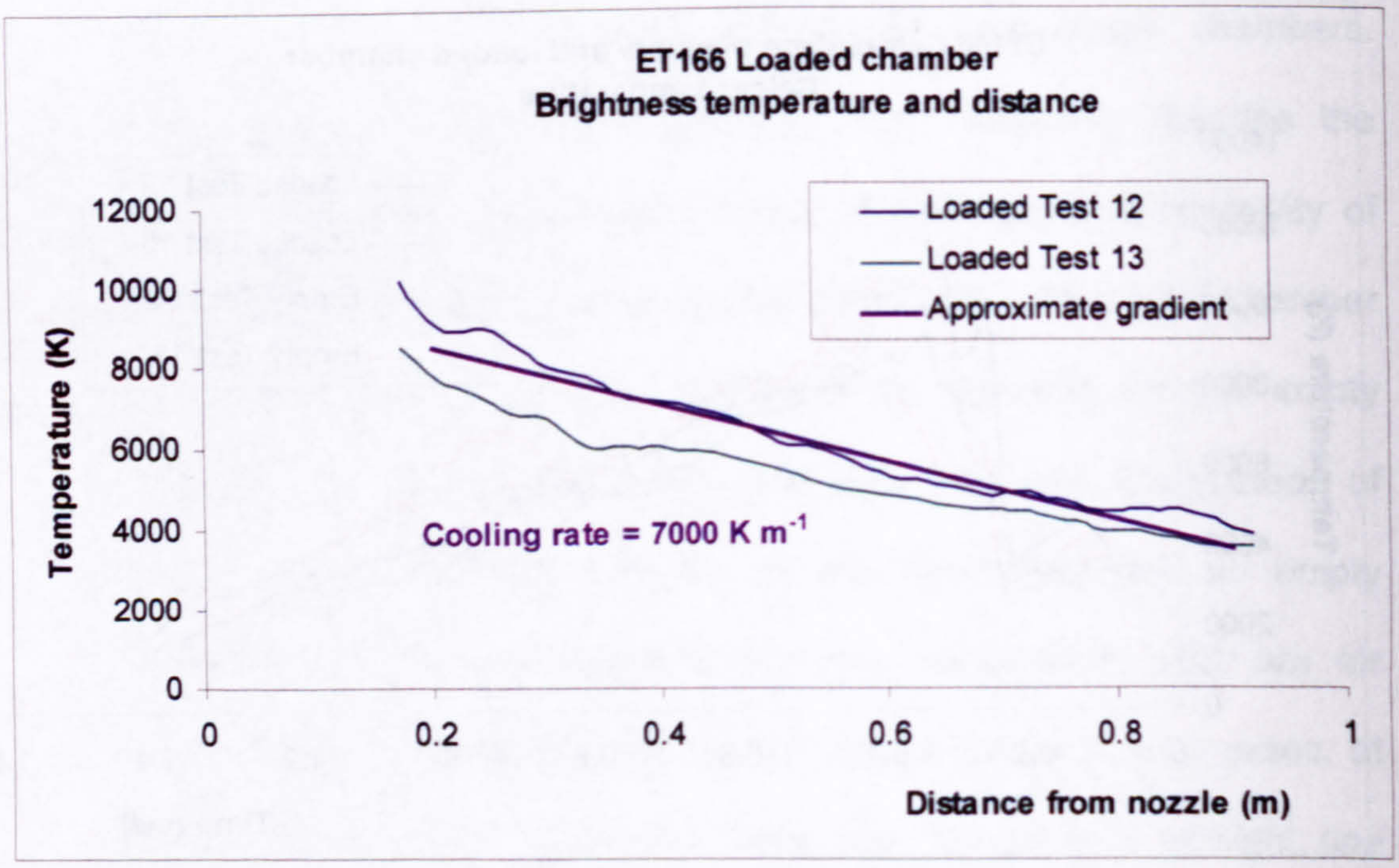

Figure 9.26 ET166 Loaded chamber tests: brightness temperature and distance from nozzle

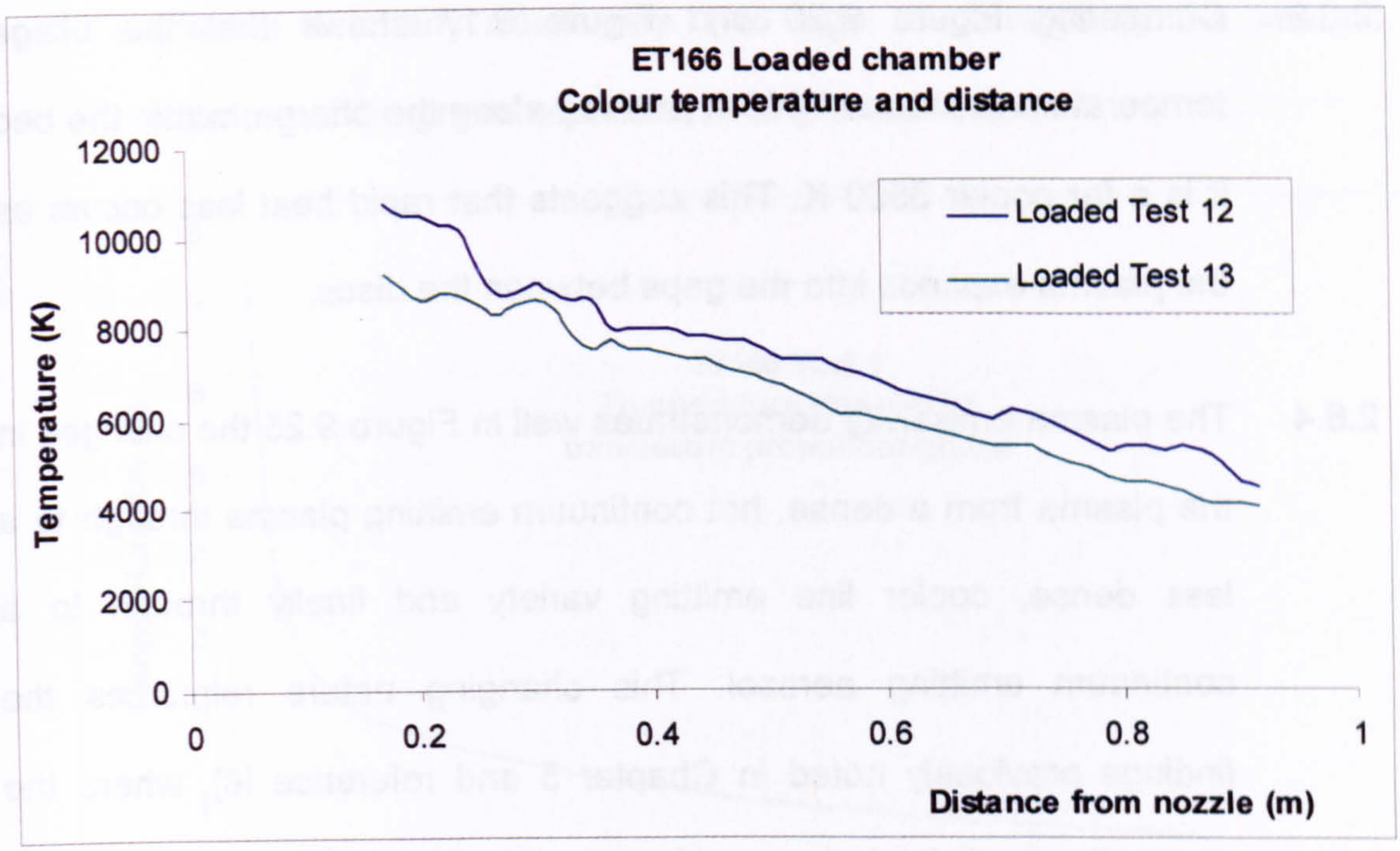

Figure 9.27 ET166 Loaded chamber tests: colour temperature and distance from nozzle

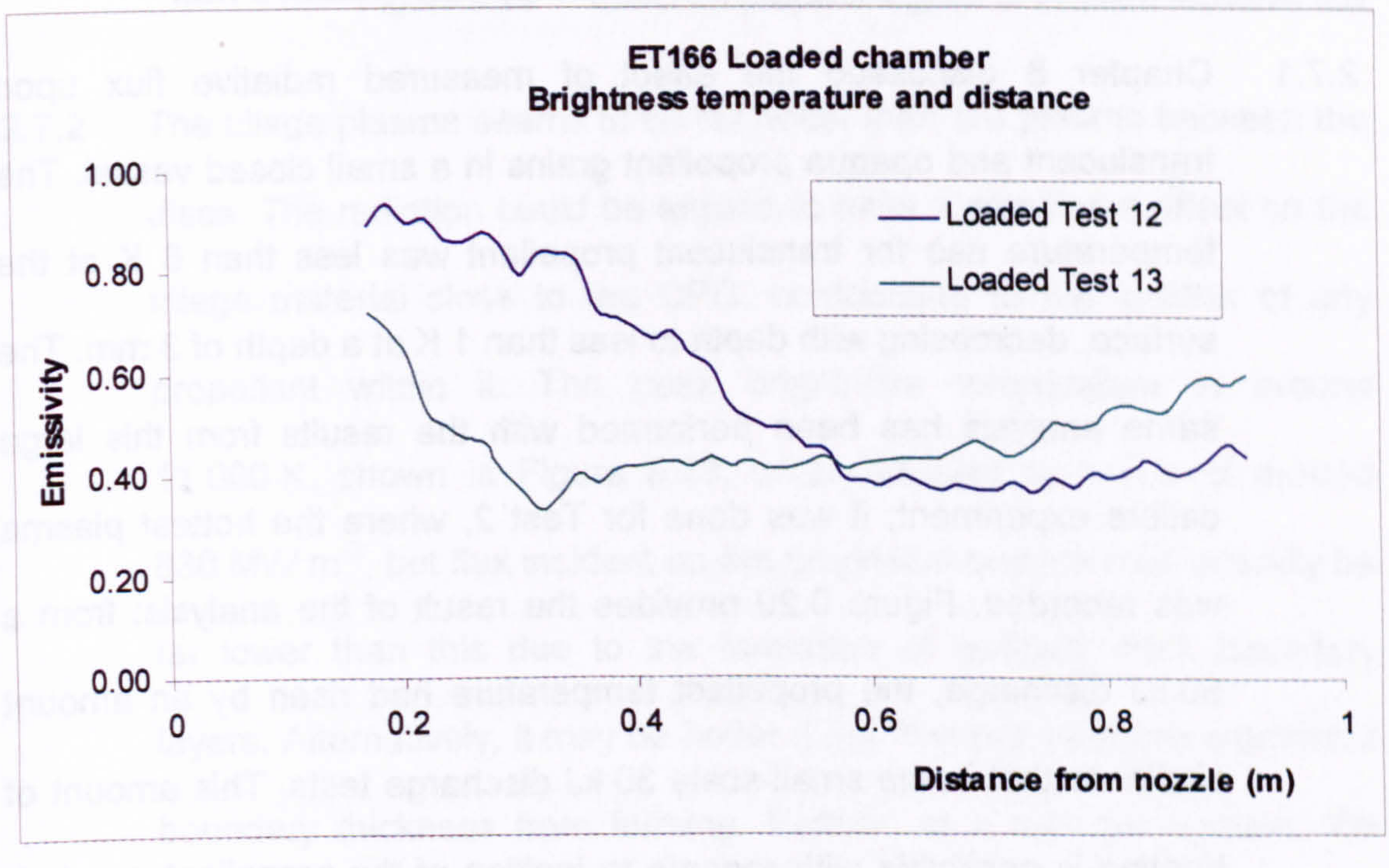

Figure 9.28 ET166 Loaded chamber tests: emissivity and distance from nozzle

2.6.3 Comparing Figure 9.26 and Figure 9.17 shows that the ullage temperature is around 7000 K midway along the charge; within the bed it is a far cooler 3500 K. This suggests that rapid heat loss occurs as the plasma expands into the gaps between the discs.

2.6.4 The plasma emissivity demonstrates well in Figure 9.25 the changes in the plasma from a dense, hot continuum emitting plasma through to a less dense, cooler line emitting variety and finally through to a continuum emitting aerosol. This changing nature reinforces the findings previously noted in Chapter 5 and reference [6], where the same three distinct types of emission from ETC plasma were discussed.

2.7 Temperature rise of propellant due to incident radiative flux

2.7.1 Chapter 8 discussed the effect of measured radiative flux upon translucent and opaque propellant grains in a small closed vessel. The temperature rise for translucent propellant was less than 6 K at the surface, decreasing with depth to less than 1 K at a depth of 3 mm. The same analysis has been performed with the results from this large calibre experiment; it was done for Test 2, where the hottest plasma was recorded. Figure 9.29 provides the result of the analysis: from a 50 kJ discharge, the propellant temperature had risen by an amount similar to that in the small-scale 30 kJ discharge tests. This amount of heating is negligible with regards to ignition of the propellant, nor is it

affected it in any other way. (No sign of damage to the internal structure of the grains was seen in any of the tests.)

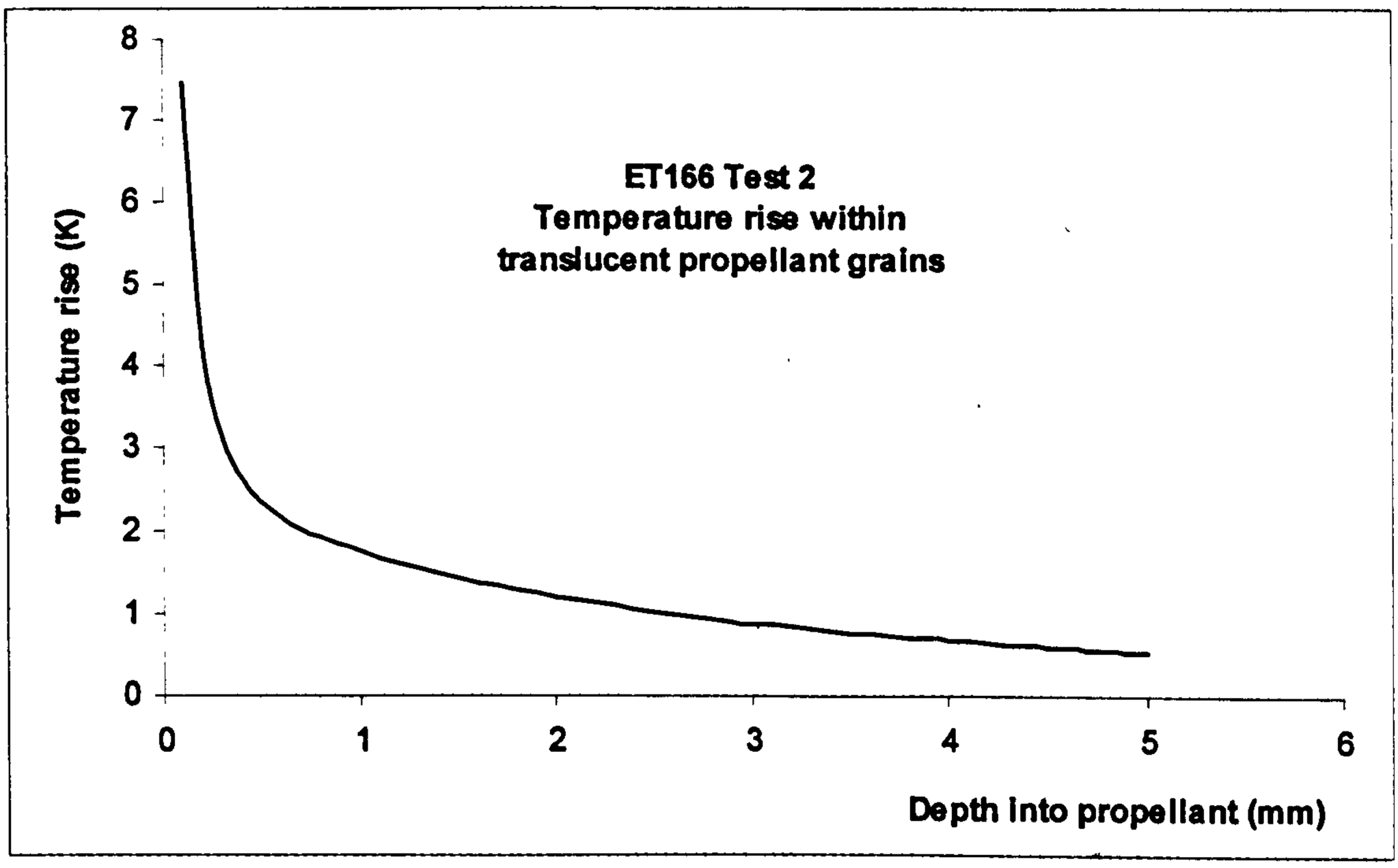

Figure 9.29 Effect on propellant grain of incident radiative flux

2.7.2 The ullage plasma seems to be far hotter than the plasma between the discs. The radiation could be argued to have a significant effect on the ullage material close to the CPG, contributing to the ignition of any propellant within it. The peak brightness temperature is around 11 000 K, shown in Figure 9.23, which equates to a flux of around 830 MW m^{-2}, but flux incident on the propellant surface may actually be far lower than this due to the formation of optically thick boundary layers. Alternatively, it may be hotter if the flow prevents any significant boundary thickness from forming. Further, in a real gun system, the plasma from a CPG would expand down an ullage tube made from a combustible material – a mixture of nitrocellulose (around 60%) and

cardboard. This material on receiving the radiation from the hotter plasma smoulders rather than deflagrates and so it is unlikely that the combustible ullage tube ignites, in turn igniting the propellant. The plasma vents through holes around 10 mm in diameter in the combustible ullage tube and into the propellant bed. It could be that the radiation has a significant effect on the propellant immediately on the other side of the holes close to the CPG. The magnitude and importance of any effect has yet to be determined, however: more work is required to elucidate this point further.

2.8 Estimation of flux transfer due to condensation of copper vapour

2.8.1 The heat flux due to condensation of metallic vapour onto the propellant surface can be estimated from measurements of the thickness of the deposit onto the polyethylene (which is assumed to have similar thermal properties to the propellant). Figure 9.30 illustrates SEM measurements of the deposit cross section. The thickness was difficult to gauge accurately due to the swarf from the metallic coating spreading into the polyethylene during polishing of the mounted sample, but the thickness is shown to lie between 0.5 μm and 1.5 μm.

2.8.2 Taking the deposit thickness as 1 μm, the mass of copper deposited per unit area would be 8.96 g m^{-2}; with the specific latent heat of vaporisation at 4.8 kJ g^{-1}, the energy liberated would be 43 kJ m^{-2}. Next, the time for condensation to occur had to be estimated. From the spectrographic work reported in this chapter, the maximum time would

need to be less than 50 μs, giving a minimum flux of 860 MW m^{-2} (similar to radiation from plasma at 11 000 K). This compares to 20 MW m^{-2} quoted earlier for a typical gunpowder igniter (Chapter 7 Section 3.2).

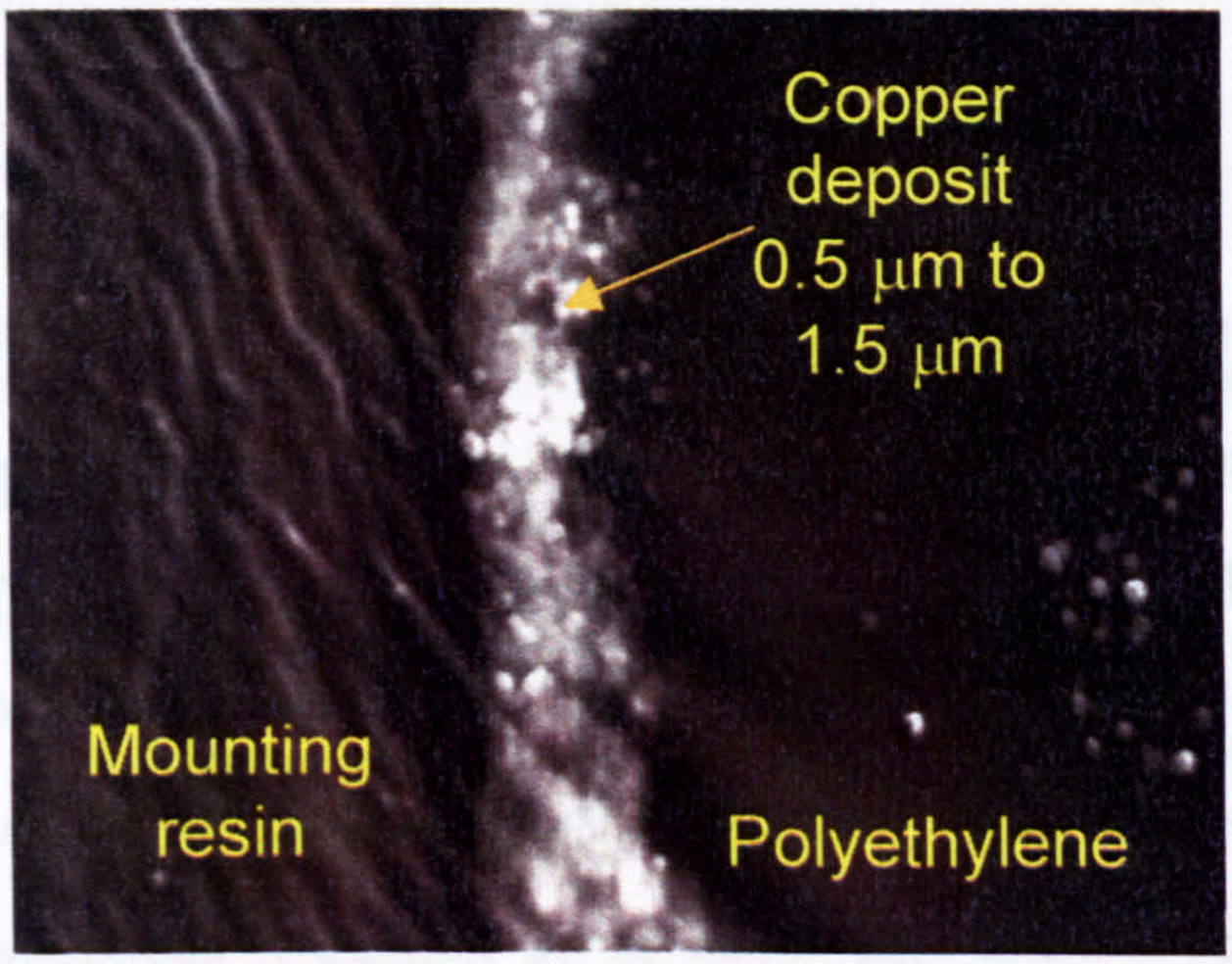

Figure 9.30 Measurement of the thickness of copper vapour residue

2.8.3 The deposition thickness used here was taken from a disc midway along the chamber. No measurement has yet been made of the deposit thickness further up the chamber, which is possibly less than the 1 μm in this estimation and significantly reduces the flux. However, the time required for the condensation to occur is possibly less than the 50 μs used, which significantly increasing the flux.

2.8.4 Hence, the flux from this process of copper vapour deposition is likely to be many hundreds of megawatts per unit area – at least an order of magnitude greater than from a conventional gun-powder ignition system. Further, the ability to transfer energy to the propellant surface

is not dependent on the optical properties of the propellant, unlike radiant energy transfer processes. Nor does it require the energy requirements of an ETC system based upon radiative energy transfer processes. For ignition by vapour deposition, a vapour generator rather than a plasma generator is all that is required.

3 Conclusions and summary of Chapter 9

3.1.1 This chapter was aimed at testing the hypothesis for ignition by vapour deposition in a large-calibre ETC test vessel under realistic loading conditions. The hypothesis has been supported by estimations of the vapour flux being at least an order of magnitude greater than in typical conventional ignition systems. Within the bed, the flux due to radiative energy transfer was found to be negligible, especially towards the projectile end, away from the plasma generator. The contribution from radiative heat transfer may well be measurable along the central ullage, although the optically thick boundary layers may greatly reduce the radiative flux. Within a real gun system the propellant may be shielded from the radiative effects of the ullage tube plasma by the combustible cartridge material, but work is necessary to determine the importance of this effect.

3.1.2 A full set of experimental data has been recorded, therefore, that will be used for validating EDEN-IB. Apart from the flux and time to ignition at different locations within the bed, these data include the localised pressure within the bed, the plasma expansion velocity under a number

of different conditions, as well as capillary pressure and plasma surface brightness temperatures.

---

1 M. J. Taylor, "ET166 – Correlation of Copper Vapour Deposition and Propellant Grain Ignition", unpublished QinetiQ report FST/CDT/58-ETL/ERD026, January 2001

2 A. M. Voronov, H. K. Haak and Th. H. G. G. Weise, "The Interaction of Electrothermally Supplied Energy with Compact Solid Propellants", IEEE Transactions on Magnetics, Vol. 35, 1, January 1999

3 M. J. Taylor, "ET114 – Estimation of Radiant Energy from a Plasma Jet", DERA internal document WSS/WS4/58-ETL/ERD008, Experiment No. ET114, February 2000

4 CRC Handbook of Chemistry and Physics, 79th Edition **10 - 17**

5 C. Welfare, QinetiQ, private communications, 2001

6 M. J. Taylor, "Measurement of the Properties of Plasma from ETC Capillary Plasma Generators", IEEE Transactions on Magnetics, Vol. 37, 1, January 2001

Appendix A - Spectrographic terms, data acquisition and analytical techniques

1 Introduction

1.1.1 Appendix A is intended to define certain terms related to spectrographic elements of the work used regularly within the main body of this Thesis, but which are not necessarily everyday terms. Those operating within the realm of electromagnetic emission spectroscopy will be familiar with these definitions. Further, the Appendix will then expand on the spectrographic data acquisition, calibration and analytical techniques used in this work.

1.1.2 Although the application of time-resolved emission spectroscopy to ETC research is not new, it is believed that use of the spectral analytical techniques and definition of plasma temperature in terms of a Planckian blackbody temperature is indeed novel. Alternative analytical techniques will be explored, as will the relevance of a Planckian definition for temperature. A worked example will be presented to emphasise the advantages of using blackbody theory in ETC research.

2 Spectrographic terms

2.1 Introduction

2.1.1 All matter with a temperature above absolute zero emits electromagnetic radiation. For matter in the condensed phase, this radiation spectrum will be a function of surface rather than bulk properties. The main property will be temperature but other factors such as texture and material type will also be important. For gaseous phase matter the issues are more complicated and pressure as well as

temperature need to be considered. The following definitions are generally applicable to condensed matter and gases with pressures above a few tens of megapascals, but care needs to be exercised when considering gases at low pressure.

2.2 Blackbody radiation

2.2.1 A perfect emitter is known as a 'blackbody.' This term is a misnomer because when the surface is hot enough to emit visible light (around 800 K) it is anything but black. The term blackbody originates from a body whose visual appearance at room temperature is indeed black due to its absorption characteristics being proportional to its emission characteristics at the same wavelengths, according to Kirchoff's radiation law.

2.3 Spectral radiant flux density, radiant flux density and radiated energy

2.3.1 The electromagnetic thermal energy emitted per unit time per unit area per unit wavelength into a solid angle of 2π is known as the spectral radiant flux density or spectral power density, ϕ. The radiant flux density or radiant power density, Φ is the integral of ϕ over the entire electromagnetic spectrum and the radiated energy density, ε is the integral of Φ with respect to time. The total energy radiated from an entire body, E is thus the integral of ε with respect to surface area.

2.4 The Planck radiation law, continuum emitters and the Stefan-Boltzmann radiation law

2.4.1 For a perfectly emitting (i.e. a blackbody) plane surface , the radiant flux density is given by the Planck radiation law:

$$\Phi_B = \int_0^\infty \phi_B(\lambda, T)d\lambda = \int_0^\infty \frac{2\pi hc^2}{\lambda^5}(e^{hc/\lambda kT} - 1)^{-1}d\lambda = \sigma T^4 \qquad \textbf{Equation A.1}$$

where

ϕ_B is the blackbody spectral radiant flux density,

λ is the wavelength of the electromagnetic energy,

T is the thermodynamic temperature,

h is Planck's constant,

c is the speed of light in a vacuum,

k is Boltzmann's constant, and

σ is the Stefan-Boltzmann constant.

2.4.2 Since the only free variable in the blackbody spectral radiant flux density is temperature, non-intrusive spectrographic measurements can be used to accurately calculate the surface temperature of a body. Blackbody or approximate blackbody emitters are often known as continuum emitters, because their spectral profile is continuous at all wavelengths.

2.4.3 The fourth power term on the right-hand side of Equation A.1 is known as the Stefan-Boltzmann radiation law and shows how the radiated increases energy rapidly with temperature. A derivation of the Planck and Stefan-Boltzmann radiation laws can be found in reference [1].

2.5 Temperature variation of the blackbody spectral radiant flux density

2.5.1 The visible region of the electromagnetic spectrum ranges from around 400 to 700 nm. The experimental wavelength range associated with the work in this Thesis is 200 – 1000 nm. Figure A.1 shows graphically how the spectral radiant flux density of a perfect emitter changes with temperature over this wavelength range: temperature variations are from 1000 to 6000 K. The radiant flux density (i.e. the area beneath the curve in Figure A.1 for all wavelengths) varies from 5.7×10^4 W m^{-2} at 1000 K, to 7.3×10^7 W m^{-2} at 6000 K.

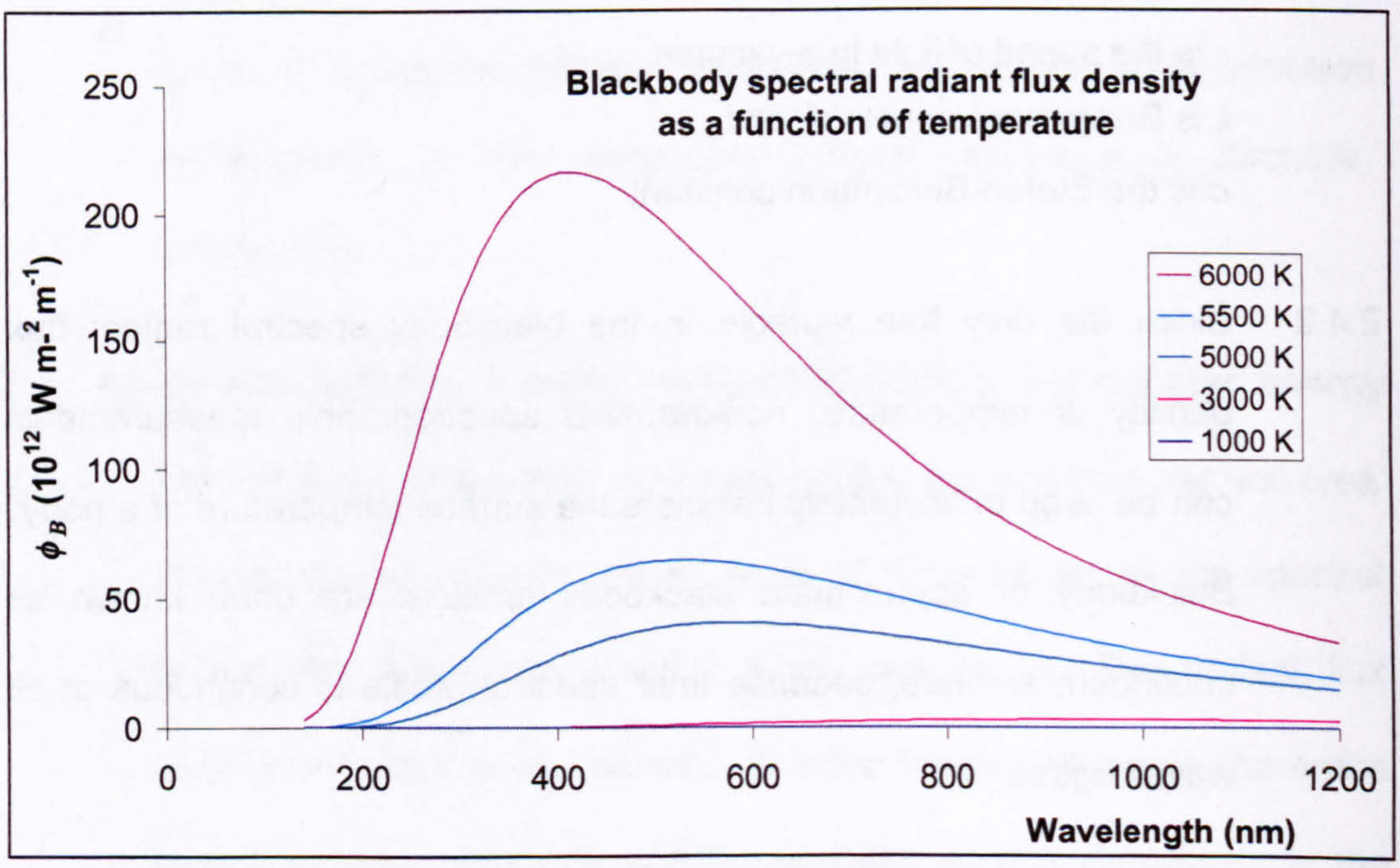

Figure A.1 Blackbody spectral radiant emission as a function of temperature

2.5.2 Surfaces with temperatures below 1500 K become difficult to examine with the spectral data acquisition equipment used and at exposure times relevant to ETC gun experiments. This is because the emitted radiation is too low to provide a good quality signal.

2.6 Greybody radiation and emissivity

2.6.1 A non-perfect emitter will emit thermal radiation less than ϕ_B, thus reducing Equation A.1 by a factor, $\varepsilon\ (\lambda,\ T)$ known as the emissivity of the surface. The emissivity is not necessarily a strong function of wavelength or temperature for small temperature changes and can often be replaced by a single constant value for many purposes. Such a body is called a 'greybody.' Graphite is used for calibration purposes (see below) and its emissivity has been taken a 0.8 for temperatures below around 2000 K and within the experimental wavelength range.

2.7 Optical thickness

2.7.1 An object whose radiation emanates from the surface (i.e. less than a few tens of microns into the body) is known as an optically thick body; one where the flux is emitted from deep within is known as an optically thin body. Condensed phase matter is in general optically thick (transparent and translucent objects are exceptions) and gas phase matter is generally optically thin. Even so, it is possible for an optically thin object to be an effective blackbody if its dimensions are such that it absorbs all radiation entering it. Deep space could be seen to fall within this category. Knowledge of the nature of the emitter's optical depth is essential for some of the analytical techniques used in this Thesis, to avoid drawing incorrect conclusions.

2.8 Emitting gases

2.8.1 The optical thickness and thus the emissivity of gases are closely linked to the pressure exerted within the gas. Emission spectrographic measurements are reported in the Thesis of gun propellant gases ranging in pressure from 0.1 MPa (atmospheric pressure) up to above 100 MPa. These measurements highlight how the emissivities of gases vary with pressure.

2.9 Line emitters, line broadening and line reversal

2.9.1 A low pressure gas with non-interacting atoms or molecules will emit thermal radiation and the emissivity of such a gas is zero for all but very discrete wavelength values. The values of wavelengths with non-zero emissivity are associated with the electronic structure of the emitting particle such that:

$$\Delta E = h\,c\,/\,\lambda \qquad \textbf{Equation A.2}$$

where

ΔE represents the difference between the upper and lower energy levels of the electronic transition from which the emitted photon originates. Such emitters are called 'line emitters' because their spectral profile is zero interspersed with high values at specific wavelengths. For an ideal gaseous emitter of sufficient depth, the magnitude of the spectral radiant flux density at the *specific wavelengths* is given by Equation A.1 alone. Thus, the temperature of a gas can be deduced from the magnitude of one spectral line. More generally, the relative magnitudes of more than one line are used, as

the gas depth is rarely sufficient to allow the Planckian magnitude to be reached. This method is examined in some detail below.

2.9.2 As the gas pressure increases, inter-particle interactions distort the electronic structure during the process of photonic emission, broadening the spectral lines in what is called 'pressure broadening'. In the case of plasma, the local electric field effects produce increased line broadening – electric field (or Stark) broadening. For very hot plasma, the high particle velocity increases the broadening still further with Doppler broadening. Doppler broadening is insignificant for this work, however, because the temperatures are relatively low (less than a few tens of thousands of kelvin).

2.9.3 In both Stark and pressure broadening, the broadened line-shape is Lorentzian, which allows for further analysis of temperature and ionisation levels. However, for reasons given below, no effort has been made by the Author towards such analytical techniques. However, Stark broadening is discussed in connection with some ETC emission spectroscopic measurements made by other workers in the field [2].

2.9.4 At moderately high pressures, the spectrum becomes a complex mix of line and continuum so that any analytical techniques must be applied with great caution. As pressures increase still further, the discrete line emission profile eventually broadens into that of a continuum emitter (i.e. the wavelength sensitivity of the emissivity becomes less and less significant). Line reversal often subsequently occurs at these high

pressures, where dips due to self-absorption are measured in the spectral profile centred on the same wavelengths as the line peaks due to emission.

2.10 Thermodynamic, brightness and colour temperatures

2.10.1 A thermally emitting body can be assigned three temperatures to it: its thermodynamic temperature (as obtained from a thermometer), its brightness temperature and its colour temperature. Brightness and colour temperatures are measured from the body's emitted spectra. In the case of a blackbody in thermal equilibrium, all three temperatures are the same.

2.10.2 The brightness (or blackbody) temperature of a body, T_b is defined as the temperature of a blackbody that emits the same amount of radiation per unit area as the body itself. In graphical form, the area beneath the spectral radiant flux density profile would equate to that of a blackbody at its brightness temperature. This quantity is useful in energy transfer problems where the absolute temperature is not necessarily required but an effective temperature for radiative energy transfer is needed. Such a temperature is often used for comparison with computer models where a body is often assumed to be black.

2.10.3 The colour temperature, T_c of a body is defined as the temperature of a blackbody from which the radiant energy has the same spectral distribution as that from its surface. In many cases were the emissivity is a weak function of wavelength, the colour temperature is close to the

thermodynamic temperature. The colour temperature may also be used to estimate the thermodynamic temperature, T of an emitter whose spectral distribution is totally dissimilar to that of a blackbody (for example, a line emitter). Here, the spectral radiant flux density distribution is set equal to that of a blackbody at T_c for one (or more) points. The assumption is that the emitter has an emissivity of unity for at least one point in its spectrum, but this might not be the case in causing T_c to be lower than T.

2.10.4 Figure A.2 indicates how T_b and T_c can be obtained from an experimental spectrum and shows examples of broadened line emitters and self-absorbing continuum emitters. LOVA 4 is an HMX-based gun propellant containing trace elements of metallic sodium and potassium; the figure depicts the spectrum of a flame from LOVA 4 burning freely in air at atmospheric pressure (green line). This spectrum was acquired with the burning zone of the condensed propellant outside the spectrographic field-of-view. EX97 is an RDX-based gun propellant containing the same trace elements; in the figure is a spectrum of the pressurised propellant hot combustion gases at 74 MPa (red line). The trace elements cause self-absorption in the high pressure spectrum of the propellant gases during combustion, but once the propellant has burnt completely, the absorption lines disappear and broad features associated with water vapour dominate. Only the effect of potassium is visible on this particular spectrum of EX97. The LOVA 4 spectrum is given in relative units but that for EX97 is in absolute units.

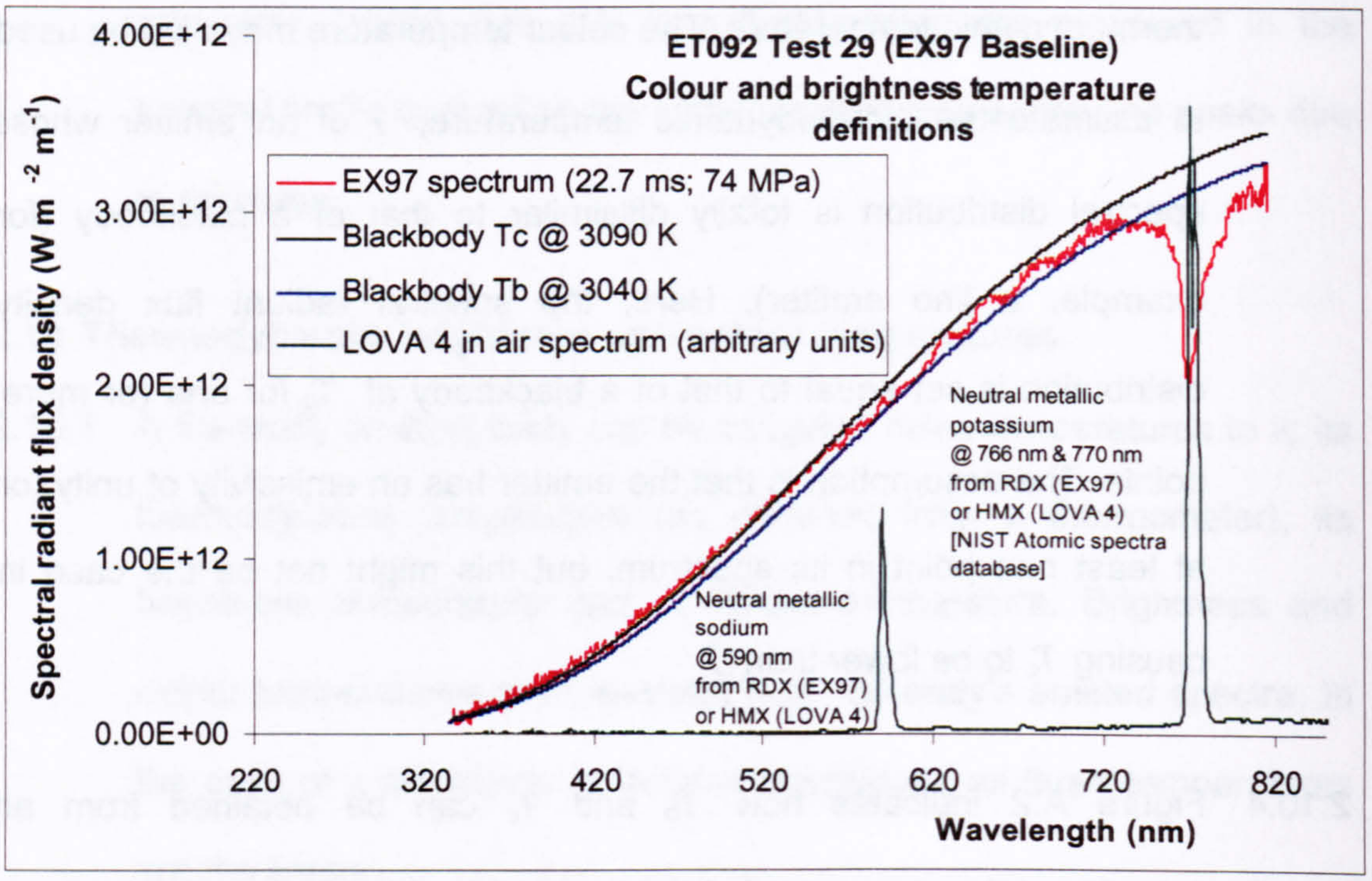

Figure A.2 Graphical definitions of brightness and colour temperature

2.10.5 The blue curve is a theoretical blackbody spectral profile with the same area beneath it for the experimental range as the red EX97 spectral curve, and which defines the brightness temperature, T_b of EX97. The black curve is a theoretical blackbody spectral profile 50 K higher than the brightness temperature, the profile of which matches the EX97 spectral profile for most of the distribution for the wavelength range measured and defines the colour temperature, T_c of EX97. The thermodynamic temperature of the gases might be closer to T_c than T_b, although the radiant energy transferred to the vessel walls will be from a blackbody closer to T_b than T_c. If $T_b \approx T_c$ then this infers that the thermodynamic temperature has been measured. Throughout this Thesis, an error is often applied to thermodynamic temperatures

obtained by spectral means: this error is a measure of the difference between T_b and T_c.

2.11 Hidden assumption in colour and brightness temperature measurements

2.11.1 The danger associated with quoting either temperature from these spectrographic measurements is the assumption that the spectrum in the wavelength range shown is representative of the entire spectrum. Here, knowledge of the emitting system is central to preventing erroneous conclusions being reached. However, most often the assumption must be made based upon the closeness of fit of the measured spectral profile to a blackbody emitter over a range of temperatures. In one test, plasma spectra with T_b from 3000 K to 60 000 K were successfully fitted to theoretical blackbody curves via one fitting parameter – blackbody temperature. This example is shown later in Appendix A.

3 Spectrographic data acquisition and calibration

3.1 Data acquisition

3.1.1 Time-resolved spectroscopy was identified early as an important research method for the Author's study of ETC plasma propellant interactions. The equipment described below was purchased on the Author's behalf specifically to allow this study to proceed.

3.1.2 Time-resolved spectra were recorded by an Acton Research Corporation (ARC) SP-306-I triple grating monochromator with an

imaging fibre adaptor ARC FC-446-030. A (coarse) 150 groove mm^{-1} grating blazed at 300 nm was used for this work, but other (finer) gratings were available. A central wavelength set to 700 nm gave a wavelength range from approximately 369 to 1027 nm at approximately 0.6 nm resolution. The computer controlled detector had an EEV model 30-11 kinetics, 1024 X 256 pixel, front illuminated, charge-coupled device (CCD) solid-state chip with a mask applied to it. The mask on the CCD covered the entire chip apart from, nominally, one active row (row 252) on which the spectrum from the monochromator was imaged. Incident photons excited the pixel's surface and electrons were liberated: these free electrons accumulated within the pixel, the latter acting as a 'potential well'. The number of free electrons accumulated could be measured by their charge once an acquisition sequence (or exposure) had been completed, and this number was expressed as counts. More than 60 000 electrons in one potential well saturated the well. A 'quantum efficiency' is associated with the CCD photosensitive material (silicon) and is a function of wavelength. This means that it takes on average, for example, 4 photons at a given wavelength to liberate an electron. In such a case, the quantum efficiency would be the reciprocal of this value (i.e. 0.25). The quantum efficiency of silicon peaks at around 675 nm and drops to zero at 400 nm and 1100 nm; this defines the wavelength range of the instrument. To increase this range into the ultraviolet (UV), a scintillator coating (*Lumigen*) was applied to the silicon surface which responded to UV radiation by

emitting radiation between 400 nm and 1100 nm. Figure A.3 is a typical spectral response curve for silicon, shown together with the effect of using the Lumigen coating.

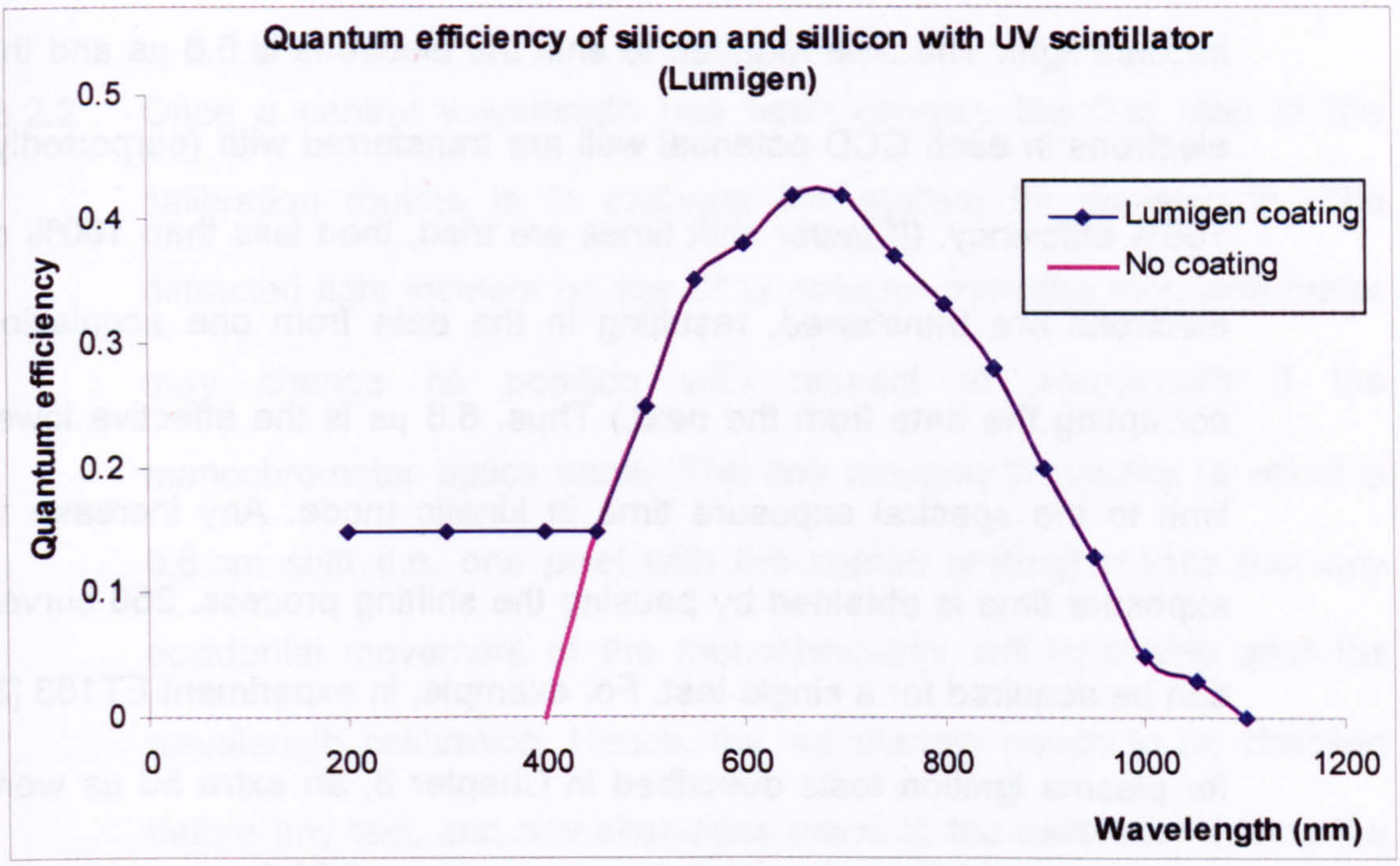

Figure A.3 'Quantum efficiency' of silicon

3.1.3 The spectrograph can be used in two modes: standard and kinetic. In standard mode the light from the monochromator is incident on the single unmasked row of pixels throughout the time that a mechanical shutter is open. The opening and closing of the shutter takes around 6 ms so data acquisition times need to be longer than this in standard mode to record anything. In addition, the actual 'exposure time' has an error of several milliseconds associated with the time that the shutter is opening and closing. Further, the spectrum is integrated over the entire exposure time and so any spectral changes are not recorded.

3.1.4 With the CCD detector in time-resolving 'kinetic' mode, the shutter remains open and the liberated electrons stored in the potential well are shifted below an opaque mask after a predetermined 'exposure time'. Thus, spectral data are protected from further exposure to incident light. The time required to shift the electrons is 6.6 μs and the electrons in each CCD potential well are transferred with (purportedly) 100% efficiency. (If faster shift times are tried, then less than 100% of electrons are transferred, resulting in the data from one acquisition corrupting the data from the next.) Thus, 6.6 μs is the effective lower limit to the spectral exposure time in kinetic mode. Any increase in exposure time is obtained by pausing the shifting process. 250 curves can be acquired for a single test. For example, in experiment ET163 [3] for plasma ignition tests described in Chapter 8, an extra 50 μs were added to the shift to give a total exposure time of 56.6 μs, and for the conventional ignition tests 220 μs of exposure time were added to the shift, giving a total exposure of 226.6 μs. For the total of 250 usable data rows available in this time-resolvable 'kinetic' mode, a total time of 14.15 ms was available to record the plasma radiated energy, with 56.65 ms for the conventional test radiant energy.

3.2 Calibration

3.2.1 Due to some idiosyncrasy with the movement of charge in the kinetic mode (there is a 'six phase' system of charge moving from the active rows), the signal (in counts) recorded in standard mode for spectra

from a constant intensity source is less than that recorded in kinetic mode. This non-equivalence between kinetic and standard operation has proved a problem, so a multistep calibration routine has been devised by the Author to addresses it.

3.2.2 Once a central wavelength has been chosen, the first step in the calibration routine is to calibrate the system for wavelength. The diffracted light incident on the CCD detector from the monochromator may change its position with respect to wavelength if the monochromator optics move. The tiny movement needed to effect a 0.6 nm shift (i.e. one pixel with the coarse grating) means that any accidental movement of the monochromator will invariably alter the wavelength calibration. Hence, the wavelength needs to be checked before any test, and any alterations made to the calibration (using the procedure supplied with the system). Acquiring a single spectrum (in standard mode) from a mercury argon discharge lamp, and checking the location of the emission lines against their known values can easily achieve this calibration. (It has been found in practice that if the system is out by a single pixel, then re-centring the diffraction grating on a different wavelength a few times before returning to the original one often resets the calibration.)

3.2.3 Once the wavelength calibration is acceptable, the absolute calibration of the system can be performed. Absolute calibration partly involves allowing for absorption from various optics (including mirrors and

windows used in the experiment, the 40 m length of 400 µm diameter silicon objective fibre and the spectrograph monochromator optics) as well as the quantum efficiency of the CCD, known here as system relative spectral response calibration. It also means allowing for the fibre acceptance angle, known here as absolute sensitivity calibration. Because the geometry of individual experiments often changes while everything else remains the same, the calibration procedure keeps system response calibration and absolute sensitivity calibration separate.

3.2.4 System response has to be measured because theoretical adjustment to the experimental spectra would be difficult. Ideally, measurement would be performed by a spectral irradiance lamp with absolutely known output. However, due to the varying nature of the experimental designs at Fort Halstead, it was more practicable to use irradiance lamps calibrated in relative terms: these were a tungsten lamp, normalised at 560 nm for wavelengths between 336 nm and 1100 nm, and a deuterium lamp normalised at 350 nm for wavelengths between 200 nm and 400 nm. These lamps were powered by constant current supplies. Calibration of the lamps and power supplies was performed by the National Physical Laboratory (NPL) every three years (or every 1000 h of use). The tungsten halogen lamp involved in for this work was an EG&G Gamma Scientific RS-20 lamp (HM0251) with an RS-3 lamp monitor and control unit/power supply (HK1560). The deuterium lamp is a Cathodeon Ltd V04 discharge lamp (AR032) with a C710

power supply (00580). Relative spectral irradiance calibration was undertaken for the tungsten and deuterium lamps by the UK National Physical Laboratory in July/August 1998, reference QD21/98/004/BCG2 and QD24/98/002/DCEE2 respectively, to produce the relative spectral radiant flux density data.

3.2.5 The absolute sensitivity calibration was performed with a piece of electrically heated graphite and over only the tungsten lamp wavelength range. Once the following procedure has been carried out on this wavelength range, then the spectra calibrated for system response for the lower wavelengths was spliced to the absolutely calibrated higher wavelength data. A high current power source (i.e. an arc welder source) was used to heat a rectangle of graphite (80 mm x 15 mm x 2 mm) the latter was held in a purpose-built rig and heated until it was glowing brightly (at a temperature up to 2000 K). The graphite was located where the experimental surface'was to be, so that in the case of a plasma jet, for example, the graphite was placed where the plasma surface would be. If this surface was more than a few millimetres from the spectrograph objective optical fibre terminus, then the collection angle would mean the graphite only filled a portion of its field of view. In such cases, a collimating mirror was used to reduce the field of view to a spot a few millimetres in diameter. The collimated nature of the field of view also allowed for small variations in the plasma surface from the location the graphite spectra were recorded. Spectra of the graphite are then recorded (again in kinetic

mode). If the graphite's spectral radiant flux density is ϕ_g, then the spectral radiant energy collected is :

$$G = \Lambda\, t_g\, \phi_g / R \qquad \textbf{Equation A.3}$$

where

Λ is the fraction of emitted light collected by the spectroscope objective fibre optic from the solid angle of 2π

t_g is the known exposure time of the graphite acquisition

R is the inverse of the spectrograph detector relative spectral response and needs to be determined for use as a calibration correction curve. The units of spectral magnitude are defined to be in counts.

3.2.6 The recorded graphite spectrum required calibration for the spectrograph detector relative spectral response. This was achieved by acquisition of spectra (in kinetic mode) from the tungsten spectral irradiance lamp, the relative spectral radiant flux density of which was stated by the lamp's suppliers, National Physical Laboratory (NPL) as:

$$\phi_{NPL} = k_{NPL}\, \phi_W \qquad \textbf{Equation A.4}$$

where

k_{NPL} is a constant associated with the collection parameters of NPL's measurement and

ϕ_W is the tungsten irradiance lamp's spectral radiant flux density.

3.2.7 The lamp must be used with the same optics as the experiment but may need a different geometry to ensure that light is not collected from any single point, which would invalidate its calibration. Further, a different exposure time may be required from that used with the

graphite sample. The spectral radiant energy collected from the tungsten lamp will be:

$$W_c = \Lambda_W t_W \phi_W / R \qquad \textbf{Equation A.5}$$

where

Λ_W is the fraction of emitted light from the tungsten lamp collected by the monochromator and

t_W is the exposure time of the tungsten irradiance lamp acquisition.

3.2.8 The units of the spectral magnitude are again defined in counts. The correction curve, R is produced by dividing the lamp suppliers given relative spectral radiant flux density (Equation A.4) by the acquired tungsten lamps spectrum (Equation A.5):

$$R = \phi_{NPL} / \phi_W = \phi_{NPL} \Lambda_W t_W / W_c k_{NPL} \qquad \textbf{Equation A.6}$$

3.2.9 This correction curve magnitude will have units of W m^{-2} m^{-1} s / counts. k_{NPL} is unknown, as is Λ_W. Both are independent of wavelength and so calibration using R is relative rather than absolute.

3.2.10 Comparison of the graphite spectrum, G with that of a theoretical blackbody emitter will permit absolute calibration.

3.2.11 The theoretical blackbody spectral radiant flux density can be calculated from the Planck radiation formula, ϕ_B given by Equation A.1.

3.2.12 The thermodynamic temperature, T of the graphite sample can be determined by comparing the profile of the spectral curve with that given by the Planck radiation formula, because graphite emissivity has

a negligible variation with wavelength over the experimental wavelength range. Then:

$$\varepsilon_g \, \phi_B = \phi_g \qquad \textbf{Equation A.7}$$

and from equations Equation A.3 and Equation A.7:

$$\Lambda = R \, G / \varepsilon \, \phi_B \, t_g \qquad \textbf{Equation A.8}$$

where

R is determined from Equation A.6 and

ε_g is the spectral emissivity of graphite (taken as 0.8 for the visible region of the spectrum at all temperatures). Λ will be a dimensionless quantity less than or equal to unity (usually of the order of 10^{-12}). It is purely a function of the geometry of the collection arrangement and, as long as this remains constant, the absolute calibration technique is valid.

3.2.13 All experimental spectra are then divided by the acquisition exposure time, multiplied by the system sensitivity calibration curve and divided by Λ. Obviously, there are a number of potential sources of experimental error in this calibration process, but for emitters that approximate to a blackbody, comparison of the absolutely calibrated spectra with a theoretical blackbody allows some assessment of the calibrated spectra, because there is only one fitting parameter (blackbody temperature). If a good fit to experimental data can be obtained with a theoretical blackbody curve over a wide range of

blackbody temperatures then the calibration procedure is likely to have been carried out correctly.

3.2.14 Figure A.4 compares an experimental spectrum acquired from electrically heated graphite that has been calibrated for system response, with a spectrum from a theoretical blackbody generated using Equation A.1. The fit allows the graphite temperature to be calculated to better than 5 K.

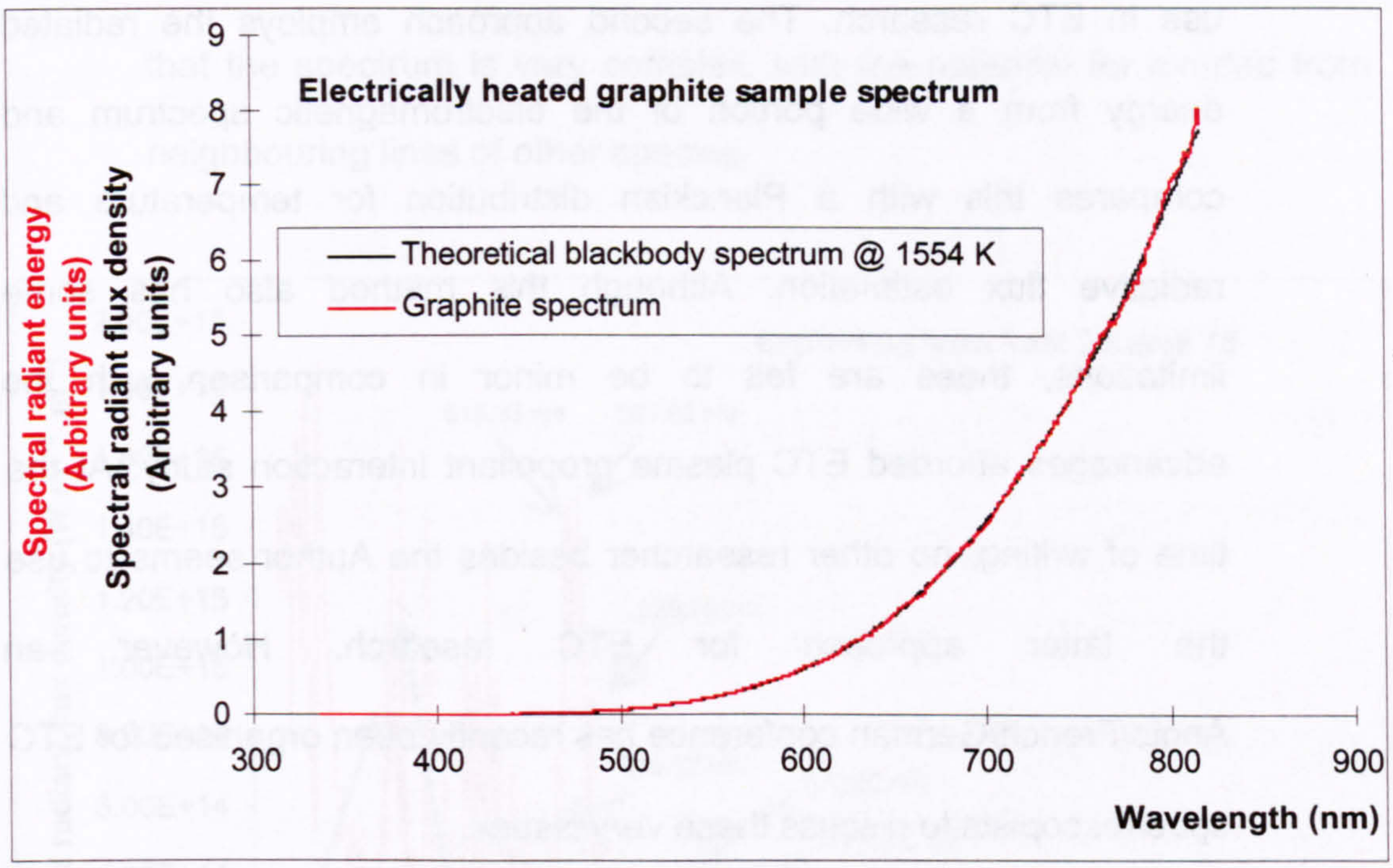

Figure A.4 Spectra of experimental electrically heated graphite and a theoretical blackbody

4 Analytical techniques

4.1 Introduction

4.1.1 Research into ETC plasma propellant interactions must address two issues: an understanding of the fundamental physics of the interaction

itself and validation measurements for computer simulation code development. This section describes two different approaches to analysing calibrated spectra for ETC research, aimed at addressing these issues. The first approach, preferred by a number of workers in the field [2, 4, 5] uses the relative intensity of known spectral lines to obtain a temperature for ETC plasma, and the broadened profile of the lines to estimate electron number density. The spectral line approach has some limitations that, in the Authors opinion, render it of limited use in ETC research. The second approach employs the radiated energy from a wide portion of the electromagnetic spectrum and compares this with a Planckian distribution for temperature and radiative flux estimation. Although this method also has some limitations, these are felt to be minor in comparison with the advantages afforded ETC plasma propellant interaction study. At the time of writing, no other researcher besides the Author seems to use the latter approach for ETC research. However, an Anglo/French/German conference has recently been organised for ETC spectroscopists to discuss these very issues.

4.2 Spectral line analysis approach

4.2.1 As described above, a hot low-density gas emits line radiation. Copper has been extensively used as a typical material for initiating ETC plasma discharges. Hence, emission spectroscopic measurements of ETC plasma often reveal strong copper lines; several known lines exist in the experimental wavelength range covered in such studies. The

Author used the technique during the early days of his research for temperature determination, but some obvious weaknesses resulted in the development of other analytical techniques. As such, the spectral line analysis was never used by the Author to determine free electron number density.

4.2.2 Figure A.5 illustrates the spectrum of copper plasma recorded from an exploded copper wire: the eight lines with published data available for temperature analysis are clearly indicated. It is immediately apparent that the spectrum is very complex, with the potential for overlap from neighbouring lines of other species.

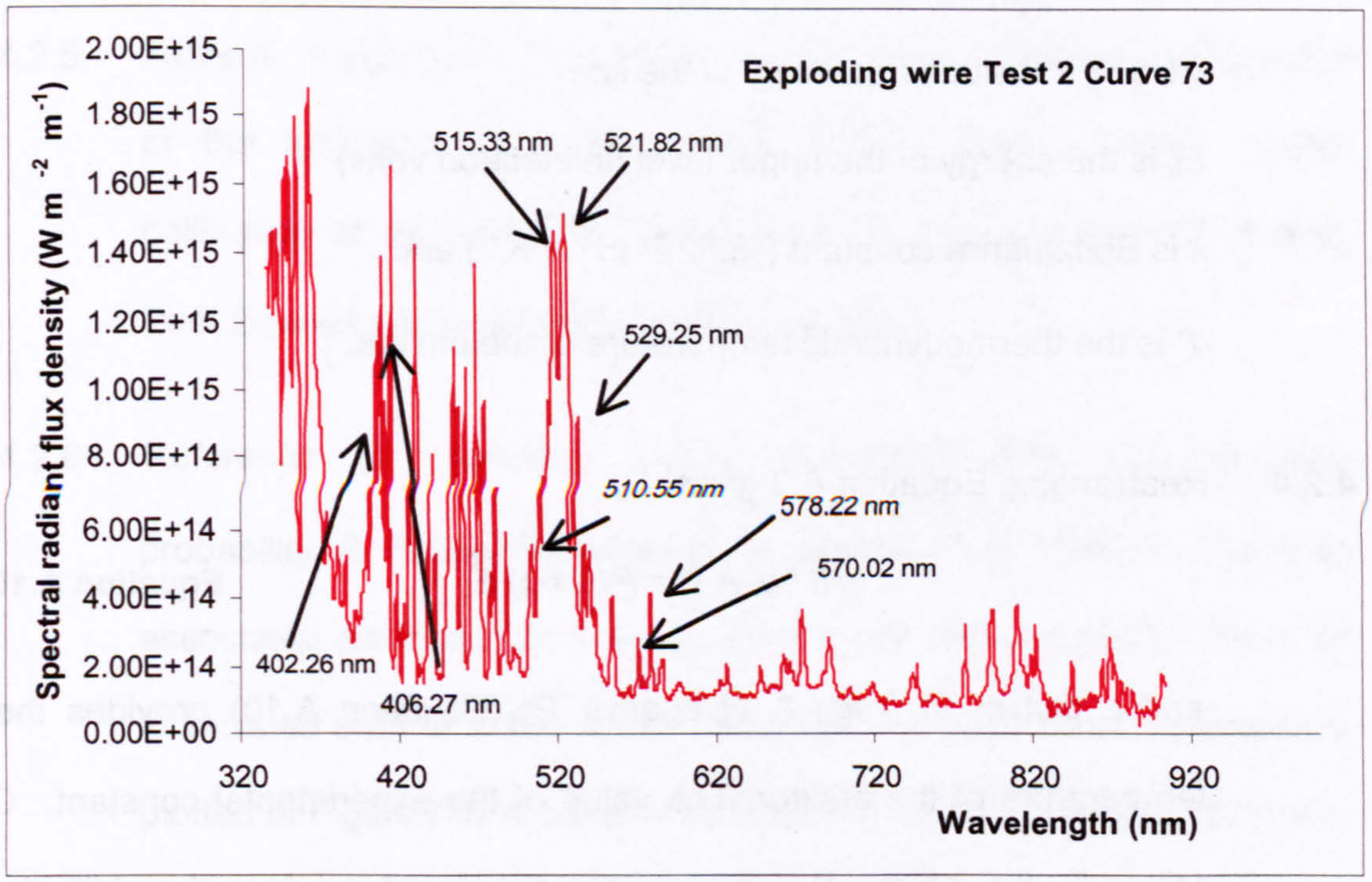

Figure A.5 Absolutely calibrated spectrum of copper plasma from an electrically exploded copper wire

4.2.3 This spectrum was recorded using the 150 groove mm^{-1} (coarse) grating, but finer gratings could have been used for better resolution: recalibrating the spectrograph system for a grating change was too great an effort for the small gain in benefit, however. The technique used in spectral line analysis for obtaining a temperature is known as the Boltzmann's Plot. The intensity, I of a spectral line is given by:

$$I = C\, g_u\, A\, \nu\, exp\,[-E_u / k\, T] \qquad \textbf{Equation A.9}$$

where

C is a constant of the experiment

g_u is the statistical weight of the upper energy level of the electron decay orbit

A is the transition probability that such a decay will occur

ν is the transition frequency of the line

E_u is the energy of the upper level (in electron volts)

k is Boltzmann's constant (8.62E-05 eV K^{-1}) and

T is the thermodynamic temperature of the emitter.

4.2.4 Rearranging Equation A.9 gives:

$$ln\,[I / g_u\, A\, \nu] = (-1 / k\, T)\, E_u \qquad \textbf{Equation A.10}$$

and a plot of $ln\,[I / g_u\, A\, \nu]$ against E_u (Equation A.10) provides the temperature of the emitter. The value of the experimental constant, C (given by the intercept) becomes less significant, as does the ability to calibrate the spectrograph system absolutely. Relative line values are

sufficient to enable the value of the gradient to be determined. Table A. 1 sets out the electronic transition data used by the Author.

Wavelength, λ (nm)	Frequency, ν (Hz)	A (s^{-1}) [6]	g_u [6]	E_u (eV)	I
402.26	7.45E+14	19000000*	4	6.87	0.6545
406.27	7.38E+14	21000000*	6	6.87	0.9101
510.55	5.87E+14	2000000*	4	3.82	0.5795
515.33	5.82E+14	60000000*	4	6.19	0.9851
521.82	5.75E+14	75000000*	6	6.19	1.0153
529.25	5.66E+14	10900000^{+}	4	7.74	0.5721
570.02	5.26E+14	240000*	4	3.82	0.1814
578.21	5.18E+14	1650000^{+}	2	3.79	0.2715

Table A. 1

4.2.5 Table A. 1 also gives the spectral values at the specified wavelengths of the spectrum in Figure A.5, although from previous relative calibration of the spectrum. The location of these values for plotting from Equation A.10 are shown in Figure A.6.

4.2.6 Reference [6] specifies errors associated with the transition probability, *A*. Figures indicated by an asterisk (*) in Table A. 1 have an associated error of ± 25 – 50%, whilst those with a cross ($^{+}$) have an associated error of ± 10 – 25%. The effect of these errors on the values plotted in Figure A.6 is somewhat mitigated by the logarithmic function, as shown in Figure A.7.

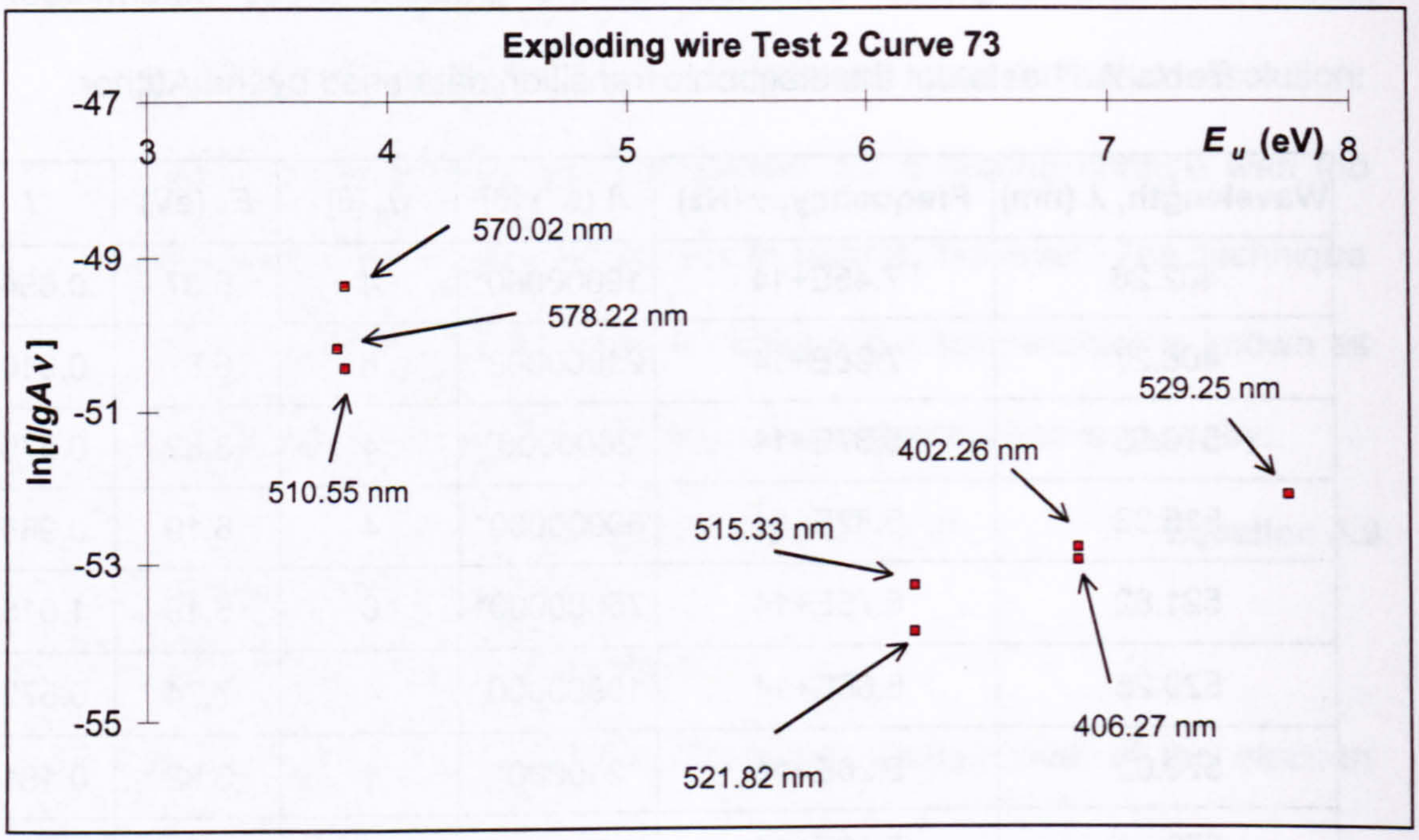

Figure A.6 Boltzmann's Plot spectral location

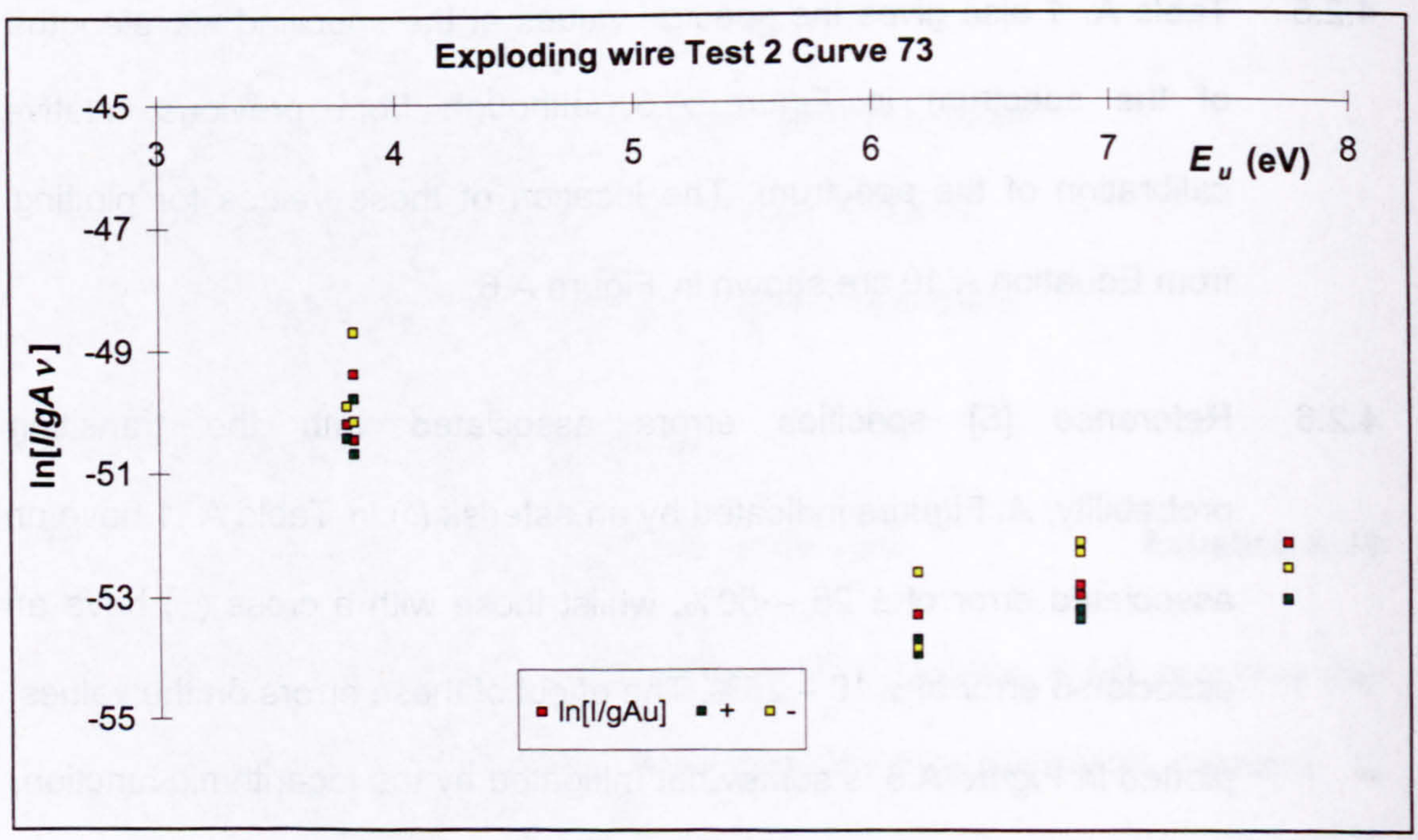

Figure A.7 Boltzmann's Plot spectral location errors in *A*

4.2.7 The plotted results form two clumps of data points, each clump having a large statistical distribution. The plasma temperature is obtained from

a linear regression line through the data and is shown as giving large errors in the temperature.

4.2.8 Curved confidence bands represent the 95% confidence interval for a regression line. This can be calculated from:

$$(a + b X) \pm (t) (S_P) [n^{-1} + (X - \bar{x})^2 / (n - 1) (r)^2]^{0.5} \qquad \textbf{Equation A.11}$$

where

a is the least squares regression line intercept coefficient

b is the least squares regression line slope coefficient

X is the upper energy level value as given by the regression line at a measured value of $ln [I / g_u A \nu]$

t is a standard statistical t-table value for a 95% confidence interval

S_P is the standard deviation in the abscissa values

n is the number of data points

$\bar{x}$ is the mean of the experimental upper energy level values.

4.2.9 r is the residual standard deviation given by:

$$S_e [(n - 1)(n - 2)^{-1} (1 - R^2)]^{0.5} \qquad \textbf{Equation A.12}$$

where

S_e is the standard deviation in the ordinate values and

R is the sample correlation coefficient.

4.2.10 The error in the slope is given by:

$$b \pm (t) (S_P) [(n - 1) (R)^2]^{-0.5} \qquad \textbf{Equation A.13}$$

4.2.11 Figure A.8 shows the results of this statistical analysis on the spectrum in Figure A.5. The Boltzmann's plot suggests the plasma has a

temperature of 13 800 K, but the regression error analysis shows the temperature may range from 8200 K to 45 500 K. This range does not include the increased spread resulting from the errors in *A* (Figure A.7), which would increase the errors in temperature even further.

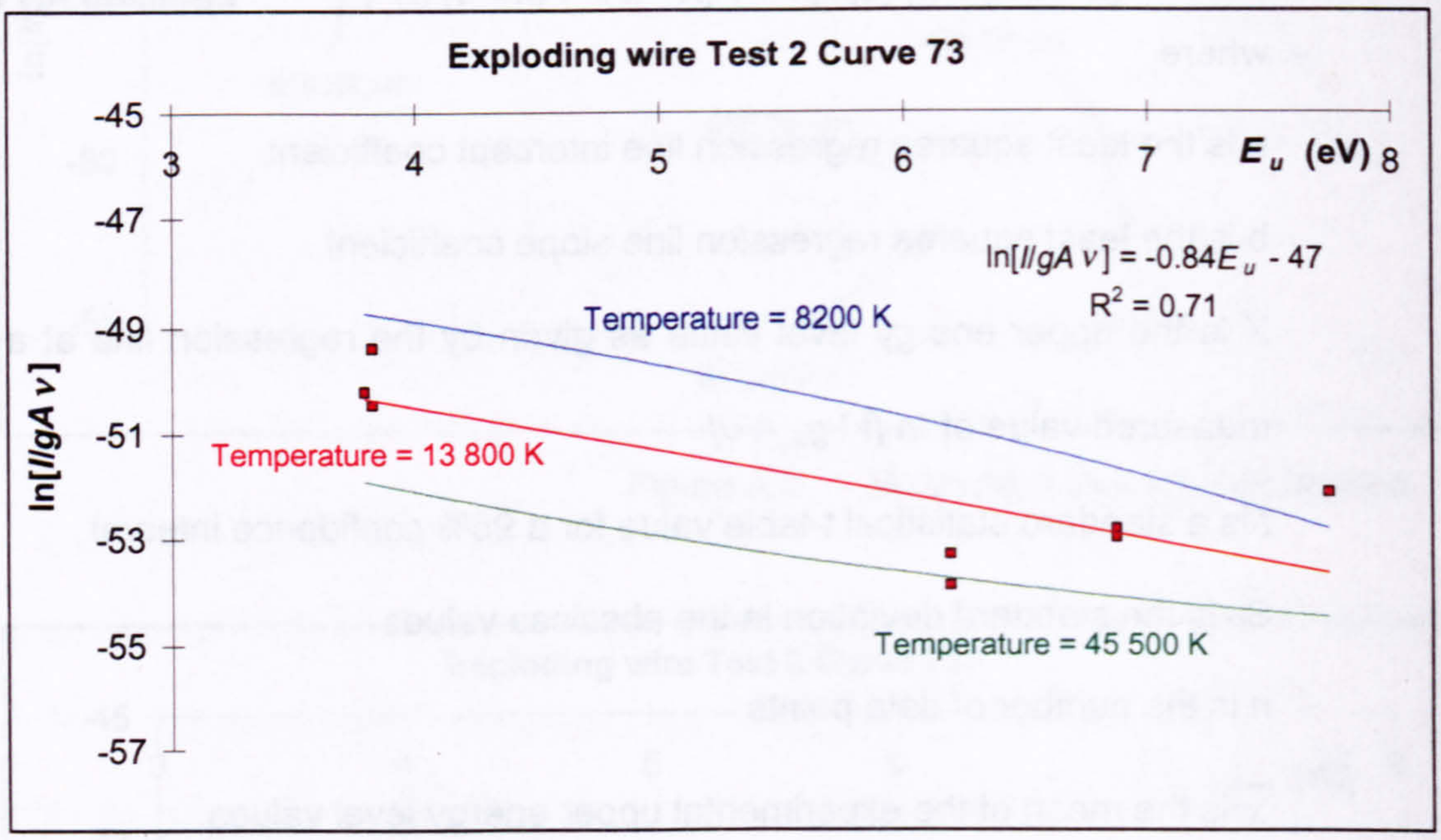

Figure A.8 Boltzmann's Plot analysis

4.2.12 The work described in references [2] and [5] briefly outline error analysis based on standard deviation. The quoted errors are 25% [2] and 1.7% [5]. No account appears to have been taken of the statistical variability of the regression line resulting from the data spread, but some effort has been made in both references to improve the methods performance.

4.2.13 Varghese et al [2] must have used a fine (unspecified) grating to acquire spectra from copper plasma, as their quoted resolution is

around 0.2 nm. They then used a Lorentzian profile to reconstruct the spectral line profiles, thus removing some of the effects of neighbouring lines, low levels of background continuum radiation and self-absorption. Their paper quotes enough information to allow the results to be re-analysed using the statistical error analysis in Equation A.11 to Equation A.13. Figure A.9 provides the results of this exercise.

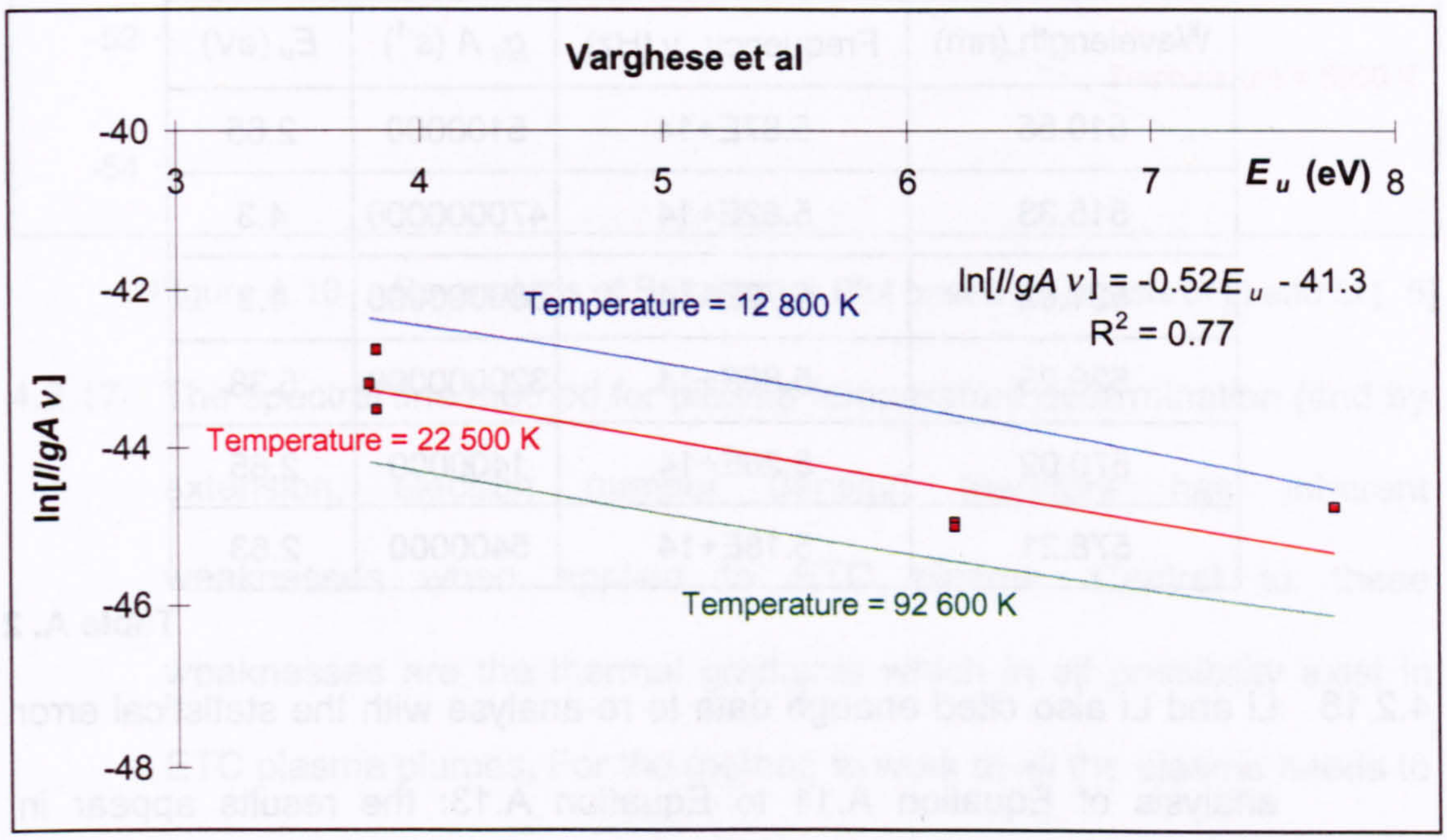

Figure A.9 Re-analysis of Boltzmann's Plot based on the results of Varghese et al [2]

4.2.14 The temperature of the Boltzmann's Plot is found to be 22 500 K, with the statistical error analysis outlined above setting the temperature between 12 800 K and 92 600 K. Their own result places the temperature between 17 400 K and 29 500 K. Even after the attempt to remove some of the problems associated with this method, the

temperature variability (even by their own analysis) leaves little confidence in its use for model validation.

4.2.15 Li and Li [5] used different atomic transition values cited from Coraliss and Bozman [7], rather than the CRC values quoted by others. These values are shown in Table A. 2. (Only the product $g_u A$ is cited by Li and Li, and no reference is made to errors in A.)

Wavelength (nm)	Frequency, ν (Hz)	$g_u A$ (s^{-1})	E_u (eV)
510.55	5.87E+14	5100000	2.65
515.33	5.82E+14	470000000	4.3
521.82	5.75E+14	580000000	4.3
529.25	5.66E+14	320000000	5.38
570.02	5.26E+14	1400000	2.65
578.21	5.18E+14	5400000	2.63

Table A. 2

4.2.16 Li and Li also cited enough data to re-analyse with the statistical error analysis of Equation A.11 to Equation A.13: the results appear in Figure A.10. The temperature of the Boltzmann's Plot is found to be 5900 K, with the statistical error analysis giving the temperature between 4300 K and 9700 K. Their result places the temperature between 5800 K and 6000 K. The analysis from this method does improve the situation, although the justification for using the values of Coraliss and Bozman rather than those of CRC needs to be better than just a more favourable result.

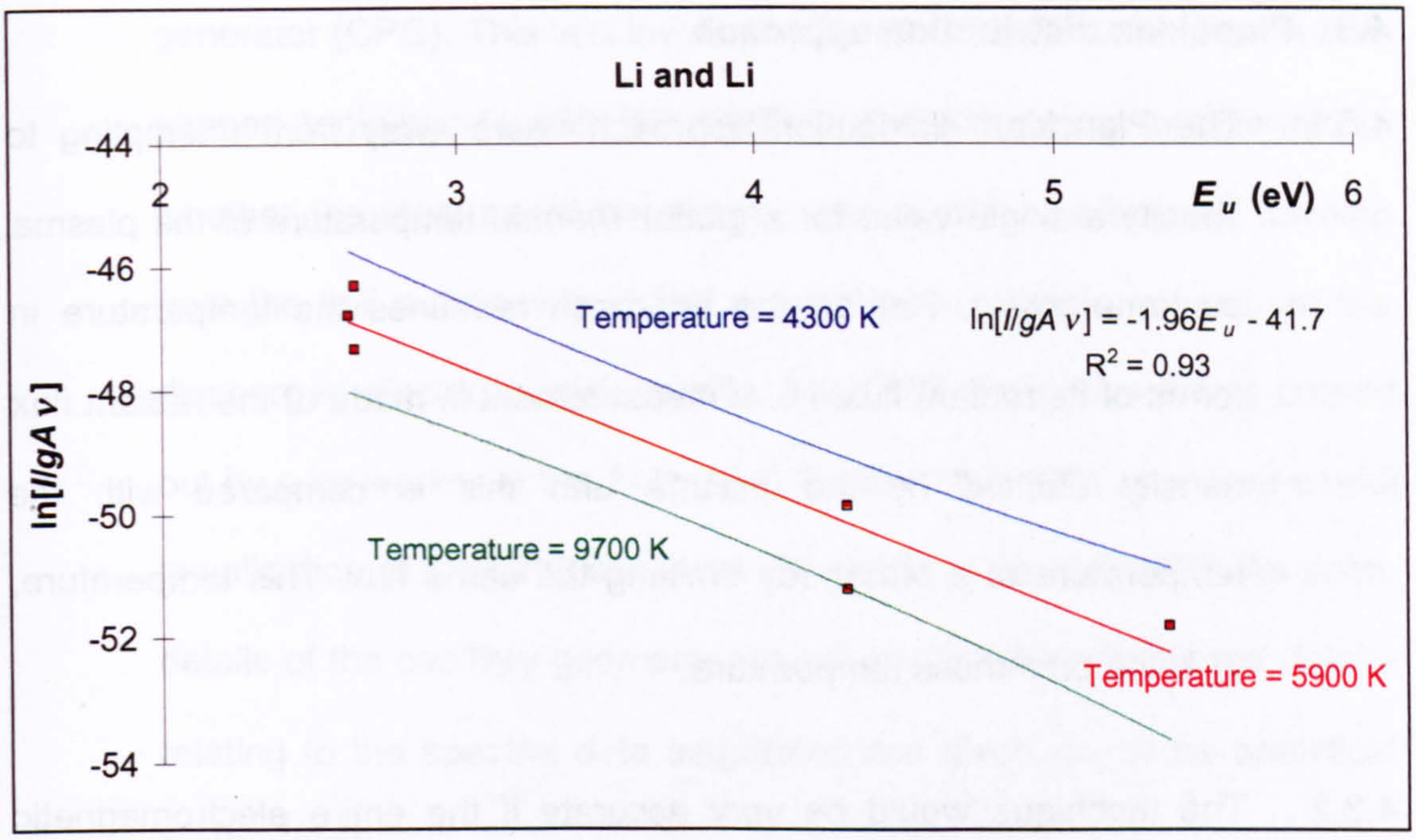

Figure A.10 Re-analysis of Boltzmann's Plot based on results of Li and Li [5]

4.2.17 The spectral line method for plasma temperature determination (and by extension, electron number density) therefore has inherent weaknesses when applied to ETC plasma. Central to these weaknesses are the thermal gradients which in all possibility exist in ETC plasma plumes. For the method to work at all the plasma needs to be optically thin and so any thermal gradients will distort the single value of a particular line. Furthermore, the method is only applicable to the latter part of the discharge, when the plasma has expanded sufficiently to become predominantly a line emitter. Varghese et al [2] admitted that this analysis was restricted in ETC research to expanded plasma where both the temperature and electron number density were low.

4.3 Planckian distribution approach

4.3.1 The Planckian distribution approach veers away from attempting to specify a single value for a global *thermal* temperature of the plasma, as none exists. Rather, the approach redefines the temperature in terms of its radiant flux, i.e. a measurement is made of the radiant flux density emitted by the plasma and this is compared with the temperature of a blackbody emitting the same flux. This temperature, T_b is the brightness temperature.

4.3.2 The technique would be very accurate if the entire electromagnetic spectrum were to be measured. However, in practice, only a portion of the spectrum is measured and therefore unquantifiable errors appear. An indication for error assessment is the difference between the brightness temperature, T_b and the colour temperature, T_c. For a perfect Planckian emitter this difference would be zero. In the unlucky case of an object that emits as a blackbody within the experimental wavelength range but has zero emissions elsewhere in the spectrum, then this assessment is obviously misleading. However, in the general case where a good proportion of the emitted energy has been measured, it might seem reasonable to assume that extrapolation to all wavelengths is fair if the difference between T_b and T_c is small.

4.3.3 An example of the practicalities of this technique is the following description of work performed to measure the plasma brightness temperature of a high power discharge from a capillary plasma

generator (CPG). This test involved a parallel nozzle rather than a bell-shaped sonic nozzle with the capillary, the aim being to determine whether the ideal pencil-like plasma plume structure seen to develop from the bell nozzle was in fact a result of the nozzle rather than the discharged electrical power profile. The CPG design work was carried out by a co-worker of the Author [8]. Further, the tests appeared useful in validation of the CPG computer simulation code, EDENET. As such, details of the capillary geometry are not explained here, but the details relating to the spectral data acquisition are given, as is the analytical methodology.

4.3.4 Figure A.11a is a photograph of a test arrangement similar to that used for the test discussed here. Two mirrors can be seen in the photograph: a rectangular plane mirror (used in this particular test for photography) and, below this, a smaller circular collimating surface-coated mirror with a 50 mm focal length. The CPG body with the central nozzle can be seen in the rectangular mirror. Figure A.11b is a photograph of a similar CPG body design with the capillary, c rear electrode, e and front annular electrode, f removed; a biro pen alongside gives the scale. The rectangular mirror in this particular test enabled the plasma jet to be photographed along the axial direction. The circular mirror imaged the plasma radiation from the leading edge onto the spectrograph optical fibre objective. The fibre (with a red polymer sheath) terminated in an SMA optical fibre connector. One important difference between the photograph and the test under discussion was that a 95 μm reduction

fibre was added to the 400 μm spectrograph fibre in order to reduce the radiation entering the spectrograph system, which would otherwise have saturated the CCD detector from the very bright source.

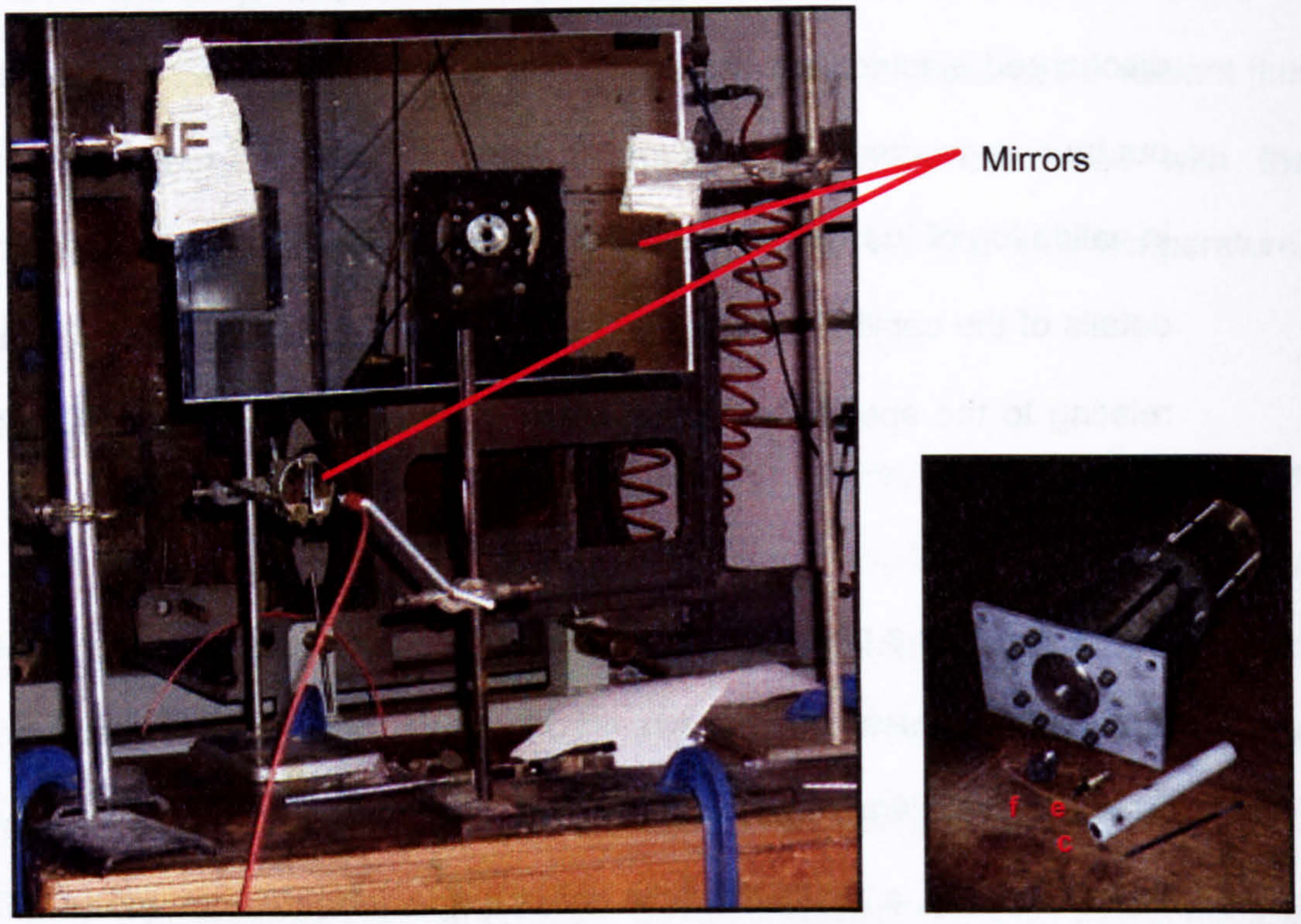

Figure A.11 Experimental set-up for spectral data acquisition during ET141

4.3.5 The spectrograph fibre can be seen taped to a retort stand just to the right of the circular mirror and facing the latter. Focusing is achieved by connecting a helium-neon laser to the spectrograph fibre via an SMA connector 10 m from the objective terminus (the fibre is 40 m in length). The location of the fibre terminus was finely altered with respect to the mirror until the laser light focused at a suitable location along the axis, producing a focused spot typically two or three millimetres in diameter. Moving a piece of white card along the axis where the plasma radiant

flux was to be measured indicated that the geometry of this spot remained visually unchanged.

4.3.6 Before the test was conducted, mercury, graphite, tungsten and deuterium calibration curves were acquired as described earlier. A certain background value associated with the CCD operation is always present and a background curve-set, with the same acquisition exposure time, must be acquired for each spectral curve-set. This background *file* can be subtracted automatically from the data file by the spectrograph software. All lamps were removed, a new background curve-set recorded and the spectrograph *armed* for data acquisition. Once armed, the system waited for a 5 V square-wave trigger pulse, and data acquisition began on the negative edge of this pulse. During spectral acquisition, the spectrograph transmitted a signal for data logger recording of its acquisition routine. Each spectral curve can be analysed in this way with respect to the rest of the experimental time-varying parameters (current, voltage etc). Triggering of the spectrograph usually occurs before that of the capacitor bank electrical discharge; the amount of pre-trigger time is dependent on the spectral acquisition exposure time. A maximum of 250 spectral curves is available for recording purposes and normally at least 20 curves remain left at the beginning of the acquisition sequence. It has been found that edge effects on the CCD detector distort the first 17 spectral curves.

4.3.7 Spectra acquired have a format with irregular spaced wavelength values, because the dispersion of the spectrum on the CCD chip is nonlinear with respect to wavelength. WinSpec, the spectral analysis software supplied with the spectrograph system is very limited in its ability to perform complex analytical routines: in particular, it is not able to output the spectrum in regularly spaced wavelengths. Hence, the spectra must be converted into a format more adequately suitable for spectrographic analysis. The software purchased for this purpose was Grams32, from Galactic Industries Corporation, requiring spectra to be converted to Grams32 format. The conversion could be done using WinSpec, so all relevant data for this test were duly converted.

4.3.8 Within Grams32, a program called *xy2even.ab* could be used to convert the wavelength to regularly spaced values. This was performed on all spectral data (apart from the mercury lamp data, which were not required for calibration of the experimental data but only as a record to show that the system was wavelength calibrated). All data were then divided by their experimental acquisition exposure time to obtain unit time values. For this particular test, the graphite exposure time was 10 s, the time for tungsten was 100 s, for deuterium was 3 min and the experimental exposure time was 30 µs, including shift time.

4.3.9 The tungsten and deuterium curve-sets were then divided into the appropriate calibrated NPL data to give calibration curve-sets for the two wavelength ranges. The experimental data were multiplied by both

calibration curve-sets, but the graphite curve-set was only multiplied by the tungsten (the tungsten spectrum becomes very low at wavelengths below 336 nm).

4.3.10 Three sets of spectral data calibrated for system response exist therefore: 'tungsten' calibrated graphite; tungsten calibrated plasma and 'deuterium' calibrated plasma. A single graphite spectrum from the spectral curve-set was then copied into a Microsoft Excel worksheet called '*Graphite*', in a workbook entitled '*Radiant flux density calculation - 1.xls*'. This was a controlled workbook, compiled by the Author [9]. The choice of which of the 252 graphite spectral curves to use was arbitrary, but the curve was noted for future reference. The 'solver' routine in Excel was used to reduce to a minimum the sum of the squares of the differences between the experimental graphite curve and a theoretical blackbody curve (represented in arbitrary units). Two fitting parameters were used – temperature and a scaling constant – to adjust the blackbody curve spectral profile to match the experimental graphite curve: the result can be seen in Figure A.4. Once the colour temperature of the graphite was obtained, this value was entered into the '*radiant flux density* ' worksheet in the same workbook. This temperature controlled the spectral profile of a second theoretical blackbody curve (this time in absolute units). The graphite curve was also copied into this worksheet. The 'solver' routine in Excel was again used to reduce to a minimum the sum of the squares of the differences between the experimental graphite curve and a theoretical blackbody

curve, but this time the magnitude of the graphite curve was adjusted by altering the geometrical scaling factor, Λ. This is the value discussed earlier for Equation A.3 that measures the fraction of emitted light collected by the spectroscope objective fibre and is thus a geometrical constant of the experiment. Λ is typically around 10^{-12}, indicating the very limited fraction of total radiation measured by the collimated collection method.

4.3.11 Experimental data (deuterium and tungsten calibrated data are still separate) were now copied into the same workbook, to a worksheet called '*Splice*'. The 'solver' routine in Excel was again used to reduce to a minimum the sum of the squares of the differences between the deuterium and tungsten calibrated curves between 370 and 400 nm (i.e. part of the spectral overlap). The deuterium calibrated curve was adjusted by a scaling factor and subsequently all deuterium curves were scaled accordingly. Figure A.12 illustrates an example of the closeness of fit. The tungsten calibrated data become susceptible to noise variation at wavelengths below 400 nm, and so the deuterium data were used for wavelengths lower than this, being spliced to the remainder of the tungsten spectral data. The spliced data were automatically copied into the worksheet 'radiant flux density' and the spectra divided by Λ. This completed the absolute calibration process for this particular curve. Each curve required for analysis had to be manually copied in turn from Grams32 into 'Splice', in a procedure

which was therefore rather time-consuming. However, this allowed for errors and anomalies to be identified and noted.

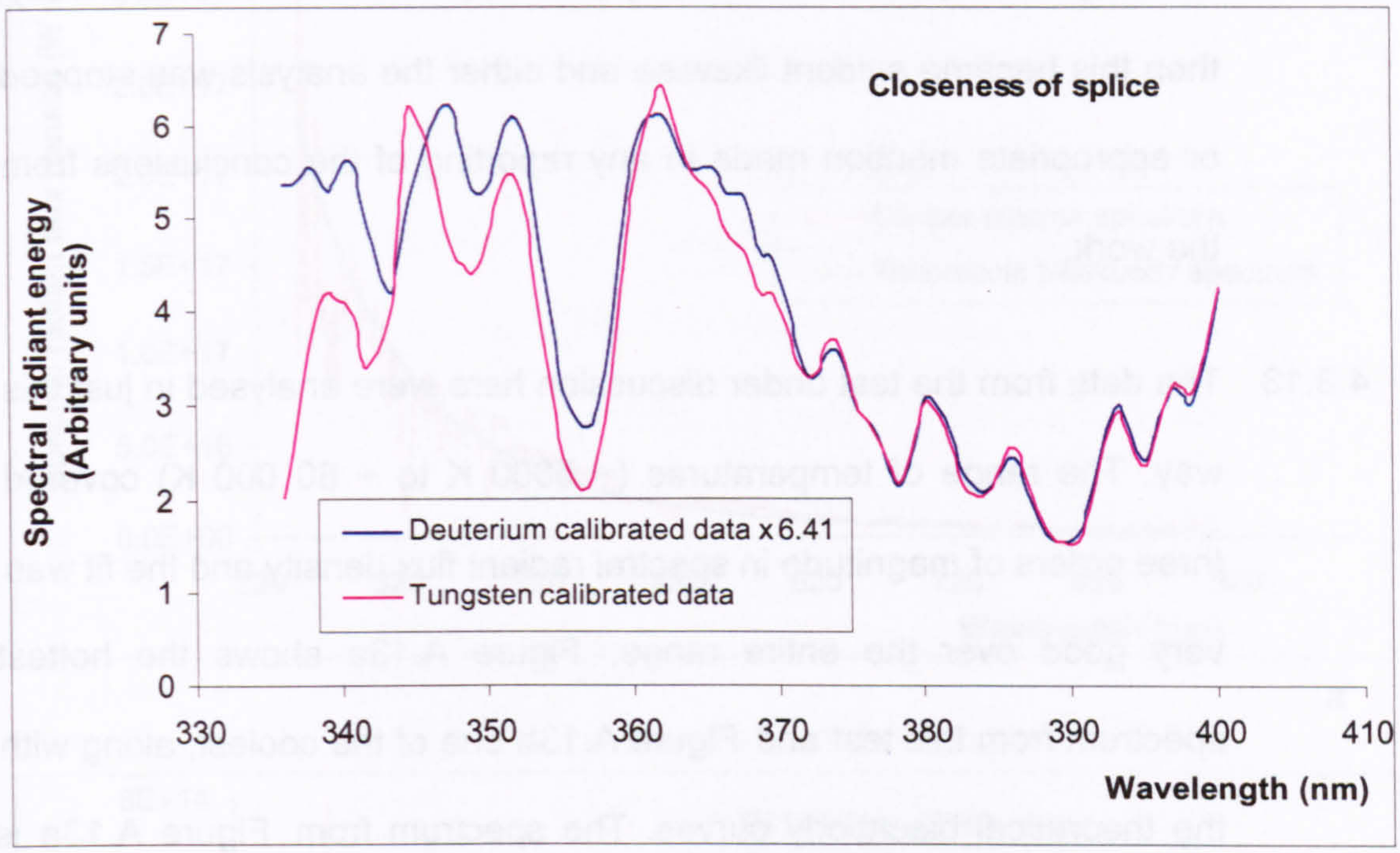

Figure A.12 Splice of deuterium and tungsten calibrated data

4.3.12 The absolutely-calibrated data were then compared with a theoretical blackbody spectrum curve by curve. Curve fitting was achieved with one parameter (i.e. temperature): the curve fitting was accomplished through numerical integration of the spectral profile of both the experimental and blackbody curves with respect to wavelength. Solver' was again used to reduce the division of the two numerical integration sums to unity, by adjusting the blackbody temperature. Then the radiated power over the entire wavelength range of the plasma was that of the blackbody at temperature, T_b. The value of T_b was noted and each experimental spectral curve treated likewise in turn. The quality of the fit to the blackbody was visually checked for closeness. If there had

been any errors in the multi-step calibration procedure, then this became evident through an inability to fit the data to the blackbody. Similarly, if the plasma was a very poor approximation to a blackbody, then this became evident likewise and either the analysis was stopped or appropriate mention made in any reporting of the conclusions from the work.

4.3.13 The data from the test under discussion here were analysed in just this way. The range of temperatures (~ 5000 K to ~ 60 000 K) covered three orders of magnitude in spectral radiant flux density and the fit was very good over the entire range. Figure A.13a shows the hottest spectrum from this test and Figure A.13b one of the coolest, along with the theoretical blackbody curves. The spectrum from Figure A.13a is believed to be the hottest ETC plasma for which temperature has been measured. The spike in Figure A.13b at around 386 nm could belong to iron [10]. The same spectrum was seen in Chapter 6, Figure 6.6. The elevated temperature could be due to exothermic reactions in progress involving oxidation of this species, although 7800 K is somewhat extreme for this activity. More likely, it is associated with the strong carbon 2 Swan' band structure shown in Figure 6.7 of Chapter 6, although no reference to this particular feature has been found by the Author.

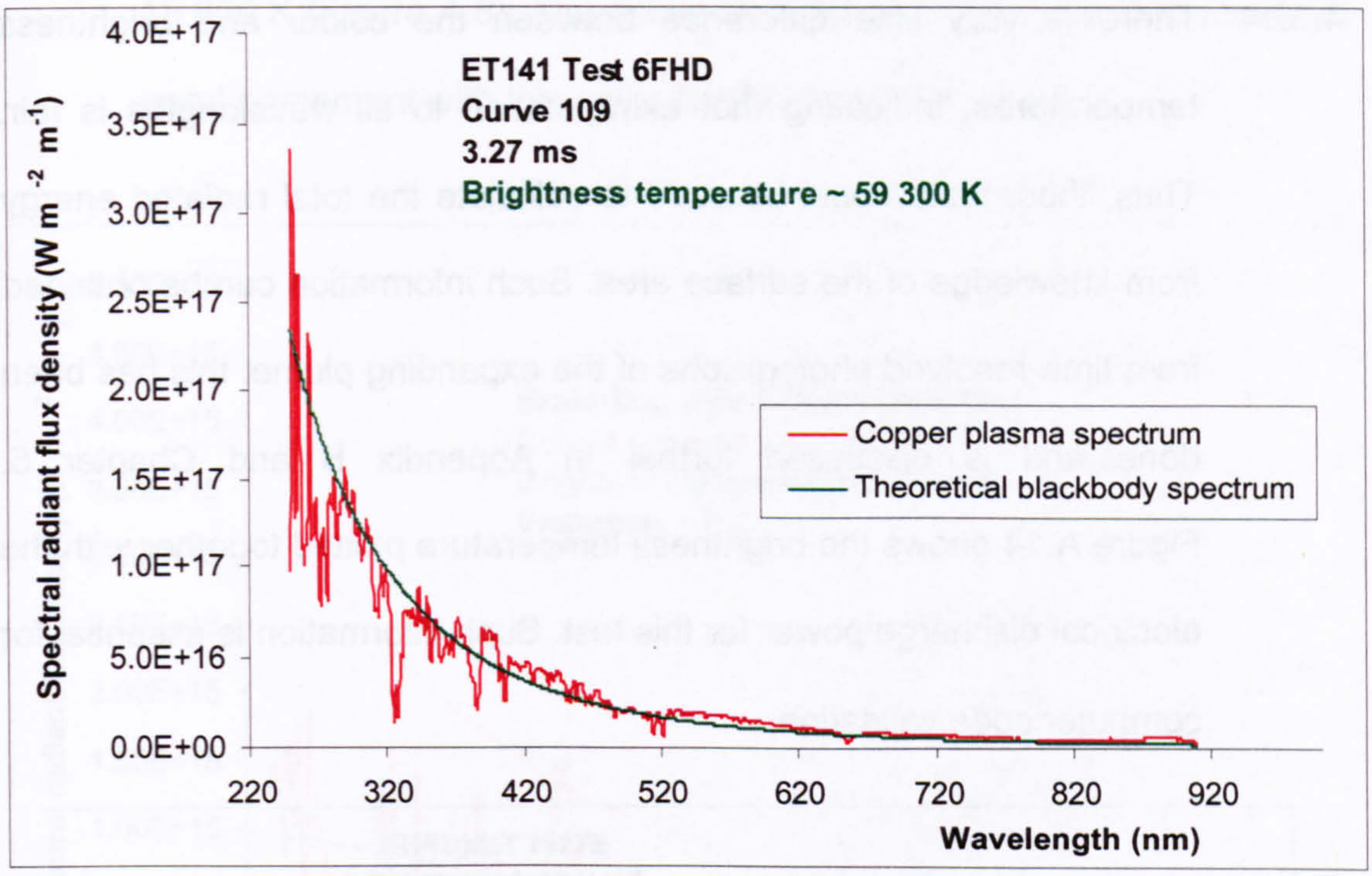

a

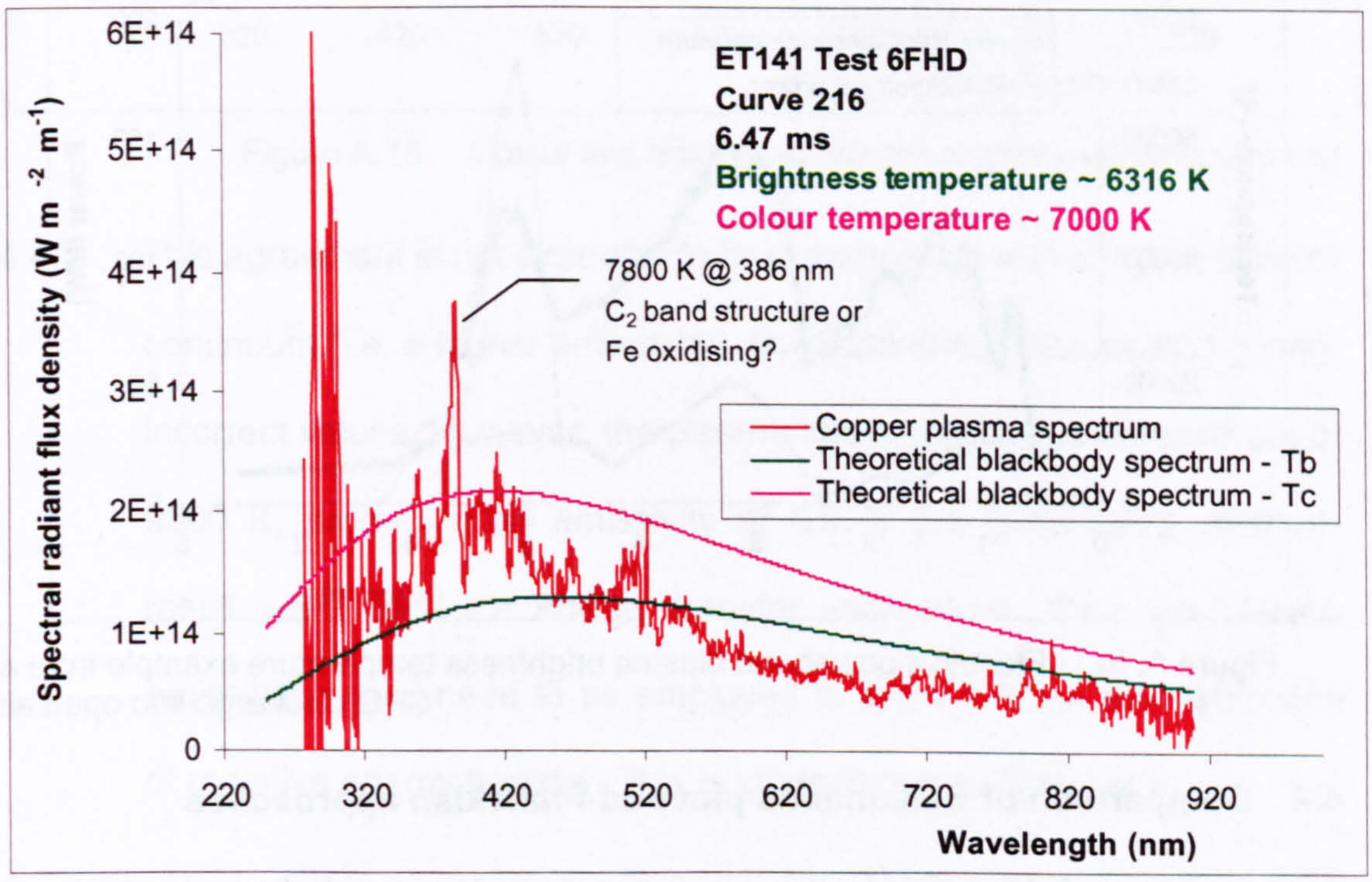

b

Figure A.13 Demonstration of the suitability of the Planckian method – three orders of magnitude of flux with one fitting parameter: temperature

4.3.14 There is very little difference between the colour and brightness temperatures, indicating that extrapolation to all wavelengths is fair. Thus, these data could be used to calculate the total radiated energy from knowledge of the surface area. Such information can be obtained from time-resolved photographs of the expanding plume: this has been done and is discussed further in Appendix B and Chapter 5. Figure A.14 shows the brightness temperature plotted together with the electrical discharge power for this test. Such information is essential for computer code validation.

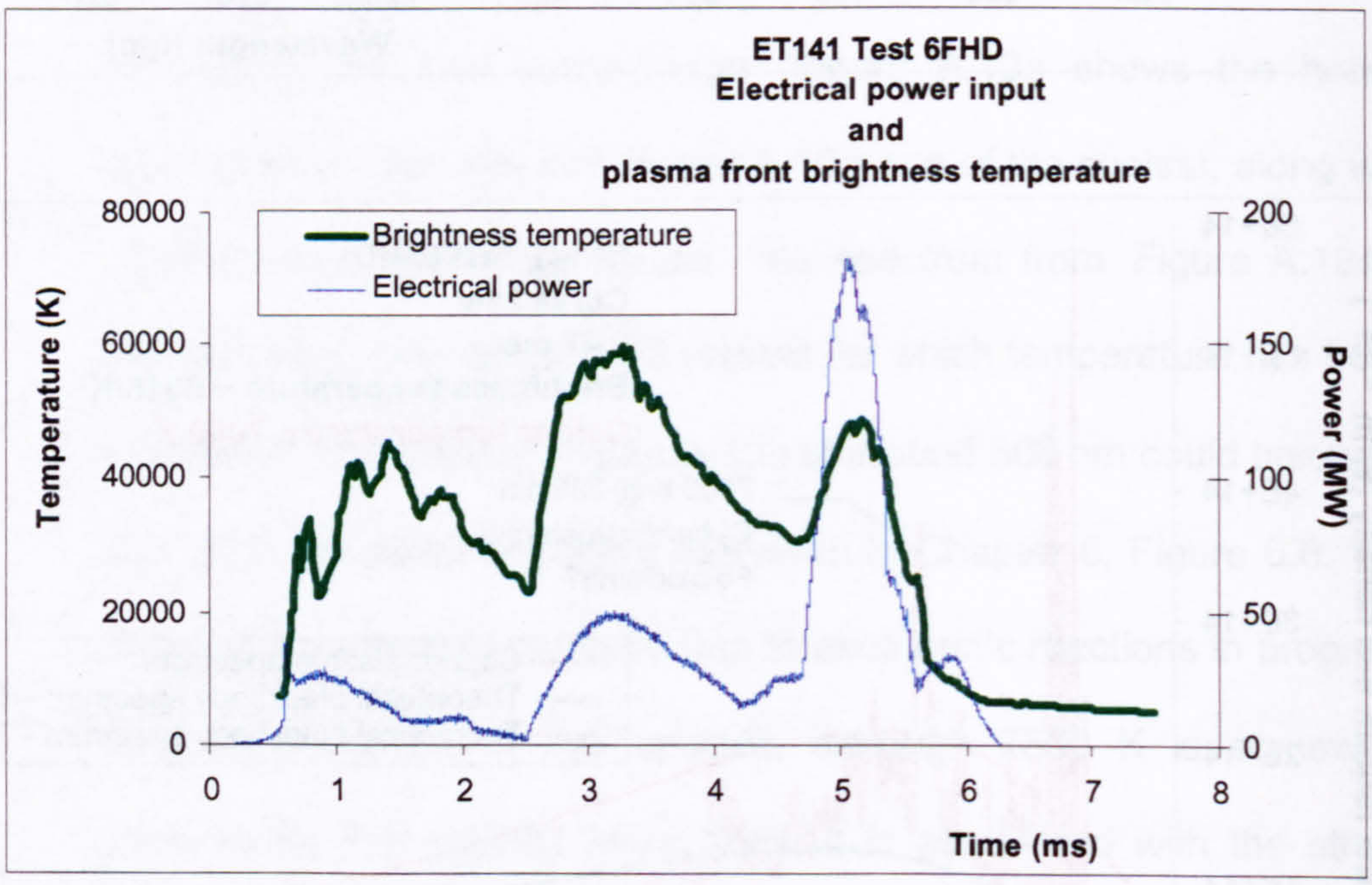

Figure A.14 Electrical power and plasma brightness temperature example from a CPG discharge into open air

4.4 Comparison of Boltzmann's plot and Planckian approaches

4.4.1 Figure A.15 provides the same spectrum from exploding wire tests as Figure A.5. This spectrum was analysed previously using the Boltzmann's plot method, which gave a temperature of around

13 800 K (Figure A.8). The colour temperature of 13 000 K is clearly in good agreement with this value for this particular case.

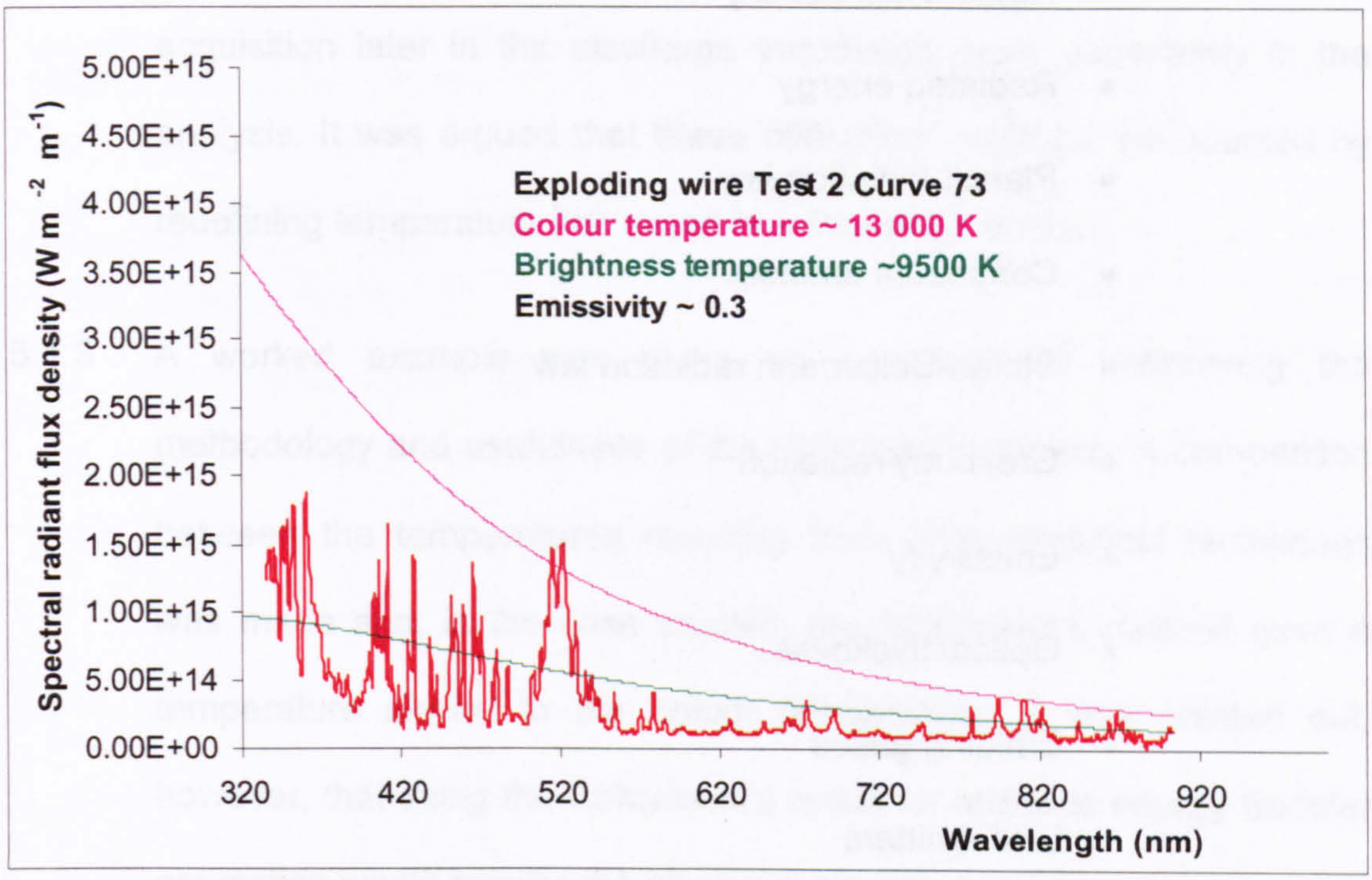

Figure A.15 Colour and brightness temperature of exploding wire test

4.4.2 This agreement is not expected to hold for plasma with a higher level of continuum (i.e. a higher emissivity), the Boltzmann's plot method giving incorrect values. However, the plasma has a brightness temperature of 9500 K, producing an emissivity of 0.3. If the Boltzmann's method result were used for energy transfer estimations, then the plasma emissivity would need to be employed to avoid a large overestimation of radiative energy transfer. This is taken further in Chapter 6.

5 Summary

5.1.1 Various definitions used throughout the main body of the Thesis have been explained. They were:

- Blackbody radiation
- Spectral radiant flux density
- Radiant flux density
- Radiated energy
- Planck radiation law
- Continuum emitters
- Stefan-Boltzmann radiation law
- Greybody radiation
- Emissivity
- Optical thickness
- Emitting gases
- Line emitters
- Thermodynamic temperature
- Brightness temperature
- Colour temperature

5.1.2 Spectrographic data acquisition and calibration techniques developed by the Author for the work covered in the Thesis were then described. Following this, the relative advantages and disadvantages of two analytical techniques were discussed in the context of ETC research. It was argued that the use of spectral lines for temperature (and free electron number density) determination was inappropriate in ETC work. This was mainly due to a lack of confidence in the result, with a large statistical variation given by regression analysis. In addition, the ETC

plasma is seen to be a continuum emitter during the more interesting moments of the discharge. Furthermore, the lack of a single value for thermodynamic temperature along the line of sight of the spectral data acquisition later in the discharge introduces more uncertainty in the analysis. It was argued that these difficulties could be surmounted by redefining temperature into terms of a Planckian emitter.

5.1.3 A worked example was given as a means of underlining the methodology and usefulness of the Planckian approach. A comparison between the temperatures resulting from both analytical techniques was made and, in the case studied, the Boltzmann's method gave a temperature similar to the colour temperature. It was pointed out, however, that using the Boltzmann's result for radiative energy transfer estimation would require the plasma emissivity to be known.

---

1 M. Garbuny, "Optical Physics", Academic Press: New York and London, 1965

2 J. M. Kohel, L. K. Su, N. T. Clemens and P. L. Varghese, "Emission Spectroscopic Measurements and Analysis of a Pulsed Plasma Jet", IEEE Transactions on Magnetics, Vol. 35, 1, January 1999

3 M. J. Taylor, "Investigation of Plasma Ignition of Opaque and Translucent Propellant", Unpublished QinetiQ report, December 2001

4 O. E. Hankins, M. A. Bourham, J. Earnhart and J. G. Gilligan, "Visible Light Emission Measurements from a Dense Electrothermal Launcher Plasma", IEEE Transactions on Magnetics, Vol. 29, 1, January 1993

5 B. Li and H. Li, "Discussions on Emission Spectroscopy Measurements from a Dense Electrothermal Launcher Plasma", 19th International Symposium of Ballistics, Interlaken, Switzerland, May 2001

6 CRC Handbook of Chemistry and Physics, 79th Edition **10** - 103

7 C. H. Coraliss and W. R. Bozman, "Experimental Transition Probabilities for Spectral Lines for Seventy Elements", Washington: National Bureau of Standards monograph S3, US Government Printing Office, 1962

8 Grant Savell, "ET141 - Investigation of the Enhanced Burning Effect using Different Nozzle Configurations and Different Propellant Compositions", unpublished QinetiQ report WSS/WS4/01-ETG/ERD053, June 2000

9 M. J. Taylor Design document: Excel spreadsheet 'Radiant flux density calculation' (Ref. Project N°. TG06/5/2/2. Work item: Experimental studies; Plasma properties. Files: DERA/WS4/1/1/2/10/1/3 and DRA/WX6/7/7/7/4) Version 1.0, 25th August 1999

10 CRC Handbook of Chemistry and Physics, 79th Edition 10-34

Appendix B – Photographic recording

1 Introduction

1.1.1 Much of the work covered by this Thesis has required the acquisition of photographic data. This includes work covered on exploding wires (Chapter 4) as well as expanding plasma plumes (Chapters 5 and 6). All the photographic work described has been performed by the Author. Appendix B will describe the operation and calibration techniques used in this work.

2 The Ultranac camera

2.1 Construction

2.1.1 Available to the Author for his work was an intensified ultra-high speed, image converter camera. The computer controlled 'Ultranac' camera [1] captures between 8 and 24 frames at the rate of 2000 to 20 000 000 s^{-1}, each frame being independent for exposure and interframe time. Further, it has a built-in triggering capability, designed to trigger events during an experiment. The output images are digital.

2.1.2 The Ultranac camera has a standard bayonet-type objective camera lens: a range of focal length lenses is available for use with it. Incident light is focussed onto an image converter tube via a hinged prism. When the camera is in standby mode, the prism is positioned to reflect the light to a CCD viewfinder camera. This camera is connected to an external video screen for composure and focusing. During an exposure, the prism is positioned to reflect light to the image converter tube. The image converter tube is a photocathode: incident light on a

phosphorus-coated window stimulates photo-emission of electrons. These electrons are accelerated along the axis of the photocathode tube, causing an avalanche effect within the low pressure gas filling the tube. The direction of this 'electron beam' can be controlled with spatial and temporal precision by charged deflection plates. The beam is then focused onto an output phosphorus-coated window for conversion of the kinetic energy of the electrons back to light. An image can thus be 'written' onto the output window and recorded by either photographic film or, as in this work, a digital camera. The Ultranac camera records from 8 to 24 images onto the one output window. Hence, more images are captured at the expense of image resolution.

2.1.3 Three computers control the Ultranac camera: one to control the operation of the image converter (i.e. exposure and interframe timing); one controls the digital camera (controlling exposure time and relaying images) and the third controls the other two as well as interfacing with the operator. Each of these computers has its own 'Windows' based programme manager. Clearly, operating the Ultranac system does require an investment in training!

2.1.4 The Ultranac camera is encased in mu-metal inner and steel outer jackets for protection against the hostile electromagnetic and potentially explosive environment. The entire housing sits on wheels fitted with pneumatic tyres.

2.1.5 Fibre optic communication with the camera prevents any high voltages being reached within the communications room. Trigger pulses can be relayed to and from the camera. Two pulses from the camera were used by the Author to indicate the start and end of an exposure sequence, and these pulses were recorded by the instrumentation officer, along with the other instrumentation (e.g. plasma voltage and current). Hence, the moment that each image was recorded with respect to the experiment could be obtained from inspection of the start pulse and the exposure and interframe timing. The end pulse served as a check that there had been no errors in the calculated frame timing. The digital images captured by the Ultranac camera were relayed to the camera control computer.

2.2 Image geometry

2.2.1 Image geometry was rectangular, with the short length representing the horizontal plane. This is problematic in much of the work conducted by the Author, because plasma plumes exiting from plasma generators have a long horizontal axis. With simple cameras, this problem can be solved by simply rotating the camera through 90°, but this was not possible here. Neither was it feasible to rotate the experiment due to engineering constraints, plus a low ceiling within the experimental area. A solution was gained through use of a 'Dove (Delaborne) prism' – a compound prism which rotates an image through 90°. This device was placed immediately in front of the objective lens on a stand commissioned by the Author. The stand has a movement system with

three degrees of freedom, allowing image composure to be performed. Figure B.1 shows the Ultranac camera together with Dove prism and stand.

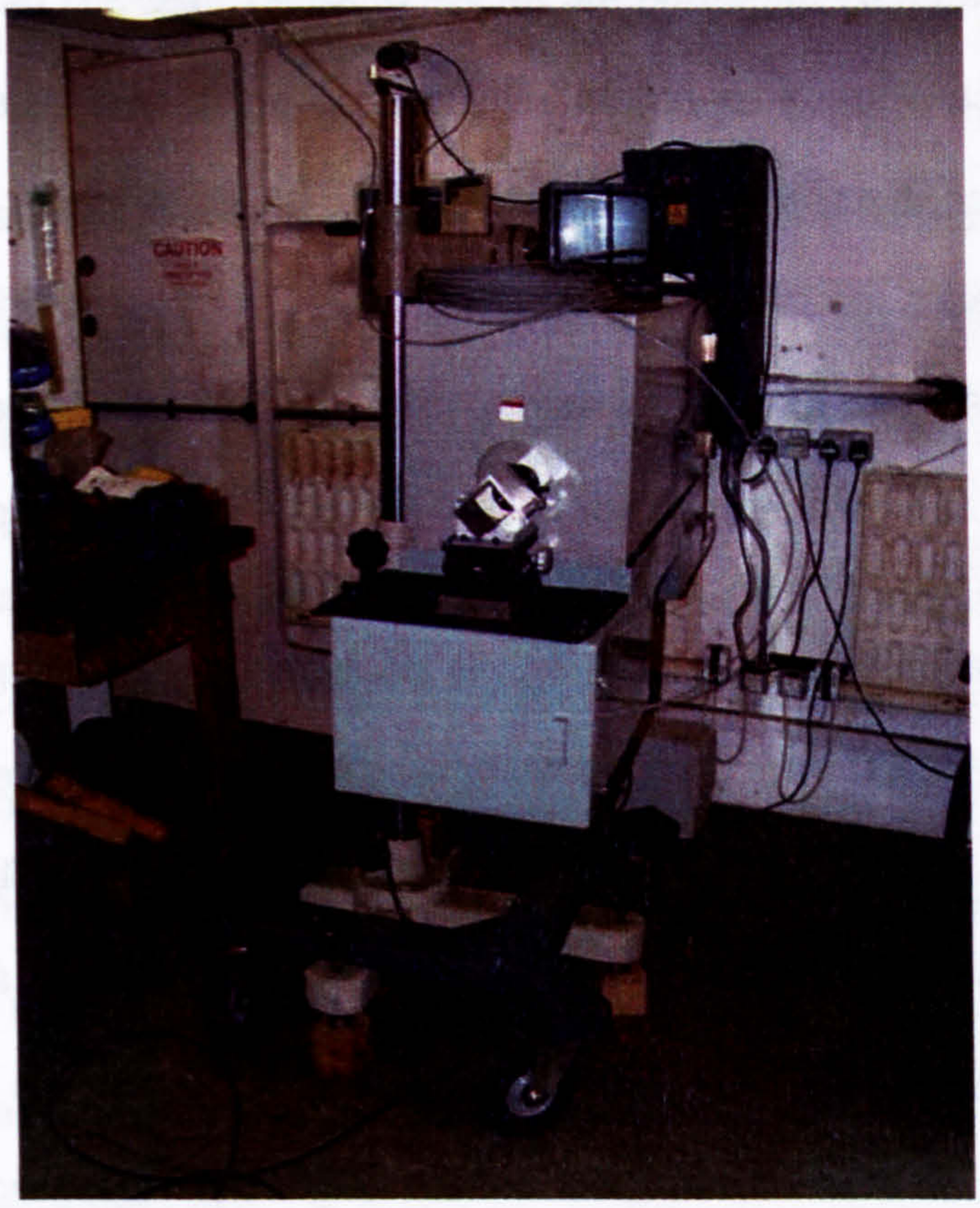

Figure B.1 Ultranac camera with Dove prism

2.3 Image output

2.3.1 The type of image output is unique to the Ultranac camera. The system has its own image analysis software package, but because of its limited scope a commercial image analysis software package was purchased by the Author for this work. This was Image-Pro Plus V4 (Media-Cybernetics). Image Pro-Plus had an image conversion file added to it to enable the Ultranac files to be read.

3 Image calibration

3.1 Calibration of Ultranac camera for spatial measurement

3.1.1 Images can be calibrated for geometry as required and this was performed by capturing the image of an A1 size test card, placed in the location of the experiment. The test card, made by the Author for this purpose, had an array of black 1 cm squares. With this image, the axial and radial co-ordinates of experimental images could be determined with respect to a fixed origin in the equipment. The origin for the capillary plasma generator is usually taken to be the capillary nozzle.

3.1.2 Calibration for absolute length is performed by measuring the number of pixels along a given line. Several different lengths are measured and a graph plotted. A linear regression line gives the calibration factor, f. This is the ratio of the measured length, d (in metres) and the number of pixels, p covering the distance. Measuring the length of any object in pixels can thus be converted to unit length by multiplying the number of pixels by f. Errors in the measurement of digital images will occur, but they are shown here to be negligible. δf, the error in f, is given by [2]:

$$\sqrt{\left(\frac{\partial f}{\partial p}\delta p\right)^2 + \left(\frac{\partial f}{\partial d}\delta d\right)^2} \qquad \textbf{Equation B .1}$$

where

$$f = \frac{d}{p} \qquad \textbf{Equation B. 2}$$

and so

$$\frac{\partial f}{\partial p} = -\frac{d}{p^2} \qquad \textbf{Equation B.3}$$

and

$$\frac{\partial f}{\partial d} = \frac{1}{p} \qquad \textbf{Equation B.4}$$

3.1.3 The error in pixels, δp is ± 2 (for a sharp image) and the error in length, δd is ± 10^{-3} m (using a calibrated ruler). 196 ± 2 pixels were counted to cover an image 0.265 ± 0.001 m in length. The calibration factor, f is given as (1.352 ± 0.015) x 10^{-3} metres per pixel: the error in the calibration factor, δf is within 1% and can thus be safely ignored.

3.1.4 The calibration process needs to be performed over a range of distances (pixels) in order to verify the linearity of the optics. (In the case of a non-linear pixel to distance calibration where nonplanar focusing mirrors etc. are being employed, the appropriate factor needs to be used for individual image sizes.) Figure B.2 shows that the Ultranac imaging is both horizontally and vertically linear during the calibration card test.

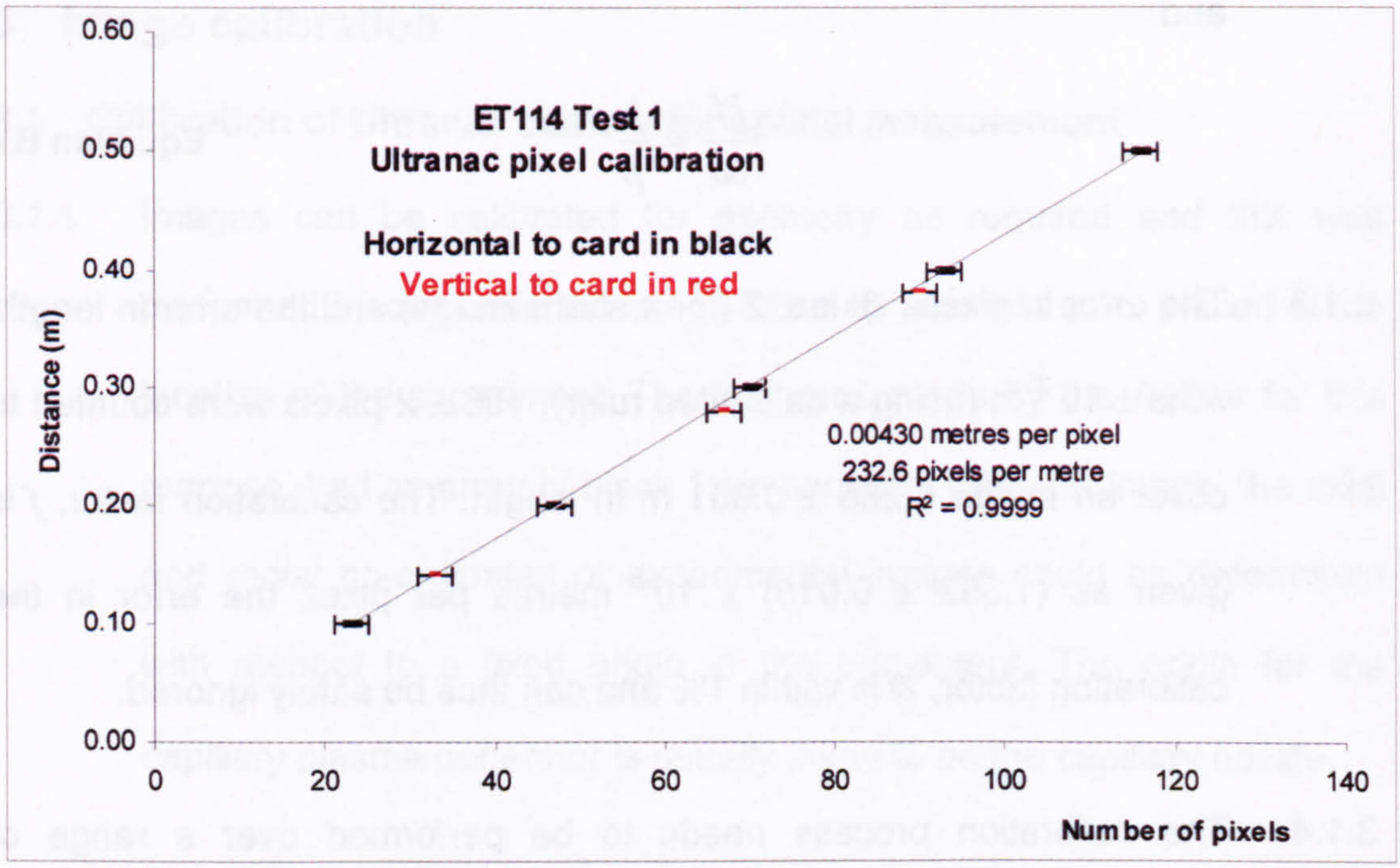

Figure B.2 Linearity of Ultranac calibration

3.1.5 The Ultranac produces 2D images of the 3D plume. To calculate radiative flux measurement of plasma plumes requires determination of the radiative flux density (Appendix A) and absolute measurement of the 3D surface area. The 3D surface area can be obtained from the 2D profile by revolving the latter, assuming cylindrical symmetry. A method for this has been produced by the Author [3] and is discussed below. Calculations were achieved by employing three proprietary software programs: “Image-Pro Plus V4”, to obtain the vector positions of the image surface outline; “DADiSP version 4.1”, to perform a 100 point interpolate between the vector position data points and “Microsoft Excel”, to obtain surface areas and volumes of revolution.

3.1.6 The 2D grey-scale images have a depth (intensity) from zero up to a maximum of 60 000 counts. There is a background of 263 counts,

which was subtracted from each image as the initial step in the surface area estimation. The next step involved producing a suitable profile for the revolution process using the *'count and measure'* dialogue box in Image-Pro Plus V4. The plasma plumes have no hard edge and so defining the surface area is subject to errors. Figure B.3 shows the approach to the problem of determining the edge of the plasma. The three images, a, b and c are identical. The red outline is the profile in the case of choosing 200, 300 and 400 counts respectively. It appears clear from the figure that 300 counts is closer to the visual hot plume than the other choices, but this is artificial because the visual image can be manipulated to show a hot plume of almost any size. The intensity profile across the plume from image b is shown in the graph in Figure B.3: again, no clearly defined plume edge is evident. The difference in the final 3D surface area is around 10-15% between the 200 and 400 count options, compared with that of 300 counts. The final criteria decided upon were based on stopping radiative flux analysis at 3000 K. Images at this temperature, determined from spectrographic analysis (Appendix A), were explored and had a digital image count of around 300 for this particular experimental set-up. Since the analysis was halted at 3000 K, and 3000 K was equivalent to 300 counts in the images, it seemed reasonable to choose 300 counts as a basis for defining the plasma edge. (This method has also been used to calibrate the Ultranac camera for temperature measurement, see Section 3.2.1.) This method is not perfect of course but the lack of any

improved criteria has meant that it has continued, especially as the overall error target was around 50% and this estimation only resulted in at the very most 10%.

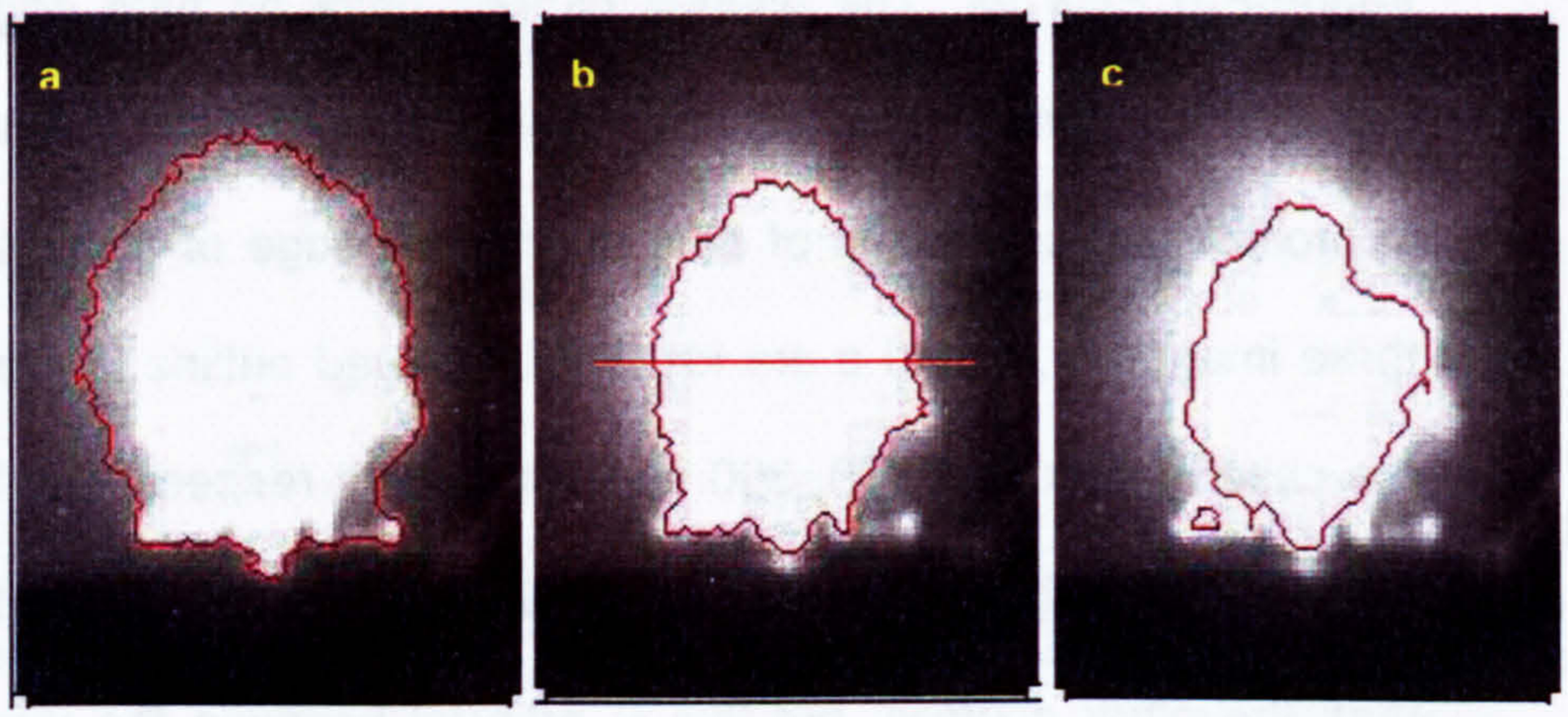

	200 counts	300 counts	400 counts
Surface area (m^2)	2.39E-01	2.10E-01	1.89E-01
% difference	13.8 % larger	-	10.0 % smaller

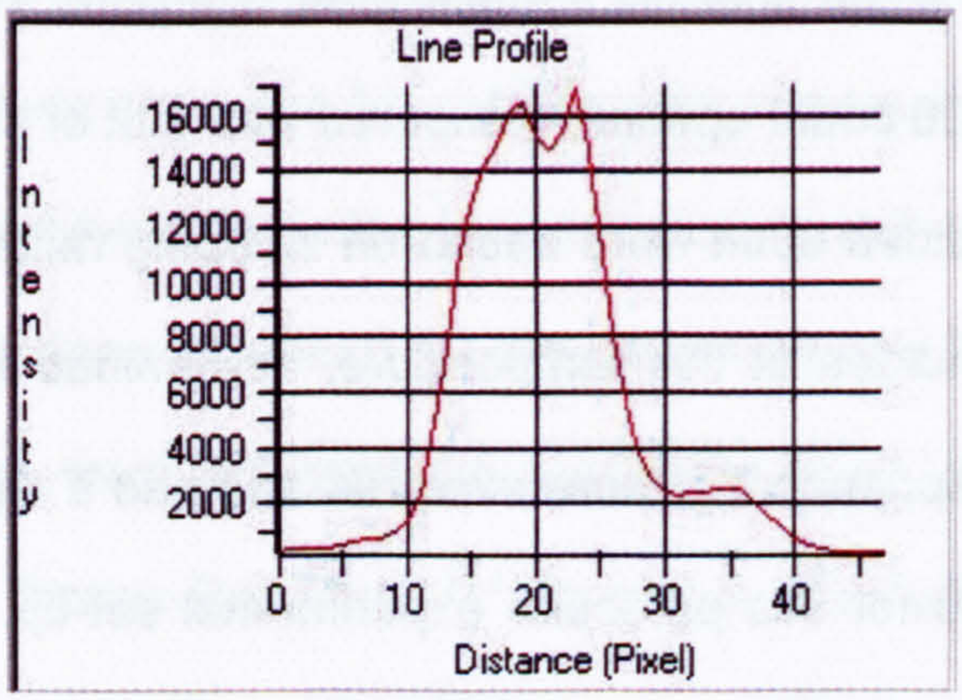

Figure B.3 Estimating the edge of the plasma

3.1.7 The next step in the 3D surface area estimation was to isolate the particular region being analysed in the plume image. This was done by cutting the image sections into two halves co-axially with the capillary. Image-Pro Plus V4 was then used to determine the vector co-ordinates

of the outer edge of each bisected section (i.e. where the depth reached 300 counts) and these co-ordinates were sent by direct data exchange (DDE) to Microsoft Excel. Figure B.4 shows an example of the results of this exercise performed upon a bisected whole plume.

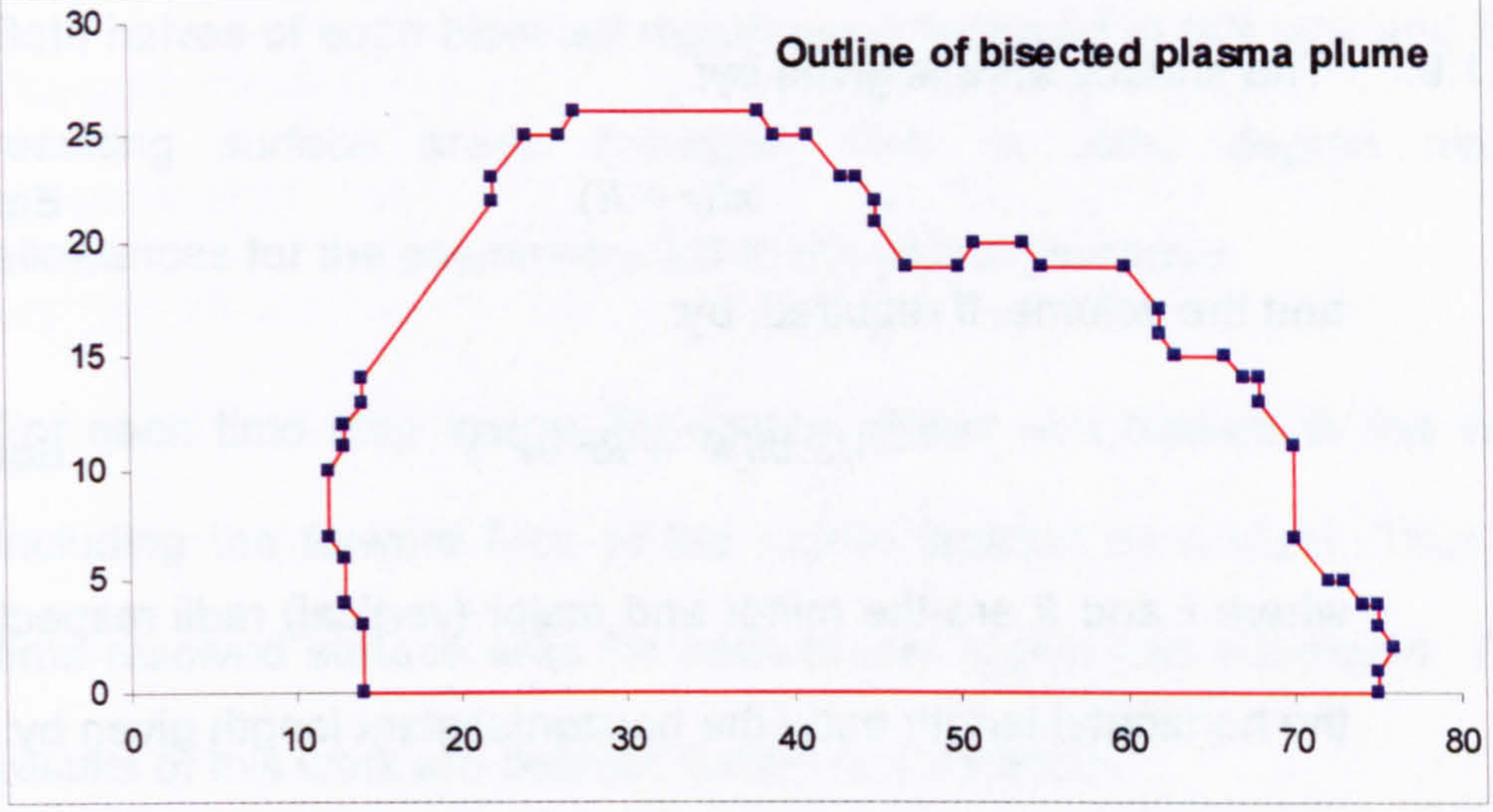

Figure B.4 Example of bisection of a plume image at 300 counts

3.1.8 The surface and volume of revolution performed in the Excel spreadsheet assumes the plume to be composed of many segments: each segment has the geometry of a frustum of a cone, as in Figure B.5, the minor and major (vertical) radii of which are given by the Y co-ordinates. The surface area (excluding the vertical faces) of each segment is calculated and the separate results summed to give the plume segment 3D surface area. This will be in pixels^2, but multiplication by the calibration factor, f^2 provides the area in SI units.

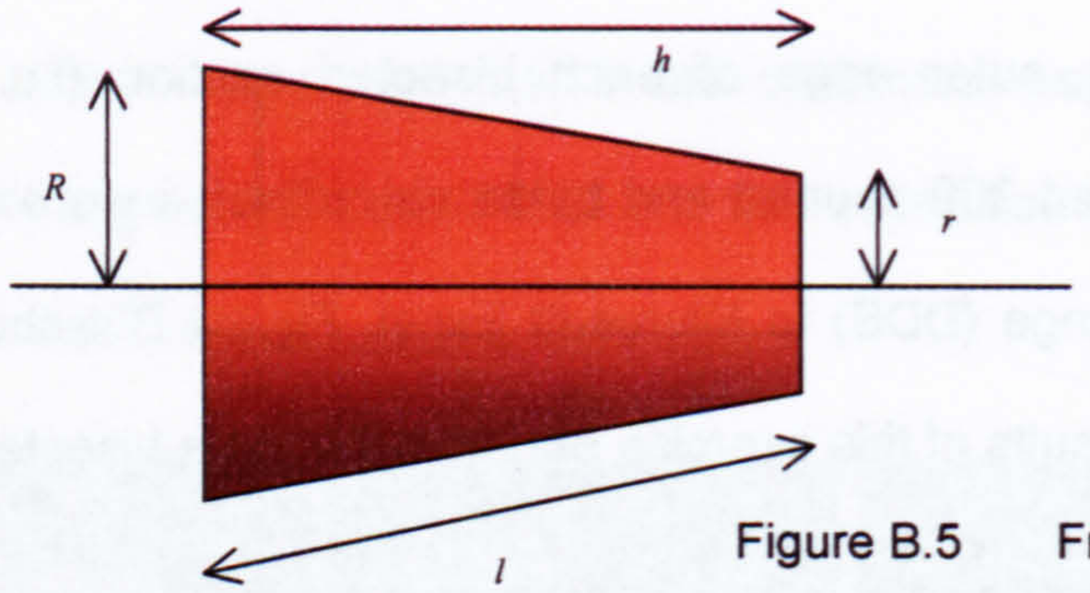

Figure B.5 Frustum of a cone

3.1.9 The surface area is given by:

$$\pi l(r+R) \qquad \textbf{Equation B.5}$$

and the volume, if required, by:

$$1/3\,\pi h(R^2+Rr+r^2) \qquad \textbf{Equation B.6}$$

where r and R are the minor and major (vertical) radii respectively, h is the horizontal length and l the horizontal slant length given by:

$$((R-r)^2+h^2)^{1/2} \qquad \textbf{Equation B.7}$$

3.1.10 Known geometrical shapes have been generated and analysed by the model and calculated by hand. There is agreement to within 0.5%.

3.1.11 Heavily lobed plumes will give large surface areas from cavities formed within the plasma geometry. In the context of radiating surfaces, it is debatable whether the inside surface area of a lobe cavity can be reasonably regarded as emitting: radiant energy may well be re-absorbed within the lobe. Inspection of each plume segment showed the occasional lobe cavity, which was manually removed from the DDE data, to effectively cover over the lobe cavity for the purposes of the surface area analysis. (The plasma generally becomes asymmetrical

and lobed only towards the end of the electrical discharge when the plume is radiating comparatively little power with respect to its early stages. Errors in the final estimation of radiant energy associated with lobe cavities will therefore be small.)

3.1.12 Both halves of each bisected region were analysed in this way and the resulting surface areas averaged. This to some degree made allowances for the asymmetry within the plume geometry.

3.1.13 For each time step image, the plume region was treated in this way including the forward face of the plume (treated as a disk). Thus, a time-resolved surface area for each plume region was estimated. The results of this work are detailed further in Chapter 5.

3.2 Calibration of Ultranac images for temperature measurement

3.2.1 Images recorded by the Ultranac camera have been calibrated for temperature measurement between 1000 K and 2000 K, based upon the arguments presented in Section 3.1.6 above. The Ultranac digital images are very sensitive to the temperature of a thermally radiating body through the Stefan-Boltzmann radiation law. The intensity (in counts) of the images increases with the fourth power of temperature of the radiating body. By recording images of a blackbody emitter at a known temperature and plotting the image intensity against temperature, a calibration factor can be found.

3.2.2 There is a method for determining the temperature of rectangular segments of electrically heated graphite, an approximate blackbody emitter. These segments are around 10 cm long, 4 cm wide and 0.3 cm thick. The spectrograph (Appendix A) is used to record the spectrum of the graphite, and this spectrum is then compared to that of a theoretical blackbody. Because the heated graphite radiation is a good greybody emitter (emissivity taken to be 0.8 for the spectrograph wavelength and temperature range), the temperature of the graphite can be obtained simply through the curve-fitting technique set out in Appendix A. The method is accurate to better than 5 K at temperatures greater than 1000 K.

3.2.3 The heated graphite sample, located at the position where the body temperature was to be recorded, was used to calibrate the Ultranac camera for temperature measurement. An image of the graphite was obtained, with the same experimental arrangement (camera location, exposure time and so on) as would be used to measure the plasma temperature. The spectrum of the graphite sample was also recorded at the same time. In this way, the Ultranac pixel intensity could be deduced as a function of temperature once the known emissivity of the graphite was allowed for. (This method can equally be applied to any type of camera.) The only other consideration is that the body being measured is a blackbody, or a grey body with a known emissivity. This can be determined by measuring the emitting body spectrum.

3.2.4 Figure B.6 demonstrates the results of the Ultranac temperature calibration. The blue markers are from a single piece of graphite, the temperature of which was raised by increasing the electrical current through it. However, being performed in air, the graphite sample eventually burnt away. The pink markers indicate results from a new piece of graphite. There is an obvious discrepancy in the results. One explanation is that the spectrograph was not central to one or other sample (thought, from the data spread, to be the new sample, the results from which were discarded). This will have the effect of measuring a lower temperature (the temperature of the sample being regular apart from near the edges and ends where it is lower). The error in the calibration is taken to be 2%, as the error in the blackbody curve-fitting was less than 30 K in 1500 K.

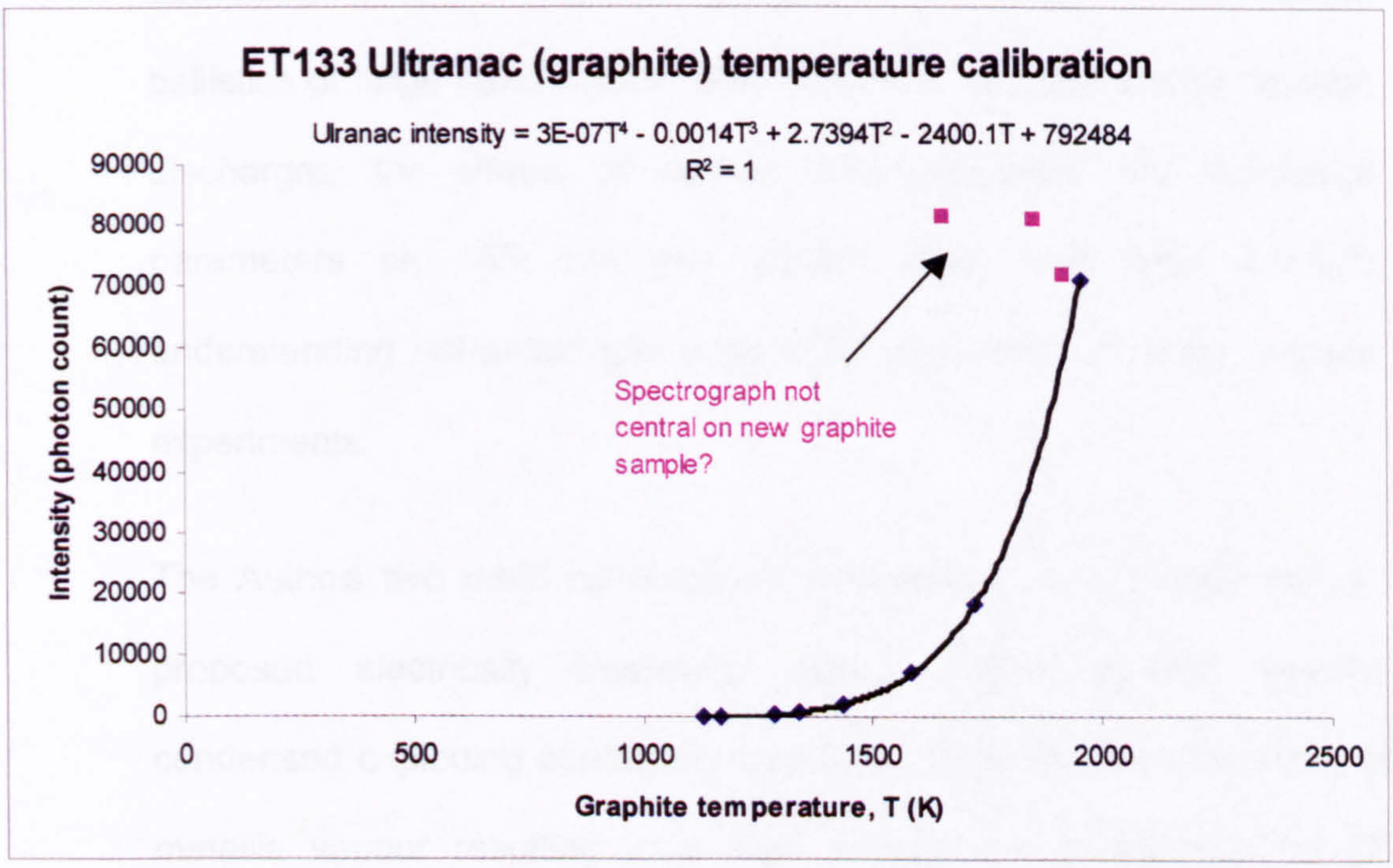

Figure B.6 Ultranac calibration curve

3.2.5 The maximum temperature that the Ultranac will measure without saturation is 1950 K under these conditions of exposure time and so forth. This method was used to estimate the temperature of the copper vapour cloud resulting from an ETC plasma discharge (Chapter 6).

---

1 Ultranac image converter camera Astromed/IMCO ICS 20 CCD image capture system

2 J. R. Taylor, "Introduction to Error Analysis: the Study of Uncertainties in Physical Measurements (2nd edition)", University Science Books, 1982

3 M. J. Taylor, "Volumes of revolution calculation - 1.xls", DERA internal design documentation held on files DERA/WS4/1/1/2/10/1/3 and DRA/WX6/7/7/7/4, August 1999

Summary and Further Work

This Thesis has covered the work conducted by the Author as well as others who aim to understand the mechanisms underpinning the operation of the electrothermal chemical gun. This has included the initial formation of plasma from electrically exploding wires, through to the development of plasma venting from the capillary and interacting with a densely packed energetic propellant bed.

The interaction processes leading to plasma ignition of the propellant have been studied, but much more work has been performed by the Author than is covered by this Thesis. Such work includes: the detrimental effects of high energy ignition discharges on the internal ballistics of large calibre guns; the benefits of reduced energy ignition discharges; the effects of various CPG properties and discharge parameters on 155 mm gun ignition delay and work towards understanding enhanced gas generation rates seen in small – scale experiments.

The Authors two main contributions discussed in this Thesis are: a proposed electrically insulating vapour barrier located around condensed exploding conductors and the hypothesis for deposition of metallic vapour resulting in a high energy flux to the surface of propellant, leading to propellant ignition. Although neither of these

concepts can be claimed as new to science, they are at least new in the application of gun propulsion systems.

The vapour barrier hypothesis was formulated to explain the experimentally observed phenomenon whereby electrical current bypasses (seemingly low resistance) condensed conducting material in favour of a path through (seemingly high resistance) plasma. It is important in a number of fields where the passage of current through condensed material or through surrounding plasma is significant. The importance may arise from the need to disrupt the condensed material by applying strong magnetic fields (as in the disruption of metallic shaped charge jets); in the requirement to generate a metallic vapour efficiently from electrically exploding wires (as per ETC ignition systems); or in the necessity to re-use the condensed material after a discharge (as with lightning divertor strips).

The hypothesis for the ignition of energetic materials by metallic vapour deposition relies on the transfer of latent heat during condensation. It is important for the efficient transfer of energy from an exploded wire (or other such metallic vapour generating device) to the surface of energetic material. This flux is obtained far more efficiently through condensation than from radiative energy transfer, because the energy required to evaporate copper, for instance, is 6 $\dot{k}J\ g^{-1}$. To heat it to temperatures at which an equivalent radiative flux would be emitted (around 11 000 K) requires a *further* 14 $kJ\ g^{-1}$. This hypothesis allows

optimised electrothermal ignition systems to be designed with lower energy requirements and thus a smaller weaponisation cost.

Work is still in progress to understand the plasma propellant interaction processes better both at ambient and at gun pressures, although little mention has been made in the Thesis of the work at elevated pressure due to length limitations. The main emphasis of this is currently in the field of enhanced gas generation rates measured for some propellant compositions. A new method for measuring the propellant surface regression velocity under dynamic closed vessel conditions and during ETC discharges is being devised by the Author. This requires the insertion of fibre optics into the charge, the length of which then reduces at the same rate as the propellant surface recedes. Measurement with the remaining unburned length of fibre allows the surface regression velocity and hence the propellant gas generation rates to be obtained. The current method relies on measurement of the chamber pressure and the use of internal ballistics models to calculate the gas generation rates. This method is open to errors if the heat transfer to the chamber walls is not well known, or uncertainties arise regarding the effective free volume of the chamber. Both these topics are pertinent to ETC plasma discharges at higher pressures.

Other instrumentation being worked on by the Author is a pressure transducer for use in a high electric field environment. This would be employed in recording the capillary pressure during actual gun firings,

where pressures of hundreds of megapascals prevent the insertion of conventional pressure transducers. A novel method, suggested by the Author, of inserting a Bragg grating into the rear electrode is under test. This device may have wider applications in other areas where environmental conditions preclude the use of traditional piezoelectric transducers.

Acknowledgements

I would like to acknowledge the many hours of useful discussions, aid with some of the calculations, help with experimentation and general toleration of myself by colleagues during the course of the work conducted for this Thesis. In particular, I should like to thank Graham Parry for the original inspiration to study at Ph.D. Level and Graham Smith for the departmental time permitted for me to write up the work. Also, I would like to acknowledge the help given on all aspects of technical issues by Mike Firth, Steve Gilbert, Clive Woodley, Pete Chapman, Ian Badger'Dewar, Steve Fuller, Grant Hainsworth, Clive Inglis, Roy Kidley, Brian Leggett, Gordon Thomson, Joe Roberts and Grant Savell.

Author's Publications (Not including internal DERA and QinetiQ reports)

M. A. Firth, C. R. Woodley, M. J. Taylor, S. R. Fuller and G. F. Savell, "The UK ETC Gun Programme for the Millennium", Proceedings of the European Forum on Ballistics of Projectiles 2000, Saint-Louise, France April 2000

*†M. J. Taylor, "Measurement of the Properties of Plasma from ETC Capillary Plasma Generators", IEEE Transactions on Magnetics, Vol. 37, 1, January 2001

M. J. Taylor and C. R. Woodley, "Variation in Enhanced Gas Generation Rates in Electrothermal-chemical Closed Vessel Studies", Proc. 19th International Symposium on Ballistics, pp 179 – 186, Interlaken, Switzerland, 7th – 11th May 2001

*M. J. Taylor, "Ignition of Propellant by Metallic Vapour Deposition for an ETC Gun System", Propellants, Explosives, Pyrotechnics, Vol. 26, pp 137–143, August 2001

*M. J. Taylor, "Formation of Plasma Around Wire Fragments Created by Electrically Exploded Copper Wire", J. Phys D: Appl. Phys. Vol. 35, 7, pp 700-709, 2002

*†M. J. Taylor, "Consideration of the Energy Transfer Mechanisms Involved in SPETC Ignition Systems", 11th Electromagnetic launch Symposium, St. Louis, France, 14th – 17th May 2002

*M. J. Taylor and J. Dunnett, "A Description of the Wire Explosion Process for ETC Plasma Generators", 11th Electromagnetic Launch Symposium, St. Louis, France, May 14th – 17th, 2002

†‡M. J. Taylor, "Energy Transfer Mechanisms Involved in Plasma Ignition of Solid Propellants", 20th International Symposium on Ballistics, Orlando, Florida, September 2002

*‡M. J. Taylor, "Spectral Acquisition and Calibration Techniques for the Measurement of Radiative Flux Incident upon Propellant", Submitted to Propellants, Explosives, Pyrotechnics July 2002

*‡M. J. Taylor, "Direct Measurement of Radiative Flux Incident upon Propellant during Plasma Propellant Interactions", Submitted to Propellants, Explosives, Pyrotechnics July 2002

*‡M. J. Taylor, "Evidence for the Hypothesis of Ignition of Propellants by Metallic Vapour Deposition", Submitted to Propellants, Explosives, Pyrotechnics July 2002

*Peer reviewed
†Oral presentation
‡ Forthcoming